CHALMERS

Proceedings of the 23rd European VLBI Group for Geodesy and Astrometry Working Meeting

May 2017
Gothenburg, Sweden

edited by R. Haas and G. Elgered

Proceedings of the 23rd European VLBI Group for Geodesy and Astrometry Working Meeting

edited by
Rüdiger Haas and Gunnar Elgered

Cover: The Onsala twin telescopes just before the inauguration on 18 May 2017.
(Photo Onsala Space Observatory)

May 2017, Gothenburg, Sweden

ISBN 978-91-88041-09-8

Preface

The 23rd Working Meeting of the European VLBI Group for Geodesy and Astrometry (EVGA), held at Chalmers University of Technology, initiated a week that was fully packed with VLBI activities in Gothenburg and at the Onsala Space Observatory.

The EVGA Working Meeting 2017 started with an ice breaker and registration on Sunday, 14 May, followed by the actual conference which was held on Monday and Tuesday, 15 and 16 May. Almost 100 participants from 20 countries (Fig. 1), both from inside and outside Europe (Appendix-A), contributed with many interesting presentations on the current status of geodetic and astrometric VLBI and corresponding technical development and scientific results. In total there were 52 oral talks and 34 posters. The corresponding articles of the majority of these presentations are collected in this proceedings book. The conference dinner on Tuesday evening closed the meeting.

However, it did not end here. The week continued with VLBI related activities. The 18th IVS Analysis Workshop and various IVS splinter meetings were held on Wednesday, 17 May, also at Chalmers. This also included a meeting on compatibility issues concerning the VGOS equipment worldwide, both the existing as well as that under development. A brief summary of this important meeting is included in Appendix-B.

Figure 1: Picture of the EVGA 2017 participants in front of the conference venue at Chalmers University of Technology (Photo: Joakim Strandberg).

On Thursday, May 18, the new VGOS-type Onsala twin telescopes were inaugurated. Details on this ceremonial event, including pictures and the speeches given, are included in Appendix-C.

This intense VLBI week was finally concluded by the 37th IVS Directing Board Meeting, held at Chalmers.

Coming back to the EVGA Working Meeting 2017, we want to thank all participants for sharing their findings with the audience during interesting oral and poster presentations. We want to thank the scientific organising committee for putting together a very interesting meeting program. The program and the list of participants are provided in Appendix-A. We are of course also grateful to all authors for preparing their proceedings contributions. The electronic version of these proceedings will be made available on the EVGA webpage `evga.org`.

The large number of participants at the EVGA 2017 Working Meeting, and the high quality and interesting oral and poster presentations are very good indications that European VLBI community is active and on a good track. This time the Onsala twin telescopes were inaugurated. The next EVGA Working Meeting in 2019 will most probably be connected to the inauguration of another new VGOS telescope in Europe. But before that, in the spring of 2018, we foresee the inauguration of the twin telescopes in Ny-Ålesund in connection to the next IVS General Meeting. I am thus convinced that we will see a strong contribution of the EVGA to VGOS!

Finally, I together with the organising committee want to thank the Chalmers University of Technology Foundation for their generous support provided for the inauguration of the Onsala twin telescopes, including the printing and distribution of this proceedings book.

November 2017
Rüdiger Haas (EVGA chair)

EVGA 2017 organising committees

Scientific Organising Committee (SOC)

- Rüdiger Haas (Chair), Chalmers tekniska högskola, Sweden
- Sabine Bachmann, Bundesamt für Kartographie und Geodäsie, Germany
- Alessandra Bertarini, Reichert GmbH / Bundesamt für Kartographie und Geodäsie, c/o Max Planck Institute for Radio Astronomy, Germany
- Johannes Böhm, Technische Universität Wien, Austria
- Evgeny Nosov, Institute of Applied Astronomy of the Russian Academy of Sciences, Russia
- Nataliya Zubko, Finnish Geospatial Research Institute, Finland

Local Organising Committee (LOC)

- Rüdiger Haas (Chair)
- Camilla Andersson
- Thomas Hobiger
- Niko Kareinen
- Grzegorz Kłopotek

Series of events during the EVGA2017

Date	Time	Event	Location
14 May	18:00-20:00	Icebreaker and registration	foyer Palmstedssalen
15 May	08:45-17:45	Oral presentations Day-1	Palmstedssalen
	17:45-20:45	Poster session	foyer Palmstedssalen
16 May	09:00-17:45	Oral presentations Day-2	Palmstedssalen
	19:00-23:00	Conference dinner	Wijkanders Restaurang
17 May	08:45-17:00	Various splinter meetings	HA4, EDIT 3364, EL42
18 May	10:45-15:45	Onsala Twin Telescopes inauguration	Onsala
19 May	09:00-18:00	IVS Directing Board Meeting #37	EDIT 3364

Contents

Technology Sessions

Observations Sessions

Analysis Sessions

Technological Developments for VGOS at IGN Yebes Observatory

J. A. López-Fernández, P. de Vicente, J. A. López-Pérez, F. Colomer, L. R. Santos

Abstract Most of the technological developments at Yebes Observatory are focused on the construction of the four VGOS radio telescopes that configure the RAEGE Network (Yebes, Canary Island, Santa MarÃa and Flores islands in Azores, Portugal). The areas covered by these developments are broadband receiver, low noise amplifiers, feed development, generation of phase cal tones, RFI monitoring and radio telescope performance optimization and control. Yebes activities also include the refurbishment and start operations of other radio telescopes which belong to other institutions like Ny-Ålesund TTW or BKG legacy receivers.

Keywords VGOS, RAEGE, RFI, LNA, OFC

1 RAEGE

The Spanish IGN, together with Portuguese colleagues in EMA (Azores, Portugal), continues the construction of a network of four new Fundamental Geodynamical and Space Stations. The RAEGE project was described previously (Gómez-González et al., 2015). The Spanish-Portuguese VGOS network RAEGE will cover three continental plates, with sites in Spain at Yebes (Eurasian Plate) and Tenerife (African Plate), and in Portugal on the Azorean islands of Santa Maria (Eurasian Plate) and Flores (North American Plate).

The radio telescopes, elevation-over azimuth turning-head 13.2 m diameter with a ring-focus optical design and fast moving capabilities, are identical at the four stations. They have been made by MT Mechatronics and currently three of them are already built.

Yebes RAEGE radio telescope is equipped with a broad band receiver (see next section) and is currently participating in VGOS trial sessions (VT) together with GGAO, Westford and Wettzell (MIT, 2017).

The radio telescope in Santa Maria (Azores) is complete, and first light has already being achieved with its triband receiver developped at Yebes laboratories, Fig. 1.

Fig. 1: Installation of the receiver at the Santa Maria RAEGE station.

José Antonio López-Fernández · Pablo de Vicente · José Antonio López-Pérez · Francisco Colomer
Instituto Geográfico Nacional, Observatorio de Yebes, Cerro de la Palera s/n, E-19141 Yebes, Spain

Francisco Colomer
Joint Institute for VLBI ERIC (JIVE), Oude Hoogeveensedijk 4, 7991PD Dwingeloo, the Netherlands

Luis R. Santos
EMA-Espaço, Estrutura de Missão dos Açores para o Espaço, Secretaria Regional do Mar, Ciência e Tecnologia, Rua do Mercado, n.21 9500-326 Ponta Delgada, Portugal

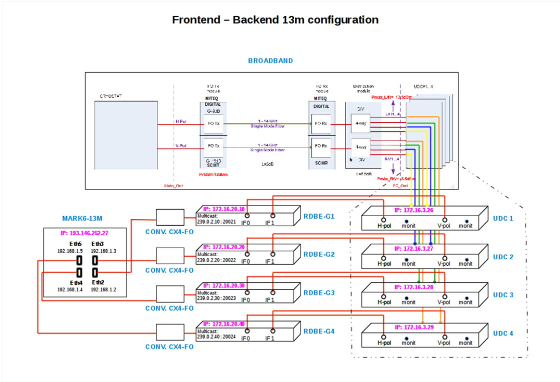

Fig. 2: Frontend-backend configuration.

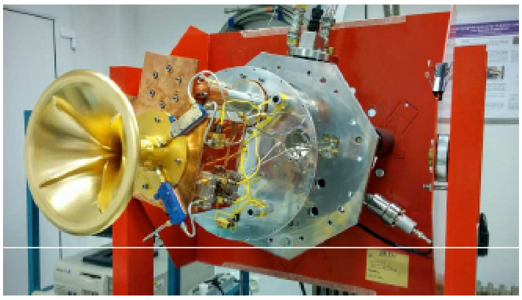

Fig. 3: Broadband VGOS receiver.

The infrastructure works for the RAEGE station in Gran Canaria (Spain) is now focused on getting the approval from the nature protection authorities. The construction of the radio telescope is foreseen for 2018 and we estimate to put in operation in Spring 2019.

Preliminary work in Flores (Azores) is being conducted to characterize the presence of radio frequency interference and the soil investigation. Currently the site has been selected and the operation of the radio telescope is estimated also in 2019.

2 Broadband receiver

The block diagram is shown in Fig. 2. The front-end consists of a dewar with a dual linear polarization quadruple-ridged flared horn (QRFH) feed, directional couplers for noisecal and phasecal injection and two ultra-low noise hybrid amplifiers developed at the Yebes laboratories. The cryostat, Fig. 3, is built over a Sumitomo SRDK-408S2 cold head in a cylindrical dewar made of stainless steel. The top and bottom covers are made of aluminum. In the top cover a vacuum window lets the broadband radiation go through. The receiver and its performance is described in Garcia et al. (2016) and de Vicente et al. (2016).

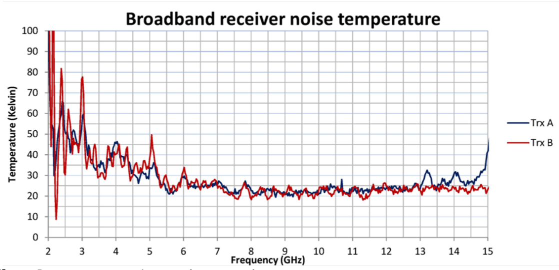

Fig. 4: Measured receiver noise temperature.

The bottom cover hosts all the RF connectors (signal outputs and calibration inputs), vacuum flanges, the pressure monitor, DC cabling, and housekeeping connectors. Inside the cryostat there is a cylindrical radiation shield made of aluminum and with multilayer isolation (MLI). The temperature of this stage is less than 40 K. Removing the radiation shield, the entire receiver can be easily reached. It is the coldest part of the receiver at a temperature < 10 K. The cold stage is made of copper. The RF output signals from the dewar are sent to RF over-fiber transmitters, allowing signal transportation through single-mode fiber up to the 40-m radio telescope back-end room (450 meters). In this place, the optical receivers are installed, together with an RF distribution module and four up/down converters. These converters are fed by the outputs of the distribution module. They allow the selection of four dual polarization sub-bands in the range 2 – 14 GHz and its conversion to base-band to feed the VLBI back-ends. NoiseCal and PhaseCal modules were developed too. The backend uses four RDBEs.

The measured receiver noise temperature is shown in Fig. 4. It can be seen that noise temperature values are distorted by large RFI at low frequencies. Due to these RFI signals, the optical fiber transmitter preamplifier had to be removed, to avoid saturation and intermodulation products. The actual Tsys value is estimated to be 43 K at 45 degrees elevation. The aperture efficiency has also been measured with values between 40 and 70 % all over the band, Fig. 5.

3 LNAs

Y214G series 1 are ultra-wide band, 2 – 14 GHz low noise cryogenic amplifiers designed and built at the Observatorio de Yebes for the development of a receiver for the VGOS next generation geodetic VLBI band. Amplifier Y214G 1012 has been modified to improve the output 1 dB compression point by using a GaAs commercial transistor in the third stage (López-Fernández et al., 2016).

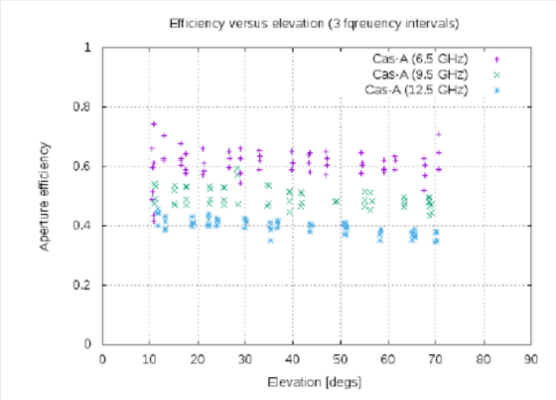

Fig. 5: Measured aperture efficiency.

Wideband cryogenic LNAs with quite good performance in the 2 – 14 GHz band have been demonstrated, but they usually present a high input reflection in the low frequency end. As cryogenic isolators for such a wide band are not feasible, the only possible alternative to obtain a good input match is to use a balanced configuration made up of two 3 dB 90Âº directional couplers (hybrids) and two LNAs.

We have designed and manufactured three different types of multioctave stripline 3 dB 90Âº hybrid couplers for the 2 – 14 GHz band. All of them are specially conceived to operate when cooled to 20 K. Its coupling and reflection characteristics show very little temperature dependence (Malo et al., 2016).

4 PhaseCal

Microwave Photonics is the field combining radio-frequency (RF) engineering and photonic technologies to realize unique applications in microwave photonic filtering, ultra-broadband coherent communications, and radio-frequency arbitrary waveform generation. Optical Frequency Combs (OFC) are photonic systems which offer outstanding phase-noise performance, leading to a revolution in optical synthesis and metrology.

We have developed a system (Carpintero et al., 2017) that, integrating different optical frequency comb structures based on mode locked ring-lasers, enables the characterization of the phase delay in the microwave cables connecting the feed of a radio-astronomy antenna receiver site to the instruments over the frequency band spanning from 2 GHz to 14 GHz. A first structure has been realized to achieve a wide optical frequency comb, improving the spectral flatness among the optical modes through the integration of a Mach-Zender interferometer within the laser structure.

A second structure that has been developed is a 30 mm long resonator cavity mode locked laser, generating a repetition rate as low as 2.7 GHz. Such device allows to generate an electrical comb within the range from 2.7 GHz to 20 GHz, with 2.7 GHz spacing. In order to obtain kHz spacing tones further improvement using pulse gating is needed, see Fig. 6.

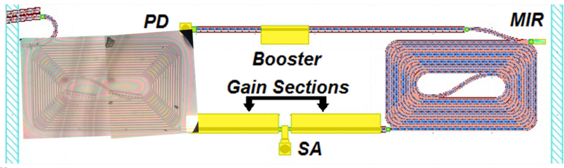

Fig. 6: Optical frequency comb generator.

5 Other activities

The existence of RFI can damage the amplifying stages of these ultra low noise receivers or drive them into saturation and, hence, generate intermodulation. These effects prevent the detection of cosmic radio signals and can even blind the receiver, making it useless. In June, the workshop “Detection and measurement of RFI in radio astronomy” will be held at Yebes Observatory. The purpose of this workshop is to join the efforts of scientists and engineers in the analysis of the impact of RFI, its detection and measurement and hardware and software solutions to minimize their effects. A tutorial will be given to show other stations how to use the portable RFI equipment available at Yebes Observatory. It will allow stations to carry out RFI measurements on their own with Yebes equipment, which can be borrowed at no cost other than transportation.

Yebes TDC has also carried out support activities to other stations like the implementation of the control system and installation of a triband receiver for Ny-Ålesund twin telescopes (Beltran et al., 2016) or the refurbishment of legacy S/X receiver for BKG AGGO station (Vaquero et al., 2016).

References

Gómez-González J, Santos L R, López-Fernández J A, Colomer F (2015) Status of Spanish-Portuguese RAEGE project. In: R. Haas and F. Colomer (eds.), *Proc. 22nd EVGA Working Meeting*, 55–58.

MIT Haystack Observatory (2017) MIT Haystack Observatory VGOS Network Analysis. 6 April 2017.

Garcia-Carreño P et al. (2016) Geodetic VLBI Ultra Low Noise Broad-band Receiver for 13 meter VGOS radiotelescopes. In: *Proc. 46th European Microwave Conference*.

de Vicente P, González J, Barbas L, Córdoba B (2016) Preliminary results from the 13.2 m Yebes antenna after the VGOS update. Technical Report IT-CDT 2016-5.

López-Fernández I et al. (2016) Y214G 1012 2–14 GHz cryogenic low noise amplifier report. Technical Report IT-CDT 2016-28.

Malo I et al. (2016) Cryogenic 3 dB 90^o stripline hybrid couplers for the $2--14$ GHz band: Design, manufacturing and measurement. Technical report, IT-CDT 2016-20.

Carpintero G et al. (2017) Towards monolithic integrated optical frequency combs for microwave signal generation. In: *ESA MTT Technology and Techniques workshop, Noordwijk*, The Netherlands.

Beltran F J, Barbas L, de Vicente P (2016) Ny-Ålesund 13.2 m control system: Installation and Basics. Technical report IT-CDT 2016-17.

Vaquero B, Serna J M, López-Fernández J A, Patino M, López-Pérez J A, Henche S (2016) Yague J M, Abad J A, Fernández J (2016) AGGO S/X Bands Cryogenic Receiver Upgrade. Technical report IT-CDT 2016-2.

Broadband VLBI System GALA-V and its Application for Geodesy and Frequency Transfer

M. Sekido, K. Takefuji, H. Ujihara, T. Kondo, M. Tsutsumi, Y. Miyauchi, E. Kawai, S. Hasegawa, Y. Koyama, Y. Hanado, J. Komuro, K. Terada, K. Namba, R. Takahashi, K. Okamoto, T. Aoki, T. Ikeda, K. Watabe, T. Suzuyama, R. Kawabata, M. Ishimoto, T. Wakasugi, M. Umei

Abstract We have developed a new broadband VLBI system, which includes broadband feed, data acquisition system, and data processing software to derive precise group delay observable. The system is intended to be compatible with the VGOS (VLBI Global Observing System) specifications. A newly developed broadband NINJA feed has been mounted at the Cassegrain focus of Kashima 34 m antenna, as well as at two small diameter VLBI antennas. The RF-Direct sampling (RDS) technique was introduced by using high speed sampler K6/GALAS(OCTAD-G). The RDS has great benefit not only simplification of the data acquisition system by eliminating analog frequency converter, but also increasing phase stability of the signal. This characteristic is essentially contributing to sub-pico second precision delay measurement achieved by wideband bandwidth synthesis. We conducted a series of broadband VLBI experiments between two small telescopes installed at NICT (Tokyo) and NMIJ (Tsukuba) for measurement of clock difference between UTC(NICT) and UTC(NMIJ). The results demonstrated that the broadband VLBI system enables pico-second precision observations even with small diameter radio telescopes.

Keywords Broadband Feed, RF-Direct Sampling

Mamuro Sekido · Kazuhiro Takefuji · Hideki Ujihara · Tetsuro Kondo · Masanori Tsutsumi · Yuka Miyauchi · Ejii Kawai · Shingo Hasegawa · Yasuhiro Koyama · Yuko Hanado · Junichi Komuro · Kenjiro Terada · Kunitaka Nanba · Rumi Takahashi · Tetsuro Aoki · Takatoshi Ikeda
National Institute of Information and Communications Technology, 4-2-1 Nukui-kita, Koganei, Tokyo, Japan

Kenichi Watabe · Tomoya Suzuyama
National Institute of Advanced Industrial Science and Technology/ National Metrology Institute of Japan, 1-1-1 Umezono, Chuou-3, Tsukuba, Ibaraki 305-8563, Japan

Ryoji Kawabata · Masayoshi Ishimoto · Takahiro Wakasugi · Miko Umei
Geospatial Authority of Japan, 1, Kitasato, Tsukuba 305-0811, Japan

1 Introduction of the GALA-V Project

The cConcept of broadband VLBI system for the next generation geodetic VLBI system has been discussed by the IVS working group (Niell et al., 2006). And it has been realized as the VGOS (VLBI Global Observing System). Stimulated by the VGOS concept, we have started the development of a broadband VLBI system named GALA-V for applications to perform accurate frequency comparison on long baselines.

We employed small diameter antennas (MARBLE1 and MARBLE2) as relocatable VLBI station. Standard signals generated by the atomic clocks to be compared are used for frequency standards at each small VLBI stations, and they are compared by observations. The disadvantage of the small collecting area of the antenna is compensated by two techniques.

One technique is to expand the observation bandwidth. The signal-to-noise ratio (SNR) is proportional to the square-root of the signal bandwidth, then increasing frequency width of signal channel from conventional 8 MHz to 1024 MHz gains $\sqrt{128} = 11$ times improvement.

The second technique is to joint VLBI observations with a larger diameter antenna, because the sensitivity of VLBI observation is proportional to the product of diameter of the antenna pair.

Fig. 1 depicts an image of the GALA-V project and 34 m and 2.4 m diameter antennas used in the project. Once the 'large-small' diameter antenna pair works as VLBI station, the delay observable on the 'small-small' diameter antenna pair can be computed by using the closure relation from two 'large-small' baseline data sets of the same epoch, where radio source structure effects are supposed to be compensated or small enough to be eliminated.

This report describes topics of GALA-V system development.

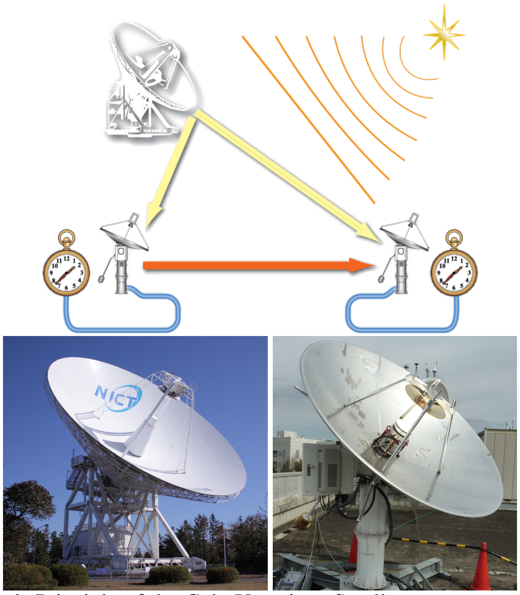

Fig. 1: Principle of the Gala-Y project. Small antennas are used as tool for geodesy by joint observation with a large diameter antenna. Kashima 34 m (left) and 2.4 m diameter Cassegrain antennas (right) are capable of super broad frequency (3-14 GHz) observation via new broadband NINJA feeds.

2 Broadband Feed and Signal Chain

New VGOS telescopes are starting up in many countries, and almost all of new VGOS stations employ either the Eleven Feed System (Yang, et al., 2011) or the Quadruple-Ridged Flared Horn (Akgiray, et al., 2013) for the receiver. Since these feeds have wide opening angle around 120 degrees, ring focus optics have been chosen for new telescopes being built. However, in our case, Kashima 34 m antenna's full viewing angle of subreflector from the focal point is fixed by geometry to be 34 degrees. Due to this reason, we have developed our own multi-mode feed named IGUNA-H (Ujihara, 2016) for 6.5-15 GHz frequency range as the first prototype. A second prototype NINJA feed for the 3.2-14 GHz frequency range has been used at Kashima 34 m and two small diameter telescopes in our project. A picture of the broadband feeds mounted at Kashima 34 m antenna is displayed in Fig. 2. For quick development and for cost restriction, room temperature LNA has been used, then modified system temperature (Tsys∗) is about 150-300 K for 3-14 GHz frequency range.

The received signal is transmitted to the observation room via a broadband optical signal transmission system. An amplitude slope of the signal over the frequency is inevitably caused by insertion loss of any microwave components, including frequency response of the A/D converter, though this causes a significant signal loss at higher frequency. Thus, the compensation of the amplitude slope by using a passive equalization device is important in the signal chain.

Fig. 2: Picture of the broadband feed system of the Kashima 34 m antenna with the NINJA feed on the left and the IGUANA-H feed on the right hand side.

3 RF-Direct Sampling and Phase Calibration with Radio Source

As it has already mentioned in the "Vision of VLBI2010" (Niell et al., 2006), RF-direct Sampling (RDS) technique has several advantages. Not only it enables simplified backend system, digitalization at early stage of signal chain brings benefit of stable phase relation of signal between channels. That is essentially important for precise group delay measurement. The block diagram of RDS and signal in frequency domain are illustrated in Fig. 3. The observed radio frequency signal is converted to digital data by using highspeed sampler K6/GALAS. The extraction of four channels of 1024 MHz width are made by FPGA digital signal processing implemented in the sampler. Frequency allocation within the input signal is selectable with 1 MHz resolution. The acquired data of each channel comes out by 2048 Msps in 1 bit or 2 bit quantized via

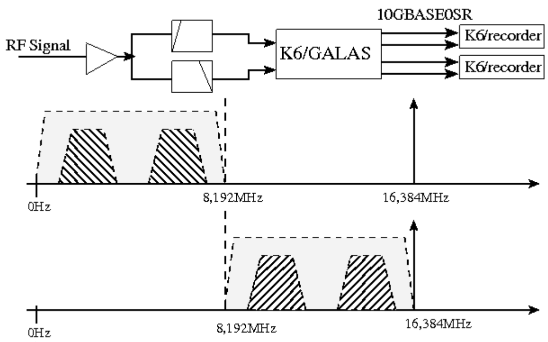

Fig. 3: Diagram of RF-Direct Sampling with 16 GHz sampler K6/GALAS. Two RF inputs (DC-8 GHz and 8-16 GHz) are digitized, and four channels with 1 GHz frequency width are extracted by digital BBC function inside the sampler.

VDIF/VTP/UDP data stream through 10GBASE-SR interfaces. We have been routinely using an off-the-shelf computer with 10GBASE-SR NIC and RAID disk system for recording of 8192 Mbps data stream.

Conventionally, phase calibration (Pcal) signals have been used to recover linear phase response of the entire VLBI observation system for precise group delay measurement. The target of phase correction via Pcal signal is an extra phase added at the stage of frequency conversion and a phase delay in the signal transmission path. It is unavoidable that the unknown initial phase of the local oscillator is inserted in the analog frequency conversion. In case of the RDS data acquisition, the phase relation between channels are frozen at digitization, and further filtering and frequency conversion are made by digital signal processing. Any cause of phase variation, such as small changes of signal transmission path length and changes of sampling timing, are limited . Therefore, conventional Pcal signal is less important in RDS data acquisition.

Even though the RDS technique is used, linear phase relation is not always preserved in the raw data, because the physical signal paths to two A/D converters and delay steps in the digital signal processing might be slightly different between channels. Hence, we introduce phase calibration by using natural radio source to recover linear phase relation. When cross correlating, the phase at frequency ω is given by $Cor(\omega) = A(\omega)\exp\{j\phi(\omega)\}$. The phase $\phi(\omega)$ includes several components as follows,

$$\begin{aligned}\phi(\omega) = \phi_{\text{geom}} + \Delta\phi_{\text{atm}} + \Delta\phi_{\omega,\text{ion}} + \Delta\phi_{\omega,\text{feed}} \\ + \Delta\phi_{\omega,\text{trans}} + \Delta\phi_{\omega,\text{DAS}} + \phi_{\omega,\text{src}},\end{aligned} \qquad (1)$$

where Δ means difference between two radio telescopes. The suffixes 'geom', 'atm', 'ion', ' feed', ' trans', ' DAS', and ' src' represent geometrical delay, neutral atmospheric propagation delay, ionospheric dispersive delay, frequency dependent feed characteristics, signal transmission path, data acquisition system, and radio source structure, respectively. Here we omit the source structure effect, since it is a subject to be discussed separately.

Let us suppose an ideal radio source which is located at identical celestial coordinates as a point source in all observing bands. We observe such a radio source as a reference scan with sufficient integration time to achieve good SNR. The correlation phase of the 'reference scan' $\phi(\omega)_{\text{ref}}$ is used for calibrate the phase of the ith scan $\phi(\omega)_{\text{i}}$, where the instrumental phases $\Delta\phi_{\text{feed}}$, $\Delta\phi_{\text{trans}}$, and $\Delta\phi_{\text{DAS}}$ are supposed to be constant over time. Consequently, the calibrated cross correlation phase contains differential ionospheric delay and constant group delay offset, i.e.

$$\begin{aligned}\Delta\phi_{\text{i}} &= \phi(\omega)_{\text{i}} - \phi(\omega)_{\text{ref}} \\ &= \phi_{\text{geom,i}} - \phi_{\text{geom,ref}} + \Delta\phi_{\text{atm,i}} - \Delta\phi_{\text{atm,ref}} \\ &\quad + \Delta\phi_{\omega,\text{ion,i}} - \Delta\phi_{\omega,\text{ion,ref}} \\ &= \phi_{\text{geom,i}} + \Delta\phi_{\omega,\text{atm,i}} - \frac{\Delta TEC_{\text{i}} - \Delta TEC_{\text{ref}}}{\omega} \\ &\quad + A \times \omega \quad .\end{aligned} \qquad (2)$$

The constant A corresponds to the group delay of geometry and neutral atmosphere of the reference scan. The dispersive differential ionospheric contribution can be separately estimated and excluded by the $1/\omega$ dependency of the correlation phase. Finally, all causes of non-linearity of the phase originating from instrumental effects and data acquisition are eliminated and linear phase characteristic is recovered for the broad frequency range. The only drawback is the inclusion of the group delay offset A, though it can be absorbed in the clock offset.

It has been reported that radio source structure effects become significant when the projected baseline length gets longer (e.g. Xu et al., 2016). This effect needs to be investigated and to be taken into account for intercontinental baselines.

4 Broadband Group Delay and Comparison with Conventional Multi-channel Delay

Linear phase response over frequency range 3–12 GHz can be realized, as described in the previous section. Based on this calibration technique, extremely precise group delays can be determined by coherently synthesizing broadband signals. This wide-band bandwidth synthesis software has been developed by Kondo and Takefuji (2016). Hereafter we call the group delay obtained by synthesizing broadband cross correlation data as 'broadband-delay'. Fig. 4 shows an example of broadband-delay obtained between Kashima 34 m and Ishioka 13 m radio telescope with frequency array of 3.2, 4.8, 8.8, and 11.6 GHz. Each point in the plot is a broadband-delay derived by one second integration. The data shows that the delay precision reaches to sub-picosecond level for one second of integration. Additionally, a random walk like delay change in the order of a few tens of picoseconds has been observed during hundreds seconds of timescale. The most probable cause of this delay behavior is the propagation delay due to inhomogeneous distribution of water vapor in the atmosphere.

As described in Section 1, delay observables between a 'small-small' antenna pair are derived by closure delay relation. In 2016, a series of broadband VLBI

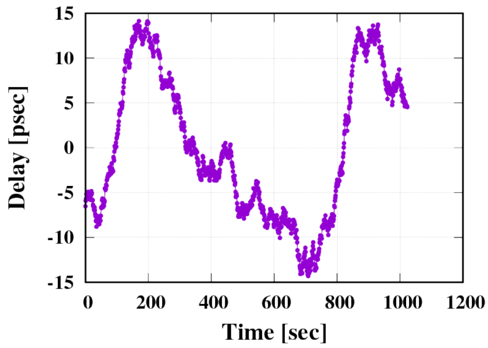

Fig. 4: Broadband delay observed on Kashima34 – Ishioka 13 m baseline, after removing a slow delay change caused by the geometrical delay. Each point is derived from broad bandwidth synthesis with 1 second integration. The delay measurement precision has been evaluated about 4.e-13 sec. at one second.

experiments were conducted 10 times with two small VLBI antennas and a 34 m antenna (O). The two small antennas were a 1.6 m diameter broadband antennas (MARBLE1:A) installed at the National Metrology Institute of Japan (NMIJ) in Tsukuba and a 2.4 m diameter broadband antenna (MARBLE2:B) installed at the headquarter of NICT in Tokyo. The frequency arrays of the GALA-V observations were not always the same for all of the ten sessions. The nominal frequency array of the GALA-V project is 3.5, 5.1, 9.9, and 13.1 GHz, which results in 3.8 GHz effective bandwidth (EBW). The minimum EBW is 1.78 GHz when frequency array was 5.9, 7.1, 8.7, and 10.6 GHz. Reference scans, which are used for correlation phase calibration, were included three times in every sessions with about 1200 s duration. These scans were used for the evaluation of the delay measurement precision. Time series of broadband-delays (τ_{OA}, τ_{OB}) have been derived with one second integration. Then, the delay observables of the 'small-small' baseline (τ_{AB}) were computed by linear combination of τ_{OA} and τ_{OB}. These broadband-delay data are plotted in Fig. 5.

For the comparison between broadband-delay and conventional multi-channel delay in X-band, observations in X-band with 2000 s duration were conducted with the 11 m diameter antenna pair of the Kashima – Koganei 100 km baseline. Roughly speaking, the 2.4 m and 34 m diameter antenna pair has an equivalent sensitivity of a $\sqrt{2.4 * 34} = 9$ m antenna pair. VLBI observations of 3C273B with Kashima 11 m – Koganei 11 m baseline were made on 10 April 2017 with the X-band frequency array 8210.99, 8220.99, 8250.99, 8310.99, 8420.99, 8500.99, 8550.99, and 8570.99 MHz with each 8 MHz bandwidth. The effective bandwidth of this array is about 133 MHz. To reach sufficient SNR, 9 s of integration time was chosen. The multi-channel delay after removing slow geometrical delay change is superimposed with open circle in Fig. 5. Since the typical rms residual of geodetic VLBI analysis of Kashima 11 m – Koganei 11 m baseline is around 30 ps, scattering of the multi-channel delay in this plot represents proper performance of the observation system.

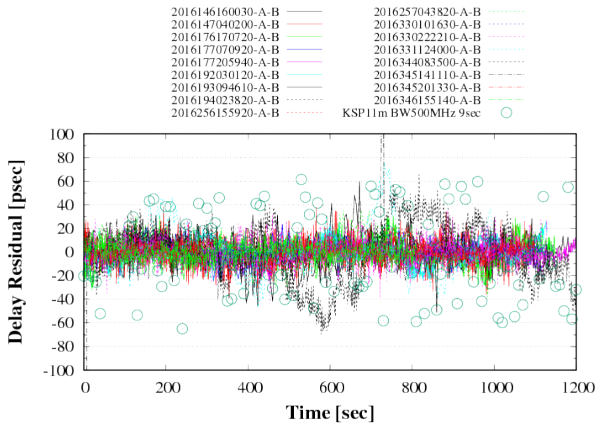

Fig. 5: Broadband-delay of MARBLE1–MARBLE2 baseline data observed in 2016 are plotted with lines of each color. Slow geometrical delay changes are removed from these data in advance. The numbers of the notations indicate time tag of the scans in yyyydddHHMMSS format. Broadband-delays were derived every one or 4 s intervals. Conventional multi-channel delays of Kashima 11 m – Koganei 11 m baseline were observed with 8 channels at X-band within 500 MHz width. These data are plotted by 9 s interval with open circles.

This plot tells us several findings:

1. Broadband delay has a significantly higher precision than conventional multi-channel delay with X-band.
2. Broadband-delay shows random walk like delay change with a few tens of pico seconds of amplitude within hundred seconds of timescale. Potential cause of delay changes would be
   a. change of electrical path from feed system to the sampler.
   b. drift of sampling timing
   c. excess delay change caused by signal propagation medium.

We suspect that the most probable cause of this will be (c), which is attributed to small scale inhomogeneity of the atmosphere. Contributions from the other error sources (a) and (b) should exist. However, 20 ps (=16 mm) amplitude change within a few hundreds of seconds is too large, thus these are unlikely to be the dominating error sources.

5 Conclusions

We have developed new broadband VLBI system, which includes broadband feed, data acquisition system, and data processing software to derive precise group delay observable. It was demonstrated that the broadband-delay observable has the potential to measure group delays with sub-picosecond precision. Even a small (1.6 - 2.4 m) diameter antenna pair can make precise group delay measurements by broadband observation and joint observation with large diameter antenna. The delay precision was superior to conventional multi-channel delay observations with an 11 m diameter antenna pair.

Acknowledgements

This research activities is supported by JGN research testbed network by 10 Gbps network link. The development of the broadband receiver was supported by a grant of the Joint Development Research of National Astronomical Observatory of Japan (NAOJ). The figures in this paper were generated by gnuplot and general mapping tools.

References

Akgiray A, Weinreb S, Imbriale W A, Beaudoin C (2013) Circular Quadruple-Ridged Flared Horn Achieving Near-Constant Beamwidth Over Multioctave Bandwidth: Design and Measurements. *IEEE Trans. Antennas Propag.*, 61(3), 1099–1108, doi:10.1109/TAP.2012.2229953.

Hobiger T, T. Kondo T, Koyama T (2007) MK3TOOLS & NetCDF - storing VLBI data in a machine independent array oriented data format. In: J. Böhm, A. Pany, H. Schuh (eds.) *Proc. of 18th EVGA Working Meeting*, 194–195, http://www.evga.org/files/2007EVGA-proc_Vienna.pdf.

Kondo T, Takefuji K (2016) An algorithm of wideband bandwidth synthesis for geodetic VLBI. *Radio Sci.*, 51, doi:10.1002/2016RS006070.

Niell A, Whitney A, Petrachenko B, Schlüter W, Vandenberg N, Hase H, Koyama Y, Ma C, Schuh H, Tuccari G (2006) VLBI2010: Current and Future Requirement for Geodetic VLBI System. In: D. Behrend, K. D. Baver (eds.) *IVS 2005 Annual Report*, NASA/TP-2006-214136, 13–40.

Petrachenko W T, Niell A E, Corey B E, Behrend D, Schuh H, Wresnik J (2010) VLBI2010: Next Generation VLBI System for Geodesy and Astrometry. In: S. Kenyon, M. C. Pacino, U. Marti (eds.) *Geodesy for Planet Earth, International Association of Geodesy Symposia 136*, Springer-Verlag Berlin Heidelberg, ISBN 978-3-642-20337-4, 999–1006.

Ujihara H (2016) Development of wideband feed for Kashima 34 m Antenna. *Radio Sci.*, 52, doi::10.1002/2016RS006071.

Xu M H, Heinkelmann R, Anderson J M, Mora-Diaz J, Schuh H, Wang G L (2016) The Source Structure of 0642+449 Detected from the CONT14 Observations. *AJ*, 152(5), 11, doi:10.3847/0004-6256/152/5/151.

Yang J, Pantaleev M, Kildal P-S, Klein B, Karandikar Y, Helldner L, Wadefalk N, Beaudoin C (2011) Cryogenic 2–13 GHz Eleven Feed for Reflector Antennas in Future Wideband Radio Telescopes. *IEEE Trans. Antennas Propag.*, 59(6), 1918–1934.

Sensitivity and Antenna Noise Temperature Analysis of the Feed System for the Onsala Twin Telescopes

J. Flygare, M. Pantaleev, B. Billade, M. Dahlgren, L. Helldner, R. Haas

Abstract The demand for higher precision measurements in Very Long Baseline Interferometry (VLBI) continues to grow, which drives the technical development of next generation international VLBI stations called the VLBI Global Observing System (VGOS). The VGOS design includes the idea of twin telescopes, i.e. two identical telescopes that will be used for continuous observations to study geodynamical processes. Such a twin telescope system has recently been installed at the Onsala Space Observatory, Sweden. The Onsala twin telescopes (OTT) are 13.2 m diameter, dual-reflector systems with a ring-focus sub-reflector. In this paper we present the estimated performance, focusing on the achievable system equivalent flux density ($SEFD$), sky noise modeling, and antenna noise temperature. We evaluate the system for two different cryogenic wideband quad-ridge flared horn (QRFH) feed setups operating over 3 – 18 GHz and 4.6 – 24 GHz. Analysis based on measured feed data shows a low antenna noise temperature and that SEFD of 1000 Jy can be achieved for the system. The result from Y-factor test shows T_{REC} = 10 K over most of the frequency band.

Keywords Very Long Baseline Interferometry (VLBI), VLBI Global Observing System (VGOS), Wideband, Feed, System Equivalent Flux Density (SEFD), Quad-Ridge Flared Horn (QRFH)

1 Introduction

The technique of Geodetic Very Long Baseline Interferometry (Geo-VLBI) is well established as a high precision technique to determine geodetic and geodynamic parameters. It is used extensively to give accurate time estimation and reference frames for the earths global coordinate systems. Since the first VLBI development in the 1970‘s and until now, the position accuracy has increased with a factor of 10^3. The VLBI Global Observing System (VGOS) is the latest step in the realization of this improvement with a goal of a position accuracy of 1 mm. As pointed out in Schönberger et al. (2015), the twin telescope concept is advantageous for several reasons, and due to the short distance between the identical telescopes the difference in atmospheric conditions should be minimal. In 2013 the first twin telescopes were installed at Wettzell Geodetic Observatory, Germany and currently the construction is ongoing for the Ny-Ålesund Geodetic Observatory in Svalbard, Norway. The Onsala twin telescopes (OTT) are the newest addition to the VGOS project, and can be seen in Fig. 1. The telescopes were inaugurated with great celebrations on the 18th of May, 2017.

Fig. 1: The Onsala twin telescopes, OTT-North on the left and OTT-South to the right.

In this paper we focus on the sensitivity performance of the OTT based on measured data. The Figure-of-Merit (FoM), the system equivalent flux

Jonas Flygare · Miroslav Pantaleev · Bhushan Billade · Magnus Dahlgren, Leif Helldner · Rüdiger Haas
Onsala Space Observatory, Department of Space, Earth and Environment, Chalmers University of Technology, SE-439 92 Onsala, Sweden
Email: jonas.flygare@chalmers.se

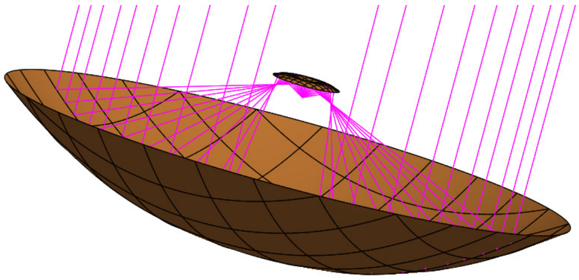

Fig. 2: OTT ring-focus geometry illustrated in GRASP.

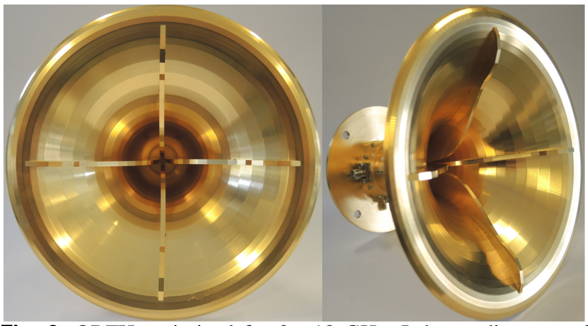

Fig. 3: QRFH optimized for 3 – 18 GHz. It has a diameter of 148 mm and a length of 102 mm.

density ($SEFD$), is specified to be below 2100 Jy for 3 – 18 GHz and elevations down to 30° above the horizon. In Eq. 1 it can be seen that for a given incoming flux density, S_{in}, the Signal-to-Noise Ratio (SNR) increases with a decreasing $SEFD$,

$$SNR = \frac{S_{\mathrm{in}}}{SEFD}\sqrt{t \cdot f_{\mathrm{BW}}}, \tag{1}$$

where t is the integration time and f_{BW} is the bandwidth. Therefore, minimizing $SEFD$ as much as possible translates to high sensitivity and shorter integration time for observations. $SEFD$ is proportional to the ratio of total system noise temperature, T_{sys}, over effective collecting area of the telescope, A_{eff}, according to Eq. 2,

$$SEFD = \frac{2k_{\mathrm{B}}T_{\mathrm{sys}}}{A_{\mathrm{eff}}}, \tag{2}$$

where k_{B} is the Boltzmann constant. The effective area of the telescope is defined as $A_{\mathrm{eff}} = \eta_{\mathrm{a}}A_{\mathrm{phy}}$ where η_{a} is the aperture efficiency and A_{phy} is the physical collecting area of the dish. Total system noise temperature is defined as $T_{\mathrm{sys}} = T_{\mathrm{A}} + T_{\mathrm{REC}}$, where T_{A} is the antenna noise temperature and T_{REC} is the receiver noise temperature including mismatches, feed ohmic losses and the noise temperature of the cryogenic Low-Noise Amplifiers (LNA). In Sec. 3 we discuss T_{A} more and the modeling of the sky noise temperature and spill-over calculation.

2 Telescope geometry

The OTT dish geometry is of ring-focus dual-reflector type with a D = 13.2 m and a half-subtended angle θ_0 = 65° and was designed and delivered by MT Mechatronics (MTM). A simplified picture of the ring-focus geometry is shown in Fig. 2 with a 1.5 m on-axis sub-reflector. This geometry results in a telescope focus close to the sub-reflector and not at the main-reflector apex, therefore no rays are reflecting from the center hole of the main-reflector. Rays from the main-reflector outer rim reflect into boresight of the feed and rays from close to the center hole reflect at the sub-reflector outer rim into the feed. This construction results in a higher aperture efficiency compared to common unshaped dual-reflector systems (Milligan, 2005). The subtended angle is suitable for linearly dual-polarized broadband feeds such as the quad-ridge flared horn (QRFH) (Akgiray et al., 2011) and the Eleven Feed (Yang et al., 2011). The ring-focus antenna geometry makes the system sensitive for horizontal radio frequency interference (RFI) due to the sub-reflector shape, and depending on the local situation a broadband feed with a strict cut-off above the lowest part of the S-band could be needed (Schüler et al., 2015), which is a inherent feature of the QRFH. Both the QRFH and the Eleven Feed are very well known technologies and have been studied thoroughly for the VGOS project. These feed concepts give near-constant beamwidth, ultra-wideband frequency performance and a compact footprint. The Eleven Feed has a constant phase center location and QRFH can be easily fed with one single-ended LNA per polarization. The receiver system and cryogenic dewar was designed so that it could house either of the feed concepts and be interchangeable.

3 Noise temperature modeling

To calculate the $SEFD$ we need to accurately estimate the antenna noise temperature, T_{A}. This was done using a complete system simulator, provided by Marianna Ivashina at the antenna group at Chalmers University of Technology (Ivashina et al., 2011). The software combines the feed beam patterns with the dish geometry and calculates the full beam pattern of the telescope through physical optics (PO) and physical theory of diffraction (PTD) in the GRASP software. Then, by integrating the noise temperature distribution, $T(\theta,\phi,f)$, of the sky (Fig. 5) and ground over all angles weighted with the beam pattern according to Eq. 3,

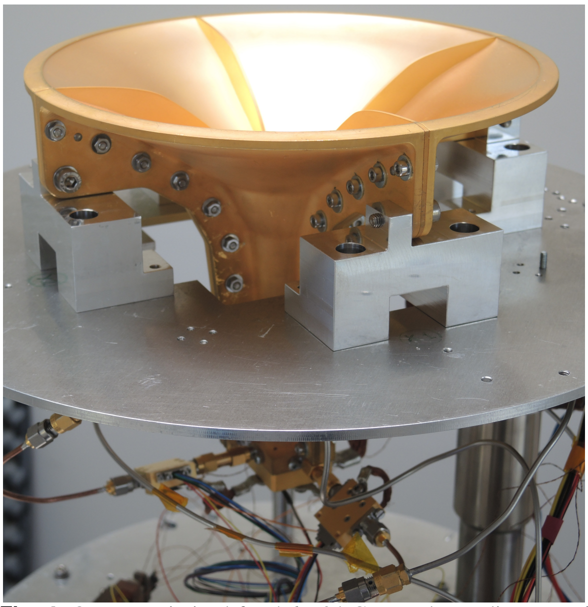

Fig. 4: QRFH optimized for 4.6 – 24 GHz. It has a diameter of 202 mm and a length of 182 mm. The feed is shown mounted inside the dewar for test with the LNAs visible at the bottom.

$$T_{\mathrm{A}} = \frac{\iint\limits_{4\pi} G(\theta,\phi,f) T(\theta,\phi,f) \sin\theta \,\mathrm{d}\theta \,\mathrm{d}\phi}{\iint\limits_{4\pi} G(\theta,\phi,f) \sin\theta \,\mathrm{d}\theta \,\mathrm{d}\phi} \tag{3}$$

we can estimate the antenna noise temperature T_{A}. In this calculation $G(\theta, \phi, f)$ is the beam pattern of the telescope, θ is elevation, ϕ azimuth and f is frequency. The significant contributions to the antenna noise are the sky-noise from the main beam and the spill-over terminated on the ground ($T_{\mathrm{g}} = 290$ K). The noise distribution for the full sphere surrounding the telescope is given according to Eq. 4,

$$T(\theta,\phi,f) = \begin{cases} T_{\mathrm{s}}(\theta,\phi,f) & 90^\circ \geq |\theta| > 0^\circ \\ T_{\mathrm{g}} & 0^\circ \geq |\theta| \geq -90^\circ \end{cases} \tag{4}$$

From the noise temperature calculations together with the aperture efficiency, we can accurately estimate the $SEFD$ of the complete telescope system. For clarification, a schematic over the system simulator process is shown in Fig. 6.

4 Feed system performance

In this section we show the performance of a 3 – 18 GHz QRFH, see Fig. 3, estimated on the OTT with measured feed beam patterns. The feed was optimized and

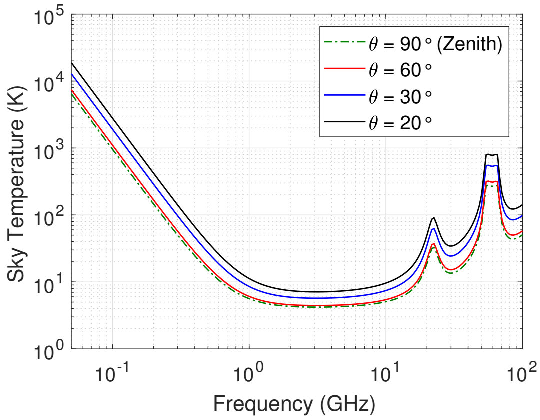

Fig. 5: Sky temperature over 0.2 – 100 GHz, four elevations.

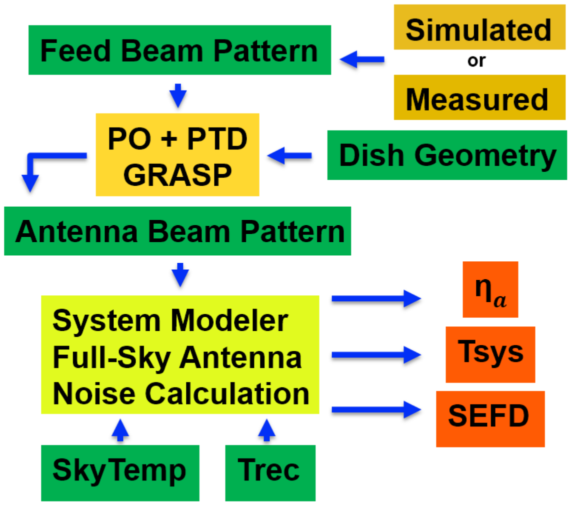

Fig. 6: Schematic of the steps in the system simulator illustrating the full calculation procedure.

delivered by the California Institute of Technology, Pasadena, CA, USA, for these frequencies. We also show the performance of a QRFH over 4.6 – 24 GHz, see Fig. 4, designed at Onsala and the antenna group at Chalmers for a different project (Dong et al., 2017) and how it could be a possible upgrade in the future for OTT. T_{REC} was measured at Onsala for both receiver systems using the standard Y-factor method with a hot (absorber) and cold (sky) load. The systems includes cryogenic low-noise amplifiers (LNA) supplied by the company Low Noise Factory (LNF) based in Gothenburg, Sweden. Antenna noise temperature was calculated using measured feed beam patterns in the system simulator described in Sec. 3.

Aperture efficiency for the 3 – 18 GHz QRFH (6 : 1 bandwidth) is above 50 % across the band with an average of 58 %, see Fig. 7. This is slightly below the expected 60 % and most likely depends on ridge misalignment in the feed during the assembly. The 4.6 – 24 GHz

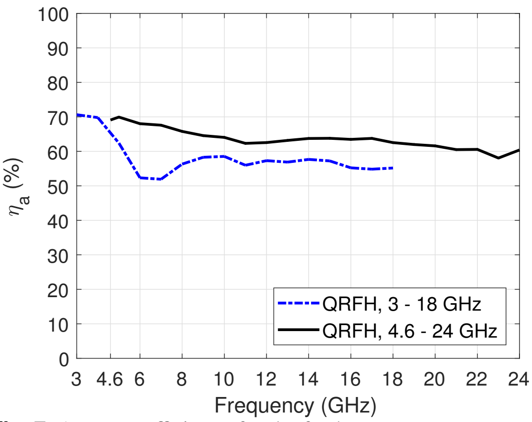

Fig. 7: Aperture efficiency for the feed systems.

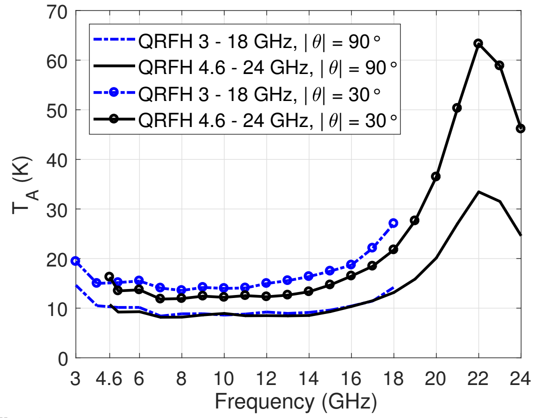

Fig. 8: T_A for the feed systems shown for two elevations.

QRFH (5.2 : 1 bandwidth) shows high and constant aperture efficiency above 60 % across almost the entire band with an average of 63 %.

Both feeds show similar performance in antenna noise, $T_A = 10$ K in zenith elevation, for the overlapping frequencies. The 4.6 – 24 GHz QRFH show slightly better performance due to higher spill-over efficiency, see Fig. 8. The difference in T_A between the feeds for lower elevation means that a bigger fraction of the side-lobes are terminated on the ground for the 3 – 18 GHz feed at this range of elevation. At the upper end of the frequency band in Fig. 8 we see an increase in sky-noise from the water-vapor line at 22.2 GHz which is an unavoidable feature of the surrounding sky temperature, see Fig. 5. The receiver noise of both systems is measured to excellent $T_{REC} = 10$ K over most of the frequency band, see Fig. 9. Total system noise temperature for each of the two systems, T_{sys}, are between 20 – 25 K over most of the bands for zenith elevation and 10 K higher for the lower elevation $|\theta| = 30°$. In both systems we add another 2 K to the total system noise accounting for back-end noise contribution. According to Eq. 2 this results in $SEFD = 1000$ Jy, clearly fulfilling the requirement of lower than 2100 Jy over the 3 – 18 GHz band, see Fig. 10. For the frequency range 21 – 24 GHz, $SEFD$ is degraded due to the very strong absorption in the water-vapor line and can not be expected to achieve the same performance as the rest of the band.

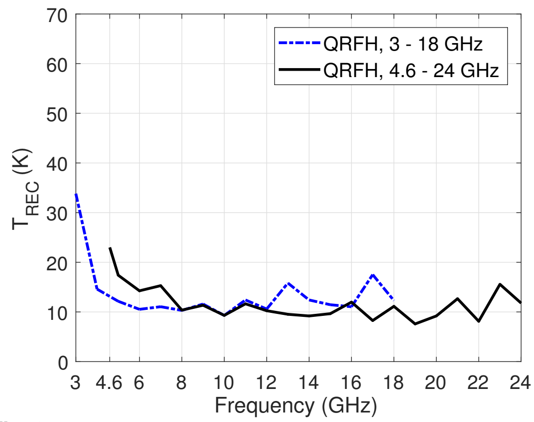

Fig. 9: T_{REC} for the feed systems.

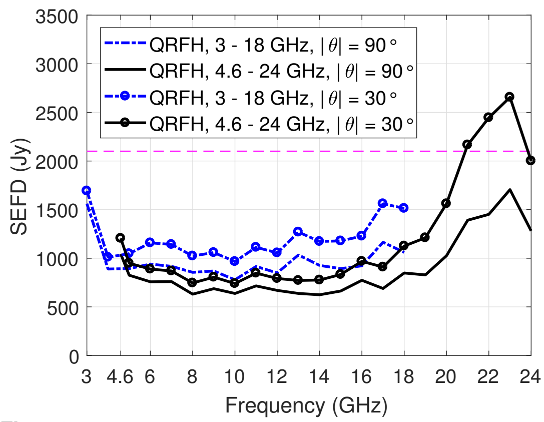

Fig. 10: $SEFD$ for the feed systems shown for two elevations. The dashed purple line shows the maximum allowed $SEFD$ over 3 – 18 GHz.

5 Conclusions

Through full system antenna noise analysis, the OTT feed systems show $SEFD = 1000$ Jy over most of the 3 – 18 GHz and all elevations. This is clearly fulfilling the specification of maximum 2100 Jy allowed. Both QRFH systems presented here show excellent $T_{REC} = 10$ K and should be considered as good candidates for operation. The OTT is indeed a high-end VGOS system that will contribute substantially to next generation of Geo-VLBI research.

Acknowledgement

The authors would like to thank Sander Weinreb at Caltech for providing us with the QRFH feed design for 3 – 18 GHz. We would like to thank Jian Yang from the Antenna Group at Chalmers University of Technology, Sweden and Bin Dong from National Astronomical Observatories, Chinese Academy of Sciences, China for the development and design of the 4.6 – 24 GHz QRFH and assisting with beam pattern measurements. We would also like to thank José Manuel Serna Puente, José Antonio López Fernández and Samuel López Ruiz at Observatorio de Yebes, Spain for beam pattern measurements. The authors would also like to thank Peter Forkman at Onsala for supplying an accurate sky model for the Y-factor measurements.

References

Akgiray A, Weinreb S, Imbriale W (2011) Design and measurements of dual-polarized wideband constant-beamwidth quadruple-ridged flared horn. *Proc. IEEE Antennas Propag. Soc. Int. Symp. (APSURSI2011)*, 1135–1138.

Dong B, Yang J, Dahlström J, Flygare J, Pantaleev M, Billade B (2017). Optimization and Realization of Quadruple-ridge Flared Horn with New Spline-defined Profiles as a High-efficiency Feed for Reflectors over 4.6–24 GHz. submitted to *IEEE Trans. Antennas. Propag.*

Ivashina M, Iupikov O, Maaskant R, van Cappellen W, Oosterloo T (2011) An optimal beamforming strategy for wide-field surveys with phased-array-fed reflector antennas. *IEEE Trans. Antennas. Propag.*, 59(6), 1864–1875.

Milligan T A (2005) Modern Antenna Design. 2nd Edition. *NJ, USA: Wiley-IEEE Press*.

Schönberger C, Gnilsen P, Böhm J, Haas R (2015) Twin Telescopes at Onsala and Wettzell and their contribution to the VGOS System. In: R. Haas, F. Colomer (eds.), *Proc. 22nd European VLBI Group for Geodesy and Astrometry Working Meeting*, 120–124.

Schüler T, Kronschnabl G, Plötz C, Neidhardt A, Bertarini A, Bernhart S, Nothnagel A (2015) Initial Results Obtained with the First TWIN VLBI Radio Telescope at the Geodetic Observatory Wettzell. *Sensors*, 15(8), 18767–18800.

Yang J, M. Pantaleev M, Kildal P-S, Klein B, Karandikar Y, Helldner L, Wadefalk N, Beaudoin C (2011) Cryogenic 2-13 GHz Eleven Feed for Reflector Antennas in Future Wideband Radio Telescopes. *IEEE Trans. Antennas. Propag.*, 59(6), 1918–1934.

Design, Implementation and Tests of the Signal Chain for the Twin Telescopes at Onsala Space Observatory

M. Pantaleev, L. Helldner, R. Haas, K.-Å. Johansson, L. Petterson, J. Dahlström, M. Dahlgren, U. Kylenfall, B. Billade, J. Flygare

Abstract We give an overview on the design, realisation and tests of the signal chain for the twin telescopes at Onsala Space Observatory. The choice of feed and frequency band was dictated by the requirement for keeping compatibility with the S-band system and existing reference frame established from the observations performed for decades with the OSO 20 m and in the same time creating system that will be flexible for adding new frequency bands above 14 GHz. We describe the design details and test results for the two developed systems: a cryogenic front-end with 3–18 GHz Quad-Ridged Feed Horn (QRFH), installed on the northern telescope and a cryogenic front-end with Eleven Feed for the 2–14 GHz range, installed on the southern telescope. We present the criteria and the selection process related to evaluation of key system components as for example the feed, LNA and RFoF link. We give also details on the design of the signal chain, including RF signal distribution to the back-end, noise and phase calibration and the system for monitoring and control of the RF chain.

Keywords VGOS, QRFH, Eleven Feed, RFoF, Signal Chain, RF Chain

1 Introduction

The Onsala Space Observatory (OSO) was involved in VLBI since the first experiments in 1968. The diverse advanced equipment acquired during the years as well as the longest time series in the VLBI database makes OSO to be an unique fundamental space geodetic site. In order to meet the new VGOS standards, activities for purchase of VGOS-compatible telescopes and equipment started as early as 2011. The contract for the delivery and installation of a twin pair of antennas was awarded to MT Mechatronics (MTM) (MTM, 2015) and the construction of the signal chain was decided to be accomplished by the Electronics Laboratory at OSO. A general overview on the Onsala twin telescope project is given in Elgered et al. (2017). Here we present the main activities related to the design and construction of the signal chain.

Miroslav Pantaleev · Leif Helldner · Rüdiger Haas · Karl-Åke Johansson · Lars Petterson · Jens Dahlström · Magnus Dahlgren · Ulf Kylenfall · Bhushan Billade · Jonas Flygare
Chalmers University of Technology, Department of Space, Earth and Environment, Onsala Space Observatory, SE-439 92 Onsala

2 System overview

The Onsala twin telescopes (OTT) are located approximately 800 meters from the 20 m antenna building which hosts the control room for the 20 m and the 25 m antennas as well as two H-masers. We were faced with a problem of how to decide on the transfer of frequency standard and RF signals and also to make decision for the location of the back-ends. Three possible placements for the back-end system were discussed: a) the towers of the telescopes, b) the 25 m antenna building (located 50 m from the OTT), and c) the 20 m antenna control room. After careful consideration of advantages and disadvantages for each of these alternatives we decided to place the back-ends in the 20 m antenna control room and transfer the time and frequency standards from the existing maser in the 20 m antenna building to the OTT. For the distribution of the RF as well as time and frequency standards we decided to use RF over Fiber (RFoF) links.

In the OTT project we define the signal chain as the system that captures the EM signal from the antenna reflector system and provides amplification, filtering subband division and transportation to the back-end, and also supplies noise and phase calibration signals. Part of the signal chain are also the components providing control and monitoring of the active elements and monitoring of the RF signals. Fig. 1 depicts a context diagram of the signal chain. The RF chain is a sub-system of the

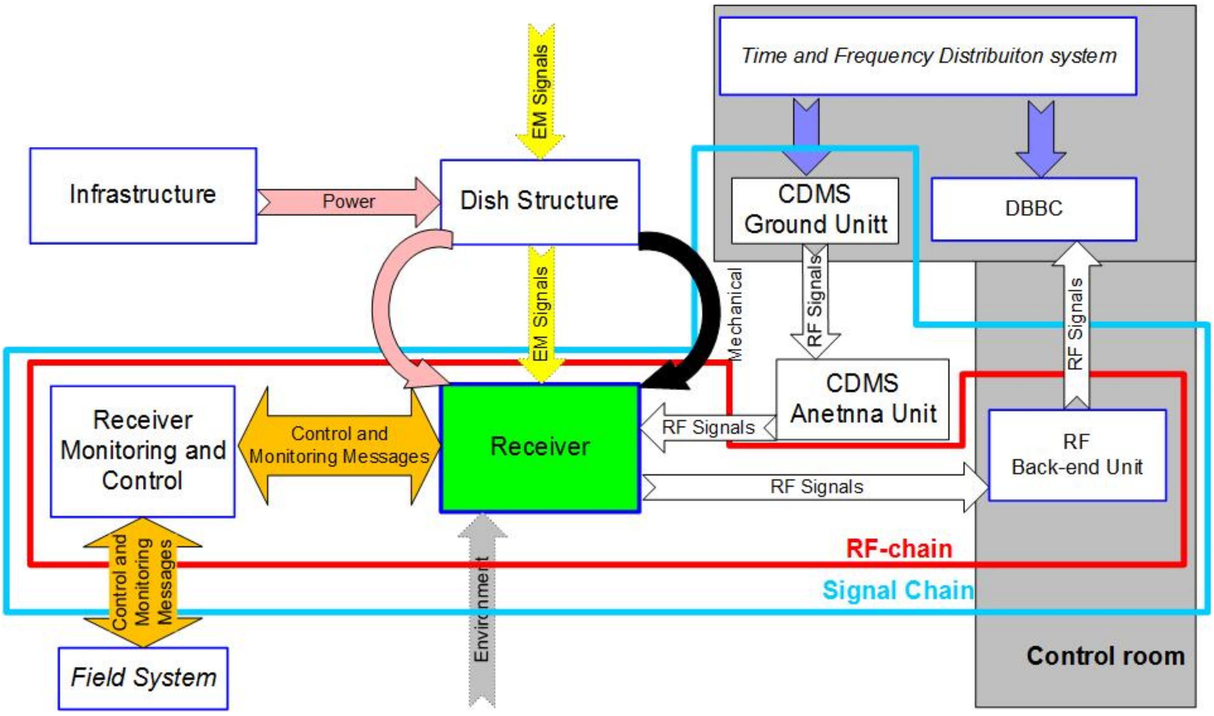

Fig. 1: Signal chain - context diagram.

signal chain that converts the EM signals received from the telescope and delivers them to the back-end. The RF chain consists of four functional units, interconnected in the following order: cryogenic receiver, RF front-end, RFoF link and RF back-end. The receiver that houses the feed and the cryogenic LNAs is located inside the elevation cabin and interfaces mechanically and optically to the antenna reflector. The RF signals are transported via RFoF link to the control room located in the 20 m antenna building. The RF Back-end unit provides amplification, filtering and sub-band division and supplies the signals to the Digital Base Band Converter (DBBC). The time and frequency distribution system uses reference signals from the H-maser which is also located at the 20 m antenna control building. 5 MHz and 1 pps are supplied to the DBBC and the ground unit of the Cable Delay Measurement System (CDMS) that is located in the same temperature-stabilised room as the H-maser.

The work on the signal chain started in 2015 with definition of the various sub-systems and selection of suppliers for the key components as for example feed, RFoF and CDMS. The detailed design of the cryostat, RF distribution and control system was carried out at the Electronics Laboratory at Onsala and was accomplished by the spring of 2016. The procurement, assembly and test of all locally designed sub-systems was finished and tested in the lab by the end of 2016. In January 2017 the first receiver was installed and tested on the north telescope followed by installation and tests with the second receiver on south telescope in April 2017.

3 Selection of feeds

The MTM antennas are equipped with axis-symmetric ring focus dual reflector systems. The diameter of the primary and secondary reflectors are 13.2 m and 1.55 m, respectively. This antenna geometry requires a feed with wide illumination angle. The feed selection was dictated by a few factors: frequency range, sensitivity and polarisation properties. After considering some input from the IVS working group and also taking in to account the local RFI situation at OSO, as well as the requirements for keeping compatibility with the S-band system and

Fig. 2: The interior of the two cryogenic receivers.

existing reference frame established from the observations performed for decades with the OSO 20 m telescope, we decided to have two different type of feeds covering different frequency bands for the OTT. It was decided that one of the telescopes will be equipped with 3–18 GHz Quad-Ridged Feed Horn (QRFH) (Akgiray et al., 2013) and the other one with an Eleven Feed for the 2–4 GHz range (Yang et al., 2011).

The purchase of the QRFH was agreed with Sander Winereb at California Institute of Technology (Caltech). A contractual agreement was set up between OSO and Caltech to scale up in frequency the existing 2–14 GHz QRFH design and optimize the performance to provide optimal efficiency for the 3–18 GHz for the MT Mechatronics ring focus reflector system. The optimisation was carried out using CST Microwave studio (CST, 2016). The goal was to obtain 60 % efficiency over 90 % of the 3–18 GHz frequency range at a fixed focus position of the feed. Two feeds were purchased with the provision that the cryostat with the Eleven feed could be upgraded with QRFH at a later stage. Details on the feed analysis are given in Flygare et al. (2017).

4 Construction of the cryogenic receivers

The cryogenic receiver is the first component of the signal chain. The function of the cryogenic receiver as part of the signal chain is to capture the signals from the antenna via the feed horn, couple phase and noise calibration, and provide low noise amplification. Therefore, the receiver integrates the broad band feed and the first stage amplifier at cryogenic temperature to provide ultimate sensitivity for receiving sky signals. The receiver design was driven by the requirements to allow exchange of different type of feeds. Pictures of the two cryostats are shown in Fig. 2. Special care in the cryostat design was taken in order to provide good mechanical references between the feed mechanical position and the interface to the antenna. This will secure that the phase centre of the feed will be well aligned with the focal point of the reflector system. For the support of the receiver we used glass-fiber pipes with openings on the side to access the cryostat interior and mount components. The feed is mounted on an aluminum plate bolted to the glas-fiber support and connected with flexible copper braids to the cold head to transfer the heat and at the same time to prevent transfer of mechanical vibrations from the cold head to the feed. The heat load due to infrared radiation is minimised using Multi-Layer Insulation based on aluminum foil wrapped around the heat shields. The optical interface of the feed towards the sub-reflector is provided by an infrared window that minimises the heat load towards the 20 K stage and a vacuum window providing the hermetical sealing. The infrared window is constructed from thin teflon sheets separated by plastic mesh. The vacuum window is a self-supported Mylar film clamped with O-ring. The mechanical design of the vacuum window and infrared window was made suitable for both Eleven feed and QRFH. The signal from the feed is fed first to a directional coupler for inserting noise calibration signal and then passed to the LNA. The first stage gain Low Noise Amplifiers (LNA) for the two receivers were purchased from Low Noise Factory (LNF, 2016).

5 RF front-end and back-end units

The RF front-end unit is the component following the cryogenic receiver. To avoid potential problems with the dynamic range of the RF oF link as well as to mitigate possible saturation of the amplifiers in the signal chain from strong RFI signals we decided to split the RF-band at the output of the receiver to two sub-bands and use two RFoF links for the Low and High sub-bands of each polarisation. Thus the function of the RF front-end unit is to provide additional amplification of the RF signal and also to divide the signal to two sub-bands.

The RFoF links were purchased from RF Optics (RF Optics, 2016). The installation of all fibers was made taking in to account very good thermal insulation. They are placed at least 0.8 m below the surface, where possible, and insulated with thick foam everywhere else. The fibre cable used is LS Cable LSGS-06-OC0190-02 G.652D single mode fiber. This cable type was selected because its excellent thermal coefficient of delay.

In the control room the optical signals are down-converted to RF. At the output of the optical receivers for the Low and High sub-bands we have installed filter bank for forming four IF channels that are passed to the DBBC. Several options for the filter banks were discussed. The goal was to design system that will provide full VGOS operations in the future and at the same time to be compatible the present Haystack-system to allow VLBI sessions as early as possible. At present time (end of 2016) Haystack is using 512 MHz bandwidth around center frequencies of 3.3, 5.5, 6.6, and 10.5 GHz. After discussion with Jim Lovell and Gino Tuccari (Lovell et al., 2016) we adopted the IF bands as listed in Table 1.

The OTT equipment located in the 20 m control room is shown in Fig. 3. The RFoF receivers supplies signals to the RF back-end unit which splits the RF to four sub-bands and feed them to the DBBC. There is additional functionalities providing the possibility to mon-

Table 1: Filter bands for four channels fed to the DBBC.

Band	Bandwidth (-20 dB) [GHz]	Pass-band [GHz]	LO [GHz]	IF [GHz]
1	1.8–4.1	2.0–3.8	–	2.0–3.8
2	3.7–7.7	3.8–7.6	7.7	0.1–3.9
3	7.5–11.5	7.6–11.4	7.5	0.1–3.9
4	11.3–15.3	11.4–15.2	11.3	0.1–3.9

itor the spectra of the RF signal as well to analyse the phase calibration signal for each of the four sub-bands.

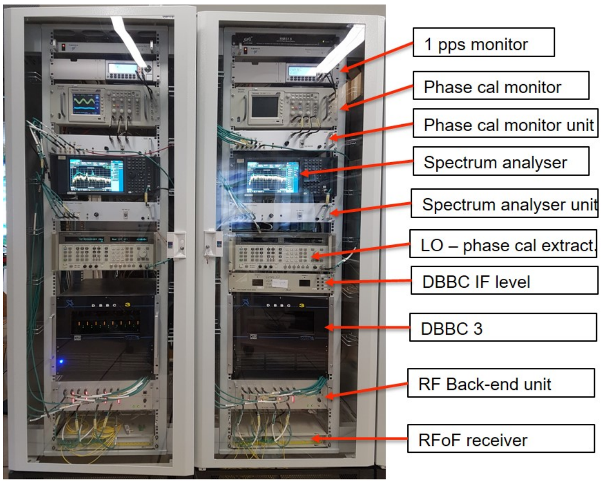

Fig. 3: The OTT equipment in the control room of the 20 m building. The left cabinet is for OTT-S, the right for OTT-N.

6 Phase and Cable delay measurement

As described in the previous section we decided to distribute the time and frequency normal over RFoF link from the H-maser at the 20 m to the two telescopes. The complexity of finding the best technical solution was additionally complicated because of the selection of strategy for integrating Cable Delay Measurement System (CDMS). We considered two alternative solutions for transferring the time and frequency normal: a) actively compensated link from Menlo Systems (model RFCD1500), and b) using the CDMS from MIT Haystack (CDMS, 2016). After some experiments and considering the project time line we decide to go for the CDMS with ground and RFoF transmitter both unit installed at the H-maser in the control room of the 20 m and RFoF receiver and antenna unit installed at the receiver in each of the antennas.

7 Test Results

The integration of the QRFH was accomplished in November 2016 and the equivalent receiver noise was tested using Y-factor method with the sky as cold load and absorber at ambient temperature as hot load. The testing was done at the newly build Y-factor measurement facility at the Electronics Laboratory at OSO. The results are shown in Fig. 4. The careful design of the cryostat opening that does not truncate the beam, the efficient cooling of the feed and especially the use of amplifier with very low equivalent noise temperature made possible to reach excellent receiver noise. As seen in the figure the equivalent receiver noise is in the order of 10 K for approximately the half of the receiver band. The rise in receiver noise at the low part of the band is due to mismatch between the feed impedance and the input impedance of the LNA. For the integration of the Eleven feed we decided to use passive feeding network in front of the LNAs thus decreasing the number of amplifiers from eight (four per polarisation) to two (one LNA per polarisation). Due to the usage of this feeding network the receiver noise of the receiver with the Eleven feed is higher than the QRFH.

In order to accurately estimate the overall system sensitivity, one needs to accurately estimate the spill over noise contribution after the reflector system. The estimation of the overall on-sky sensitivity of QRFH was done using a GRASP system simulator (Ivashina et al., 2011). The sensitivity for range of antenna elevation angles was performed with the system simulator using measured QRFH and Eleven feed data and using the receiver noise test results from Fig. 4 to estimate the equivalent system noise. Fig. 5 depicts the simulated system sensitivity for QRFH for zenith angle. The VGOS sensitivity specification is set in Petrachenko et al. (2009) as 2000 Jy over all elevation angles. Our analysis showed that the sensitivity of the QRFH receiver is well below the specification for the whole range of

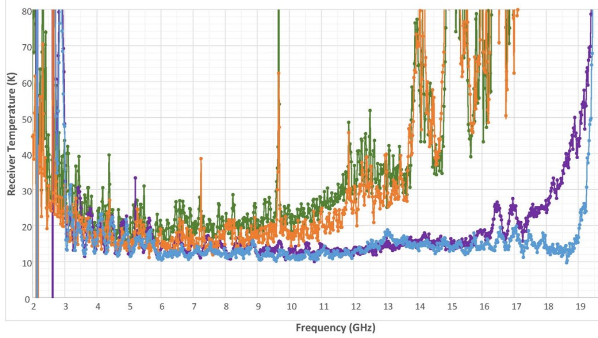

Fig. 4: Y-factor tests of the receivers with the Eleven feed (orange and green) and the QRFH (light and dark blue).

elevation angles. We did the same analysis of the sensitivity of the receiver with the Eleven feed and the results showed that the system will achieve SEFD below 2000 Jy. Details on the feed analysis are given in Flygare et al. (2017).

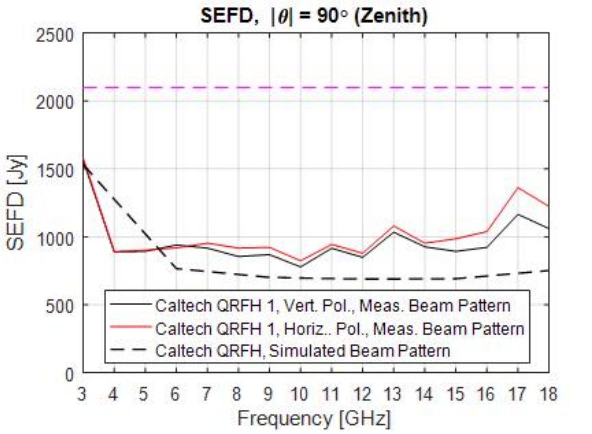

Fig. 5: Calculated SEFD using measured QRFH beam patterns and Y-factor test results.

8 Conclusions and Future Plans

We have successfully designed, built and tested signal chain for the OTT. Two receivers were constructed, one with QRFH and one with Eleven feed. The plan to bring the OTT in full network operation and participate in the CONT17 session in the autumn of 2017.

Acknowledgements

The Onsala twin telescopes project if funded from National Infrastructure programme of the Knut and Alice Wallenberg (KAW) Foundation. We acknowledge the support with the Beam Pattern Measurements from Jian Yang from the Antenna Group, Department of Signals and Systems at Chalmers University of Technology, and Bin Dong, guest researcher from JLRAT, China. We are thankful to Sander Weinreb and Ahmed Mohamed at Caltech Institute of Technology for the numerous discussions during their work on optimising the QRFH design for our antennas.

References

Akgiray A, Weinreb S, Imbriale W, Beaudoin C (2013) Circular quadruple-ridged flared horn achieving near-constant beamwidth over multioctave bandwidth: Design and measurements. *IEEE Trans. Antennas Propag.*, 61(3), 1099–1108.

CDMS (2016) http://www.haystack.mit.edu/workshop/ivtw2016/presentations/grajagopalan-ivtw20161.pdf

CST (2016) CST MICROWAVE STUDIO, http://www.cst.com/Content/ Products/MWS/Overview.aspx.

Elgered G, Haas R, Conway J, Hammargren R, Helldner L, Hobiger T, Pantaleev M, Wennerbäck L (2017) The Onsala twin telescopes: the status at the time for the inauguration. In: R. Haas, and G. Elgered (eds.), *Proc. 23rd EVGA Working Meeting*, 136–139.

Flygare J, Pantaleev M, Billade B, Dahlgren M, Helldner L, Haas R (2017) Sensitivity and antenna noise temperature analysis of the feed system for the Onsala twin telescopes. In: R. Haas, and G. Elgered (eds.), *Proc. 23rd EVGA Working Meeting*, 10–14.

Ivashina M, Iupikov O, Maaskant R, van Cappellen W, Oosterloo T (2011) An optimal beamforming strategy for wide-field surveys with phased-array-fed reflector antennas. *IEEE Transactions on Antennas and Propagation*, 59(6), 1864–1875.

Low Noise Factory (2016) http://www.lownoisefactory.com/

Lovell J, Tuccari G, Haas R (2016) Private communication.

MT-Mechatronics GmbH (2015) http://www.mt-mechatronics.com/

Petrachenko B, Niell A E, Behrend D, Corey B, Böhm J, Charlot P, Collioud A, Gipson J, Haas R, Hobiger T, Koyama Y, MacMillan D, Malkin Z, Nilsson T, Pany A, Tuccari G, Whitney A, Wresnik J (2009) Design Aspects of the VLBI2010 System. *Progress Report of the IVS VLBI2010 Committee*, ftp://202.127.29.33/pub/VLBI2010/V2C/PR\protect\discretionary{\char\hyphenchar\font}{}{}V2C_090417.pdf

RF Optics (2016) http://rfoptic.com/

Yang J, Pantaleev M, Kildal P-S, Klein B, Wadefalk N, Ivashinna M (2011) Cryogenic 2–13 GHz Eleven Feed for Reflector Antennas in Future Wideband Radio Telescopes. *IEEE Transactions on Antennas and Propagation*, 59(6), 1918–1934.

Improvement of PCAL Signal Distribution on RT-32 Radio Telescopes of ”Quasar” VLBI Network

E. Nosov, D. Marshalov

Abstract Using multi-tone phase calibration in VLBI observations can potentially give better results than the conventional single-tone technique. At the same time it increases the requirements to phase calibration (PCAL) signal quality. Distortions of PCAL signal can eliminate all benefits of multi-tone calibration up to making it completely unusable. To prevent this and to examine the condition of PCAL signals at "Quasar" VLBI network stations we performed a series of test measurements with RT-32 radio telescopes. The measurements included estimation of amplitudes and phases of all PCAL tones in all channels in standard S/X geo mode and their dependence on the antenna elevation. The results were used to perform troubleshooting on the stations which has already resulted in a significant improvement of PCAL signal quality which, in turn, is expected to lead to better calibration results, both single- and multi-tone. The paper presents brief report of the measurements taken and the results achieved.

Keywords VLBI, radio telescope, phase calibration, PCAL, Svetloe station

1 Introduction

Comparison of VLBI results received from CONT14 with single- and multi-tone calibration showed significant difference between them for Zelenchukskaya station. One of the possible reasons for that can be poor quality of PCAL signal on the station. A strong dependence of the calculated delay of PCAL signal in S-band and the antenna elevation has been registered, while the dependence in X-band is minor. To clarify this dependence we performed a series of measurements with RT-32 radio telescopes of ”Quasar” VLBI network (Finkelstein et al., 2004, 2008, 2009).

Evgeny Nosov · Dmitry Marshalov
Institute of Applied Astronomy of Russian Academy of Sciences, IAA RAS, Kutuzova nab. 10, Saint-Petersburg, Russia

2 Test conditions

During the measurements we moved the antennas in different ways, mostly up and down, to check the influence on PCAL amplitude, phase and delay. The signal chain equipment was set to standard S/X geo mode: 6 channels in S-band, 8 channels in X-band, all in upper sidebands, 8 MHz bandwidth, 10 kHz PCAL tones offset, 1-bit quantization, Mark5B recorder. A custom C-based utility was created to perform fast PCAL extraction from Mark5B records. It extracts PCAL signals of all channels in time domain with throughput of about 5 seconds of data per 1 second of computation (on regular PC). The extracted PCAL signals are then analyzed in frequency domain and both amplitude and phase of all tones in all channels are calculated for each second of data. As we are not interested in absolute values of the phases, only in their variation in time, we estimate all phases relatively to their initial values. Among other things it simplifies subsequent group delay estimation decreasing the influence of phase response non linearity. We estimated PCAL delay fluctuations in S- and X-band by fitting line to phase plot combined of all channels in a band. The declination of the line recalculated to units of time gives us estimation of PCAL delay.

3 Results of initial measurements

The initial measurements show unusual phase fluctuation of PCAL tones in S-band in Zelenchukskaya and Svetloe stations. Especially huge fluctuations were observed in Svetloe (Fig. 1). The corresponding PCAL delay fluctuations for S- and X-bands are presented in Fig. 2.

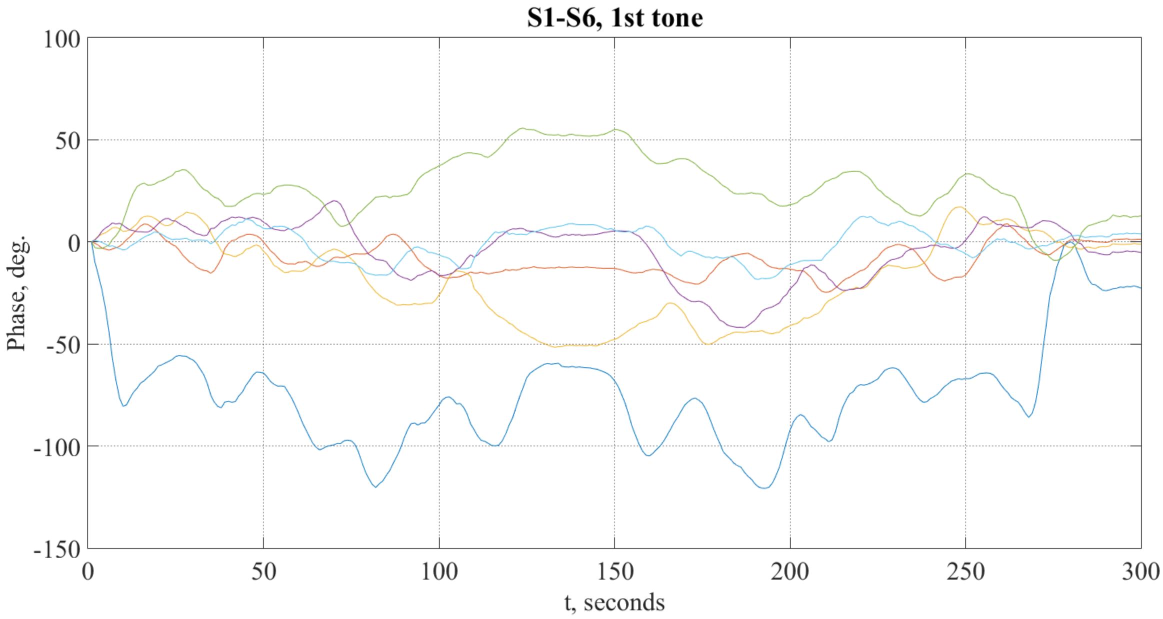

Fig. 1: Phase fluctuation of 1st PCAL tones in six S-band channels for Svetloe station before troubleshooting. The elevation angle was changed from 80 to 10 deg. (1-140 s) and back (140-280 s). Date of record: 28.11.2016.

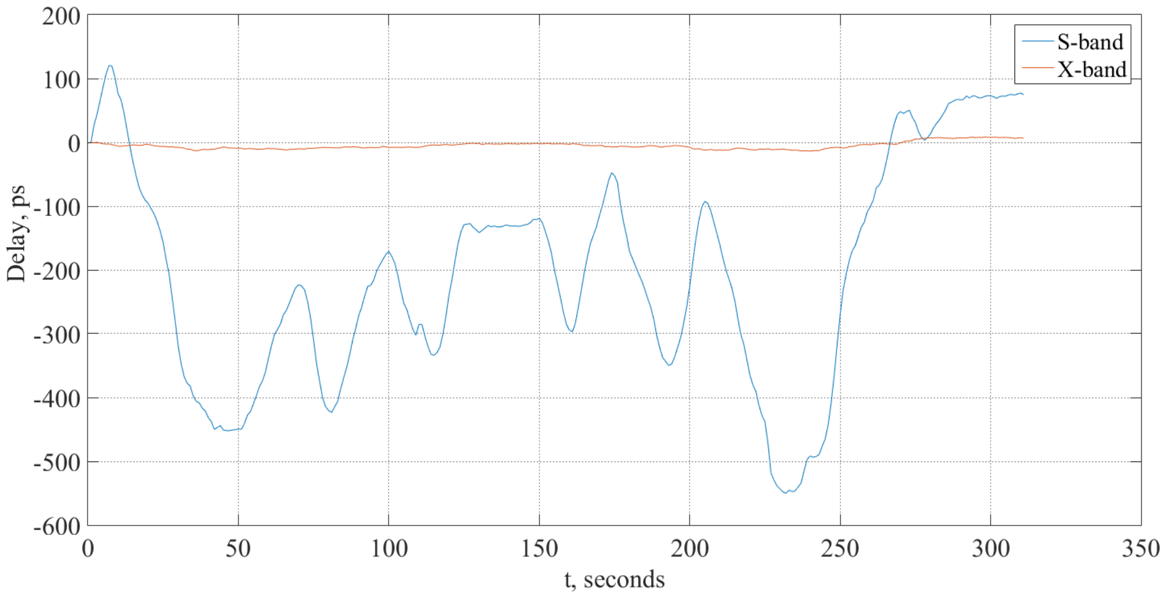

Fig. 2: PCAL delay fluctuations estimated in S- and X-bands for Svetloe station before troubleshooting. The elevation angle was changed from from 80 to 10 deg. (1-140 s) and back (140-280 s). Date of record: 28.11.2016.

One can see that there is a clear dependence of tones phases on antenna elevation. Phase of each PCAL tone varies in its own way, which is true even for neighboring tones in one channel (not shown on Fig. 1). The symmetry of the plot indicates that phase behavior is well reproduced when antenna goes up and down. This behavior could not be explained by fluctuation of LO phase because in that case all phases would fluctuate in the same way and it would not be seen in delay plot. It means that the problem is not directly caused by quality of reference clock or LO. As well, it could not be directly caused by group delay variation of signal chain because in that case all phases would fluctuate in the same direction. The observed delay variation of hundreds of picoseconds could hardly be explained by variation of physical delay in equipment or cables. It can be conclude from presented figures that using of PCAL for calibration in Svetloe was meaningless at that moment. One of the main assumption to explain observed behavior of PCAL was existence of delayed copy of PCAL in signal chain. It could be caused by parasitic propagation path and/or reflections in signal chain. The other possible explanation is the distortion of PCAL caused by influence of RFI in S-band that depends on antenna position and can result in saturation of some part of signal chain. Both reasons assume that each recorded tones of PCAL are sum of true tones and a few of parasitic tones with phase and amplitude dependent on antenna elevation.

4 Troubleshooting in Svetloe station

To find the problem we inspected the signal chain on RT-32 radio telescope in Svetloe station. We found strong parasitic way of PCAL injection through the feed. One of the main reasons for that was a fracture in PCAL injection cable for X-band that resulted in radiation of PCAL signal. Part of PCAL power got to the signal chain in a regular manner through the cable while another part of the power was injected through the air to the feed after a few reflections. As the cable was not properly fixed the amount of radiation and reflections could be changed with antenna elevation. Minor cause of radiation was using metric and imperial thread connectors together. The connectors look very similar and can fit to each other, but the connection shielding is not enough for strong and short PCAL pulses. To decrease the radiation of PCAL we made new cables with high EMI shielding and appropriate connectors. Also we moved attenuators in PCAL line from the far end to the PCAL generator output which decreased the radiation even more. Some other fixes were also performed. After that we repeated the measurements moving the antenna up and down. The resulting PCAL delay fluctuations are presented on Fig. 3. One can see that the fluctuations are reduced from a few hundred of picoseconds to about 20 picoseconds peak-to-peak. Furthermore, the delays in S- and X-bands look very similar now. The residual fluctuations most probably are related to cable delay in cable loop of the antenna.

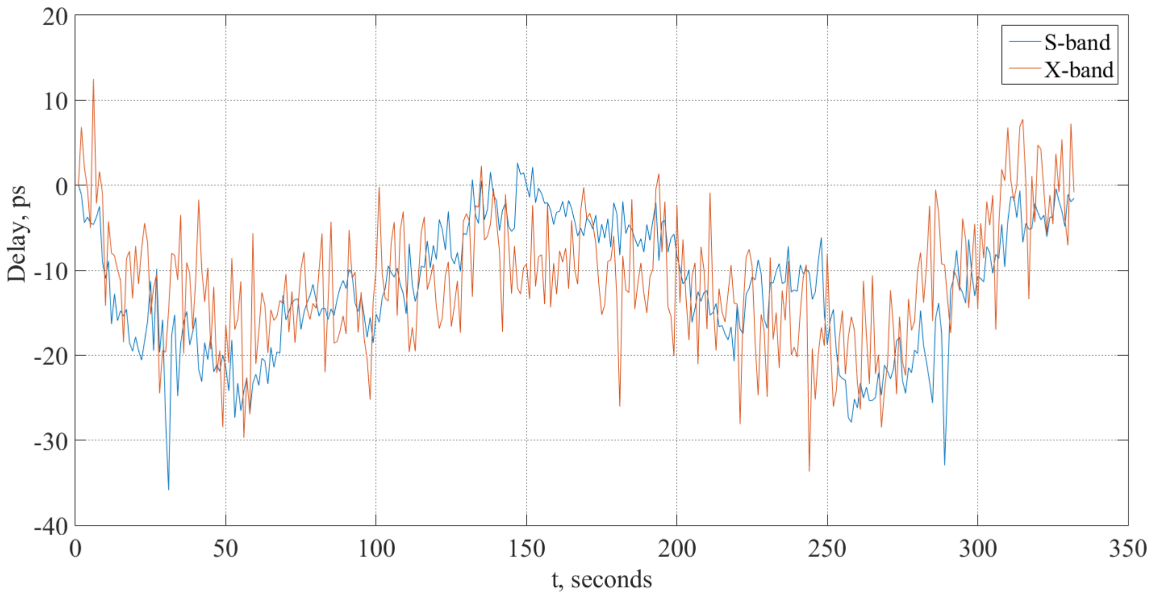

Fig. 3: PCAL delay fluctuations estimated in S- and X-bands for Svetloe station after troubleshooting. The elevation angle was changed from 10 to 80 deg. (1-160 s) and back (160-320 s). Date of record: 11.05.2017.

It can be both the delay of reference clock of PCAL generator and the delay in IF cables.

5 Conclusions

- The troubleshooting performed at Svetloe station has allowed to decrease observable PCAL delay fluctuations over antenna elevation from a few hundred of picosecond to about 20 picosecond peak-to-peak.
- PCAL and clock distribution system for radio telescopes of ”Quasar” VLBI-network will be reviewed during coming modernization of signal chain with new wideband digital backend.
- Precise cable delay measurement system is required to separate delay variations in signal chain from variations of reference clock. It is extremely important if the VLBI-formatter is located on the antenna.
- Periodical checks of PCAL quality during antenna movements help to control and prevent degradation of signal chain and clock distribution system.
- A few obvious lessons should be learned by station engineers:

1. PCAL signal is a strong source of radio interference. A good shielding and impedance matching is necessary to reduce parasitic propagation ways.
2. The best place to locate attenuator (if required) is near or inside the PCAL generator. It helps to reduce radiation.
3. All cables should be tightly fixed to improve stability and prevent its degradation and dependence on antenna elevation. Reliable connector sealing should also be ensured.

References

Finkelstein A, Ipatov A, Smolentsev S (2004) Radio Astronomy Observatories Svetloe, Zelenchukskaya and Badary of VLBI Network "Quasar". In: R. Vandenberg and K. D. Baver (eds.), *IVS 2004 General Meeting Proc.*, 161–165, NASA/CP-2004-212255.

Finkelstein A, Ipatov A, Smolentsev S (2008) The Network "Quasar": 2008–2011. In: A. Finkelstein and D.Behrend (eds.), *IVS 2008 General Meeting Proc.: "Measuring the future"*, 39–46, St. Petersburg, "Nauka".

Finkelstein A, Salnikov A, Ipatov A, Kaidanovsky M, Bezrukov I, Mikhailov A, Surkis I, Skurikhina E (2009) E-VLBI Technology in VLBI Network "Quasar". In: *8th International e-VLBI Workshop Proc.*, PoS(EXPReS09) 098, 2009.

VLBI-DORIS Interference Investigation at Wettzell

T. Klügel, T. Schüler, A. Phogat, S. Mähler, C. Plötz, G. Kronschnabl, A. Bertarini, A. Neidhardt, J. Saunier, F. Didelot, J.-M. Walter

Abstract The Geodetic Observatory Wettzell (GOW) is a Fundamentalstation of Geodesy where all important systems of the space geodetic techniques are collocated within a distance of less than 250 meters. Detailed investigations aiming at the integration of a DORIS beacon where conducted in 2015 and 2016 yielding a permanent installation of that system at Wettzell. Since DORIS transmits signals at 2.04 GHz with a power comparable to smartphones, care has to be exercised not to harm the sensitive receiving systems of the three VLBI telescopes at Wettzell. All of them have feeds ranging down to S-band frequencies. We describe the VLBI-DORIS interference investigations carried out. These comprise field measurements of signal power and attenuation as well as the conduct of real VLBI experiments with the DORIS beacon being switched on. In conclusion, the permanent installation of a DORIS system at GO Wettzell is possible as long as certain conditions are met. Mainly, a suitable location is necessary which is a compromise regarding DORIS visibility and DORIS signal attenuation in direction to the radio telescopes in order to avoid interference on the VLBI antennas. Such a location acting as a natural barrier between the beacon and the telescopes is available at Wettzell.

Thomas Klügel · Torben Schüler · Apurva Phogat · Swetlana Mähler · Christian Plötz · , Gerhard Kronschnabl
Geodetic Observatory Wettzell, Federal Agency for Cartography and Geodesy (BKG), Sackenrieder Str. 25, DE-93444 Bad Kötzting, Germany

Alessandra Bertarini
Rheinische Friedrich-Wilhelms Universität Bonn, IGG, Nußallee 17, DE-53115 Bonn, Germany

Alexander Neidhardt
Geodetic Observatory Wettzell, Technische Universität München, Sackenrieder Str. 25, DE-93444 Bad Kötzting, Germany

Jerôme Saunier
Institut national de l'information géographique et forestière (IGN), Saint-Mandé, France
François Didelot, Jean-Marc Walter
Centre national d'études spatiales (CNES), Toulouse, France

Keywords DORIS, VLBI-DORIS interoperability, Geodetic Observatory Wettzell, GGOS

1 Introduction

Geodetic fundamental stations play an important role for the realisation of the Global Geodetic Observing System (GGOS). All space geodetic techniques are collocated within a distance of less than 500 meters at these core sites. Fortunately, VLBI telescopes, laser ranging systems and GNSS receivers do not interfere with each other. Unfortunately, the simultaneous operation of VLBI and DORIS at one site may generate problems with electromagnetic compatibility (EMC).

Beaudoin et al. (2012) investigated the RF compatibility of VLBI with DORIS at Goddard Space Flight Center (GSFC) by means of numerical modelling and field experiments. He suggests the use of radio-frequency (RF) blockers close to the DORIS antenna to attenuate the signal appropriately. Il'in at al. (2010) state that standard VLBI observations are not affected by DORIS. Their investigations are based on measurements at the receiver output at the legacy Badary VLBI station, where the DORIS beacon is only 100 m away. However, for wide-band receivers the authors emphasize that the DORIS signal must be carefully filtered. Usually, the VLBI and DORIS systems are separated by more than 2 km at other stations where both techniques are employed, namely Hartebeesthoek (South Africa) as well as Metsähovi (Finland).

The VLBI system is designed to receive extremely weak signals down to −110 dBm. In contrast, the DORIS beacon emits signals at a frequency of 2,036 MHz and a 40 dBm output power. There is the potential of a coupling between the DORIS signals and the VLBI S-band receiving chain generating spurious signals. In the worst case, an overloading of the Low Noise Amplifiers (LNAs) with the risk of damaging

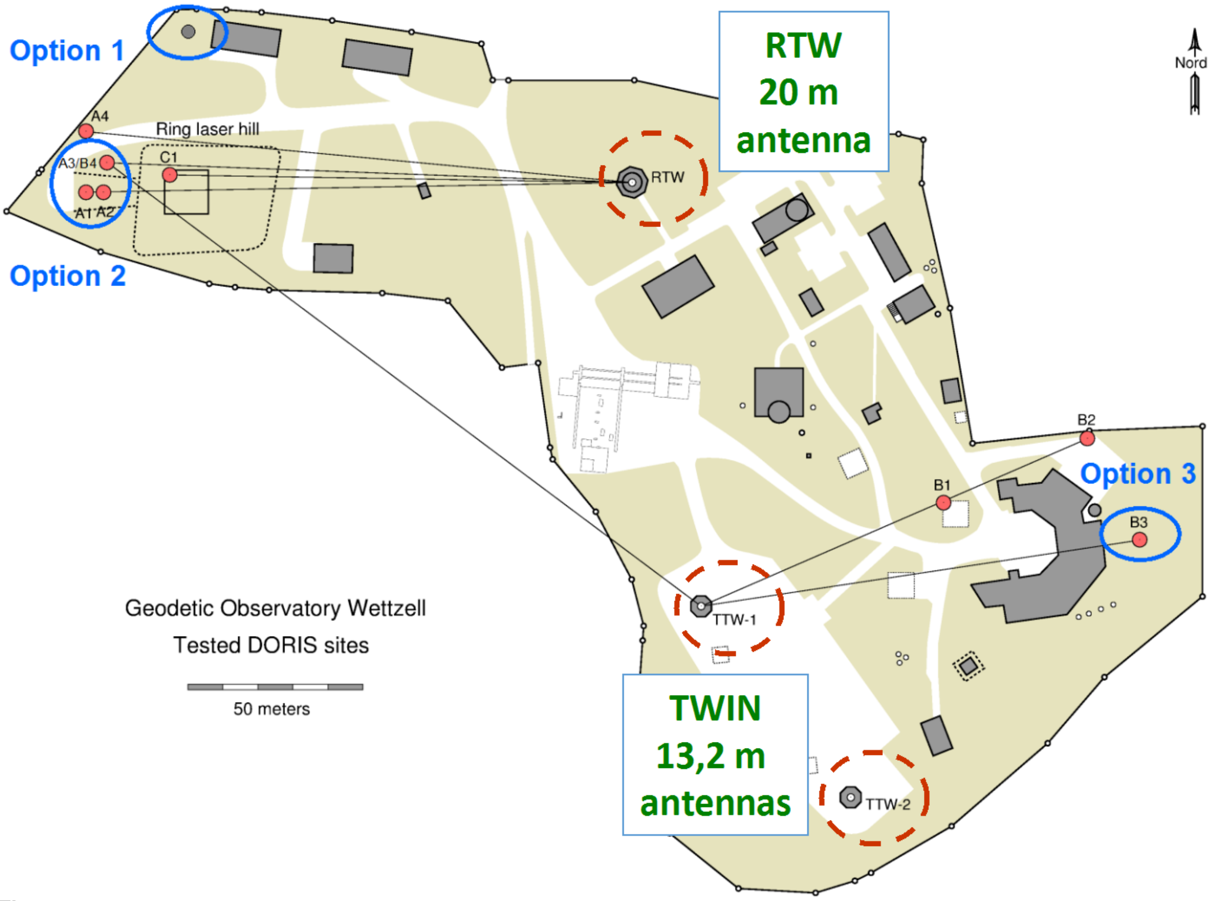

Fig. 1: Potential DORIS sites tested at Wettzell. The sites should be far enough from the VLBI telescopes and shielded by buildings (options 1 and 3) or the ring laser hill (option 2).

them is possible. Although the recorded S-band frequencies (2.1–2.4 GHz) are not expected to be directly influenced, the LNAs in the front-end could saturate.

In order to find a solution for a common operation, we investigated the RF interference situation at the LNA inputs of both the 20 m radio telescope (Wz, RTW) as well as the TWIN-1 telescope (Wn, tri-band S/X/Ka-feed). This was done by varying the telescope azimuths and elevations relative to the emitting source and testing different locations and RF blocking structures.

2 DORIS Overview

The DORIS system is based on the analysis of the Doppler shift between a ground station and the moving satellite. It is used to determine satellite orbits and coordinates of the ground stations. A number of approx. 60 ground stations ("DORIS beacons") emit signals at fixed frequencies both at 401 as well as 2,036 MHz. These are received and analysed on-board of the satellite. The accuracy may reach a few centimetres over a data ingestion interval of one month. Though slightly worse than GPS in terms of coordinate accuracy, the good global network coverage and the permanent data acquisition make the system a valuable supplement for the measurement of station coordinates, Earth rotation, and the gravity field.

First DORIS operations at Wettzell date back to the year 2003. The beacon was always set into stand-by mode during VLBI operations in order avoid potential interferences with VLBI. At that time, this mode of operation turned out to be inappropriate for an adequate DORIS data retrieval, and DORIS operations ceased for about 10 years. In 2014, a new attempt towards a full 4-technique VLBI-SLR-GNSS-DORIS station was made. This initiative benefited from new IDS goals, since the co-location of DORIS with other space techniques was now actively promoted in the framework of GGOS. In 2015, the pre-requisites for the operation of a DORIS beacon at Wettzell were fulfilled, including the site investigation, the negotiation of the cooperation agreement and the frequency clearance. In the same time, the compatibility between the DORIS beacon and the VLBI systems was evaluated.

3 RFI Investigations

In order to find a solution for common operations, RF interference at the LNA inputs of the Wettzell 20 m telescope (Wz) and the TWIN-1 telescope (Wn) was investigated. Wz is in routine operation since 1984 and equipped with a classical geodetic S-/X-band receiving system. The TWIN-1 telescope (Wn) features a tri-band-feed including S-/X-/Ka-bands. The investigations were carried out under varying telescope azimuths and elevations. Different RF blocking structures were tried out, and different locations were occupied. In a first survey in December 2014, the three different locations shown in Fig. 3 were identified as possible options.

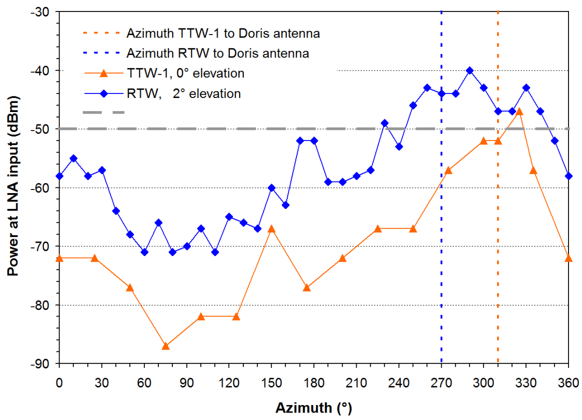

Fig. 2: Azimuth-dependency of the received DORIS power at the RTW (Wz) and TTW-1 (Wn) radio telescopes at distinct low elevations. The line at −50 dBm indicates the critical power level where LNA non-linearities must be taken into account. The DORIS beacon is at site A3 (marked as "Option 2" in the map).

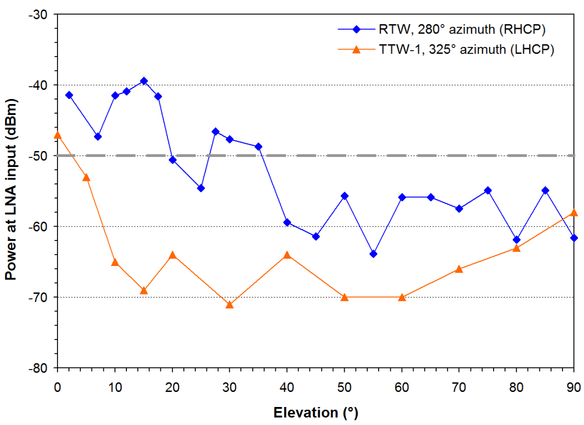

Fig. 3: Elevation-dependency of the received DORIS power at the RTW (Wz) and TTW-1 (Wn) radio telescopes.

The received power was measured at the receiver output and corrected for amplifier gain and cable losses. The graphs represent the maximum power in the spectrum analyser at a frequency of 16.248 MHz, that is, the DORIS S-band minus the LO frequency of 2,020 MHz. The measured power strongly depends on the orientation of the VLBI telescope. As visible in Fig. 2, the maximum is reached when pointing towards the DORIS antenna at elevations below 15°. However, an increased power is noticeable in Fig. 3 at higher elevations, too. Possible reasons are spillover effects or reflections at the sub-reflector, in particular at the TWIN telescope Wn which is optimised for broadband reception.

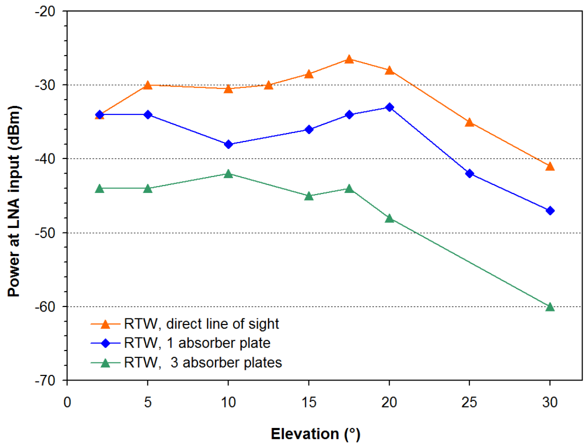

Fig. 4: Attenuation effect of absorber plates on 20 m telescope Wz (RTW) at location C1.

We found that the received power at the VLBI system may exceed the LNA-safe operations point anywhere at the station as soon as a direct line-of-sight geometry is present — a situation which shall be avoided. The *safe operations point* for typical LNAs is on the order of −50 dBm or −80 dBW according to Petrachenko et al. (2013). In these cases the original polarization (right-hand circular polarization or RHCP) dominates.

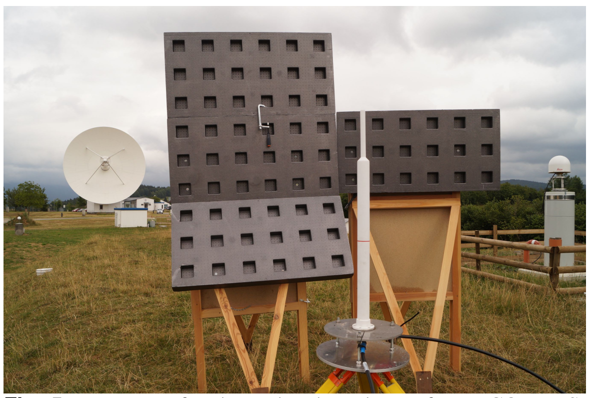

Fig. 5: Test setup for three absorber plates of type COMTEST MT65.

The introduction of RF barriers (e.g. absorber plates, see Fig. 3) or obstacles (such as buildings or hills) reduces the received power by up to 20 dB. This is illustrated in Fig. 4. A similar attenuation of 12—16 dB was obtained by Koepping et al. (2014) using a steel mesh blocker. However, at dedicated orientations the power is still at the upper limit. In these cases the percentage of LHCP and RHCP is equal indicating that the signal is reflected many times before entering the receiver.

When the measured power in direct line-of-sight is combined with common path loss models for open or suburban terrain (see e.g. Hata 1980), a loss of about 12.5 dB can be expected when doubling the distance. Consequently, a distance of 300–400 m between the VLBI and DORIS antennas is sufficient to achieve the required level of attenuation for safe operations. However, it has to be ensured that the DORIS antenna is never within the maximum gain lobe of the VLBI antenna. This additional gain could overload or even destroy the LNA.

4 Long-Term VLBI-Test

The position behind the ring laser hill yields the highest signal attenuation due to the shielding effect of the hill and the long distance to the radio telescopes. This site was chosen to test the contemporaneous operation of DORIS and VLBI over one month. In order to further reduce the impact of the DORIS emissions, the beacon is normally in stand-by mode and only automatically switched on when a satellite with DORIS-equipment on-board is visible.

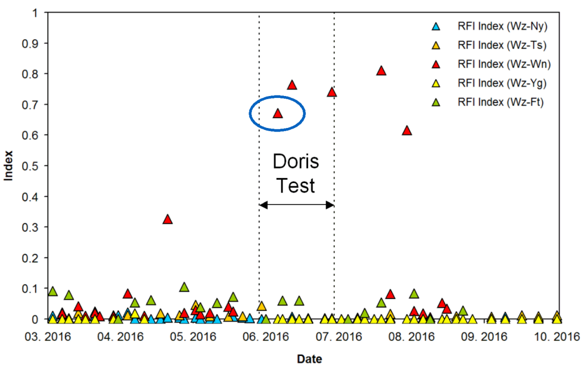

Fig. 6: RFI index on different baselines (local baseline: red triangles) derived from the correlation of IVS R1 and R4 sessions between March and October 2016.

A measure of RFI are the “G codes” in the correlation process, marking scans where no proper correlation is possible. For the routine experiments R1 and R4 the RFI index, that is the relative frequency of the G codes, is shown before, during and after the test interval in Fig. 5. As expected and investigated by Schüler et al. (2015), the local baseline Wz–Wn (WV) is much affected by local RFI, as RFI signatures are highly correlated in the records of both telescopes. However, there is no increase during the DORIS test, nor at the local neither at the long baselines.

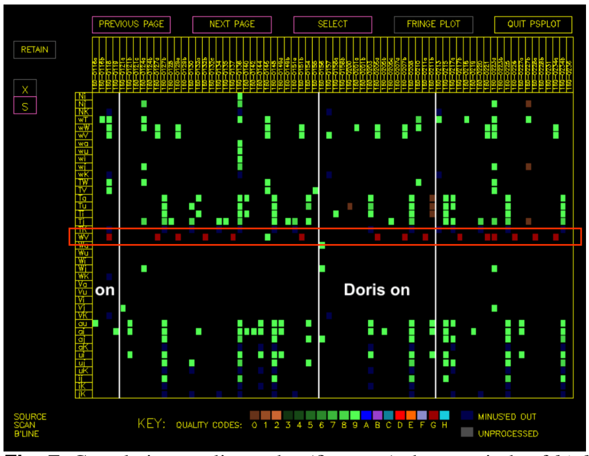

Fig. 7: Correlation quality codes (first part) show periods of *high* RFI impact on the local baseline Wz—Wn (WV), independently from the state of the DORIS beacon. R1 experiment from June 7, 2016.

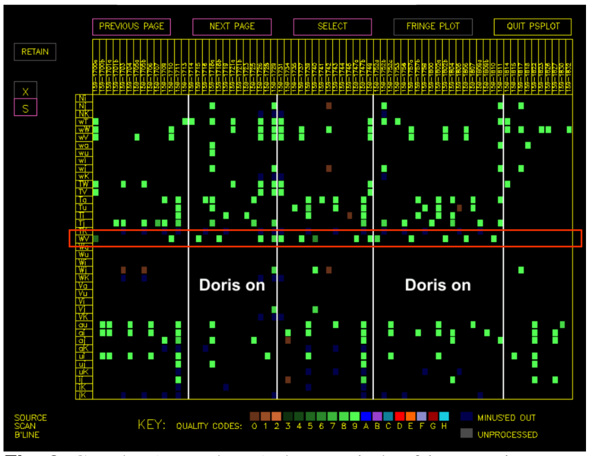

Fig. 8: G codes (second part) show periods of *low* RFI impact on the local baseline Wz—Wn (WV).

A closer look on individual scans of the local baseline Wz—Wn (WV) reveals that G codes appear independently of DORIS being on or off (see Fig. 7 and 8). It is concluded that local RFI certainly degrades the S-band correlation results of the local baseline. However, it is not caused by the DORIS beacon.

5 Conclusions

The common operation of a VLBI antenna and a DORIS beacon at a distance below 400 m is possible. As the DORIS beacon has enough power to saturate or destroy the LNA, the signal must be attenuated e.g. by using obstacles between the antennas (hills, buildings, RF blocker) or increasing the distance. The maximum gain lobe of the VLBI antenna shall never point towards the DORIS antenna.

In the case of the Geodetic Observatory Wettzell, an installation behind the ring laser hill (no direct line-of-sight to any of the VLBI telescopes) is the preferred choice giving the best compromise:

1. *VLBI:* enough attenuation exploiting both distance and natural barrier
2. *Operation on demand:* 25-30 % duty cycle, no effect on satellite reception
3. *DORIS:* elevation mask around 10^o (acceptable for IDS)
4. *Local ties:* precise co-location with VLBI, SLR, GNSS is easily possible and was accomplished

The nominal operation of the Wettzell DORIS station *WEUC* started on September 27, 2016. Although the desired minimum DORIS elevation of 5^o is not reached in each direction, the station yields good results. On the VLBI side, there is no degradation of the correlation results detectable since then.

References

Beaudoin C, Corey B, Hilliard L, Petrachenko B (2012) RF Compatibility of VLBI with DORIS and SLR at GGOS Stations: an Experimental Methodology to Validate the Models. In: D. Behrend and K. D. Baver, *I*VS 2012 General Meeting Proc., NASA/CP-2012-217504, 3–7.

Hata M (1980) Empirical Formula for Propagation Loss in Land Mobile Radio Services. *IEEE Transactions on Vehicular Technology*, 29(3): 317–325.

Il'in G, Smolentsev S, Sergeev R (2010) About the Compatibility of DORIS and VLBI Observations. In: D. Behrend and K. D. Baver, *IVS 2010 General Meeting Proc.*, NASA/CP-2010-215864, 180–183.

Koepping G, Hopkins A, Young C, Hilliard L (2014) RFI Blocker Testing at GGAO to Enable Space Geodetic Technique Colocation. GSFC Science Jamboree, July 17, 2014.

Petrachenko B, Corey B, Beaudoin C (2013) VGOS RFI Survey. In: N. Zubko and M. Poutanen (eds.), *Proc. 21th EVGA Working Meeting*, 33–38.

Schüler T, Kronschnabl G, Plötz C, Neidhardt A, Bertarini A, Bernhart S, La Porta L, Halsig S, Nothnagel A (2015) Initial Results Obtained with the First TWIN VLBI Radio Telescope at the Geodetic Observatory Wettzell. *Sensors*, 15(8), 18767–18800. doi:10.3390/s150818767.

Unified Model for Surface Fitting of Radio Telescope Reflectors

M. Lösler, C. Eschelbach, R. Haas

Abstract The main reflector of VLBI radio telescopes is affected by several disturbing forces. Temperature, wind, insolation or snow load deform the surface of the reflector and impair the receiving properties. Depending on the elevation orientation of the main reflector, the dead load of the dish w.r.t. the gravitation field of the Earth influence the surface negatively. In recent years, surface deformations and variations of the focal length have been analyzed by several groups. The common mathematical model to describe the main reflector is an ordinary rotational paraboloid. Due to the reflector design improvements, the surface of the main reflector of many of the upcoming VGOS radio telescopes cannot be parameterized by an ordinary rotational paraboloid. We present a unified mathematical model that overcomes this limitation and which is valid for the ordinary surface design as well as the new ring-focus reflector design of VGOS radio telescopes. The model is used for an independent confirmation of the specifications of the new Onsala twin telescopes at the Onsala Space Observatory.

Keywords Reverse Engineering, VGOS, Paraboloid, Ring-Focus, Focal-Length, Surface, Deformation, Close-Range Photogrammetry

1 Introduction

A VLBI radio telescope is a large geodetic space instrument that usually receives signals of quasi-stellar radio sources in space. The receiving properties of such a telescope depend on the design of the radio telescope. The diameter of the main reflector of most of the existing radio telescopes lies within the range of 20 m up to 40 m, but there are also a few telescopes with larger diameter like the 100 m radio telescope Effelsberg. Due to the dimension, the main reflector is affected by several disturbance forces, e.g. the dead load of the dish w.r.t. the gravitation field of the Earth or weather conditions like insolation, wind or snow load. Some of the forces deform the main reflector as a function of the elevation orientation e.g. the path length of the signal. Clark and Thomsen (1988) parameterize the path length variations as a function of the change of the position of the vertex, the displacement of the receiver and the focal length variation w.r.t. the elevation orientation. The focal length is a design parameter of the main reflector and can be derived by e.g. high precision photogrammetric measurements of the reflector surface (Fraser, 1986; Luhmann, 2010). These observations can also be used to validate the surface quality, i.e. the alignment of the panels of the reflector or to detect deformations (Edmundson and Baker, 2001; Shankar et al., 2009). The root-mean-square (RMS) specifications of the surface quality of the reflectors and the path length variations are <200 μm and <300 μm, respectively, for the upcoming VGOS – *VLBI2010 Global Observing System* – radio telescopes (Petrachenko et al., 2009). In the framework of reverse engineering, the parameter estimation of surfaces is a main part of industrial metrology.

2 Surface Model of Ordinary Paraboloid

The main reflector of most of the existing radio telescopes can be parameterized as a type of a quadric surface, i.e. a paraboloid. The canonical form of an ordinary paraboloid, i.e. the vertex is located at the origin and the principal axis is $\begin{pmatrix} 0 & 0 & 1 \end{pmatrix}^{\mathrm{T}}$, reads

Michael Lösler (michael.loesler@fb1.fra-uas.de) · Cornelia Eschelbach (cornelia.eschelbach@fb1.fra-uas.de)
Frankfurt University of Applied Sciences, Laboratory for Industrial Metrology, Nibelungenplatz 1, DE-60318 Frankfurt am Main, Germany

Rüdiger Haas
Chalmers University of Technology, Onsala Space Observatory SE-439 92 Onsala, Sweden

$$a^2 x_i^2 + b^2 y_i^2 = z_i, \tag{1}$$

where $\mathbf{p}_i = \begin{pmatrix} x_i \; y_i \; z_i \end{pmatrix}^{\mathrm{T}}$ represents the coordinates of the i-th object point and a and b are the datum-independent form-parameters of an ordinary elliptic paraboloid (OEP). By shifting and rotating, the object point $\mathbf{p}_i$ can be transformed to a superordinate reference frame e.g. the measurement system, e.g. (Lösler, 2011):

$$\mathbf{p}_i = \mathbf{Q}\left(\mathbf{P}_i - \mathbf{P}_0\right). \tag{2}$$

Here point $\mathbf{P}_i = \begin{pmatrix} X_i \; Y_i \; Z_i \end{pmatrix}^{\mathrm{T}}$ corresponds to $\mathbf{p}_i$ in the superordinate reference frame, $\mathbf{P}_0 = \begin{pmatrix} X_0 \; Y_0 \; Z_0 \end{pmatrix}^{\mathrm{T}}$ is the translation vector and $\mathbf{Q}$ represents the rotation sequence of the unit quaternion $\mathrm{q} = q_0 + \mathbf{q}$ with the scalar part q_0 and the imaginary part $\mathbf{q} = \varsigma q_1 + \xi q_2 + \zeta q_3$, with $\varsigma^2 = \xi^2 = \zeta^2 = \varsigma\xi\zeta = -1$, (Nitschke and Knickmeyer, 2000; Lösler and Nitschke, 2010), i.e.

$$\mathbf{Q} = \left(q_0^2 - \mathbf{q}^{\mathrm{T}}\mathbf{q}\right)\mathbf{I} + 2\left(\mathbf{q}\mathbf{q}^{\mathrm{T}} + q_0\left[q\times\right]\right), \tag{3}$$

with the skew-symmetric matrix

$$\left[q\times\right] = \begin{pmatrix} 0 & -q_3 & q_2 \\ q_3 & 0 & -q_1 \\ -q_2 & q_1 & 0 \end{pmatrix}, \tag{4}$$

where $\mathbf{I}$ is the identity matrix.

In general, the main reflector is designed to be rotation-symmetrical. If $a \neq b$ the paraboloid is deformed w.r.t. the ideal design and the focal point degenerates to a focal line. By setting $a = b$, the ordinary elliptic paraboloid becomes an ordinary rotational paraboloid (ORP), i.e.

$$a^2\left(x_i^2 + y_i^2\right) = z_i, \tag{5}$$

and the focal length f reads

$$f = \frac{1}{4a^2}. \tag{6}$$

The simplification of Eq. (1) is used by many groups as mathematical model, e.g. Sarti et al. (2009); Holst et al. (2012); Kallio et al. (2015), even though a difference between a and b impairs the receiving properties significantly.

3 Unified Model of Radio Telescope Main Reflector

Following the VLBI2010 agenda (Niell et al., 2006), a new generation of radio telescopes was designed. These so-called VGOS radio telescopes are much more compact, i.e. the diameter of the main reflector is about 12 m, and faster, i.e. 12°/s in azimuth and 6°/s in elevation (Petrachenko et al., 2009). Moreover, the design of the main reflector is improved, in contrast to conventional radio telescopes. In conventional radio telescopes, the feed obstructs the path and results in fields of low intensity. As shown by Cutler (1947) this shading effect can be reduced by an improved reflector design. By stretching the paraboloid at the principal axis, the vertex as well as the focal point become circles (Prata et al., 2003). This design is known as ring-focus paraboloid.

In recent years, a lot of VGOS radio telescopes have been planned, were under construction or have already been installed. Most of these telescopes use the improved ring-focus design (Neidhardt et al., 2011; Gómez-González et al., 2014; Ipatov et al., 2015; Helldner et al., 2015). Due to the new main reflector design, a generalized mathematical model is needed to describe the surface because Eq. (1) as well as Eq. (5) are not suitable for ring-focus telescopes.

Therefore, we here propose an extended model of Eq. (1), which represents an elliptic ring-focus paraboloid (ERFP). The extended mathematical model is given by

$$a^2\left(x_i - rn_{x,i}\right)^2 + b^2\left(y_i - rn_{y,i}\right)^2 = z_i, \tag{7}$$

where r is the radius of the vertex circle and $\mathbf{n}_i = \begin{pmatrix} n_x \; n_y \end{pmatrix}^{\mathrm{T}}$ is the normalized vector that points in the direction of the elliptic paraboloid. The vector $\mathbf{n}_i$ is not an unknown parameter because this vector can be expressed as a function of the point $\mathbf{p}_i$ by substituting

$$n_{x,i} = \frac{x_i}{\sqrt{x_i^2 + y_i^2}} \tag{8}$$

and

$$n_{y,i} = \frac{y_i}{\sqrt{x_i^2 + y_i^2}}, \tag{9}$$

respectively.

In analogy to Eq. (5), Eq. (7) becomes a rotational ring-focus paraboloid (RRFP) by setting $a = b$, i.e.

$$a^2\left(\left(x_i - rn_{x,i}\right)^2 + \left(y_i - rn_{y,i}\right)^2\right) = z_i, \tag{10}$$

with focal length $f = \frac{1}{4a^2}$, cf. Eq. (6).

The generalized mathematical model (7) becomes universal because four types of paraboloids can be described, cf. Table 1, and the parameters of conventional radio telescopes as well as VGOS related radio telescopes with ring-focus can be fitted. Figure 1 depicts the four estimable paraboloid types.

Table 1: Paraboloid types that can be expressed by the universal model (7) depending on the form-parameter a, b and r.

	$a = b$	$a \neq b$
$r = 0$	ordinary rotational	ordinary elliptic
$r \neq 0$	rotational ring-focus	elliptic ring-focus

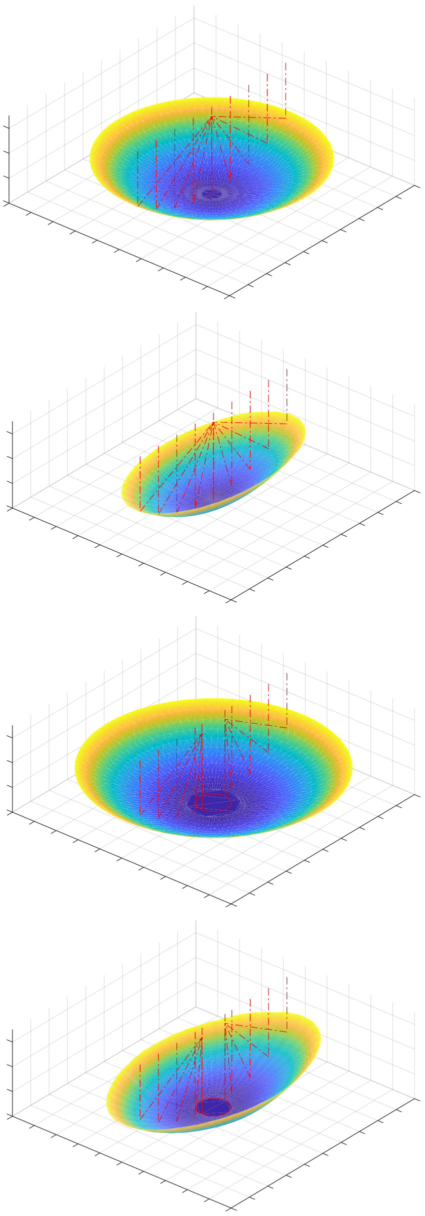

Fig. 1: Paraboloid types (from top to bottom): ordinary rotational paraboloid (ORP), ordinary elliptic paraboloid (OEP), rotational ring-focus paraboloid (RRFP) and elliptic ring-focus paraboloid (ERFP), and ray path lines (red dashed lines).

4 Parameter Estimation

As well-known from linear algebra, Eq. (1) is a special form of a quadric surface specified by

$$\mathbf{P}_i^{\mathrm{T}}\mathbf{U}\mathbf{P}_i + \mathbf{P}_i^{\mathrm{T}}\mathbf{u} + u_0 = 0, \tag{11}$$

where $\mathbf{U}$ is a symmetric matrix that contains the elements of the so-called quadratic function

$$\mathbf{U} = \begin{pmatrix} u_1 & \frac{u_4}{\sqrt{2}} & \frac{u_5}{\sqrt{2}} \\ \frac{u_4}{\sqrt{2}} & u_2 & \frac{u_6}{\sqrt{2}} \\ \frac{u_5}{\sqrt{2}} & \frac{u_6}{\sqrt{2}} & u_3 \end{pmatrix} \tag{12}$$

and the vector $\mathbf{u}$ contains the coefficients

$$\mathbf{u}^{\mathrm{T}} = \begin{pmatrix} u_7 & u_8 & u_9 \end{pmatrix} \tag{13}$$

of the quadric (Drixler, 1993). To eliminate the mixed terms in Eq. (11), each quadric can be transferred into a certain normal form by a principal axis transformation. As a result of the principal axis transformation the translation vector $\mathbf{P}_0$ as well as the quaternion q, which defines the rotation sequence, are determined, cf. Eq. (2). Moreover, the type of the quadric can be classified and specific form-parameters are estimable.

The big advantage of using Eq. (11) instead of Eq. (1) is the bilinear normal equation systems. Thus, rough approximation values are sufficient to solve the unknown parameters u_i, with $i = 0 \ldots 9$. On the other hand, the drawback of Eq. (11) is the universal scope, i.e. the lack of specifying the desired form-type. Beside the paraboloid, Eq. (11) describes sixteen further forms like plane, ellipsoid, cylinder or cone (Khan, 2010). If the observed point cloud is close to the vertex, the quadric surface may describe an ellipsoid instead of a paraboloid (Drixler, 1993; Lösler and Nitschke, 2010). Thus, explicit formulated models like Eq. (1) are needed to force the desired form-type. Furthermore, Eq. (7) is out of scope of Eq. (11). For this reason, the use of Eq. (11) is only recommended for deriving appropriate approximation values for the least-squares adjustment. Of course, for some radio telescopes an approximation of the focal length f can be taken from the main reflector design and initial spatial transformation parameters $\mathbf{P}_0$ and q can be predicted by the measurement setup (Sarti et al., 2009; Holst et al., 2012). But in the framework of reverse engineering, advanced information is seldomly available (Dutescu et al., 2009) and, thus, appropriate approximation values are important to ensure convergence.

To solve Eq. (7) within a least-squares adjustment, an error in variables model (EIV) is needed. Such a EIV model can be expressed as mixed model, also known as Gauß-Helmert model (Koch, 2014; Lösler et al., 2016). Due to the different paraboloid types, cf. Table 1, a Gauß-Helmert model with restrictions is recommended (Caspary and Wichmann, 2007; Lösler and Nitschke, 2010). Table 2 summarizes the required restrictions to switch over the four models.

Table 2: Restrictions to transform the universal model of an elliptic ring-focus paraboloid (ERFP) to its simplifications, i.e. an ordinary rotational paraboloid (ORP), an ordinary elliptic paraboloid (OEP) and a rotational ring-focus paraboloid (RRFP).

Restriction / Type	ORP	OEP	RRFP	ERFP
$a-b=0$	×	−	×	−
$q_1q_2+q_0q_3=0$	×	−	×	−
$r=0$	×	×	−	−
$\mathrm{q}^\mathrm{T}\mathrm{q}=1$	×	×	×	×

5 Onsala twin telescopes

The Onsala Space Observatory is located 45 km south of Göteborg at the Swedish west coast. Since the end of the 1960s, the observatory has been participating in numerous geodetic and astrometric VLBI campaigns.

The observatory is part of the International VLBI Service (IVS). In 2016, the building phase of the Onsala twin telescopes (OTT) project started. This project includes two VGOS specified radio telescopes, named OTT-N and OTT-S. The inauguration and start of operation of the two new VGOS systems is planned for 2017 (Haas, 2013; Elgered et al., 2017).

Figure 5 depicts the new VGOS-type radio telescopes at Onsala Space Observatory during the construction phase 2016.

Fig. 2: The Onsala twin telescopes – two identical VGOS-type radio telescopes (Photo: Roger Hammargren).

Continuous quality inspections, which prove the compliance with the specification e.g. the focal length or the alignment of the panels, were carried out by MT Mechatronics GmbH. The main reflector was observed using high precision close-range photogrammetric methods, cf. Fig. 3. The measurement accuracy is specified as 5 μm + 5 μm/m by the manufacturer (personal communication MT Mechatronics GmbH). In total, 224 representative adjustment points were measured. These points are distributed on six rings on the main reflector, cf. Fig. 4. For an independent validation of the data, the 224 discrete points were introduced to the proposed mathematical model (7) and the form-parameters were derived. It should be noted that the panel adjustment is not finalized yet. Thus, the derived results must be interpreted as preliminary results but they prove the high-grade execution of construction work of the mechanical engineers.

Fig. 3: Observing representative points on the main reflector of OTT-S using high precision close-range photogrammetric methods (Photo: Rüdiger Haas).

The estimated results are presented in Table 3 and Table 4 for OTT-N and OTT-S, respectively. The approximation values were derived by Eq. (11) using a principal axis transformation. For both radio telescopes, the form-parameters a and b of the ERFP differ in a range of about 2.2e – 5, which corresponds to a focal length variation of about 0.6 mm, cf. Eq. (6).

A further analysis was carried out by applying the restriction for a RRFP type radio telescope, cf. Table 2, and the parameter a was transformed to the focal length f by Eq. (6). The overall RMS of the RRFP adjustment was 82 μm and 102 μm for OTT-N and OTT-S, respectively. As an example, Figure 4 depicts the estimated deviations for OTT-N, i.e. the signed orthogonal distance ∇, between the observed points and the estimated RRFP surface.

Table 3: Approximation values and adjustment results of OTT-N for ERFP and RRFP paraboloid types, respectively.

Parameter	Approx	ERFP	RRFP
X_0	+4.507 m	+0.2187 m	+0.2187 m
Y_0	-0.007 m	+0.0296 m	+0.0296 m
Z_0	-1.746 m	-1.7203 m	-1.7203 m
q_0	+0.30447	+0.458686	+0.313149
q_1	-0.64258	-0.542601	-0.638285
q_2	-0.30107	-0.457090	-0.309742
q_3	-0.63540	-0.535032	-0.631340
a	+0.21611	+0.259967	+0.259955
b	+0.21615	+0.259945	+0.259955
r	+0 m	+0.7402 m	+0.7402 m
f	–	–	+3.6995 m

Table 4: Approximation values and adjustment results of OTT-S for ERFP and RRFP paraboloid types, respectively.

Parameter	Approx	ERFP	RRFP
X_0	+4.403 m	+0.7902 m	+0.7902 m
Y_0	-0.224 m	-0.4263 m	-0.4263 m
Z_0	-1.938 m	-3.3518 m	-3.3518 m
q_0	+0.82484	+0.825731	+0.824836
q_1	+0.05458	+0.027741	+0.056183
q_2	-0.56150	-0.563408	-0.561274
q_3	+0.03716	-0.003509	+0.038230
a	+0.22583	+0.259930	+0.259933
b	+0.22574	+0.259937	+0.259933
r	+0 m	+0.7396 m	+0.7396 m
f	–	–	+3.7001 m

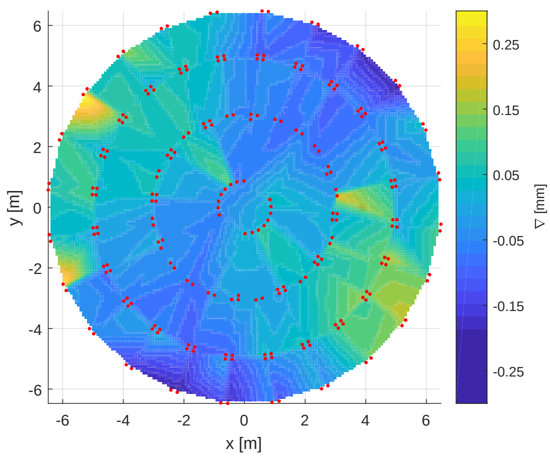

Fig. 4: Deviations, i.e. the signed orthogonal distance ∇, between the observed points (red dots) and the estimated rotational ring focus paraboloid surface of the OTT-N radio telescope.

To evaluate the influence of the radius r of the ring-focus design on the focal length f, the correlation coefficient can be used (Caspary and Wichmann, 2007):

$$\rho_{r,f} = \frac{\operatorname{cov}(r, f)}{\sigma_r \sigma_f}. \qquad (14)$$

The correlation coefficient results in values between -1 and $+1$ and describes the linear dependence between two parameters. Whereas $\rho = 0$ implies no linear correlations, a coefficient of $\rho = \pm 1$ represents a total dependence. The estimated $\rho_{r,f} \approx 0$ and, therefore, the dependence of both parameters is negligible.

Up to now, no advanced information was used during the analysis process, which is usual in reverse engineering. To evaluate the influence of a known radius $\widetilde{r}$ of the ring-focus design on the focal length f, the form-parameter can be restricted. The specified radius of the Onsala twin telescopes is $\widetilde{r} = 0.74$ m and the further restriction reads

$$\widetilde{r} = r. \qquad (15)$$

Applying Eq. (15), the focal length becomes $f = 3.6997$ m for both radio telescopes. Compared to the intended focal length of $\widetilde{f} = 3.7$ m, this value demonstrates the high quality of the pre-adjustment of the main reflectors.

6 Conclusion

In recent years, many research groups investigated on the force-deformation behavior of the main reflector of radio telescopes. Most of these investigations focused on the surface deformation or on the variations of the focal length. Technical innovations were introduced to the measurement process to achieve reliable results, and improvement of computer technology was used to process large amounts of data, but the mathematical model was kept unchanged.

Due to the reflector design improvements, the surface of the main reflector of the upcoming VGOS radio telescopes cannot be parameterized by an ordinary rotational paraboloid. The goal of our investigation was to formulate a unified mathematical model that describes the previous surface design as well as the ring-focus reflector design. The proposed data analysis concept is a two-stage process. Firstly, appropriate approximation values are derived by a quadric surface using the principal axis transformation. Thus, advanced information about the paraboloid type becomes unnecessary. Especially in the framework of reverse engineering it is important to have a self-provided and independent algorithm because prior information is maybe incomplete or rare. The second step is the adjustment process using the unified model, Eq. (7). Additional restriction can be introduced to switch over four surface types including the simplest case, i.e. an ordinary rotational paraboloid, and the most complex case, i.e. an elliptic ring-focus paraboloid.

At Onsala Space Observatory two VGOS-type radio telescopes are under construction, which are identical in design. For construction supervision several quality inspections were carried out to prove the compliance with the specifications. Two photogrammetric data sets were provided by MT Mechatronics GmbH. These data sets were used to verify the proposed algorithm and to derive independent results. Since the panel adjustment is not finished yet, the derived results must be interpreted as preliminary results. However, the results proved the high-grade execution of construction work of the mechanical engineers up to now.

Acknowledgements We gratefully acknowledge MT Mechatronics GmbH for supporting this research by providing two photogrammetric data sets of the Onsala twin telescopes.

References

Caspary W, Wichmann K (2007) *Auswertung von Messdaten – Statistische Methoden für Geo- und Ingenieurwissenschaften*, Oldenbourg, München.

Clark TA, Thomsen P (1988) Deformations in VLBI antennas. *NASA Technical Memorandum 100696*, NASA, Greenbelt.

Cutler CC (1947) Parabolic-antenna design for microwaves. In: *Proceedings of the IRE*, 35(11), 1284–1294.

Drixler E (1993) *Analyse der Form und Lage von Objekten im Raum*, Bayer. Akademie d. Wissenschaften, Deutsche Geodätische Kommission, C409, München.

Dutescu E, Heunecke O, Krack K (2009) Estimation of Surface Parameters of Radio Telescopes using Terrestrial Laser Scanner (in German). *avn*, 116(6), 239–245.

Edmundson K, Baker L (2001) Photogrammetric measurements of the Arecibo primary reflector surface. In: *17th annual Coordinate Measurement Systems Committee Conference*.

Elgered G, Haas R, Conway J, Hammargren R, Helldner L, Hobiger T, Pantaleev M, Wennerback L (2017) The Onsala twin telescopes project. In: R. Haas and G. Elgered (eds.), *Proc. 23rd EVGA Working Meeting*, 136–139.

Fraser CS (1986) Microwave antenna measurement. *Photogrammetric Engineering and Remote Sensing*, 52(19), 1627–1635.

Gómez-González J, López Fernández JA, Colomer F, Santos LR (2014) An Atlantic Network of Geodynamical and Space Stations - The RAEGE Project. In: D. Behrend, K. D. Baver, K. L. Armstrong (eds.), *IVS 2014 General Meeting Proc.: "VGOS: The New VLBI Network"*, 20–24.

Haas R (2013) The Onsala twin telescope project. In: N. Zubko, and M. Poutanen (eds.), *Proc. 21st EVGA Working Meeting*, 61–66.

Helldner L, Haas R, Pantaleev M (2015) Recent developments at the Onsala Space Observatory: VGOS Twin Telescope project and broadband upgrade. In: *4th International VLBI Technology Workshop (IVTW 2015)*.

Holst C, Zeimetz P, Nothnagel A, Schauerte W, Kuhlmann H (2012) Estimation of focal length variations of a 100-m radio telescope's main reflector by laser scanner measurements. *J. Surv. Eng.*, 138(3), 126–135, doi:10.1061/(ASCE)SU.1943-5428.0000082.

Ipatov A, Ivanov D, Ilin G, Olifirov V, Mardyshkin V, Surkis I, Fedotov L, Gayazov I, Stempkovsky V, Bondarenko Y (2015) Russian Radio Interferometer of New Generation. In: R. Haas and F. Colomer (eds.), *Proc. 22nd EVGA Working Meeting*, 75–79.

Kallio U, Kukko A, Kaartinen H, Kallunki J, Rönnberg H, Uunila M (2015) An experimental scanning of the Metsähovi radio telescope dish. In: R. Haas and F. Colomer (eds.), *Proc. 22nd EVGA Working Meeting*.

Khan SA (2010) Quadratic Surfaces in Science and Engineering. *Bulletin of the IAPT*, 2(11), 327–330.

Koch KR (2014) Robust estimations for the nonlinear Gauss Helmert model by the expectation maximization algorithm. *J Geod*, 88(3), 263–271, doi:10.1007/s00190-013-0681-9.

Lösler M, Nitschke M (2010) Estimation of the Parameters of a Spatial Ellipse (in German). *avn*, 117(3), 113–117.

Lösler M (2010) Robust Parameter Estimation of the Spatial Helmert-Transformation (in German). *avn*, 118(5), 187–191.

Lösler M, Haas R, Eschelbach C (2016) Terrestrial monitoring of a radio telescope reference point using comprehensive uncertainty budgeting – Investigations during CONT14 at the Onsala Space Observatory. *J Geod*, 90(5), 467–486, doi:10.1007/s00190-016-0887-8.

Luhmann T (2010) *Nahbereichsphotogrammetrie - Grundlagen, Methoden und Anwendungen*, Wichmann, Berlin, 3nd edn.

Neidhardt A, Kronschnabl G, Klügel T, Hase H, Pausch K, Göldi W (2011) VLBI2010 - Current status of the TWIN radio telescope project at Wettzell, Germany. In: W. Alef, S. Bernhart, and A. Nothnagel (eds.), *Proc. 20st EVGA Working Meeting*, 67–70.

Niell A, Whitney A, Petrachenko B, Schlüter W, Vandenberg N, Hase H, Koyama Y, Ma C, Schuh H and Tuccari G (2006) VLBI2010: Current and Future Requirements for Geodetic VLBI Systems. In: D. Behrend and K. D. Baver (eds.), *IVS Annual Report 2005*, NASA/TP-2006-214136, 13–40.

Nitschke M and Knickmeyer EH (2000) Rotation Parameters – A Survey of Techniques. *J Surv Eng*, 126(3), 83–105, doi:10.1061/(ASCE)0733-9453(2000)126:3(83).

Prata A, Moreira FJS, Amaro LR Displaced-Axis-Ellipse Reflector Antenna for Spacecraft Communications. In: *Proceedings of the 2003 SBMO/IEEE MTT-S International*, Microwave and Optoelectronics Conference, 391–395, doi:10.1109/IMOC.2003.1244891.

Petrachenko B, Niell A, Behrend D, Corey B, Boehm J, Charlot P, Collioud A, Gipson J, Haas R, Hobiger T, Koyama Y, MacMillan D, Malkin Z, Nilsson T, Pany A, Tuccari G, Whitney A, Wresnik J (2009) Design Aspects of the VLBI2010 System. *Progress Report of the IVS VLBI2010 Committee*, NASA/TM-2009-214180.

Sarti P, Vittuari L, Abbondanza C (2009) Laser scanner and terrestrial surveying applied to gravitational deformation monitoring of large VLBI telescopes' primary reflector. *J Surv Eng*, 135(4), 136–148, doi:10.1061/(ASCE)SU.1943-5428.0000008.

Shankar NU, Duraichelvan R, Ateequlla CM, Nayak A, Krishnan A, Yogi MKS, Rao CK, Vidyasagar K, Jain R, Mathur P, Govinda KV, Rajeev RB, Danabalan TL (2009) Photogrammetric measurements of a 12-metre preloaded parabolic dish antenna. In: *National Workshop on the Design of Antenna and Radar Systems (DARS)*, ISRO Telemetry Tracking and Command Network (ISTRAC).

On the way to Regular, Transatlantic VGOS Sessions Using an Elevenfeed and DBBC2's

A. Neidhardt, C. Plötz, G. Kronschnabl, W. Schwarz, S. Mähler, T. Schüler

Abstract The first transatlantic VGOS-sessions were successfully operated. Special is that different receiving hardware is used at the sites. The Geodetic Observatory Wettzell is the first site using the new broadband Elevenfeed, two DBBC-2's in combination with two FILA10G, and a Mark6, controlled by the NASA Field System. First experiences show that it was and is a continuous process of learning, testing, and implementing. This paper explains the currently used systems and setups. Results from additional investigations in antenna performance and in mechanical deformation are shown. Implementations made to get the system running are demonstrated. Finally, we show made progress but also current issues.

Keywords VGOS, Elevenfeed, DBBC, transatlantic sessions

1 Introduction

The year 2016 was the starting signal for transatlantic VLBI Global Observing System (VGOS) sessions. The core network of the new broadband systems consisting of the antennas at the Kokee Park Geophysical Observatory (KPGO) in Hawaii, the Goddard Geophysical and Astronomical Observatory (GGAO) in Maryland, and Westford in Massachusetts were extended by the additional sites Wettzell in Germany and Yebes in Spain (see Fig. 1). "On Thursday, 9 June 2016 (day of year 161), fringes were obtained between GGAO, Westford, and Wettzell in all four VGOS observing bands (a.k.a. bands A, B, C, and D)" (Ruszczyk, 2016).

Different to the American sites and Yebes, the Wettzell VGOS system uses an Elevenfeed, two DBBC-2's, two FILA10G's, and a Mark6 System with an extension chassis. After a long test and learning process, Wettzell is the first site having experiences with this new European-driven system family.

2 The VGOS system at Wettzell

The Wettzell VGOS system is designed as a TWIN telescope consisting of two antennas which are identical in construction. Nevertheless, both antennas of the Twin Telescope Wettzell (TTW) are currently equipped with different receiving systems. The northern antenna Wn (TTW1) has a receiving feed for S/X/Ka band frequency with RHCP and LHCP polarisation in order to support legacy IVS S/X band observations as well as Ka band experiments. The southern antenna Ws (TTW2) is a fully operational, fast VGOS-compliant antenna (see Fig. 3). Both antennas designed and built by Vertex Antennentechnik GmbH support fast slewing. The VGOS system uses an Elevenfeed with a continuous frequency band from 2 to 14 GHz with linear polarization which is incorporated in a cryostat with amplifiers running on 9 Kelvin and requiring reduced maintenance. The dewar with the feed and the phase calibration unit is mounted on a rail system, so that it can be replaced with another system within a few days. The system uses an adjustable sub-reflector which automatically compensates path lengths errors at different elevations. The downconverter of the receiving chain supports 8 IF downconverter and a Holzworth synthesizer to allow the tuning of local oscillator (LO) frequencies. The front-end is completely developed at the Wettzell observatory. The front-end in the elevation cabin is currently connected to the back-end in the control room using coax-cables. Optical fibers to propagate the whole frequency band

Alexander Neidhardt
Technische Universität München, Forschungseinrichtung Satellitengeodäsie, Geodätisches Observatorium Wettzell, Sackenrieder Str. 25, D-93444 Bad Kötzting, Germany

Christian Plötz · Gerhard Kronschnabl · Walter Schwarz · Svetlana Mähler · Torben Schüler
Federal Agency for Cartography and Geodesy, Geodätisches Observatorium Wettzell, Sackenrieder Str. 25, DE-93444 Bad Kötzting, Germany

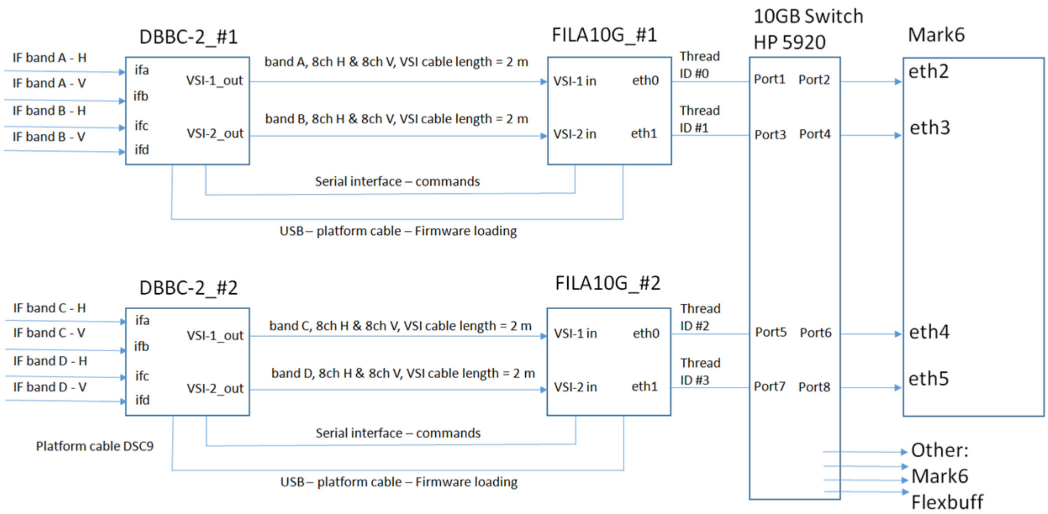

Fig. 2: A sketch of the Wettzell back-end.

Fig. 1: The network of the early transatlantic VGOS sessions showing the geographic position of the Wettzell VGOS site (extracted from Ruszczyk (2016)).

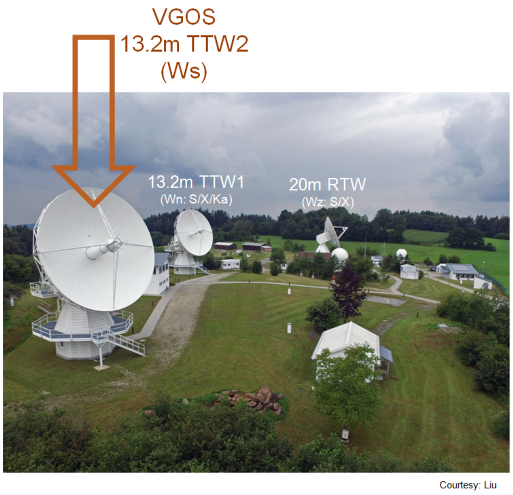

Fig. 3: The Wettzell VGOS antenna of the Twin Telescope Wettzell (TTW).

without the conversion to IF bands are also possible in the future.

The back-end (see Fig. 2) consists of a very new DBBC-2 #1 for the horizontal and vertical bands A (currently starting at frequency 2984 MHz) and B (currently starting at frequency 5224 MHz). DBBC-2 #2 is an upgraded version of one of the earliest DBBC's and is used for the other two bands C (starting at frequency 6344 MHz) and D (starting at frequency 10184 MHz). The DBBC-2's (both with software personality Dbbc2_pfb_v16_010916_1_adb2.bit) do an automatic gain control and run a Polyphase Filter Bank (PFB) mode to sample the whole bands with a bandwidth of 512 MHz using junks of 32 MHz. Each DBBC streams the 32 channels sampled over two VSI cables to a connected FILA10G formatter (with the software personality Fila10g_v3.3.2_1_150715.bit). It realizes the timing and formatting into VDIF frames. Each band corresponds to an individual thread in the format. The VDIF frames of the individual threads are sent on different 10 Gbit/sec Ethernet fiber links over a 10 GBit/sec Switch to one Mark6 system (using software release 1.20 of dplane and 1.0.24 of cplane and a version of vbs_fs, a VDIF Fuse file system emulator written at JIVE ERIC, Dwingeloo) with four input Ethernet ports. The Ethernet switch, an HP 5920, breaks the rigid, direct connection and can be used to easily change recording devices in the future, so that the configuration of the FILA10G's determines which recorder receives the data without changing of the communication fibers. This implementation builds a new transfer network for VLBI data as described in Neidhardt (2017). This configuration simplifies the integration of a Flexbuff system, which is currently under test using a DELL PowerVault MD3460 Storage

Array with currently up to 72 Terabyte of storage volume.

All systems are controlled by the NASA Field System using version 9.12.10 of the VGOS branch. It supports all VGOS functionalities for the US-systems RDBE and also for the DBBC's. A relevant difference to legacy versions of the Field System is, that schedule files (SKD-files) also contain individual procedures for station specific tasks to setup sessions. These procedures are no more part of the station code and are automatically generated using the Field System program "drudg", so that every change must be committed to the VGOS scheduler. The e-RemoteCtrl server (in the version r667_20130411) also runs on the Field System PC. It is the remote control software developed at the Wettzell observatory (see Neidhardt (2013)). e-RemoteCtrl clients are installed at the different control rooms and on mobile Linux devices to operate the VGOS antenna from remote.

3 Lessons learned from system tests and quality control

The way to become a VGOS site using different equipment to all other sites was a "stony walk" of several learning lessons. The following is a rough itemization of the main findings and perceptions at the location of a site on this way to a VGOS station:

- General issues
  - The new ring-focus antennas suffer from strong Radio Frequency Interferences (RFI) in low and high elevations: the dish shape requires a different approach to avoid RFI at all, if possible
  - Requirement of a stable, modern phase calibration unit: The rise time of the existing legacy phase calibration units is too slow, so that the phase calibration signal in band A over-saturates while band D just sees a very weak signal; additionally, the used unit had no gating so that positive and negative pulses passed the output, which had to be solved with an RF-switch gating only the positive pulses
  - Clear detection of the polarizations of the different bands: the detection of the polarizations was difficult due to a different parallactic angle between US-stations and Wettzell; it was necessary to swap the IF cables several times and watch the correlator reports for feedback
  - IF distribution back-end requires equalizers and post-amplifiers: like in legacy systems, IF bands should be flat and without differences of the power levels within the bands; spectra at Wettzell show differences around 10 dB
  - All eight IF bands must be transferred over the same type of cables from the front-end to the back-end: different cable types resulted in different delays for the different bands and "Fourfit" was not able to manage this
  - Use the same type of back-end devices for all eight bands: the internal behavior of different back-ends, like digital BBCs, might apply different delays (e.g., a back-end chain with an ADS3000+ applied about 200 nsec offset compared to a pure DBBC-2 chain which led to problems with Fourfit)
  - Requirement of a cable calibration unit: different to early assumptions, VGOS systems require a cable calibration system to deal with different delays in the different frequency bands on different cables
- DBBC-2 issues using PFB mode with 4 bands of 512 MHz bandwidth per band and 256 MHz per polarization
  - Always use the most stable firmware and report bugs to HatLab: continuous firmware and software improvements had to be done while implementing the VGOS mode; tests showed that the 64 MHz VSI clock frequency alignment to the digital data stream to an external FILA10G was not stable which required an upgrade to enable the feature "vsi_align"; there were "ghost tones" from time to time, caused by an incorrect data capture from the analog digital converter (trigger edge of data converter clock)
  - Check the power supply of the DBBC if it supports the higher power consumption of PFB mode: especially older models of the DBBC-2 use a weak power distribution board which cannot support the higher power requirements when more FPGA blocks are used like with the PFB mode
  - Use the found VGOS setup for DBBC/-FILA10G from Wettzell: originally, there was no setup available from Haystack for this equipment, so that the first tests from the Wettzell team were used to find the right configuration, which is now available
  - There are still sporadic losses of channels or complete IF bands: this is still under investigation; complete reboots before each session reduces the probability of failures
- Mark6 issues

– Always use installations from Haystack: directly shipped Mark6 systems do not have any installations what required exhausting installation and test periods by the Wettzell team
– Always end recording states using "record=off": before a new activity is commanded to the Mark6, a reset of the recording state is essential, because the system might be pending e.g. if no data arrive on one of the Ethernet ports
– Always follow a strict sequence of commands to mount modules: the Mark6 is very sensitive to wrong orders of the commands during the mounting or unmounting process, so that the Wettzell team found the following sequence as suitable: init module, create group, open group and after recording close group and unmount group.
– Reduced monitoring capability is still an issue: there is no feedback about the mounting and filling status of the disks, so that slow disks can not be identified; the network behavior or direct clock jumps are not monitored in real-time, which can be done using the program "dboss"; "scan_check" also offers not always correct numbers, so that separate programs like the "scan_check" of Jive5ab from JIVE ERIC might be used

The experiences at Wettzell showed that an additional monitoring of the data quality is essential. The available feedback from the systems themselves offer just reduced information which does not help to detect issues. Therefore, the Wettzell team wrote a Linux script which uses the DiFX utilities from W. Brisken and "vbs_fs" from H. Verkouter to mount the disks in parallel to dplane on the Mark6. The script runs after each recording of a scan, triggered in the procedure "postob". It searches the latest, valid scan, copies 200 MByte including all VDIF threads, runs "dqa -d" to separate the single bands, creates spectrum plots with "m5spec" from the DiFX utilities, creates image files of the spectrum plots with GNU plot, copies the image files into a backup directory for later investigations, uses a separate script to read out disks used and their volumes, and combines everything to an HTML page as live feedback for the operator. The scripts can be downloaded from: http://vtcdoc.iapg.bgu.tum.de/mk6_scan_plotting.

4 Antenna performance

The performance of Ws is quite good. Regular SEFD measurements show good results (see Fig. 4). Also the measured beam patterns of the whole system align quite well with the calculated patterns from the design analysis before the construction of the feed.

Additionally, regular geodetic surveys are processed about once per month from three locations using total station Leica TS50 and 26 reflectors in the telescope back-structure and on the cabin. The measurement is done within special sessions with a length of 9 hours where the antenna position is changed in steps of 20 degree in azimuth and 30 degree in elevation. This re-

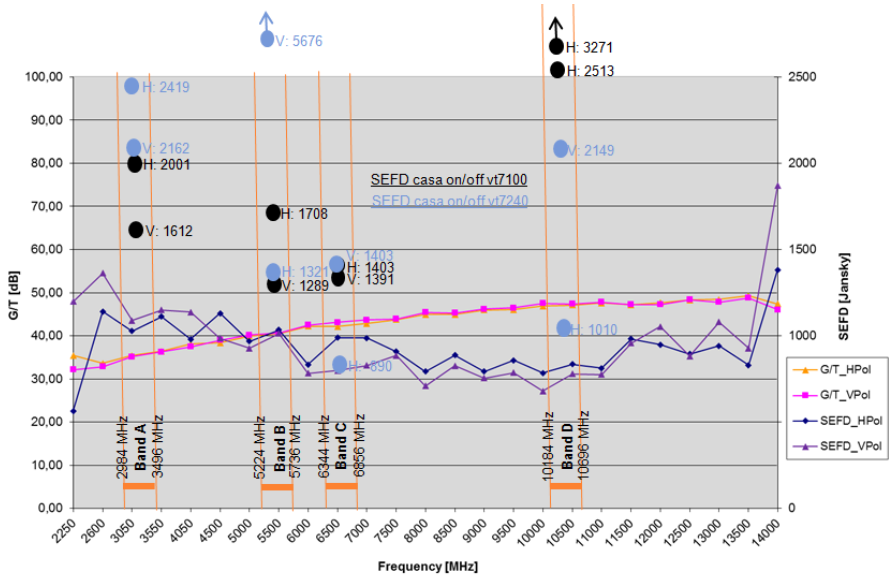

Fig. 4: The early results from "blue-sky" tests with the pure Elevenfeed and according values from the regular SEFD measurements before session vt7100 and vt7240 using the whole receiver chain.

sults in 700 scans per session. The tracking and analysis uses the semi-automated procedures and programs from Lösler (2017), which apply a suitable telescope model.

These regular geodetic surveys show seasonal variation effects of about 0.5 mm in X direction, about 0.4 mm in Y direction, and about 1.9 mm in Z direction. The application of thermal corrections from six temperature sensors in the concrete tower reduces the height changes to about 0.5 mm.

5 Conclusion and outlook

The Wettzell team had to learn from several sessions on the way to become a VGOS site using a different equipment based on an Elevenfeed, DBBC-2's, FILA10G's, and a Mark6 recorder. While there are still some issues, Ws is meanwhile a VGOS antenna which participates to all regular VGOS test sessions.

To enable the capabilities of a Twin Radio Telescope, a QRFH feed is ordered which should replace the S/X/Ka tribandfeed of the second antenna TTW1 (Wn). It is designed to be tested in the current VGOS setup of the Ws antenna and uses an improved dewar, a better window design, and noise calibration installations. It will be delivered to Wettzell in spring 2018.

Acknowledgments

We want to thank all colleagues of the IVS community and especially the colleagues at the Haystack observatory, NASA GSFC, the Yebes observatory, the MPIfR Bonn for supporting us.

References

Neidhardt A, Ettl M, Mühlbauer M, Kronschnabl G, Alef W, Himwich E, Beaudoin C, Plötz C, Lovell J (2013) Safe and secure remote control for the Twin Radio Telescope Wettzell. In: Zubko, N.; Poutanen, M. (eds.) *Proc. 21st meeting of the European VLBI Group for Geodesy and Astrometry*, 25–28, Finnish Geodetic Institute.

Neidhardt A (2017) Applied Computer Science for GGOS Observatories. Communication, Coordination and Automation of Future Geodetic Infrastructures. ISBN 978-3-319-40137-9. Springer International Publishing Switzerland.

Lösler M, Lossin T, Neidhardt A, Lehmann R (2017) Untersuchung zur automatisierten Bestimmung des IVS-Referenzpunktes am TWIN Radioteleskop Wettzell. QUCOSA (Quality Content of Saxonia), HTW Dresden, QUCOSA.

Ruszczyk C (2016) First Transatlantic VGOS Fringes. In: D. Behrend, Kyla Armstrong (eds.). *IVS Newsletter*, Issue 45.

The Jumping Jive Monitoring Work Package: Centralized System Monitoring and Automation as key Feature Also for VGOS

A. Neidhardt, A. Szomoru, M. Schönberger, J. Bachem, K. Kirschbauer, U. Hugentobler, E. Barbieri

Abstract 12 institutes from 8 different countries have teamed up in the JUMPING JIVE project, which was awarded with nearly 3 million Euro by the Horizon 2020 Framework Program of the EU for the next 4 years. The project is led by JIVE, the Joint Institute for VLBI ERIC, located in Dwingeloo (the Netherlands). The Technical University of Munich at the Geodetic Observatory Wettzell participates to this project integrating monitoring systems for global VLBI interfaces. This work might have a relevant impact to the VGOS operations, because it is the first founded implementation with a focus on centralized structures for VLBI networks. Monitoring systems and remote control abilities will be evaluated to find common interoperability. It will adapt existing software for integration into a central infrastructure.

Keywords Monitoring, control, infrastructure

1 Introduction

The importance of seamless auxiliary data grows to improve data quality and to reduce downtimes of VLBI networks. Growing numbers of globally distributed radio telescopes, real-time possibilities and remote abilities additionally require a central monitoring, overview and failure management to deal with distributed requirements. The Technical University of Munich (TUM) and the Wettzell Observatory can take over a leading and connecting role in this field, because techniques to deal with remote operations and monitoring of VLBI telescopes have been developed there over almost a decade now.

As scientists of JIVE ERIC also see the advantages and necessity to improve the global infrastructure of globally distributed networks as one of the key feature in the future, they joint together as one of 12 institutes for a new EU-funded project. The TUM is partner in the work package 8 "Global VLBI interfaces", where centralized monitoring and control should be established. Because similar aspects are also relevant for future VGOS networks of the IVS, integrations and implementations in this field offer a suitable synergy.

Alexander Neidhardt · Urs Hugentobler · E. Barbieri
Technische Universität München, Forschungseinrichtung Satellitengeodäsie, Geodätisches Observatorium Wettzell, Sackenrieder Str. 25, DE-93444 Bad Kötzting, Germany

Arpad Szomoru
Joint Institute for VLBI ERIC, Postbus 2, NL-7990 AA Dwingeloo, The Netherlands

M. Schönberger · J. Bachem
Federal Agency for Cartography and Geodesy, Geodätisches Observatorium Wettzell, Sackenrieder Str. 25, DE-93444 Bad Kötzting, Germany

K. Kirschbauer
Ostbayerische Technische Hochschule Regensburg, Prüfeninger Str. 58, DE-93049 Regensburg, Germany

2 Joining up Users for Maximising the Profile, the Innovation and the Necessary Globalisation of JIVE (Jumping JIVE) and the TUM work package

"Jumping JIVE" (see the logo in Fig. 1) is funded with 3 million Euro by the European Union from the Horizon 2020 Framework Program for 4 years. The project is led by JIVE ERIC. 12 partners from 8 different nations work in 10 work packages to establish the possible infrastructure for future VLBI observations. Projects like the Square Kilometer Array (SKA) or upcoming new antennas in Africa (African VLBI Network (AVN)) and all around the world open new possibilities for VLBI. Further partnerships with countries in such regions are suitable and should bring European and international experts together to define the technical innovations based on scientific requirements. New techniques, the Low Frequency Array (LOFAR) or other new telescopes need to be integrated into existing networks and common analysis processes. Besides astronomical research, geodetic and satellite tracking capabilities are valuable to use existing systems for geoscience or space science (Neidhardt, 2017a).

Fig. 1: The logo of the EU-funded project "Jumping JIVE".

The team of the TUM is partner for the aspect of global VLBI interfaces in work package 8 together with the Chalmers University and led by JIVE ERIC. The work package consists of two tasks: re-factoring of legacy scheduling software and remote access and control. TUM's focus lays on the second task. One aspect here is the evaluation of existing monitoring and control software. The second aspect is the integration of suitable packages into a centralized infrastructure for astronomical and geodetic VLBI. The second part is separated into remote monitoring of operational, diagnostic, and analysis data and a real remote access to control single parameters (see Fig. 2). But remote control is limited to administrative and security permissions, so that it will be difficult to establish a single operation center. Therefore, the focus will be on collecting monitoring data, a suitable presentation and an essential failure and alert management.

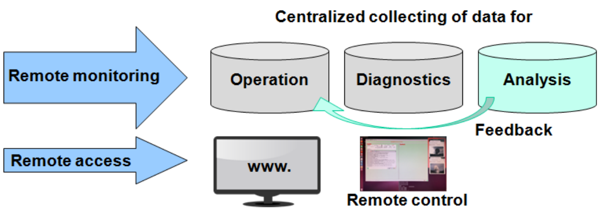

Fig. 2: Active remote access and passive monitoring of data for operation, diagnostics and analysis.

3 Monitoring software which is used or planned for VLBI

The collection and evaluation of existing and possible future monitoring tools was recently finished (see Neidhardt (2017b) for the following parts). The report collected known tools used or planned in the VLBI community. It separates between pure passive monitoring environments and software for active operation control. The evaluation of the software is based on an individual, qualitative estimation, which is represented by a rating using quantitative numbers.

Used criteria were:

- Industrial importance
- Open source
- Use for VLBI
- User community
- Developer community/ Size of developer team
- Readiness for production and release policy
- Community support
- Documentation
- Platform support (Linux for central server; also others for data provider)
- Simplicity to install
- Simplicity to use for non-specialists
- Simplicity to extend with own parts
- Supported techniques/protocols for the use in VLBI
- Web based access possibilities
- Usability for distributed VLBI networks
- Coherent design and use of programming languages
- State-of-the-art techniques
- Access control
- Maintainability and possibility of migration
- Future relevance
- Individual notes

Evaluated monitoring tools were:

- "MoniCA" or "openMoniCA" (Australia Telescope National Facility and AuScope geodetic VLBI telescopes): MoniCA is a Java-based graphical application for viewing real-time and archival monitor data. It was developed for the Australia Telescope National Facility by CSIRO and is an open-source project.
- ZABBIX & SysMon (Wettzell Observatory): Zabbix is an open-source software written by Alexei Vladishev for the monitoring of networks, applications, services, servers, and network hardware. It uses a databases as data archive. SysMon is the Wettzell implementation of a simple monitoring software without graphical output. It is a consequent implementation of the suggestions from the

White Paper of the IVS Monitoring and Control Infrastructure (MCI) group. A description can also be found in Neidhardt (2017).

- Telegraf - InfluxDB - Grafana (TIG) (NASA FS): TIG uses loosely coupled software packages to provide a system for collecting, storing, processing, and visualizing time-series data. The use of TIG for VLBI was presented first at the Technical Operations Workshop at Haystack, USA 2017.
- Radboud Radio Lab VLBI monitor (EVN, mm-VLBI): The VLBI Monitor code is open source since Feb. 2nd, 2016, and was developed for the Event Horizon Telescope. It is a mixture of different Web-based utilities.
- Monitoring and Control Infrastructure MCI (MIT Haystack Observatory): The Monitoring and Control Infrastructure (MCI) group was founded, which wrote a white paper defining the goals and implementations of a centralized monitoring system. MIT MCI is a very individual development for the US-VGOS antennas using Python programs.
- Industrial monitoring tools (Nagios, Zabbix, etc.): There is a bunch of industrial monitoring tools, which are all similar and focus on monitoring of computers, servers, and networks. An internal study at the Wettzell observatory found Zabbix as the most useful for observatory needs.
- SKA Telescope Manager (SKA): SKA developes a completely individual system, where no information can yet be found.
- Individual Linux scripts: There are several individual and specific monitoring scripts and programs, which do individual tasks.
- Goddard Mission Services Evolution Center (GMSEC) Architecture: The GMSEC middleware or architecture is currently under development by the NASA, Goddard Space Flight Center and will be used by different NASA projects especially for satellite missions. It currently plays no role for VLBI.

The evaluation of the above environments came to the results that the most suitable and valuable packages are ZABBIX & Sysmon, other industrial monitoring tools, TIG, and partly MoniCA. A central infrastructure must at least offer interfaces for these packages to inject monitoring data. The central presentation on a Web page can be realized with only one of the packages. Because of long experience with ZABBIX at the Wettzell observatory, ZABBIX is planned to be used as presentation layer.

Evaluated tools for VLBI remote control, operation and automation were:

- e-RemoteCtrl (Wettzell, O'Higgins, AuScope, partly Ny-Ålesund and Hartebeesthoek, tested for TIGO in Chilé): The work for e-RemoteCtrl started in the year 2008/2009 at the Wettzell observatory to control the Antarctic telescope at O'Higgins. It was extended within the EU-funded project NEXPReS (see Neidhardt (2013)) and during a research exchange to the University of Tasmania, Hobart. The software is written in C/C++ under the GNU Lesser license and available in the version of 2014/2015 using wxWidgets 2.8.
- Dynamic Observation (AuScope tests): The software is a test setup by the AuScope network in Australia and Tasmania to treat each antenna as a dynamic resource. An operation center gets feedback from the antennas and creates new observation schedules for the coming period of 15 minutes. The software is a combination of scripts written in different programming languages.
- Remote control and monitoring of e-VLBI experiments at JIVE ERIC: During an e-VLBI run the correlator requires direct access to specific equipment at the stations for real-time control and monitoring. It is a list of tools to support these needs.
- SSH/VPN-tunnels to or VNC/Remote-desktop of the NASA Field System PC: These are techniques known from home or business PCs to forward desktops or to do a remote login on remote computers.

The evaluation of the environments described above came to the results that the most suitable and valuable packages are the single data server of the e-RemoteCtrl software on the Field System PC or the complete e-RemoteCtrl software, because it is developed with the focus on VLBI remote tasks and security issues. A disadvantage is the missing upgrades. All remote control tools suffer from individual regulations at the observatories, so that there is no wide acceptance. Therefore, dynamic observation might play a big role in the future, because the control stays at the observatory and updates just concern schedules. It is an interesting aspect, see Lovell (2016).

4 A central infrastructure

The central infrastructure finally should consist of two centers: a main center at JIVE ERIC in Dwingeloo and a center at the Wettzell observatory. The center at Wettzell can also be used for IVS needs. The data are propagated from software at the telescopes to both centers. The data center consists of two parts: a real-time monitoring tool based on ZABBIX/SysMon and a file archive for historic data on a separate Web server. The possible hard-

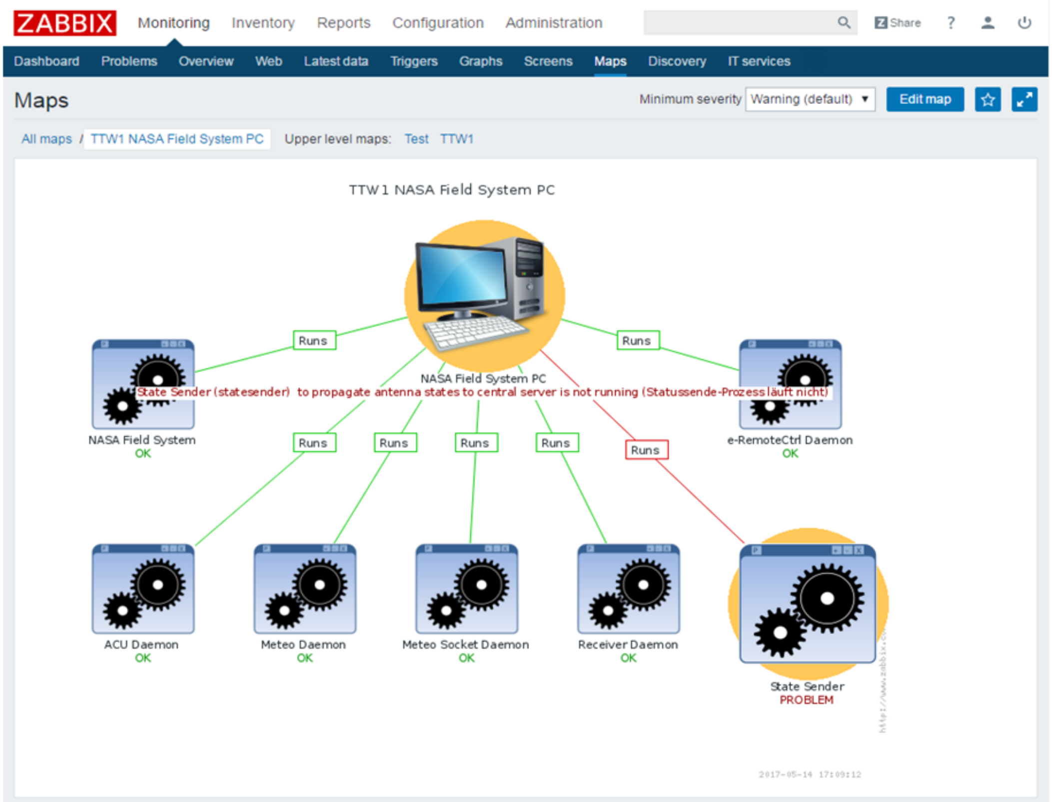

Fig. 3: A possible ZABBIX map for the NASA Field System PC with interactive links to following maps of the subsystems and the propagation of alerts.

ware and the integrated software is currently under test at the Wettzell observatory for laser ranging and VLBI. The used software is publicly available and can also be installed at the observatories (see Neidhardt (2017c)).

The central design of the Web presentation is based on a hierarchy of ZABBIX maps (see Fig. 3). The top level starts with a world map showing all monitored antennas. There can be a world map for each individual network situation or the world map can dynamically be changed. The maps for the antennas are static. The lowest layer consists of one screen for each individual device/item. The screen combines graphs and other graphical elements, e.g. to show alert states (see Fig. 4). It is possible to zoom in or out just by selecting the time interval.

The installed software at the telescope can be an individual script, a ZABBIX agent or in best case the e-RemoteCtrl sender. It already supports the data injection to SysMon. It is also planned to upgrade the graphical client to wxWidgets 3.0 and to re-write the state machines to improve the timing for very remote sites. There are also plans to integrate it into the NASA Field System as an add-on.

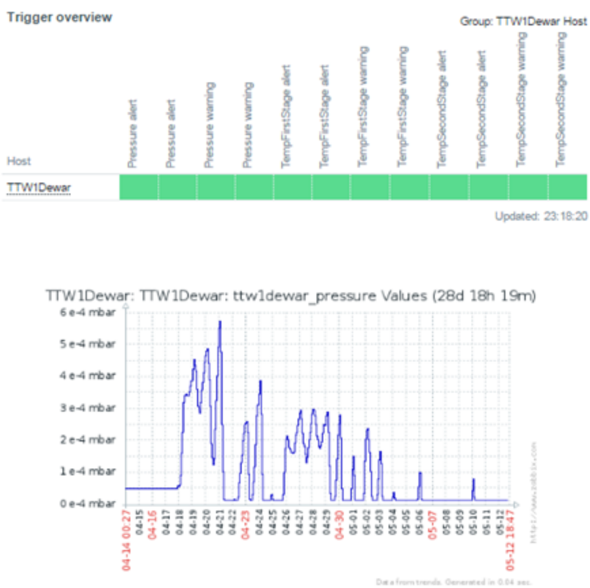

Fig. 4: Possible graphs and displays on a ZABBIX screen to present alert levels and trends of the collected values.

5 Conclusion and participation

The installations and adaption of the system are still under progress. Nevertheless, VLBI stations will be allowed to send in monitoring data soon. A first attempt focus on already available data sets from the NASA Field System, which can be propagated by sending standardized files via Secure Copy (SCP) to the test server of the Wettzell center. If the tests are successful, a version will be installed at JIVE ERIC.

References

Lovell J, Plank L, McCallum J, Shabala S, Mayer D (2016) Prototyping Automation and Dynamic Observing with the AuScope Array. In: D. Behrend, K. Baver, K. Armstrong (eds.) *International VLBI Service for Geodesy and Astrometry 2016 General Meeting Proceedings - "New Horizons with VGOS"*, National Aeronautics and Space Administration, Goddard Space Flight Center.

Neidhardt A, Ettl M, Mühlbauer M, Kronschnabl G, Alef W, Himwich E, Beaudoin C, Plötz C, Lovell J (2013) Safe and secure remote control for the Twin Radio Telescope Wettzell. In: N. Zubko, M. Poutanen (eds.) *Proc. 21st Meeting of the European VLBI Group for Geodesy and Astrometry*, 25–28, Finnish Geodetic Institute.

Neidhardt A (2017a) Globale Infrastruktur zur Beobachtung des Weltalls. In: TUMcampus. Ausgabe 2, https://www.tum.de/fileadmin/w00bfo/www/TUMcampus/2017_2/2017_2_TUMcampus.pdf.

Neidhardt A (2017b) Evaluation of software packages (for system monitoring). Deliverable 8.4. 730884 "JUMPING JIVE" H2020-INFRADEV-2016-2017/H2020-INFRADEV-2016-1.

Neidhardt A (2017c) System Monitoring Topics. Notebook of the TOW 2017. http://www.haystack.mit.edu/workshop/TOW2017/files/Seminars/sysmon_notes.pdf.

Neidhardt A (2017d) Applied Computer Science for GGOS Observatories. Communication, Coordination and Automation of Future Geodetic Infrastructures. ISBN 978-3-319-40137-9. Springer International Publishing Switzerland.

VGOS 1.1: A DBE Opportunity and Data Transmission Challenge

B. Petrachenko

Abstract The basic technical specifications for VGOS have not changed for a decade; they were presented in detail in 2012 at the VLBI2010 Workshop on Technical Specifications at Bad Kötzting, Germany. In the interim, circumstances have changed sufficiently in two areas to warrant a review and possible upgrade of the specifications. First, advances in Digital Back End (DBE) capabilities make it possible to envision a frequency scheme whereby any output channel can be selected from anywhere in the VGOS 2 – 14 GHz input range, as opposed to being restricted to four 1 GHz bands. This is desirable to mitigate some the negative impacts of RFI and source structure, the two dominant risk factors for VGOS. Second, there is a strong desire on the part of many stations to transmit data to the correlator via the internet as opposed to via physical transport of removable media. This poses a challenge at existing correlators where anticipated input data rate capabilities do not match data production rates at the stations. New, more distributed, correlator models are being considered.

Keywords Continuous Frequency DBE, Distributed Correlator

1 Introduction

The technical specifications for the VLBI Global Observing System (VGOS) were established about a decade ago (Niell et al., 2006; Petrachenko et al., 2009). The most important parameters are summarized below:

- SEFD: less than 2500 Jy.
- Azimuth and elevation slew speeds: 12°/s and 6°/s respectively.
- Polarization: dual, either linear or dual circular.
- Input frequency range: 2.2–14 GHz
- Band structure: four 1 GHz bands that can each be placed anywhere in the input frequency range
- Channel structure: 16 32 MHz channels per band for a system total of 64 32 MHz channels.
- Data rate: 16 Gbps
- Data transmission mode: physical shipment of media augmented by some eTransfer for rapid turnaround of results.

These parameters have remained stable over the intervening years with one small exception being that the lower limit of the input frequency range has been raised from 2.2 GHz to 3 GHz to avoid excessive S-band RFI at many stations. However, if possible, stations are still encouraged to include the 2.2–3 GHz range to allow mixed mode observing with legacy stations. This is needed to tie the VGOS network to the legacy network. In addition it has tacitly been assumed that, as technology advances, consideration will be given to increasing the number of channels per band, the total data rate, and the fraction of data transmission that uses eTransfer.

More recently, a DBE opportunity and data transmission challenge have stimulated thoughts of more profound changes to the VGOS system. Specifically, advances in digital technology have enabled the design of DBEs with bandwidths large enough to contemplate continuous coverage of the full 3–14 GHZ input range; and the combination of a desire on the part of many stations to eTransfer all data to the correlator and limited input bandwith at existing correlators has motivated a reconsideration of the case for distributed correlation.

2 Continuous Frequency Coverage

Advances in FPGA and sampler technology make the development of DBEs with IF bandwidths greater than 1 GHz practical and economical. Already two units of this type are available within the IVS community. They are the DBBC3L developed by Gino Tuccari, which in-

B. Petrachenko
Natural Resources Canada, 588 Booth St, Ottawa, Ontario, Canada

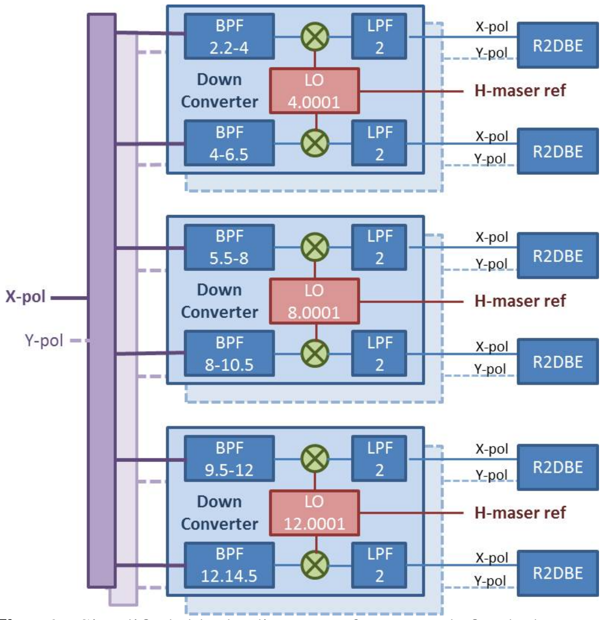

Fig. 1: Simplified block diagram of proposed fixed down-converters for an R2DBE-based system.

cludes eight single polarization IFs, each with 4 GHz input bandwidth and the R2DBE, developed at Haystack Observatory/MIT, which handles two 2 GHz IFs, nominally one per polarization. The full 2.2–14 GHz VGOS input range can be handled cost effectively either by a single 8-IF DBBC3L or six R2DBEs.

Continuous Frequency Coverage has a number of benefits:

- **Down conversion is simpler, less expensive and more phase stable.** The original VGOS spec requires that each of the four 1-GHz bands be selected anywhere in the input range using up/down converters (UDCs). A UDC is a complex circuit using two frequency conversions (one up and one down), two LOs (one of them with a 10 GHz frequency range), and a significant amount of circuitry operating above 30 GHz. In contrast, since continuous frequency coverage operates with fixed contiguous bands, there is no need for flexible frequency selection [In fact a small amount of flexibility is still required to ensure that channels can be aligned.] and hence fixed down converters can be used. See Figure 1 for a simplified block diagram of proposed fixed down-converters for an R2DBE-based system. Each fixed down converter requires only one frequency conversion, one LO and no circuitry operating above 14 GHz. For these reasons, down conversion in a continuous frequency system is simpler, less expensive, and more phase stable.
- **Treatment of RFI is improved.** With a four-bandx system, it is essential for phase connection that no band is made unusable by RFI. Hence, it is necessary that four clear 1-GHz bands exist in the intersection of RFI from the entire network. Unfortunately, in the real world, it is not likely that the remaining clear frequency bands are also at locations that are optimal for resolving phase and for separation of the geometric and ionosphere delay. In contrast, since the frequency allocation is so wide for continuous frequency mode, moderate losses of spectrum due to RFI can be tolerated since the uncontaminated part of the band on each baseline is in general significant enough to easily extrapolate phase across the gaps caused by RFI.
- **Fringe detection is improved, especially in the presence of spurious phase trends.** In a four-band system there are large gaps between the bands. Determining the correct delay observable requires that phase between the bands be bridged without error. Since there are no gaps in a continuous frequency system (or only minimal gaps at RFI locations) this problem is almost entirely eliminated. Furthermore, in real systems there are spurious phase trends resulting from uncalibrated instrumental effects or source structure. Simulations show that, in the presence of these spurious phase trends, the continuous frequency mode is more than a factor of two more likely to come up with a sensible delay than a four-band system.
- **Higher output data rates can be achieved.** With a four band system, the highest output data rate that can efficiently be achieved is 32 Gbps. With a continuous frequency system, because of the larger available bandwidth, output data rates as high a 64 Gbps or even 88 Gbps can be achieved. Higher data rates have the benefit of enabling either shorter times to reach SNR targets or lower flux limits, which in turn enable larger source lists and hence better support of the ICFF.
- **Source structure in three dimensions may be possible.** With the original four-band system, source structure could still be treated in two dimensions. In other words four two dimensional maps could be made, one for each band, and then inter-band implications could be considered in a separate step. With the new continuous frequency system, it is more natural (especially since overall SNR is low) to treat source structure in three dimension. In a direct sense the third dimension would be frequency but under some often realistic conditions frequency can further be considered synonymous with depth. To the best of my knowledge this is uncharted territory and hence presents both an opportunity and a challenge. Other broadband systems, e.g. eVLA and BRAND EVN might

also benefit from exploration of three dimensional mapping or modelling.

Clearly the continuous frequency mode for VGOS is now feasible and cost effective. Furthermore it has many benefits. It is strongly recommended that all new systems be built with continuous frequency capability. Because of their nature, these systems will be backward compatible with the four-band systems and will open a door for future improved operations.

3 Distributed Correlation

When VGOS was first conceptualized, it was recognized that high data rates and rapid source switching would require the trasmission of vast amounts of data to the correlator. For this reason it was believed that, at the start of operations, the majority of data would be trasmitted physically by shipping record media while a smaller subset, required for rapid turn-around of initial products, would be transmitted using eTransfer.

However, with the operational phase of VGOS nearing, shipping of media no longer appears to be a univerally valid assumption. At least one station has no plans to physically ship media to the correlator and a significant number of other stations (that have exerienced the convenience of using eTransfer for legacy operations) have a strong preference to continue to use eTransfer for VGOS as well. In fact a significant number of stations have 10 Gbps eTransfer capability, which is more than enough for full VGOS 24/7 operations.

At the same time, the eTransfer capability at other stations falls far short of the VGOS requirement. Hence at the start of operations, a mix of physical shipment of media and eTransfer will be needed, much like current legacy operations. The main problem with this model is that the internet bandwidth at the correlators, while adequate for legacy operations, falls far short of the requirement for full VGOS operations. All the same, this model will work provided that the number of VGOS stations using eTransfer is strongly limited at the start of operations. With time this problem may resolve itself if internet bandwidths at the correlator increase at the same rate as VGOS operational requirements.

An alternate approach is the use of distributed correlation. Although not new this idea is a good fit to the current circumstance. Its implementation is made more realistic by the comparatively recent advent of software correlators, which require only standard computing resources and no special purpose VLBI hardware. As a result any location that has computing resources and a good internet connection can participate as a node in a distributed correlator. Examples include computing resources in the cloud, super computers, the computer centres at institutes, computer resources at stations with good internet connections, or existing IVS correlation facilities.

The idea is that small chunks of data, perhaps in units of one scan, can be shipped to a particular dis-

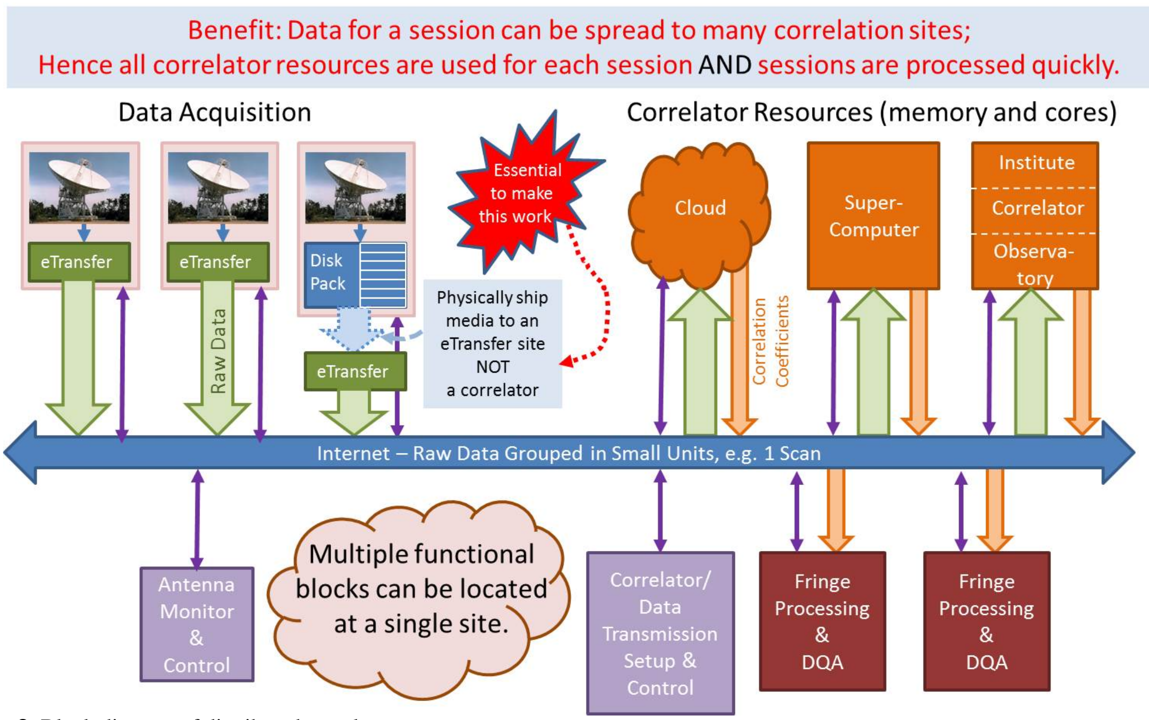

Fig. 2: Block diagram of distributed correlator.

tributed node with a control computer specifying to which node to ship the scan. This makes it possible to focus all correlator resources on a single session so that it can be processed as quickly as possible.

The main drawback of the distributed correlator model is that all stations must have an eTransfer capability. If even one station needs to physically ship media to a correlator then all remaining stations must also eTransferred their data to that correlator. This is effectively a return to the monolithic correlator model. Fortunately, there is a way around this problem. Stations that cannot eTransfer data can physically transport their media (as quickly as possible) to locations (hopefully not too far away) that *do* have good eTransfer capability. This will effectively act as if the station is capable of eTransfer, albeit delayed by a day or two. Hence, until all stations have cost effective eTransfer capability, this expedient can salvage the distributed correlator model hence enabling the most efficient and rapid production of final results. See Figure 2 for a simplified block diagram of a distributed correlator

It is still too early to tell whether increases in internet bandwidth at current IVS correlators will match the expansion of VGOS operational requirements. However, it is recommended that these two rates be monitored carefully to ensure that correlation does not become a serious VGOS bottleneck. At the same time distributed correlation should be studied and perhaps developed since, in the long run, it provides an attractive alternative for VGOS.

References

Niell A E, Whitney A, Petrachenko B, Schlüter W, Vandenberg N, Hase H, Koyama Y, Ma C, Schuh H, Tuccari G (2006) VLBI2010: Current and Future Requirements for Geodetic VLBI Systems. In: D. Behrend and K. D. Baver (eds.), *IVS 2005 Annual Report*, NASA/TP-2006-214136, 13–40.

Petrachenko B, Niell A E, Behrend D, Corey B, Böhm J, Charlot P, Collioud A, Gipson J, Haas R, Hobiger T, Koyama Y, MacMillan D, Malkin Z, Nilsson T, Pany A, Tuccari G, Whitney A, Wresnik J (2009) Design Aspects of the VLBI2010 System: Progress Report of the IVS VLBI2010 Committee. In: D. Behrend and K. D. Baver (eds.), *IVS 2008 Annual Report*, NASA/TP-2009-214183, 13–67.

An IVS Pilot Study for Distributed Correlation in the VGOS era

A. Bertarini, G. Tuccari, R. Haas, J. McCallum, S. Weston

Abstract In this study we explore the feasibility of distributed correlation as a potential VGOS correlation architecture. Specific challenges are that the amount of data to be transferred to the correlator is going to increase enormously, hence also the correlation time and the capacity of the RAIDs at the correlators to store the data will increase. This study will identify whether distributing the correlation of one experiment among more correlators will help to keep the latency from observation to analysis within a reasonable time; now the guideline set by the IVS from observation to analysis should not be more than two weeks.

Keywords Correlation, VGOS, Geodetic VLBI

1 Introduction

In this study we present the first test made toward the goal of distributed correlation. The general idea of this study is to send segment of data to multiple correlators; one main correlator receives the data at the beginning and the end of the experiment for clock and drift adjustment, prepares the vex and v2d files required for the correlation within DiFX and distributes them to the branch correlators that then correlate their allocated segment of data within the experiment, ideally all using the same DiFX version. After the correlation the branch correlators send the visibilities to the main correlator for fringe fitting and further geodetic processing.

Alessandra Bertarini
Reichert GmbH und Bundesamt für Kartographie und Geodäsie
Bonn, Germany

Gino Tuccari
Istituto di Radioastronomia, Italian National Institute for Astrophysics, Italy

Rüdiger Haas
Chalmers University of Technology, Onsala Space Observatory, SE-439 92 Onsala, Sweden

Jamie McCallum
University of Tasmania, Private Bag 37, 7001 Hobart, Australia

Stuart Weston
Institute for Radio Astronomy & Space Research, AUT University, Auckland, New Zealand

2 Background

The VGOS requirements forcasted for 2020 are summarized in Table 1.

Table 1: VGOS requirements (forecast for 2020) (Petrachenko et al., 2015).

Observation cycle of 1 source	30 s
Data rate	16 Gbps
Session length	24 h/day
Periodicity	7 days/week
Number of sites	24

The expected amount of data per day, that a VGOS correlator will have to handle is about 1000 TB /day hence huge in comparison to the data arriving at the correlator for the legacy system which is about 30 TB/-day for a 10 station 512 Mbps R1 session. Some consequences are as follows.

- The correlators need to buy new RAIDs for storage.
- There is a need of more bandwidth to and from the correlators.
- IVS needs more VGOS correlators.
- Maybe use cloud computing.
- Maybe use distributed correlation.

In this study we begin to explore the distributed correlation.

3 Distributed correlation

For the pilot test presented here, we selected Bonn to be the main correlator and Hobart (Tasmania), Onsala (Sweden) and Workwarth (New Zealand) as branch correlators. We agreed to use the IVS experiment R1.785 because R1.785 was observed at 256 Mbps, and we wanted to start with a low data rate to shorten the electronic data transfer.

Each of the branch correlators received 1 hour of data from the 10 stations involved in R1.785, i.e. Hobart, HartRAO, Ishioka, Katherine, Ny-Ålesund, Onsala, Shanghai, Warkworth, Wettzell and Yarragadee. Using the clock information provided by the main correlator, each branch correlator correlated the assigned hour of data, using identical v2d and vex files provided from the main correlator. After the correlation the branch correlators sent the visibilities to the main correlator for further processing. In parallel, the main correlator correlated all the experiment for regular submission to the data centers. Then the results produced by the branch-correlator processing and the main correlator can be compared and the strategy can be evaluated (still pending).

4 Does distributed correlation work?

We cannot yet give a definitive answer since the project just started and requires more tests, but we can say that

- it works best if all the participating stations transfer their data electronically. If using modules, the stations have to spread the data over multiple modules: one per correlator involved,
- each station should have enough storage in the form of RAIDs or FlexBuff that can be accessed simultaneously by all the correlators,
- the main and branch correlators should have the same DiFX version,
- this study is DiFX-centric, but not all IVS correlators use DiFX. This implies that the main correlator should master all the various file formats used by the various correlator architectures, or the branch correlators should be able to convert the file produced by the main correlator into their control format.
- we are unsure whether this system would work for military-based institutions,
- the correlator reliability drops with the power of the number of the correlators involved. E.g. reliability $\sim \eta^{Ncorr}$, if $\eta = 0.9$ and $N = 5$ then we expect 59 % successful correlation.

5 Future planning

We need to continue with R1.785 analysis to see whether the final results are consistent with those obtained from the correlation performed fully at Bonn. We need to perform more structured tests adjusting the number of correlated hours per branch correlator to be proportional to the number of computing nodes and bandwidth available at the branch correlators. Also we need to check whether the latency from observation to analysis stays within 15 days.

Acknowledgements

We thank S. Casey and R. Hammargren from Onsala, L. La Porta from Bonn correlator, U. Michiko from GSI, C. Plötz from BKG Wettzell, J. Quick from HartRAO, M. Siebert from NMA and B. Xia from Shanghai Astronomical Observatory for their help and assistance during this test.

References

Petrachenko B, Bertarini A, Alef W, Behrend D, Cappallo R, Hase H, Ma C, Niell A, Nothnagel A, Zhang X (2015) VGOS Data Transmission and Correlation Plan. In: K. D. Baver, D. Behrend, K. L. Armstrong (eds.) *International VLBI Service for Geodesy and Astrometry 2014 Annual Report* NASA/TP-2015-217532.

Towards Cloud Correlation of VLBI Data

S. Weston, S. Gulyaev, B. Kim, A. Litchfield, D. Hall, J. Curtis, T. C. Yun, A. Ruthven, G. Davies, B. Lagos, D. Christie

Abstract Currently VLBI data is correlated in several international Correlation Centres; they receive data from individual radio telescope stations either on diskpacks via regular mail service or via fibre using e-transfer mode. The latter is often limited by connectivity of existing correlation centres, which can dramatically slow down the turnover of the data. This work reports on the initial steps towards development of a cloud correlation infrastructure for geodetic VLBI data. Initially a blade server at the Auckland University of Technology (AUT) campus using Virtual Machines (VMs) enabled the emulation of a cloud server. The network was provided by Research and Education Advanced Network New Zealand (REANNZ). Use was made of real VLBI data to emulate data transfers from remote locations and to provide a meaningful benchmark dataset for correlation. This was correlated with a speed-up factor of 0.8 using the DiFX software correlator. In partnership with the New Zealand office of Catalyst IT Ltd we moved this project into their Commercial Cloud and report on the first correlation of a VLBI dataset in a true commercial cloud environment. Using a new paradigm of multiple head nodes we reached a speed-up factor approaching 2.5, therefore, in principle, allowing real-time cloud correlation.

Keywords VLBI, radio astronomy, software correlation

Stuart Weston · Sergei Gulyaev · Bumjun Kim · Alan Litchfield
Institute for Radio Astronomy & Space Research, AUT University, Auckland, New Zealand

Dylan Hall · Jamie Curtis
REANNZ, New Zealand

T. Charles Yun
School of Information, University of Michigan, Ann Arbor, MI, USA

Andrew Ruthven · Glyn Davies · Bruno Lagos · Don Christie
Catalyst IT Ltd, New Zealand

1 Introduction

Over the previous decade with the pace of development in commodity computing it became possible to process VLBI data on commercially available computing hardware. This enabled the development and introduction of software correlation solutions with Japan software correlator (Hirabayashi et al., 2000), DiFX (Deller et al., 2007; Deller et al., 2011) and SFXC (Keimpema et al., 2015) software correlators. DiFX has become the correlator of choice for the International VLBI Service for Geodesy and Astrometry (IVS) (Nothnagel et al., 2016).

As broadband networks have improved, more and more stations have moved to transferring VLBI data via the network, and thus can be transferred anywhere. But correlation is still performed on a large and usually dedicated server at one of a small number of dedicated sites. We ask; is the total cost of ownership (Hardware, Network, Infastructure, Staff) of large systems at dedicated sites for correlation a cost effective use of budgets? Where compute and storage can be provided on demand, is the cloud a cost effective alternative?

In this work we present an implementation of the DiFX software correlator in a commercial cloud computing environment. Described are the first tests of cloud correlation undertaken using real data from the network of the southern hemisphere radio telescopes. Results are provided for performance comparisons for several experiments correlated on dedicated hardware and in a commercial cloud environment.

2 Datasets

For environment comparison, two data sets have been used. The first was a two antenna observation using the Warkworth 30 m (Woodburn et al., 2015) and the Hartebeesthoek 26 m at 6.7 GHz used for fringe testing in February 2016 with PKS 0537-441. This was recorded at both antennas on a Mark 5 (Whitney, 2003) with sixteen 16 MHz bands at 2 bit.

For the second data set Australia Telescope National Facility (ATNF) Correlator kindly provided a subset 1.5 hours of the raw dataset for experiment v534a which used six antennas (15 baselines) of the Long Baseline Array (LBA) at 6.642 GHz in March 2016. This was recorded with an LBA hard-disk recording system (LBADR) (Phillips et al., 2009) at Parkes, Mopra, ATCA, Hobart and Ceduna, and a Mark 5 at Warkworth 30 m with four 16 MHz bands at 2 bit.

3 Environments

In this section, the environment and data used to test cloud correlation in New Zealand are described.

3.1 Network

The data were transferred from radio telescopes to the cloud using the REANNZ network (REANNZ, 2016). Network capacity to and from New Zealand is currently now 100 Gbps, within Auckland City exists a 100 Gbps ring circuit and to the University 10 Gbps is available. At very short notice 10 Gbps was facilitated between REANNZ and Catalyst IT Limited.

3.2 Cloud Environments

The New Zealand cloud computing capability was provided to us by AUT (Local Cloud) and by Catalyst IT Limited (Catalyst IT Limited, 2016). The use of Virtual Machines (VMs) is now well established in industry for development and production services. Once a VM is configured for the requirements it is easy to package up and distribute and replicate. Using snapshots allows an easy and fast (minutes) method to replicate more VMs but also provides the ability to move between different snapshots and hence the states of VMs. Performance loss by using VMs vs a Native Operating is minimal these days.

3.2.1 Local Cloud

Before using a commercial cloud service for correlation of radio astronomical data, we simulated a cloud-like environment using a local (AUT) research cluster operated by the Service and Cloud Computing Research Lab (SCCRL).

This cluster has been in operation since 2014 and provides a range of researchers and students with a secure platform for development and research projects. The cluster was made available to the LWCC project to build a proof-of-concept.

The cluster has been built to support projects with differing requirements, therefore it has been designed with maximum flexibility in mind, without an emphasis on production values typically found in commercial data centres. Projects can be built on the cluster to suit the requirements of operating systems, software, and additional hardware. On the server VMWare vSphere V5.5 was used.

The use of the cluster was limited to the design and development of the LWCC. It was intended that once the proof of concept had been established (that correlation is achievable in a cloud context and how that may be achieved), the deployment would be transitioned to a different environment that could afford greater levels of service and quality management. To that extent, no adjustments were made to the cluster to accommodate the project.

Following initial set up, expected performance issues were found to be true. While the servers themselves operated speedily, there were bottlenecks occurring on the internal cluster network. This is mainly due to the limited capacity of the internal network interface cards. Another issue was related to immediate storage requirements, that is the ability to temporarily store large volumes of data. To enable large data volume processing requirements, the project team introduced an existing but older model server onto the cluster. The third main issue was having to traverse the university security firewall and proxy system, the university fibre backbone was not sufficient for this project and REANNZ provided a separate switch and configured Virtual LAN (VLAN).

3.2.2 Commercial Cloud

The Catalyst Cloud (Catalyst IT Limited, 2016) is a New Zealand public cloud service. It is designed to make use of free and open source software and generic hardware. The underlying software platform deploying and managing the Catalyst cloud services uses OpenStack and Ceph running on Ubuntu Linux. Where Catalyst has made modifications or written custom software, these have been either contributed back upstream or made available with a free and open source software licence.

The hardware platform is OEM servers made by Intel and using Xeon E5 v4 series CPUs. Each server which runs compute instances (a hypervisor) has two Xeon processors, each of which typically has at least 18 cores where the preference is to provide more cores rather than more speed. With hyper threading enabled this typically provides 72 threads per server. The amount of memory per server is scaled based on the number of cores in the hypervisor; there are typically 512 or 768 GB per hypervisor.

The Catalyst Cloud block storage service is based on Ceph, for building reliable storage systems on generic hardware. The system is designed to be completely distributed, without a single point of failure, scalable to the exabyte level and to be both self-healing and self-managing.

Catalyst block storage servers have a combination of spinning drives and solid state drives. Data is replicated three times on different servers in the same region. This allows for hard drives and servers to fail without loss of data. Write operations always go to solid state first and are flushed asynchronously to spinning drives. The storage servers have a large amount of RAM to allow for caching of data.

All servers within the Catalyst Cloud are networked together using a number of bonded 10 Gbps connections to provide at least 20 Gbps networking, with the storage layer and compute interconnects on separate networks.

4 Results

In this section we present the results of cloud correlation conducted first in a cloud-like environment using VMs and then in an actual commercial cloud environment. To quantify our results, we use the Speedup factor, S, which is normally defined as the ratio of the total observation time and the time taken to correlate these observations:

$$S = \frac{Obs\_Time}{Corr\_Time} \tag{1}$$

In Section 6 we modify this definition.

4.1 Local Cloud

Head node was a c1.c16r8 (16 vCPUs, 8 GB RAM) and the worker nodes were c1.c4r3 (4 vCPUs, 2 GB RAM).

We can see that as VMs (2 cores, 8 threads) are added the correlation of dataset v534a in Figure 1 achieves a maximum speedup of 0.9 at NP= 15.

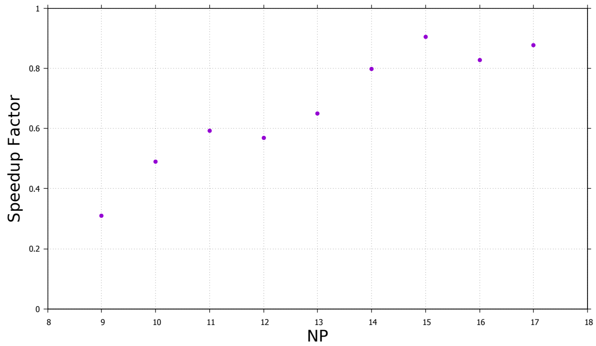

Fig. 1: AUT Blade Server showing Speedup factor vs Number of Processors for experiment v534a.

Associated with Figure 1 is Figure 2, which shows that as we add additional VMs the network bandwidth available for DiFX is being constrained. This is due to network load balancing within the blade server between VMs by VMWare.

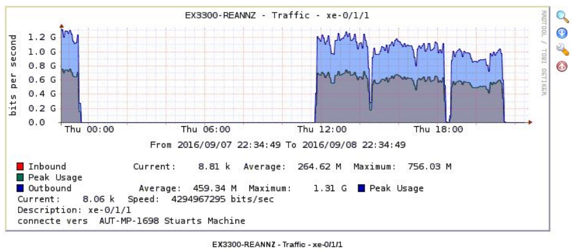

Fig. 2: Showing the network traffic on the local switch as more VMs are added in sync with Figure 1 rerunning correlation of v534a on the AUT Blade Server.

4.2 Commercial Cloud

Figure 3 shows the first fringe obtained entirely within a commercial cloud environment.

Comparing the correlation of HHWA03 using different file systems in Figure 4 we see that only for the minimum number of processors does RAID0 provide any noticable benefit. We appear to reach a plateau at $NP = 8$ in the Speedup factor. For experiment “V534a” in Figure 5 we can see that here we reach a plateau in Speedup factor for NP= 14. Both exhibit a dip in the Speedup factor for a higher NP.

5 A new paradigm with Ansible

The Ansible (ANSIBLE, 2017) library of cloud support modules makes it easy to provision instances, networks,

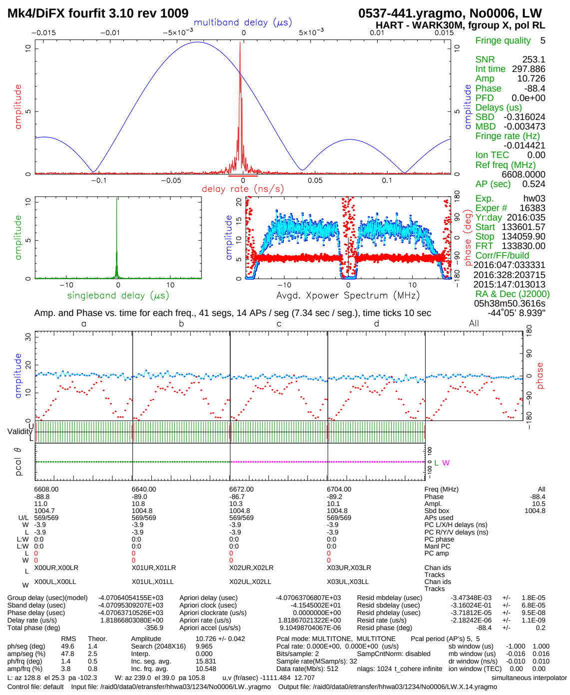

Fig. 3: The first fringe produced entirely in a commercial cloud using DiFX for dataset HHWA03.

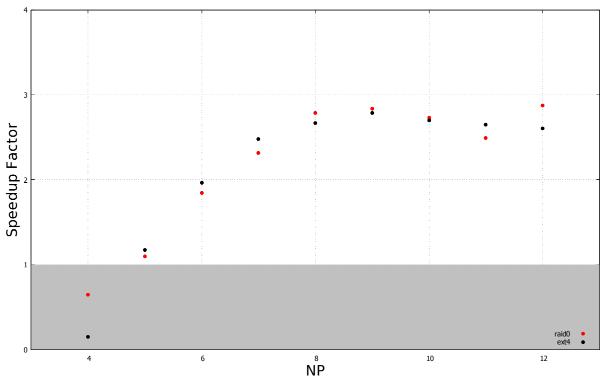

Fig. 4: The Speedup factor vs Number of Processors in the commercial cloud for the HHWA03 dataset using different file systems (RAID0 red dots and EXT4 black dots) in the cloud storage containers.

and complete cloud infrastructure. The simple Playbook language can be used for application deployment and virtualization automation. Ansible ensures cloud deployments work seamlessly across public, private, or hybrid cloud as easily as you can build a single system.

We propose the paradigm where we have a master node coordinating several head to worker node clusters as shown in Figure 6. From scanning the VEX file Ansible has been used to create and deploy the node clusters as required. Another example of this has been demonstrated for geographically distributed correlation, see Bertarini et al. (2017).

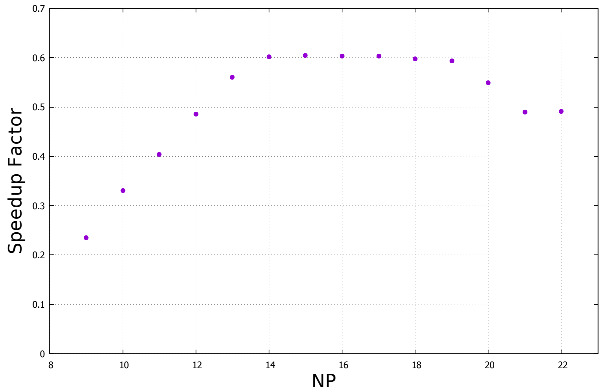

Fig. 5: The Speedup factor of V534a in the commercial cloud vs Number of Processors.

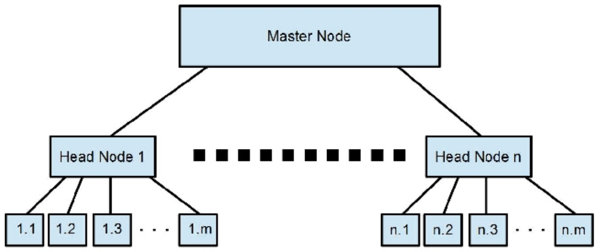

Fig. 6: The proposed DiFX Cloud paradigm cluster

Using Ansible scripts prepared by Catalyst IT Ltd [1] we broke v534a into two sequential time segments. Shown in Figure 7 is the instantaneous speedup for the two jobs on different head nodes running in parallel initiated from the master node. Of interest is the sudden drop in the Speedup factor in Figure 7 at about 0.5 hrs for Head-1, and at a later time of 1.0 hrs for Head-2. As yet we have not determined the cause of this drop in the Speedup factor; without that we would see an overall Speedup of ≈ 2.5.

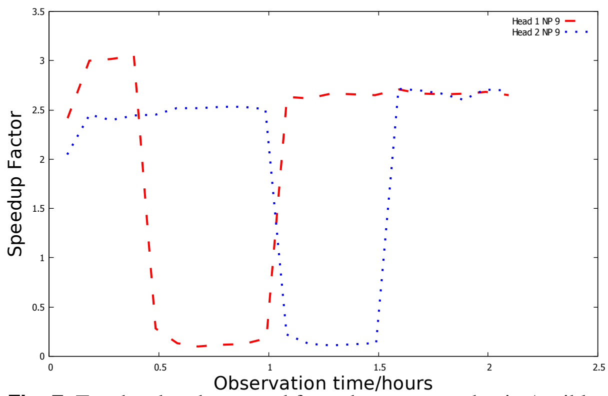

Fig. 7: Two head nodes started from the master node via Ansible - Head 1 in red and Head-2 in blue for the first 2.083 Hours of "V534a".

[1] These scripts are available from the Author

6 Discussion

In the cloud environment, it makes sense to modify the Speedup factor as on each head node the subset of correlation will be processed in different periods of time. Here we use :

$$S^* = \frac{\sum_{i=1}^{n} Obs\_Time_i}{Max(Corr\_Time_i)} \quad (2)$$

where $Max(Corr\_Time_i)$ is the maximum correlation time from the individual head nodes. An example of using Equation 2 is shown in Table 1. The Speedup factor S^* is calculated by dividing the total observation time (4.166 hours) by the correlation time on Head 1 (4.882 hours) according to Equation 2 giving $S^* = 0.853$.

Table 1: Example of a multi-head node speedup using the HHWA03 dataset and Equation 2.

	Head 1	Head 2
Obs Time	2.083	2.083
Corr Time	4.882	4.187
Speedup	0.426	0.497
Speedup*	0.853	

The other extreme is if we assume that as soon as one correlation job finishes the system can immediately proceed to correlate the next job in the sequence, and so we have to report the weighted average speedup of the individual jobs as given in Equation 3 (this came from correspondence on the 28th June 2017 with A. Deller) below:

$$\overline{S} = \frac{\sum_{i=1}^{n} S_i * Obs\_Time_i}{\sum_{i=1}^{n} Corr\_Time_i} \quad (3)$$

where S_i comes from :

$$S_i = \frac{Obs\_Time_i}{Corr\_Time_i} \quad (4)$$

7 Conclusion

For the first time, it has been demonstrated that DiFX can correlate VLBI data in the Cloud using VMs, and using tools such as Ansible the cloud resources required can be scaled on the fly. The Speedup factor achieved shows that real-time correlation is possible and future eVLBI can rely on the cloud correlation paradigm.

8 Acknowledgements

We thank Jonathan Quick for his assistance in operating the Hartebeesthoek 26 m for the fringe test experiment hw03 in February 2016. Also Cormac Reynolds of ATNF for providing part of the dataset for v534a used in this work. The Long Baseline Array and Australia Telescope Compact Array are part of the Australia Telescope National Facility, which is funded by the Commonwealth of Australia for operation as a National Facility managed by CSIRO. This work used the facilities and staff of the Service and Cloud Computing Research Lab (at the Auckland University of Technology) and to whom we are grateful. Also a big thank you to Catalyst NZ Ltd for making the resources available in their cloud infrastructure and providing some consultancy time. Also their quick response in cooperation with REANNZ to facilitate a high speed network link from the NZ research network to their Cloud. Stuart Weston is a recipient of a CSIRO Astronomy & Space Science, Australia Telescope National Facility Graduate Research Scholarship.

References

ANSIBLE, 2017, ANSIBLE, https://www.ansible.com/cloud

Bertarini A, Tuccari G, Haas R, McCallum J, Weston S (2017) An IVS Pilot Study for Distributed Correlation in the VGOS era. In: R. Haas and G. Elgered (eds.), *Proc. 23rd EVGA Working Meeting*, 49–50.

Catalyst IT Limited, 2016, Catalyst Cloud, https://www.catalyst.net.nz/catalyst-cloud

Deller A. T., Brisken W. F., Phillips C. J., Morgan J., Alef W., Cappallo R., Middelberg E., Romney J., Rottmann H., Tingay S. J., Wayth R., 2011, Publ. Astron. Soc. Pac., 123, 275

Deller A. T., Tingay S. J., Bailes M., West C., 2007, Publ. Astron. Soc. Pac., 119, 318

Hirabayashi H., et al., 2000, Publ. Astron. Soc. Jpn., 52, 955

Keimpema A., Kettenis M. M., Pogrebenko S. V., Campbell R. M., Cimó G., Duev D. A., Eldering B., Kruithof N., van Langevelde H. J., Marchal D., Molera Calvés G., Ozdemir H., Paragi Z., Pidopryhora Y., Szomoru A., Yang J., 2015, Experimental Astronomy, 39, 259

Nothnagel A., Artz T., Behrend D., Malkin Z., 2016, Journal of Geodesy, pp 1–11

Phillips C., Tzioumis T., Tingay S., Stevens J., Lovell J., Amy S., West C., Dodson R., 2009, in 8th International e-VLBI Workshop LBADR: The LBA Data Recorder. p. 99

REANNZ, 2016, REANNZ, https://reannz.co.nz/

Whitney A. R., 2003, in Minh Y. C., ed., New technologies in VLBI Vol. 306 of Astronomical Society of the Pacific Conference Series, Mark 5 Disk-Based Gbps VLBI Data System. p. 123

Woodburn L., Natusch T., Weston S., Thomasson P., Godwin M., Granet C., Gulyaev S., 2015, Publ. Astron. Soc. Aust., 32, e017

The Progress of VLBI Terminal and Software Correlator in SHAO

W. Zheng, Z. Renjie, J. Zhang, L. Tong, L. Liu, J. Li, S. Guo, F. Tong, F. Shu

Abstract To meet the requirement of VGOS and deep-space missions, Shanghai Astronomical Observatory (SHAO) has carried out development works on new VLBI terminal and correlator. There are three VLBI terminals under development. The VGOS terminal is for wideband observation and the maximum input data speed is up to 16 Gbps with VDIF output data format. The dedicated deep-space terminal has narrow band observation ability with 1-16 bits quantization. A general purpose software VLBI correlator for space probe tracking, geodesy and astrophysics is under development. It has been applied to CE-3 lander phase referenced VLBI positioning and will be used in Chang'E-5 mission's dual objects same beam VLBI tracking as well as routine IVS data processing. According to several comparison based on geodesy observations, the results of Shanghai software correlator (SCORR) are consistent with DiFX correlator results very well. For the technology research purpose, a prototype terminal based on Roach board and a GPU + CPU software correlator are under development too.

Keywords VLBI terminal, software correlator

1 Introduction

Supported by the China's Lunar Exploration Project (CLEP) Shanghai Astronomical Observatory (SHAO) has carried out development works on VLBI digital baseband converter (BBC) for many years. CDAS (Chinese VLBI Data Acquisition System) is the first generation digital BBC installed at the Chinese VLBI Network (CVN) stations for astronomy, geodesy and deep space observations. It has 4 Intermediate Frequency (IF) channels and it has the maximum 2048 Mbps data rate output with 2-bit quantization capabilities. Due to the different requirements of astronomy, geodesy and deep-space observations, the second generation VLBI backend-CDAS2 platform is designed by SHAO. For weak quasar observations, CDAS can work in the ultra-wide bandwidth with 1 or 2-bit quantization, while in deep-space probe observation case, it can work in the narrow bandwidth with multi-bit quantization.

The Shanghai software correlator (SCORR) was further developed for CLEP, and then it was used in the geodesy project of Crustal Movement Observation Network of China (CMONOC) for monitoring the change of crustal movement, the morphology and change of the gravity field in China. The first generation of SCORR was written in C and Pthread and run on the Multi-processor server. The second generation can be run on the cluster with MPI library, OpenMP. For astronomy and geodesy usages, a conversion program is designed to transfer the special CVN output format to Mk4 format and FITS-IDI format. Mk4 is the input format of Haystack Observatory Postprocessing System (HOPS), a widely-used geodetic data processing soft. FITS-IDI can be used as the input format of AIPS, a widely-used astronomy data processing software. A precision analysis between the SCORR and DiFX shows that SCORR meets the requirement of geodetic data processing and it is competent for IVS data processing (Liu et al., 2017).

Weimin Zheng · Zhu Renjie · Juan Zhang · Li Tong · Lei Liu · Jiyun Li, Shaoguang Guo · Fengxian Tong · Fengchun Shu
Shanghai Astronomical Observatory, Chinese Academy of Sciences, Shanghai 200030, China

Weimin Zheng · Fengchun Shu
Key Laboratory of Radio Astronomy, Chinese Academy of Sciences, Nanjing 210008, China
Shanghai Key Laboratory of Space Navigation and Positioning Techniques, Shanghai 200030, China

2 VLBI Terminal at SHAO

2.1 Geodesy Backend – CDAS2-PFB

The CDAS2 platform contains a CPCI standard card with ADC and FPGAs. It can accept two IF channels,

Fig. 1: CDAS2-PFB modules and the Mark6.

with 512 MHz bandwidth/IF. It also can be connected to record backend through two 10 Giga Ethernet ports.

For VLBI Global Observation System (VGOS) usage, we designed the CDAS2-PFB terminal which consists of four CDAS2 platforms. The Polyphase filter bank (PFB) algorithm and VDIF formatter are implemented. Each platform can be connected to one Mark6 recorder by 10 Giga Ethernet. Figure 1 depicts the CDAS2-PFB module and the Mark6.

Due to the PFB algorithm, the frequency and bandwidth of each channel is fixed. The data flow in each CDAS2-PFB module is showed in Figure 2. There are two independent threads in the FPGA before sent to 10 Giga Ethernet. Each thread converts a 512 MHz bandwidth signal to 16 baseband channels. The data rate for each thread is 2048 Mbps. So each CDAS2-PFB module has 4096 Mbps data rate with VDIF data format. Four modules provide 16 Gbps in total. The Field System computer can control the complete backend, including CDAS2 and Mark6 by Ethernet.

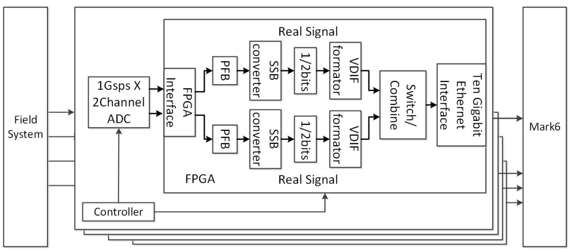

Fig. 2: Schematic diagram of the CDAS2-PFB.

2.2 Deep-space backend – CDAS2-DDC

In deep-space exploration missions, many onboard beacons just emit very narrow bandwidth signals such as the telemetry signals or Differential One-way Range (DOR) signals. In these cases, the narrow band and multi-bit quantization sampling is more suitable than the normal wideband and 1 or 2 bit sampling. In this case, one CDAS2 platform module is enough for the application.

Two IFs of S/X band are connected to CDAS2-DDC backend. The data recorder is a commercial server with 12 hard-disks. Figure 3 depicts the backend on top of the recorder.

In the deep-space applications, the frequency and bandwidth of each channel should be tunable. So the Direct Digital Conversion (DDC) algorithm is adapted.

Figure 4 depicts the data processing chart of one channel in CDAS2-DDC. Because of the bit width of Mark5B format, not all of the 16 channels can be sent to the recorder when the quantization is more than two bits. Table 1 shows the relationship between channel and sample-bit. If the sample-bit is greater than two, more sample-bits will cause less channels output.

The multi-bit sampling usually is used with the narrow bandwidth mode. The advantage of multi-bit sampling is to increase the signal-to-noise ratio (SNR) and to increase the detectability of probe signals.

Figure 5 depicts the comparison of different bit case from 1-bit to 16-bit. The original signal is an AM modulated signal and its signal spectrum is presented in Figure 8-(a). The baseband bandwidth is 2 MHz. The most obvious phenomenon is that the higher the sampling-bit, the weaker are the fake harmonic components.

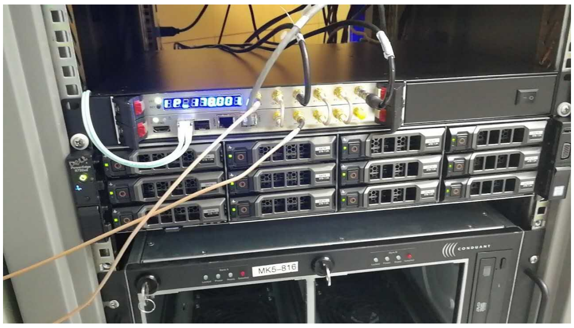

Fig. 3: CDAS2-DDC and recorder.

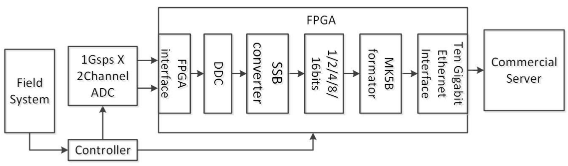

Fig. 4: Schematic diagram of the CDAS2-DDC.

Table 1: Available multi-bit modes.

	1CH	2CH	4CH	8CH	16CH
1-bit	2/4/8/16/32MHz	2/4/8/16/32MHz	2/4/8/16/32MHz	2/4/8/16/32MHz	2/4/8/16/32MHz
2-bit	2/4/8/16/32MHz	2/4/8/16/32MHz	2/4/8/16/32MHz	2/4/8/16/32MHz	2/4/8/16/32MHz
4-bit	2/4/8/16MHz	2/4/8/16MHz	2/4/8/16MHz	2/4/8/16MHz	——
8-bit	0.1/0.2/0.5/1/2/4MHz	0.1/0.2/0.5/1/2/4MHz	0.1/0.2/0.5/1/2/4MHz	——	——
16-bit	0.1/0.2/0.5/1/2MHz	0.1/0.2/0.5/1/2MHz	——	——	——

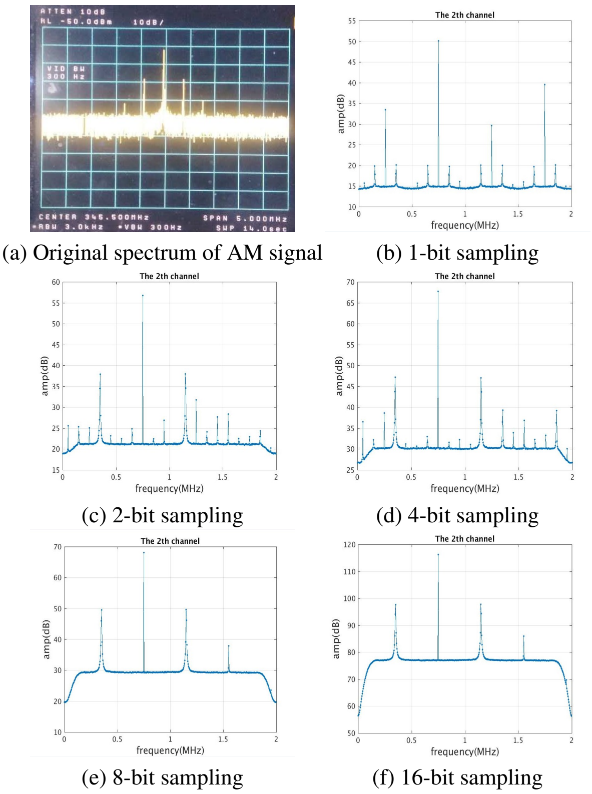

(a) Original spectrum of AM signal (b) 1-bit sampling

(c) 2-bit sampling (d) 4-bit sampling

(e) 8-bit sampling (f) 16-bit sampling

Fig. 5: Comparison of multi-bit sampling.

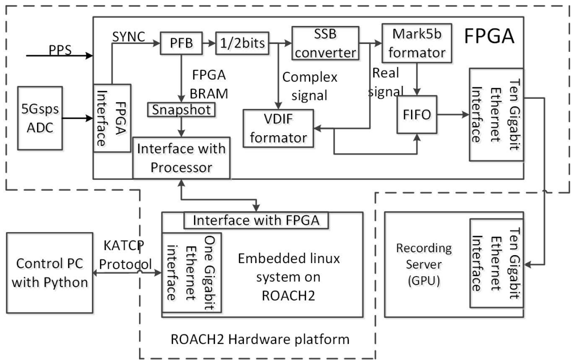

Fig. 6: The structure of the universal backend based on ROACH2.

2.3 General Backend – CDAS2-ROACH2

Both the CDAS and CDAS2 platform are specially designed, and the developing cycle is a time consuming process. Considering short the developing cycle, SHAO plans to develop a general purpose VLBI terminal based on ROACH2 (ROACH2, 2013) platform, in collaboration with Xinjiang Astronomical Observatory (XAO). This universal terminal is not only a general purpose VLBI terminal but can also a be used for single dish pulsar observations. SHAO focuses on the VLBI function.

This backend consists of a ROACH2 and a GPU board, as shown in Figure 6. In the VLBI mode and using the PFB algorithm, its function is similar to CDAS2-PFB. The onboard GPU can not only record but also analyze the sampling data from ROACH2.

Table 2 lists the differences of the three terminals in structure, algorithm, performance and applications.

3 CVN Software Correlator – SCORR

The data processing flow of SCORR is described in the following. The station data are transmitted to the *Data Preprocess* module by e-VLBI or shipment. *Data Preprocess* recovers the formatted data and stores them in buffer files of series of one-second data. *Phase Calibration Signal (PCAL) extractor* is used to extract the phase and amplitude of PCAL. *Fringe searcher* searches the residual delay and delay rate from the probe narrow band telemetry signals. It is very useful in the probe orbit maneuver period. *Spacecraft Delay Model Reconstruction* uses the residual delay and delay rate from *Fringe searcher* to compensate for the forecast delay model and gets the precision delay model. *Correlation* uses the precision delay model to do correlating.

In the lunar mission, the output format of SCORR adopts CVN output format. We hope to upgrade SCORR to a general purpose software correlator and service the astronomy, geodesy and deep-space observations. For this reason, a transform program has been designed to translate the special CVN output format to Mk4 format and FITS-IDI format. Mk4 format is proposed by Haystack Observatory, as well as the input format of HOPS which is a popular geodetic data processing software. FITS-IDI format is used for AIPS, a widely-used astronomy data processing software.

Table 2: Comparisons of the features of three VLBI terminals.

	CDAS2-PFB	CDAS2-DDC	CDAS2-ROACH2
Algorithm	PFB	DDC	PFB
Total Bandwidth	4 IF x 2 Pol x 512 MHz	2 IF x 1 Pol x 512 MHz	2 IF x 1 Pol x 512 MHz
Max.Data Rate	16 Gbps	2 Gbps	2 Gbps
Data Format	VDIF	MK5B/VDIF	MK5B/PSR Fits
Interface	SFP+x4	SFP+x1	SFP+x1
Sample-Bits	1/2	1/2/4/8/16	1/2
Sub-Bandwidth	32 MHz	0.1/0.2/0.5/1/2/4/8/16/32 MHz	32 MHz
Max.Channels	4 IF x 2 Pol x 16 CH	16 CH	16 CH
Key Processer	Xilinx XC7K355T	Xilinx XC7K480T	Xilinx XC6VSX475
Recorder	Mark6	Commercial Server	GPU
Target	VGOS	Deep Space Exploration	VLBI Pulsar, Maser(with XAO)

Table 3: The specification of SCORR.

Frequency Channel	16~16384
Output Formate	CVN, FIT-IDI, Mk4
Developing Language and Libraries	C, C++, CUDA, IPP, MPI, Pthread, OpenMP
Computing Platform	Cluster+GPU+Storage Servers
Data Recorded Format	Mark5, VDIF
Applications	Deep Space, Geodesy, Astronomy, Spacecraft phase-reference VLBI experiments, and so on

3.1 Probe Fringe Searcher

When tracking deep-space probes, the VLBI software correlator always needs a precision delay model. But due to the probe orbit maneuver, sometimes the predicted delay error can be quite large. So *the probe fringe searcher* can search the fringe and fringe rate independent of the predicted delay model, and then use the results to compensate for the predicted delay and delay rate. This function was used in CE-2(Chang'E-2) and CE-3(Chang'E-3) of CLEP. In CE-5 (Chang¡'E-5), we are planning to track the orbiter and the ascender in some special same beam VLBI cases. New dual objects algorithm is under development.

Figure 7 depicts the flow chat of the new probe fringe searcher. In the *Local Correlation* module, the signal received by station multiplies the conjugate of the signal at frequency $f_{0(emission frequency)}$; *Doppler Frequency* gets the high precision Doppler frequency shift Δf, which is relative to $f_{0(emission frequency)}$; In the *Delayrate-Reconstruction* module, $\Delta f/f_0$ replaces the delay rate in the prior model; *Correlator* does correlating based on the prior model; *Simple Postprocessor* gets residual delay and the residual delay rate.

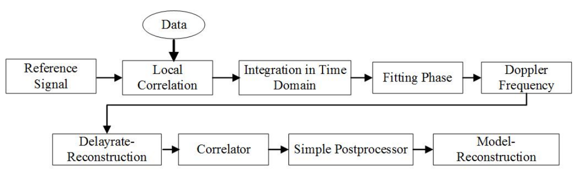

Fig. 7: Flow chart of the probe fringe searcher

3.2 Two Dynamic Objects Same-beam VLBI

When two dynamic probes fall into the same antenna beam, such as in the the Rendezvous and Docking (RvD) of CE-5 Orbiter and Ascender, as Figure 8 shows, the VLBI correlator needs to arrange two phase centers to track the different dynamical objects. For a real-time system, the calculation speed should be increased by a factor of two. GPU and IPP library will be used to accelerate.

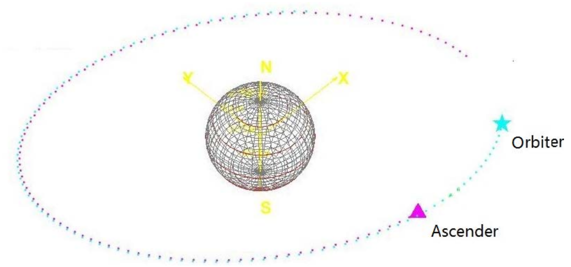

Fig. 8: An example demonstrates that the Orbiter and Ascender are rendezvousing and docking.

3.3 Precision Comparisons between SCORR and DiFX

DiFX (Deller et al., 2007; Deller et al., 2011) is the most widely used VLBI software correlator. Since the second half of 2016, we have carried out the precision compar-

Table 4: Precision comparisons between SCORR and DiFX.

	k14349	cn1502	apsg38
Data sources	IVS	CVN	IVS
Use same delay model	Y	N	N
S band MBD Difference (< 10 ps)	Y	Y	Y
X band MBD Difference (< 3 ps)	Y	Y	Y
SNR Difference (< 0.5 %)	Y	Y	Y

ison between SCORR and DiFX (version 2.4.1) based on the geodesy observations. Firstly, the two correlators processed the same set of observation data, respectively, and then used HOPS to finish postprocessing (Liu et al., 2017). The comparison results presented in Table 4 indicate that the discrepancy of SCORR and DiFX are very small.

4 Conclusion

The CVN digital backend CDAS and the software correlator SCORR are developed by SHAO. To meet the requirements of astronomy, geodesy and deep-space applications, a new VLBI backend CDAS2 and a general purpose software correlator have been developed. According to the comparison with DiFX, SCORR's accuracy is verified. They both will be used in the new VGOS system and lunar missions.

5 Acknowledgements

This work is sponsored by the Natural Science Foundation of China (11373061, 11573057), the Key Laboratory of Radio Astronomy of Chinese Academy of Sciences, the CAS Key Technology Talent Program, the Program of Shanghai Subject Chief Scientist (14XD1404300), the Chinese Academy of Sciences innovation project (CXJJ-17-Q113), Shanghai Natural Science Foundation of China (15ZR1446800) and the Chinese lunar exploration project. The authors appreciate the support of CVN data processing center.

References

Liu L, Zheng W, Zhang Ju, Shu F, Tong F, Tong L (2017) Precision Analysis of Chinese VLBI Network Software Correlator for Geodetic Applications. *Acta Geodaetica et Cartographica Sinica*, 46(7), 805–814, doi:10.11947/j.AGCS.2017.20160600

ROACH2 (2013) https://casper.berkeley.edu/wiki/ROACH-2_Revision_2.

Deller A T, Tingay S J, Bailes M, West C (2007) DiFX:A Software Correlator for Very Long Bsedline Interferometry Using MultiProcessor Computing Environments. *Publications of the astronomical society of the Pacific*, 119:318–336.

Deller A T, Brisken W F, Phillips C J, Morgan J, Alef W, Cappallo R, Middelberg E, Romney J, Rottmann H, Tingay S J, Wayth R (2011) DiFX-2: A More Flexible, Efficient, Robust and Powerful Software Correlatior. *Publications of the astronomical society of the Pacific*, 123:275–287.

Geometric Variations of a Geodetic Radio Telescope

S. Bergstrand, R. Haas, M. Herbertsson, C. Rieck, J. Spetz, C.-G. Svantesson

Abstract We have measured the key deforming parameters of the Onsala 20 m telescope with laser based tracker, scanner and electronic distance meters. The parameters show both thermal and elevation dependence at an order of some millimeters, and are therefore potential significant contributors to a scale error in VLBI analysis.

Keywords radio telescope, laser tracker, laser scanner, deformation parameters

1 Introduction

Compared to previous VLBI generations, local measurements have become an increasingly important issue in connection with the tighter VLBI2010/VGOS/GGOS specifications. Signal chains and other electronic components are under constant development, and local tie methods are being improved (IERS WG, 2015; Lösler et al., 2016; Poyard et al., 2017) e.g. as a mean to better understand the scale error between SLR and VLBI in ITRF2014 (Altamimi et al., 2016) but the mechanical parts have attracted less attention. Clark and Thomsen (1988) is the standard work in the area, which in later years has been extended (Sarti et al., 2009; Artz et al., 2014). Artz et al. (2014) reported a general deformation model for the Effelsberg telescope and based an analysis on a combination of recent and historical data, and suggested a similar investigation for the more common 20 m sized telescopes in the regular IVS networks/sessions. Following the model by Artz et al. (2014), we have employed a number of contemporary laser based length measuring devices in order to characterize the deformations of the Onsala 20 m telescope. Noting that stations are identified by DOMES number and sites are geographical locations, a co-location and site surveying reference for this work is slightly misleading, as local ties provide information of the external relationships between the geometrically defined reference points (GRP) of geodetic stations on a site, whereas deformation analysis captures information of internal variations that largely have been elusive to those surveys. In this study we focus on the internal structural deformations of the telescope in order to explore the possibilities to detect the systematic effects that are, or alias as, tropospheric, temporal or vertical errors in the geodetic analysis. Quantification of these deformations therefore has potential to put valuable constraints on systematic VLBI errors.

Sten Bergstrand · Magnus Herbertsson · Carsten Rieck · Jörgen Spetz · Claes-Göran Svantesson
Research Institutes of Sweden, Brinellgatan 4, SE-504 62 Borås

Rüdiger Haas
Chalmers University of Technology, Department of Space, Earth and Environment, Onsala Space Observatory, SE-439 92 Onsala

2 Methods and results

Clark and Thomsen (1988) characterized telescope deformation in terms of elevation dependent length changes ΔL and divided these into parts relating to focal length $\Delta F(\epsilon)$, vertex position $\Delta V(\epsilon)$ and receiver position $\Delta R(\epsilon)$, i.e.

$$\Delta L = \alpha_F \Delta F(\epsilon) + \alpha_V \Delta V(\epsilon) + \gamma \alpha_R \Delta R(\epsilon), \qquad (1)$$

where $\alpha_{F/V/R}$ are telescope specific linearly dependent scaling coefficients, and $\gamma = 1$ for primary and $\gamma = 2$ for secondary focus telescopes.

Artz et al. (2014) presented the separate contributing components that we list in Tab. 1, and which we here complement with the instrumentation that we have utilized for the measurements. Due to different telescope constructions some components have been slightly altered in the progression of the project.

Table 1: Telescope deformation category (CA), components (CO), description, measuring method and equipment used.

CA	CO	Description	Method	Instrument
V	L_1	Height of secondary axis	Invar + tracker	Electromagnetic inducer, Leica LTD800
V	L_2	Vertex separation from elevation axis	(tracker)	Leica LTD800
F	L_3	Deformation of the main paraboloid	Scanner (EDM)	Leica HDS7000, Micro-Epsilon optoNCDT ILR 1181
R	L_4	Impact of defocused optics	Gain+EDM	Micro-Epsilon optoNCDT ILR 1181
R	L_5	Effects of a second reflection	EDM	Micro-Epsilon optoNCDT ILR 1181
R	L_6	Displacement of feed horn at secondary focus	(EDM/tracker)	Micro-Epsilon optoNCDT ILR 1181

3 Invar

The main constituent of L_1 is the monument height, whose near 1:1 correlation with temperature has been monitored continuously for more than twenty years (Johansson et al., 1996). Additional movements have been observed during geodetic VLBI sessions, but as the 5 minute smoothing/sampling interval is schedule independent and the magnitude of the movements is small, it has not triggered any elevation dependence studies. The amplitude of the daily L_1 variation is of order 1 mm.

4 Laser tracker

The most precise measurements are performed with a laser tracker, which is a laser interferometer on a dual axis rotating head where encoders detect angular movements. In addition to the invar measurements that monitor the monument height's thermal dependence, we examined whether we could detect an elevation dependent variation of L_1 as well. First measurements were made on the back of the reflector to the supposedly stable platform which co-rotates with the antenna azimuth atop the telescope concrete tower. The initial laser interferometer results from the tracker indicated systematic movements, but at closer examination the results did not supersede the measurement uncertainty. In order to lever the movement, we therefore mounted the tracker's retroreflector on a carbon fiber spinnaker boom which we protruded backwards from the platform. The effect, which is measurable at an order of 0.1 mm and corresponds to a telescope pointing error of 3 arcsec, is minor but at an order of 10 % of the specification not negligible. Some attempts were also directed towards quantifying the variations of L_2, but the inaccessibility of axis supports combined with a set of complex mechanical relations prohibited any qualified measures of this component. At Effelsberg where the reflector rests on a beam, this bending effect was more easily measured and turned out to be a significant contributor. It is plausible that L_2 variations could be captured with a tracker, but that would require intermittent decommissioning of essential electronic equipment and was therefore disregarded for this project.

5 Laser scanner

Where tracker measurements are extremely accurate in discrete points, they are not optimized to characterize surfaces. To measure the elevation dependent deformation L_3 of the reflector, we employed a metrology grade scanner which is a better tool for surface measurements although the accuracy of single points is not competitive to those of a tracker. The manufacturer recommended having the scanner's primary axis aligned with the vertical in order to preserve the instrument bearings and encoders. Adhering to the overall priority to make measurements as close to operating conditions as possible, the first attempts to scan the surface was made from a position close to the antenna vertex. However, the reflected signal from the smooth surface at flat angles proved insufficient to extract relevant data, and the scanner needed to be elevated from the vertex to increase the measuring attitude. We therefore had to relax the initial priority on an unloaded structure, and constructed a lightweight pneumatic controlled gimbal and a clamp which we attached to the subreflector quadrupod for an inverted scanner setup. This construction has also been reused by other instruments for related investigations of the telescope (Holst et al., 2017). Keeping the paraboloid vertex as reference, the telescope rim advances around 6 mm at low elevations compared to the zenith.

6 Electronic distance meter

For monitoring of observation axis movement which in terms of distance components essentially is L_4 and L_5, we attached lightweight, industrial grade laser EDMs as close to the center of the antenna as possible and pointed towards the subreflector. The EDMs were utilized to monitor both elevation and thermal dependence of the subreflector distance, which at an order of 3 mm is of comparable magnitude to the elevation compensation made during astronomical observations. In instances where an invar rod solution is not practical for L_1 measurements, an EDM solution may offer comparable results.

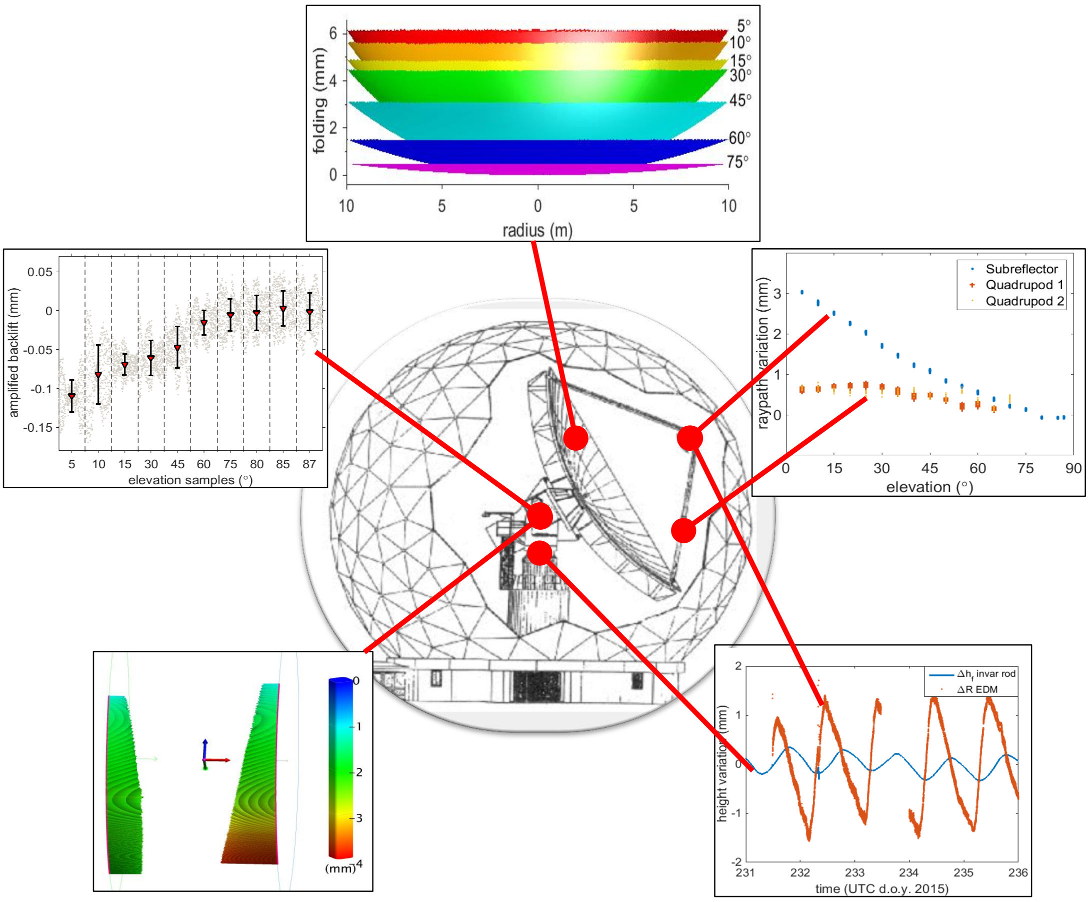

Fig. 1: Structural deformation of the Onsala 20 m telescope. Clockwise from top: elevation dependent main reflector deformation compared to 85° (L_3); elevation dependent subreflector distance and lower quadrupod supports' length (L_4, L_5); thermally induced subreflector distance (L_4) and monument height (L_1); elevation dependent collapse/bending of counter-weights (L_2 indicator); elevation dependent height variation of secondary axis (L_1).

7 Discussion

The telescope was primarily constructed for astronomical purposes, and the technical documentation for focal length, etc. appears to be set for 45° elevation. As the geodetic benchmark is zenith observations, the difference to low elevations become even more accentuated. To continue the dissemination of the deformation components, L_6 is short and its variations minor compared to that of the subreflector distance. A complete quantification of the path length variations therefore includes some more components than presented here. The overall effect of the deformations is not considered, but will be analyzed in a future publication (in progress). Nevertheless, given the VGOS sub mm accuracy objective, the magnitude of the deformations indicates that the effects need to be quantified at the recently deployed 13.2 m telescopes as well. As rms-evaluations are suited for goodness of fit but has limited implications for accuracy, metrologically traceable equipment are recommended for these quantifications.

8 Conclusions

These are direct measurements of the telescope deformations and path length variations. In order to achieve the GGOS objective of 1 mm accuracy for space geodetic observations, corresponding deformations need to be quantified at more sites. As a number of high productive legacy telescopes, e.g. Kokee Park and Ny-Ålesund are about to be decommissioned, it is imperative to measure the structural deformations of these stations before they are demounted and their properties are lost for future TRF and CRF generations.

Acknowledgements

This work was part of the SIB60 project in the European metrology research programme. The EMRP is jointly funded by the EMRP participating countries and the European Union. We are grateful for the support of all the technical and operating staff that has assisted throughout the project.

References

Artz T, Springer A, Nothnagel A (2014) A complete VLBI delay model for deforming radio telescopes: the Effelsberg case. *J Geod*, 88(12), 1145–1161, doi:10.1007/s00190-014-0749-1

Altamimi Z, Rebischung P, Métivier L, Collilieux X (2016) ITRF2014: A new release of the International Terrestrial Reference Frame modeling nonlinear station motions. *J Geophys Res Solid Earth*, 121, doi:10.1002/2016JB013098

IERS Working Group on Site Survey and Co-location (2015) https://www.iers.org/IERS/EN/Organization/WorkingGroups/SiteSurvey/sitesurvey.html

Clark T A, Thomsen P (1988) Deformations in VLBI antennas. *NASA Technical Memorandum 100696*, Goddard Space Flight Center, Greenbelt, Maryland, 96 pp.

Holst C, Schunck D, Nothnagel A, Haas R, Wennerbäck R, Olofsson H, Hammargren R, Kuhlmann H (2017) Terrestrial Laser Scanner Two-Face Measurements for Analyzing the Elevation-Dependent Deformation of the Onsala Space Observatory 20-m Radio Telescope's Main Reflector in a Bundle Adjustment. *Sensors*, 17(8), 1833, doi:10.3390/s17081833

Johansson L A, Stodne F, Wolf S (1996) The PISA project – variations in the height of the foundation of the 20 meter radio telescope. *Research report 178*, Department of Radio and Space Science with Onsala Space Observatory, Chalmers University of Technology, Göteborg, Sweden

Lösler M, Haas R, Eschelbach C (2016) Terrestrial monitoring of a radio telescope reference point using comprehensive uncertainty budgeting – Investigations during CONT14 at the Onsala Space Observatory. *J Geod*, 90(5), 467–486, doi:10.1007/s00190-016-0887-8

Poyard J-C, Collilieux X, Muller J-M, Garayt B, Saunier J (2017) IGN best practice for surveying instrument reference points at ITRF co-location sites. *IERS Technical Note*, No. 39

Sarti P, Vittuari L, Abbondanza C (2009) Laser Scanner and Terrestrial Surveying Applied to Gravitational Deformation Monitoring of Large VLBI Telescopes' Primary Reflector. *J Surv Eng*, 135(4), 136–148, doi:10.1061/_ASCE_SU.1943-5428.0000008

Accuracy Assessment of the two WVRs, Astrid and Konrad, at the Onsala Space Observatory

P. Forkman, G. Elgered, T. Ning

Abstract Two Water Vapour Radiometers (WVRs), Astrid and Konrad, have been operating at the Onsala Space Observatory during the time period 2013–2016. There are several data gaps due to different types of instrument failures and therefore we also use estimates of the equivalent zenith wet delay (ZWD) from the two GNSS reference stations: ONSA and ONS1. They provide an almost continuous time series during the four years. ZWD root-mean-square differences are 0.38 cm between ONSA and ONS1, 0.92 cm between ONS1 and Astrid, and 0.75 cm between ONS1 and Konrad. For the horizontal linear gradients we see correlation coefficients of the order of 0.9 between ONSA and ONS1 and 0.5 between ONS1 and Konrad.

Keywords Water Vapour Radiometer, Zenith Wet Delay, GNSS, GPS

1 Introduction

Water Vapour Radiometers (WVRs) provide independent information on the signal propagation path delay due to atmospheric water vapour, often referred to as the wet delay.

WVR estimates of the wet delay can be used directly in the VLBI data analysis but also as validation data for delays estimated from the VLBI data themselves.

The two WVRs at the Onsala site have been in operation for a long time. Astrid did the first comparison measurements with radiosondes at the Gothenburg-Landvetter Airport in May 1980. Konrad's first field campaign was in Kiruna, at the Esrange Space Center, in August 2000. We are now considering a new WVR for installation at the Onsala site and have identified a need for an assessment of the accuracy, reproducibility, and repeatability using the existing WVR data from recent years. Here we give an overview of results obtained from the time period 2013–2016.

In Section 2, we describe the instrumentation followed by the data analysis in Section 2. Section 3 present the results and Section 4 the conclusions and plans for a new WVR.

Peter Forkman · Gunnar Elgered
Chalmers University of Technology, Onsala Space Observatory, SE-439 92 Onsala, Sweden

Tong Ning
Lantmäteriet, SE-801 82 Gävle, Sweden

2 Instrumentation

The two WVRs, Astrid (Fig. 1) and Konrad (Fig. 2), have been used at the observatory since 1980 and 2000, respectively. Both measure the sky brightness temperature approximately 1 GHz below the water vapour line at 22.2 GHz and in the atmospheric window at 31.4 GHz.

The GNSS stations ONSA, first established in the CIGNET network in 1987, and ONS1, established as a back-up station in 2011, are sites in the national reference network SWEPOS®. They also continuously offer the observational data to the open access networks of

Fig. 1: The WVR Astrid.

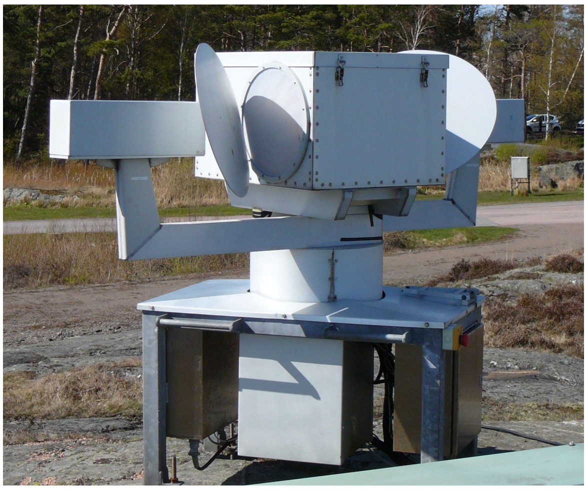

Fig. 2: The WVR Konrad.

Fig. 3: GPS stations ONSA (left) and ONS1 (right).

IGS and EUREF. Figure 3 shows the two sites. Note that the ONSA site is equipped with a sheet of absorbing material (ECCOSORB®) just below the antenna in order to reduce multipath effects.

3 Data analysis

Unfortunately, there are several data gaps due to different types of instrument failures — both WVRs are becoming old. Therefore, in order to have simultaneous data for comparisons, we also use estimates of the equivalent zenith wet delay (ZWD) and horizontal linear gradients from the two GNSS reference stations: ONSA and ONS1. They offer almost continuous and independent time series for the parameters of interest during the four years. The only GPS data gap is for the ONSA station in the summer of 2015 due to a failing pre-amplifier.

3.1 WVR data analysis

A common method for calibration of the sky brightness temperatures measured by the WVR is the tip curve method, where observations spread over a range of elevation angles are used in order to get an extrapolated sky brightness temperature at zero air mass equal to the cosmic background radiation (Elgered and Jarlemark, 1993). Additionally an elevation pointing offset can be estimated. Here we estimate both so called hot load corrections, low pass filtered with a time constant of ≈ 5 h, and daily elevation offsets. Because of atmospheric inhomogeneities we expect a correlation between the residual offsets of the two channels (see Figure 4). The sky brightness temperatures are finally used to calculate the ZWD (Elgered, 1993).

Subsequently, based on the equivalent ZWDs observed in specific directions, the horizontal linear gradients (east and north) were calculated according to the four-parameter model described by Davis et al. (1993).

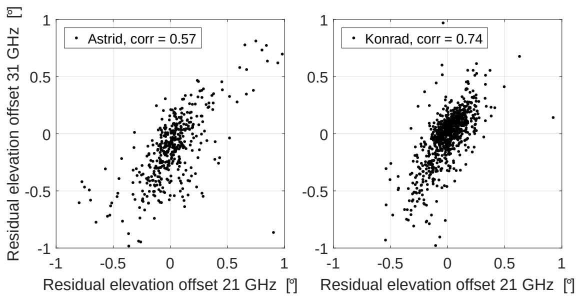

Fig. 4: Estimated daily elevation offsets for the two channels of Astrid (left) and Konrad (right).

3.2 GPS data analysis

The data have been analyzed using the method described by Ning et al. (2013) where the ZWD and the linear east and north gradients are estimated simultaneously in the processing.

4 Results

We first present the results for the equivalent ZWD and then for the gradients. The first comparison is between the two GNSS stations. The estimated ZWD is illustrated in Figure 5. We note that the observed bias between ONS1 and ONSA of 0.36 cm is consistent with earlier results showing the influence of the suppres-

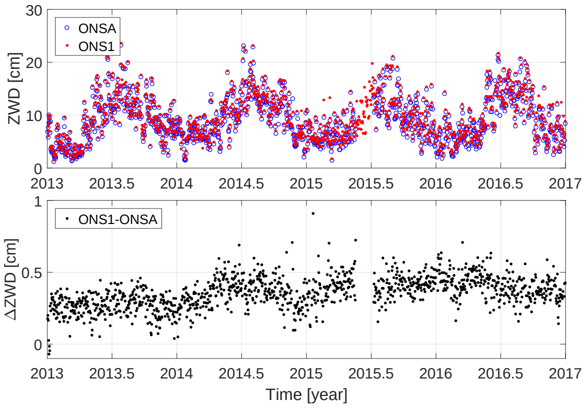

Fig. 5: Time series of estimated ZWD and their differences using GPS data from ONSA and ONS1.

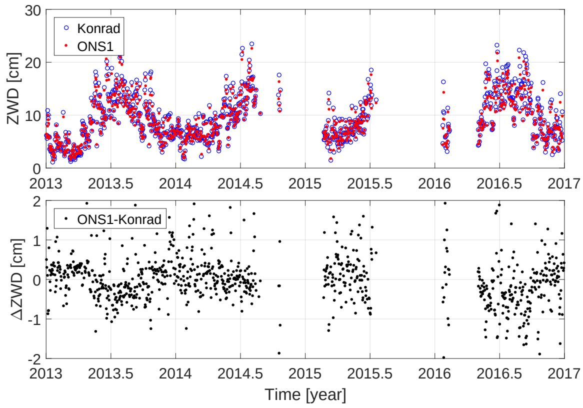

Fig. 7: Time series of estimated ZWD and their differences using Konrad data and GPS data from ONS1.

sion of multipath using a microwave absorber at ONSA, which is not the case for ONS1 (Ning et al., 2011).

We chose to use ONS1 data for the WVR comparison because of the slightly better data coverage over the four years. In Figures 6 and 7 we calculate daily averages of the ZWD based on hourly averages where the data coverage is at least 75 % of the default observation schedule for each instrument.

Table 1 summarizes the results (depicted in Figures 6 and 7) in terms of bias, standard deviation (SD) and root-mean square (RMS) of the differences, ΔZWD.

Table 1: Instrument comparison results for the ZWD.

Instruments compared	Bias (cm)	SD (cm)	RMS (cm)
ONS1−ONSA	0.35	0.14	0.38
ONS1−Astrid	0.44	0.81	0.92
ONS1−Konrad	0.06	0.75	0.75

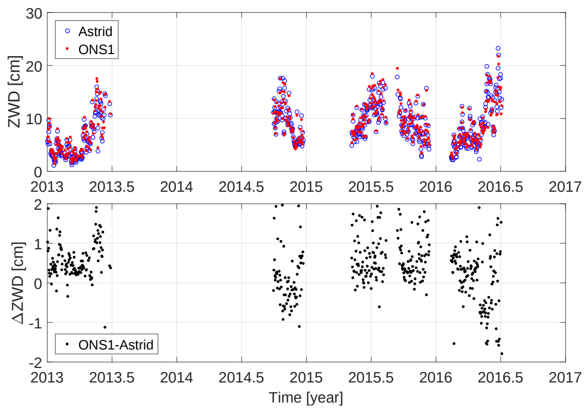

Fig. 6: Time series of estimated ZWD and their differences using Astrid data and GPS data from ONS1.

When comparing gradients estimated from WVR and GPS data it is noted that the WVR measures gradients in the water vapour whereas the GPS measure gradients in the refractive index (determined by both the wet and the dry atmosphere). Unfortunately the Astrid WVR was affected by an unstable pointing in the azimuth coordinate during the period. In principle we can estimate a pointing offset for subsets of the data over the period by fitting the data in order to have an agreement in the horizontal gradients with the other instruments. This was, however, not the aim of this study and we chose to focus on a comparison using Konrad data and GPS data only. All estimated gradients are shown in Figure 8. We note that the size and variability of the WVR gradients are significantly larger compared to the GPS gradients. This is consistent with earlier results (Gradinarsky and Elgered, 2000).

Figure 9 depicts the correlations for the gradients over the whole four year period. The upper graphs illustrates that even though the GPS observations see the same atmosphere and observes the same satellites the agreement is not ideal. Furthermore, when using GPS as ground truth, we must add an additional uncertainty due to the fact that the hydrostatic delay is also included whereas the WVRs are only inferring the gradients due to the water vapour. The lower graphs show the correlation between ONS1 and Konrad. The observed correlations do not differ by more than 5 % for the individual years and a value around 0.5 is also a typical value reported for comparisons between gradients estimated from WVR data and different GNSS data (Lu et al., 2016).

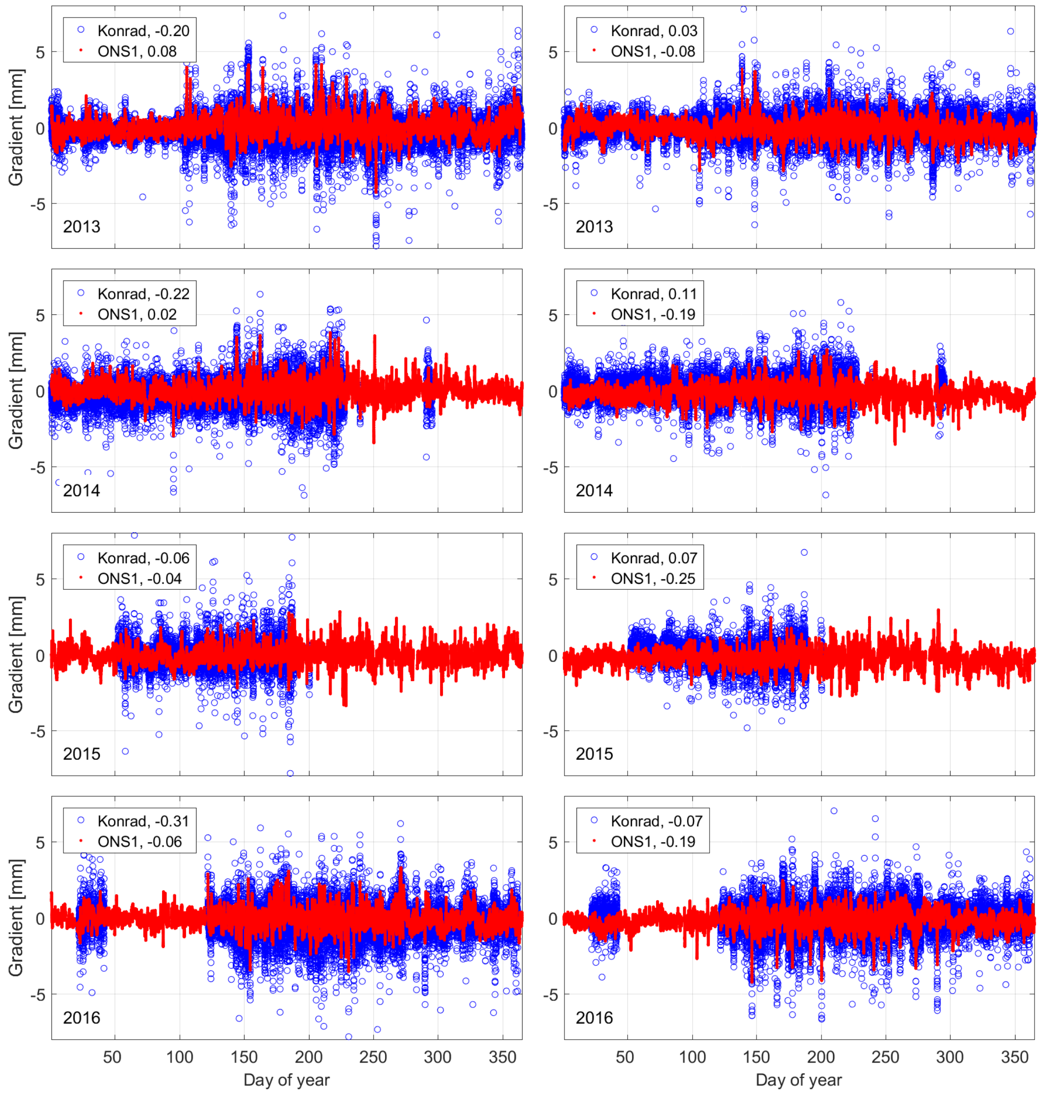

Fig. 8: Time series of estimated gradients using Konrad data and GPS data from ONS1. East and north gradients are displayed in the left and right columns, respectively. Average gradients are shown in the upper left corners. The average north gradient due to an increasing ground pressure with decreasing latitude, is seen in the GPS results, typically of the order of −0.2 mm.

5 Conclusions and future work

We find that in spite of their old age the two WVRs give biases in the ZWD comparable to historical results. The standard deviations are slightly worse. Ning et al. (2012) report typical standard deviations around 0.7 cm between ONSA and Astrid for ZWD averages over 1.5 h. Also when comparing horizontal gradients we find consistent results to those reported earlier. The main problem with the WVRs is the frequent hardware failures causing a significant data loss.

We plan for a new installation of a WVR. Presently Omnisys Instruments in Gothenburg is developing a prototype WVR for the European Space Agency. When this instrument is completed a field campaign will be carried out at Onsala. Thereafter a copy will operate at the site for a long term. The prototype instrument is shown in Figure 10.

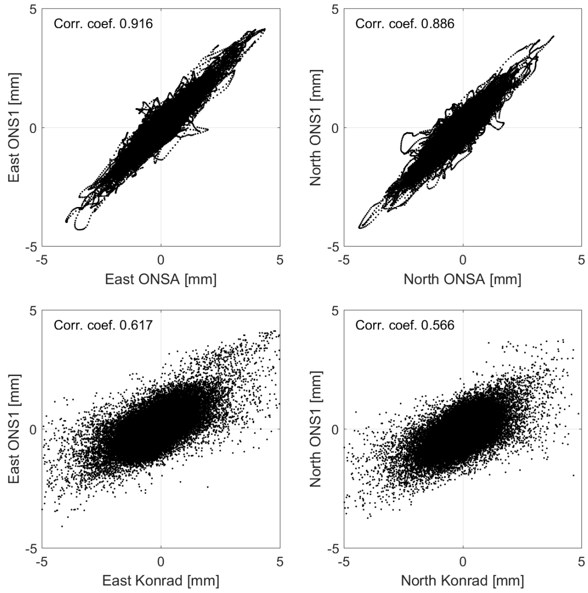

Fig. 9: Correlations between estimated east (left) and north (right) gradients. Upper graphs show the correlation between the two GPS stations and the lower graphs between the GPS station ONS1 and the Konrad WVR.

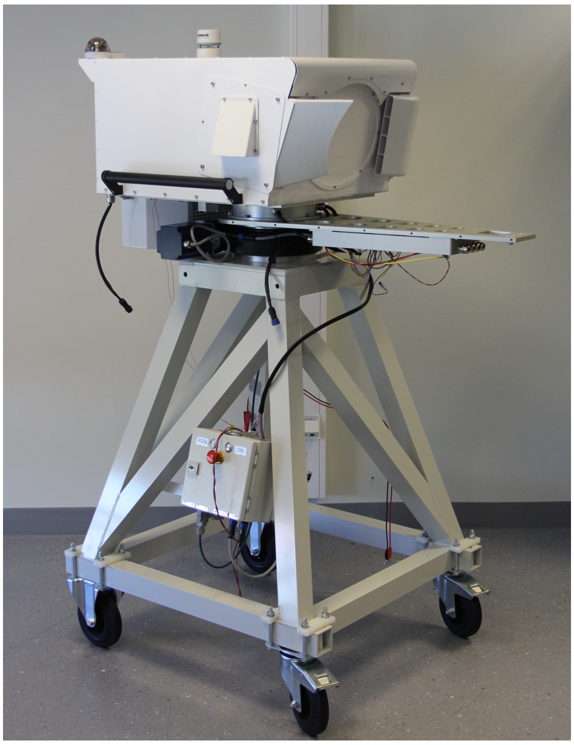

Fig. 10: The WVR under development at Omnisys Inc.

References

Davis J L, Elgered G, Niell A E, Kuehn C E (1993) Ground-based Measurement of Gradients in the "Wet" Radio Refractive Index of Air. *Radio Sci.*, 28(6), 1003–1018.

Elgered G (1993) Tropospheric Radio Path Delay from Ground-Based Microwave Radiometry. In: M. Janssen (ed.) *Atmospheric Remote Sensing by Microwave Radiometry*, Wiley & Sons, 215–258.

Elgered G, Jarlemark P O J (1988) Ground-Based Microwave Radiometry and Long-Term Observations of Atmospheric Water Vapor. *Radio Sci.*, 33, 707–717.

Gradinarsky L P, Elgered G (2000) Horizontal Gradients in the wet path delay derived from four years of microwave radiometer data. *Geophys. Res. Let.*, 27, 2521–2524.

Lu C, Li X, Li Z, Heinkelmann R, Nilsson T, Dick G, Ge M, Schuh H (2016) GNSS tropospheric gradients with high temporal resolution and their effect on precise positioning. *J. Geophys. Res. Atmos.*, 121, 912–930, doi:10.1002/2015JD024255

Ning T, Johansson J M, Elgered G (2011) The Impact of Microwave Absorber and Radome Geometries on Ground-Based GNSS Measurements of Coordinates and Atmospheric Water Vapour. *Adv. Space Res.*, 47(2), 186–196, doi:10.1016/j.asr.2010.06.023

Ning T, Haas R, Elgered G, Willén U (2012) Multi-technique comparisons of ten years of wet delay estimates on the west coast of Sweden. *J. Geod.*, 565–575, doi:10.1007/s00190-011-0527-2

Ning T, Elgered G, Willén U, Johansson J M (2013) Evaluation of the atmospheric water vapor content in a regional climate model using ground-based GPS measurements. *J. Geophys. Res.*, 118, 1–11, doi:10.1029/2012JD018053

Communication, Coordination, and Automation for Future Geodetic Infrastructures

A. Neidhardt

Abstract This paper is an overview of ideas, implementations, and results from seven years of technical research in computer science for developments of future geodetic infrastructures. It explains the four pillars found: stable and safe scientific software, an extended common software toolbox, autonomous production cells, and remote access and monitoring. This is combined to coordinated multi-agent systems offering solutions for operational aspects of the Global Geodetic Observing System (GGOS) with regard to "Industry 4.0". The paper is a summary of a textbook published by Springer Int. Switzerland, see Neidhardt (2017).

Keywords GGOS, infrastructure, automation, control, communication, coordination

1 Introduction

Several large projects have been realized at the Geodetic Observatory Wettzell during the past decade. A new laser ranging system, VLBI Twin Telescopes, several local sensors, to name just a few main projects, required from the Wettzell developer team to write software. "Connecting hardware devices, controlling workflows, scheduling tasks, managing error situations, communicating between distributed equipment, and designing a more automated operation took many years for several project members to develop." (Neidhardt, 2017).

Several aspects of applied computer science were apparent. While local solutions were finished, it became more and more clear that aspects like coordination, communication, automation, control, and operation require a more general approach if GGOS should become one global observing system. This was the starting point to collect ideas and implementations to discuss and offer solutions for future requirements of a GGOS.

These aspects could be structured as four main topics which are the pillars "holding" the infrastructure of GGOS.

2 First pillar: Stable and Safe Scientific Software

The style (coding layout and code policies) which is used for writing the source code is essential to keep the programs comprehensive. A big issue is the inclusion of existing legacy code using suitable converter classes with clear interfaces to keep "older" code more manageable. Automatic document generators help to implement an agile documentation landscape. High-quality, test-driven developments use unit tests, static inspections and dynamic analysis to get a suitable test coverage. Test metrics provide quantitative classifiers for software quality. Continuous integration (see Fig. 1) offers daily overviews. Code repositories use version management systems to track all changes and updates. This ideally supports agile development.

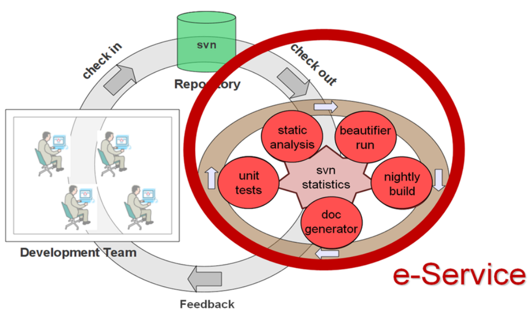

Fig. 1: The round-trip used for continuous integration (Neidhardt, 2017).

Alexander Neidhardt
Technische Universität München, Forschungseinrichtung Satellitengeodäsie, Geodätisches Observatorium Wettzell, Sackenrieder Str. 25, DE-93444 Bad Kötzting, Germany

3 Second pillar: Common Software Toolboxes

Software is decomposed into modules and components partly using generative ways to support parametrized applications. This splits a development into domain and application engineering so that most of the engineers can use predefined, parametrized domains for specific tasks to implement their own applications, like communication over network. Remote procedure calls standardize this communication and also all related tasks. The results are remote function calls which look similar to local calls. They organize data conversion, implement call semantics, and guarantee safety and security. The result is a new middleware with the following layers:

- Manually written "glue code": it contains "handwritten", individual code mainly used to combine modules and components to main programs.
- Completely generative modules and components: it contains generated parts of a specific problem case.
- Template metaprogramming components: it contains object-oriented components which are unrolled and unfolded by the compiler itself.
- Generative template pattern components: it contains object-oriented components using templates to be adaptable to different types of variables.
- Object-oriented components: it contains all pure object-oriented components without generative parts but which use the advantages of the object-oriented paradigm.
- Structured modules: it contains all simple, structured modules mainly to control lower layered hardware.

4 Third pillar: Autonomous Production Cells

Designing of control tasks means a mapping of real structures to software units. An intelligent controlling of hardware includes different layers of feedback loops which use data from sensors to make decisions for the commanding of actuators. Every hardware is represented in the form of standardized software stubs. Autonomous production cells (see Fig. 2) using autonomous software cells provide techniques for planning, controlling, user interfacing, hardware driving, and failure managing. A coordination cell uses metrics for static and dynamic planning. Separate autonomous hardware cells control the individual hardware. All data are organized in a hybrid, autonomous data management cell. A parallel system monitoring is used to fulfill safety criteria and to show state overviews.

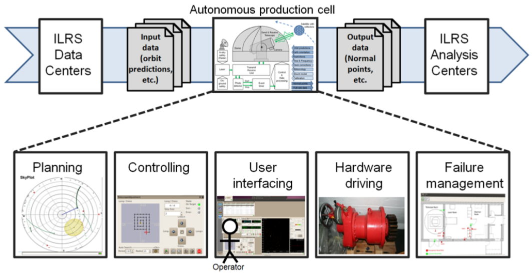

Fig. 2: A possible structure of an autonomous production cell for laser ranging (Neidhardt, 2017).

5 Fourth pillar: Remote Access and Monitoring

It is feasible to extend the existing systems with functionalities for remote access to support orders from external partners and offer reports to them (see Fig. 1). Because worldwide networks do not guarantee continuous access, systems have to increase their ability to run completely autonomously. This can be implemented using multi-agent systems where each agent uses an internal feedback loop. An agent can control existing software, like the NASA Field System, as legacy code. Additional requirements, like web cameras, remotely controlled switches, and a suitable graphical remote interface, extend the local architecture to replace the senses of an operator at the system. Remote access requires network security using role-based access control and ciphering algorithms, restricted network enclaves, and different types of firewalls.

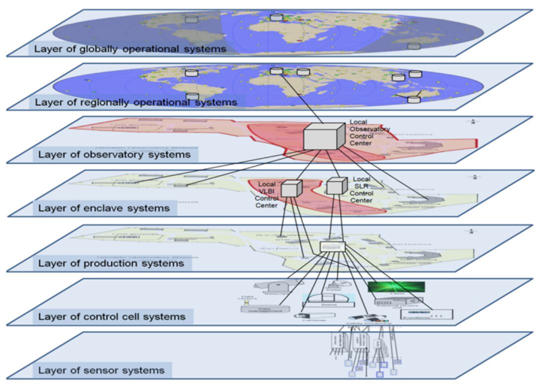

Fig. 3: Communication and coordination layers for GGOS products (Neidhardt, 2017).

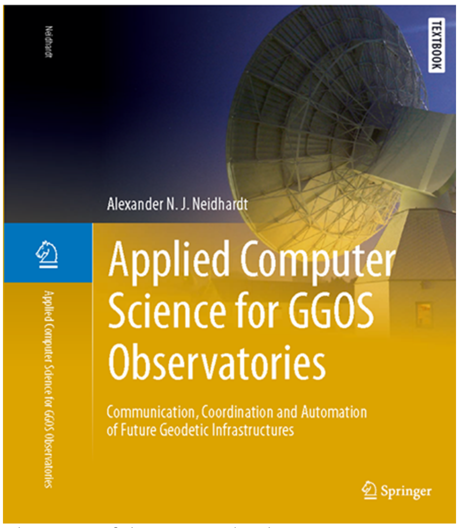

Fig. 4: The cover of the new textbook.

6 Conclusions

The main topics described require a global networking within GGOS which can be compared to "Internet of Things" or "Industry 4.0" in the field of industrial implementations. But it is a paradigm change to leave the individual and loose net of participating geodetic sites which offer their data products and start thinking in terms of global coordination, communication and automation beyond institute structures. Nevertheless, it has high potential and is a very interesting new aspect of cooperation.

All these ideas and solutions found are published as textbook by Springer Int. Switzerland, see Neidhardt (2017). This book combines elementary theory from computer science with real-world challenges in global geodetic observation, based on examples from the Geodetic Observatory Wettzell, Germany. It starts with a step-by-step introduction to developing stable and safe scientific software for successful software projects. The use of software toolboxes is another essential aspect that leads to the application of generative programming. An example is a generative network middleware that simplifies communication.

One of the book's main focuses is on explaining a potential strategy involving autonomous production cells for space geodetic techniques. The complete software design of a satellite laser ranging system is taken as an example. Such automated systems are then combined for global interaction using secure communication tunnels for remote access. The network of radio telescopes is used as a reference.

Combined observatories form coordinated multi-agent systems and offer solutions for operational aspects of the G lobal Geodetic Observing System (GGOS) with regard to "Industry 4.0".

References

Neidhardt A (2017) Applied Computer Science for GGOS Observatories. Communication, Coordination and Automation of Future Geodetic Infrastructures. ISBN 978-3-319-40137-9. Springer International Publishing Switzerland.

The MIT/NASA Broadband Signal Chain: Present State, VGOS Compliance, and Beyond

C. A. Ruszczyk, G. Rajagopalan, R. McWhirter, C. Eckert, P. Elósegui

Abstract The VGOS implementation of the MIT/-NASA broadband signal chain incorporates a number of new technological developments, including the Calibration Delay Measurement System (CDMS) and the ROACH2-based digital backend (R2DBE). The former is a key component for accurate estimation of instrumental delays in the signal chain; the latter supports full 1-GHz bandwidth sampling capability. The CDMS adds active picosecond-level cable delay measurement capabilities to the MIT Haystack (MHO)–designed calibrator to correct for cable delays, signal phase, and amplitude across the full VGOS band. The R2DBE is currently undergoing zero-baseline testing against the RDBE-G, with upcoming deployment at the Westford station for further field testing.

Keywords VGOS, CONT17, signal chain, CDMS

1 Introduction

The VGOS implementation of the MIT/NASA broadband signal chain has been deployed at the KPGO site and passed the operation readiness review in September 2017. The following sections describe the existing system capabilities, how the system will be brought into VGOS compliance, and the future of the calibration systems.

2 VGOS VLBI Signal Chain: Frontend and Backend

The MIT Haystack–developed VGOS VLBI signal chain (Figure 1) is separated into the frontend, located at the antenna, and the backend, located in the control center and connected by fiber for the high-frequency band (4.5–14 GHz) and coaxial cable for the low band (2–5 GHz). A separate coax provides the connection from the calibration ground unit to the antenna unit located next to the feed.

Characteristics of the frontend (Figure 2) include a noise temperature of 40 K over the range of 2–14 GHz (maximum excluding atmosphere), with a feed efficiency of greater than 50 %. The aperture efficiency is approximately 70 % over a range of 2–14 GHz. The spur-free dynamic range minimum is 90 dB in 1 Hz bandwidth, and the dual linear H/V polarization provides –20 dB isolation. The feed has support for pre-LNA instrumental phase and amplitude monitoring.

The backend of the signal chain (Figure 3) supports the frontend receiver signal to independently tune four IF conversion sampled bands. To accomplish this the RF Distributor (RFD v. 2.0) provides one low band (2–5 GHz) output and three high band outputs

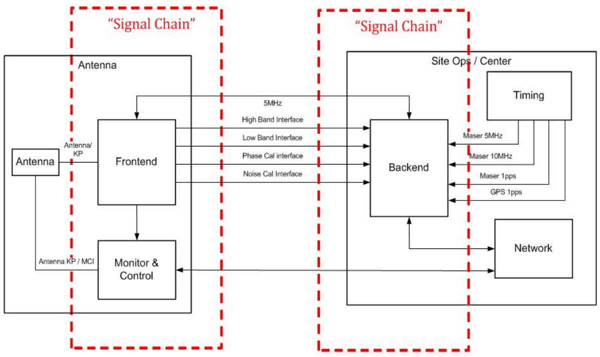

Fig. 1: The VGOS VLBI signal chain architecture.

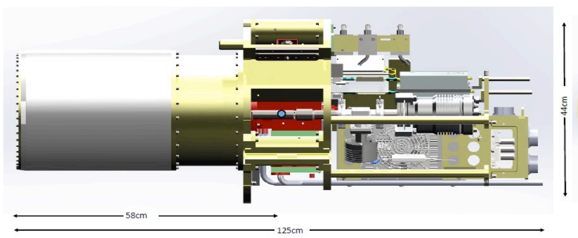

Fig. 2: The VGOS VLBI signal chain frontend.

Chester A. Ruszczyk · Ganesh Rajagopalan · Russel McWhirter · Christopher Eckert · Pedro Elósegui
MIT Haystack Observatory, Westford, MA, USA

Fig. 3: The VGOS VLBI signal chain backend.

(4.5–14 GHz). The backend also supports 2–14 GHz RF down-conversion to 2 GHz baseband output via the Up Down Converters (UDCs v. 2.0), that are programmed to tune the IF bands. The present version of the ROACH digital backend geodetic (RDBE-G v.3.0) digitizes 512 MHz IF bandwidth, and the polyphase filter bank (PFB v3.0) channelizes it into 16×32 MHz complex signals and outputs a 2-bit per channel VDIF format. The data is sent via 10G Ethernet to a Mark6 recorder that records data to disk modules at rates of up to 16 Gbps.

The calibration system (Figure 4), described in detail in Section 4, allows for determination of instrumental delays in the VGOS system, including cable delays, signal phase, and signal amplitude.

3 R2DBE-G v. 4.0

Haystack's 4th-generation digital backend, the R2DBE-G v. 4.0, is based upon the ROACH2 and utilizes a Vertix 6 FPGA. The ADC's chosen for the R2DBE's were developed by ASAIA, in support of the EHT, and consists of a 5 Gigasample per second ADC (2, 4, 8, 16 Gbps) that allows the Haystack signal chain to be 100 % VGOS compliant by supporting greater than the full 1024 GHz band. The R2DBE supports two IF $\times$ 2048 GHz horizontal and vertical polarizations (H&V-pol)) with the bandwidth digitized into 64×32 MHz complex signals in 2-bit VDIF format for a 1024 GHz band.

The R2DBE's 2U form factor (see Figures 5 and 6) is the same as that of the RDBE-G, with a slightly updated configuration with four 10G optical SFP+ interfaces versus the CX4 interface of the RDBE-G.

The software interface supports VSI-S and has a command set that is backward-compatible with v3.0. The same features supported by the RDBE-G, multicast capabilities for monitoring (PCAL, TSYS), have been extended to support 64 channels versus 32 channels for the earlier version.

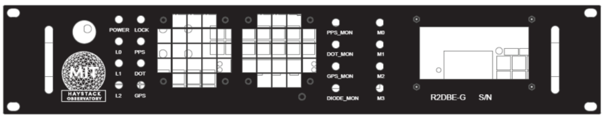

Fig. 5: R2DBE-G front panel.

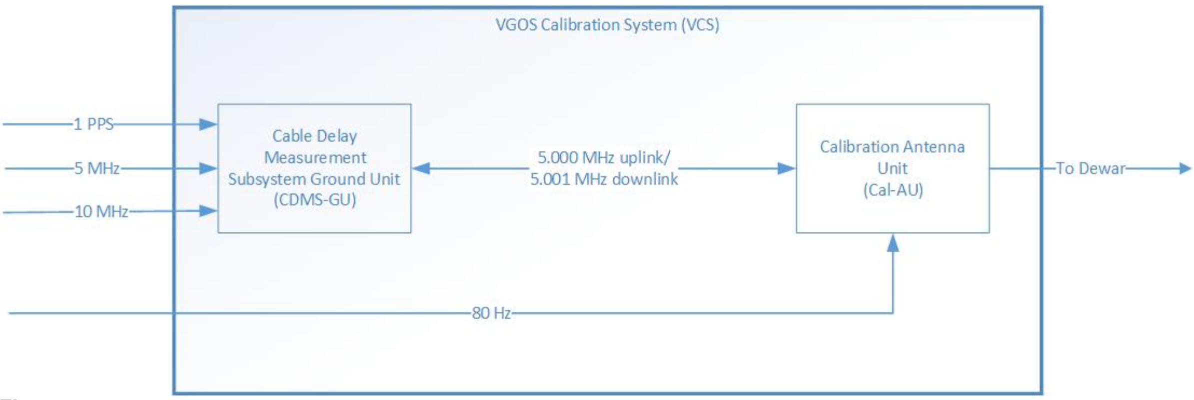

Fig. 4: The new VGOS Calibration System (VCS) CDMS.

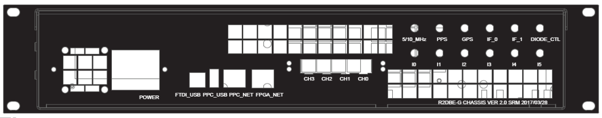

Fig. 6: R2DBE-G back panel.

3.1 Testing

The polyphase filter bank (PFB) has been verified using simulation tools. Extensive zero-baseline testing is being performed with the RDBE-G v3.0 PFB personality for both 1024 GHz and the entire supportable 2048 GHz bandwidth. Following the conclusion of the zero baseline, the R2DBE will start to be tagged along for the VT sessions for further verification and integration with the correlation process (see Fig. 7). The R2DBE-G design has been provided to Digicom™ for purchase by the community. The firmware and the software will be released after stability testing is completed.

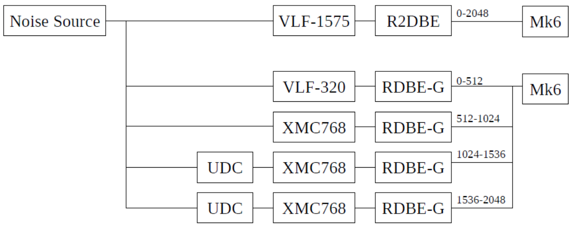

Fig. 7: RDBE-G/R2DBE testing.

4 Calibration: CDMS

The Haystack cable delay measurement system (CDMS) provides monitoring of the electrical length of the signal-carrying cables to enable corrections for cable length variations induced by mechanical, thermal, and any other effects with an RMS accuracy of ≤1 picosecond.

CDMS delay stability is designed to exceed the following standards (Allan standard deviations):

- 1.8e-14 at 30 s
- 5.5e-15 at 100 s
- 9.0e-16 at 600 s
- 1.0e-16 at 50 min

The default cable for delay calibrations is assumed to be an LMR400 coaxial cable. Fiber optic cable support is available upon request. Unfortunately, a modification to the antenna unit is required for the switch.

The new VGOS Calibration System (VCS) CDMS is integrated with upgraded versions of the existing noise and phase/delay calibration subsystems designed by Haystack. The VCS is separated between the frontend and backend of the VGOS signal chain. See figures 8 and 9.

4.1 Stability Testing

The system was tested to verify that stability meets the requirements by inserting the ground and antenna units in a temperature-controlled chamber. The goal was to determine the Allan standard deviations for the system. Figure 10 is an example of a duration for the stability of the system.

The system was also tested for accuracy with an electrically controlled trombone inserted into the coaxial link. Predefined incremental steps, executed at fixed times, were sent to the electrical/mechanical switch to cause the trombone to increase the length to a predetermined calibrated amount.

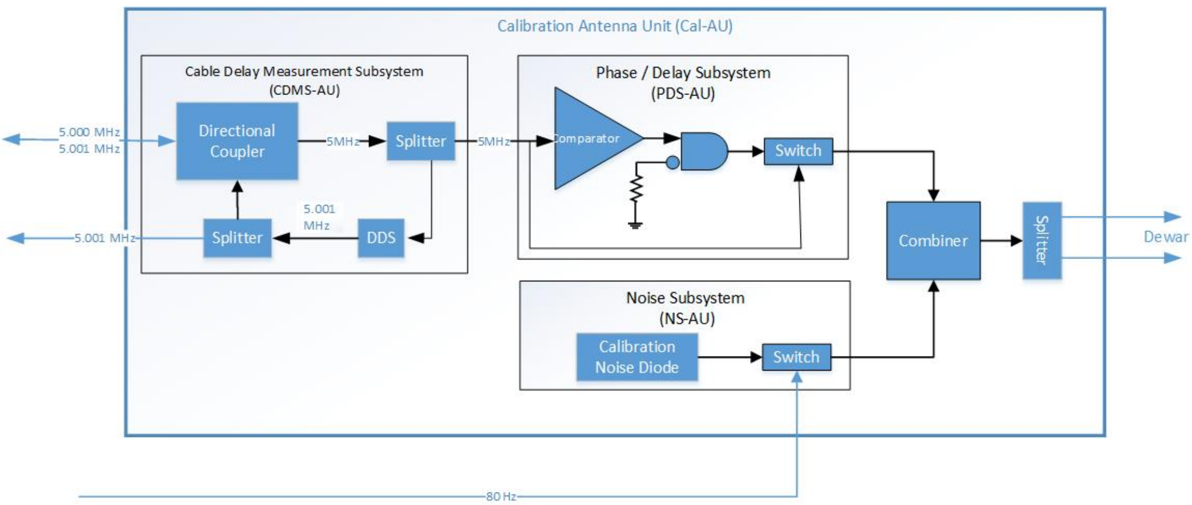

Fig. 8: The CDMS antenna unit.

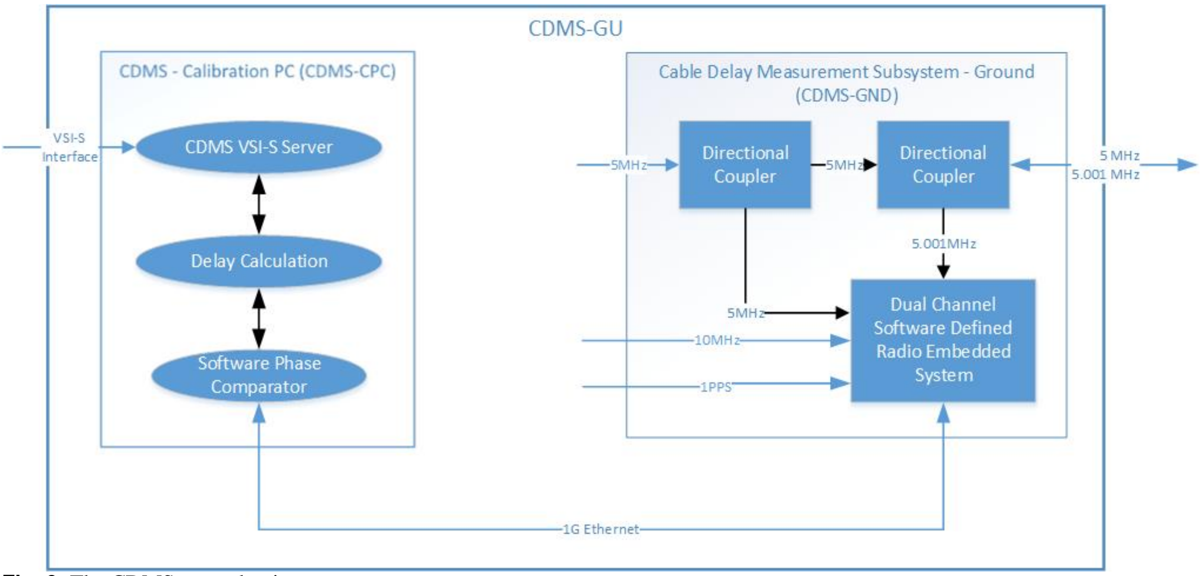

Fig. 9: The CDMS ground unit.

The mechanical changes were then verified by the CDMS that was measuring the proper length changes in picoseconds. The results are shown in Figure 11. At the end of the trombone's maximum length, the controller was reset to the starting reference point and the results verified over a long duration.

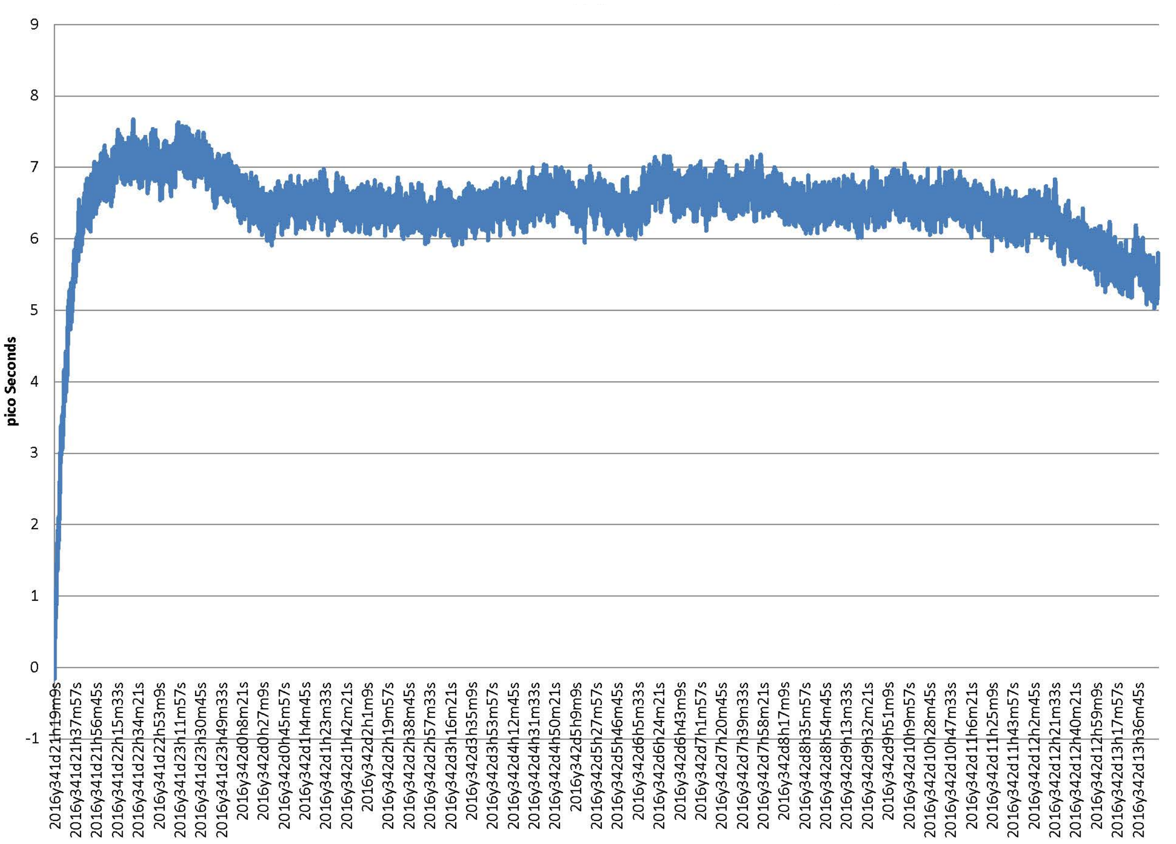

Fig. 10: Results of stability test in a temperature-controlled chamber.

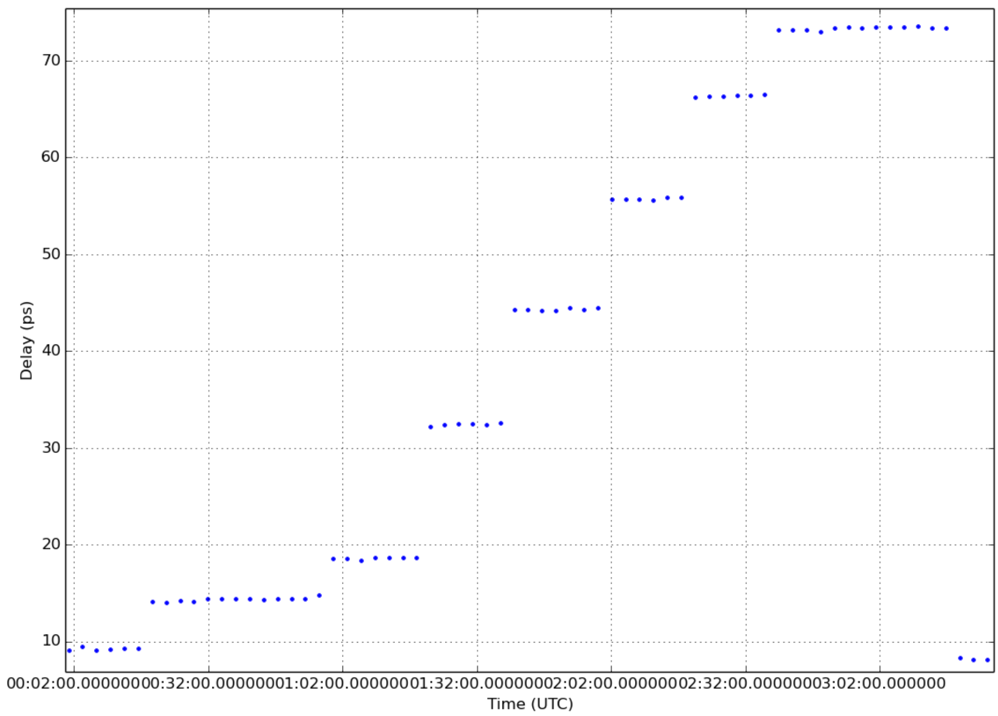

Fig. 11: Results of test with trombone inserted into link.

5 Conclusion

Haystack has officially deployed and supported a VGOS signal chain for the past three years. The work described in this document addresses how the signal chain will meet and support the specifications determined by the community with the R2DBE work. The CDMS system has likewise been deployed and is under analysis through the correlation process; results will be provided later.

DBBC3: The new Flexible, Wide-band VLBI Backend

G. Tuccari, W. Alef, M. Wunderlich, S. Buttaccio, D. A. Graham, H. Rottmann, A. Bertarini, A. Roy, S. Dornbusch, A. Felke, S. Casey, M. Lindqvist

Abstract The successor of the DBBC2 (Digital Base-Band Converter), the most widely adapted digital VLBI backend, is the DBBC3. It has been developed with financial support by RadioNet3 (FP7-Grant Agreement no. 283393) and can sample up to 4 GHz wide bands. In its largest configuration it can output up to 128 Gbps from 8×4 GHz input bandwidth. The first DBBC3s have been delivered to astronomical and geodetic customers. Progress since the last EVGA meeting and future plans are described.

Keywords VLBI, EVN, VGOS, digital backends

1 Introduction

The DBBC3 (Digital Base-Band Converter 3) has been developed with support by RadioNet3 (FP7-Grant Agreement no. 283393) in the Joint Research Activity DIVA (Tuccari et al., 2014). It is the successor of the DBBC2, the most widely adapted digital VLBI backend. Firmware development for the DBBC3 is ongoing to make it fully backwards compatible with the DBBC2. The DBBC3 is a versatile backend, as it can serve the needs of the EVN (European VLBI Network), EHT (Event Horizon Telescope), and the geodetic VGOS network. The DBBC3 can be flexibly configured, as it can be equipped with up to 8 sampler/processing combinations. Thus it offers up to 8 IFs on input with 16 Gbps to 128 Gbps using 2-bit samples on output (the hardware can support a maximum of 512 Gbps).

It is a cost-effective backend which is compatible with nearly every other backend type and out-competes other less flexible solutions. The DBBC3 has reached the production stage, while the firmware is still being extended to allow different observing modes. It was successfully used in latest EHT session. Additionally the DBBC3 is widely suitable to more applications like space science.

Gino Tuccari · Walter Alef · Michael Wunderlich · David Graham · Helge Rottmann · Alessandra Bertarini · Alan Roy · Sven Dornbusch · Armin Felke
Max Planck Institute for Radio Astronomy, Auf dem Hügel 69, DE-53121 Bonn, Germany

Gino Tuccari · Salvo Buttaccio
INAF Istituto di Radioastronomia, Sezione di Noto, Contrada Renna, IT-96017 Noto (SR), Italy

Simon Casey · Michael Lindqvist
Onsala Space Observatory, SE-439 92 Onsala, Sweden

2 DBBC3 components

Similarly to the DBBC2 the DBBC3 consists of a chassis with a control computer, which is used to load firmware to various FPGAs in the system, send setup parameters to all the boards, and provide time information to all parts of the DBBC3.

The analogue IF signal cables are connected to the so-called Giga COnditioning MOdule (GCOMO). This analogue board takes pre-filtered signals with either 1 GHz, 2 GHz, or 4 GHz bandwidth. The IF signals can be in the base-band of 0 GHz to 4 GHz, or can be down-converted from somewhere in the range from 4 GHz to 15 GHz to base-band.

In the next stage the analogue signals are digitised by the analogue-to-digital 3L sampler board (ADB3L). It has four 1 GHz sampler chips, which can be configured for a variety of functions: single and multiple input bands, real or complex sampling. The four sampler chips in real mode can sample a total of up to 4 GHz bandwidth interleaved. In this mode the sampling clock for the four samplers is shifted precisely by 90 from one to the next. Other options are to sample two signals of 2 GHz instantaneous bandwidth each, or four different signals of 1 GHz bandwidth each. For interleaved sampling a novel automatic calibration routine was de-

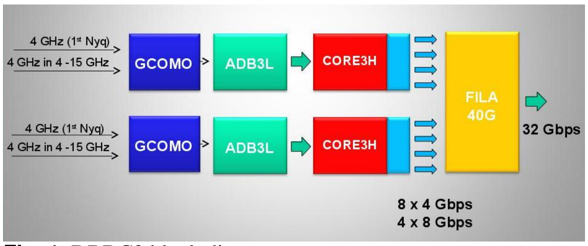

Fig. 1: DBBC3 block diagram.

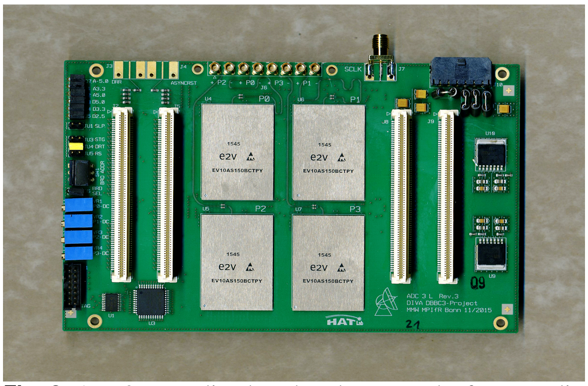

Fig. 2: ADB3L sampling board.In the centre the four sampling chips can be seen.

veloped. The sampling representation is 10 bits and the equivalent sample rate for each ADB3L is 8 GSps.

The digitised signal is next processed by the CORE3 board which consists mainly of a single powerful FPGA. On input the data can have either 8 bit to 10 bit representation. In order to handle this enormous input data-rate the FPGA provides a maximum of 5 TMACS (Terra multiplication-accumulations per second). The processed data can be output via up to eight serial links of 10 Gbps Ethernet with a data-rate of more than 32 Gbps.

The pass-band filtering which can be achieved with this board is 100 dB for signals outside of the desired band. Available and planned processing modes are wide-band DDC (Digital Down Conversion), wide-band PFB (Poly-phase Filter-Bank), DCS (Direct Sampling Conversion):

- Direct sampling conversion of 4 GHz wide bands. If the input data is pre-filtered bandwidths of 2 GHz and 1 GHz and smaller can be converted using decimation.
- PFBs with 256 MHz / 64 MHz / 32 MHz
- DDCs with 128 MHz / 64 MHz / 32 MHz / 16 MHz / 8 MHz / 4 MHz / 2 MHz
- mixed DDC/PFB modes and PFB/DDC modes will most likely be developed

A so-called FILA-40G post-processing and recording unit was developed by Onsala Observatory. It can be used for further processing and recording of the data

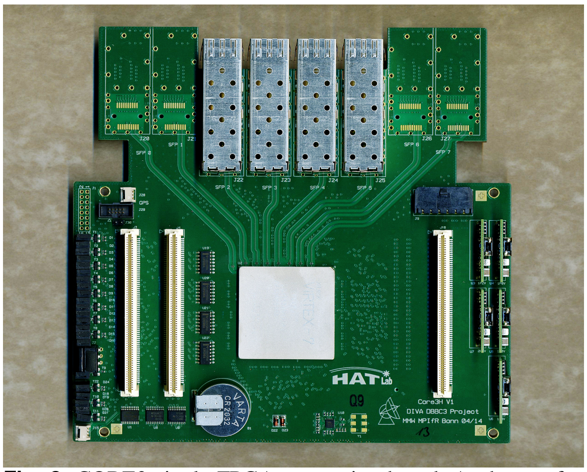

Fig. 3: CORE3 single FPGA processing board. At the top four 10 GE output connectors are visible. Four more can be populated.

output by the CORE3 board. The FILA-40G unit is realized by means of a high-end computer in a RAID chassis with a number of 10 GE and 40 GE ports and a large number of fast disks. It was designed for the functions needed for further processing of the data including the capability to record at 32 Gbps for short periods of time. The complete list of functions includes:

- UT time synchronisation
- Input data masking and decimating
- Corner turning of the data streams
- Packet filtering and burst mode
- Pulsar gating
- VDIF threads forming
- Disk recording

Ancillary boards in the DBBC3 are: the clock and timing board GCAT (GHz Clock And Timing), the phase adaptor for the ADB3L board PHA, GPS 1 PPS distribution etc.

3 DBBC3 development and production status

There are a number of DBBC3s which have been delivered to customers at astronomical and geodetic observatories, or which are under construction.

- VGOS systems with 8 or 6 IFs: Auscope (3 stations 6 IFs each), Onsala (2), Ny-Ålesund (2), Wettzell, Shanghai, Metsähovi
- EHT systems with 4 IFs: APEX, Pico Veleta
- EVN systems with 2 IFs: Yebes, Effelsberg
- other systems with 2 IFs: Sejong (Korea)

Various laboratory tests have been performed for all the systems including a final zero baseline test in DSC and DDC modes. Geodetic tests were done in DSC mode between Hobart and Ishioka antennas. The systems delivered to the EHT antennas at APEX and Pico Veleta were used to record the latest EHT session in April 2017. The latter systems will be compared to the R2DBE backends developed by MIT Haystack Observatory.

Work on the firmware is ongoing. The DSC (full band mode) is operational for EHT and VGOS. It is also useful to provide compatibility to the new Japanese backends. Different flavours of DDC/FPB are under development. High priority has the backwards compatibility to the DBBC2.

Other planned functions are an automatic digital band-pass equaliser, as the very wide IF band-passes are usually not flat, but rather tilted with bumps from reflections in the cables, an RFI logger, a phase-cal detector etc.

To further improve compatibility with all sorts of VLBI backends, which all have only a very limited range of processing capabilities, it is planned to implement adaptive bandwidth and range selection. In preparation for the BRAND project (Tuccari et al., 2017), which will have a next version of DBBC3 as backend this will be dynamic and on the fly to react to time variable RFI. A novel dual frequency cable delay measurement integration in DBBC3 should further improve the geodetic functionalities. To some extent also firmware which will be developed for the BRAND project will back-ported to the DBBC3 like for instance RFI mitigation, etc.

Acknowledgements

The activities that led to this publication were supported by RadioNet3. RadioNet3 received funding from the European Union's Seventh Framework Programme for research, technological development and demonstration under grant agreement no 283393.

References

Tuccari G, Alef A, Buttaccio S, S. Casey S, Felke A, Lindqvist M, Wunderlich M (2014) DBBC3 - EVN and VGOS All-Inclusive VLBI System. In: D. Behrend, K. D. Baver, K. L. Armstrong (eds.), *IVS 2014 General Meeting Proceedings*, 86–90, Science Press (Beijing), ISBN 978-7-03-042974-2.

Tuccari G, Alef W, Pantaleev M, Flygare J, López Pérez J A, López Fernández J A, Schoonderbeek G W, Bezrukovs V (2017) BRAND: A very wide-band receiver for the EVN. In: R. Haas and G. Elgered (eds.), *Proc. 23rd EVGA Working Meeting*, 81–83.

BRAND: A Very Wide-band Receiver for the EVN

G. Tuccari, W. Alef, M. Pantaleev, J. Flygare, J. A. López Pérez, J. A. López Fernández,
G. W. Schoonderbeek, V. Bezrukovs

Abstract BRAND stands for BRoad bAND EVN, a project to build a prototype primary focus receiver with the very wide frequency range from 1.5 GHz to 15.5 GHz, to investigate secondary focus solutions, and to make a survey of the EVN telescopes in order to set the stage for equipping all EVN stations with such a receiver as soon as possible. The project has received funding from the European Union's Horizon 2020 research and innovation programme under grant agreement No 730562 and is a Joint Research Activity (JRA) in the RadioNet programme. We present the motivation, aims, scope and status of the project which was started on January 1st, 2017.

Keywords VLBI, EVN, radio astronomy receiver, digital backends, digital receiver

1 Introduction

The aim of the RadioNet JRA BRAND EVN is developing a wide-bandâ ”digital” VLBI-receiver for the EVN and also other telescopes. The frequency range of the BRAND receiver protoype will be from 1.5 GHz to 15.5 GHz. Up to date a radio astronomical receiver with a frequency ratio of 10:1 has never been realised before. The project engineer is Gino Tuccari from INAF/MPIfR, the project manager is Walter Alef from MPIfR. BRAND EVN is a truly European project with partners in Germany (MPIfR), Italy (INAF), Sweden (ONSALA), Spain (IGN), The Netherlands (ASTRON), and Latvia (VIRAC).

Initially we will develop and build a prototype for prime focus, as wide-band prime focus feeds are much more advanced than similar feeds for secondary focus. But, as EVN has a lot of antennas which can only mount secondary focus receivers, another work package will also do research in a wide-band feed for secondary focus. The timeline for a first VLBI test at Effelsberg is summer 2020, which is ambitious but not unrealistic. The aim of BRAND EVN for the next decade is to enable all EVN stations to install a BRAND receiver as soon as possible!

2 Scientific opportunities and advantages

Assuming that all telescopes of a network are equipped with wide-band BRAND receivers, simultaneous multi-frequency observations will be possible similar to VGOS, but with much wider frequency coverage. While it is expected that such a wide-band system will be less sensitive than modern narrow-band receivers, the enormous bandwidth and data-rate of the BRAND receiver will overcompensate the sensitivity losses.

To make full use of this bandwidth, fringe-fitting has to be done over the very wide frequency range, thus integrating coherently all the data. Of course a precondition is that the ionospheric contribution to the delay is determined by fringe-fitting a quadratic term over frequency in addition to the traditional linear slope. This

Gino Tuccari
Max Planck Institute for Radio Astronomy, Auf dem Hügel 69, DE-53121 Bonn, Germany, and INAF Istituto di Radioastronomia, Sezione di Noto, Contrada Renna, IT-96017 Noto (SR), Italy

Walter Alef
Max Planck Institute for Radio Astronomy, Auf dem Hügel 69, DE-53121 Bonn, Germany

Miroslav Pantaleev · Jonas Flygare
Onsala Space Observatory, SE-439 92 Onsala, Sweden

José Antonio López Pérez · Félix Tercero
Instituto Geográfico Nacional, Madrid, Spain

Gijs Schoonderbeek
ASTRON, Netherlands Institute for Radio Astronomy, Dwingeloo, The Netherlands

Vladislavs Bezrukovs
Ventspils International Radio Astronomy Center, Venstpils, Latvia

problem has been solved already for VGOS. A solution for astronomy will be developed in the framework of CASA (McMullin et al., 2007) by the RadioNet JRA RINGS.

Another advantage of this coherent fringe-fit is that precise registration of simultaneous images at different frequencies will become possible, as the phases as a function of frequency are all related to each other, which is not the case for fast frequency switching.

The BRAND approach will also be superior to VGOS due to the quasi continuous frequency coverage which will result in smaller gaps between sub-bands, which eases the fringe-fitting over the full band. Gaps will be caused by RFI which will be treated in two stages. The strongest RFI will be suppressed right after the receiving horn by High Temperature Super Conducting (HTSC) filters. Remaining weaker RFI will be suppressed in the digital stage.

The UV-coverage will also be vastly improved due to wide frequency band. This still holds even though images will have to made for several frequency ranges.

Joint observations with geodetic VGOS antennas will become possible, so that the long-standing collaboration between astronomy and geodesy can be continued in a somewhat limited scope. But astronomers will still be able to measure precise positions of astronomical antennas, and can contribute to the determination of the radio celestial reference frame. Occasionally huge arrays for special astronomical observations can be formed by adding VGOS antennas to a "BRAND array" when needed.

With a full "BRAND EVN" astronomers can measure variations of polarised emission as a function of frequency over a very wide frequency range with very precise, unambiguous rotation measures.

Studies of several different maser types in different frequency bands can be made simultaneously with proper alignment of the different maser species.

Further opportunities arise for flux variation studies in several bands simultaneously, which is especially interesting for intraday variability investigations. Pulsar searches and observations can be performed over a wide frequency range without timing ambiguities.

3 Technical Feasibility and proposed technical realisation

Broad-band receivers for VLBI with a frequency range of 1.5 GHz to 15.5 GHz have become the next technical challenge in building radio astronomy receivers. Broadband LNAs and feeds have become available for instance for the VGOS project. But also in the RadioNet3

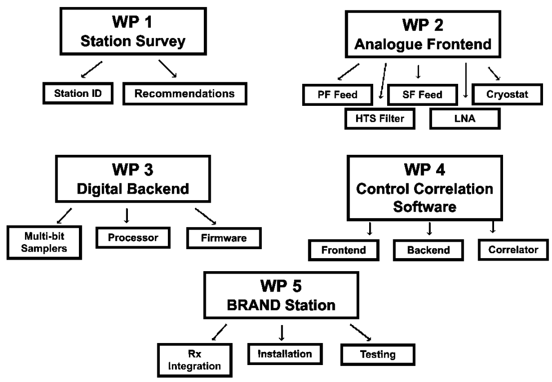

Fig. 1: Block diagram of the work packages.

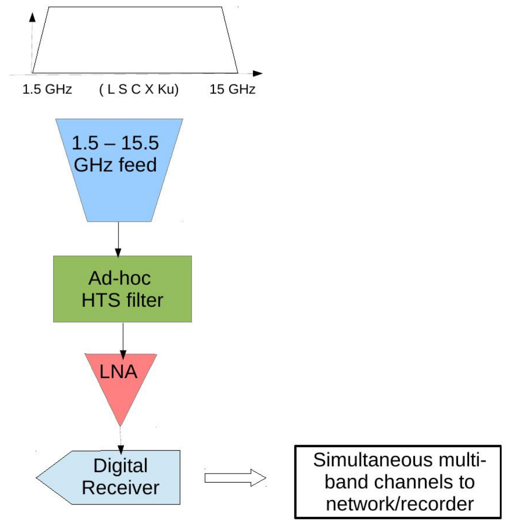

Fig. 2: Schematic view of the proposed BRAND receiver.

JRA DIVA a receiver from 1.5 GHz to 5.5 GHz was developed.

Backends with very high data rates have been developed for for example by JRA DIVA — DBBC3 with 2×4 GHz input and 32 Gbps output. Now DBBC3s with 8×4 GHz have been produced for VGOS antennas.

High bit-rate recorders exist, either as stationary Flexbuff recorders or as up to four Mark6s with up to 64 Gbps for the EHT, or as FiLA40G recorder/postprocessing units at Onsala (see JRA DIVA).

The proposed technical realisation (see Fig. 1 for an overview of the WPs) starts with a survey of the characteristics of the antennas in the EVN and the RFI situation. This information will be assembled in a document which can serve EVN stations in proposing for resources for a BRAND receiver. It will also be used as a start to define standards for the prototype which should fit most antennas.

BRAND EVN will be a single cooled receiver for astronomy covering the band from 1.5 GHz to 15.5 GHz with a linear polarisation feed (see Fig. 2), followed by

HTSC filters to protect the LNA and samplers from the strongest interference, so that both will not be saturated.

After the usual analogue amplification the signal is digitised by a sampler which can handle the 14 GHz wide band in one chunk in 8-bit representation.

The digitised RF signal will be processed by high-performance FPGAs. Firmware will be written to convert the linear polarisation to circular, to remove remaining RFI signals, to form sub-bands with poly-phase filter-banks, digital down-conversion or a mixture thereof. The total output bit-rate will be up to 128 Gbps for 2-bit samples onto Ethernet for local recording or transfer via the Internet.

Acknowledgements

This publication has received funding from the European Union's Horizon 2020 research and innovation programme under grant agreement No 730562 (RadioNet).

References

McMullin J P, Waters B, Schiebel D, Young W., Golap K (2007) CASA Architecture and Applications. In: R. A. Shaw, F. Hill, D. J. Bell (eds.) *Astronomical Data Analysis Software and Systems XVI* (ASP Conf. Ser. 376), 127.

VGOS Development for Ishioka 13-m Antenna

T. Wakasugi, M. Umei, T. Toyoda, M. Ishimoto, R. Kawabata, B. Miyahara

Abstract The Geospatial Information Authority of Japan (GSI) has constructed a new VLBI station which meets the requirements of VGOS in Ishioka, Japan. The station started its operation at February 2015 and had carried out more than 50 sessions in parallel with Tsukuba until the end of 2016. Because the accurate geodetic position of Ishioka is obtained from those sessions, the station took over the role of Tsukuba from the beginning of 2017. Ishioka also conducted some experiments with a broadband system in 2016. This report presents the geodetic results derived from the legacy S/X-band sessions and the status of the broadband experiments.

Keywords Ishioka Tsukuba VGOS broadband

1 Introduction

The Geospatial Information Authority of Japan (GSI) has started the construction of a new geodetic VLBI station in Ishioka since 2011 (Fig. 1). The station is designed for the next-generation VLBI system called VGOS, which is promoted by the International VLBI Service for Geodesy and Astrometry (IVS). The construction of the antenna was completed in March 2014 and its operation was started at February 2015 after some initial performance checks and operational tests. In addition, gravity measurement equipment and GNSS continuously operating reference stations were also installed in the same site to contribute to the Global Geodetic Observing System (GGOS) as a core observatory. The station is located at about 17 km northeast of Tsukuba where there is the headquarters of GSI. We named this new geodetic observing site the Ishioka Geodetic Observing Station (iGOS) (Ishimoto et al., 2016).

Takahiro Wakasugi · Michiko Umei · Tomoo Toyoda · Masayoshi Ishimoto · Ryoji Kawabata · Basara Miyahara
Geospatial Information Authority of Japan, 1 Kitasato, Tsukuba city, 305-0811 Japan

2 IVS Regular S/X-band Sessions

2.1 Relative Position between Tsukuba and Ishioka

Ishioka participated in more than 50 IVS S/X-band regular sessions in parallel with Tsukuba. Figure 2 shows the baseline length between Tsukuba and Ishioka. Orange diamonds are results obtained from each session. The vertical axis represents the baseline length with respect to 16,606,290 mm. Ishioka works well in most of sessions and the repeatability fits within about 5 mm. The relative position of Ishioka with respect to Tsukuba was estimated at $-2,226,596.39$ mm, $-13,403,258.77$ mm and $9,547,971.71$ mm for X, Y, and Z components respectively.

Colocation surveys were conducted in both sites already, so we can verify the results of VLBI by compared with the GNSS data. The purple dots indicate the GNSS results adapted by adding the VLBI-GNSS tie vectors at each site. As you can see, both results reasonably correspond with each other. That means that the relative position of Ishioka to Tsukuba was well established.

2.2 Intensives with Ishioka

One of the important sessions for GSI and IVS is the intensive sessions to rapidly obtain the UT1-UTC parameter. GSI started the weekend intensive sessions (INT2) in 2002 with the Tsukuba-Wettzell baseline. The whole processes from data transfer to analysis are conducted by unmanned operation at GSI, then results are submitted to IVS and IERS within a few minutes from the end of each session. Thus INT2s contribute to monitor the

Fig. 1: The panoramic view of the new geodetic observing site in Ishioka.

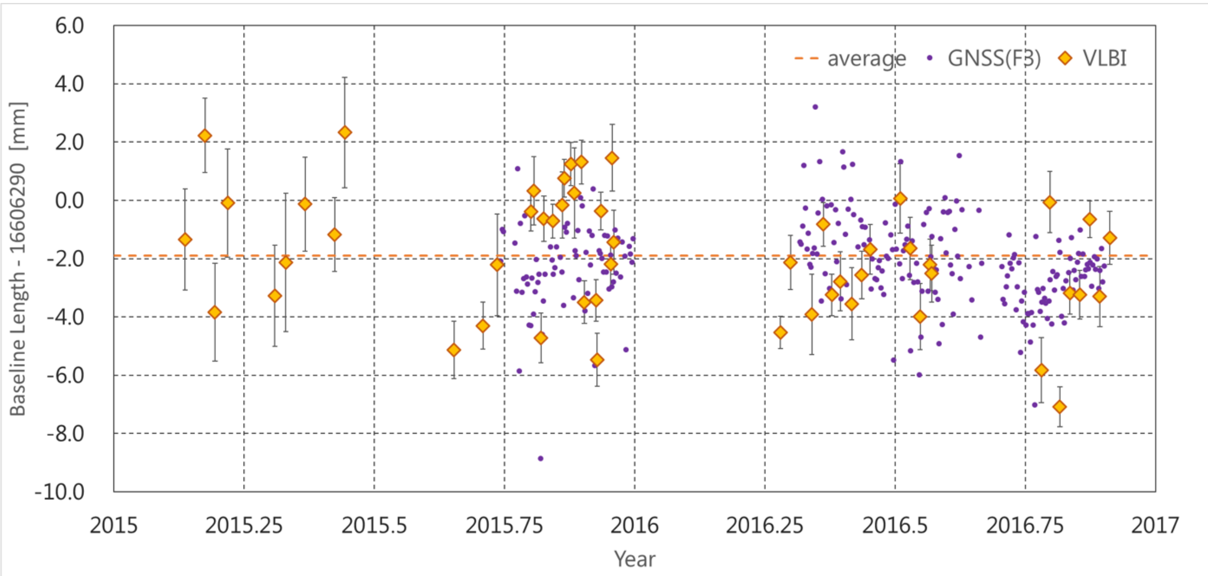

Fig. 2: The baseline length between Tsukuba and Ishioka obtained from S/X-band sessions from 2015 through the end of 2016.

irregular fluctuation of UT1-UTC and improve the accuracy of prediction value [Wakasugi and Hara. (2017)].

Ishioka started trial observations in October 2016 in order to prepare for the termination of the operation of Tsukuba at the end of 2016. The results of UT1-UTC estimation with respect to the IERS final solution are shown in Fig. 3. The result derived from the Ishioka-Wettzell baseline are consistent with that from the Tsukuba-Wettzell baseline. As a result, Ishioka started the intensive sessions officially as the successor of Tsukuba from the beginning of 2017.

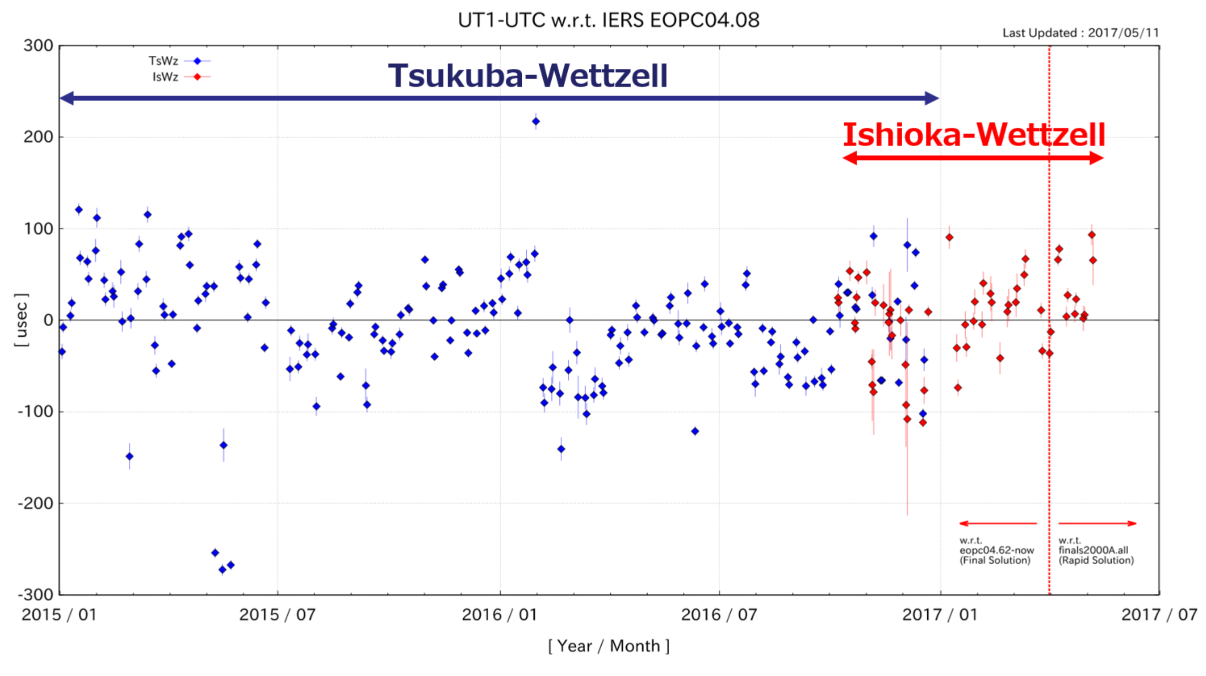

Fig. 3: The estimated UT1-UTC with Tsukuba (blue dots) and Ishioka (red dots).

3 Broadband Experiments

Some pieces of new equipment such as a receiver, a frequency converter, a high speed sampler and a recorder for broadband experiments are ready for Ishioka. Some initial performance checks with the equipment were conducted at the beginning of 2015.

The first international broadband experiments for the station were carried out in 2016. Because only one receiver can be installed in the station, it is necessary to replace existing observing equipment with the new one in order to receive a broadband signal. It takes usually about a week for completing whole exchange processes including cooling and system checks. Therefore the broadband experiments in 2016 were conducted from August to September intensively.

The details of those experiments are summarized in Table 1. The first international fringe for Ishioka was detected in the experiment on Aug. 9 with Hobart station supported and correlated by the National Institute of Information and Communication Technology (NICT). Ishioka obtained fringes in all four bands with GGAO and Westford stations in the VGOS Trial named VGP001 coordinated by IVS. Through these experiments, we confirmed the compatibility of equipment for broadband observation with overseas VGOS systems.

4 Future perspective

Ishioka will continue legacy S/X-band sessions for a while in order to establish relative positions with existing stations in the world. On the other hand, the development and the operation of the broadband system are very significant challenges as well. In the end of 2017, the station will participate in the continuous campaign VLBI experiment coordinated by IVS, called CONT17, as a VGOS station. Then the station will gradually transit to VGOS experiment keeping pace with overseas stations.

5 Conclusions

Ishioka was constructed in 2014 and had observed more than 50 IVS regular sessions with Tsukuba until the end of 2016. Those sessions produced the reliable geodetic position of Ishioka. Accompanying the termination of operation and demolishment of Tsukuba, Ishioka took over the role of Tsukuba including IVS Intensive sessions for the rapid estimation of UT1-UTC. Ishioka succeeded in obtaining the first fringe with overseas stations during intensive broadband experiments conducted in August and September 2016. The station will continue the legacy S/X-band sessions for a while and gradually transit to VGOS with the continuous campaign CONT17 at the end of 2017 as a start.

Table 1: Summary of intensive broadband experiments in 2016.

Date	Experiment	Front-end	Bach-end	Mode	Fringes
Aug. 6	Test with Kashima	QRFH	ADS3000+	8 Msps x 16 ch	Yes
Aug. 9	Test with Hobart	QRFH	GALAV (NICT)	2 Gsps x 4 bands	Yes
Aug. 11	Trial VGT003	QRFH	ADS3000+	64 Msps x 8 ch x 2 pol x 2 bands	Failed
Aug. 18	Test with Tsukuba	QRFH	ADS3000+	64 Msps x 16 ch	Yes
Aug. 23	Test with Marble (NICT)	QRFH	GALAV (NICT)	2 Gsps x 4 bands	Yes
Aug. 30	Trial VGT004	QRFH	ADS3000+	64 Msps x 8 ch x 2 pol x 2 bands	Yes
Sep. 20	Trial VGP001	QRFH	ADS3000+	64 Msps x 8 ch x 2 pol x 4 bands	Yes

References

Ishimoto M, Umei M, Wakasugi T, Kawabata R, Toyoda T, Miyahara B, Fukuzaki Y (2016) Status on the Ishioka Geodetic Observing Station. *IVS NICT-TDC News*, 36, 9–12,

Wakasugi T, Hara T (2017) Tsukuba VLBI Analysis Center. *International VLBI Service for Geodesy and Astrometry 2015+2016 Biennial Report*, in press,

VOGS Interoperability Observing Sessions (IOS) Results, Lessons Learned, and Guidelines

C. A. Ruszczyk, M. Titus, A. Burns, J. Barrett, A. Niell, P. Elósegui

Abstract The VGOS network has expanded over the last two years from a single baseline of two prototype systems at Westford, Massachusetts, and the Goddard Geophysical and Astronomical Observatory (GGAO), Maryland, to a thriving network of at least 6 stations. The two prototype systems share many of the broadband attributes that characterize a VGOS system—in particular, the implementation of the signal chain. Using the implementation of similar technology at the two ends of a relatively short baseline (about 600 km) was a desirable feature, since it greatly simplified the challenge of understanding the novel VGOS data, hence also helping to improve those systems. Recently, new systems have come online, including the 12-m antenna at the Kokee Park Geophysical Observatory (KPGO), Hawaii, and 13-m antennas at Yebes, Spain; Wettzell, Germany; and Ishioka, Japan. The KPGO system is an improved version of the Westford and GGAO systems; the signal chain technology of the other three systems, on the other hand, differs quite substantially from their predecessors. The expansion of the VGOS network will continue to involve embracing heterogeneity while maintaining compatibility, which is a challenge. We will present our ongoing observational efforts, a series of carefully designed and executed trial sessions aimed at the seamless integration into the VGOS network of new stations as they come online. These efforts are necessary for the successful expansion of VGOS into a truly global network.

Keywords VGOS, observations, lessons, guidelines

Chester A. Ruszczyk · Mike Titus · Alex Michael Burns · John Patrick Barrett · Arthur Niell · Pedro Elósegui
Massachusetts Institute of Technology, Haystack Observatory, Westford, MA, USA.

1 Introduction

The International VLBI Service for Geodesy and Astrometry (IVS) VLBI Geodetic Observing (VGOS) network (see Fig. 1), currently consisting of 6 globally distributed VGOS telescopes, has been taking part in biweekly 24-hour observing sessions.

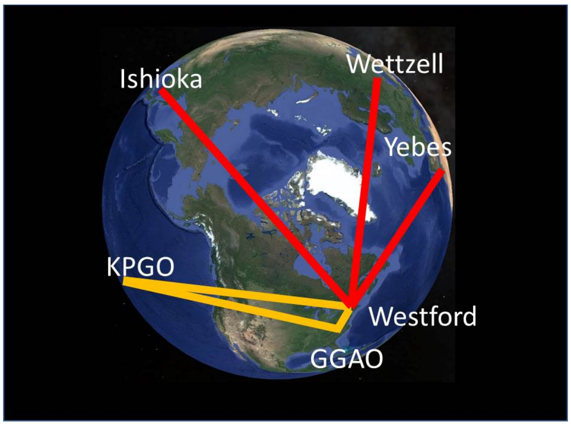

Fig. 1: VGOS Interoperability Observing Session (IOS) network.

The primary goals of the Interoperability Observing Sessions (IOS) sessions are:

1. Explore compliance and interoperability among different realizations of a VGOS system, consisting of:
   - The NASA network (Westford, GGAO, and KPGO)
   - Wettzell, Yebes, and Ishioka
2. Demonstrate consistency for operational readiness and data quality
3. Implement end-to-end network operations integration, including:
   - Consistent station operations
   - Correlation and post-correlation processing

- Database generation and geodetic "rapid" analysis

4. Provide feedback to improve the quality of the VGOS data and increase reliability of operations
5. Perform VGOS operations 24×7

To test implementation of these goals, the VLBI Trial (VT) sessions were designed; these are currently being executed (see Table 1).

From these end-to-end sessions, the rapid analysis results process was generated for the GGAO to Westford (Wf) baselines, based on more than 3 years of observations (Sec. 2). Lessons from the tests continue to be documented for all stations so that performance can be improved (Sec. 3) and procedures for participation updated (Sec. 4). Likewise, guidelines were established for all new stations that wish to participate in the VGOS sessions based upon the last two years of experience (Sec. 5). All of these topics are covered in the following sections, with the ultimate goal of enabling stable operations for the growing VGOS network. This progress could not have been accomplished without the contributions of all participating members (Sec. 7).

2 2017 Rapid Analysis Results

For the rapid analysis groundwork, the GGAO to Westford baseline (~600 km), for which observations were first run in December 2013 and continue through 2017, baseline-length residuals (mm) were plotted for observations including 1-, 6-, and 24-hour sessions. The last of the estimates plotted were from the VT7100 session. The rapid analysis results are shown in Figure 2, which plots the baseline-length residual for each session.

The baseline length was determined to be 600796020.4 mm with a weighted RMS of 1.0 mm and a chi2pdof of 2.5. The longer error bars are

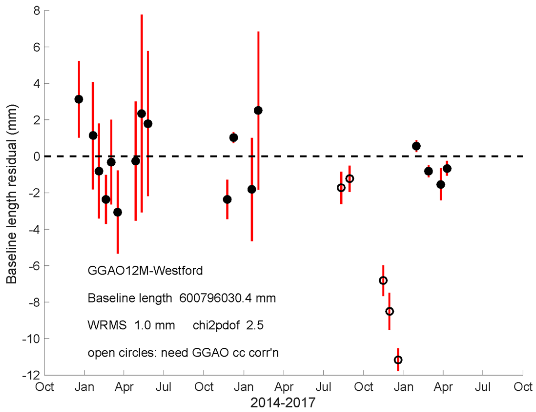

Fig. 2: Results: GGAO to Westford rapid analysis 2014–2017.

associated with the 1-hour observations; the mid-length error bars with 6-hour observations; and the short error bars to the full 24-hour observation sessions. (It should be noted that the solid circles incorporate cable calibration corrections and the open circles still require corrections.)

It is expected that similar figures for the other baselines (i.e., KPGO, Yebes, Wettzell) will be added, pending the stability of their configurations.

3 Lessons

We have separated the lessons learned from the test sessions into individual station reports and overall VGOS end-to-end operation reports.

The following list of issues was compiled after examination of all stations' operational procedures:

1. A lack of logging incidents during observing to aid in correlation processing, e.g. equipment failures during the session
2. Action, or slow reaction, based on reports filed from the correlator on data quality issues
3. Delay in disk shipment due to budgets impacting correlation turnaround time
4. e-transfer requiring 2-step process for data conversion into the proper format and limited bandwidth
5. Instrumentation challenges:
   - Different equipment features
   - Lack of a unified software interface and varying feature sets
   - Lack of plug-and-play capability in the design of the command control software
   - Problems diagnosed not leading to resolution in data quality

For item 2, it is understood that the end stations do not necessarily have control over bug fixes and are beholden to the development effort.

Overall operation of the VGOS network, including correlation and analysis, has demonstrated the following issues:

1. Correlation and analysis lacks a rapid turnaround of results.
2. Shipping issues associated with the end stations result in a delay to the start of correlation of up to two weeks.
3. Correlation space restructuring at Haystack impacted the initial VT series, but has since been corrected.
4. The software is not ready for prime time, or release to other correlation centers, which leads to procedures not being propagated to other correlators.

Table 1: 2017 VGOS VT Observing Sessions (https://lupus.gsfc.nasa.gov/sess/master17-vgos.html).

Session Type	Session Code	Date (yyyy/mm/dd)	DOY (ddd)	UT Time (hh:mm)	Duration (hrs)	Stations
VT	VT7017	2017/01/17	017	18:00	24	GsWfWsYj
VT	VT7030	2017/01/30	030	18:00	24	GsWfWsYj
VT	VT7044	2017/02/13	030	18:00	24	GsWfWsYj
VT	VT7058	2017/02/27	044	18:00	24	GsWfWsYj
VT	VT7072	2017/03/13	058	18:00	24	WfWsYj
VT	VT7086	2017/03/27	072	18:00	24	GsWfWsYj
VT	VT7100	2017/04/10	086	18:00	24	GsWfWsYj
VT	VT7114	2017/04/24	100	18:00	24	GsWfWsYj
VT	VT7128	2017/05/08	114	18:00	24	GsWfWsYj
VT	VT7142	2017/05/22	128	18:00	24	GsK2WfWsYj
VT	VT7156	2017/06/06	142	18:00	24	GsK2WfWsYj
VT	VT7170	2017/06/19	156	18:00	24	GsK2WfWsYj

After the initial VT series report (Ruszczyk and Titus, 2017), subsequent series have seen a marked improvement to overall operations of the first five established VGOS systems (Ruszczyk et al., 2017).

4 Established Station Guidelines

Station participation in the VT series is based upon stable and recoverable operations during the 24-hour session. Technical problems are expected from both hardware and software failures and due to the fact that most new pieces of equipment in the VGOS system are being stressed for the first time.

If a technical problems prevents a station from participating in a single or multiple 24-hour VT sessions, or upgrades to hardware or software of FPGA bit code, a station must follow specific issued guidelines in order to be reinstated into the subsequent VT session.

The guidelines specify that the following steps must be performed:

1. A successful fringe test proving operational readiness with a operational station
2. A single scan of approximately 30 secs
3. Ad hoc observing (source, time, standard configuration, 30-second scan)
4. e-transfer data to correlator in a specified format
5. A go / no go for next session or request for additional fringe tests (provided from the correlator)

Once these steps are completed, an existing station may rejoin the network for the next 24-hour session. Failure to follow the steps will result in the data not being processed at the correlator.

5 New Station Guidelines

As new VGOS stations begin to come online, the expectation is that the stations have verified functionality of their VLBI signal chain before participation. Note that the correlation process should not be used as a debugging tool for equipment that has not been vetted. After the station equipment has been proven to operate correctly and is able to be configured and controlled properly, the station will:

1. Perform a successful fringe test (same as existing stations) on all 4 VGOS bands
2. Join a VT schedule and tag along for 1 hour to confirm:
   - Configuration information
   - Prove operational readiness (e.g., Ready, Start, Stop messages)
3. Tag along for 24-hour sessions to prove overall stability of signal chain and operations
4. Prove stability before being integrated into the core network, by demonstrating the following:
   - Stability over multiple sessions
   - Acceptable data quality as indicated by correlation results

6 Conclusions

We are living in an exciting time, as VGOS stations continue to interoperate and flush out operational and system issues, and as new stations come online. Many challenges remain when incorporating new instrumentation, including the first true stress test over prolonged periods and interoperability. The issue of data quality versus data quantity is being carefully investigated, as is the stability of the overall VGOS network and the ability to repeat observing sessions.

VGOS operations have come a long way toward operating at the level of standards that exist for legacy IVS sessions, but stations must still break away from the ad hoc engineering operations that exist for most new systems and those that are integrating new equipment. We continue to work to integrate new VGOS solutions and verify integration to the overall network from end to end. After much progress, we continue to move toward achieving the VGOS goals of 24×7 operations.

7 Acknowledgments

We would like to acknowledge and thank the sites members for participating in the VGOS sessions and to continual improve their systems and processes: Katie Pazamickas and Jay Redmond (GGAO); Alex Burns and Mike Poirier (Westford); Lawrence Chang, Chris Coughlin, and Kiah Imai (KPGO); Gerhard Kronschnabl, Alexander Neidhardt, and Christian Plötz (Wettzell); Laura Barbas, Javier González, and Pablo de Vicente (Yebes); Rioji Kawabata, Masayoshi Ishimoto, Takahiro Wakasugi, and Michiko Umei (Ishioka).

We also thank the dedicated staff at NVI: Dirk Behrend, Sergei Bolotin, John Gipson, Frank Gomez, Ed Himwich, and Cynthia Thomas, along with the many others who have made VGOS a reality.

References

Ruszczyk C, Titus M (2017) MIT Haystack Observatory VGSO Network Anaylysis. NASA Document SGP-VLBI-ANYS-0030 04 2017.

Ruszczyk C, Titus M, Barrett J (2017) MIT Haystack Observatory VGSO Network Anaylysis. NASA Document SGP-VLBI-ANYS-0031 08 2017.

Bonn Correlator: Preparing for VGOS and EHT

W. Alef, A. Bertarini, S. Bernhart, L. La Porta, A. Müskens, H. Rottmann, T. Schüler, J. Wagner

Abstract After about seven years of operation the HPC cluster of the Bonn correlator centre was renewed in 12/2015 to accommodate future vastly increased datarates of VGOS and EHT[1] observations. Its capacity should be sufficient for the next five to seven years. We will give an overview of the cluster and the correlator performance. We review organisational changes and the correlator activity since the last meeting. The first correlations with playback from Mark 6 recorders were cumbersome, but recent software developments have lead to a satisfactory solution. Unfortunately tests could not be done with VGOS data as none has been made available to us. A second 1 GigE line to the Internet via the University of Bonn was connected to the correlator. Due to rapidly falling costs for Gb-Internet connections we will soon be able to improve the correlator connectivity, if need arises.

Keywords instrumentation: interferometers, VGOS operations broadband, VLBI correlation

Walter Alef · Helge Rottmann · Jan Wagner
Max Planck Institute for Radio Astronomy, Auf dem Hügel 69, DE-53121 Bonn, Germany

Alessandra Bertarini · Laura La Porta · Simone Bernhart
Reichert GmbH / Bundesamt für Kartographie und Geodäsie, c/o Max Planck Institute for Radio Astronomy, Auf dem Hügel 69, DE-53121 Bonn, Germany

Arno Müskens
Rheinische Friedrich-Wilhelms Universität Bonn, Institut für Geodäsie und Geoinformation (IGG), Nußallee 17, DE-53115 Bonn, Germany

Torben Schüler
Bundesamt für Kartographie und Geodäsie, Geodätisches Observatorium Wettzell, Sackenrieder Str. 25, DE-93444 Bad Kötzting, Germany

[1] http://eventhorizontelescope.org

1 Introduction

The VLBI correlator at the Max Planck Institute for Radio Astronomy (MPIfR) has been a joint project of the MPIfR and the German Federal Agency for Cartography and Geodesy (BKG) with support from the IGG, University of Bonn. In the beginning of 2017 the geodetic correlation was outsourced by the BKG to the company Reichert GmbH in Bonn, who has now taken over the role of the IGG. As the trained staff could be kept, continuity for geodetic correlation could be maintained.

Highlights since last meeting are that a new compute cluster was erected, the correlation of data from the Event Horizon Telescope (EHT), native playback of Mark 6 data, a second 1-Gbit Internet connection via Bonn University, and the installation of the cluster file system BeeGFS to better administer the 870 TB storage of data from the antennas.

2 The new correlator cluster at MPIfR

After seven years of operation the High Performance Computer (HPC) cluster at the VLBI correlator centre at the MPIfR was replaced in December of 2015 by a new cluster of much more powerful elements. It was designed to match the requirements for both VGOS and mm-VLBI correlation up to about 2020. The cluster consist of:

- 68 nodes with 20 compute cores each (= 1360 cores total), which results in an increase in computing power of about 10 times that available with the old cluster
- three head nodes which allows more than one correlation to be executed in parallel
- 56 Gbps Infiniband interconnect between all nodes
- more than 1 PB of disk space organised in several RAID units, each with redundancy. About 880 TB are organised in a BeeGFS parallel cluster file sys-

Fig. 1: New HPC cluster at MPIfR seen through a glass wall.

tem which offers to the correlator software one point of access to the data recorded at the antennas
- 15 Mark 5 playback units
- six Mark 6 playback units each with four bays for playback of EHT and VGOS data

The correlated data and other important files are backed-up daily. The Internet connectivity has recently been improved by connecting a second 1-Gbit line to the Internet via Bonn University.

Geodetic data is correlated with DiFX (Deller et al., 2011) version 2.4 while for data recorded on Mark 6 units the development version (2.5) has to be used. For the correlation of RadioAstron (Kardashev et al., 2012) data a special branch of DiFX is available. For RadioAstron a final new version was developed (Bruni et al., 2014), which is now frozen.

Up to three parallel correlations have been tested and no reduction in speed has been observed. A native playback mode for Mark 6 modules is about 90 % ready. An initial attempt was made to implement multiple data streams per station, which could allow undersampled data streams to be merged. It was decided though to handle this problem outside of DiFX.

Mark 6 playback via Haystack's vdifuse package delivered only low data-rates at the Bonn correlator, even with the same setup as used at Haystack. A solution was found by switching to J. Wagner's fuseMk6 software which performs as expected up to 16 Gbps.

The database for experiment status and disks has been extended to incorporate more and more information to increase its usefulness for controlling the whole correlation, including export and archiving of the data. Data export is in FITS and HOPS format. Initial data analysis is done with HOPS, AIPS, and PIMA. The final products are archived on the MPIfR archive server.

3 Correlation

The geodetic analysts fully support all geodetic observations correlated at Bonn. With about 2.1 FTEs (1.5 by BKG/Reichert GmbH, and 0.6 by IGG) they are responsible for scheduling a number of geodetic observing series, for preparing and supervising the correlation, as well as for the postprocessing of the correlated data. The latter includes fringe-fitting and creation of the file formats required by the subsequent geodetic analysis. The geodetic group also maintains a web page via which all data transfers to/from the correlators are coordinated.

All of the astronomical correlation is handled by MPIfR staff and support scientists. The cluster and DiFX software are maintained and improved by MPIfR staff, with financial support from BKG. MPIfR is also in charge of hardware maintenance and repair. General IT-support is given by MPIfR's IT division.

Correlation could be sped up due to the faster HPC cluster, the BeeGFS, which for instance reduced the correlation time of the INT3s by 33 %, and a more streamlined operation. As a result the amount of geodetic correlation was increased by about 20 % in the last two years without an increase in manpower. Total numbers of observations correlated since the last meeting are:

Fig. 2: View of the Mark 5 and Mark 6 units through a glass wall.

- 104 R1
- 12 EURO
- 19 T2
- 12 OHIG
- 103 INT3 (in eVLBI mode)
- 8 RDs Cheng'E3 VLBI observations

Only about two stations send modules to the Bonn correlator still. To cope with the slowly increasing demand, an additional 1-Gbit Internet line via Bonn University was connected to the correlator cluster. Even better Internet connectivity is becoming affordable now, as prices in Germany are dropping and the MPIfR is close to glass fibres of other providers.

Astronomical correlation is centred around "very high resolution" astronomy. About 15 observations with RadioAstron with up to 20 antennas were correlated, where enormous baseline lengths of several earth diameters are reached regularly.

The other area is mm-VLBI, where at the highest frequencies presently used in VLBI, resolutions are achieved which approach the event horizon of the nearest supermassive Black Holes. Two session per year of the Global 3mm-VLBI Array (GMVA) with up to 15 participating antennas, 2 Gbps data-rate, and up to 700 TB of data were correlated. End or March 2017 a first session including the Atacama Large Millimeter/submilimeter Array was observed in an new mode which required a contiguous bandwidth of 512 MHz yielding a data-rate of 4 Gbps. For the Event Horizon Telescope (EHT) observing at 230 GHz half of the 2015 session was correlated at Bonn, as will be the April 2017 session.

In addition a number of tests for the development of the DBBC VLBI backend were supported.

4 Preparations for VGOS

Correlation efficiency could and will be increased further. Fringe search is still needed for geodetic correlation, while for instance the VLBA uses continuously monitored values of GPS time versus the formatter clock, which saves time and effort.

Other delays in correlation are caused by errors in transferred data. The software used for the transfers has to be made more robust and needs to better recover from unstable Internet connections. The transfer process itself should be automatically initiated and controlled by the correlator, based on planned correlation dates, ancillary information and available space. Appropriate data buffers have to be provided at the stations.

One bottleneck in correlation will remain. In order to reach the VGOS aims the highest data quality possible will be required! Thus, in order to scrutinise the results and help to debug problems at stations, experienced staff will still be needed. For instance losing one/more antennas will already deteriorate the geodetic observables, even for big arrays.

Both VGOS and the EHT will make heavy use of Mark 6 recording. This can be attributed to the very high data-rates of up to 64 Gbps which make Internet transfer at least initially unfeasible. The Mark 6 system uses several units with up to four modules in parallel. The data is recorded and scattered over more than one module. While for Mark 5 data the so-called native mode was implemented by NRAO, and has proven to be the most efficient method for correlation, for Mark 6 the scattered data has to be gathered before correlation, either in a separate process or on the fly with a fuse file system.

Haystack has developed vdifuse which gathers the data on the fly and offers the data on the modules to the correlator as files in a directory. MPIfR in collaboration with W. Brisken (LBO) has started to implement a native Mark 6 mode which is now about 90 % ready. The native mode would avoid the overhead of the often networked fuse file system.

As an alternative to vidfuse at MPIfR we installed fuseMk6 which allowed much faster playback of Mark 6 data. While we could test Mark 6 correlation extensively with EHT data, we have not received any VGOS data from Haystack for testing. We expect though to gain a lot of experience with Mark 6 recording by correlating the MPIfR half of the 2017 EHT data. Fringe search has started and correlation is imminent.

5 Conclusions

The Bonn VLBI correlator was replaced in 12/2015 after about seven years of operation. The new HPC cluster is about 10 times as powerful as the old cluster. The throughput of the cluster was slightly increased for traditional geodetic observations due to better efficiency in the correlation process and the BeeGFS cluster file system. So far the cluster could not be tested for VGOS as no data has been made available by Haystack observatory.

Playback of Mark 6 data is now working well, as could be proven with data from the Event Horizon Telescope. More software will be needed to improve the correlation process further. In particular the buffering of data at the stations and transfer via the Internet has to be automated and handled centrally by the correlator.

References

Bruni G, Anderson J, Alef W, Lobanov A, Zensus A J (2014) Space-VLBI with RadioAstron: new correlator capabilities at MPIfR. In: *Proc. 12th European VLBI Network Symposium and Users Meeting*, ID: 119.

Deller A T, Brisken W F, Phillips C J, Morgan J, Alef W, Cappallo R, Middelberg E, Romney J D, Rottmann H, Tingay S J, Wayth R (2011) DiFX-2: A More Flexible, Efficient, Robust, and Powerful Software Correlator. *PASP*, 123, 275–287.

Kardashev N S, Kovalev Y Y, Kellermann K I (2012) The Radio Science Bulletin, 343, 22–29.

On the use of Linear Polarizers in VLBI: the PolConvert Algorithm

I. Martí-Vidal

Abstract With the advent of new-generation broadband receivers in VLBI, it is now possible to extend the observing bandwidths up to several GHz; a continuous frequency coverage even across different bands. However, the wideband receivers have to detect the signal in a linear polarization basis, which is not convenient for VLBI. Thus, the VLBI signals have to be converted into a circular basis for a robust fringe-fitting and phase calibration. In these proceedings, I discuss about a polarization conversion algorithm (PolConvert), designed for a linear-to-circular conversion at a post-correlation level. This algorithm allows us to calibrate and convert the linear-polarization VLBI correlations into a pure circular basis with a high flexibility and a minimum residual polarization leakage.

Keywords techniques: interferometric, techniques: VLBI, polarization, methods: data analysis

1 Introduction

The signals recorded in VLBI are typically given in a circular polarization basis: there are two data streams being registered, right-circular polarization and left-circular polarization (RCP and LCP, respectively). The use of this polarization basis has many advantages for VLBI. The most important one is that the parallactic-angle effect becomes a mere phase correction:

$$R^{corr} = R \times \exp(j\psi) \quad ; \quad L^{corr} = L \times \exp(-j\psi),$$

where ψ is the parallactic angle of the observed source (for a given antenna), R and L are the RCP and LCP streams (for that antenna), respectively, and R^{corr} and L^{corr} are the streams properly corrected for parallactic angle. In this basis, the correction of the cross-correlation $R_a R_b^*$ (where a and b are the indexes of the two antennas in the baseline) would be as simple as

$$(R_a R_b^*)^{corr} = R_a R_b^* \exp[j(\psi_a - \psi_b)].$$

The parallactic angle correction is a fundamental step that has to be applied prior to the fringe-fitting, especially in VLBI phase-referencing observations, where the gain interpolation from the calibrator to the target has to be free of any unmodelled geometric effects. Furthermore, this correction has opposite signs for R and L, so that the only way of combining polarizations, to get a higher SNR in the fringe detections, is to correct for the ψ effect *before* the fringe fitting; right at the beginning of the data calibration.

If we cross-correlate the VLBI fringes in a linear polarization basis (i.e., X and Y, where X is the horizontal dipole and Y is vertical, in the frame of the antenna mount), the parallactic-angle correction becomes bit more complicated. For example, the correlation product $X_a X_b^*$ is corrected as (e. g. Smirnov, 2011)

$$\begin{aligned}(X_a X_b^*)^{corr} &= X_a X_b^* \cos\psi_a \cos\psi_b + \\ &+ X_a Y_b^* \cos\psi_a \sin\psi_b + Y_a X_b^* \sin\psi_a \cos\psi_b + \\ &+ Y_a Y_b^* \sin\psi_a \sin\psi_b.\end{aligned} \tag{1}$$

If we further add the different antenna-gain corrections for X and Y (since, for linear polarizers, these do not commute with the parallactic-angle correction), the expression becomes even more difficult to treat. Notice that, in order to correct $X_a X_b^*$, we would need to know the complex gains for X and Y at both antennas. However, such gains are only known *after* a global fringe-fitting and a full phase calibration, for which we need to have applied the parallactic-angle correction *before*. Therefore, the only way to solve this calibration problem is to perform the fringe-fitting *and* the parallactic-angle correction *simultaneously* and self-consistently for all the polarization products. Such an approach is impractical. Even if the data could be fully calibrated, the resulting visibility $X_a X_b^* + Y_a Y_b^*$ would *not* corre-

Ivan Martí-Vidal
Onsala Space Observatory, Space Earth and Environment, Chalmers University of Technology, SE-439 92 Onsala, Sweden

spond to the Fourier transform of Stokes I, but to

$$\frac{(X_a X_b^* + Y_a Y_b^*)^{corr}}{2} = \mathcal{F}\left[I\cos(\psi_a - \psi_b) + jV\sin(\psi_a - \psi_b)\right]|_{(u,v)}, \quad (2)$$

which is a baseline-dependent complex function (a non-trivial extension of the Aperture-Synthesis). All these problems are the reason to convert the data streams into a circular basis for VLBI.

The VLBI community is evolving toward the use of wideband receivers. Wide fractional bandwidths in VLBI are the key to increase both the sensitivity to weak sources and the accuracy in the group-delay estimates. The latter advantage is especially important for Geodesy and Astrometry, so that wideband receivers have become, indeed, critical components for the new-generation VLBI geodetic stations. However, the traditional way of polarimetric conversion from linear to circular (i.e., the use of quarter-wave plates at the receiver's frontend) is not possible with wideband receivers, since the polarization leakage far from the center frequency would be too large. Doing the conversion digitally, at the receiver's backend, would be a possibility, although the relative phases (and amplitudes) among polarizers (together with their eventual time evolution) would have to be known (i.e., monitored, in some way) with a high precision, for a successful conversion. Furthermore, any error in such estimates might spoil the observations, with the introduction of large leakage-like effects among the polarization products.

2 Post-correlation conversion: PolConvert

Processing the data streams *after* the VLBI correlation is the most efficient and secure strategy for the conversion into a pure circular basis. It is efficent, since it is applied to a volume of data much smaller than the raw antenna signals, and there is no need of hardware implementation; it is secure, since the process is fully reversible, without need of re-correlation. We have developed an algorithm (PolConvert) that performs such a conversion on VLBI data, given either in DiFX/SWIN or FITS-IDI format. We have also implemented and tested it on real VLBI data (e.g., Martí-Vidal et al., 2016). The algorithm is able to handle even observations in a *mixed* polarization basis; that is, using antennas with linear-polarization and circular-polarization feeds in the same experiment. The program can also be used to convert data from phased arrays (it is indeed the official software used for the ALMA-VLBI polarimetry, where the ALMA antennas are phased up as one single linear-polarization VLBI station).

How does this work? If G_x and G_y are the complex gains that calibrate the X and Y data streams of a given antenna, the polarization conversion can be written as a function of one single parameter, $\rho = G_x/G_y$, which is assumed to be either constant or slowly varying in time. Hence, the algorithm estimates the gain ratio between polarizers (i.e., the "cross-polarization gain"), ρ, with an antenna-based solver that uses cross-polarization products as observables. Given its global formulation, we could call this algorithm *Global Cross-Polarization Fringe Fitting* (GCPFF). The globalizer is just a minimization problem of the error function (Martí-Vidal et al., 2016)

$$\chi^2 = \sum_k \omega_k \left[\left(\frac{(RR_k^*)^{corr}}{(LL_k^*)^{corr}} - 1\right)^2 + \lambda\left((RL_k^*)^2 + (LR_k^*)^2\right)\right] \quad (3)$$

where k is the visibility index, ω_k the visibility weight, and λ is a Lagrange multiplier, to provide numerical stability to the solutions (this multiplier was not given in Martí-Vidal et al., 2016). This χ^2 function depends on the cross-polarization gain ratios of all the antennas, which affect the RR, LL, RL, and LR correlation products in different ways (depending on whether the antennas have linear or circular polarizers). For example, if the baseline is *mixed*, so it is formed by a linear (denoted by $+$) and a circular (denoted by $\odot$) antenna, the $(RR^*)^{corr}/(LL^*)^{corr}$ ratio becomes

$$\left[\frac{RR_k^*}{LL_k^*}\right]^{corr} = \frac{XR_k^*\rho_+^{-1} - jYR_k^*}{XL_k^*\rho_+^{-1} + jYL_k^*}(e^{\psi_+})(e^{\psi_\odot^*})(\rho_\odot^{-1})^*.$$

The minimization of Eq. 3 is performed using a non-linear solver, after correction for the fringe rates using an ordinary linear least-squares minimization.

The PolConvert algorithm has already been successfully applied to several VLBI observations: from 86 GHz GMVA (Martí-Vidal et al., 2016), to 6 GHz eEVN (see Figs.1 and 2), 43/86 GHz ATCA-KVN, 86 GHz ALMA-GMVA and 230 GHz ALMA-EHT. In all cases, the algorithm has produced a satisfactory calibration and conversion of all the correlation products. Besides, and since the cross-polarization gains of all antennas, as well as their parallactic angles, are taken into account in the GCPFF process, the electric-vector position angle (EVPA) is fully calibrated after the conversion. Having the absolute EVPA calibration, as a byproduct of the GCPFF calibration, is a *major advantage* for astronomical VLBI. The EVPA calibration has been, until now, an important limitation of the use of circular polarizers, since observations of calibrators with different (non-VLBI) stations were always needed to derive the absolute EVPA. Such EVPA estimates did also depend on critical assumptions, especially if the

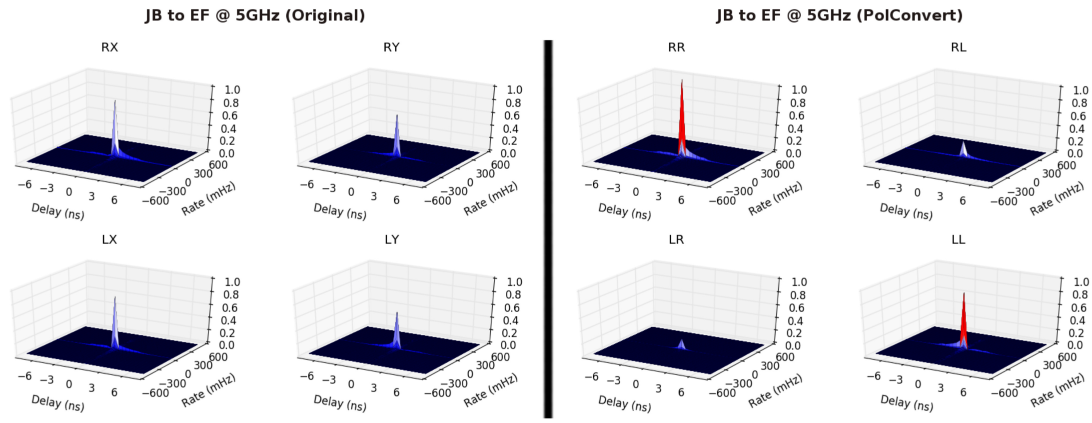

Fig. 1: Left, delay-rate plots of the correlation products between Effelsberg (EF) and the Lovell Telescope (JB) at C band, during observations of a calibrator source in an eEVN experiment (EO014, PI: M. Olech). EF was observing with linear polarizers, while the rest of the eEVN stations used circular polarizers. Right, the same visibility after the GCPFF calibration and conversion with PolConvert. The cross-polarization gains derived with the GCPFF are shown in Fig. 2.

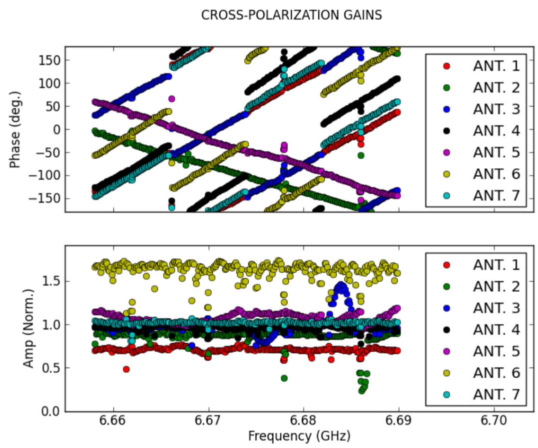

Fig. 2: Cross-polarization gains (i.e., either G_R/G_L or G_x/G_y) of seven eEVN antennas participating in the EO014 experiment. These gains are derived using the GCPFF approach, as implemented in PolConvert. EF (Antenna 2) is shown in green.

calibrators were resolved at VLBI scales. Now, with the use of linear polarizers in VLBI (properly calibrated with PolConvert), the longstanding EVPA problem is just a matter of the past.

Acknowledgements

The European VLBI Network is a joint facility of independent European, African, Asian, and North American radio astronomy institutes. Scientific results from data presented in this publication are derived from the following EVN project code(s): EO014. The author acknowledges M. Olech for the use of these data.

References

Marti-Vidal I, Roy A, Conway J, Zensus A J (2016) Calibration of mixed-polarization interferometric observations. *A&A*, 587, 143, doi:10.1051/0004-6361/201526063.

Smirnov O M (2011) Revisiting the radio interferometer measurement equation. I. *A&A*, 527, 106, doi:10.1051/0004-6361/201016082.

The HOB Experiments

L. McCallum, J. McCallum, J. Lovell

Abstract At Hobart, we ran a 14-week long observing program in 2016, with weekly 24-h sessions including both telescopes, the co-located 12 m (Hb) and 26 m (Ho) antennas. While in one week a special session with only Hb and Ho at X-band (HOB) was run, the next week Ho was added into an AUSTRAL S/X-experiment, including the whole AuScope network (+Yg and Ke). Here we report on the results of these experiments, primarily concentrating on the measured local baseline. While the repeatability of the HOB sessions with better than 1 mm is satisfying, the phasecal measurement at Hb, if applied, was identified to cause a systematic error of 2 cm on the measured baseline.

Keywords Sibling telescopes, local tie, phase calibration

1 Introduction

The transition to VGOS using new telescopes co-located with legacy antennas raises the question of whether the long time series of the legacy antenna can be smoothly transferred to the VGOS antenna. Shall there be common observations, and if so, for how long? At Hobart, we have been operating the 26m Ho telescope alongside the AuScope 12m Hb telescope since 2010. Studying the results from a series of R1/R4 experiments with both telescopes participating revealed a baseline length repeatability of about 9 mm and a variation in the local baseline length of up to 2 cm (Plank et al., 2015). Curiously, this was not seen during Cont14.

Another motivation for this work is the fact that in IVS experiments, the baselines of co-located telescopes are typically excluded from the analysis (e.g. Wettzell, Yebes, Hobart). The common reason for this is high radio-frequency interference (RFI) in S-band, which dominates the correlation on the local baseline.

To investigate local baselines more closely, we ran a 14-week long observing program in 2016, with weekly 24-h sessions including both Hobart telescopes. In alternating weeks, the Hobart 26m was either added to an existing AUSTRAL S/X-experiment (Plank et al., 2017) or joined a special session with only Hb and Ho at X-band (HOB).

In the following Section the HOB series is introduced. The results, mainly in terms of baseline length are presented in Section 3, with some emphasis on effects of the phase calibration correction at Hb (Section 3.3). We conclude in Section refsec:conclusions.

2 The HOB series

For this investigation, six successful HOB sessions were used (Table 1). Comprising only two antennas, Hb and Ho, these sessions of 24-h duration were undertaken approximately every second week in the time between September and December 2016. The scheduling, correlation and post-processing was done at the University of Tasmania.

2.1 Observing mode

The HOB sessions were observed in a modified mode to the usual IVS/AUSTRAL experiments. Due to strong local RFI and the fact that relative ionospheric propagation delays are expected to be insignificant, the HOB sessions were observed only in X-band. Using the standard AUSTRAL frequencies at X-band, we opted for eight channels of 16 MHz, each recording upper and lower sideband and using 2-bit sampling. This gives an effective sampling of 1 Gbps.

Lucia McCallum · Jamie McCallum · Jim Lovell
University of Tasmania, AuScope VLBI, Private Bag 37, 7001 Hobart, Australia

Table 1: Overview of HOB and AUG sessions in 2016, as listed on the IVS master schedule (http://ivscc.gsfc.nasa.gov/sess/master16.html). All sessions lasted for 24 hours.

session	code	date	doy	start	stations
AUS-HOB004	HOB004	SEP16	260	19:00	HbHo
AUS-GEO029	AUG029	SEP21	265	18:00	HbKeYg -Ho
AUS-HOB005	HOB005	SEP25	269	16:30	HbHo
AUS-GEO030	AUG030	OCT07	281	19:00	HbHoKeYg
AUS-HOB006	HOB006	OCT21	295	19:00	HbHo
AUS-GEO031	AUG031	OCT23	297	16:30	HbHoKeYg
AUS-HOB007	HOB007	NOV02	307	18:00	HbHo
AUS-GEO032	AUG032	NOV06	311	16:30	HbHoKeYg
AUS-HOB008	HOB008	NOV18	323	19:00	HbHo
AUS-GEO033	AUG033	NOV24	329	19:30	HbHoKeYg
AUS-HOB009	HOB009	DEC01	336	07:00	HbHo
AUS-GEO034	AUG034	DEC09	344	19:00	HbHoKeYg

2.2 Scheduling

For scheduling, the Vienna VLBI Software (VieVS) was used (Böhm et al., 2012). Aiming for a high number of observations, the usual criteria of high sky coverage was adapted for an additional restriction in the slewing time of the antennas. As a consequence, we achieve a better balance between the antennas observing sources at different parts of the sky, and their slewing time. On average, 28 scans per hour were observed in the HOB sessions. Given the relatively slow slewing speed of the Ho antenna, this number is quite high.

2.3 Analysis

The data were correlated and fringe-fitted using HOPS and Calc/Solve. The X-band level 3 databases were then imported to νSolve (Bolotin et al., 2014), checked for ambiguities and clock breaks and the delays were exported as NGS-file. The final analysis was done in VieVS. Since the data were taken on a single baseline, Earth orientation was fixed. As we were interested in the relative baseline between the two antennas, we estimated corrections to the station positions. Despite both antennas running from the identical maser, one clock was estimated. On the other hand, we found that estimating zenith wet delays at both stations is numerically non-stable and the troposphere was fixed to the a priori values. As a comment we would like to point out that fixing all parameters at one station and estimate those at the other would be another analysis possibility which we might apply in the future.

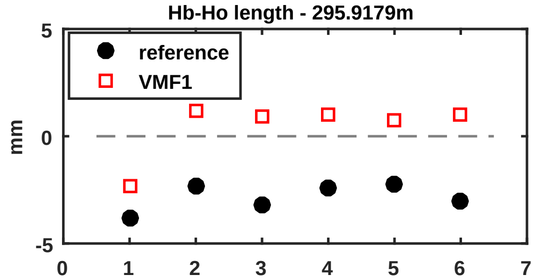

Fig. 1: Results of the six HOB sessions. The presented values are the session-wise estimated baseline lengths between Hb and Ho, minus the local tie measurement. The results for the reference solution (*black circles*) are shown as well as those from using station-dependent hydrostatic delays from VMF1 (*red squares*).

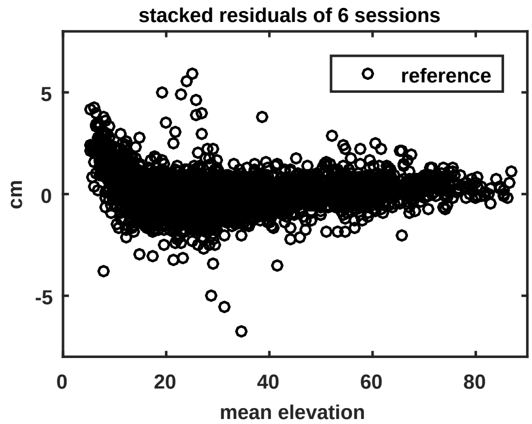

Fig. 2: Residuals of the HOB sessions in the reference solution. A correlation with elevation is clearly visible.

3 Results

The results are assessed in terms of baseline length between the two telescopes in Hobart. The baseline is estimated for each session, and then compared to the local tie measurement of 295.9170 m. In a first solution - henceforth referred to as reference solution -, we find a repeatability of 0.6 mm and a mean offset to the local tie measurement of -2.8 mm (Fig. 1).

Through investigation of this offset, we discovered a clear correlation of the residuals of the observations after the least-squares adjustment with elevation. As shown in Fig. 2, at mean elevations $< 20°$ the residuals quickly rise, up to 5 cm.

3.1 Troposphere modelling

Since no residual troposphere in terms of zenith wet delays were estimated in the solution, it was obvious to

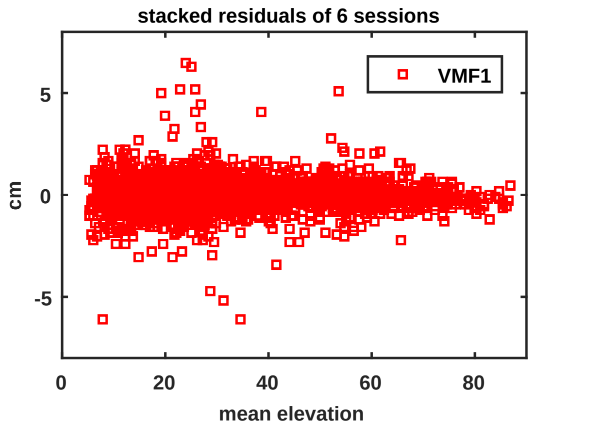

Fig. 3: Residuals of the HOB sessions when using station-dependent zenith hydrostatic delays from VMF1.

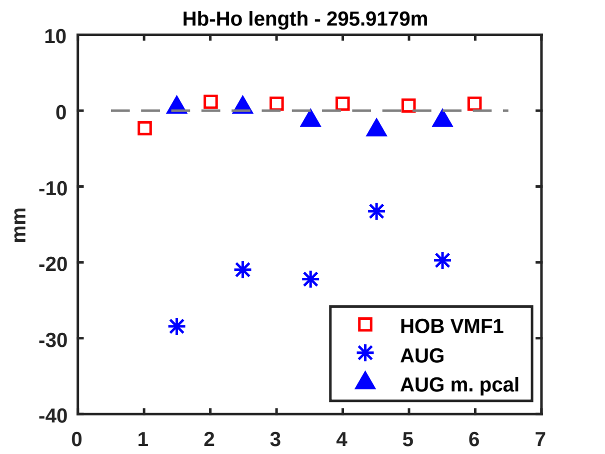

Fig. 4: Results AUG (*blue*) and HOB (*red*) sessions. Shown are the session-wise estimated baseline lengths between Hb and Ho, minus the local tie measurement. The HOB results (*red squares*) are those using the VMF1 hydrostatic delays, as shown in Fig. 1. AUG results using the phase cal signals in Hb (*blue stars*) are clearly offset from the HOB results, while those using manual phase cal (*blue triangles*) show good agreement.

search for the reason of these rising residuals with low elevations in the troposphere. Due to the proximity of the antennas we actually did not expect considerable differences in the wet delay in addition to the dry part which is applied in the theoretical model. The VieVS software does allow for a priori modelling also of the wet part, using numerical weather models and VMF1 data. Using this option, our initial assumption was confirmed in that applying wet delays does not remove the large residuals at low elevations.

However, we did find clear improvements when replacing the in situ pressure measurements with zenith hydrostatic delays from weather models provided for each of the two stations with the VMF1. Applying the alternative pressure values makes the large residuals at low elevation disappear, although a slight correlation with elevation remains (Fig. 3). Local pressure values are used to model the a priori hydrostatic tropospheric delay, using the model of Saastamoinen. In Hobart, the weather sensor is located next to the control building mounted on a pole of approximately 5 m height. This is roughly at half the height of the VLBI reference point of the Ho 26m telescope. However, the Hb 12m dish is about 24 m lower than the reference point of Ho, making the measured local pressure value not very representative. In standard VLBI this may not be a problem for the measurements since residual tropospheric delays can be compensated for through the estimates for zenith wet delays. In the analysis of the HOB sessions, however, we find this problematic.

Besides improving the residuals, using alternative pressure values also has a significant effect on the measured length of the baseline. For five out of the six HOB sessions, the length changes about 4 mm compared to the reference solution. Moreover, the new solution shows an improved repeatability of 0.2 mm and, even more convincing, an improved offset from the local tie value of only 0.4 mm. The first of the sessions was excluded from this statistics. Possible reasons for this outlier will have to be investigated.

3.2 AUG sessions

With the results of the HOB sessions being quite satisfying, next they are compared to those of the AUG sessions. AUG030 through AUG034 were observed in between the HOB sessions, in every other week. In addition to the Hb and Ho antennas, the other two AuScope telescopes in Katherine (Ke) and Yarragadee (Yg) contributed. The scheduling of these sessions was done without sub-netting, so that all four antennas observed together in each scan. Using the standard AUSTRAL mode of 1 Gbps, there are about 22 scans per hour in these AUG sessions.

First results of the AUG sessions, however, revealed a repeatability of only 5.4 mm and a mean baseline that is 2 cm shorter than the local tie measurement (Fig. 4).

Investigations of the reason for this significant offset included changes in the analysis options, excluding different antennas, extracting only the Ho-Hb baseline of the AUG sessions, changing the reference clock, and extracting only the X-band data. While some of those changes did have minor effects on the results, none could remove this 2 cm offset.

3.3 Phasecal at Hb

We then discovered that in the HOB sessions we used manual phase calibration during the fringe fitting process while in the AUG sessions the measured phase calibration signal was used at Hb, Ke, and Yg.

Consequently, the AUG sessions were re-processed, this time using the manual phasecal option. For the re-processing, the correlator output (Mk4-files) were fringe-fitted again using fourfit, then the X-band and S-band databases were combined using νSolve and the data were exported as level 4 NGS-files for the final analysis in VieVS.

Comparing the group delay measurements of sessions using phase calibration and those using manual phasecal, we found systematic differences up to 6 cm, having a clear dependency with the local antenna azimuth in Hobart. We assume that this is caused by a cable twisting, with the largest effects seen a the extreme ends of the cable wrap. For more information please also see Mayer et al. (2017).

Using manual phasecal at Hobart in the AUG sessions, the results for the Hb-Ho baseline improved considerably, to 1.4 mm repeatability and an offset from the local tie measurement of only −1 mm (Fig. 4). This leads to the conclusion that the phasecal measurement at Hb introduced an additional signal into the measurements, leading to spurious variations. Given the stability of the solution using manual phasecal, it appears that these errors are in the phasecal uplink cable. Of course, more detailed investigations on this issue need to be undertaken.

4 Conclusions

The dedicated 14-week observing program of six HOB and five AUG sessions is well suited to investigate observing and analysis options for the local Hobart-Hobart baseline. After some tweaks in the analysis, results in terms of baseline length repeatability of better than 1 mm for the HOB sessions and of 1.4 mm for the AUG sessions were found. For the HOB sessions, using zenith hydrostatic delays from VMF was identified as a good alternative to the otherwise identical local pressure values from a single weather station. In the meantime, a new weather sensor has been ordered to provide readings from a height level appropriate for the Hobart 12m telescope.

In the course of this work, a clear systematic effect of the phasecal signal at the Hobart 12 m antenna was discovered. The additional delays of up to 6 cm cause a decrease of the mean baseline length of 2 cm. When omitting the phasecal signal in the processing, the agreement between the estimated baseline using both the HOB and AUG series to the local tie measurements is at the level of about 1 mm, with no significant offset. We think that this is a good indication that the phasecal signal is erroneous and actually introduces more error than it corrects for.

Acknowledgements

This study was supported by the Austrian Science Fund (FWF) (project J 3699-N29). The data was collected at the University of Tasmania through the AuScope initiative, under contract with Geoscience Australia. AuScope Ltd is funded under the National Collaborative Research Infrastructure Strategy (NCRIS), an Australian Commonwealth Government Programme.

References

Böhm J, Böhm S, Nilsson T, Pany A, Plank L, Spicakova H, Teke K, Schuh H (2012) The new Vienna VLBI Software VieVS. In: *Proceedings of the 2009 IAG Symposium*, International Association of Geodesy Symposia, 136, doi:10.1007/978-3-642-20338-1_126

Bolotin B, Baver K, J. Gipson J, Gordon D, MacMillan D (2014) The VLBI Data Analysis Software νSolve: Development Progress and Plans for the Future. In: D. Behrend, K. D. Baver, K. L. Armstrong (eds.) *International VLBI Service for Geodesy and Astrometry 2014 General Meeting Proceedings: "VGOS: The New VLBI Network"*, Science Press, Beijing, China, ISBN 978-7-03-042974-2, 253–257.

Mayer D, Böhm J, Krásná H, McCallum L (2017) The influence of phase calibration at the station Hobart12 on the ICRF. In: R. Haas, and G. Elgered (eds.), *Proc. 23 EVGA working Meeting*, 177–180.

Plank L, Lovell J, Böhm J, Mayer D (2015) Hb-Ho: Observations with the sibling telescope in Hobart. In: R. Haas, F. Colomer (eds.), *Proc. 22nd EVGA Working Meeting*, ISBN 978-989-20-6191-7, 112–116, `http://evga2015.raege.net/EVGA2015{_}proceedings.pdf`.

Plank L, Lovell J, McCallum J, Mayer D, Reynolds C, Quick J, Weston S, Titov O, Shabala S S, Böhm J, Natusch T, Nickola M, Gulyaev S (2017) The AUSTRAL VLBI observing program. *J Geod*, 91, 803–817, doi:10.1007/s00190-016-0949-y.

Proposed Establishment of a new Fundamental Geodetic Station in Antarctica

L. Combrinck, A. de Witt, P. E. Opseth, A. Færøvig, L. M. Tangen, R. Haas

Abstract The Global Geodetic Observing System (GGOS) requires a globally distributed network utilizing next generation Satellite Laser Ranging (SLR) and Very Long Baseline Interferometry (VLBI) technology to meet the objectives of GGOS. It is expected that about 30 core sites will be established globally to ensure adequate network density and geometry. The proposal presented here highlights opportunities for VLBI network densification. We consider both southern Africa and Antarctica sites for the establishment of new VLBI sites. We have made *u-v* coverage plots and geodetic VLBI simulations for several sites, and evaluate these in terms of their scientific value. Both the southern Africa and Antarctica sites should be equipped with VGOS compatible antennas.

In particular we propose the establishment of a new core fundamental station in Antarctica, operated and funded by an international consortium. This core GGOS site could be located at either the Norwegian (Troll) or South African Antarctica (SANAE IV) bases. Troll is located 235 km from the coast in Dronning Maud Land at 72°01′ S, 2°32′ E, at a height of 1270 m above sea level on the Jutulsessen nunatak. SANAE IV is located 170 km from the coast at a height of 800 m on the Vesleskarvet nunatak in Queen Maud Land at 72°40′ S, 2°50′ W. Unlike most other Antarctica research bases, both these stations are located on exposed bedrock, not on ice, making them suitable for geodetic installations. A specially designed Geodetic/Astrometric antenna (perhaps equipped with a radome) suitable for the harsh Antarctica environment will have to be constructed for installation in Antarctica. The Antarctica locations will create the longest possible North-South baseline (at this stage).

We further propose the relocation of the geodetic VLBI antenna (20-m) currently located at Ny-Ålesund at 79° N, Svalbard to South Africa (Matjiesfontein) or even another suitable site such as Gamsberg in Namibia to form part of the African VLBI Network (AVN).

Simulations have shown that adding a station in Antarctica has a very positive improvement on *u-v* coverage, with Matjiesfontein being the second best option. We present an overview of the envisioned GGOS stations, details and modalities of these projects and expected scientific and other benefits.

Ludwig Combrinck · Alet de Witt
Hartebeesthoek Radio Astronomy Observatory, Krugersdorp, South Africa

Per Erik Opseth · Are Færøvig · Leif Morten Tangen
Statens Kartverk, Hønefoss, Norway

Rüdiger Haas
Onsala Space Observatory, Chalmers University of Technology, Sweden

Keywords GGOS, Antarctica, VLBI, GGRF, AVN

1 Introduction

During March 2016 a suggestion was made by Statens Kartverk (Norway) that the currently operational 20-m VLBI radio telescope located at Ny-Ålesund (see Fig. 1) be donated to HartRAO (South Africa). This antenna can thus be relocated and installed at an appropriate location in South Africa, or elsewhere in Africa. There are several possible re-location sites, Mauritius, Madagascar, Matjiesfontein (South Africa), Gamsberg (Namibia), or Kilimanjaro (Kenya). A possible location could be Gamsberg if it is decided to rather make the 20-m part of the African VLBI Network (AVN); this could then be the first astronomy/astrometric/geodetic antenna within the AVN. For details on the AVN see Gaylard et al. (2012) and Loots (2015). For the simulations presented in this article, we included Antarctica to estimate what the effect of including a new antenna on this continent would have compared to a standard VLBI geodetic network. The idea of including Antarctica as a possible site stems from the fact that current geodetic infrastructure on Antarctica is very sparse. Currently there are two VLBI antennas located on Antarctica (O'Higgins and Syowa), these are both small antennas (9 m and 11 m respectively) and are not fully dedicated to geodesy or astrometry, although both have made very important contributions to the geodetic networks. Therefore the installation of a geodetic/astrometric quality antennna will drastically improve network geometry and *u*-*v* coverage. There is no Satellite Laser Ranging (SLR) equipment either, therefore such a VLBI antenna installation should be done with the view towards a complete Fundamental Station for Antarctica, which includes the installation of all other major geodetic equipment as well as supportive geophysical instrumentation.

We made *u*-*v* coverage plots and performed geodetic VLBI simulations for different sites to evaluate their scientific merit. Astrometry simulations will be done at a later stage to also compare the accuracy of source positions.

Logistically some sites are easier than others, the science case for Antarctica is the most convincing, however it is also the most challenging installation due to difficult logistics and harsh weather conditions. These are not insurmountable, as both Norway and South Africa have extensive experience of construction and the difficult logistical requirements that will be required for such a project.

The Ny-Ålesund antenna will be suitable for installation at a selected site in southern Africa after some upgrades and renovation (new motors, encoders, modern servo drives and control systems, receivers and cooling systems) but will be unsuitable for installation in Antarctica due to its age and possible deficiencies. A new, specifically designed antenna for Antarctica, with specifications to be VGOS compatible and be large enough to allow celestial reference frame work will have to be designed and manufactured for installation in Antarctica. The structural requirements for Antarctica are severe due to the harsh environment and high velocity winds encountered.

We had our first meeting concerning the 20m-antenna project at Hønefoss during 12-14 February 2017 followed by a site visit to Ny-Ålesund during 22-24 May 2017. It was estimated that the 20-m antenna will be phased out over 3 years (twin VGOS antennas replacing the 20-m), so that the 20-m should become available for disassembly and removal from about June 2020.

The proposal expressed in this paper is twofold, on the one hand we propose to relocate the Ny-Ålesund 20-m to southern Africa (upgraded to be VGOS compatible as far as practical), and on the other hand we propose to develop a complete Fundamental Geodetic Station in Antarctica, part of the GGOS network, part of the Global Geodetic Reference Frame (GGRF) infastructure, operated and maintained by a global consortium (i.e. an internationally funded and operated station).

Fig. 1: The Ny-Ålesund 20-m VLBI antenna. The antenna was constructed during the summers of 1993 and 1994, and has been operational since 1 January 1995. Its pedestal consists of steel subsections, making removal and re-assembly practical.

2 Simulations

We performed geodetic VLBI simulations in terms of Earth Orientation Parameters (EOP) errors as an indicator of proposed site suitability. The reference network is based on the standard IVS-R1675 network configuration. The Vienna VLBI Software (VieVS; Böhm et al., 2009) was used for scheduling, simulating and analysing these sessions. The scheduling parameterisation resembles the IVS-R1675 sessions as closely as possible. For the simulation of observations the default atmospheric turbulence parameters in VieVS ($C_n = 2.5 \cdot 10^{-7}\ m^{-1/3}$, $H = 2000$ m, $v_e = 8\ m/s$, etc.) were used for every station. This does not resemble the true troposphere variability at every site but at the moment there is not enough information about troposphere turbulence at these stations. In order to get statistical information about the estimated parameters, the sessions were Monte Carlo simulated 50 times and then analysed. A standard geodetic analysis was performed with the same models and parameters for every session. The results are tabulated in Tab. 1. The best total relative improvement results from adding a station to Antarctica (using the coordinates of the Norwegian Troll base) followed by Matjiesfontein (South Africa). This is not surprising as the extended north-south baselines decrease the y pole error substantially; measurement of UT1-UTC also improves.

The quality of a VLBI image can be determined by the density and distribution of *u*-*v* tracks in the *u*-*v* plane, therefore one can use this characteristic to eval-

Table 1: Average formal EOP errors and their standard deviations using R1675 as reference. It is clear that Antarctica is the best choice followed by Matjiesfontein, with Gamsberg a close 3rd (based on sum of errors).

Network	UT1 - UTC (ms)	x_pole (μas)	y_pole (μas)	dX (μas)	dY (μas)	sum$_{error}$
R1675	3.27 ± 0.08	27.28 ± 0.70	51.41 ± 1.32	24.04 ± 0.62	22.94 ± 0.59	128.94 ± 3.30
R1675 + Antarctica	2.72 ± 0.07	20.88 ± 0.50	37.90 ± 0.91	19.94 ± 0.48	18.91 ± 0.45	100.35 ± 2.40
R1675 + Matjiesfontein	2.91 ± 0.07	20.60 ± 0.51	43.94 ± 1.08	19.40 ± 0.48	18.82 ± 0.46	105.67 ± 2.60
R1675 + Gamsberg	2.81 ± 0.07	20.40 ± 0.53	44.61 ± 1.17	20.10 ± 0.53	19.17 ± 0.50	107.09 ± 2.80
R1675 + Kilimanjaro	3.05 ± 0.06	22.15 ± 0.45	45.76 ± 0.94	20.82 ± 0.43	20.32 ± 0.42	112.10 ± 2.30
R1675 + Mauritius	2.99 ± 0.08	23.00 ± 0.64	45.29 ± 1.26	20.94 ± 0.58	20.29 ± 0.56	112.51 ± 3.13
R1675 + Kenya	2.99 ± 0.07	22.86 ± 0.55	47.04 ± 1.14	20.73 ± 0.50	20.34 ± 0.49	113.96 ± 2.75

uate the benefits of densifying a particular VLBI network or to ascertain the benefits by creating extended baselines by adding additional stations to increase the geometrical size of the network. These *u*-*v* tracks are created through the 2-D projection of the various VLBI baselines on the *u*-*v* plane; this plane is perpendicular to the line of sight of the antenna when pointed to a radio source. In Fig. 2 we show the *u*-*v* plots for various sites added to the standard VLBI network in the Southern Hemisphere. A new station in Antarctica provides by far the best improvement in *u*-*v* coverage.

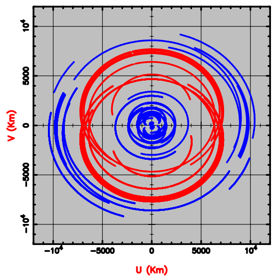

(a) Antarctica

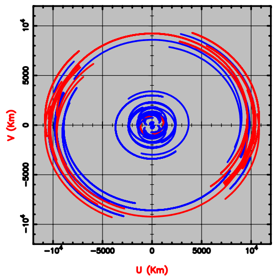

(b) Gamsberg

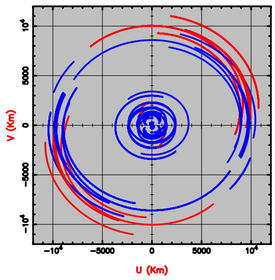

(c) Kenya

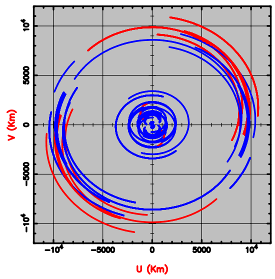

(d) Kilimanjaro

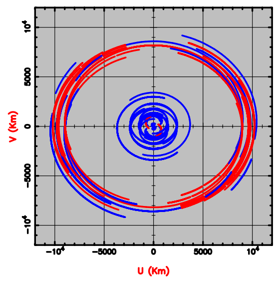

(e) Matjiesfontein

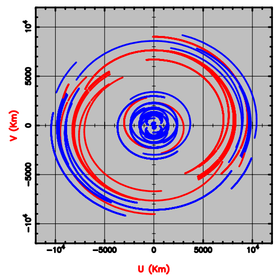

(f) Mauritius

Fig. 2: Plots of the *u*-*v* coverage for a source at -60° declination, observed over a period of 24 hours. The blue tracks are from the standard Southern Hemisphere VLBI network and the red tracks due to an additional station as labelled in figures (a) to (f).

3 Possible locations for the 20-m VLBI and new-built antennas

There are 3 sites which warrant serious consideration for a geodetic/astrometric antenna. In the southern part of South Africa (Matjiesfontein) and then either the Norwegian Troll (Fig. 3) base or the South African SANAE IV base (Fig. 4), which both are located in Antarctica within about 200 km from each other. The basic logistics for transporting an antenna to Antarctica exists. These are not greenfield sites and adding a fundamental geodetic station should be within the capacity of the existing infrastructure, even if some expansion or capacity increase may have to included in the station design.

3.1 *Antarctica (new-built)*

1. Both South Africa (SA Agulhas II) and Norway have supply ships capable of transporting large equipment to Antarctica
2. Both countries have snow tractors and sledges of adequate capacity
3. The antenna could be moved from the ice shelf to either base
4. Both bases have airstrips; aeroplanes can land at Troll throughout the year (the only base where this is possible)

3.2 *Matjiesfontein (re-located 20-m)*

1. This is a green-fields site (no major infrastructure).
2. High speed optical fibre is 4 km distant
3. The site is suitable for radio and optical equipment (semi-arid, low rainfall)
4. A geophysical and a GNSS station have already been installed.

Fig. 3: The Norwegian Antarctica base (Troll). The photo was taken during the summer of 2007.

Fig. 4: The South African Antarctica base (SANAE IV), the photo was also taken during the summer of 2007.

5. A major paved road and train line is 4 km distant so access is relatively easy

4 Site surveys

Site surveys/evaluations need to be conducted during the next three years to ascertain the suitability of candidate sites. The southern Africa sites are easy to access, however the Antarctica sites require interaction with other stakeholders (Norwegian Polar Institute, South African National Antarctica Programme) and will need much preparatory work and institutional approval and support. Basic site surveys should include:

1. Wind direction and strength (Fig. 5)
2. Topography (Fig. 6 and Fig. 7)
3. Geology (bedrock type, stability, strength)
4. Logistical support/additional requirements
5. Power, communications
6. Accessibility (ship, plane, sledge, helicopter)
7. Most appropriate location on site
8. Other

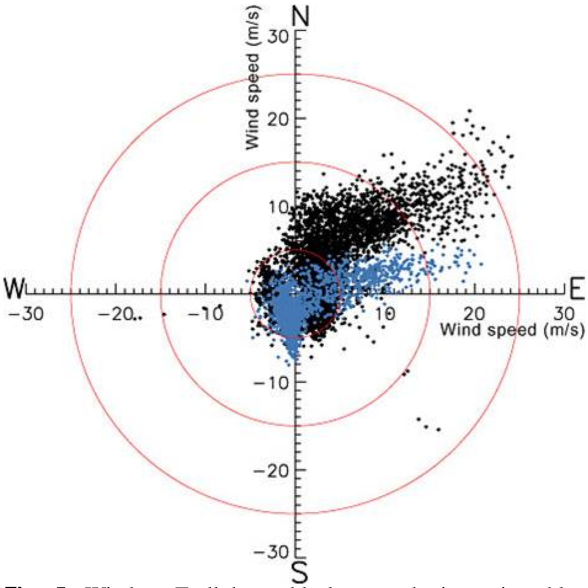

Fig. 5: Wind at Troll base: black-atmospheric station, blue-airfield (Hansen, 2009).

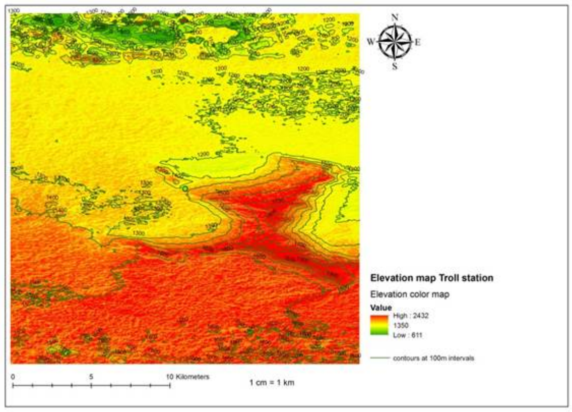

Fig. 6: The topography at Troll base exhibits a hilly terrain. A safe location for the new-built VLBI antenna must be found to shield it from the prevailing north-east winds (see Fig. 5). Data from the Shuttle Radar Topography Mission (SRTM; USGS, 2004) was used to generate elevation maps for the Troll and SANAE IV (Fig. 7) sites.

5 Conclusions

In the near future there will be an opportunity to relocate the Ny-Ålesund) 20-m VLBI antenna to southern Africa. This relocation has a good science case. The funding model for this could be linked to the AVN project, and this needs to be explored.

Establishment of an international consortium will be required for a Fundamental Station in Antarctica and it should lead to the establishment of a GGRF/GGOS node in Antarctica; the science case for this is very good.

In summary, we see two opportunities for VLBI and geodesy; southern Africa and Antarctica. Each of these locations have their own challenges; Norway and South

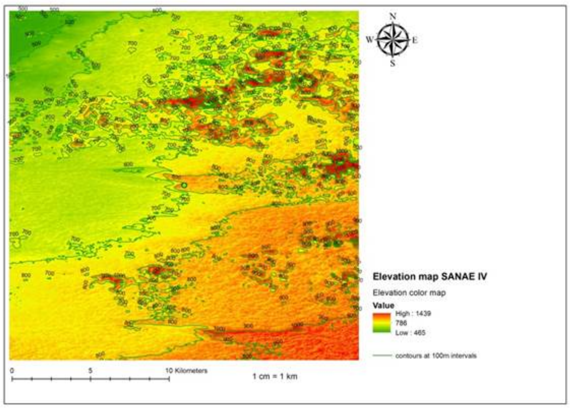

Fig. 7: The topography at the SANAE IV base is flat in general, except for a cliff which breaks the flatness of the terrain. In general it is more exposed than the Troll base.

Africa can play a major role in both these two ventures, with benefits to the global community, improvement in geodetic and astrometric products as well as global reference frame support.

The issue of data transfer will be a challenge, as there is no optical fibre to Antarctica at this stage (although this is a well known requirement, there are many practical obstacles due to the moving ice on the continent). Other options will have to be considered, and perhaps, such a requirement will provide enough impetus for the first fibre optic cable to be laid to Antarctica.

References

Böhm J, Böhm S, Nilsson T, Pany A, Plank L, Spicakova H, Teke K, Schuh H (2009) The new Vienna VLBI Software VieVS. In: S. Kenyon, M. C. Pacino, U. Marti (eds.) *Proc. 2009 IAG Symposium*, IAG Symposia 136, 1007–1011, https://link.springer.com/chapter/10.1007/978-3-642-20338-1_126.

Gaylard M J, Bietenholz M F, Combrinck L, Booth R S, Buchner S , Fanaroff B L, MacLeod G C, Nicolson G D, Quick J F H, Stronkhorst P, Venkatasubramani T L (2012) An African VLBI Network of radio telescopes. In: I. Basson, A. E. Botha (eds.), *Proc. SAIP2011*, 473–478, http://adsabs.harvard.edu/abs/2011saip.conf..473G

Hansen G, Aspmo K, Berg T, Edvardsen K, Fiebig M, Kallenborn R, Krognes T, Lunder C, Stebel K, Schmidbauer N, Solberg S, Yttri K E (2009) Atmospheric monitoring at the Norwegian Antarctic station Troll: Measurement programme and first results. *Polar Research*, 28(3), http://www.tandfonline.com/doi/abs/10.1111/j.1751-8369.2009.00134.x, doi:10.1111/j.1751-8369.2009.00134.x.

Loots A (2015) The African VLBI network project. *AAS Meeting Abstracts*, 225, id 126.02, http://adsabs.harvard.edu/abs/2015AAS...22512602L

USGS (2004) Shuttle Radar Topography Mission, 1 Arc Second scene SRTM_u03_n008e004. http://glcf.umd.edu/data/srtm/

Simulation Results for KOKEE12M-WETTZ13S Intensives

K. Baver, J. Gipson

Abstract Using the VLBI scheduling software *Sked*, we generated a series of schedules at two-week intervals spanning a year for the KOKEE12M–WETTZ13S baseline using VGOS broadband observing and the standard KOKEE-WETTZELL baseline using standard operational (S/X) observing. This paper describes the simulations and reports the results. The initial simulations indicate that the use of KOKEE12M and WETTZ13S should improve five metrics. The best VGOS INT01 configuration tested increases the number of scheduled sources from 16.08 to 20.53 sources, increases the number of scheduled observations from 19.18 to 56.29 observations, reduces the UT1 formal error from simulations from 7.68 to 3.38 μs, reduces sensitivity to atmospheric turbulence from 16.69 to 14.01 μs, and reduces sensitivity to source loss from 12.66 to 9.22 μs. But further testing is recommended.

Keywords UT1, Intensives, scheduling, VGOS

1 Introduction

UT1-UTC is an important IVS product, and one-hour IVS Intensive sessions provide low latency UT1 estimates throughout the week. A long east-west baseline is needed to estimate UT1, and baselines between the Kokee Park site in Hawaii, USA and the Wettzell site in Germany fulfill this criterion, as shown in Figure 1. The Kokee Park S/X 20-m antenna (KOKEE) and the Wettzell S/X 20-m antenna (WETTZELL) have provided the primary baseline for IVS-INT01 sessions for many years. Now it is time to plan for future VGOS INT01 observing using Kokee Park and Wettzell broadband antennas.

Karen Baver · John Gipson
NVI, Inc., 7257D Hanover Parkway, Greenbelt Maryland, 20770, USA

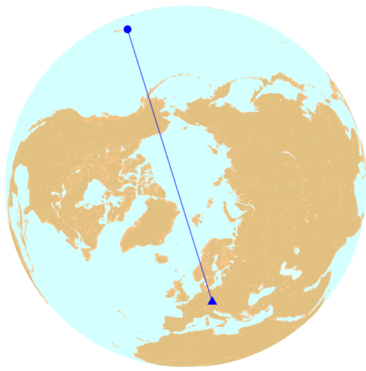

Fig. 1: Baseline between the sites at Kokee Park (Hawaii, USA) and Wettzell (Germany) shown on a polar projection.

Using the *Sked* scheduling program, we ran simulations using several schedule configurations in order to identify a good configuration for VGOS INT01 observing. We tested the baseline between Kokee Park's 12-m broadband antenna (KOKEE12M) and Wettzell's southern twin 13-m antenna (WETTZ13S) in its broadband configuration. As a control, we used KOKEE-WETTZELL schedules in the operational INT01 style.

Gipson and Baver (2016) has shown that an INT01 session's UT1 formal error depends on the availability of sources. The available set of sources changes over time; the mutual visibility of the sources varies throughout the year, and the ability to observe a source fluctuates as its strength fluctuates. So we tested each schedule configuration for 26 days of the year (DOYs) spaced two weeks apart, starting on January 10 at 18:30 UT, using 12 flux catalogs that had been used operationally between 2012 and 2016. This generated 312 schedules for each VGOS INT01 schedule configuration and for the control configuration. We identified seven viable schedule configurations and ran their schedules through *Calc/Solve* simulation solutions to simulate, as far as possible, actual observations. For these simulations, we assumed that all scheduled observations were successful and that the measurement uncertainties calculated through *Sked* were correct.

We used five metrics for the tests. The most important metric is the UT1 formal error from the *Solve* simulations, with a lower value being better. The second metric is sensitivity to atmospheric turbulence, which we measured using the RMS about the mean of the UT1 estimates from 300 *Solve* solutions that applied random noise that simulated atmospheric turbulence. A lower value is better. The third metric is sensitivity to source loss, which we measured using the RMS about the mean of the UT1 estimates from *Solve* solutions in which each source in a schedule was deleted in turn. This simulates source loss, which could occur if the source flux model is outdated. A lower value is better. The final two metrics are the average number of scheduled sources and the average number of scheduled observations. For both metrics, a higher value is better. Gipson and Baver (2016) discusses the metrics in more detail.

A full report on the simulations is under development (Baver and Gipson , 2017b), but this proceedings paper reports general information about the best VGOS INT01 configuration identified. VGOS INT01 latency is also discussed.

2 Antenna Characteristics

Figure 2 shows the Kokee Park and Wettzell S/X and broadband antennas used in this study. Table 1 reports the characteristics of the four antennas. The broadband antennas are smaller and faster. WETTZ13S' azimuth and elevation slew rates are four times those of WETTZELL. The KOKEE12M azimuth slew rate is six times that of KOKEE, and its elevation slew rate is 2.5 times that of KOKEE. Higher slew rates reduce the amount of time spent slewing, which means that more time is available for observing, which might result in more observations. The VGOS antennas' data acquisition rate is 8192 Mbps, 64 times that of the S/X antennas in their INT01 observing mode. The SEFD characterizes a station's sensitivity, with a lower number being better. This is a function of the size of the antenna (with larger being better), the antenna efficiency, and the antenna's electronics. The VGOS antennas' SEFDs are generally larger than the S/X antennas' (a maximum of four times at S-band for KOKEE12M vs. KOKEE), indicating that they are less sensitive.

The formula for an observation's SNR is given by

$$SNR = C * F * \frac{\sqrt{T * DR}}{\sqrt{SEFD_1 * SEFD_2}} \qquad (1)$$

where C is a constant, F is the flux of the source being observed, T is the span of the observation, DR is the data rate, and $SEFD_1$ and $SEFD_2$ are the SEFDs of the antennas. The VGOS antennas' increased data rate more than compensates for their increased SEFDS. For a given integration time T, the SNR of an observation using the VGOS antennas will be much higher than the SNR for an observation using the S/X antennas, resulting in more precise observations. Alternatively, for a given SNR, the integration time will be much less, allowing for more scheduled observations.

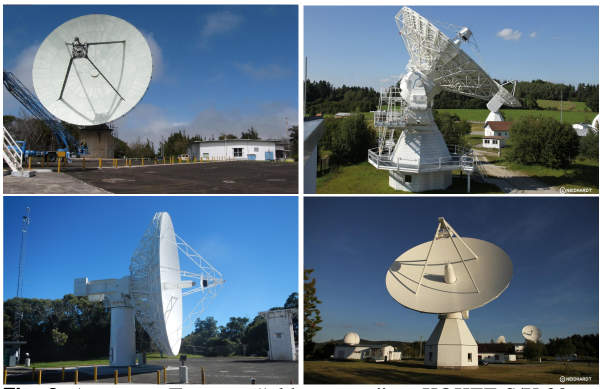

Fig. 2: Antennas. Top row: "old veterans" — KOKEE S/X 20 m (left) and WETTZELL S/X 20 m (right). Bottom row: "new kids" — KOKEE12M broadband 12 m (left) and WETTZ13S broadband 13 m (right). The photos of the Wettzell antennas are courtesy of Alexander Neidhardt (FESG, TUM). The KOKEE photo is from the Kokee Park 2009 IVS annual report. The KOKEE12M photo is from the Kokee Park 2015+2016 IVS biennial report. Both Kokee Park photos are being used with permission from Chris Coughlin (Harris Corporation).

Table 1: Characteristics of the four antennas. The slew rates are in degrees per second. The data acquisition rates are in Mbps. The SEFDs are in Jy.

	KOKEE	WETTZELL	KOKEE12M	WETTZ13S
Band	S/X	S/X	Broadband	Broadband
Size	20 m	20 m	12 m	13 m
AZ slew rate	2	3	12	12
EL slew rate	2	1.5	5	6
Data rate	128	128	8192	8192
SEFD X-band	2000	750	3000	1400
S-band	750	1115	3000	1050

3 VGOS INT01 Schedules

Baver and Gipson (2017b) discusses the tested schedule configurations in detail. Here we only mention the two biggest differences between the S/X and VGOS INT01 schedules and their likely effect on the number of scheduled observations and the UT1 formal error.

The first difference is in the amount of the sky that can be observed by the two pairs of antennas. Figure 3 shows azimuth/elevation plots of the four stations, with the areas enclosed by the heavy, dark lines showing the mutual visibility of the plotted station with its observing partner. No obstructions intrude on the KOKEE and WETTZELL sky lines, and S/X INT01 schedules use a horizon mask of 8°. This produces a large area of mutual visibility as shown in Figure 3 (top row). In contrast, a significant amount of KOKEE12M's northwest sky is blocked by KOKEE, producing a much smaller area of mutual visibility, as shown in Figure 3 (bottom row). Simulations done for Baver and Gipson (2017a) show that the reduction of the mutual visibility area has a detrimental effect on the UT1 formal error.

The second difference is in the observation length ranges for the two pairs of antennas. S/X INT01 observation lengths range from 40 to 200 seconds. In contrast, the VGOS INT01 configuration reported here allowed observations ranging from 20 to 40 seconds. The shorter duration is due to the VGOS antennas' higher data rate. Shorter observation lengths should yield more observations, which should reduce the UT1 formal error. In Figure 4, azimuth/elevation plots display observations, shown as circles, from a sample KOKEE-WETTZELL schedule and the corresponding KOKEE12M-WETTZ13S schedule. The plots illustrate the fact that VGOS INT01 schedules will have many more observations than S/X INT01 schedules. Our study showed that, on average, a VGOS INT01 schedule has approximately 2.5 to three times as many observations as an S/X schedule made under the same conditions. In Figure 4, the S/X schedule has 18 observations, and the VGOS INT01 schedule has 52 observations.

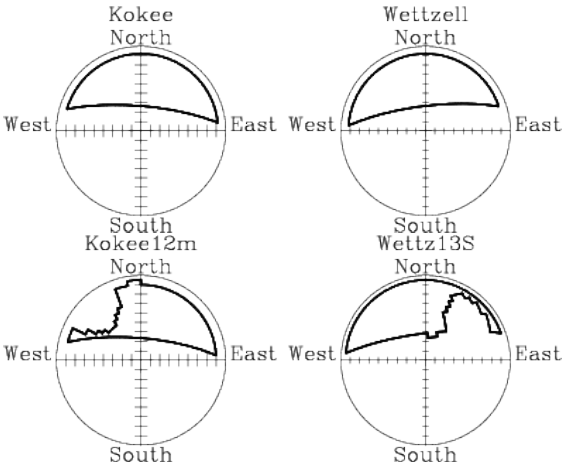

Fig. 3: Top row: observation spaces (interiors of the darkened crescents) for KOKEE (left) and WETTZELL (right). Bottom row: observation spaces (interiors of the irregular darkened polygons) for KOKEE12m (left) and WETTZ13S (right).

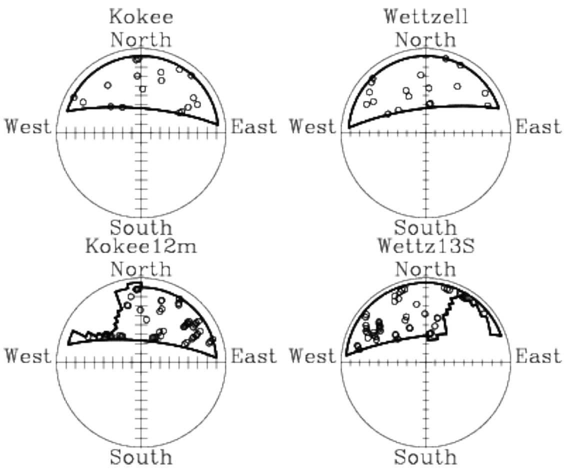

Fig. 4: Top row: observations from a sample S/X INT01 schedule of KOKEE (left) and WETTZELL (right) plotted by azimuth and elevation. Bottom row: the corresponding VGOS INT01 schedule of KOKEE12M (left) and WETTZ13S (right). Both schedules were made for DOY 052 using the 16Aug25 flux catalog.

4 Simulation Results

Table 2 shows five metrics from the *Solve* simulations. Each control (S/X) or VGOS INT01 metric value is averaged over 312 schedules (for the 12 flux catalogs applied at 26 DOYs). All metrics improve for the VGOS INT01 case. The number of scheduled sources is increased by 28% (from 16.08 to 20.53), and the number of scheduled observations is nearly tripled (from 19.18 to 56.29). The sensitivity to atmospheric turbulence is decreased by 16% (from 16.69 to 14.01 μs), and the sensitivity to source loss is decreased by 27% (from 12.66 to 9.22 μs). Most importantly, the UT1 formal error is more than halved (from 7.68 to 3.38 μs).

Table 2: Metric averages over 312 schedules that represent 26 DOYS using 12 flux catalogs.

	S/X (control)	VGOS INT01
Number of scheduled sources	16.08	20.53
Number of scheduled observations	19.18	56.29
UT1 formal error (μs)	7.68	3.38
Atmospheric turbulence sensitivity (μs)	16.69	14.01
Source loss sensitivity (μs)	12.66	9.22

As stated earlier, the set of sources that are mutually visible varies throughout the year and affects the INT01 sessions' UT1 formal errors. Figures 5 – 9 plot the metrics at the 26 tested DOYs for a single flux catalog. Two caveats should be mentioned. First, the corresponding plots using other flux catalogs would be similar but different. Second, no flux catalog would actually be used for an entire year. Fluxes change so rapidly that a flux catalog tends to become out of date within two weeks to a month. In spite of these caveats, these plots are representative and look similar to the plots averaged over all 12 flux catalogs. For all 26 DOYs, the VGOS INT01 schedules have more scheduled observations, have more scheduled sources, and have lower UT1 formal errors than the S/X schedules. In terms of sensitivity to atmospheric turbulence or source loss, the VGOS INT01 schedules are, on average, better, but there are some DOYs for which the S/X schedules are better.

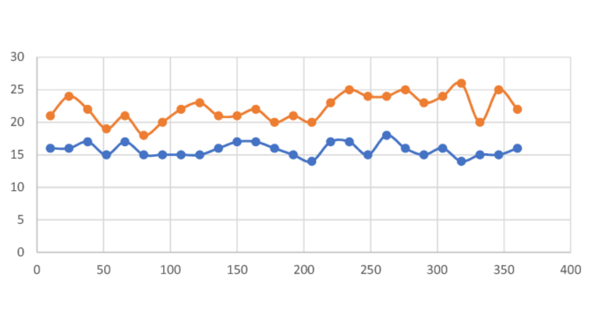

Fig. 5: Number of scheduled sources at the 26 DOYs for flux catalog 16Aug25 for VGOS INT01 (red/light) and S/X.

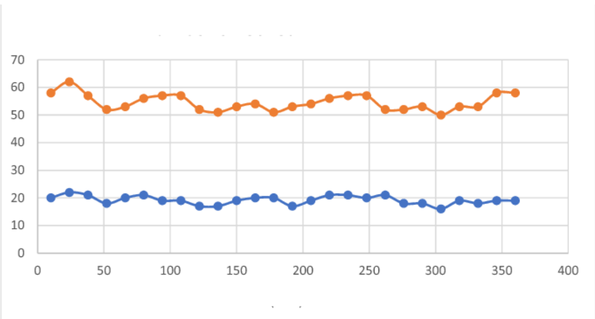

Fig. 6: Number of scheduled observations at the 26 DOYs for flux catalog 16Aug25 for VGOS INT01 (red/light) and S/X.

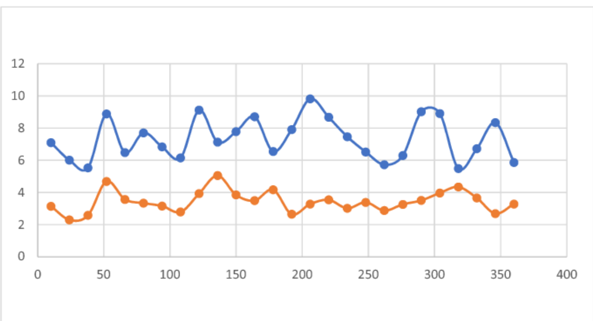

Fig. 7: UT1 formal error (μs) at the 26 DOYs for flux catalog 16Aug25 for VGOS INT01 (red/light) and S/X.

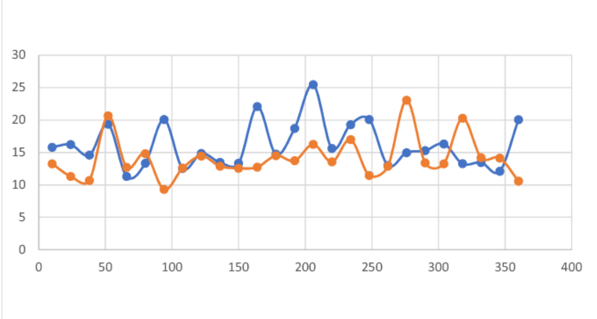

Fig. 8: Sensitivity to atmospheric turbulence (μs) at the 26 DOYs for flux catalog 16Aug25 for VGOS INT01 (red/light) and S/X.

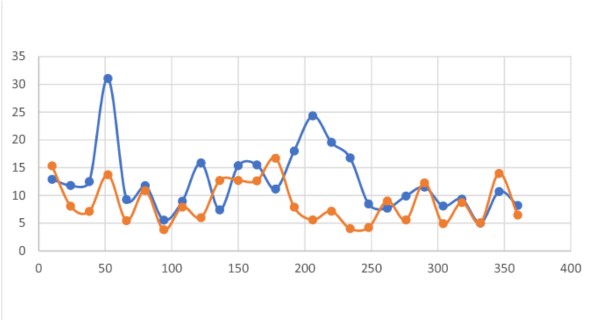

Fig. 9: Sensitivity to source loss (μs) at the 26 DOYs for flux catalog 16Aug25 for VGOS INT01 (red/light) and S/X.

5 VGOS INT01 Latency

The uncertainty in UT1 predictions grows rapidly with time, so reduced latency is an important goal for Intensive sessions. E-transfer of a session's data to a correlator is a key factor in reducing latency. Currently, the Kokee Park bandwidth is too low to support e-transfer of the larger amount of data that VGOS observing will produce, so VGOS INT01 observing in Kokee Park's current state would cause an operational bottleneck.

A typical S/X INT01 session records 43 GB of data at each site. A VGOS INT01 session should record ~1.7 TB of data at each site, which is roughly 40 times as much data. Currently, the Kokee Park site's internet bandwidth is 100 Mb/s. This makes the current Kokee Park transfer time for an S/X INT01 session $(8*43*1000Mb)/(100\ Mb/s)$, which equals 3440 seconds, or approximately one hour. So, with the Kokee Park site's current bandwidth, it would take ~40 hours to transfer a VGOS INT01 session to a correlator.

Kokee Park plans to increase its bandwidth to 1 GB/s during the summer of 2017. This will decrease the transfer time by a factor of 10, enabling transfer of a VGOS INT01 session to a correlator within four hours. So, after the upgrade, quasi-realtime e-transfer of VGOS INT01 sessions will become realistic.

6 Next Steps

The results here are sufficiently promising that it would be reasonable to start test sessions once KOKEE12M becomes able to observe routinely. On the other hand, additional simulations could be beneficial. The KOKEE12M horizon mask had not been finalized at the time of the simulations; especially, the effect of KOKEE in KOKEE12M's northwest quadrant had not been fully mapped. Also the work done for Baver and Gipson (2017a) has suggested a new parameter to test in the VGOS INT01 schedule configurations.

7 Conclusions

The best VGOS INT01 schedule configuration tested to date outperforms the operational S/X schedule configuration for five metrics (UT1 formal error, sensitivity to atmospheric turbulence, sensitivity to source loss, number of scheduled sources, and number of scheduled observations) when averaged over a set of 312 schedules. The results are sufficiently promising that test observing could begin, although more work could also be done first to improve the VGOS INT01 schedule configuration, especially with respect to the KOKEE12M horizon mask.

There is a known obstacle to VGOS INT01 observing — an excessively long time to e-transfer a large amount of data from Kokee Park due to its current bandwidth. But a planned upgrade should solve this.

References

Gipson J, Baver K (2016) Improvement of the IVS-INT01 sessions by source selection: development and evaluation of the maximal source strategy. *J. Geodesy*, 90:287-303, doi:10.1007/s00190-015-0873-6.

Baver K, Gipson J (2017) Reduction of the IVS-INT01 UT1 Formal Error through New Sked Algorithms. In: R Haas and G. Elgered (eds.), *Proc. 23rd EVGA Working Meeting*, 127–131.

Baver K, Gipson J (2017) First VGOS INT01 (KOKEE12M—WETTZ13S) Simulations. In progress.

Recent Developments in Scheduling With VieVS

M. Schartner, J. Böhm, D. Mayer, L. McCallum, A. Hellerschmied

1 Introduction

Generating a good schedule is critical for each VLBI experiment, because the schedule determines the quality of the parameters which should be derived by the session. Within the IVS, usually a schedule is prepared with a scheduling software, like SKED (Gipson, 2012) or VieVS. With the VieVS scheduling software it is possible to create schedules automatically, semi-manually or manually. It supports different optimization strategies and parameters, like a station based approach optimizing the sky coverage over each station. However, the large amount of different optimization parameters can lead to troubles finding a good set of parameters to use for the scheduling process. Previously it was time consuming to test different parameters with VieVS because each time the parameters had to be changed manually and a new schedule had to be created. Then these schedules had to be selected manually to simulate observations. Afterwards the simulated session files had to be selected manually again to run a least squares adjustment to estimate geodetic parameters. This procedure was highly inefficient and time consuming. With the new changes in the VieVS software all steps can now be done automatically.

2 VieVS multi scheduling tool

The VieVS software is organized in different modules. To analyse a VLBI session the modules VIE_INIT, VIE_MOD and VIE_LSM are necessary. Vie_INIT reads in all files and prepares files in the VieVS internal format. VIE_MOD models the theoretical time delay for each observation and VIE_LSM calculates the target parameters in a least squares adjustment.

Three extensions to the core modules, VIE_GLOB, VIE_SCHED and VIE_SIM are also available. VIE_GLOB is used to run a global VLBI solution, VIE_SCHED is the dedicated scheduling module and VIE_SIM is used to simulate observations including white noise, tropospheric turbulences and clock drifts (Pany et al., 2011).

While VIE_GLOB is well connected with the rest of VieVS, VIE_SCHED and VIE_SIM were kind of standalone features. This is now changed, Figure 1 shows the new interactions between VIE_SCHED and VIE_SIM. It is now possible to create a schedule for a VLBI session, to simulate this session multiple times and perform a least squares adjustment for each simulated session automatically. This is a lot more efficient, because similar calculations only need to be done once and no user interaction is required except for the start when everything is set up. To speed things up even further an improved multicore support is added for the scheduling part, which can be used if the computer has a multicore CPU.

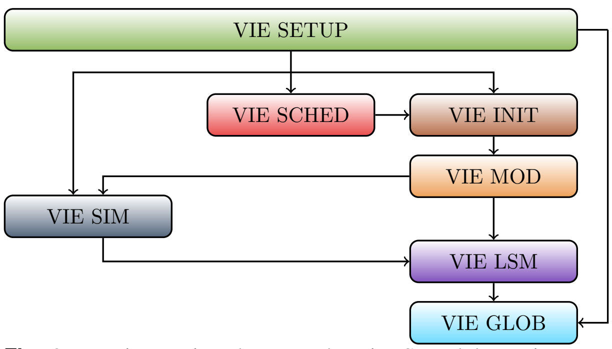

Fig. 1: New interactions between the VieVS modules. It is now possible to schedule, simulate and analyse sessions at once.

Matthias Schartner · Johannes Böhm · David Mayer · Andreas Hellerschmied
TU Wien, Gußhausstraße 27-29, AT-1040 Wien, Austria

Lucia McCallum
University of Tasmania, Private Bag 37, 7001 Hobart, Australia

3 Test case 1: impact of a new station in Africa

The first test case investigates the impact of a new station in Africa on an existing network. Therefore a network with seven stations was used and an eighth station was added at different locations in Africa (Fig. 2). Each red dot represents one station in the existing network. Each green dot represents a possible station location for the eighth station. Altogether 99 possible station locations were taken into account. For each location 12 schedules were created with different starting dates. Each session lasts for 24 hours and was simulated 100 times. This ends up with almost 120000 simulated sessions. Figure 3 shows the results. Due to the huge amount of data, it is possible to either look at the repeatability or at the mean formal errors of certain parameters, which agree quite well with each other.

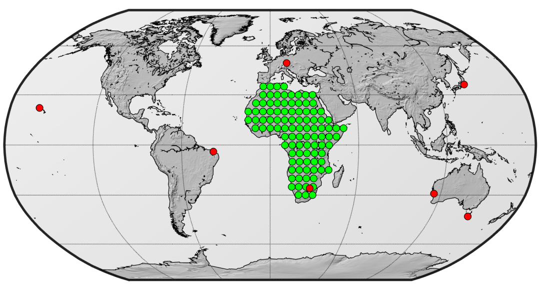

Fig. 2: Investigated network: seven fixed stations (red dots) plus one station with 99 possible positions (green dots)

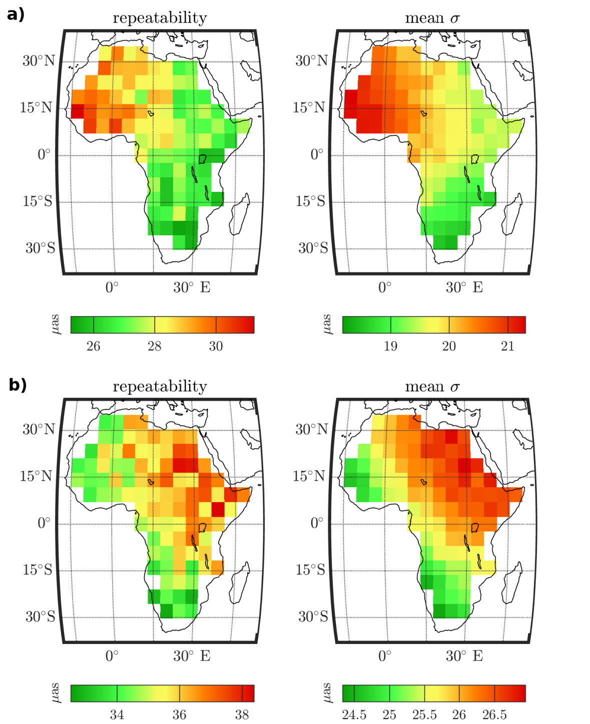

Fig. 3: Results from Monte Carlo simulations. Left column is repeatability over each simulation, right column is mean formal error. **a)** polar motion x-axis, **b)** polar motion y-axis

Figure 3 shows that it is difficult to get one preferred station location where all parameters benefit most. For example, while for improving the polar motion in x direction the south and the east parts of Africa are preferred, for polar motion in y direction the south and the west lead to the best results. It was unexpected that the south is among the best possible locations, because with HART15M there is already a station available in the south. This needs further research. It should also be noted here, that the effect of only one existing network is studied. With different networks the results could change. To find the best possible location of a new antenna in Africa in general, different networks need to be investigated.

4 Test case 2: Choosing appropriate weight factors

Selecting a good set of parameters is not an easy task. However, with the changes in the VieVS software it is now easier to test different parameter setups. To understand what weight factors are best suited it is necessary to understand how the VieVS scheduling tool works (Sun et al., 2014). The schedule is created scan by scan. To select a next scan, all available scans are considered with simple models. Some conditions are applied to reduce the otherwise huge number of possible next scans to speed up the calculation. For the remaining scans, more rigorous models are used to calculate all necessary parameters and to perform internal checks. Each scan is then given several scores. Usually a score for the improvement of the sky coverage, a score for the number of observations and a score for the total time it takes to observe the scan. The weight factors now simply specify how these scores are added together to get a final score. The scan with the highest final score is then used as the next scan and the whole process starts again. This means using good weight factors directly influence the schedule, because via the weight factors the scans are selected. Figure 4 shows all investigated sets of different weight factors. A total of 92 possible sets of parameters were used.

Two different networks were used to search for a good set of parameters, the Austral network and a global network. The main difference between the networks is that the Austral network consists of 5 stations and no subnetting is used to create the schedules. For the global network 8 stations were used with subnetting. For the

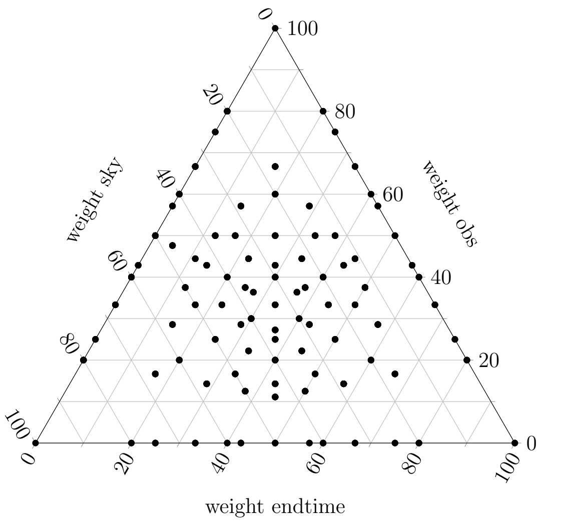

Fig. 4: Relative ratio between the three main weight factors used in VieVS. Ninety-two different sets of parameters (black dots) were used to create schedules.

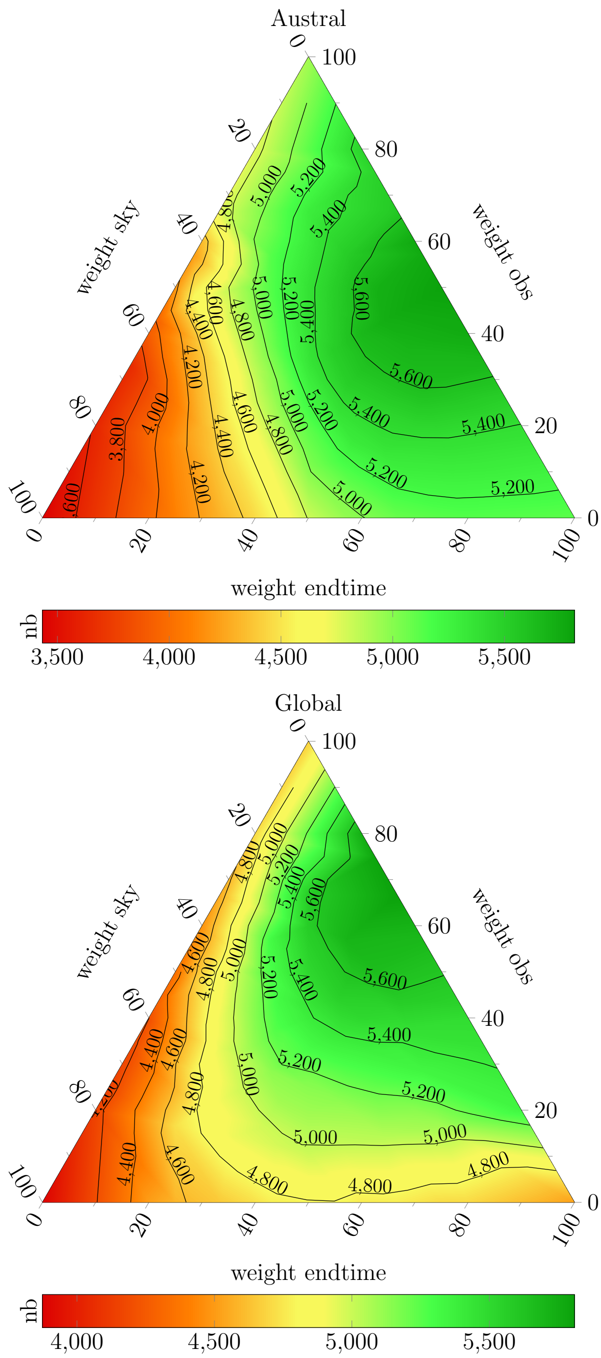

Fig. 5: Mean number of observations investigated at 92 sample points. Space between sample points is interpolated. The maximums for Austral network and global network correspond quite well.

Austral network 6 schedules with different start points were created for each set of parameters and each schedule was simulated 50 times. This adds up to 27600 simulated sessions. For the global network 10 schedules were created and again simulated 50 times which adds up to 46000 simulated sessions, which means in total more than 73600 sessions were simulated. Figure 5 shows the mean number of observations per schedule for each set of parameters. Usually a high number of observations is a good indicator for a good schedule. A clear maximum can be seen, which corresponds quite well between the Austral and the global network. Figure 6 shows the mean estimates of the polar motion along the x-axis. The result is quite different between the Austral and the global network. While for the Austral network, parameters with a high weight for the scan endtime lead to good results, for the global network a more balanced set of parameters leads to better results. The result looks almost identical for other parameters, like polar motion in y-direction or station coordinates. It should also be noted here, that the parameters which lead to the highest number of observations are not the parameters which show the best result. Therefore we recommend to simulate a schedule and look at the expected precision of the estimated geodetic parameters.

Table 1 lists sets of parameters, which lead to the best results when used in VieVS. The large amount of schedules was necessary, to reduce the noise in the results. This means that two sets of parameters, which are close to each other, can give very varying results. Therefore it is recommended to use the multi scheduling tool to create multiple schedules with similar parameters and to simulate the schedules to pick the best one.

5 Conclusion

With the new changes in VieVS it is possible to create large scale Monte Carlo simulations automatically which can be used for several research. It is shown, that it is difficult to select a good station location for a new antenna. Looking at different parameters like polar motion or station coordinates would lead to different pre-

Table 1: List of parameters which should be used to create a schedule.

Network	weight endtime	weight nobs	weight sky
Austral	0.6	0.2	0.2
global	0.4	0.4	0.2

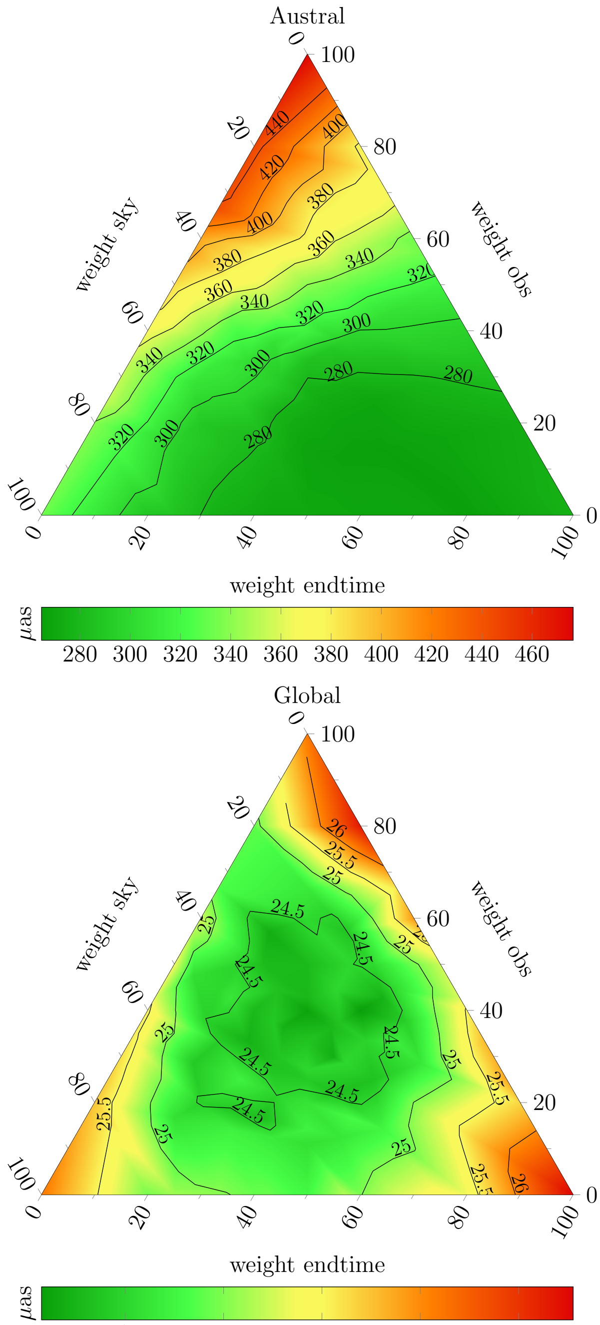

Fig. 6: Mean result for polar motion in x-direction after simulating each schedule 50 times. Note that the best results do not correspond with the areas of the highest number of observations in Figure 5. Different weight factors for the Austral network and a global network show best results.

ferred locations. To create a good schedule it is critical to use an appropriate set of weight factors in VieVS. The most suitable set of weight factors depends on the station network and the session task, which means that for each network different parameters should be used. With the new changes in VieVS it is now easier to try different parameters and get a good result.

References

Böhm J, Böhm S, Nilsson T, Pany A, Plank L, Spicakova H, Teke K, Schuh H (2012) The new Vienna VLBI Software VieVS. In: S. Kenyon, M. C. Pacino, U. Marti (eds.) *Proc. IAG Scientific Assembly 2009*, IAG Symposia Series, 136, 1007–1011, doi:10.1007/978-3-642-20338-1_126.

Gipson J (2012) Sked - VLBI Scheduling Software. NASA Goddard Space Flight Center, `ftp://gemini.gsfc.nasa.\protect\discretionary{\char\hyphenchar\font}{}{}gov/\protect\discretionary{\char\hyphenchar\font}{}{}pub/\protect\discretionary{\char\hyphenchar\font}{}{}sked/sked_Manual_v2012May09.pdf`

Hellerschmied A, Böhm J, Neidhardt A, Kodet J, Haas R, Plank L (2015) Scheduling VLBI Observations to Satellites with VieVS. In: C. Rizos, P. Willis (eds.), *Proc. IAG Commission 1 Symposium 2014: Reference Frames for Applications in Geosciences (REFAG2014)* IAG Symposia, doi:10.1007/1345 2015 183.

Lovell J E J, McCallum J N, Reid P B, McCulloch P M, Baynes B E, Dickey J M, Shabala S S, Watson C S, Titov O, Ruddick R, Twilley R, Reynolds C, Tingay S J, Shield P, Adada R, Ellingsen S P, Morgan J S, Bignall H E (2013) The AuScope geodetic VLBI array. *J Geod*, 87, 527–538.

Pany A, Böhm J, MacMillan D, Schuh H, Nilsson T, Wresnik J (2011) Monte Carlo simulations of the impact of troposphere, clock and measurement errors on the repeatability of VLBI positions. *J Geod*, 85:39, doi:10.1007/s00190-010-0415-1.

Plank L, Hellerschmied A, McCallum J, Böhm J, Lovell J (2017) VLBI observations of GNSS-satellites: from scheduling to analysis. *J Geod*, 91:867, doi:10.1007/s00190-016-0992-8

Sun J, Böhm J, Nilsson T, Krásná H, Böhm S, Schuh H (2014) New VLBI2010 scheduling strategies and implications on the terrestrial reference frames. *J Geod*, 88(5), 449–461.

VLBI With GNSS-signals on an Intercontinental Baseline – A progress report

R. Haas, T. Hobiger, G. Klopotek, N. Kareinen, J. Yang , L. Combrinck, A. de Witt, M. Nickola

Abstract VLBI-observations of GNSS-signals have been discussed for several years as a apossible approach to improve the accuracy of the terrestrial reference frame. Several experimental observing sessions have been performed during the last years, primarily with regional VLBI networks in Europe and Australia. Here we present VLBI observations of GNSS-signals performed on an intercontinental baseline between Onsala (Europe) and Hartebeesthoek (Africa). These observations are part of a ESA pilot project within the Alcantara programme of the European Space Agency (ESA) and aim at achieving synergies between VLBI and GNSS. Data were collected during several sessions in 2017, successfully correlated and post-processed, and analyzed with a geodetic VLBI data analysis software. The results show that ... We briefly describe these sessions, and present first preliminary results.

Keywords VLBI, GNSS, satellite observations, DiFX, Fourfit, C5++

1 Introduction

A global geodetic terrestrial reference frame, such as the international terrestrial reference frame (ITRF) (Altamimi et al., 2011, 2016) is of great importance for society (United Nations, 2015). However, the current quality of the global terrestrial reference frame is regarded as still being insufficient for studies concerning global change processes, such as sea level rise (Blewitt et al., 2010). In particular the quality of the so-called local ties at co-location stations is often suspected to be the reason for the insufficient qualify of the ITRF (Altamimi et al., 2011; Seitz et al., 2012).

As one promising approach to improve the consistency and accuracy of the global terrestrial reference frame the idea of co-location onboard satellites has been proposed (Rothacher et al., 2009). This includes dedicated multi-technique co-location satellites such as the Chinese APOD (Tang et al., 2016) or the proposed E-GRASP satellite (Biancale et al., 2017), but involves also VLBI observations of GNSS satellites. Concerning the latter, simulation studies performed by Plank et al. (2014) showed promising results for VLBI observations of GPS satellites in a seven station European VLBI network, providing 3D station position repeatabilities on the order of 5–10 mm.

Test observations of GNSS signals were performed during the last years mainly with VLBI stations in either Europe or Australia. Often observations were performed on a single baseline only. The stations involved were primarily Onsala, Medicina, Noto, Wettzell in Europe, e.g. (Tornatore et al., 2011; Haas et al., 2014, 2015) and Hobart and Ceduna in Australia (Plank et al., 2017).

These stations involved are equipped with L-band receiving systems, the European stations with dual circular polarisation, and the Australian ones with dual linear polarisation. Most of the L-band systems are bandwidth restricted, i.e. it is not possible to observe simultaneously both the GPS L1 (1575.42 MHz) and L2 (1227.60 MHz) frequency bands. Often the GPS L2 is even out of the receiver capabilities, and form some even GPS L1 is difficult to reach. However, for the latter at least the GLONASS L1 (1600 MHz) was reachable.

Most of the telescopes involved do not yet allow continuous tracking of orbiting objects, so that a stop-and-go type of observing strategy with update intervals on the order of 10 s to 15 s had to be used to follow the satellites.

Inspired by the promising simulation study (Plank et al., 2014) and the successful test observations (Tor-

Rüdiger Haas · Thomas Hobiger · Grzegorz Klopotek · Niko Kareinen · Jun Yang
Chalmers University of Technology, Department of Space, Earth and Environment, Onsala Space Observatory, SE–439 92 Onsala, Sweden

Ludwig Combrinck · Alet de Witt · Marisa Nickola
Hartebeesthoek Radio Observatory, Krugersdorp, 1740, South Africa

natore et al., 2011; Haas et al., 2014, 2015; Plank et al., 2017), ESA initiated a called for a pilot project within its Alcantara programme on the topic of Synergies between VLBI and GNSS. The goals of this pilot project are to study whether VLBI observations of GNSS signals really can be used to improve the terrestrial reference frames, to test intercontinental networks, and in particular the impact of Galileo. We submitted a proposal to this call and were lucky to get a contract for this pilot project.

2 Observations

As part of the ESA pilot project, we performed in 2017 a number test experiments on the Onsala – Hartebeesthoek baseline. The telescopes used are the 25 m radio telescope at Onsala (ONSALA85) usually used for astronomical VLBI, and the 26 m radio telescope at Hartebeesthoek (HARTRAO) which is used for both geodetic and astronomical VLBI. While ONSALA85 was involved in the first intercontinental geodetic VLBI observations in the late 1960'ies and has been observing the S-band part of geodetic S/X measurements together with the Onsala 20 m telescope (ONSALA60), which did the X-band part, in the late 1970'ies, it has not been used for geodetic VLBI since then. The station coordinates of ONSALA85 were determined from local tie measurements (Lundqvist, 1982) and VLBI at C-band (Charlot et al., 2001). HARTRAO on the other hand is regularly used in geodetic VLBI in the IVS observing programme and thus should have updated and reliable coordinates.

Between January and July 2017 we organised in total eight so-called OHT-sessions. The backbone of these sessions is the Onsala-Hartebeesthoek baseline. Since the aim of the pilot project was to do real network observations, we tried to include additionally further telescopes. For the most recent sessions in May and July we were able to include additionally the Russian station Zelenchukskaya. This station is also regularly participating in the geodetic VLBI observing plan and has well established coordinates and promises to improve the observing geometry.

The observing plans were scheduled with the VieVs scheduling tool (Hellerschmied et al., 2015). The first tests were done focussing on to observe GPS satellites. Then we also included GLONASS observations. However, we realized soon that the inclusion of GLONASS caused difficulties due to the necessity to adjust the observation frequency bands. Thus, we left the idea of combined GPS and GLONASS observations again. Instead, we added Galileo to the observing plan for the more recent sessions. Galileo satellites also use the same L1 center frequency as GPS, though the signal characteristics are quite different.

Table 1 gives an overview of the so-far performed OHT-sessions, with their dates, durations, participating stations and GNSS observed. In the sequence of this manuscript we will concentrate on the first three sessions which involved one intercontinental baseline only.

Table 1: Overview of the VLBI sessions

Session	date	duration	stations	satellites
OHT1	2017-01-24	1 h	O8 - Hh	GPS
OHT2	2017-01-31	4 h	O8 - Hh	GPS + GLONASS
OHT6	2017-04-07	4 h	O8 - Hh	GPS + Galileo
OHT7	2017-05-22	2.5 h	O8 - Hh - Zc	GPS + Galileo
OHT8	2017-07-24	24 h	O8 - Hh - Zc	GPS + Galileo

The setup chosen for the OHT experiments was to observe four channels of 16 MHz bandwidth (for OHT6 32 MHz), two in each polarisation, centered on the GPS/Galileo L1 center frequency. For OHT2 the observing frequencies were adapted to the corresponding GLONASS satellites, and on GPS L1 for GPS satellites. Except for OHT1, also natural radio sources were observed, typically at the beginning and the end of the session and in regular intervals during the session. These radio sources were rather near by the satellites, Therefor the observing frequencies for the radio sources were slightly offset in order to avoid potential leaking of satellite signals through e.g. side lobes.

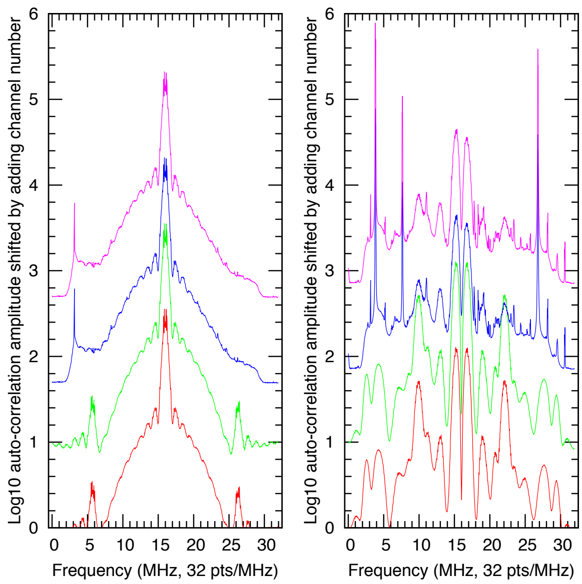

Fig. 1: Examples of spectra observed locally at Onsala during session OHT6: Bandpass of a GPS satellite (left) and a Galileo satellite (right). Shown are four channels covering 32 MHz.

The plots presented in Fig. 1 are examples of the spectra locally observed at Onsala during OHT6. Shown are 4 observing channels of 32 MHz bandwidth. The difference in the signal characteristics between GPS (left) and Galileo (right) is clearly visible.

3 Data processing

The observed raw data were e-transferred to Onsala and correlated there with the software correlator DiFX (Deller et al., 2011). The a priori delays necessary for the correlation of the satellite observations were determined with the C5++ software (Hobiger et al., 2010) using near-field modeling following Duev et al. (2012). Fringe-fitting was performed with the *Fourfit* program.

It turned out that the 10 s long scans gave rather high SNR values, on the order of 10000 and more. As an example the finge plot of GPS satellite PG03 observed during OHT1 is presented in Fig. 2. With 10 s of data SNR values of more than 11000 can be achieved. We thus decided to split up the data into smaller pieces of 1 s for the correlation and fringe fitting, which still provided sufficiently high SNR values.

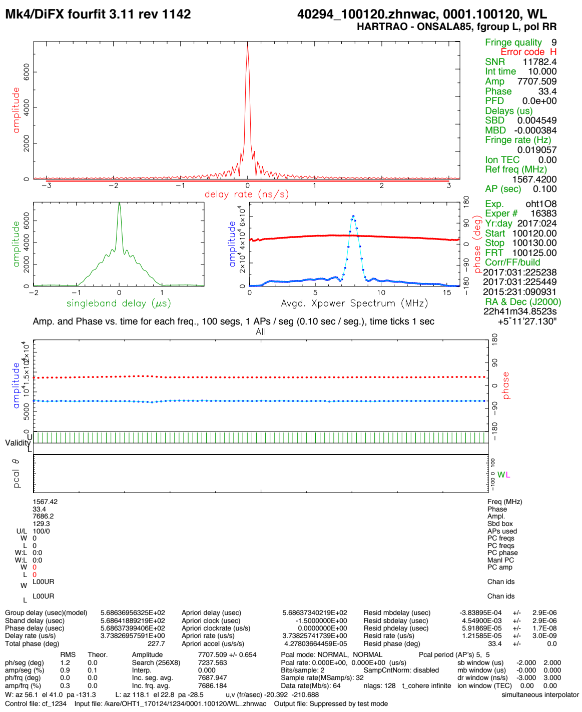

Fig. 2: Fringe plot for GPS satellite PG03 observed on the baseline Onsala-Hartebeesthoek during session OHT1.

4 Preliminary results

After correlation and fringe fitting the resulting delay values were analysed using the C5++ software. Standard routines were used for the processing. Tropospheric information was used based on the GPT2 model and ionospheric corrections were applied based on global TEC maps provided by the IGS.

Since HartRAO is an active IVS station with well established coordinates in the ITRF it was used as reference station for the data analysis, both concerning the station position as well as concerning the reference clock. Station position corrections were estimate for ONSALA85, as well as clock offsets and rates. For both station involved in the sessions, zenith wet delay (ZWD) and station-dependent ionospheric biases were estimated. Additionally, for each satellite observed, a satellite-specific time bias was estimated. The latter were introduced to partly take care ionospheric influences, as well as instrumental delays due to the interaction of individual satellite signal structure and filter characteristics of the receiving systems.

Unfortunately, the ionospheric corrections based on global TEC maps do not give sufficient detail and thus do not sufficiently remove the ionospheric effects from the observed single frequency delays. As a consequence, the other parameters that are estimated in the data analysis will partly be absorbing remaining ionospheric contributions. Therefore it is not meaningful yet to investigate the estimated parameters in detail.

Instead, as a quality measure, we have a look at the post-fit residuals of the first three sessions. The post-fit residuals of OHT1, OHT2 and OHT3 are presented in Fig. 3, Fig. 4, and Fig. 5, respectively

It becomes evident that there are still systematics left in the residuals. There is e.g. a kind of ”saw-tooth” pattern within the 5 minutes long observing epochs per

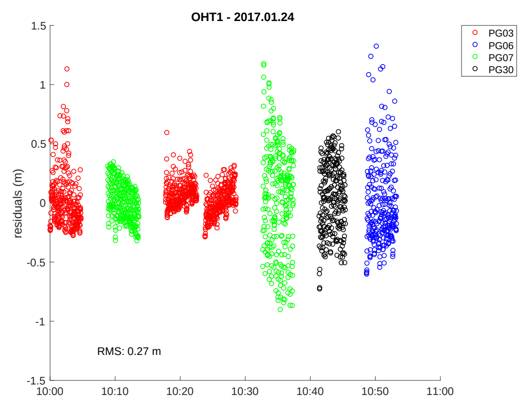

Fig. 3: Post-fit residuals for OHT1.

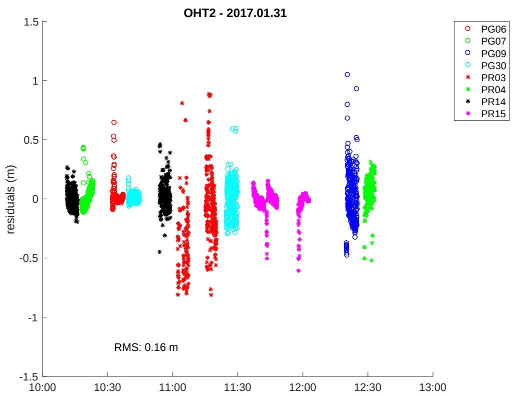

Fig. 4: Post-fit residuals for OHT2.

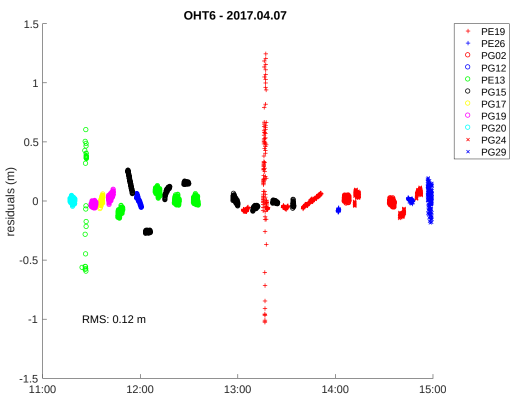

Fig. 5: Post-fit residuals for OHT6.

satellite (see e.g. PG07 in Fig.3). This might be related to the stop-and-go type of observation strategy where the telescopes were repointed every 10 s to follow the satellite passes. There are also ”satellite jumps” visible, both between different satellites, but also when coming back to the same satellite (see e.g. PG03 and PG07 in Fig. 3, or PG06 in Fig. 4, or PG13 in Fig. 5). Sometimes there are ”satellite patterns”, i.e. residuals fading in or fading out (see e.g. PR15 in Fig. 4), probably due to tracking issues. And sometimes satellites show rather large residuals due to so far unknown reasons (see e.g. PE19 in Fig. 5). Thus, more work is needed in order to understand these features. Table 2 provides some statistical information on the analysis of all three stations.

Table 2: Statistics for the first three OHT sessions

Session	duration	observations	post-fit RMS (m)
OHT1	1 h	1948	0.27
OHT2	4 h	3340	0.16
OHT6	4 h	5144	0.12

5 Conclusions

During 2017 we performed a serie of successful VLBI observations of GNSS signals on an intercontinental baseline between Onsala and Hartebeesthoek. Signals of GPS, GLONASS and Galileo satellites were observed and correlated. Even with data sets as short as 1 s sufficiently high SNR is achieved.

The geodetic analysis of these data was done with C5++ and a number of parameters were estimated, including station position, station clock parameters, and troposphere parameters. The lack of ionospheric correction with sufficient detail and accuracy leads to that the estimated parameters are influenced by these remaining ionospheric effects. The post-fit residuals are on the order of 12-27 cm. However, a number of systematic effects are left in the post-fit residuals, e.g. a ”saw-tooth” pattern within the satellite scans, and ”satellite jumps”. So, more work is needed to understand these systematics and to improve the performance. Further observing sessions, preferably including more stations and with at least 24 h observation time are planned to address these issues. One aspect that in particular requires improvement is the handling of ionospheric effects.

However, in general, we think that the approach to observe GNSS-signals with VLBI radio telescopes is promising. We thus support the ideas of to equip one or several of the second generation Galileo satellites with artificial senders for VLBI observations.

References

Altamimi Z, Collilieux X, M7'e9tivier L (2011) ITRF2008: an improved solution of the international terrestrial reference frame. *J Geod*, 85(8), 457–473,

Altamimi Z, Rebischung P, Métivier L, Xavier C (2016) ITRF2014: A new release of the International Terrestrial Reference Frame modeling nonlinear station motions. *J. Geophys. Res. Solid Earth*, 121, 6109–6131, {doi:10.1002/2016JB013098

Biancale R, Pollet A, Coulot D, Mandea M (2017) E-GRASP/Eratosthenes: a mission proposal for millimetric TRF realization. *Geophysical Research Abstracts*, 19, EGU2017-8752.

Blewitt G, Altamimi Z, Davis J, Gross R, Kuo C Y, Lemoine F G, Moore A W, Neilan R E, Plag H-P, Rothacher M, Shum C K, Sideris M, Schöne T, Tregoning P, Zerbini S (2010) Geodetic Observations and Global Reference Frame Contributions to Understanding Sea-Level Rise and Variability. In: J. A. Church, P. L. Woodworth, T. Aarup, W. S. Wilson (eds.), Understanding Sea-Level Rise and Variability, 1st edition, Blackwell Publishing Ltd., 256–284, doi:10.1002/9781444323276.ch9

Charlot P, Campbell R, Alef W, Borkowski K, Conway J, Foley A, Garrington S, Kraus A, Nothnagel A, Sovers O, Trigilio C, Venturi T, Xinyong H (2001) ITRF2000 Positions of

Non-geodetic Telescopes in the European VLBI Network. In: D. Behrend, A. Rius (eds.), *Proc. 15th Working Meeting on European VLBI*, 194–200.

Collilieux X, Wöppelmann G,(2011) Global sea-level rise and its relation to the terrestrial reference frame. *J Geod*, 85(1), 9–22, doi:10.1007/s00190-010-0412-4

Deller A T, Brisken W F, Phillips C F, Morgan J, Alef W, Cappallo R, Middelberg E, Romney J, Rottmann H, Tingay S J, Wayth R (2011) DiFX-2: A More Flexible, Efficient, Robust, and Powerful Software Correlator. *Pub Astron Soc Pac*, 123(901), 275–287.

Duev D A, Molera Calves G, Pogrebenko S V, Gurvits L I, Cimo G, Bahamon T B (2012) Spacecraft VLBI and doppler tracking: algorithms and implementation. *Astronomy & Astrophysics* 541, A43, doi:10.1051/0004-6361/201218885.

Haas R, Neidhardt A, Kodet J, Plötz Ch, Schreiber K-U, Kronschnabl G, Pogrebenko S, Duev D, Casey S, Marti-Vidal I, Yang J, Plank L (2014) The Wettzell-Onsala G130128 experiment – VLBI-observations of a GLONASS satellite. In: D. Behrend, K. D. Baver, K. L. Armstrong (eds.), *IVS 2014 General Meeting Proc.*, Science Press (Beijing), 451–455.

Haas R, Hobiger T, Hellerschmied A, Neidhardt A, Kodet J (2015) GLONASS-VLBI: Onsala-Wettzell test observations. In: R. Haas, F. Colomer (eds.), *Proc. 22nd EVGA Working Meeting*, 107–111.

Hellerschmied A, Böhm J, Neidhardt A, Kodet J, Haas R, Plank L (2015) Scheduling VLBI observations to satellites with VieVS. In: T. van Dam (ed.), *REFAG 2014, International Association of Geodesy Symposia 146*, doi:10.1007/1345_2015_183

Hobiger T, Otsubo T, Sekido M, Gotoh T, Kubooka T, Takiguchi H (2010) Fully automated VLBI analysis with c5++ for ultra rapid determination of ut1. *Earth Planets Space* 62, 993–937, doi:10.5047/eps.2010.11.008.

Lundqvist G (1982) Precision Surveying at the 1-mm level using radio interferometry. In: *Proc. Symposium No. 5-IAG*, NOAA Technical Report NOS 95 NGS 24, 99.

Plank L, Böhm J, Schuh H (2014) Precise station positions from VLBI observations to satellites: a simulation study. *J Geod* 88(7):659–673, doi:10.1007/s00190-014-0712-1

Plank L, Hellerschmied A, McCallum J, Böhm J, Lovell J (2017) VLBI observations of GNSS-satellites: from scheduling to analysis. *J Geod* 91(7):867–880, doi:10.1007/s00190-016-0992-8.

Rothacher M, Beutler G, Behrend D, Donnellan A, Hinderer J, Ma C, Noll C, Oberst J, Pearlman M, Plag H-P, Richter B, Schöne T, Tavernier G, Woodworth P (2009) The future global geodetic observing system. In: H.-P. Plag, M. Pearlman (eds.), Global Geodetic Observing System - Meeting the Requirements of a Global Society on a Changing Planet in 2020. Springer, 237–272, doi:10.1007/978-3-642-02687-4

Seitz M, Angermann D, Bloßfeld M, Drewes H, Gerstl M (2012) The 2008 DGFI realization of the ITRS: DTRF2008. *J Geod*, 86(12), 1097–1123.

Tang G, Sun J, Li X, Liu S, Chen G, Ren T, Wang G (2016) APOD Mission Status and Observations by VLBI. In: D. Behrend, K. D. Baver, K. L. Armstrong (eds.), *IVS 2016 General Meeting Proceedings - "New Horizons with VGOS"*, NASA/CP-2016-219016, 363–367.

Tornatore V, Haas R, Duev D, Pogrebenko S, Casey S, Molera Calvés G, Keimpema A (2011) Single baseline GLONASS observations with VLBI: data processing and first results. In: W. Alef, S. Bernhart, A. Nothnagel (eds.), *Proc. 20th EVGA Working Meeting*, 162–165.

United Nations General Assembly (2015) UN General Assembly resolution: A global geodetic reference frame for sustainable development. `http://www.un.org/ga/search/view_doc.asp?symbol=A/69/L.53`

Schaer S, Beutler G, Rothacher M, Springer T A (1996) Daily global ionosphere maps based on GPS carrier phase data routinely produced by the CODE. In: R. E. Neilan, P. A. Van Scoy, J. F. Zumberge (eds.), *Pro. IGS Analysis Center Workshop*, International GNSS Service. 181–192.

Sekido M, Kondo T, Kawai E, Imae M (2003) Evaluation of GPS-based ionospheric TEC map by comparing with VLBI data. *Radio Science* 38, doi:10.1029/2000RS002620.

Lunar Observations and Geodetic VLBI – A Simulation Study

G. Klopotek, T. Hobiger, R. Haas

Abstract The recent OCEL (Observing the Chang'E Lander with VLBI) sessions allow the geodetic VLBI community to gain new experience concerning observations of an artificial lunar radio source. Although the analysis of obtained data is still ongoing, the performance of the OCEL sessions, in terms of lunar-based parameters, is still rather unclear. In order to address this and related questions, we carried out Monte Carlo simulations using the c5++ analysis software and OCEL schedules with the purpose to evaluate the accuracy with which the position of an artificial radio source on the surface of the Moon can be determined with geodetic VLBI. We present the results of our study and discuss the limiting factors of this concept. Our simulation results can provide valuable insights concerning global observations of lunar radio transmitters and stimulate new observing ideas for space geodesy.

Keywords The Moon, geodetic VLBI, OCEL, c5++, Monte Carlo simulations

1 Introduction

In late 2013, a Chinese lander and a rover were deployed on the surface of the Moon to carry out scientific tasks related to the Chang'E-3 (CE-3) mission (Li et al., 2015). The landing site was located in the northwest part of the visible side of the Moon and both probes were equipped with X-band transmitters in order to send the acquired data back to Earth. In April 2014, first geodetic VLBI observations of signals transmitted by the lander were carried out on the Onsala–Wettzell baseline. Motivated by this initial experiment, observations of the lander with a global network of VLBI stations were proposed to the International VLBI Service for Geodesy and Astrometry (IVS) Program Committee. This resulted in twelve OCEL (Observing the Chang'E Lander with VLBI) sessions, organized between the years 2014 and 2016 (Haas et al., 2017). The global distribution of VLBI sites scheduled for this project is shown in Fig. 1.

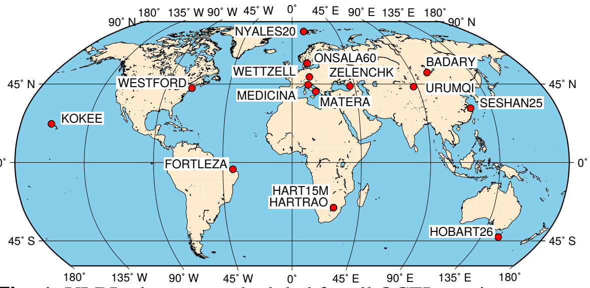

Fig. 1: VLBI telescopes scheduled for all OCEL sessions.

As the geodetic analysis of the OCEL experiments is still ongoing, the performance of these sessions, in terms of lunar-based parameters, has not been investigated yet. Therefore, we present the results of Monte Carlo simulations carried out with the purpose to determine the horizontal position components of a lunar lander located at the landing site of the CE-3 mission. We provide information on the network geometry and describe the simulation setup of this study. We show how the estimated horizontal position components of a lunar lander depend upon the precision of lunar observations. In addition, we highlight the limiting factors of this new observation concept as well as additional aspects that need to be taken into account when including lunar objects into geodetic VLBI schedules. An outlook concerning observations of an artificial lunar radio source by geodetic VLBI forms the last part of this study.

Grzegorz Klopotek · Thomas Hobiger · Rüdiger Haas
Chalmers University of Technology, Department of Space, Earth and Environment, Onsala Space Observatory, SE–439 92 Onsala, Sweden

2 Data

In order to investigate the concept of lunar observations incorporated into geodetic VLBI schedules, the OCEL schedules were utilized in our simulations. As stated by Haas et al. (2017), the combination of lunar and quasar observations for creating the 24-hour OCEL schedules was carried out in a semi-automatic fashion using SKED (Gipson et al., 2010). The aim was to achieve an alternating sequence of two type of thirty minute long observing blocks. The first type were "standard geodetic blocks", i.e. scheduled using the standard automated scheduling strategy in SKED, and the second type were "lunar blocks". The latter were scheduled manually with alternating observations to the CE-3 lander and near-by radio sources. The scans to the CE-3 lander were fixed to be 30 s long, while the length of the radio source scans was determined as usual to achieve the target SNR. For most OCEL sessions these blocks spanned throughout the whole 24-hour session and alternated with same-length blocks of automatically-scheduled quasar observations. However, in particular for the early OCELs, the lunar lander was not active throughout the whole 24 h, so that only a fraction of the 24 h session could be filled with lunar blocks. Furthermore, due to the "Pacific gap", i.e. the rather low density of VLBI stations between East Asia and the Americas in the OCEL sessions, it occurred often that the lunar lander was only visible for a single station durin several hours, thus permitting to schedule lunar blocks. On average, this scheduling strategy resulted in about 16 % of lunar observations per session. The list of OCEL schedules along with session-specific information is presented in Tab. 1.

3 Simulation setup

All simulations were performed with the c5++ analysis software (Hobiger et al., 2010), in which VLBI observables are simulated by including three major error sources, i.e. zenith wet delays (ZWD_1 and ZWD_2), station clock variations (clk_1, clk_2), and a baseline noise (τ_{rnd}). This can be expressed as

$$\begin{aligned}\tau_{sim} = \tau_g + (ZWD_2 \cdot m_w(\varepsilon_2) + clk_2) \\ -(ZWD_1 \cdot m_w(\varepsilon_1) + clk_1) + \tau_{rnd},\end{aligned} \tag{1}$$

where $m_w(\varepsilon_i)$ is the wet mapping function for the elevation angle ε_i at the i^{th} station and τ_g corresponding to a geometric VLBI delay. In the case of lunar observations, τ_g is computed following Duev et al. (2012).

The simulated ZWD and clock values were modeled using a standard parametrization applied in geodetic VLBI simulations (Halsig et al., 2016; Kareinen et al., 2017). Quasar observations were generated using the Gaussian distribution with the standard deviation of 14.14 mm (47 ps). In the case of lunar observations, twenty levels of τ_{rnd} were considered. They spanned from 1.41 mm to 141.4 mm in logarithmic steps in order to investigate the relation between the precision of lunar observations and the lunar lander's position estimates. Thus, the lunar observation precision is related not only to the theoretical uncertainty of a group delay observable, which in this case amounts to few millimeters, but includes also additional error contributions.

All twelve OCEL schedules created semi-automatically in SKED were converted to VLBI experiment (VEX) files and formed the basis of the following simulations. Station positions and Earth Orientation Parameters (EOP) were fixed to their a priori values and only the lunar position of the lander was solved for. Clock offsets (w.r.t. a reference clock) and troposphere (zenith wet delays, north and east tropospheric gradients) parameters were estimated using piece-wise linear offsets and following usual temporal resolution choices for these four nuisance parameters. Each of the OCEL sessions was simulated one hundred times for each of the twenty lunar observation precision levels. The estimated horizontal position components (ϕ_{lan}, λ_{lan}) of the lunar lander along with its a priori position were used to compute two-dimensional position repeatabilities. The latter were expressed in the form of Weighted Root Mean Square errors ($WRMS_{2D}$). The height component was not included in the estimation process and it was fixed to an arbitrary value of 0.00 m.

4 Results

The computed WRMS$_{2D}$ values are presented in Fig. 2 for different levels of the lunar observation precision. For the best-performing OCEL session (RD1601) and millimeter-level precise lunar observations, the two-dimensional position accuracies settle around ten centimeters. In the presence of only measurement noise, the obtained WRMS$_{2D}$ values should linearly depend upon τ_{rnd}. However, similar repeatabilities for the lunar observation precision up to ten millimeters are related, to a major extent, to the effect of the tropospheric variation. The latter, in general, dominates the noise budget of geodetic VLBI and a better handling of this effect along with the lower measurement noise could lead in the future to an improved determination of the position of the lander on the Moon.

In the case of single-frequency observations, one needs

Table 1: OCEL schedules with information on the quantity of stations and observations per session.

		Participating VLBI telescopes													Number		
Number	Session	BADARY	FORTLEZA	HARTRAO	HOBART26	HART15M	KOKEE	KUNMING	NYALES20	ONSALA60	SESHAN25	URUMQI	WETTZELL	ZELENCHK	Stations	Lunar obs.	All obs.
#1	RD1405	Bd	-	Hh	Ho	-	-	-	Ny	On	Sh	-	Wz	Zc	8	1018	8021
#2	RD1407	Bd	-	Hh	-	-	-	-	Ny	-	Sh	Ur	Wz	Zc	7	910	7057
#3	RD1409	Bd	-	-	Ho	Ht	-	-	Ny	-	Sh	Ur	Wz	Zc	8	908	7416
#4	RD1411	-	-	-	Ho	Ht	Kk	-	Ny	-	-	Ur	Wz	-	6	662	4860
#5	RD1505	Bd	Ft	Hh	Ho	-	Kk	-	Ny	On	Sh	-	Wz	Zc	10	1488	9364
#6	RD1506	Bd	Ft	Hh	Ho	-	Kk	-	Ny	On	Sh	-	Wz	Zc	10	870	8652
#7	RD1507	Bd	-	Hh	Ho	-	Kk	-	Ny	On	-	-	Wz	Zc	8	617	6901
#8	RD1510	Bd	Ft	-	Ho	Ht	Kk	-	Ny	On	-	-	Wz	Zc	9	1524	9093
#9	RD1601	Bd	Ft	Hh	Ho	-	Kk	-	Ny	On	-	-	Wz	Zc	9	1427	8948
#10	RD1604	Bd	Ft	Hh	Ho	-	-	-	Ny	-	Sh	Ur	Wz	Zc	9	1629	10530
#11	RD1609	Bd	Ft	Hh	Ho	-	Kk	Km	Ny	On	-	Ur	Wz	Zc	11	741	7248
#12	RD1611	Bd	Ft	Hh	Ho	-	Kk	-	Ny	On	-	Ur	Wz	Zc	10	1355	8049

also to consider the impact of the ionosphere on the obtained results. For single-frequency lunar observations, externally-derived ionospheric delays e.g. based on Global Ionospheric Maps (GIM) (Schaer et al., 1996), are necessary. Utilization of such correction models would imply additional noise contributions on the level of about sixty millimeters for intercontinental baselines (Sekido et al., 2003). This value, of course, should be smaller for shorter baselines. Nevertheless, one can conclude that WRMS_{2D} computed for all OCEL sessions does not exceed 0.5 m for the precision of lunar observations of up to 70 mm, i.e. including already ionosphere delay correction uncertainties.

At a first glance of Fig. 2, one can identify major differences between the worst-performing (RD1407) and best-performing (RD1601) session in terms of the computed lunar position repeatabilities. Compared to the RD1407 network, RD1601 contains two more stations (KOKEE, FORTLEZA), which are located in the western part of the globe. Besides of an increased number of lunar and quasar observations per session, such an extension of the network provides an improved observing geometry for determination of both Earth-based and lunar-based parameters. As an example, the mean formal error of the estimated ZWD values from the RD1407 session for FORTLEZA decreased by about 11 mm in the case of the RD1601 session. On the contrary, for ZWD estimated for WETTZELL such an improvement amounts only to about 1 mm. In the case of lunar-based parameters, the impact of different network configurations on WRMS_{2D} was also investigated in this study.

As previously mentioned in Sec. 2, the scheduling process was carried out in a semi-automatic fashion where lunar baselines were created manually with no consideration on their orientation nor length. The distribution of baseline lengths for lunar observations is shown in Fig. 3. In terms of WRMS_{2D}, session RD1604 was not superior, although it is characterized by the largest number of quasar and lunar observations. On the contrary, the number of lunar and quasar observations is the smallest in the case of the RD1411 session, but it is possible to determine the lunar horizontal position components with greater precision than in the case of the worst-performing (RD1407) schedule. Based on the following, it is thought that the baseline lengths (and orientations) should be also taken into consideration when designing geodetic VLBI schedules for combination of lunar and quasar observations.

5 Conclusions & Outlook

We carried out Monte Carlo simulations using OCEL schedules in order to investigate how accurately the position of an artificial radio source on the Moon can be determined in standard geodetic VLBI mode for an object located in the north-west part of the visible side of the Moon. Based on our study, which included stochastic modeling of the three major error sources, we also highlighted dominating factors impacting the quality of these position estimates i.e. the tropospheric turbulence and network geometry. Assuming ionosphere-free group delay observables, the horizontal position components of an artificial radio source on the Moon could be determined with an accuracy of about ten centimeters. The latter was achieved for the best-performing session. For all OCEL sessions, the position accuracy is decreased by a factor of two and settles around twenty centimeters. A better determination of tropospheric parameters, reduction of contributions coming from the reference clocks and the decrease of the observation noise could improve the precision of two-dimensional

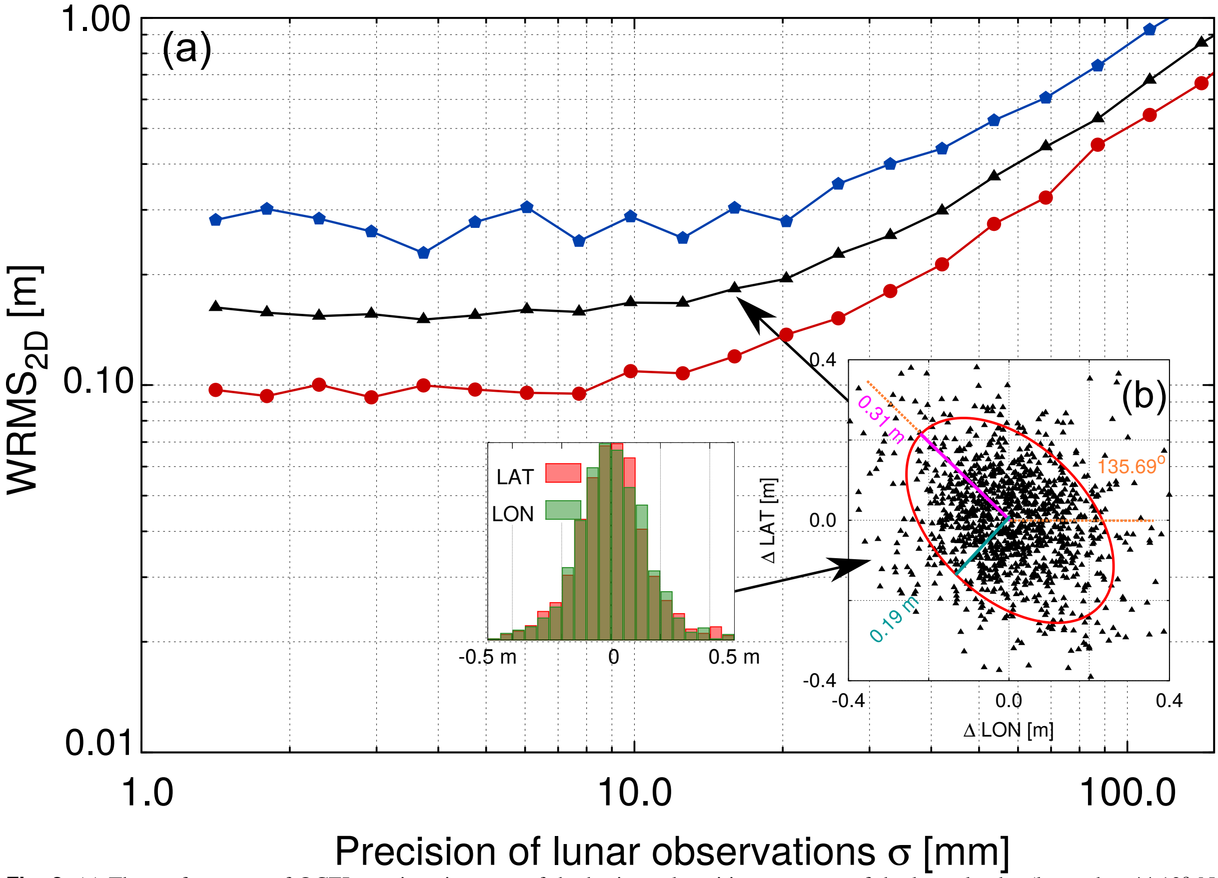

Fig. 2: (a) The performance of OCEL sessions in terms of the horizontal position accuracy of the lunar lander (located at 44.12° N and 19.51° W in the Moon's body-fixed reference frame) in dependence upon the measurement precision of lunar observations. Black triangles depict the mean performance based on all twelve sessions. The repeatabilities for the best-performing session are illustrated using red circles (RD1601), whereas the blue pentagons represent $WRMS_{2D}$ for the worst-performing OCEL session (RD1407). (b) The scatter plot and histograms of the lander's 2D position solutions are based on all OCEL sessions and a lunar observation precision of 15.97 mm. The included error ellipse represents the confidence level of 1-σ.

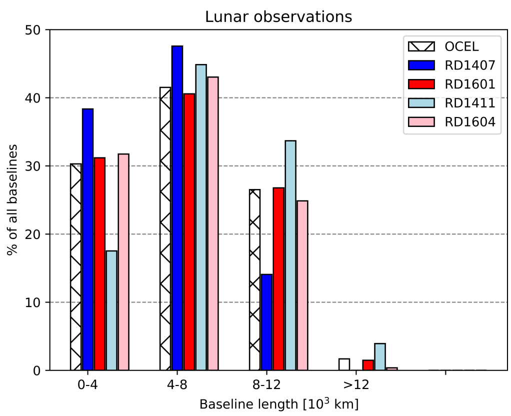

Fig. 3: The distribution of baseline lengths for lunar observations presented for all sessions (OCEL - hashed) as well as the worst-performing (RD1407 - blue) and best-performing (RD1601 - red) schedules in terms of WRMS$_{2D}$. For the sake of comparison, sessions with the smallest (RD1411 - light blue) and largest RD1604 - light red) quantity of lunar and quasar observations were also included in the figure.

lunar lander's position estimates. As presented here, the number of lunar observations per session is not the only factor important for the determination of the position components of a lunar lander. The maximization of the length of baselines used for lunar observations should be also taken into account while combining those with quasar observations within the same 24-hour geodetic VLBI sessions. Subsequent steps related to observations of lunar radio transmitters in geodetic VLBI mode concern studies on dedicated observing schedules as well as geodetic VLBI analysis of OCEL sessions.

Apart from the CE-3 mission, the performance of VLBI observations of artificial radio sources coupled with feasible processing chains is investigated nowadays by the geodetic VLBI community. An example can be observations of co-location satellites (Tang et al., 2016) or satellites of the Global Navigation Satellite Systems (GNSS) (Plank et al., 2017). Although the simulation results provide us with the knowledge on the potential of such new observation types, the observables extraction process is crucial before one can extend the field of geodetic VLBI research with new applications.

References

Duev D A, Molera Calves G, Pogrebenko S V, Gurvits L I, Cimo G, Bahamon T B (2012) Spacecraft VLBI and doppler tracking: algorithms and implementation. *Astronomy & Astrophysics* 541, A43, doi:10.1051/0004-6361/201218885.

Gipson J (2010) An Introduction to Sked. In: D. Behrend, K. D. Baver (eds.), *IVS 2010 General Meeting Proceedings*, 77–84.

Haas R, Halsig S, Han S, Iddink A, Jaron F, La Porta L, Lovell J, Neidhardt A, Nothnagel A, Plötz C, Tang G, Zhang Z (2017) Observing the Chang'E-3 Lander with VLBI (OCEL): Technical Setups and First Results. In: A. Nothnagel, F. Jaron (eds.), *Proc. First International Workshop on VLBI Observations of Near-field Targets*, Schriftenreihe des Inst. f. Geodäsie u. Geoinformation, Vol. 54, ISSN 1864-1113, Bonn. 41–64.

Halsig S, Artz T, Iddink A, Nothnagel A (2016) Using an atmospheric turbulence model for the stochastic model of geodetic VLBI data analysis. *Earth, Planets and Space* 68, 1–14, doi:10.5047/eps.2010.11.008. b03407.

Hobiger T, Otsubo T, Sekido M, Gotoh T, Kubooka T, Takiguchi H (2010) Fully automated VLBI analysis with c5++ for ultra rapid determination of ut1. *Earth Planets Space* 62, 993–937, doi:10.5047/eps.2010.11.008.

Kareinen N, Klopotek G, Hobiger T, Haas R (2017) Identifying optimal tag-along station locations for improving VLBI Intensive sessions. *Earth Planets Space* 69, 1–9, doi:10.1186/s40623-017-0601-y.

Li C, Liu J, Ren X, Zuo W, Tan X, Wen W, Li H, Mu L, Su Y, Zhang H, Yan J, Ouyang Z (2015) The Chang'E 3 Mission Overview. *Space Science Reviews* 190, 85–101, doi:10.1007/s11214-014-0134-7.

Plank L, Hellerschmied A, McCallum J, Böhm J, Lovell J (2017) VLBI observations of GNSS-satellites: from scheduling to analysis. *Journal of Geodesy* 91(7):867–880, doi:10.1007/s00190-016-0992-8.

Schaer S, Beutler G, Rothacher M, Springer T A (1996) Daily global ionosphere maps based on GPS carrier phase data routinely produced by the CODE. In: R. E. Neilan, P. A. Van Scoy, J. F. Zumberge (eds.), *Pro. IGS Analysis Center Workshop*, International GNSS Service. 181–192.

Sekido M, Kondo T, Kawai E, Imae M (2003) Evaluation of GPS-based ionospheric TEC map by comparing with VLBI data. *Radio Science* 38, doi:10.1029/2000RS002620.

Tang G, Sun J, Li X, Liu S, Chen G, Ren T, Wang G (2016) APOD Mission Status and Observations by VLBI. In: D. Behrend, K. D. Baver, K. L. Armstrong (eds.), *IVS 2016 General Meeting Proceedings*, 363–367.

Reduction of the IVS-INT01 UT1 Formal Error Through New Sked Algorithms

K. Baver, J. Gipson

Abstract Our past work has yielded information about spatio-temporal criteria for scheduling IVS-INT01 sessions' observations in order to try to improve the sessions' UT1 formal errors. We have added two new algorithms to a test version of the *Sked* program to use what we have learned in order to try to reduce the UT1 formal errors of test INT01 schedules. Here we report the results from using the new algorithms.

Keywords UT1, Intensives, scheduling, VGOS

1 Introduction

We added a new spatial and a new temporal algorithm to a test version of the *Sked* scheduling program to use lessons from our past work to try to reduce the UT1 formal errors of test INT01 schedules. Here we report on the application of these algorithms to three INT01 types: "MSS", "BA 50", and "VGOS INT01". Throughout, KOKEE and WETTZELL refer to the Kokee Park and Wettzell sites' 20-m S/X antennas, KOKEE12M to Kokee Park's broadband 12 m, and WETTZ13S to Wettzell's south broadband 13 m.

Sked selects observations in two stages. Stage 1 generates all possible observations, then discards observations that fail user-determined constraints, such as the minimum angular distance between scans. It then ranks the remaining observations by sky coverage (a schedule component that affects the UT1 formal error), passing the best N %, where N is user-specified, to stage 2. Stage 2 scores these trial observations using user-selected criteria and develops a cumulative score over all of the criteria for each observation. The observation with the highest score is scheduled. The test algorithms are implemented in stage 2. The Sked Manual (2016) describes *Sked* in more detail.

Baver and Gipson (2013) showed that UT1 formal errors improve when observations cycle evenly through three sections of the sky instead of repeating for a while in one section. So we developed the Sky Section Algorithm (SSA), which divides the sky into an arbitrary number of equal sections by azimuth and scores each trial observation by the length of time since an observation has been scheduled in the trial observation's sky section. A longer time yields a higher score. For simplicity, this is only applied to the Kokee Park station.

Gipson and Baver (2015) showed that UT1 formal errors in hypothetical schedules are minimized when observations cluster near the two corners of KOKEE and WETTZELL's mutual visibility areas near 20° elevation. Later we identified the target spots as azimuths 303.2° and 67.1° for KOKEE (290.7° and 54.7° for WETTZELL) at 18.7° elevation. So we developed the Minimization Target Algorithm (MTA), which calculates the distance from each trial observation to the closer of the target spots. A shorter distance yields a higher score. The MTA is applied to both stations.

We tested six cases: the SSA with two, three, four, and six sky sections, the MTA, and the only logical MTA/SSA combination — the MTA with SSA2. Gipson and Baver (2016) showed that an INT01 session's UT1 formal error depends on source availability, which in turn depends on source mutual visibility and strength during the session. These two factors respectively vary regularly over the year and irregularly over time. So we used the *Sked* automated scheduling mode (autosked) to generate 286 schedules for each case, testing 26 days of the year (DOYs) spaced two weeks apart starting on January 10 at 18:30 UT and testing each DOY under 11 flux catalogs from 2012–2016. For each case, we passed 25 %, 50 %, 75 %, and 100 % of the stage 1 observations to stage 2. 25% is the passing percentage (PP) used in operational INT01 schedules, and the larger percentages increase the algorithms' impact.

Karen Baver · John Gipson
NVI, Inc., 7257D Hanover Parkway, Greenbelt Maryland, 20770, USA

We evaluated the schedules with *Mini_fe*, a program that uses a simplified algorithm with elevation-dependent weighting to calculate a schedule's UT1 formal error. We ran the schedules with the best UT1 formal errors through *Solve* simulation solutions to simulate actual observations. We examined five metrics: the number of scheduled sources, the number of scheduled observations, the *Solve* UT1 formal error, atmospheric turbulence sensitivity, and source loss sensitivity. We measured atmospheric turbulence sensitivity by the RMS about the mean of UT1 estimates from 300 *Solve* solutions that applied random noise that simulated atmospheric turbulence. We measured source loss sensitivity by the RMS about the mean of UT1 estimates from *Solve* solutions in which each source in a schedule was deleted in turn. For the number of scheduled sources or observations, a higher value is better. For the other metrics, a lower value is better.

2 MSS: Operational (S/X) Schedule Type

The MSS scheduling strategy uses all geodetic sources (~90) that are mutually visible at some time during the year at KOKEE and WETTZELL; much smaller source subsets are observable during specific sessions. Table 1 shows the *Mini_fe* UT1 formal errors from MSS schedules. Increasing the passing percentage increases the number of observation choices in stage 2 from 4.3 (at PP 25 %) to 16.6 (at PP 100 %), and it increases the effect on the results; the algorithms' UT1 formal error range is 0.36 μs (7.70 to 8.06 μs) for PP 25 % and 2.45 μs for PP 100 %. Table 1 also shows that, generally, for each test case, the UT1 formal error decreases as the passing percentage increases. An exception is SSA2, which is discussed below. As the passing percentage increases, the *Sked* stage 1 algorithm that provides default sky coverage (and some UT1 formal error protection) is given less weight, and the stage 2 algorithms are given more weight.

Table 1: *Mini_fe* UT1 formal errors (μs) from MSS schedules, averaged over all DOYs and flux catalogs.

	control	SSA2	SSA3	SSA4	SSA6	MTA	MTA/SSA2
PP 25%	8.29	8.06	7.81	7.70	7.77	7.93	7.94
PP 50%	8.77	7.90	7.64	7.44	7.53	7.48	7.43
PP 75%	9.13	8.09	7.38	7.21	7.30	7.65	6.69
PP 100%	9.14	8.80	7.27	7.05	7.04	7.33	6.35

Figure 1 shows azimuth/elevation plots at KOKEE on DOY 108 using the 16May23 flux catalog. The control case used PP 25 %, and the test cases used PP 100 %. The plots are not intended to represent all DOYs and flux catalogs; instead they show what the algorithms can do. The plots are spatio-temporal, showing observation positions by circles and observation order by increasing circle sizes. The control case has bad spatial and temporal coverage; most KOKEE observations are in or near its northeast quadrant, and its northwest quadrant is not observed for the final third of the session. The temporal SSA algorithms observe the sections evenly except where SSA6 briefly lacks a source in a section. But the SSA2 observations mainly cluster between azimuths 330° and 30°, while the other SSA variants are more spatially even. The spatial MTA observes mostly near the targets as intended, but it only observes KOKEE's northeast quadrant near the start and end of the session. The MTA/SSA2, which adds the temporal algorithm, adds alternation between quadrants. So the algorithms behave as intended.

Figure 1 and Table 1 exemplify some expectations for the UT1 formal errors from the algorithms. Our past work (e.g., Gipson and Baver (2016)) has found that the worst UT1 formal errors come from limited sky coverage (away from the minimization target spots) and that extending the sky coverage from this limited coverage improves the UT1 formal error. This explains the SSA cases' behavior. Each SSA N has N sky sections and N-1 boundaries and will be satisfied if observations cluster close to the boundaries. SSA2 has one boundary, at azimuth 0°, so observations can cluster around it, giving limited sky coverage far from the minimization target points and, in turn, bad UT1 formal errors. Table 1 shows that the SSA2 UT1 formal errors are the worst of all the algorithms' UT1 formal errors for all passing percentages. The other SSAs have at least two boundaries, and more boundaries should promote more sky coverage, as long as sources are available in the increasingly smaller sky sections. The SSA3 and SSA4 do have increasingly better formal errors, but the SSA4 and SSA6 formal errors differ by only 0.01 to 0.09 μs. One possible reason is that sources cannot always be found for six small sky sections, but perhaps, also, four sky sections are sufficient. The MTA/SSA2 combines the spatial and temporal algorithms, and at its maximum effectiveness (at PP 100 %), it has the lowest UT1 formal error of all cases (6.35 μs, 0.69 μs lower than the second best case). The MTA lacks a temporal algorithm, and its UT1 formal errors tend to be higher than the SSA3-6 UT1 formal errors, perhaps indicating that the influence of the tested temporal algorithm is greater than that of the tested spatial algorithm. The best case (MTA/SSA2, PP 100 %) lowers the control PP 25 % UT1 formal error by a promising 1.94 μs.

Table 2 reports on *Solve* simulations of the generally best SSA and MTA cases, SSA4 and MTA/SSA2

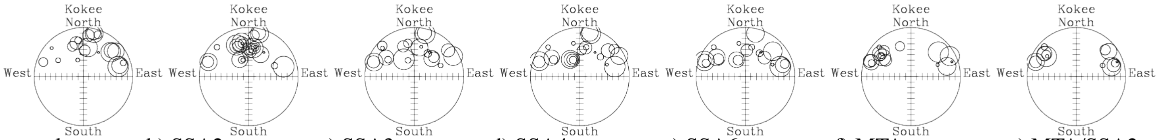

a) control b) SSA2 c) SSA3 d) SSA4 e) SSA6 f) MTA g) MTA/SSA2

Fig. 1: KOKEE azimuth/elevation spatio-temporal MSS plots for DOY 108 and flux catalog 16May23.

at PP 100 %. Each reduced the UT1 formal error and atmospheric turbulence sensitivity of control PP 25 %, although the MTA/SSA2 did better for each metric, with a reduction of 1.41 vs. 1.20 μs for the formal error and 3.92 vs. 2.59 μs for the sensitivity. But the MTA/SSA2 reduced the number of scheduled observations by 2.43 and cut the number of scheduled sources almost in half, while the SSA4 increased the number of scheduled observations by 1.38, and only decreased the number of scheduled sources by 1.67. Also the MTA/SSA2 increased source loss sensitivity by 0.71 μs, while the SSA4 lowered it by 1.41 μs. Because it improves four metrics and minimizes degradation of the fifth metric, the SSA4 seems better and merits more investigation.

Table 2: Metrics from MSS *Solve* simulations. All numbers are averages over all flux catalogs and all DOYs.

Case and Passing Percentage	Number Sched. Sources	Number Sched. Obs	UT1 Formal Err μs	Atm Turb μs	Source Loss μs
Control, 25%	16.70	19.83	7.37	16.35	12.08
MTA/SSA2, 100%	9.02	17.40	5.96	12.43	12.79
SSA4, 100%	15.03	21.21	6.17	13.76	10.67

3 BA 50: R&D (S/X) Schedule Type

We are using six IVS R&D sessions to test a new INT01 scheduling strategy, the BA 50, which uses 50 sources that balance sky coverage and source strength. Plots for the BA 50 for the 16May23 flux catalog and DOY 108 look similar to the MSS plots. Table 3 shows the UT1 formal errors from *Mini_fe* from the BA 50 schedules. Asterisks mark cases with a short schedule (DOY 290 and flux catalog 14FEB06), where autosked stopped prematurely when no observation met all of the stage 1 constraints. Operationally, a scheduler may override the constraints and manually schedule an observation. So we tried that here, and autosked finished. Table 3 shows the values from the manually completed schedule sets, which are very similar to the values from the incomplete sets.

The algorithms have an average of 2.2 choices in *Sked* stage 2 at PP 25 % and 8.1 choices at PP 100 %.

Table 3: *Mini_fe* UT1 formal errors (μs) from BA 50 schedules, averaged over all DOYs and flux catalogs. Asterisks indicate a case in which autosked created a short schedule. The final values after manual intervention are shown.

	control	SSA2	SSA3	SSA4	SSA6	MTA	MTA/SSA2
PP 25%	7.17	7.14	7.12	7.07	7.07	7.25	7.30
PP 50%	7.43	7.16	7.10	7.01	6.98	7.08*	7.03
PP 75%	7.80	7.54	7.13	6.98*	7.04	6.78	6.61
PP 100%	7.80*	8.11*	7.02*	6.95*	6.97*	6.20	6.24

The BA 50 pattern is similar to the MSS'. As the passing percentage increases, the UT1 formal error range generally increases (from 0.23 to 1.91 μs), the SSA2 UT1 formal errors increase, and the other cases' UT1 formal errors generally decrease. SSA2 is the worst SSA case, and SSA4 and SSA6 are the best. At higher PPs, the MTA/SSA2 has lower UT1 formal errors than the SSA cases. One difference with respect to the MSS is that the MTA's UT1 formal errors are comparable to the MTA/SSA2 errors instead of higher. But even with PP 100 %, the MTA-based cases only lower the control PP 25 % UT1 formal error by ~ 0.95 μs.

As with the MSS type, Table 4 shows the *Solve* simulation results for the SSA4 and MTA/SSA2 with PP 100 %. Again the pattern is similar to the MSS'. Both cases reduce the UT1 formal error and atmospheric turbulence sensitivity, but MTA/SSA2 has a greater effect. Also MTA/SSA2 reduces the number of scheduled sources greatly and reduces the number of scheduled observations, while SSA4 reduces the number of scheduled sources only slightly and increases the number of scheduled observations. But one difference compared to the MSS is that both cases increase source loss sensitivity, while only the MTA/SSA2 increases it for the MSS. MTA/SSA2 and SSA4 only lower the UT1 formal error by a modest maximum of 0.55 μs, and given the reduction of the number of sources and the increase of source loss sensitivity, neither algorithm seems useful for the BA 50.

Table 4: BA 50 *Solve* simulation metrics averaged over all flux catalogs and DOYs. The SSA4 values include the manually completed schedule but are similar to the original SSA4 values.

Case and Passing Percentage	Number Sched. Sources	Number Sched. Obs	UT1 Formal Err μs	Atm Turb μs	Source Loss μs
control, 25%	13.78	20.76	5.99	13.67	11.67
MTA/SSA2, 100%	8.47	18.65	5.44	11.92	13.56
SSA4, 100%	12.48	22.91	5.74	12.49	12.06

4 VGOS INT01: Proposed Broadband Type

We applied the algorithms to our current VGOS INT01 schedule prototype, which throughout the year uses ~90 sources selected for optimal VGOS INT01 observing. Table 5 shows the VGOS INT01 *Mini_fe* UT1 formal errors. Four cases failed to achieve a full schedule set, but manual intervention let autosked finish.

Table 5: *Mini_fe* UT1 formal error averages (μs) from VGOS INT01 schedules. Asterisks indicate cases with a short schedule. The values after manual intervention are shown. They are very similar to the values before intervention.

	control	SSA2	SSA3	SSA4	SSA6	MTA	MTA/SSA2
PP 25%	5.59	5.54	5.42	5.45*	5.43	5.57*	5.53*
PP 100%	4.91*	4.89	4.91	4.86	4.88	5.06	4.51

When the passing percentage increases from 25 % to 100 %, the number of choices increases from 2.2 to 7.6, and the UT1 formal error range increases from 0.15 to 0.55 μs. The UT1 formal error is reduced for all cases, including the SSA2 and control cases, in contrast to the MSS and BA 50 types. The control case reduction is only 0.68 μs but might be higher with another VGOS INT01 prototype. So a higher passing percentage should be considered for VGOS INT01 scheduling. The *Sked* stage 1 sky coverage algorithm might also need to be reviewed for VGOS INT01 scheduling.

With the current prototype, the PP 100 % schedule-based UT1 formal errors follow the MSS pattern in which the MTA/SSA2 UT1 formal error is lowest, and the MTA UT1 formal error is highest. But the PP 100 % UT1 formal errror range of 0.55 μs is small, so the algorithms do not affect the VGOS INT01 type much. The best case (MTA/SSA2, PP 100 %) only reduces the control PP 25 % UT1 formal error by 1.08 μs.

Table 6 lists the VGOS INT01 SSA4 and MTA/SSA2 *Solve* simulation metrics. Some patterns are common to every Intensive type. The MTA/SSA2 (and to a lesser degree SSA4) lower the UT1 formal error and atmospheric turbulence metrics but also lower the number of scheduled sources. But for the first time, MTA/SSA2 raises the number of scheduled observations (but not by as much as SSA4), and MTA/SSA2 reduces source loss sensitivity (but only slightly). Due to the small (up to 0.66 μs) reduction of the control PP 25 % UT1 formal error and the reduction of the number of scheduled sources, the algorithms are not useful for the current VGOS INT01 prototype.

Table 6: Metrics from VGOS INT01 *Solve* simulations. All metrics are averaged over all flux catalogs and DOYs.

Case and Passing Percentage	Number Sched. Sources	Number Sched. Obs	UT1 Formal Err μs	Atm Turb μs	Source Loss μs
Control, 25%	20.29	56.44	3.38	13.84	9.24
MTA/SSA2, 100%	16.89	59.88	2.72	10.54	9.07
SSA4, 100%	19.45	63.37	2.79	11.12	9.44

As shown in Fig. 2, much of KOKEE12M's northwest sky is unobservable (because KOKEE blocks it), and this eliminates some sources and should reduce the algorithms' effectiveness. So we ran hypothetical schedules without KOKEE's influence, using a constant 8.0° horizon mask at KOKEE12M, to see the effect of restoring full sky coverage. The number of *Sked* stage 2 choices is raised from 2.2 to 3.6 (PP 25 %) and from 7.6 to 13.0 (PP 100 %), but the PP 100 % UT1 formal error range only increases from 0.55 to 0.65 μs. Comparing Table 7 to Table 5, simply removing KOKEE's influence improves the *Mini_fe* schedule-based UT1 formal errors. The PP 25 % values without KOKEE are lower than the PP 25 % values with KOKEE by ~1.50 μs and are in fact lower than the PP 100 % values with KOKEE by ~0.5 to 1.0 μs. But within the hypothetical schedules, at PP 100 %, the SSA cases lower the control PP 25 % UT1 formal error by at most 0.18 μs, and the MTA-based cases lower it by at most 0.74 μs. So even without KOKEE's influence, the algorithms are not promising for the current VGOS INT01 schedule prototype.

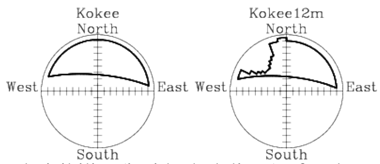

Fig. 2: Mutual visibility (inside dark lines) of Kokee Park stations with Wettzell stations. Left: KOKEE (shown) with WETTZELL. Right: KOKEE12M (shown) with WETTZ13S.

Figure 3 shows VGOS INT01 spatio-temporal plots for DOY 108 and flux catalog 16May23. The top row has realistic schedules that take KOKEE into account.

Table 7: *Mini_fe* UT1 formal error averages (μs) from hypothetical VGOS INT01 schedules that remove KOKEE's influence on the KOKEE12M horizon mask.

	control	SSA2	SSA3	SSA4	SSA6	MTA	MTA/SSA2
PP 25%	4.01	3.98	4.06	4.06	4.05	4.08	4.06
PP 100%	3.97	3.92	3.83	3.83	3.90	3.31	3.27

With the large number of rapid observations, the observing order might matter less than the S/X order, but the SSA4 does show better temporal distribution than the control case. But KOKEE's influence deflects the MTA/SSA2 observations in KOKEE12M's northwest quadrant to near azimuth 0°. The bottom row has hypothetical schedules without KOKEE's influence. Here the MTA/SSA2 behaves as intended. The SSA4 again shows better temporal distribution than the control case does.

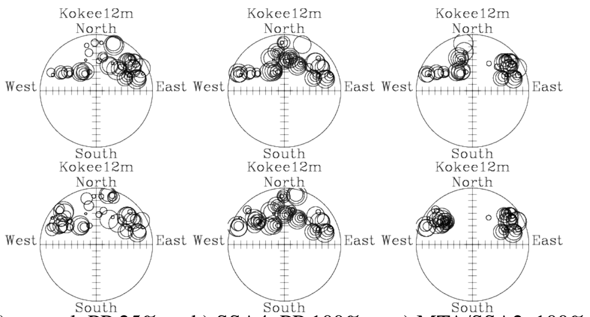

a) control, PP 25% b) SSA4, PP 100% c) MTA/SSA2, 100%

Fig. 3: KOKEE12M VGOS INT01 spatio-temporal azimuth/elevation plots, with (top row) and without (bottom row) KOKEE's influence on KOKEE12M's horizon mask.

5 Conclusions

The algorithms improve coverage as intended. In addition, adding more sources to *Sked* stage 2 by increasing the *Sked* "passing percentage" makes them more effective and generally lowers the UT1 formal error.

Generally the SSA4/6 produce the lowest schedule-based SSA UT1 formal errors, and MTA/SSA2 with PP 100 % produces the lowest schedule-based UT1 formal errors of all cases. The SSA4 and MTA/SSA2 improve the UT1 formal errors in *Solve* simulations but less than for the schedules. Also they improve the atmospheric tubulence metric but decrease the number of scheduled sources. Their effect on source loss sensitivity and the number of scheduled observations is mixed. The SSA4 is promising for the MSS. No useful algorithm was found for BA 50 or VGOS INT01 schedules.

References

Baver K, Gipson J (2013) Refining the Uniform Sky Strategy for IVS-INT01 Scheduling. In: N. Zubko, M. Poutanen (eds.), *Proc. 21st Meeting of the European VLBI Group for Geodesy and Astrometry*, 205–209, ISBN: 978-951-711-296-3.

Gipson J, Baver K (2015) Minimization of the UT1 Formal Error through a Minimization Algorithm. In: R. Haas, F. Colomer (eds.), *Proceedings of the 22nd Meeting of the EVGA*, 230–234, ISBN 978-989-20-6191-7.

Gipson J, Baver K (2016) Improvement of the IVS-INT01 sessions by source selection: development and evaluation of the maximal source strategy. *J. Geodesy*, 90:287-303, doi:10.1007/s00190-015-0873-6.

Gipson J (2016) 2016 Sked Manual, `https://lupus.gsfc.nasa.gov/files_user_manuals/sked/SkedManual_v2016Dec09.pdf`.

Planning of the Continuous VLBI Campaign 2017 (CONT17)

D. Behrend, C. Thomas, J. Gipson, E. Himwich

Abstract The IVS is currently organizing the next continuous VLBI campaign. The observational period has been fixed to run from November 28 (0 UT) to December 12 (24 UT), 2017. Unlike most CONT campaigns, CONT17 will be set up using three different networks: It is planned to have two networks of legacy S/X stations where one legacy network will include the ten stations of the VLBA. A third network will consist of VGOS broadband stations. The legacy networks will have 14 and 13 stations, respectively, each with as much a global distribution as possible. The VGOS network will be significantly smaller with six to eight stations, depending on the operational status of some of the VGOS stations. The assignment of stations to the three networks is based on EOP simulations with the anticipated observing modes. The different networks will be used to probe the accuracy of the VLBI estimates of the EOP and investigate possible network biases. With the networks fixed, work has commenced on determining media and e-transfer requirements, correlator resources, source selection, and optimized scheduling procedures.

Keywords CONT17, VLBA, VGOS, network biases

1 Introduction

Preparations are underway to organize the Continuous VLBI Campaign 2017. CONT17 will be a continuation of the series of very successful continuous VLBI campaigns that were observed at irregular intervals since 1994 (e.g., Behrend (2009); Behrend et al. (2014); Thomas et al. (2016)). The most recent CONT campaigns were observed in roughly three-year intervals.

CONT17 will be observed from 0 UT on November 28 to 24 UT on December 12, 2017, that is, fifteen consecutive UT days with three days in November and twelve days in December (cf. Figure 1). The main features of CONT17 can be summarized as follows:

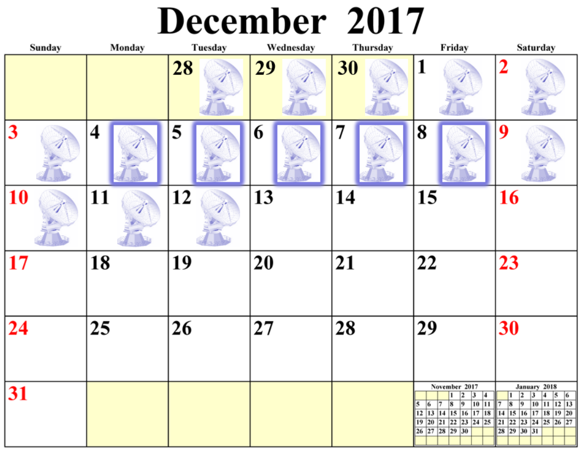

Fig. 1: Observational period of CONT17: November 28 to December12, 2017. The two legacy networks will observe the full period, whereas the VGOS demonstration network is expected to observe about a third of the fifteen days, for instance, five consecutive days in the center of the period (on the weekdays).

- two legacy S/X networks to probe the accuracy of the VLBI estimates of the EOP and to investigate possible network biases;
- one VGOS broadband demonstration network to be observed for about a third of the CONT17 period (e.g., five days from December 4 to December 8) as an initial indication of VGOS capabilities;
- continuous VLBI: fifteen consecutive days (legacy networks) with three minutes (Legacy-1) and five minutes (Legacy-2) between days for schedule changes;
- UT-day observing: days running from 0 UT to 24 UT;
- only limited station coverage in Africa and South America;
- rapid turnaround sessions: the equivalents of the R1 and R4 sessions will be shipped/e-transferred and

Dirk Behrend · Cynthia Thomas · John Gipson · Ed Himwich
NVI, Inc., 7257D Hanover Parkway, Greenbelt, MD 20770, USA

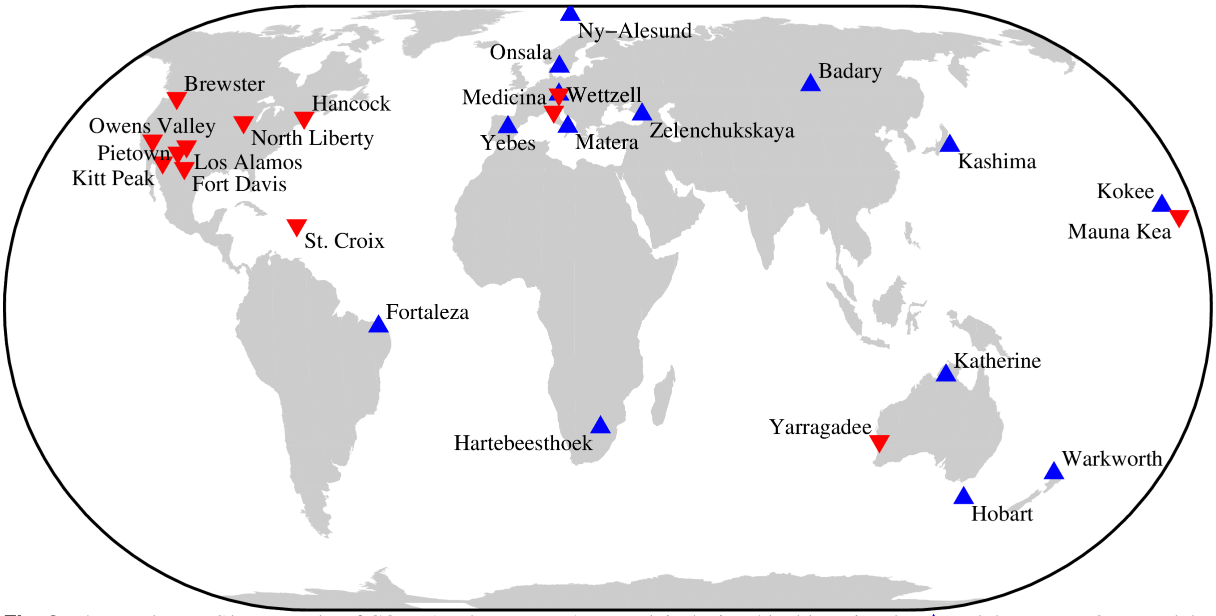

Fig. 2: The two legacy S/X networks of CONT17: the Legacy-1 network is depicted by blue triangles ▲ and the Legacy-2 network by red inverted triangles ▼. There will be 27 stations at 26 sites participating in the S/X portion of CONT17.

processed rapidly (using the data of the Legacy-1 network).

The main focus of CONT17 remains on the legacy S/X system. The VGOS broadband observing is mostly done for demonstration purposes.

The goal of CONT17 is to acquire state-of-the-art VLBI data over the fifteen-day period to demonstrate the highest accuracy of which the VLBI system is capable. This will support high-resolution Earth rotation studies, investigations of reference frame stability, and investigations of daily to sub-daily site motions among other things, and allow comparisons between VLBI and GNSS products. The availability of two global networks (and a third network of lesser extent) will allow an investigation of possible network biases.

2 Networks, Observing Modes, and Correlation

From the outset, it was planned to have at least two networks observing in parallel (e.g., Behrend et al. (2014)). Those networks were initially anticipated to be one legacy S/X network and one VGOS broadband network. For both networks there was a pool of stations that had committed to participate. While discussing the time frame for CONT17 with other VLBI groups, the Long Baseline Observatory (LBO) stated their interest in possibly joining into the effort with the Very Long Baseline Array (VLBA). The Goddard VLBI Group ran a number of simulations and prepared a proposal for geodetic observing time of the VLBA. The proposal was approved, extending the station pool significantly.

Table 1: Some features of the eventual CONT17 networks.

Network	#stations	Data rate	Correlator	Comment
Legacy-1	14	512 Mbps	Bonn	—
Legacy-2	13	256 Mbps	Socorro	VLBA
VGOS-Demo	8	8 Gbps	Haystack	—

With 27 S/X stations it was possible to co-observe two legacy networks with global coverage each and to look into network biases. Thus, a second slew of simulations was run to determine the best division of stations into the two legacy networks. A constraint was that the VLBA could not be split; it had to be treated as a single instrument. In the end the legacy station pool was split into a fourteen-station and a thirteen-station network (Figure 2 and Table 1). This split provided the best results in terms of EOP formal errors for the individual networks (Table 1). The formal errors were compared to the actual results from the CONT11 campaign, which should be equivalent to the planned networks given the basically identical network size of thirteen stations.

The VGOS demonstration network (Figure 3) will have at least six stations. It is anticipated that to those six, which already have participated in VGOS test and trial sessions, the new station at Onsala and the upgraded station at Hobart will be added. As this is work in progress, there is a chance that their addition may fall through. The simulation result listed in Table 1 assumes an eight-station network for VGOS-Demo. The slightly

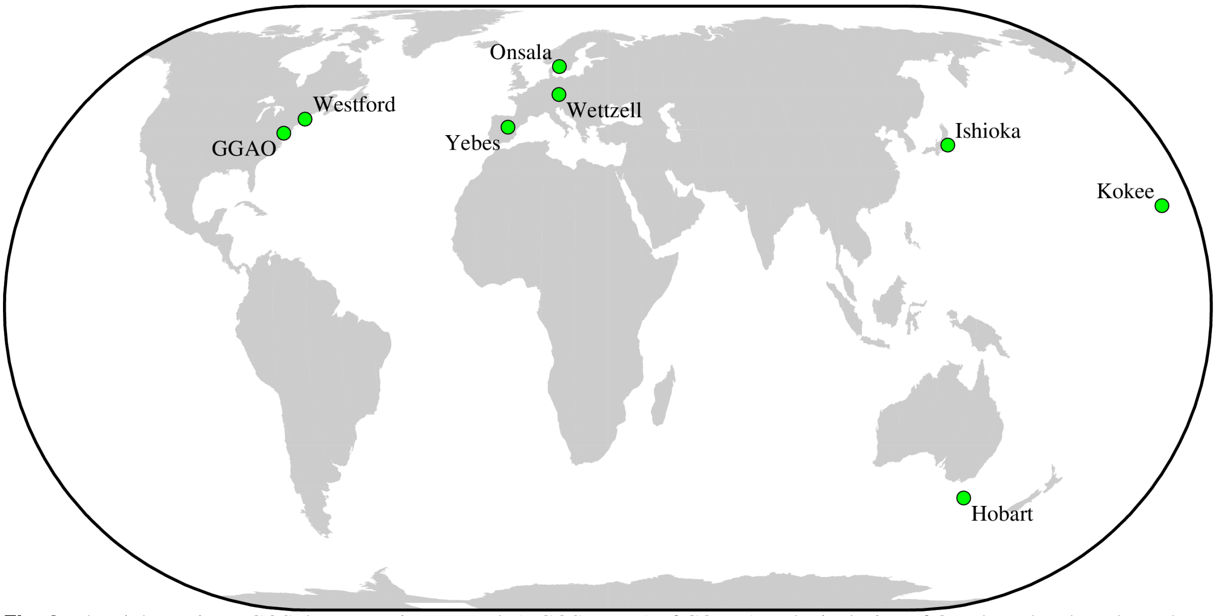

Fig. 3: The eight-station VGOS demonstration network (VGOS-Demo) of CONT17. The inclusion of Onsala and Hobart depends on the progress of their broadband signal chain roll-out.

Table 2: EOP formal errors derived from a covariance analysis without station velocity estimation for the three CONT17 networks and the actuals of the thirteen-station CONT11 network.

Network	X-pole [µas]	Y-pole [µas]	UT1 [µs]	ψ [µas]	ε [µas]
Legacy-1	13.0	13.7	0.9	36.0	13.1
Legacy-2	15.0	17.5	0.8	37.6	14.3
VGOS-Demo	22.1	22.5	0.8	43.2	18.1
CONT11 Actuals	12.9	13.1	0.7	33.5	13.8

worse formal errors for the EOP are mostly due to the limited geographic range of this network.

The observing mode for the VGOS network will be identical to the one used for the current VGOS test sessions. It is an 8-Gbps mode. Due to media, e-transfer, and data storage (at the correlators) limitations, the observing mode for the pure geodetic legacy network (Legacy-1) will be the same mode as used for CONT14, that is, a 512-Mbps recording mode. This mode is well tested, as it is also used for the even IVS-R1 sessions. For the VLBA+ network (Legacy-2) it was initially thought that a 2-Gbps mode similar to the VCS-II survey mode could be used. However, this turned out to be too risky for the three geodetic stations participating in the Legacy-2 network. For that, it was decided to fall back to the 256-Mbps mode that is used in the IVS-RDV sessions. This also allowed to test this observing mode with the three geodetic stations by adding them to upcoming RDV sessions.

The three networks will be correlated at three different correlators (Table 1). While the stations of the Legacy-1 network are expected to mostly e-transfer their data to Bonn, the Legacy-2 stations will have to ship their recording modules physically to the VLBA correlator at Socorro, NM. Bonn will likely be able to support twelve e-transfer stations; the two stations that will ship modules physically will likely be Matera and Kokee. Socorro anticipates a very fast turnaround with correlation results available by mid-to-end January. Bonn and Haystack expect the correlation work to last significantly longer. It can take from a few months up to about half-a-year. To reduce the work load on Bonn stemming from the regular IVS observing program prior to and after the CONT17 campaign, the Washington correlator will take on a part of their correlation load.

3 Observational Procedure

The observational procedure will be modeled after the CONT14 campaign (Behrend et al., 2014). In order to yield the most accurate combination and comparison with results from other space-geodetic techniques, the observing will be organized in UT days. The Intensive sessions Int1, Int2, Ru-U, and VLBA will have precedence over CONT17. For the statically scheduled IVS and Russian Intensives, observing slots will be freed in the CONT17 schedule for the Intensive stations. For the dynamically scheduled VLBA Intensives it is likely that no such slot will be provided, simply accepting the loss of observations to the two VLBA Intensive stations during that period.

For the Legacy-1 network, well-coordinated and staggered station check times of 1-hour length will be worked into the schedule. This will avoid observational gaps in the overall network. These station check times will be scheduled for all CONT17 days except the first and the last day. The VLBA will likely only do a station check directly before and after the CONT17 campaign. Thus for the Legacy-2 network no such station check times will be scheduled.

The individual observing schedules will be written using the scheduling software *sked* (Gipson, 2012). The schedules will be written by three different scheduling groups: Dirk Behrend and Cynthia Thomas (Legacy-1), David Gordon (Legacy-2), and Alex Burns (VGOS-Demo). The scheduling procedure will be similar to the scheme employed for CONT14 (Behrend, 2015).

4 Conclusion

Preparations are well underway for a three-network CONT17 campaign. There will be 29 VLBI sites participating in the campaign. As Wettzell will observe with two legacy antennas and one VGOS antenna (triple point) as well as Kokee, Onsala, and Yebes with both one legacy and one VGOS antenna, the overall number of stations participating in CONT17 will be up to 35.

The next steps in the preparation of CONT17 include:

- determination of the media requirements;
- request of additional media purchases, if necessary;
- check-out of recording modes at all stations;
- determination of station check times and assignment of appropriate Intensive slots;
- final source selection;
- preparation of final observing schedules.

More information about CONT17 will be made available on the IVS Web site at https://ivscc.gsfc.nasa.gov/program/cont17/ .

References

Behrend D (2009) Coordinating Center Report. In: D. Behrend, K. D. Baver (eds.), *IVS 2008 Annual Report*, NASA/TP-2009-214183, 77–79.

Behrend D, Thomas C, Himwich E, MacMillan D (2014) CONT14: Preparation and Prospects. In: D. Behrend, K. D. Baver, K. L. Armstrong (eds.), *IVS 2014 General Meeting Proceedings 'VGOS: The New VLBI Network'*, Science Press (Beijing), ISBN 978-7-03-042974-2, 196–200.

Behrend D (2015) Continuous VLBI Scheduling: The CONT14 Example. In: R. Haas and F. Colomer (eds.), *Proc. 22nd EVGA Working Meeting*, ISBN 978-989-20-6191-7, 145–149.

Gipson J (2012) Sked. VLBI Scheduling Software. Web document http://lupus.gsfc.nasa.gov/files_user_manuals/sked/sked.pdf

Thomas C, Behrend D, MacMillan D (2016) From CONT to VGOS: the Evolution of the CONT Campaigns. In: D. Behrend, K. D. Baver, K. L. Armstrong (eds.), *IVS 2016 General Meeting Proceedings 'New Horizons with VGOS'*, NASA/CP-2016-219016, 127–131.

The Onsala Twin Telescopes: the Status at the Time for the Inauguration

G. Elgered, R. Haas, J. Conway, R. Hammargren, L. Helldner, T. Hobiger, M. Pantaleev, L. Wennerbäck

Abstract We summarise the activities related to the Onsala Twin Telescopes (OTT), from the time when the decision was taken to fund the proposal, to the inauguration on 18 May 2017.

Keywords VLBI, VGOS, Onsala twin telescopes

1 Introduction

The Onsala Space Observatory is the European site in the International VLBI Service for Geodesy and Astrometry (IVS) that has the longest history in VLBI. First geodetic VLBI measurements were performed already in 1968 with the 25 m radio telescope. Hence Onsala is today one of the sites with the longest time series in the IVS data base. The observatory is one of the unique fundamental space geodetic sites that have a direct access to the coast line operating VLBI, GNSS, gravimetry, and sea-level monitoring. Onsala is thus an important co-location site for the Global Geodetic Observing System (GGOS). Being well aware of the VGOS standard it was clear around 2010 that Onsala needed a telescope with significantly faster slew rates than the existing radome-enclosed 20 m telescope.

A proposal for funding of twin telescopes, including the VGOS standard receiver systems, was submitted in August 2011 to Knut & Alice Wallenberg Foundation by the president of Chalmers. The decision to fund the telescopes was taken on the 26 March 2012.

We summarise the site preparations in Sect. 2, the procurement process in Sect. 3, and the construction in Sect. 4. An update of the "geodetic milestones" of the observatory are finally given in the conclusions.

Gunnar Elgered · Rüdiger Haas · John Conway · Roger Hammargren · Leif Helldner, Thomas Hobiger · Miroslav Pantaleev · Lars Wennerbäck
Chalmers University of Technology, Onsala Space Observatory, SE-439 92 Onsala, Sweden

2 Site preparation

Obtaining the building permit for the two telescopes was not straight forward. The first application was not approved. The reasons were described by Haas (2013). Finally the permit was obtained 6 February 2014. Figure 1 depicts the area of interest.

Fig. 1: The area of the OTT before the ground work started. The two sites most to the north were in the first application for the building permit, which was submitted 6 December 2012. The rejected site was in the next application (2 December 2013) replaced with the OTT south telescope. North is up.

The preparation of the grounds, including the construction of new roads, was immediately started. As can be seen in Figure 2 the area has several potential sites where the telescopes can installed directly on the bedrock. The roads were laid out around and connecting the two sites, with almost identical heights, for the telescopes, see Figure 3.

Fig. 2: The area where the OTT south telescope will be built. The photo is from 25 February 2014, credit L. Wennerbäck.

Fig. 3: The preparations of the ground are almost ready. The photo is from 4 June 2015, credit L. Wennerbäck.

3 Procurement phase

The procurement process was prepared to some detail already before the building permit was given, so that it was possible to publish the call for tender on 11 June 2014. At the end of the submission period four different offers were received. For various reasons none of them were fully compliant with our demands given the budget constraints. A period of discussions finally concluded in December 2014 and an order for the two telescopes was placed with MT Mechatronics.

Once the telescope design was specified the procurement of the telescope concrete foundations could start. It was handled separately by Chalmersfastigheter AB and an order was placed with the main contractor Hansson & Söner in August 2015.

Fig. 4: The lower part of the foundation of the northern telescope on the 28th of September 2015, credit L. Wennerbäck.

4 Construction phase

For obvious reasons the concrete foundations were to be built before the scheduled arrival of the telescopes in the spring of 2016. Already in September 2015 the work with the foundations was in progress (see Figure 4) and a couple of months later we could get an impression of the final shape (see Figure 5). In January 2016 the foundations were completed, now waiting for the arrival of the telescopes.

Fig. 5: The concrete foundation of the southern telescope on the 8th of December 2015, credit R. Haas.

There was a delay of a couple of months compared to the original time schedule and the telescope parts arrived in containers to the observatory at the end of May and early June. The installation started by mounting the equipment in the azimuth and the elevation cabins, while they were still located on the ground. Thereafter, during a period of a couple of weeks, the azimuth and elevation cabins were lifted into their final positions, see Figures 6 and 7. Once the reflectors were mounted, adjustments of the reflector panels were made, see Figure 8. The Site Acceptance Test (SAT) of the telescopes was carried out from 30 November to 2 December 2016. Figure 9 gives an impression of the site just after the SAT.

Fig. 6: Lifting the azimuth cabin of the southern telescope on the 16th of August 2016, credit G. Elgered.

Fig. 7: The reflector on its way to the northern telescope on the 18th of August 2016, credit R. Haas.

Fig. 8: Reflector prepared for adjustment measurements on the 26th of October 2016, credit R. Haas.

The two VGOS receivers were built in house by the electronics laboratory at Onsala in parallel to the telescope construction during 2016. More details on this subject are found in Pantaleev et al. (2017). The 1st VGOS receiver, with a QRFH feed, was installed in the north telescope in January 2017. In March the digital backend units, two DBBC3, were installed and commissioned, and in April the 2nd VGOS receiver, with an Eleven feed, was installed in the south telescope.

The Cable Delay Measurement Systems (CDMS) were built by MIT-Haystack. They were installed and tested in the telescopes, and on the ground, in the spring of 2017.

Further tests will be carried out for the rest of 2017 making the OTT ready for participation in geodetic VLBI. The horizon masks for the future observations are shown in Figure 10.

Fig. 9: The Onsala Twin Telescopes (OTT) on the 5th of December 2016, credit G. Elgered.

Fig. 10: The 360° horizons seen from the north (top frame) and the south (bottom frame) telescopes on the 1st of August 2017. The north direction is approximately located slightly to the left of the middle of the frames, credit G. Elgered and R. Haas.

5 Conclusions

The inauguration on 18 May 2017 added a milestone to the list of important events of the research infrastructure for geodesy and geodynamics at Onsala:

1968: First intercontinental VLBI for astronomy and geodesy using the 25 m telescope.
1980: First Mk-III experiments, with a supporting Water Vapour Radiometer, using both the 20 m (X-band) and the 25 m (S-band) telescopes.
1987: The ONSA GNSS station was started. Today it has the longest observing history in the world.
2009: Installation and start of operation of the superconducting relative gravimeter.
2012: Installation of the seismometer station, a site in the Swedish national seismic network.
2015: Inauguration of the super tide gauge station, a site in the national sea level observational network.
2017: Inauguration of the Onsala twin telescopes.

References

Haas R (2013) The Onsala Twin Telescope Project. In: N. Zubko and M. Poutanen (eds.) *Proc. 21st EVGA Working Meeting*, 61–66.

Flygare J, Pantaleev M, Billade B, Dahlgren M, Helldner L, Haas R (2017) Sensitivity and antenna noise temperature analysis of the feed system for the Onsala twin telescopes. In: R. Haas and G. Elgered (eds.), *Proc. 23rd EVGA Working Meeting*, 10–14.

Pantaleev M., Helldner L, Haas R, Johansson K-Å, Petterson L, Dahlström J, Dahlgren M, Kylenfall U, Billade B (2017) Design, implementation and tests of the signal chain for the twin telescopes at Onsala SpaceObservatory. In: R. Haas and G. Elgered (eds.), *Proc. 23rd EVGA Working Meeting*, 15–19.

Geodetic VLBI Correlation at the Vienna Scientific Cluster

J. Gruber, J. Böhm, J. McCallum

Abstract Geodetic VLBI correlation is a new challenge in the current activities at the research area Advanced Geodesy at Technische Universität Wien (TU Wien). We have implemented the Distributed FX (DiFX) software correlator and Haystack Observatory Postprocessing System (HOPS) on the Vienna Scientific Cluster 3 (VSC-3), which is a supercomputer located at TU Wien. We provide information about VLBI correlation-related activities in Vienna and we present the VSC-3 by showing some technical aspects of this high performance computer system. We have carried out a performance test to show the most efficient processing setup for DiFX on the VSC-3 and results of successfully correlated data, which includes DiFX processing and HOPS processing. Finally, we list some future challenges and tasks and comment on VGOS correlation at the VSC-3.

Keywords VLBI Correlation, Fringe Fitting, VSC, VieVS, VGOS

1 Introduction

VLBI correlation is referred to the process which determines the difference in arrival times at two stations by comparing the recorded bit streams. After the signals at each antenna site are collected and recorded, VLBI correlation initiates the analysis of a VLBI experiment. Basically a VLBI experiment can be split up into a work stream of several tasks. First the VLBI observations have to be scheduled. On the basis of this schedule the antennas observe data. The recorded bit streams are correlated and then fringe fitted to generate the fundamental VLBI observable which is used in the VLBI analysis to estimate station positions, quasar positions, Earth Orientation Parameters (EOPs) and other important geodetic parameters. So far, at our institute we are capable to schedule VLBI observations and to estimate geodetic parameters with our homemade Vienna VLBI and Satellite Software VieVS (Böhm et al., 2012). With the installation of a VLBI correlation infrastructure at our institute we have established an additional element in the VLBI processing chain of scheduling, observing, correlating and analyzing. Feedback between scheduling and correlation and analysis will help us to improve and refine the individual tasks. Furthermore, with own correlation infrastructure we are more independent to process VLBI projects and we can contribute with a wider field of capabilities to the VLBI community.

With the development of the Distributed FX-style Correlator (DiFX) (Deller, 2007), many hardware correlators have been replaced. The software is designed to run in a multi core environment parallelization to process the large amount of input data. We have installed DiFX on the Vienna Scientific Cluster (VSC) to realize VLBI software correlation at our institute.

Jakob Gruber · Johannes Böhm
TU Wien, Karlsplatz 13, AT-1040 Wien, Austria

Jamie McCallum
UTAS, Churchill Ave, Hobart TAS 7005, Australia

2 Correlation and Fringe Fitting capabilities of the VSC-3

The Vienna Scientific Cluster (VSC) is a supercomputer located in Vienna at the Arsenal TU Wien building. It consists of several cluster systems that have been designed to satisfy the demand for High Performance Computing (HPC) of a consortium of Austrian universities. The latest system is the VSC-3 which was installed in summer 2014 (see Fig. 1). At this time it was ranked 85th in the TOP500 list. The hardware capabilities which are intended for processing large amount of data and for intensive i/o workloads make the VSC-3 to an appropriate multiprocessor computing environment for the correlation of the large amount of VLBI data.

Hardware capabilities of the VSC-3

The VSC-3 was installed by ClusterVision and consists of 2020 nodes, each equipped with 2 processor. The processors are Intel Xeon E5-2650v2 processors from the Ivy Bridge-EP family with 8x2.60 GHz and 20 MB SmartCache. Details of the configuration of such a compute node are given in Tab. 1. The nodes are internally connected with an Intel QDR-80 dual-link high-speed InfiniBand fabric which features very high throughput and very low latency. Energy-efficient cooling is provided by the mineral-oil based CarnotJet System of "Green Revolution Cooling". The high-performance BeeGFS parallel Filesystem, developed for intensive i/o workloads provides the data storage facility on the VSC-3. To specify which nodes have to be used in the correlation process we make use of the SLURM workload manager which organizes the scheduled processing jobs.

Table 1: Configuration table of the compute nodes of the VSC-3.

Motherboard	Supermicro X9DRD-iF Intel Patsburg Chipset QuickPathInterconnect (QPI) 8.0GT/s Dual Xeon Sandybridge (E5 Series) Up to 256GB DDR3 1600/1333/1066/800MHz Slots: 1 (x16) PCI-E 3.0 and 4 (x8) PCI-E 3.0 slots Intel®350 Dual-Port Gigabit Ethernet Controller 8x SATA2 and 2x SATA3 ports Integrated IPMI 2.0 with Dedicated LAN Supermicro RSC-RR1U-E8 1U PCI-E Riser Rad
Chassis	SNK-P0047P passive 1U heat sink X9 Generation Motherboard Indium Foil replaces heatsink paste 1U PowerSupply 350W
CPU	2 x Intel Xeon IvyBridge-EP E5-2650v2 2.60GHz 8 Core - 20MB Cache Intel HT Technology - Intel Turbo Boost Technology 95W TDP (Thermal Design Power)
Memory	8 x 8192MB DDRIII1866 ECC Registered (512Mx8)

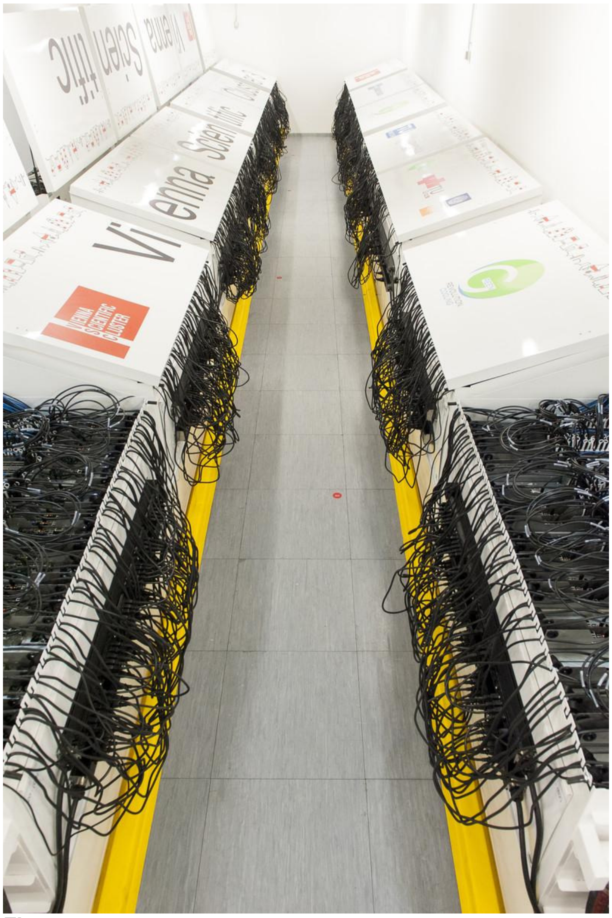

Fig. 1: Picture of the room where the 2020 nodes with liquid submersion cooling of the VSC-3 are stored. Picture taken at VSC Arsenal TU Wien building ©Claudia Blaas-Schenner.

Software correlation capabilities of the VSC-3

We have installed the Distributed FX (DiFX) software correlator version 2.4 on the VSC-3. It was developed at the Swinburne University in Melbourne, Australia by Adam Deller et al. (Deller, 2007). It is a software correlator in FX-style written in C++ and the correlation algorithms are intended to run in multiprocessor computing environments. The fundamental operations performed by the DiFX correlator can be listed as follows: streaming of digitized signals, application of the correlator model, padding the data from 2 bits to 16 bits, alignment of data within +/- 1 sample, performing an FFT, fractional-sample delay correction, complex multiplication and integration, writing output as complex visibilities. In the software correlator architecture data are loaded by data-stream nodes (one per station). These nodes are directed by a master node (FxManager) to send data to the processing elements (core nodes). The processed data are sent to the FxManager node for storage to disk.

After the generation of complex visibilities fringe fitting has to be carried out to obtain the geodetic relevant multi-band delay. This can be achieved by the Haystack Observatory Postprocessing System (HOPS). It is a software package written in C which performs basic fringe fitting, data editing, problem diagnosis, and correlator support functions. HOPS is not specifically intended to run in a multiprocessor computing environment but to have the whole correlation process chain ready at one place we have installed and integrated HOPS in our working environment on the VSC-3.

3 DiFX performance test and efficiency analysis

To evaluate the most efficient processing configuration of DiFX on the VSC-3 we have carried out performance tests. The result will help us to get a clearer understanding of the correlation processing speed on the VSC-3 of VLBI data and it will provide us information to predict the processing time for future sessions. With respect to a shared correlation network of several correlation centers we can also show our correlation capabilities to the VLBI community.

Methodology

In contrast to common benchmarking approaches of DiFX, in which fake eVLBI data streams are used to eliminate disk i/o as a bottle neck, we see our performance test in a more practical way. We want to test how DiFX performs in our working environment on the VSC-3 with real data and in a real processing environment. We do not avoid i/o issues because we want to determine the impact of the communication between the processing nodes and the hard drive. This means, i/o issues are part of this performance test, because they are part of processing real VLBI data. With this test it is difficult to ascertain the true performance of the DiFX source code but we will obtain information about processing performance of a real VLBI experiment. For more details on a benchmarking methodology and benchmarking results, see Phillips (2009).

The DiFX processing consists of several programs of the DiFX software package. A shell script is used to start DiFX and to run all the required functions. There are head operations which have to be executed just once in beginning of the whole DiFX processing, such as the generation of the machine and threads file and the generation of the .input and .calc files. Then there are processes which have to be executed once per scan such as the calcif2 program. All those functions are not intended for multiprocessor environments. Any change of the node number will not influence the processing time of this functions. The core function of the DiFX processing is "mpifxcorr" which actually carries out the correlation task. Mpifxcorr makes heavy use of the Intel Integrated Performance Primitives (IPP) library for optimization and uses MPI (Message Passing Interface) for parallelization. It is designed to run in multiprocessor environments. In this performance test we change the number of nodes to estimate the influence of number of nodes on the processing speed of this function. Furthermore we process the same data with the same cluster configuration at different times to reveal the possible impact of current workload on the shared user storage area.

Test Setup

In this test we used several scans of the session ds317 observed by the AUSTRAL network. The participating stations are Hobart 12 m, Kathereine 12 m, Yarragadee 12 m and Hartrao 15 m with a recording rate of 1 Gbps. The integration time in the DiFX processing configuration was set to 1 s and the spectral resolution of visibilities produced was set to 0.0625 MHz and was not changed for the entire performance test.

Results

The reading and writing speed on the high-performance BeeGFS parallel filesystem on the VSC-3 depends strongly on the current user workload. Our results show that the processing speed varies on average within 15 sec for the same processing setup (see Fig. 2). This means that the processing time of the same scan with the same configuration can fluctuate about 15 sec due to user workload on the storage area. Another impact on processing time is due to number of nodes used in the processing configuration. Using the same scans as used in the test shown in Fig. 2 to evaluate the impact of the number of nodes, we see that the processing time almost halves when changing from 1 to 2 nodes (see Fig. 3). By further increasing number of nodes the processing time stops decreasing at approximately 8 nodes. At this time the DiFX performance becomes data-limited rather than CPU-limited. This means that, at some point (in our case at 8 nodes), obtaining data from the data source (network socket) and transmitting it across the local network to processing nodes will no longer occur quickly enough. The decrease of processing time from 5 to 8 nodes is small in comparison to the decrease from 1 to 5 nodes. On average the decrease in processing time changing from 5 to 8 nodes is about two seconds. We think it would be more efficient to work with 5 nodes and use the remaining three nodes for processing scans in parallel. This strategy can be realized with the SLURM job array, which makes it possible to process several scans in parallel. In this test we executed each scan after another to evaluate the number of nodes at which the DiFX performance becomes data-limited, but in practice we use the SLURM job array to process several scans in parallel. For example if we want to make use of 100 nodes on the VSC-3, we will process 20 scans in parallel. Each scan will be processed by 5 nodes.

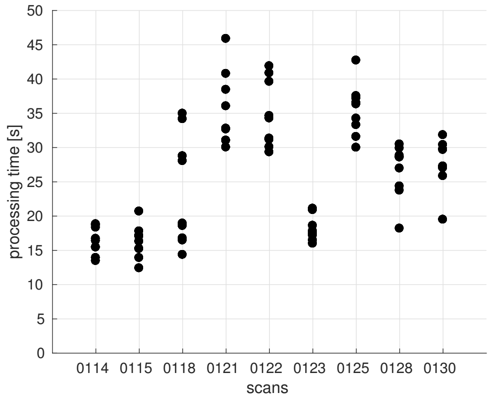

Fig. 2: Impact of current user workload of the VSC-3 storage area on processing time. The dots per scan represent the processing time of several DiFX runs for the same scan with the same processing configuration.

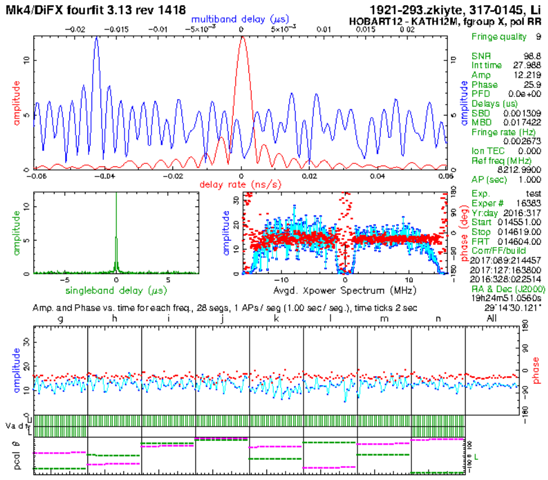

Fig. 4: Results of fringe fitting with the fourfit program of HOPS.

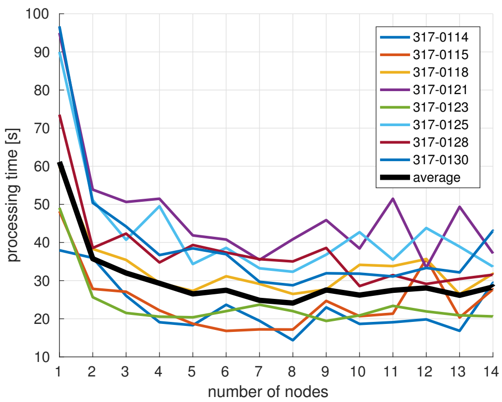

Fig. 3: Impact of number of nodes on the processing time. The colored lines represent change in processing time by changing number of nodes for each scan.

4 Experiments correlated at the VSC-3

Besides some test data we have successfully correlated the dynamic scheduling session ds317, which has been observed on 11/12/2016. We used this data also for the performance test. It was a four-antenna session of the AUSTRAL observing network Hobart 12 m, Katherine 12 m, Yarragadee 12 m and Hartrao 15 m. The session lasted 50 hours and the raw input of recorded data of the VSC-3 DiFX correlator amounts to 22.5 TB. The result of the fringe fitting process are shown in Fig. 4.

5 VGOS correlation in Vienna

The "Observing Plan" of the VLBI Global Observing System (VGOS) shows increasing requirements for the correlation and data transmission of VLBI data, see Petrachenko (2014). Due to an increasing number of observing sites per session and broadband observations more VLBI data will be generated and higher correlation capabilities are required. In view of a distributed correlation strategy, which means that data for a session will be spread to many correlation sites, the VSC-3 would have the resources to process vast amount of VGOS data as part of a shared correlation network. The VSC-3 is connected to the Global Research and Education Network with multiple 10 Gbps which would enable the transmission of recorded data.

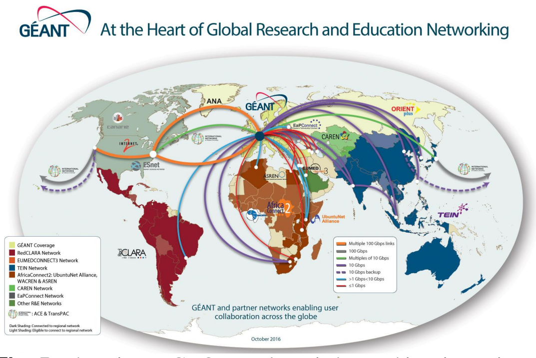

Fig. 5: The Vienna GEO correlator is located in Vienna in Europe and is connected to the Global Research and Education Network with multiple 10 Gbps links.

6 Conclusions and Outlook

We have installed DiFX and HOPS on the VSC-3 which allows us to correlate and fringe fit VLBI data. We determined the most efficient node configuration for a common four station AUSTRAL experiment and we showed the influence of the user workload on the storage area. We have successfully correlated the dynamic scheduling session ds317 and we plan to correlate several sessions per year of the AUSTRAL VLBI array in future. We are working on a refined process chain to process data automatically and we are developing a tool to convert the HOPS/MK4 output database to VGOS database to be able to feed our correlation results into VieVS. This implies the development of a tool in VieVS to detect and correct for ambiguities in the fringe fitted data.

References

Böhm J, Böhm S, Nilsson T, Pany A, Plank L, Spicakova H, Teke K, Schuh H (2012) The New Vienna VLBI Software VieVS. *Springer Berlin Heidelberg*, 1007–1011.

Deller A T, Tingay S J, Bailes M, West C (2007) DiFX: A Software Correlator for Very Long Baseline Interferometry Using Multiprocessor Computing Environments. *PASP*, 119:318–336.

Petrachenko B, Behrend D, Hase H, Ma C, Niell A, Nothnagel A, Zhang X (2014) VGOS Observing Plan. In: *Proc. IVS 2014 General Meeting*.

Phillips C, Deller A T (2009) Performance testing of the DiFX correlator. In: *Proc. 8th e-VLBI Workshop EXPReS09*.

Metsähovi Geodetic Station in Finland – New VGOS Site, Plans, and Current Status.

G. Molera Calvés, N. Zubko, J. Näränen, U. Kallio, J. Virtanen, M. Poutanen

Abstract The new VGOS radio telescope at the Metsähovi Geodetic Station is expected to be operational in 2019. In this paper, we present the latest news with an updated schedule plan of this project. We provide, as well, an overview of the rest of the instrumentation currently available at the Metsähovi Geodetic Station.

Keywords VGOS, VLBI, Metsähovi, radio telescope

1 Introduction

The Metsähovi Geodetic Station, located in Southern Finland (60.2N, 24.4E), is a key infrastructure of the Finnish Geospatial Research Institute (FGI), part of the National Land Survey of Finland (NLS). It is a Global Geodetic Observing System (GGOS) core site, i.e., member of global network of geodetic stations which is used in maintaining global terrestrial and celestial reference frames, computing precise orbits of satellites, and for geophysical studies.

Metsähovi is one of the few geodetic stations that has all major geodetic observing instrumentations co-located. These include satellite laser ranging (SLR), very long baseline interferometry (VLBI), global navigation satellite system (GNSS), superconducting and absolute gravimeters, and the DORIS beacon. The station has contributed since 1978 to several global services of the International Association of Geodesy (IAG), and due to its long existence it helps to retain sustainability in the maintenance of global reference frames.

Guifré Molera Calvés · Nataliya Zubko · Jyri Näränen · Ulla Kallio · Jenni Virtanen · Markku Poutanen
Finnish Geospatial Research Institute (FGI), National Land Survey of Finland, Geodeetinrinne 2, FI-02430 Masala, Finland.

2 VGOS project

In the autumn 2015, FGI obtained funding to build a new VGOS compatible radio telescope system (Petrachenko et al., 2009). This project is funded by the Finnish Ministry of Agriculture and Forestry and the National Land Survey. The site chosen for the new radio telescope is within 100 m from the other facilities at the Metsähovi Geodetic Station, and 500 m from the 14-metre VLBI radio telescope from Aalto University. Figure 1 shows the layout of the current site of Metsähovi.

At the end of 2016, the procurement process for the selection of the radio telescope ended. MT Mechatronics GmbH (MTM) was chosen for manufacturing, assembling, and installing the new antenna. The dish will have a diameter of 13.2-metre and mounted on a steel pedestal. The telescope installation is expected to be founder to bedrock, and be completed by the end of summer 2018. Figure 2 shows a model of the future telescope at Metsähovi.

The infrastructure works at the telescope site started in spring 2017. The area was cleared out from forest and the upper layer of soil. Immediately, the bedrock below the surface was revealed. Figure 3 shows the current status of the telescope site at the beginning of the summer 2017. The foundation work, the installation of the electrical and communication cables, and all other necessary site preparation work are scheduled for the end of this year.

The control room will be located in the main building of the Metsähovi station. As said, the main offices are located just 100 m away from the antenna. The procurement process of the signal chain components has started this year. The telescope will be equipped with QRFH feed receiver and a DBBC3 backend. We expect to have the instruments by the end of summer 2018, right after the full installation of the antenna. The first tests of the telescope equipped with the signal chain are planned by the end of 2018.

Fig. 1: Metsähovi Geodetic Station with (from left to right) GNSS-antennas, the gravity lab with the superconducting gravimeter, the main building and data centre, the SLR telescope (building in 2014) and the VLBI radio telescope from Aalto University.

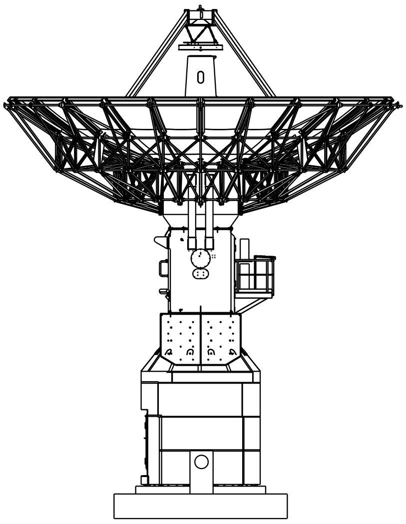

Fig. 2: Model of the new VGOS radio telescope. The 13.2 metre dish will be installed on a steel pedestal. The minimum distance from the dish to the ground will be approximately 2.5 m.

Fig. 3: Current status at the beginning of summer 2017 of the area where the new VGOS radio telescope will be located. All the infrastructure work is advancing accordingly to the initial plan.

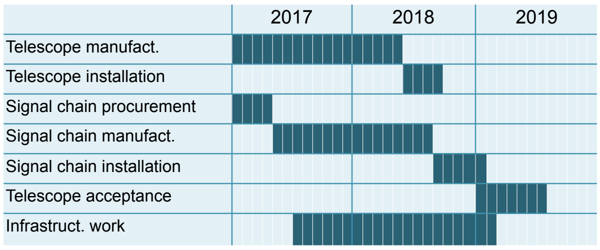

Fig. 4: Current schedule plan for the Metsähovi VGOS project

3 Metsähovi Geodetic Station

Ministry of Agriculture and Forestry and the National Land Survey of Finland has allocated a special funding for renewal of Metsähovi instrumentation and infrastructure during 2012-2018. The first large items in the project are:

- Finnish Permanent GNSS Network FinnRef (20 receivers)
- Superconducting gravimeter; new instrument in 2014
- Upgrade of the absolute gravimeter
- Satellite laser ranging; new 2 kHz system. Work ongoing, expected operational in 2017/18.
- VGOS radio telescope

The VGOS radio telescope will be valuable asset to the current major instruments or facilities that available already on site:

- Satellite laser ranging (SLR) facility, first observations were conducted in 1978. The new telescope will be operational in 2018 for observations.
- Superconducting gravimeter (GGP, ICET), since 1994. In 2014, a new SG was purchased and made available for measurements.

- Absolute gravimeter and the fundamental gravity point. Besides of a site for absolute gravimeter inter-comparison campaigns.
- Geodetic GPS receivers, since 1992 inside the IGS network, nowadays all-in-view GNSS.
- GPS receiver owned by NASA/JPL, part of the real-time NASA tracking network.
- REGINA GNSS receiver, owned by IGN, France.
- Doppler Orbitography and Radiopositioning Integrated by Satellite (DORIS) beacon owned by CNES, France (IDS).

4 Conclusions

The planning, design and preparation work for the future VGOS radio telescope to be installed at the Metsähovi Finnish Research Institute is advancing as planned. The installation of the antenna is scheduled to be completed by the ends of 2018.

The first-light and test observations will be conducted in 2019. It expected to be operational during year 2019.

References

Petrachenko B, Niell A E, Behrend D, Corey B, Böhm J, Charlot P, Collioud A, Gipson J, Haas R, Hobiger T, Koyama Y, MacMillan D, Malkin Z, Nilsson T, Pany A, Tuccari G, Whitney A, Wresnik J (2009) Design Aspects of the VLBI2010 System: Progress Report of the IVS VLBI2010 Committee. In: D. Behrend, K. D. Baver (eds.) *International VLBI Service for Geodesy and Astrometry 2008 Annual Report*, NASA/TP-2009-214183, 13–67.

HartRAO Antenna Axis Offset and its Effect on Troposphere Modelling and Antenna Coordinates

M. Nickola, A. de Witt, H. Krásná, C. Jacobs, L. Combrinck, J. Böhm

Abstract Data from geodetic VLBI sessions, which included observations with the 26-m equatorially mounted Cassegrain radio telescope at the Hartebeesthoek Radio Astronomy Observatory (HartRAO), were analysed with the Vienna VLBI Software (VieVS) to investigate the correlation between antenna coordinates and antenna axis offset. The simulation tool in VieVS was used to study the effect of the axis offset altitude troposphere correction on the estimated antenna axis offset in order to examine the 1 mm accuracy in the baseline length required by the VLBI Global Observing System (VGOS).

Keywords axis offset, altitude correction, antenna coordinates

1 Introduction

An antenna axis offset (AO) exists for radio telescopes where the rotation axes do not intersect. The antenna axis offset causes geometric and dry tropospheric delays which have to be considered in VLBI analysis.

The 26-m radio telescope at the Hartebeesthoek Radio Astronomy Observatory (HartRAO) is of equatorially mounted Cassegrain design. The rotation axes of the HartRAO 26-m radio telescope (HARTRAO) do not intersect—the VLBI reference point is represented by the intersection of the fixed Hour Angle (HA) axis with the perpendicular plane containing the moving Declination (Dec) axis (see Figure 1).

The axis offset altitude correction implemented by Sovers et al. (1998) accounts for the effect of the orientation of equatorial and X-Y antennas on the tropospheric path delay. Zenith troposphere delays of 1–2 mm, increasing to 1–2 cm when mapped to low elevation angles, result for antennas with non-zero axis offsets where the secondary rotation axis (A in Figure 2) moves vertically with changing orientation, i.e. for antennas with equatorial and with X-Y mounts (Sovers et al., 1998). A correction therefore has to be added to the zenith dry tropospheric delay (Z_d) for antennas with equatorial and with X-Y mounts (Sovers et al., 1998),

$$\delta Z_d = -Z_d(L/\Delta)\psi$$

where L is the antenna axis offset, Δ the troposphere scale height ($\approx$ 8.6 km), and ψ is an angular factor that varies with the type of mount. For equatorial mounts, such as that of HARTRAO,

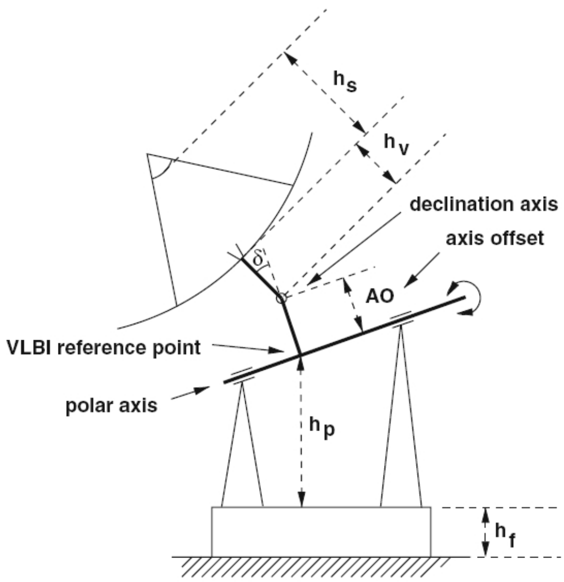

Fig. 1: Equatorial (polar) mount (Nothnagel et al., 2015).

Marisa Nickola · Aletha de Witt · Ludwig Combrinck
Hartebeesthoek Radio Astronomy Observatory, PO Box 443, Krugersdorp 1740, South Africa

Christopher Jacobs
Jet Propulsion Laboratory, California Institute of Technology/-NASA, Pasadena, CA, U.S.A.

Hana Krásná · Johannes Böhm
Department of Geodesy and Geoinformation, Vienna University of Technology, AT-1040 Vienna, Austria

$$\psi = cos\ H\ cos\ \phi_{gd}$$

where ϕ_{gd} is the geodetic latitude and H the local hour angle east of the meridian. For north-south oriented X-Y mounts,

$$\psi = sin\ E\ /\ \sqrt{1 - cos^2\ \theta\ cos^2\ E},$$

while for east-west oriented X-Y mounts, such as that of the Hobart 26-m radio telescope (HOBART26),

$$\psi = sin\ E\ /\ \sqrt{1 - sin^2\ \theta\ cos^2\ E}$$

where E is the elevation angle and θ the azimuth.

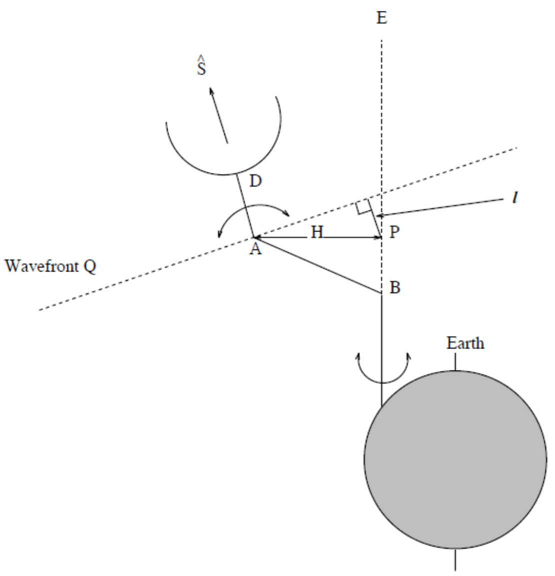

Fig. 2: Geometry of two-station VLBI network with only one station shown. Dec axis (end view represented by A) rotates in plane perpendicular to symmetry axis AD. Dec axis and polar axis (BE) are separated by distance H, the antenna axis offset. The VLBI reference point is represented by P (Combrinck and Merry, 1997).

2 Antenna Axis Offset Altitude Correction

The antenna axis offset altitude correction has been implemented in VieVS (Böhm et al., 2012) according to Sovers et al. (1998). The simulation tool in VieVS was used to simulate the effect of the axis offset altitude correction on the estimated axis offset of HARTRAO.

All IVS geodetic VLBI sessions (Nothnagel et al., 2015) in which HARTRAO participated, from August 2010 to November 2014, were also analysed with VieVS to investigate the effect of the axis offset altitude correction on the estimated antenna axis offset.

The only other participating radio telescope that is also affected by the axis offset altitude correction, is HOBART26 with its X-Y mount. All other antennas participating in the sessions analysed have Azimuth-Elevation (AZEL) mounts for which the correction is not required.

2.1 Simulations

The simulations were based on schedules from two IVS sessions, R1663 and T2094, in which HARTRAO (but not HOBART26) participated. In the simulations, zero input observation files were generated–the measured time delay was set to be equal to the theoretical time delay without adding the noise terms. The axis offset altitude correction was applied during the analysis of the simulated sessions for HARTRAO only. A simulation with the altitude correction applied, which included HARTRAO in the datum—realised with the no-net-rotation and no-net-translation condition on the antenna coordinates w.r.t. the *a priori* TRF—was also run.

The simulations show that the axis offset altitude correction has a negligible effect on the HARTRAO axis offset estimate, being in the sub-mm region (see Table 1). The axis offset altitude correction propagates to the HARTRAO antenna coordinates, and is also at the sub-mm level (see Figure 3(a)). With HARTRAO in the datum, the antenna axis offset estimate remains the same but the altitude correction propagates to the coordinates of other antennas as well. The difference in antenna coordinates is negligible however.

Table 1: AO altitude correction results - effect on estimated axis offset (dAO - difference between *a priori* and estimated axis offset, mAO - formal error). The first column depicts the simulation runs (SIM1 based on R1663 and SIM2 based on T2094), the session analysis runs with and without the AO altitude correction applied (AO +AC and AO −AC) as well as the runs to determine the effect for HOBART26 (Ho: AO +AC and Ho: AO −AC).

Simulations /	HARTRAO		HOBART26	
Session Analysis	dAO (cm)	mAO (cm)	dAO (cm)	mAO (cm)
SIM1 (+AC)	−0.041	0.001	-	-
SIM2 (+AC)	−0.061	0.002	-	-
AO +AC	1.245	0.079	-	-
AO −AC	1.252	0.079	-	-
Ho: AO +AC	1.231	0.079	0.222	0.172
Ho: AO −AC	1.239	0.079	0.216	0.172

2.2 Session Analysis

Sessions stretching from August 2010 to November 2014 in which HARTRAO participated (totalling 176) were analysed with VieVS to investigate the effect of the axis offset altitude correction on the estimated antenna axis offset and antenna coordinates. HOBART26 participated in 32 of these sessions. The sessions were run with and without the axis offset altitude correction applied and also with and without HARTRAO in the datum, while HOBART26 was not included in the datum for any of the runs.

Some of the results are depicted in Figures 3(b)–3(d). Results for only a selection of antennas are displayed due to space constraints. Results for antennas that participated in 30 or more sessions are displayed, which ensures that HOBART26 is included.

We expect the results from the session analysis to be similar to that from the simulations. From the results, we see that the difference in HARTRAO antenna coordinates for the session analysis is indeed similar to that for the simulation results (see Figures 3(a) and 3(b)). However, the difference in the estimated antenna axis offset (with and without the altitude correction applied) for the session analysis is smaller than that for the simulations, although also at sub-mm level (see Table 1). This may be caused by the propagation of the correction to the coordinates of other antennas.

The difference in antenna coordinates for stations where the correction does not apply, should theoretically be zero as is seen in Figure 3(b). The presence of HARTRAO in the datum does not affect the antenna axis offset estimates, but coordinate corrections propagate to the coordinates of other antennas, albeit only at sub-mm level (see Figures 3(c) and 3(d)).

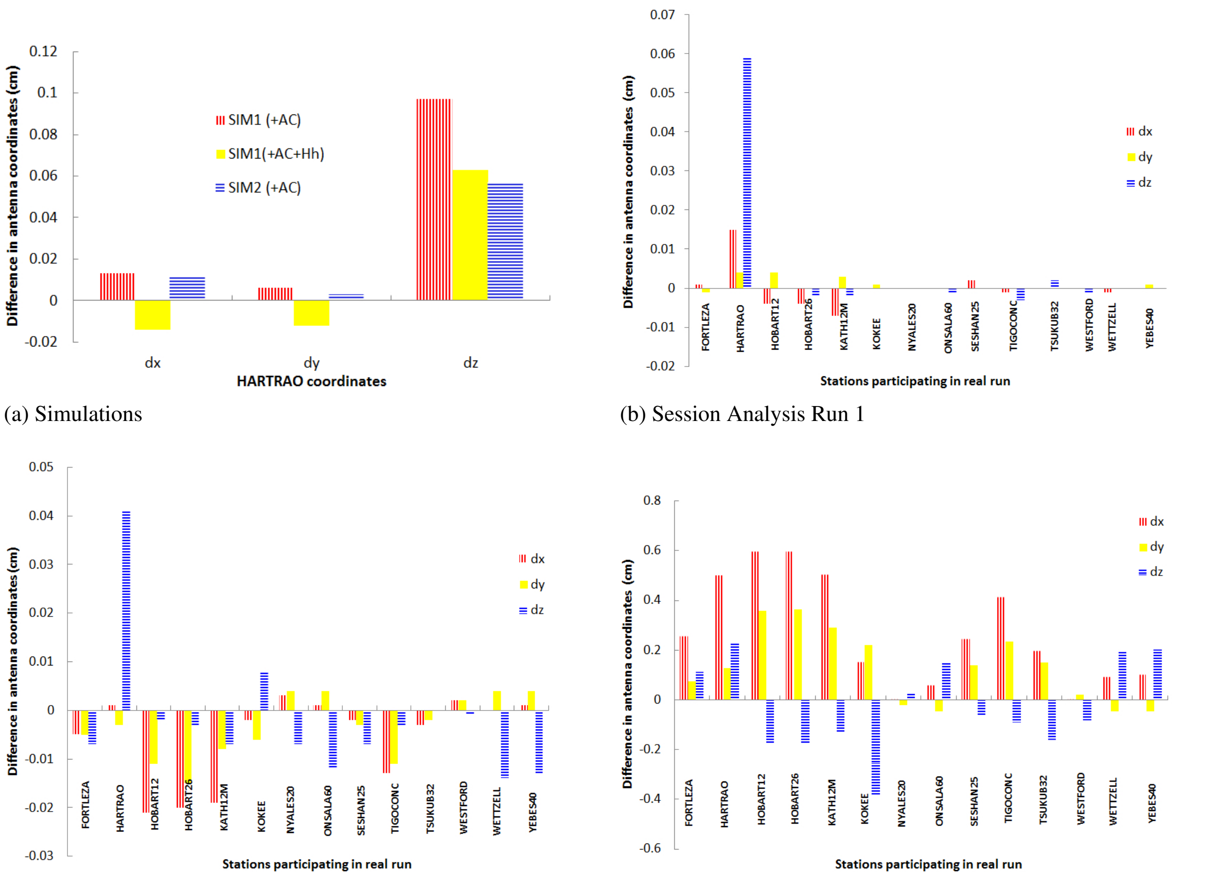

(a) Simulations

(b) Session Analysis Run 1

(c) Session Analysis Run 2

(d) Session Analysis Run 3

Fig. 3: Effect of the AO altitude correction on the estimated antenna coordinates with the difference in antenna coordinates plotted for a selection of stations: (a) simulations with AO altitude correction applied to HARTRAO only, (b) session analysis with and without AO altitude correction applied, (c) with and without AO altitude correction applied with HARTRAO in datum, and (d) with AO altitude correction applied with and without HARTRAO in datum.

3 Conclusions

The effect of the axis offset altitude correction on the estimated antenna axis offset and antenna coordinates was investigated. The axis offset altitude correction has bearing on HARTRAO (equatorial mount) and HOBART26 (X-Y mount) only, as all other stations in these sessions have telescopes with AZEL mounts to which the correction does not apply.

The axis offset altitude correction changes HARTRAO coordinates and axis offset by less than 1 mm. These preliminary results provide a smaller change in the estimated antenna coordinates than expected from the theoretical model of the axis offset altitude correction, which predicts a change of 1–2 cm in the slant troposphere delay at low elevations. We are investigating the reason for the smaller than expected shifts. We intend comparing results from VieVS and the JPL VLBI modelling and estimation software “MODEST" (Sovers et al., 1998) for a few observations to search for any inconsistencies in the coding.

A large correction to the antenna axis offset *a priori* value exists for HARTRAO in general (~1 cm) compared to that of HOBART26 (~1 mm). A difference of several millimetres between the *a priori* value for the antenna axis offset of HARTRAO and the value estimated with VieVS was also reported by Nilsson et al. (2016) and Krásná et al. (2014). The *a priori* value of the antenna axis offset was however corroborated during a recent (February 2014) local co-location survey (Muller and Poyard, 2015).

Future efforts will include analysis of CONT campaigns in which HARTRAO participated to compare the antenna axis offset estimated from CONT02, CONT05, CONT08 and CONT11. The minor influence of the axis offset altitude correction on the antenna coordinates of HOBART26 will also be investigated in our upcoming work.

Acknowledgements

 U.S. Government sponsorship acknowledged for part of this research. HartRAO is a facility of the National Research Foundation (NRF) of South Africa.

References

Böhm J, Böhm S, Nilsson T, Pany A,Plank L, Spicakova H, Teke K, Schuh H (2012) The New Vienna VLBI Software VieVS. In: S. Kenyon, M. Pacino, U. Marti (eds), *Geodesy for Planet Earth*, International Association of Geodesy Symposia, 136, 1007–1011, doi:10.1007/978-3-642-20338-1_126

Combrinck W L, Merry C L (1997) Very long baseline interferometry antenna axis offset and intersection determination using GPS. *J. Geophys Res.*, 102(B11):24741–24744.

Krásná H, Nickola M, Böhm J (2014) Axis offset estimation of VLBI telescopes. In: D. Behrend D, K. D Baver, K. Armstrong (eds.), *Proc. IVS 2014 General Meeting*, 339–343.

Muller J M, Poyard J C (2015) Hartebeesthoek local tie survey. *IGN report* http://itrf.ensg.ign.fr/doc_ITRF/RT199_V1_POYARD+_Hartebeesthoek_LocalTie-Feb2014.pdf

Nilsson T, Mora-Diaz J A, Raposo-Pulido V, Heinkelmann R, Karbon M, Liu L, Lu C, Soja B, Xu M, Schuh H (2016) Antenna axis offsets and their impact on VLBI derived reference frames. In: T. van Dam (ed.), *REFAG 2014*, International Association of Geodesy Symposia, 146, 53–58, doi:10.1007/1345_2015_126

Nothnagel A et al. (2015) The IVS data input to ITRF2014. *International VLBI Service for Geodesy and Astrometry*, doi:10.5580/GFZ.1.1.2015.002.

Nothnagel A (2008) Conventions on thermal expansion modelling of radio telescopes for geodetic and astrometric VLBI. *J. Geodesy*, 83(8), 787–792, doi:10.1007/s00190-008-0284-z.

Sovers O J, Fanselow J L, Jacobs C S (1998) Astrometry and geodesy with radio interferometry: experiments, models, results. *Rev. Mod. Phys.*, 70(4), 1393–1454,

A Celestial Reference Frame Based on Kalman Filtering

B. Soja, R. Gross, C. Jacobs, T. Chin, C. Abbondanza, M. Heflin, J. Parker, X. Wu, M. Karbon, T. Nilsson, R. Heinkelmann, H. Schuh

Abstract In this study, we investigate a novel approach to the determination of celestial reference frames (CRF). Instead of a constant model for radio sources positions, we adopt a time series representation, which allows temporal variations of radio source coordinates to be taken into account. In particular, the added flexibility is beneficial for radio sources with extended structure. We compute our time series-based CRF solutions by Kalman filtering and smoothing radio source positions, which are initially obtained from single-session VLBI analysis. The temporal resolution of the estimated CRF coordinates is identical to that of the input data, i.e. usually 1-4 days. The magnitude of the coordinate variations is controlled by the amount of process noise applied in the filter, which is in turn derived from analyzing the Allan standard deviation of the corresponding radio source coordinate time series. Measures have been developed to reduce the impact of observation errors and datum effects on the noise model.

Keywords Kalman filter, celestial reference frame, source structure

Benedikt Soja · Richard S. Gross · Christopher S. Jacobs · Toshio M. Chin · Michael B. Heflin · Jay W. Parker · Xiaoping Wu
Jet Propulsion Laboratory, California Institute of Technology, 4800 Oak Grove Dr, Pasadena, CA 91109, United States of America

Maria Karbon · Tobias Nilsson · Robert Heinkelmann
GFZ German Research Centre for Geosciences, Telegrafenberg, DE-14473 Potsdam, Germany

Harald Schuh
GFZ German Research Centre for Geosciences, Telegrafenberg, DE-14473 Potsdam, Germany
Technische Universität Berlin, Straße des 17. Juni 135, DE-10623 Berlin, Germany

1 Introduction

Extragalactic radio sources exhibit time variability, for example, due to source structure and changes therein as well as hour angle and frequency variability. In the analysis of VLBI data and in the determination of celestial reference frames (CRFs), source structure effects are commonly not corrected (IERS Conventions, 2010), which may lead to a degradation of the quality of the VLBI products and frames. Currently, no source structure correction models exist that could be utilized by analysis centers with little effort. Likewise, the International Celestial Reference Frame 2 (ICRF2, Fey et al., 2015) is based on a constant coordinate model for radio sources, neglecting any temporal variability. A group of radio sources characterized as "special handling sources" has been reduced during the estimation of the ICRF2, however, the published catalog, used in the VLBI analysis, only includes constant coordinates.

An approach for considering the time variability of radio sources is to extend the coordinate model of radio sources. Karbon et al (2016) used linear splines instead of a constant coordinate model to create a CRF, which allowed strong but unstable sources to be included in the datum when applied in VLBI analysis. Especially the insufficient observation geometries in the early years of VLBI benefited from the increased selection of datum sources and the estimated nutation parameters were improved by 10%.

In this work, we take a different approach to consider radio source coordinate variabilities: a time series representation. The tool of choice is Kalman filtering, which sequentially assimilates the observational data to estimate source coordinates with high temporal resolution. The source positions are assumed to be stochastic processes, reflecting the physical nature of these objects. A potential disadvantage of the Kalman filter algorithm is a higher computational demand compared to a classical least-squares inversion.

Kalman filtering already has been successfully used in the creation of terrestrial reference frames (Wu et al.,

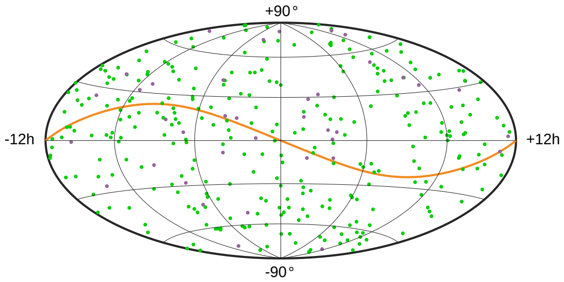

Fig. 1: Sky map of the radio sources included in this study, with dots representing defining sources, purple dots special handling sources, and the orange line the ecliptic.

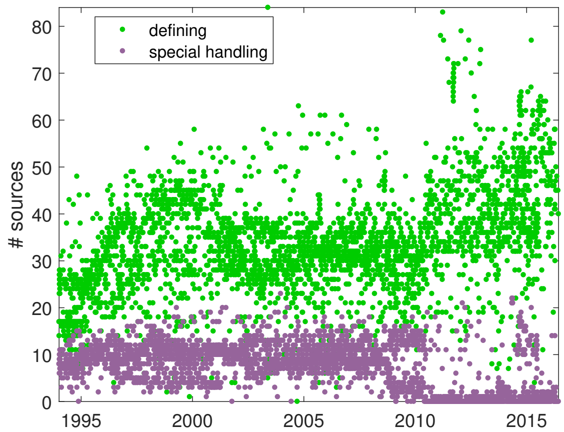

Fig. 2: The number of defining (green) and special handling (purple) radio sources per VLBI session is plotted against time.

2015; Soja et al., 2016). In the future, the International Earth Rotation and Reference Systems Service (IERS) International Terrestrial Reference System (ITRS) Combination Center at Jet Propulsion Laboratory (JPL) aims to jointly determine terrestrial and celestial reference frames, and Earth orientation parameter (EOP) time series in order to eliminate current inconsistencies. In order to achieve a joint determination, the estimation of the CRF has to be integrated into the filter-based software KALREF, which has, for example, been used to determine the JTRF2014, the recent ITRF solution by JPL (Abbondanza et al., 2017).

2 Data and Methodology

2.1 VLBI data

Only a limited data set was selected for the preliminary tests and investigations presented in this work. 3118 IVS VLBI sessions were chosen covering the time period between 1994 and 2016.5. In total, 334 radio sources were considered in this study, with 295 defining sources and 39 special handling as categorized in the ICRF2. Figure 1 shows the radio source distribution in the sky, with the majority (189 out of 334) being located in the Northern celestial hemisphere. The number of radio sources observed per session, distributed among the two categories, is displayed in Fig. 2. From around 2010 onward, the number of observed special handling sources has been drastically reduced in favor of defining sources. Hence, an improved treatment of the special handling sources, which are typically subject to source structure, is expected to have the largest impact in the early years.

2.2 VLBI analysis

The individual VLBI sessions were processed using the least-squares module of the VieVS@GFZ software (Nilsson et al., 2015). Correction models were applied according to IERS Conventions (2010) and the estimated parameters include radio sources (No-Net-Rotation constraints w.r.t. ICRF2 defining sources), all five EOP, station coordinates (No-Net-Translation and -Rotation constraints w.r.t. ITRF2014) and auxiliary parameters for clocks and troposphere. Only radio sources with three or more observations were estimated, the rest are constrained to their a priori positions.

2.3 Kalman filter setup

The estimated radio source coordinates and their covariances from the single session analysis serve as input to the Kalman filter for CRF determination. The Kalman filter is run both forward and backward in time, followed by a smoothing operation to average the estimated state vectors from the two runs. The state vector, containing the radio source coordinates, is updated for every single VLBI session (usually every 1-4 days). The coordinates are assumed to behave like random walk processes, which are easy to implement in a Kalman filter and have already been successfully applied in the creation of terrestrial reference frames (Soja et al., 2016). A source-based process noise model is utilized as described in Section 3. The datum is preserved from the single session solutions. The output consists of the filtered and smoothed radio source coordinate time series (i.e., right ascension α and declination δ).

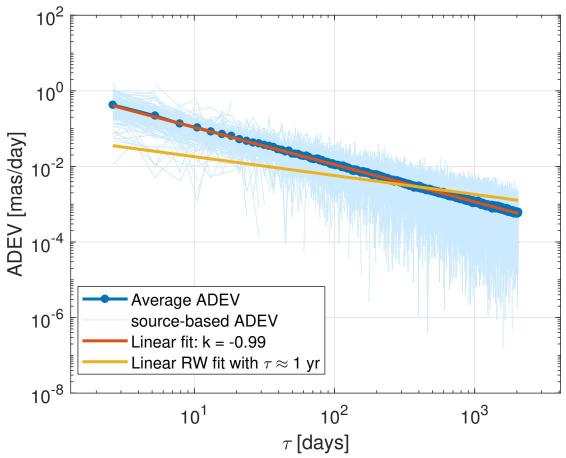

Fig. 3: ADEV for the right ascension ($\alpha \cos\delta$) time series of the individual radio sources (light blue) and the averaged ADEV of all sources (dark blue). A power-law fit is shown in red, and one assuming a random walk process in yellow.

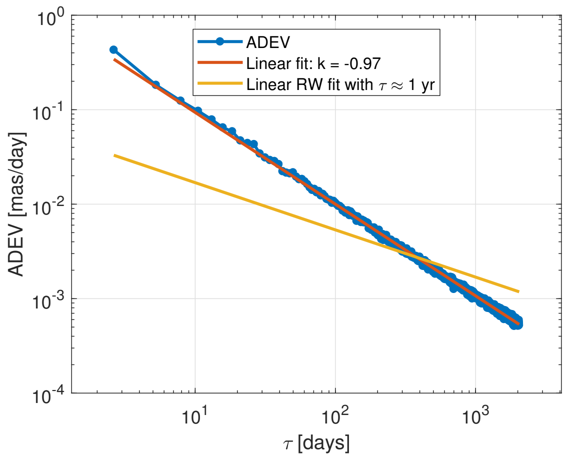

Fig. 4: ADEV and power-law fits to it (like in Fig. 3) are shown for the radio source 4C 39.25.

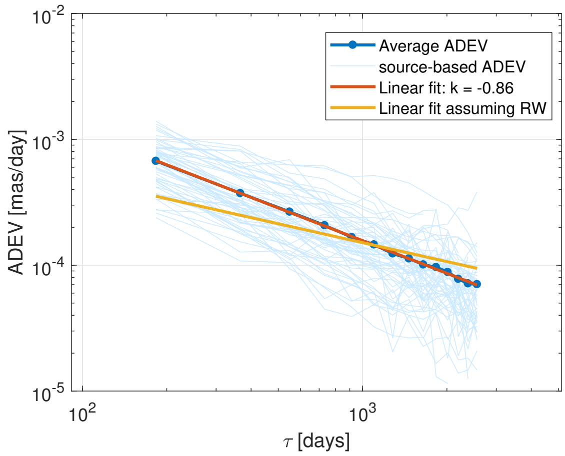

Fig. 5: Like Fig. 3, but for time series of half-yearly averages.

3 Process noise of radio source coordinates

In the Kalman filter, the process noise regulates how much weight is given to the observations in relation to the predictions based on the functional model. In general, it is desirable to utilize external information to create the process noise model, which in the case of radio sources proves to be difficult. Observations at different radio or optical frequencies might not translate to the behavior of sources at geodetic VLBI's S- and X-bands. Radio source images and structure indices could be useful, but it is not clear how they can be converted to values of process noise. Additionally, the effect of outlier flagging during both the correlation and analysis processes is likely to alter the impact of source structure on the estimated coordinates.

For these reasons, it was decided to use the same time series of radio source positions to derive the noise model that are used to determine the CRF. As described in Soja et al. (2015), the Allan standard deviation (ADEV) served as the tool of choice to determine the stochastic behavior of the 334 radio sources. Fig. 3 shows the ADEV for each individual radio source's right ascension time series and the average ADEV over all sources. Fitting a power-law model to the ADEV, the exponent k is almost identical to -1, indicating a perfect white noise process. Even for a radio source with extensive source structure like 4C 39.25 (Fig. 4), the same holds true. It is thus suspected that observational errors and datum effects are primarily the cause for the whiteness of the noise. The magnitude of the white noise seems to dominate contributions due to other reasons, such as source structure.

To remove some of the random observation error and datum effects, half-yearly averages of the positions were used instead of single-session coordinates. At least 20 data points were required per interval, which was fulfilled by 66 of the sources. The ADEV based on the half-yearly averages, shown in Fig. 5, indicates that on average, the stochastic process is no longer perfect white noise. In fact, some of the radio sources, such as 4C 39.25 (Fig. 6), exhibit temporal correlation and are better characterized by a random walk than by a white noise process.

The power spectral densities (PSDs) of the white noise driving the random walk processes are individually estimated for the 66 radio sources as outlined in Soja et al. (2015). Sky maps of the source-based process noise are shown in Fig. 7. The average PSD over all sources of $\alpha \cos\delta$ is 28 µas^2/day, and for declination it is 72 µas^2/day. The declination process noise being more than twice as large is likely related to the worse VLBI network geometry in North-South direction. Another indication that the declination process noise is more strongly affected by artificial errors is that the

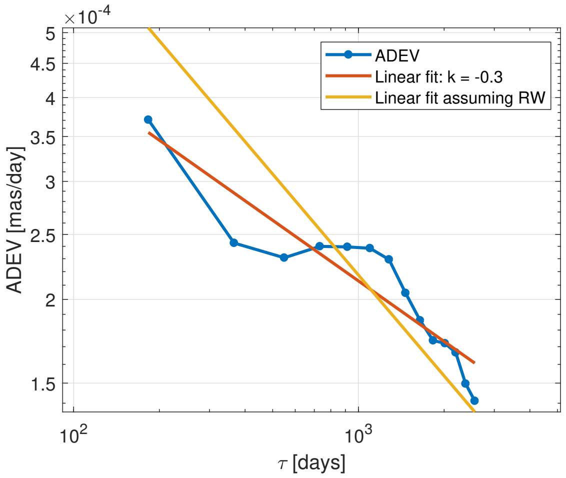

Fig. 6: Like Fig. 4, but for a time series of half-yearly averages.

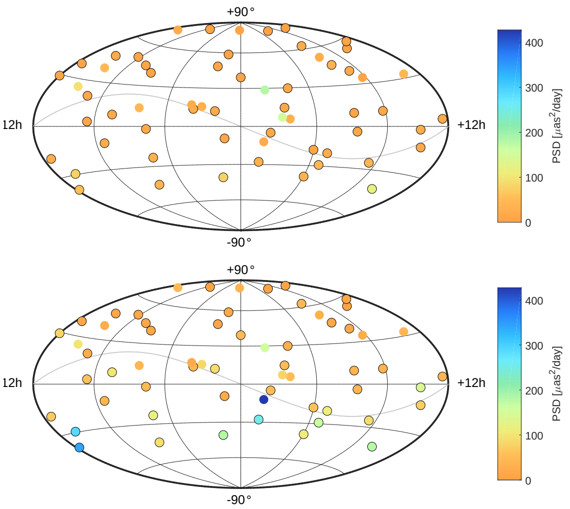

Fig. 7: Color-coded PSD values for 66 sources based on half-yearly averaged time series. Black circles indicate defining sources. Top: $\alpha \cos\delta$, bottom: δ.

radio sources at about -30° tend to have larger PSD values. Since most radio telescopes are in the Northern hemisphere, these sources are more often observed at low elevation angles, increasing tropospheric errors. Missing cable calibration at some of the Southern telescopes might contribute to this effect as well. In right ascension, the average PSD values of special handling sources are about two times as large as those of the defining sources (21 vs. 50 µas^2/day), while the difference is much smaller in the case of declination (69 vs. 83 µas^2/day). The only explanation for the different ratios is once again a stronger contribution of artificial errors to δ compared to α.

4 Kalman filter CRF solutions

Three CRF solutions have been computed using the Kalman filter as described in the previous sections, with the noise model as the only difference. In the first solution, the process noise was set to zero, resulting in a deterministic solution with constant radio source positions. Next, the source-based process noise model derived from the single-session coordinates was applied. Finally, the source-based noise model from the half-yearly averages was used for 66 sources (cf. Fig. 7), and the rest was estimated deterministically.

The different solutions are shown for radio source 4C 39.25 in Fig. 8. The deterministic estimate differs from ICRF2 by about 100 µas, most likely stemming from the different data time spans. The solution with the noise model from the individual VLBI sessions exhibits large scatter, which seems to be related to the artificial error sources discussed above. The CRF based on the half-yearly averages smoothly follows what seems to be a signal caused by changes in the structure of the source. In right ascension, a long-term pattern can be recognized, typically caused by a component of the source structure emerging from the core and first moving out of the narrow X-band beam and later out of the wide S-band beam over several years. In declination, the CRF time series is much less variable. Images of this radio source (e.g., from `vlbi.obs.u-bordeaux1.fr`) show that the source is a two-component source when observed in X-band with the two components in equatorial direction, explaining the signal seen in the CRF solution.

5 Conclusions

This study includes preliminary results related to a first demonstration of a Kalman filter CRF. The time series approach allows to take into account temporal variability in radio source positions. A source-based noise model was derived from statistical analysis of the radio source time series using ADEV. By computing the noise model from half-yearly-averaged radio source positions, the scatter in the CRF time series was reduced. In a case study of radio source 4C 39.25, the Kalman filter was able to track a signal in the source coordinates typical of a two-component radio source.

In the future, the input data will be extended, in particular, the number of radio sources. Other approaches for determining the noise model will be explored, for example, by considering the structure index or the direction of the jet. Finally, strategies for the evaluation

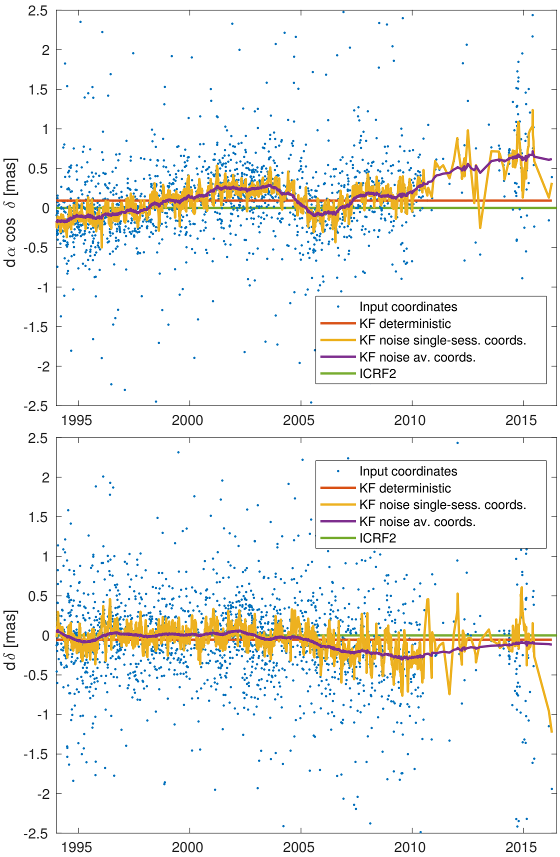

Fig. 8: Time series of radio source coordinates w.r.t. ICRF2 (top: right ascension, bottom: declination) of 4C 39.25 based on the Kalman filter CRF solutions described in Section 3.

of Kalman filter CRFs and the underlying process noise models will be developed and executed.

Acknowledgements

The authors thank the IVS for providing the VLBI data used in this work (Nothnagel et al., 2015). B. Soja's research was supported by an appointment to the NASA Postdoctoral Program at Jet Propulsion Laboratory, administered by USRA under contract with NASA.

References

Abbondanza C, Chin M, Gross R S, Heflin M B, Parker J W, Soja B, van Dam T, Wu X (2017) JTRF2014, the JPL Kalman Filter and Smoother Realization of the ITRS. *JGR*, doi:10.1002/2017JB014360

Fey A L, Gordon D, Jacobs C S, Ma C, Gaume R A, Arias EF, Bianco G, Boboltz D, Böckmann S, Bolotin S, Charlot P, Collioud A, Engelhardt G, Gipson J, Gontier A-M, Heinkelmann R, Kurdubov S, Lambert S, Lytvyn S, MacMillan D S, Malkin Z, Nothnagel A, Ojha R, Skurikhina E, Sokolova J, Souchay J, Sovers O J, Tesmer V, Titov O, Wang G, Zharov V (2015) The 2nd Realization of the ICRF by VLBI. *Astron. J.*, 150(2):58, doi:10.1088/0004-6256/150/2/58

IERS Conventions (2010), G. Petit and B. Luzum (eds.). IERS Technical Note 36, Frankfurt am Main: Verlag des BKG

Karbon M, Heinkelmann R, Mora-Diaz J, Xu M, Nilsson T, Schuh H (2016) The extension of the parametrization of the radio source coordinates in geodetic VLBI. *J Geod*, 91(7), 755–765, doi:10.1007/s00190-016-0954-1

Nilsson T, Soja B, Karbon M, Heinkelmann R, Schuh H (2015) Application of Kalman filtering in VLBI data analysis. *Earth Planets Space*, 67(1):136, doi:10.1186/s40623-015-0307-y

Nothnagel et al. (2015) The IVS data input to ITRF2014. *International VLBI Service for Geodesy and Astrometry*, doi:10.5880/GFZ.1.1.2015.002

Soja B, Nilsson T, Karbon M, Zus F, Dick G, Deng Z, Wickert J, Heinkelmann R, Schuh H (2015) Tropospheric delay determination by Kalman filtering VLBI data. *Earth Planets Space*, 67(1):144, doi:10.1186/s40623-015-0293-0

Soja B, Nilsson T, Balidakis K, Glaser S, Heinkelmann R, Schuh H (2016) Determination of a TRF via Kalman filtering of VLBI data. *J Geod*, 90(12), 1311–1327, doi:10.1007/s00190-016-0924-7

Wu X, Abbondanza C, Altamimi Z, Chin T M, Collilieux X, Gross R S, Heflin M B, Jiang Y, Parker J W (2015) KALREF – A Kalman filter and time series approach to the ITRF realization. *JGR: Solid Earth* 3775–3802, doi:10.1002/2014JB011622

ITRS Realizations in the Framework of ITRF2014: Impact of Different TRF Parameterizations on VLBI Combined Products

S. Bachmann, D. Thaller

Abstract In this paper we investigate the impact of different station coordinate parameterizations of a priori values on products of the IVS combination. Three different realizations of the latest International Terrestrial Reference System (ITRS), using different station coordinate parameterizations have been published: DTRF2014, ITRF2014, and JTRF2014. These different ITRS realizations are used as a priori station coordinates for the IVS combination process. The results of combined station coordinate time series show no significant differences in terms of statistics for the three solutions. All three solutions provide comparable results for station coordinate determination. Peculiarities can be found for JTRF2014 for stations that started observing before 1994. In this period, a tilt or an offset of the time series is visible, that is probably caused by erratic increase of available observations in combination with the Kalman filter technique. In terms of scale factor, we found a significant offset of the ITRF2014-based solution compared to the other TRF solutions by a mean value of -0.59 ppb. The other TRF solutions show no unexpected irregularities for the scale factor.

Keywords DTRF2014, ITRF2014, JTRF2014, TRF, VLBI

1 Introduction

In the framework of the realization of the latest International Terrestrial Reference System (ITRS), different terrestrial reference frames (TRF) using different parameterization models for station coordinates have been published. Namely, the DTRF2014 (Seitz et al., 2016), published by the German Geodetic Research Institute/Technical University of Munich (DGFI-TUM, Germany), the ITRF2014 (Altamimi et al., 2016), the official ITRF, published by Institut national de l'information géographique et forestière (IGN, France), and the JTRF2014 (Abbondanza et al., 2016), published by Jet Propulsion Laboratory (JPL, USA). The station coordinate models differ in term of parameterization for each of these solutions:

1. DTRF2014: piece-wise linear station model (including non-tidal atmospheric and hydrological loading)
2. ITRF2014: linear station model with additional post-seismic deformation (PSD) model (annual and semi-annual term fitted)
3. JTRF2014: weekly solution (epoch solutions, not explicitly modeling non-tidal loading).

For our comparisons, these different TRFs are used as a priori station coordinate information for the IVS combination process as described in general in Böckmann et al. (2010). The latest developments within the IVS combination as well as the generation of the IVS input contribution to the ITRF2014 are described in Bachmann et al. (2016). The combination at the normal equation level comprising Earth orientation parameter (EOP) and station coordinates is well established within the IVS and in cooperation with other space geodetic techniques (e.g. inter-technique combined TRF). The availability of accurate a priori values for station coordinates plays an important role for the estimation of combined EOP. Therefore, we study the impact of using the three different TRFs as a priori station coordinates on routinely combined VLBI products. For the station modeling of the three different TRF solutions, we applied:

1. DTRF2014: station coordinate and linear velocities for interpolation to mid-session epoch
2. ITRF2014: station coordinate, linear velocities and PSD for interpolation to mid-session epoch
3. JTRF2014: station coordinate at the respective GPS-week which applies to mid-session epoch.

Sabine Bachmann · Daniela Thaller
Federal Agency for Cartography and Geodesy (BKG), Richard-Strauss-Allee 11, DE-60598 Frankfurt am Main, Germany

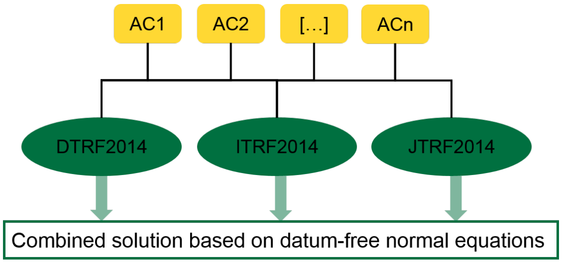

Fig. 1: Input contributions and processing scheme.

Here, we focus on results for station coordinates and the scale.

2 Input contributions

As input contributions, we used datum-free normal equations stored in SINEX files submitted by the IVS Analysis Centers (ACs), containing station coordinates, Earth Orientation Parameters (EOPs) and source positions. We used daily sessions (24 hours sessions) which are provided via the IVS data centers [1] [2] [3]. For consistency reasons, we used VLBI data observed between 1984.0 and 2015.0 as shown in Fig. 1. In total, eight different AC input contributions were used to calculate three different combined solutions alternating between the three ITRS realizations for the a priori station coordinate information. These combined solutions are then used to generate time series for station coordinates (Sect. 3) and to calculate scale time series between the combined solution and the three ITRS realizations, respectively, using a 7-parameter Helmert transformation (Sect. 4).

3 Station coordinates

We compared station coordinate time series that result from the three different TRFs used as a priori values. As an example, Fig. 2 shows the time series of the height component or station WETTZELL, Germany (reduced by ITRF2014 value at epoch 2005.0). As expected, the station coordinate using the JTRF2014 as a priori shows a regular signal corresponding to a yearly signal which has not been modeled in these solutions, contrary to the two other TRFs. Furthermore, an offset of the JTRF2014 solution is visible for the sessions before ~1994. This effect is visible in the north component of the same station, as well as an offset-like tilt (see Fig. 3, reduced by ITRF2014 value at epoch 2005.0). Investigating station coordinate time series of stations that started to observe regularly before 1994, this effect can be seen in each of these stations. We assume that this effect can be explained by the input data used for the Kalman filter technique that is used to calculate the JTRF2014 solutions: about 1993 the Global Navigation Satellite Systems (GNSS) started to observed regularly. Additionally, the Satellite Laser Ranging (SLR) technique underwent a significant improvement when the LAGEOS-2 satellite started being observed in 1992. About the same time, frequency and accuracy of VLBI observing technique improved significantly due to increasing number of telescopes, improved observing methods and improved network geometry. The integral of these changes, in combination with the Kalman filter technique, may be the reason for the effect observed in the station coordinate time series before 1994.

Station coordinate modeling is particularly interesting for stations that were affected by site displacements, caused, e.g., by Earthquakes. Figure 4 shows station TSUKUB34 (Japan), which was affected by larger Earthquakes in 2011 (also reduced by ITRF2014 value at epoch 2005.0). All three solutions provide comparable adequately defined a priori values to model the station discontinuity. No significant differences can be detected when comparing the three time series.

To compare the statistics of the different station coordinate time series generated with the three different a priori TRFs, (weighted) root mean square values ([W]RMS) are calculated. Table 1 shows the WRMS and the RMS over all stations of the combined solution referring to DTRF2014, ITRF2014 and JTRF2014, respectively. Only stations with more than 30 equal sessions for all ACs are considered to achieve comparability. The statistic values are on a comparable level and differ only on a sub-millimeter level. Due to the technique's geometry, detecting the height component is less accurate than the horizontal components. The WRMS values corresponding to the JTRF2014 seems to be lower than the respective values of the DTRF2014 and the ITR2014. This tendency can be generalized to all focused stations. Nevertheless, 50% of these stations do not show significant differences in the (W)RMS.

Table 2 shows the WRMS for the north, east and height components for DTRF2014, ITRF2014 and JTRF2014 for the contributing ACs with respect to the combined solution. Again, only stations with more than 30 successfully combined sessions are considered. Currently, a transition situation is given, where some of the ACs have already changed to use the ITRF2014 as a priori station information, others did not implement the

[1] ftp://ivs.bkg.bund.de/pub/vlbi/ivsproducts/daily_sinex/
[2] ftp://ivsopar.obspm.fr/vlbi/ivsproducts/daily_sinex/
[3] ftp://cddis.nasa.gov/pub/vlbi/ivsproducts/daily_sinex/

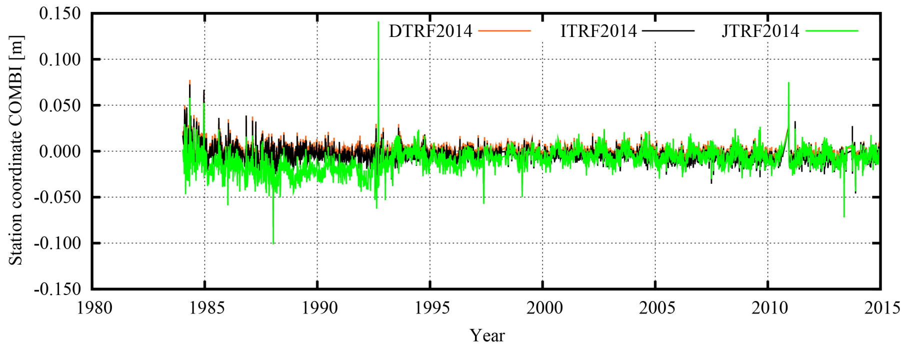

Fig. 2: Station WETTZELL (Germany) height component for DTRF2014, ITRF2014 and JTRF2014.

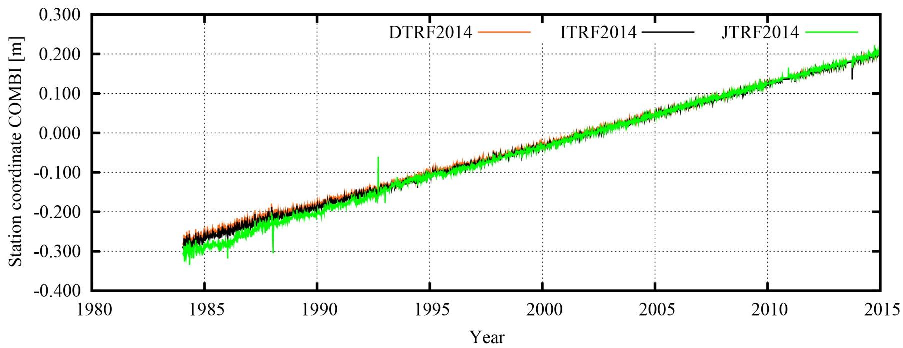

Fig. 3: Station WETTZELL (Germany) north component for DTRF2014, ITRF2014 and JTRF2014.

Table 1: WRMS and RMS over all stations for the combined solution for each of the three TRFs in North (N), East (E) and Height (H). Only stations with >30 equal sessions for all ACs are considered.

TRF name	WRMS [mm]			RMS [mm]		
	N	E	H	N	E	H
DTRF2014	3.4	4.3	7.7	4.7	5.8	11.8
ITRF2014	3.1	3.7	7.6	4.7	5.8	11.8
JTRF2014	2.6	3.1	6.6	4.5	6.9	11.3

new TRF yet and continue to use other TRFs. Since the combination procedure is based on datum-free normal equations, we do not expect to see any inconsistencies between the ACs induced by different a priori values. The differences of the WRMS between the ACs in Table 2 are not correlated with the a priori station model used by the ACs, but with the analysis software used by the respective AC.

Table 2: WRMS for individual AC solutions for each of the three ITRS realization in North (N), East (E) and Height (H). Only stations with >30 equal sessions for all ACs are considered.

	DTRF2014			ITRF2014			JTRF2014		
	N	E	H	N	E	H	N	E	H
AC1	2.0	2.5	4.6	2.1	2.5	4.7	2.0	2.4	4.6
AC2	1.3	1.6	2.8	1.3	1.6	2.8	1.3	1.5	2.8
AC3	1.7	2.0	4.1	1.7	2.0	4.0	1.7	2.0	4.0
AC4	2.9	3.2	5.9	2.9	3.1	5.8	3.0	3.2	5.9
AC5	1.5	1.7	3.1	1.4	1.7	3.0	1.5	1.7	3.1
AC6	4.4	5.0	9.8	4.3	4.9	9.8	4.4	4.9	9.8
AC7	1.8	1.9	3.2	1.7	1.8	3.1	1.7	1.8	3.2
AC8	1.8	2.0	4.0	1.8	2.0	4.0	1.8	2.0	4.0

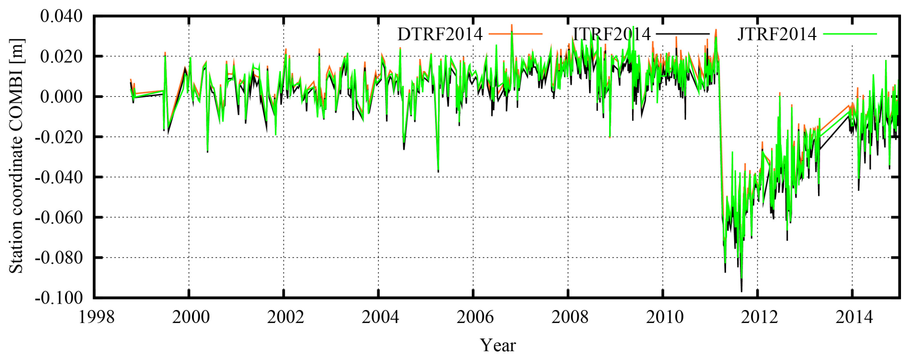

Fig. 4: TSUKUB32 (Japan) height component for DTRF2014, ITRF2014 and JTRF2014.

4 Scale comparison

VLBI and SLR together define the scale of the ITRS realization, because only these space geodetic techniques have access to this parameter. Therefore, investigating the scale is of vital interest in VLBI. To evaluate the scale parameter, we performed a session-wise comparison with respect to the routine quarterly combined solution. A 7-parameter Helmert transformation is calculated using sessions observed between 1990.0 and 2015.0. Stations with discontinuities (e.g. caused by Earthquakes) are excluded from the datum definition.

Figure 5 shows the smoothed scale time series between the combined solution and the ITRS realizations investigated in our study (DTRF2014, ITRF2014 and JTRF2014). Additionally, previous ITRS realizations, like DTRF2008 and ITRF2008, as well as the VTRF2015q2 (a TRF based on combined VLBI sessions) are shown. Peculiarities before 1994 as well as around 2004 and 2014, that are visible in each of the TRFs, can be explained by unfavorable network geometry. The figure shows a good agreement between the two DTRF solutions (DTRF2008, DTRF2014), the VTRF2015q2 solution and the JTRF2014 solution, scattering around the zero line. Between about 1998 and 2002 a variation of the JTRF2014-based scale can be observed. A noticeable difference can be observed for the two ITRF solutions, where an offset can be seen for both solutions and an additional trend for the ITRF2014-based solution is present. The offset of the ITRF2008-based solution has already been reported in, e.g., Bachmann et al. (2016). Table 3 shows the weighted mean of the scale time series as shown in Fig. 5. For the two DGFI solutions as well as the VTRF solution the weighted mean shows no significant offset. For the JTRF2014, a weighted mean of 0.19 ppb is given, probably resulting from the scale irregularities between 1998 and 2002. For the ITRF2008-based solution, a weighted mean of −0.38 ppb (corresponding to −2.4 mm on the Earth's surface) have been found, which corresponds well to the offset of 0.44 ppb found in Bachmann et al. (2016) (resulting from a 7-parameter Helmert transformation between the two TRFs [VTRF and ITRF2008], i.e., opposite transformation direction causing inverted sign). The ITRF2014-based solution on the other hand shows a weighted mean of −0.59 ppb (i.e. −3.8 mm on the Earth's surface). This value corresponds well with the scale factor between VLBI and SLR of 1.37 ppb found by Altamimi et al. (2016) and the offset of the SLR solution with respect to the ITRF2014 of about 0.7 ppb as found by V. Luceri for the SLR intra-technique combined solution (Luceri, 2017). Looking at the WRMS of the scale time series, the JTRF2014-based solution shows the smallest value of 0.78 ppb, the highest value has been detected for the ITRF2008-based solution having 1.02 ppb.

Table 3: WRMS and RMS for individual AC solutions for each of the three ITRS realization. Only stations with >30 equal sessions for all ACs are considered.

ITRS realization	Weighted Mean (ppb)	WRMS [ppb]	RMS [ppb]
DTRF2014	-0.01 ±0.01 (-0.1 mm)	0.88	2.37
ITRF2014	-0.59 ±0.02 (-3.8 mm)	0.95	2.69
JTRF2014	0.19 ±0.01 (1.2 mm)	0.78	2.23
VTRF	0.01 ±0.01 (-0.1 mm)	0.91	2.21
DTRF2008	0.02 ±0.02 (0.1 mm)	0.98	6.44
ITRF2008	-0.38 ±0.02 (-2.4 mm)	1.02	8.21

5 Conclusions

All three TRFs agree very well in terms of station coordinate estimation and repeatabilities (WRMS/RMS). The tilt that can be observed for the JTRF2014 with respect to the DTRF2014 and ITRF2014 estimates before about 1994 is presumably caused by the significant change of the amount of available data (additional GNSS, SLR and VLBI observations, see Sect. 3). The scale factor between the combined solution and the DTRF2014 does not show unexpected irregularities compared to the preceding DTRF or the VTRF2015q2 solution. The JTRF2014 shows a peculiarity around the year 2000, but for the major part of the time series the JTRF2014-based scale factor is in good agreement with the VLBI combined solution. However, the ITRF2008 and ITRF2014 solutions show a significant offset of the scale time series compared to the other TRF solutions. The origin of this scale factor (between VLBI and SLR) is not yet clear. Possible sources of impact are

- equating of station velocities
- treatment of local ties
- parameter estimation.

These open points have to be solved on the level of inter-technique combination. In future investigations, the impact of TRFs with different station coordinate modeling on EOPs and other parameters like source positions will be studied.

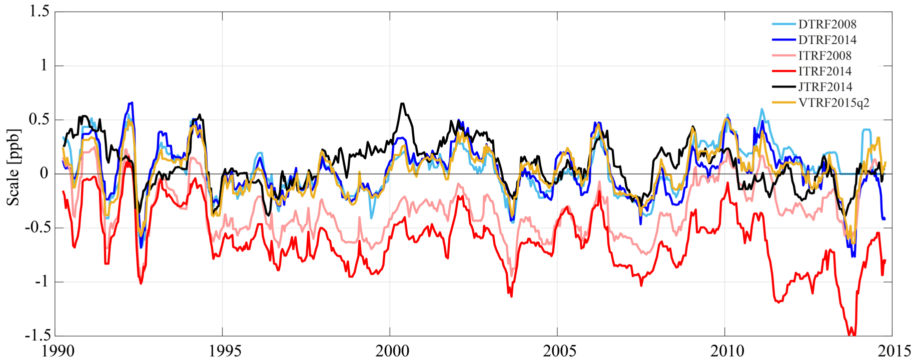

Fig. 5: Smoothed scale time series for DTRF2008 (light blue), DTRF2014 (dark blue), ITRF2008 (light red), ITRF2014 (dark red), JTRF2014 (black) and VTRF2015q2 (ocher).

References

Abbondanza C, Chin T, Gross R, Heflin M, Parker J, van Dam T, Wu X (2016) JTRF2014, the 2014 JPL Realization of the ITRS Oral presentation, EGU General Assembly 2016, Vienna, Austria,

Altamimi Z, Rebischung P, Métivier L, Collilieux X (2016) ITRF2014: A new release of the International Terrestrial Reference Frame modeling nonlinear station motions. *J. Geophys. Res. Solid Earth*, 121, 6109–6131, doi:10.1002/2016JB013098

Bachmann S, Thaller D, Roggenbuck O, Lösler M, Messerschmitt L (2016) IVS contribution to ITRF2014. *J. Geod.*, 90, 631–654, doi:10.1007/s00190-016-0899-4

Böckmann S, Artz T, Nothnagel A, Tesmer V (2010) International VLBI Service for Geodesy and Astrometry: Earth orientation parameter combination methodology and quality of the combined products. *J. Geophys. Res.*, 115, doi:10.1029/2009JB006465

Luceri V (2017) personal communication, https://ilrs.cddis.eosdis.nasa.gov/docs/2017/ILRS_ASC_EGU2017_PRESENTATIONS.pdf

Seitz M, Bloßfeld M, Angermann D, Schmid R, Gerstl M, Seitz F (2016) The new DGFI-TUM realization of the ITRS: DTRF2014 (data). Deutsches Geodätisches Forschungsinstitut, doi:10.1594/PANGAEA.864046.

Determining the Galactocentric Acceleration Vector from VLBI and its Impact on the Reference Frames

H. Krásná, O. Titov

Abstract The relative motion of the solar system barycentre around the Galactic centre can also be described as an acceleration (Galactocentric Acceleration, GA) of the solar system directed towards the centre of the Galaxy. So far, this effect has been omitted in the a priori modelling of the Very Long Baseline Interferometry (VLBI) observable. Therefore, it results in a systematic dipole proper motion (Secular Aberration Drift, SAD) of extragalactic radio sources building the celestial reference frame with a theoretical maximum magnitude of 5 – 6 µas/yr. In this paper, we present our estimation of the SAD vector obtained within global adjustments of the VLBI measurements (1979.7 – 2016.5) using the software VieVS. We show that the scale factor from the VLBI measurements estimated for each source individually discloses a clear systematic aligned with the direction to the Galactic centre-anticentre. Therefore, the radio sources located near the Galactic anticentre may cause a strong systematic effect, especially, in early VLBI years. For instance, radio source 0552+398 causes a difference exceeding 1 mm in the estimated intercontinental baseline length, which is clearly above the modelling requirements of the VLBI Global Observing System (VGOS). Furthermore, we introduce a new method for estimation of the SAD vector from the scale factor corrections.

Keywords Galactocentric acceleration, TRF, CRF

1 Introduction

The acceleration of the Solar System Barycentre (SSB) directed towards the centre of the Galaxy raises through the relative motion of the SSB around the Galactic centre on a quasi circular orbit. Table 1 summarizes recent estimates of the Galactocentric Acceleration (GA) vector obtained from the geodetic Very Long Baseline Interferometry (VLBI). In general, two methods for the estimation of the GA vector were used: (1) a posteriori fitting of the radio source proper motion field (Titov et al., 2011; Titov and Lambert, 2013, 2016) and (2) estimation of the GA vector within the global adjustment of the VLBI data (Kurdubov, 2011; Xu et al., 2012; MacMillan, 2014). It can be seen that except of Kurdubov (2011) all publications yield a consistent estimates of the maximum amplitude A of the GA vector between 5.5 and 6.5 µas/yr whereas the estimated direction of the GA vector varies especially in declination between −11 and −56 deg. Theoretically, the Galactocentric acceleration vector points to the centre of the Galaxy which is supposed to be the location of the compact radio source Sagittarius A* with the estimated coordinates α_G = 267 deg for right ascension and δ_G = −29 deg for declination (Reid and Brunthaler, 2004). In this paper we present our estimates of the Galactocentric acceleration vector obtained with the software VieVS (Böhm et al., 2012) using two different methods. Section 2 contains the GA vector estimated as global parameter in the common adjustment of the VLBI sessions whereas in Section 3 we introduce a new method for the estimation of the GA vector from the globally estimated VLBI scale factor. The impact of omitting the Galactocentric acceleration in the a priori modelling on

Hana Krásná
Technische Universität Wien, Department of Geodesy and Geoinformation, Gusshausstrasse 27-29, AT-1040 Vienna, Austria

Oleg Titov
Geoscience Australia, PO Box 378, Canberra, 2601, Australia

Table 1: Recent estimates of the GA vector from geodetic VLBI. The components of the acceleration vector are given with the amplitude A, and the equatorial coordinates of the vector direction α_G, δ_G.

	Kurdubov (2011)	Titov et al. (2011)	Xu et al. (2012)	Titov and Lambert (2013)	MacMillan (2014)	Titov and Lambert (2016)
A [µas/yr]	10.3 ± 1.1	6.4 ± 1.5	5.8 ± 0.4	6.4 ± 1.1	5.6 ± 0.4	5.9 ± 1.0
α_G [deg]	288 ± 5	263 ± 11	243 ± 4	266 ± 7	267 ± 3	273 ± 13
δ_G [deg]	0 ± 5	-20 ± 12	-11 ± 4	-26 ± 7	-11 ± 3	-56 ± 9

the estimated baseline length and the Celestial Reference Frame (CRF) is shown in Section 4.

2 Estimation of the GA vector from the global VLBI solution

Following Titov et al. (2011) the conventional equation for the group delay model (Petit and Luzum, 2010) was extended by the GA vector. Aside of that the processing followed the IERS Conventions 2010 and the technique specific VLBI analysis recommendations. Further details of the parametrisation and analysis setup for our standard global VLBI solution are given in Krásná et al. (2015). In the global solution we determined the terrestrial reference frame (position and linear velocity), celestial reference frame (position) and three components (a_x, a_y, a_z) of the GA vector. Table 2 summarizes the estimated GA vector given with its maximum amplitude A and the direction in equatorial coordinates α_G for right ascension and δ_G for declination. The first column shows the resulting GA vector from a global adjustment of nearly all available IVS sessions, i.e. ~5800 sessions from 1979.7 until 2016.5. The second column contains the GA vector determined within an adjustment of large global networks only, represented by the following specific IVS programs: the National Earth Orientation Service (NEOS-A) sessions, Rapid turnaround IVS-R1 and IVS-R4 sessions and all available two-weeks CONTinuous campaigns (CONT), i.e., ~2000 sessions from 1993 until 2016.5. Both solutions yield a value for the maximal amplitude which is consistent with the estimates published in the last few years. The direction in declination of the vector is close to its theoretical value if only the large network sessions were included in the solution which implies that this procedure is sensitive to the inclusion of weak networks.

Table 2: GA vector estimated within global VLBI solutions with software VieVS.

	1979.7 - 2016.5 ~5800 sessions	1993.0 - 2016.5 ~2000 sessions
A [µas/yr]	6.1 ± 0.2	5.4 ± 0.4
α_G [deg]	260 ± 2	273 ± 4
δ_G [deg]	-18 ± 4	-27 ± 8

3 Estimation of the GA vector from the global source-wise scale factor corrections

We developed a new method for the estimation of the GA vector. The GA vector is estimated by fitting the globally estimated scale factor F corrections. For the case of a perfect VLBI model, the measured time delay would be equal to the modelled one and the scale factor has to be equal to unity. If the additional delay produced by the acceleration of the solar system barycentre is not modelled a priori, then the scale factor manifests itself as a variable parameter, depending on the Galactocentric vector a, radio source position s and the time since a reference epoch Δt:

$$F = 1 + \frac{a \cdot s}{c} \Delta t = 1 + \Delta F. \tag{1}$$

The mathematical background with all details is introduced in Titov and Krásná (2017). We carried out again the global adjustment of the VLBI measurements where we estimated the terrestrial and celestial reference frame in the usual way and the scale factor correction for each source individually (except the 39 special handling sources). We present here the solution where the scale factor correction was treated as a time-independent parameter. It means that we built up partial derivative of the time delay τ w.r.t. $\frac{\Delta F}{\Delta t}$ as:

$$\frac{\partial \tau}{\partial \left(\frac{\Delta F}{\Delta t} \right)} = -\frac{b \cdot s}{c} \Delta t. \tag{2}$$

In such case the scale factor corrections are estimated independently of time, i.e. the annual variation [ppb/yr] is determined. Upper plots in Figure 1 show the estimated annual drift of the scale factor for each source individually if the a priori time delay was modelled according to the consensus model in IERS Conventions 2010. Lower plots show the annual effect on the scale factor from the difference between this standard solution and a solution where the GA vector was added a priori to the time delay as described in Titov et al. (2011) with the a priori amplitude of 5 µas/yr. The annual variation of the scale factor due to the GA effect reaches about 0.02 ppb/yr. Since the mean Δt in our data set is about 10 years the absolute effect on the scale grows up

Table 3: Estimates of the GA vector from the global $\frac{\Delta F}{\Delta t}$ corrections from a standard VLBI solution. Different cut-off limits for number of radio source observations (N) applied.

N	> 4	> 10	> 50	> 500	> 1 000	> 10 000	> 20 000	> 50 000
number of sources	4062	4001	3414	573	476	133	87	43
A [µas/yr]	7.1 ± 0.2	8.2 ± 0.3	5.2 ± 0.2	5.1 ± 0.3	5.0 ± 0.3	4.8 ± 0.4	5.3 ± 0.5	4.6 ± 0.7
α_G [deg]	281 ± 3	281 ± 3	281 ± 3	281 ± 4	280 ± 5	280 ± 7	281 ± 7	290 ± 13
δ_G [deg]	-51 ± 2	-55 ± 2	-35 ± 3	-34 ± 3	-32 ± 4	-28 ± 5	-34 ± 5	-24 ± 8

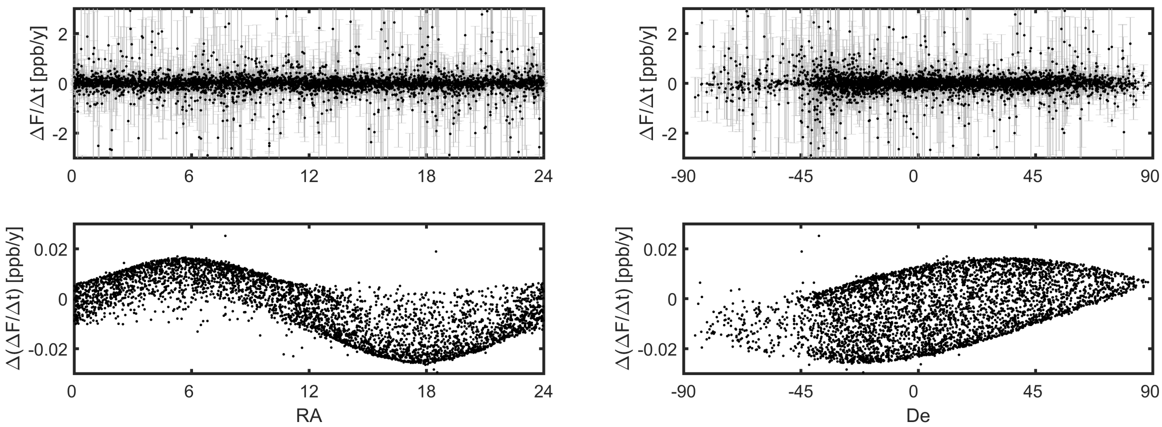

Fig. 1: Upper plots show the annual drift of the scale factor corrections $\frac{\Delta F}{\Delta t}$ from a conventional VLBI solution w.r.t. right ascension (left-hand side) and declination (right-hand side). Lower plots show the difference in $\frac{\Delta F}{\Delta t}$ from a conventional solution and a solution with GA vector modelled a priori with the amplitude 5 µas/yr.

to 0.2 ppb. The GA vector is determined by fitting the individual scale factor corrections (upper plots in Figure 1) by the following model:

$$F = a_x \cos\alpha \cos\delta + a_y \sin\alpha \cos\delta + a_z \sin\delta \tag{3}$$

using the components of the acceleration vector a_x, a_y, a_z as

$$\begin{aligned} a_x &= A \cos\alpha_G \cos\delta_G, \\ a_y &= A \sin\alpha_G \cos\delta_G, \\ a_z &= A \sin\delta_G. \end{aligned} \tag{4}$$

The resulting GA vectors from different sets of sources-wise scale corrections are summarized in Table 3. The criterion for including the scale correction to the data set was the number of observation N to the respective radio source. The first column shows the GA vector estimated from all sources with more than 4 observations, i.e., the data set consists of more than 4 000 sources. The last column shows the acceleration vector estimated from sources with more than 50 000 observations what fulfilled about 40 sources only. Estimates of the acceleration vector following a compromise between the number of observations and number of sources, i.e., (50 < N < 20 000) have a consistent maximal amplitude between 4.8 and 5.2 µas/yr and a direction in declination (from −28 to −35 deg) which is close to the theoretical value. All solutions yield a stable value for the direction in right ascension about −281 deg which should be further investigated.

4 Impact of the GA on the reference frames

Figure 2 and Figure 4 show the effect of the omitted Galactocentric acceleration in the VLBI analysis on the estimated celestial reference frame and the baseline length of selected baselines, respectively. Plotted is the difference between a conventional solution minus a solution with the GA vector modelled a priori with the amplitude of 5 µas/yr. The amplitude of the difference in CRF reaches 50 µas. The effect of the uncertainty of the GA amplitude on the CRF is modelled in Figure 3 which shows the difference in the CRF between a solution with A = 6.5 µas/yr minus a solution with A = 5.0 µas/yr. In the baseline length there is a systematic shift resulting from selected sessions in the early VLBI years. The reason is the scheduling style and the limited number of observed sources which allows the sources close to the Galactic centre or anticentre where the correction is at largest to have an hight impact on the solution. To prove that assumption we computed another solution where we applied the GA modelling for all sources with the exception of radio source 0552+398

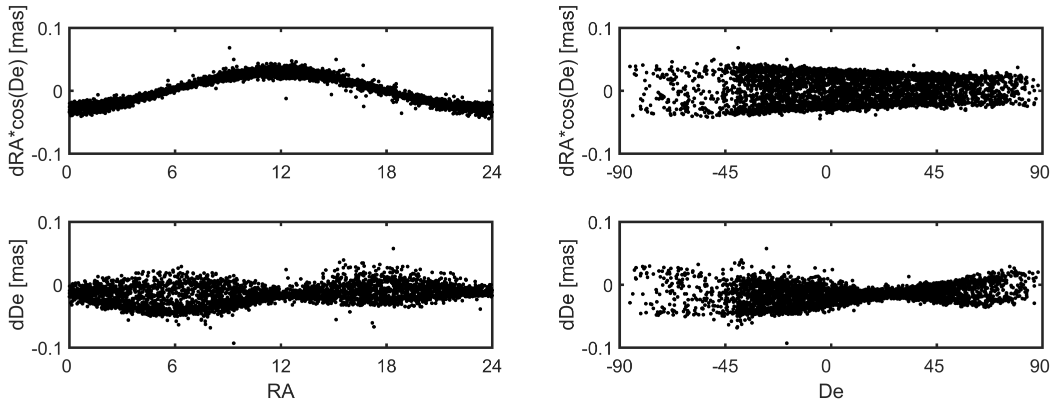

Fig. 2: Difference in source coordinates (CRF) due to the omitted GA effect. Standard solution (without GA) minus the solution with GA applied apriori (A = 5.0 µas/yr).

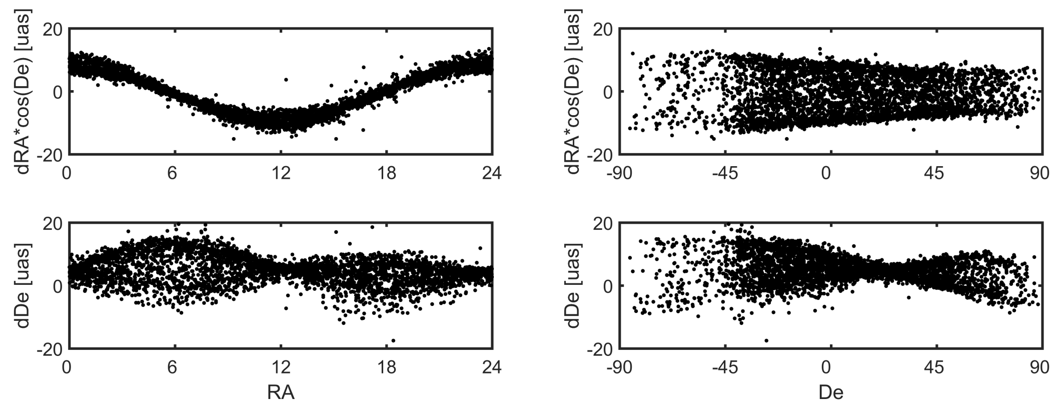

Fig. 3: Difference in CRF due to the uncertainty in the GA amplitude. Solution with A = 6.5 µas/yr minus a solution with A = 5.0 µas/yr.

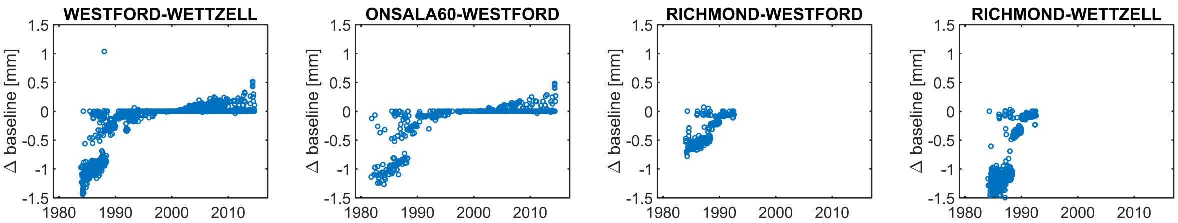

Fig. 4: Difference in the baseline length due to the omitted GA effect. Standard solution (without GA) minus the solution with GA applied apriori (A = 5.0 µas/yr).

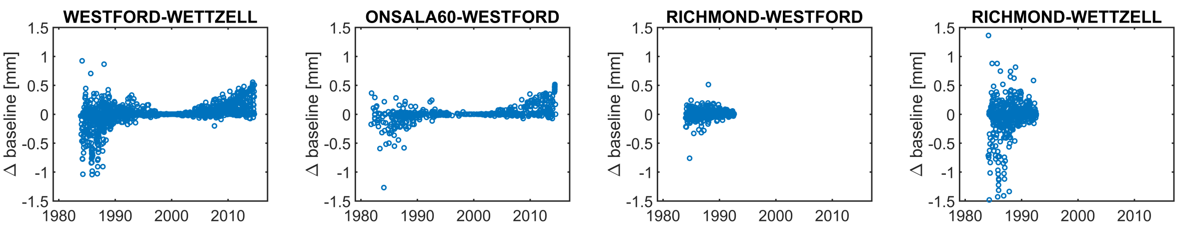

Fig. 5: Difference in the baseline length between a conventional solution minus a solution where the GA effect was modelled a priori for all sources with an exception for source 0552+398.

which is a frequently observed source near the Galactic anticentre. The difference between this solution and the conventional solution for the selected baselines plotted in Figure 5 shows that the large systematically shifted differences in the early VLBI years vanished.

5 Conclusions

We introduce a new method for estimation of the Galactocentric acceleration vector from geodetic VLBI measurements based on fitting the scale factor corrections estimated for each source individually within a global solution. From fitting the individual scale factor corrections of sources with more than 50 observations during 1979.7 – 2016.5 we got the GA vector with the amplitude of 5.2 ± 0.2 µas/yr, and the direction $\alpha_G = 281 \pm 3$ deg and $\delta_G = -35 \pm 3$ deg. The GA vector was also estimated directly within a global adjustment of the VLBI data. GA vector determined from selected large network IVS sessions after 1993 ($A = 5.4 \pm 0.4$ µas/yr, $\alpha_G = 273 \pm 4$ deg, $\delta_G = -27 \pm 8$ deg) is closer to its theoretical value than the estimate from the entire VLBI history. Neglecting the Galactocentric acceleration in the a priori VLBI observation model causes errors in the estimated baseline length which can exceed 1 mm especially in the early VLBI years, and systematic errors in the determined celestial reference frame (up to 50 µas). Results presented in this paper are computed with the VieVS software and verified with the OCCAM software package.

Acknowledgements

The authors acknowledge the IVS and all its components for providing VLBI data (Nothnagel et al., 2015). Hana Krásná works within the Hertha Firnberg position T697-N29, funded by the Austrian Science Fund (FWF).

References

Böhm J, Böhm S, Nilsson T, Pany A, Plank L, Spicakova H, Teke K, Schuh H (2012) The new Vienna VLBI Software VieVS. *IAG Symposium 2009*, 1007–1012.

Krásná H, Malkin Z, Böhm J (2015) Non-linear VLBI station motions and their impact on the celestial reference frame and Earth orientation parameters. *J Geod*, 89, 1019–1033, doi:10.1007/s00190-015-0830-4.

Kurdubov S (2011) Estimation of Solar system acceleration from VLBI. *Proc. of the 20th EVAG Working Meeting*, 112–113.

MacMillan D S (2014) Determination of Galactic Aberration from VLBI Measurements and Its Effect on VLBI Reference Frames and Earth Orientation Parameters. *AGU Fall Meeting Abstracts*.

Nothnagel et al. (2015) The IVS data input to ITRF2014. *Intenatinal VLBI Service fo Goeodesy and Astrometry*, doi:10.5880/GFZ.1.1.2015.002.

Petit G, Luzum G (2010) IERS Conventions 2010. *IERS Technical Note No. 36*.

Reid M J, Brunthaler A (2004) The Proper Motion of Sagittarius A*. II. The Mass of Sagittarius A*. *ApJ*, 616, 872–884, doi:10.1086/424960.

Titov O, Lambert S B, Gontier A-M (2011) VLBI measurement of the secular aberration drift. *A&A*, 529:A91, doi:10.1051/0004-6361/201015718.

Titov O, Lambert S B (2013) Improved VLBI measurement of the solar system acceleration. *A&A*, 559:A95, doi:10.1051/0004-6361/201321806.

Titov O, Lambert S B (2016) Search for the primordial gravitational waves with Very Long Baseline Interferometry. *Proc. of the 28th Texas Symposium on Relativistic Astrophysics*, arXiv:1603.09416.

Titov O, Krásná H (2017) Measurement of the solar system acceleration using the scale factor. *A&A*, in preparation.

Xu M H, Wang G L, Zhao M (2012) The solar acceleration obtained by VLBI observations. *A&A*, 544:A135, doi:10.1051/0004-6361/201219593.

Current Development Progress in ivg::ASCOT

A new VLBI Analysis Software

S. Halsig, A. Corbin, A. Iddink, F. Jaron, T. Schubert, A. Nothnagel

Abstract The VLBI group of the Institute of Geodesy and Geoinformation of the University of Bonn (IGG VLBI group, ivg) started the implementation of a new analysis toolbox called Analysis, Scheduling and Combination Toolbox (ivg::ASCOT) at the end of 2015. The main objective is to provide a flexible and expandable environment to easily develop new scientific projects. ivg::ASCOT is implemented in C++ and intended to perform schedules of VLBI experiments, simulations, geodetic data analysis, and intra-technique combination on the normal equation level. In this paper, the current development progress is outlined. Here, special consideration is given to the scheduling module based on singular value decomposition and impact factors, an automated ambiguity resolution, VLBI observations to near-field targets, and different possibilities to perform least squares adjustments including the classical least squares adjustment, a least squares collocation method and filter techniques.

Keywords VLBI software package, Data analysis, ivg::ASCOT

1 Introduction

In December 2015, the VLBI group at the Institute of Geodesy and Geoinformation of the University of Bonn (IGG VLBI group, ivg) started the implementation of a new analysis toolbox called Analysis, Scheduling and Combination Toolbox (ivg::ASCOT). The main objective is to provide a flexible and expandable environment to easily develop new scientific projects (Artz et al., 2016b). Further, results and source code from recent and current PhD-theses prepared at our institute can be easily merged into one consistent environment. ivg::ASCOT is implemented in C++ and intended to perform schedules of VLBI experiments, simulations and geodetic data analysis based on the IERS Conventions 2010 (Petit and Luzum, 2010). In addition to these independent single-session solutions, also a global solution of pre-processed and pre-reduced datum-free normal equations in Solution INdependent EXchange (SINEX) format[1] can be performed. Similarly, an intra-technique combination on the normal equation level is also possible in ivg::ASCOT.

Fig. 1: Logo of the VLBI analysis software package ivg::ASCOT (IGG VLBI Group - Analysis, Scheduling and Combination Toolbox).

The theoretical modeling of the VLBI delay has already been validated in the VLBI Analysis Software Comparison Campaign 2015 (VASCC2015, Klopotek et al., 2016). Therein, a good agreement between ivg::ASCOT and other widely-spread VLBI data analysis software packages has already been proven.

In this paper, the current development progress since May 2016 (which was presented in Artz et al., 2016b) is outlined. Here, special consideration is given to the scheduling module based on singular value decomposition and impact factors (Leek et al., 2015), an automated ambiguity resolution (Corbin et al., 2017), VLBI observations to near-field targets (Jaron et al., 2017), and different possibilities to perform least squares adjustments including the classical least squares adjustment, a least squares collocation method and filter techniques (for the filter approach, see Schubert et al., 2017).

Sebastian Halsig · Armin Corbin · Andreas Iddink · Frédéric Jaron · Till Schubert · Axel Nothnagel
Institute of Geodesy and Geoinformation, University of Bonn, Nußallee 17, DE-53115 Bonn, Germany

1 http://www.iers.org/IERS/EN/Organization/AnalysisCoordinator/SinexFormat/sinex.html

Further information on ivg::ASCOT can be found at http://ascot.geod.uni-bonn.de/.

2 Structure and Strategy

As already described in Artz et al. (2016b), the basic internal library of ivg::ASCOT is called `libivg`. This library defines the main functionality of the software package, including the sessions with scans and observations, classes for the Earth orientation parameters, terrestrial and celestial reference frames, but also the parameter estimation procedure and the input and output functionality.

In addition to internal libraries, ivg::ASCOT relies on external libraries and routines. First, the Conventions (2010) of the International Earth Rotation and Reference Systems Service (IERS, Petit and Luzum, 2010) are used for the theoretical modeling. The IERS FORTRAN routines[2] are compiled into a library and directly linked within ivg::ASCOT. One main advantage is the fact that updates in the conventions can easily and directly be adopted. Further, ivg::ASCOT uses the SOFA library[3] for the Earth orientation, and source code from ProjectPluto[4] for handling the JPL ephemeris. Further, ATLAS[5] and LAPACK[6] or openBLAS[7] are included for numerical calculations.

In addition, ivg::ASCOT includes different internal post-analysis tools. For example, the library `libAnalysisTools` can be used to analyze specific parameter types, such as atmospheric delays, station and source position variations. Baseline length repeatabilities can be easily calculated and transformations between different reference frame realizations can be performed or estimated. The graphical user interface (GUI) and a detailed plotting environment are provided by the library `libqtplot`.

3 Main Development

In the following, the main development progress in ivg::ASCOT since May 2016 (cf. Artz et al., 2016b) are presented.

[2] http://62.161.69.131/iers/convupdt/convupdt.html
[3] http://www.iausofa.org/
[4] http://www.projectpluto.com/jpl_eph.htm
[5] http://math-atlas.sourceforge.net/
[6] http://www.netlib.org/lapack/
[7] http://www.openblas.net/

Near-field VLBI

In addition to classical VLBI observations to natural radio sources, also observations to artificial sources, such as satellites or the Chang'E3 lander (Tang et al., 2014; Haas et al., 2017) can be processed in ivg::ASCOT. The theoretical delays are derived following the near-field delay model of Duev et al. (2012) or Sekido and Fukushima (2006). Details about implementation and testing can be found in Jaron et al. (2017).

Scheduling

A former stand-alone scheduling module based on singular value decomposition and impact factors (Leek et al., 2015) is now incorporated in ivg::ASCOT. For validation purposes, also other criteria, such as global sky coverage or the minimum standard deviation, are implemented. The output files (skd-files) can be directly used as input for the simulation module. The scheduling module is currently used operationally to schedule the INT2 sessions.

Simulation Module

Up to now, the simulation could only be used on the basis of the vgosDB data format, and was recently augmented to also use skd-files in order to use input data from other scheduling software packages. The simulated delays consist of a deterministic part, according to the theoretical modeling of a single session analysis, and three stochastic components: baseline dependent noise, clock variations by power-law processes (Kasdin, 1995), and troposphere noise based on atmospheric turbulence theory (Halsig et al., 2016). The simulation is described in Artz et al. (2013).

Least Squares Adjustment

The classical least squares adjustment including the pseudo-stochastic representation of piece-wise linear functions is not optimal to describe the stochastic characteristic of the dynamics in the neutral atmosphere. To overcome this issue, a least squares collocation method as well as a square root information filter is implemented in ivg::ASCOT. A detailed description of the filter approach is given in Schubert et al. (2017).

Automated Ambiguity Resolution

An automated procedure to resolve the group delay ambiguities and correct for the ionosphere has been developed within ivg::ASCOT. The ambiguity resolution is based on agglomerative hierarchical clustering, a distance-based clustering technique which computes a dendrogram and creates clusters with the known ambiguity spacing. So far, the procedure works for Intensive Sessions involving two stations reliably, but the functionality is currently being expanded to networks of stations. A detailed description of this approach is given in Corbin et al. (2017).

4 Independent Solution

The independent solution on a single-session basis primarily relies on the vgosDB data format (Bolotin et al., 2016), but when necessary, NGS card files [8] can also be used as the input data format. As described in Sec. 3, it is, at least for the Intensive Sessions involving two stations, possible to start the data analysis from scratch. However, concerning 24h sessions, the data analysis can only be performed if the group delay ambiguities are resolved and the ionosphere corrections are applied.

The a priori station motions are calculated following the IERS Conventions 2010, and further variations, such as non tidal atmospheric pressure loading (Petrov and Boy, 2004) or hydrological loading[9] can be applied. The theoretical delay including the relativistic corrections are also implemented according to the IERS Conventions 2010. For the Earth orientation parameters, the IERS C04 series[10] or USNO finals[11] can be used, and additionally subdaily variations are also considered following the IERS Conventions 2010.

Concerning the parameter estimation process, ivg::ASCOT is able to perform either a classical least squares adjustment using a Gauß-Markov model, which is the standard case, or a least squares collocation method and filter techniques.

In all cases, the following parameters are currently supported:

- clocks,
- baseline-dependent clock-offsets (baseline clocks),
- zenith wet delays,
- tropospheric gradients,
- station positions,
- source positions,
- EOPs.

In the standard case using a classical least squares adjustment either a polynomial representation of arbitrary degree and/or continuous piece-wise linear functions (CPWLF) with arbitrary interval length (usually 60 min.) can be used for the modeling of the atmospheric and clock correction parameters. The least squares collocation method and the square root information filter are based on covariance functions or stochastic processes, respectively.

Concerning the stochastic model of the observations, only the standard deviations derived from the fringe fitting process based on the signal-to-noise ratio are used from scratch. Since this leads to very optimistic standard deviations of the target parameters, stochastical refinement strategies can be performed in ivg::ASCOT. This includes either the use of an empirical model (Gipson et al., 2008) where constant and elevation dependent weights are introduced, or a fully populated variance-covariance matrix based on atmospheric turbulence theory (Halsig et al., 2016), which allows physically and meteorologically more reliable standard deviations.

The output of an independent VLBI session are either datum free normal equations or solutions with covariance matrices in SINEX format or an internal ivg::ASCOT format. Furthermore, the results, in particular the post-fit residuals depending on VLBI stations, baselines or sources, can be plotted by means of a graphical user interface (see Fig. 2, here exemplary for a CONT11-session). A statistical analysis of the residuals can also be performed, e.g., by creating histograms and box plots or performing time series analysis.

5 Global Solution and Combination

Global solutions are based on pre-processed and pre-reduced datum-free normal equationsfrom independent single-session data analysis in SINEX format, and are used, for example, to derive celestial and terrestrial reference frames. Not only ivg::ASCOT independent solutions, but also solutions from other VLBI software packages such as the regular contributions to the officially combined product ofthe International Service for Geodesy and Astrometry (IVS, Nothnagel et al., 2016) can be processed. Furthermore, the functionality to include contributions based on observations on the X/Ka-band is prepared. Within the framework of the global solutions it is possible to reduce nuisance parameters, such as zenith wet delays or clock parameters, or perform a priori transformations.

Session-by-session intra-technique combinations on the normal equation (Böckmann, 2010) or on the solution level (Iddink et al., 2014) complete the initial functionality of the software package. A reliable weighting procedure for different contributions is planned for the near future. Up to now, inter-technique combinations between different space-geodetic tech-

[8] http://lacerta.gsfc.nasa.gov/mk5/help/dbngs_format.txt

[9] http://lacerta.gsfc.nasa.gov/hydlo/

[10] http://www.iers.org/IERS/EN/DataProducts/EarthOrientationData/eop.html

[11] http://maia.usno.navy.mil/ser7/finals.daily

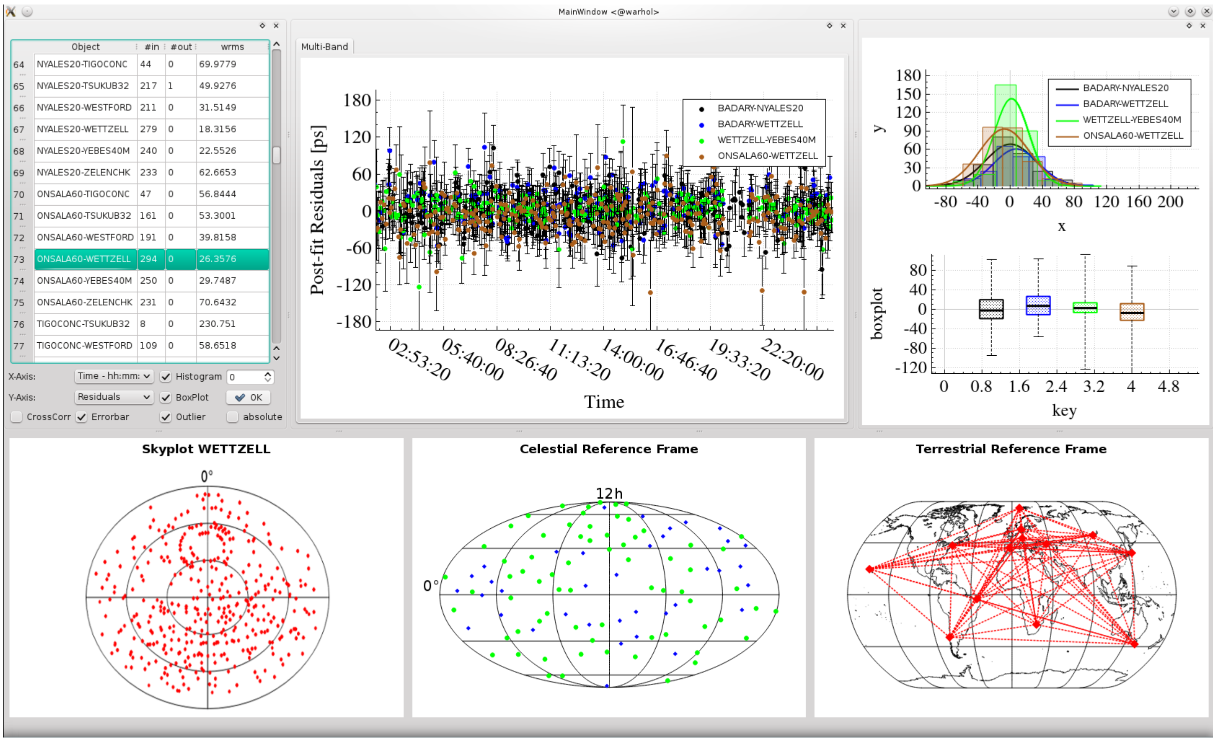

Fig. 2: Post-fit residual analysis plot for a single-session (here, the CONT11-session 11SEP20XA) including a list of stations, baselines and sources with number of observations and WRMS of residuals, a residual plot, a statistical analysis, a skyplot, the observed sources and the network geometry.

niques, such as GNSS, VLBI or SLR, are not yet possible in ivg::ASCOT.

6 Conclusion and Future Work

At the present stage of the development, ivg::ASCOT allows to perform independent solutions to estimate typical VLBI parameters, and global solutions to estimate celestial and terrestrial reference frames. Combinations of output of various analysis centers are also possible. The scheduling module is used operationally to schedule INT2 sessions. Additionally, the analysis of observations to near-field targets is integrated into the software package. Further developments will be primarily based on topics of PhD-theses.

References

Artz T, Nothnagel A, La Porta L (2013) VLBI observations of geostationary satellites. In: N. Zubko and M. Poutanen (eds.), *Proc. 21nd EVGA Working Meeting,* Reports of the Finnish Geodetic Institute, ISBN: 978-951-711-206-3, 217–221.

Artz T, Halsig S, Iddink A, Nothnagel A (2016) ivg::ASCOT: The Development of a new VLBI Software Package.. In: D. Behrend, K. D. Baver, K. Armstrong (eds.), *IVS 2016 General Meeting Proceedings, "New Horizons with VGOS"*, 217–221.

Böckmann S (2010) Robust determination of station positions and Earth orientation parameters by VLBI intra-technique combination. PhD-thesis, Universität Bonn.

Bolotin S, Baver K, Gipson J, Gordon D, MacMillan D S (2016) Transition to the vgosDb Format. In: D. Behrend, K. D. Baver, K. Armstrong (eds.), *IVS 2016 General Meeting Proceedings, "New Horizons with VGOS"* 222–224.

Corbin A, Halsig S, Iddink A, Jaron F, Nothnagel A (2017) Automated ambiguity resolution with clustering and analysis of Intensive Sessions within ivg::ASCOT. In: R. Haas and G. Elgered (eds.), *Proc. 23rd EVGA Working Meeting*, 234–238.

Duev D A, Molera Calves G, Pogrebenko S V, Gurvits L I, Cimo G, Bocanegra Bahamon T (2012) Spacecraft VLBI and doppler tracking: algorithms and implementation. *Astronomy and Astrophysics*, 541, A43, doi:10.1051/0004-6361/201218885.

Gipson J, MacMillan D S, Petrov L (2008) Improved Estimation in VLBI through Better Modeling and Analysis. In: A. Finkelstein, D. Behrend (Eds.) *IVS 2008 General Meeting Proceedings, "Measuring the Furure"*, 157–162.

Haas R, Halsig S, Han S, Iddink A, Jaron F, La Porta L, Lovell J, Neidhardt A, Nothnagel A, Plötz C, Tang G, Zhang Z (2017) Observing the Chang'E-3 Lander with VLBI (OCEL). In: A. Nothnagel, F. Jaron (eds.), *Proc. First International Workshop on VLBI Observations of Near-field Targets*, Schriftenreihe des Inst. f. Geodäsie u. Geoinformation, 54, ISSN 1864-1113.

Halsig S, Artz T, Iddink A, Nothnagel A (2016) Using an atmospheric turbulence model for the stochastic model of geodetic VLBI data analysis. *Earth, Planets and Space*, 68:106, doi:10.1186/s40623-016-0482-5

Iddink A, Nothnagel A, Artz T (2014) Rigorous VLBI intra-technique combination strategy for upcoming CRF realizations. In: N. Capitaine (ed.), *Proc. Journees 2013 Systemes de Reference Spatio-Temporels*, 81–83, ISBN: 978-2-901057-69-7.

Jaron F, Halsig S, Iddink A, Nothnagel A, McCallum L (2017) Near-Field VLBI Delay Models - Implementation and Testing. In: R. Haas and G. Elgered (eds.), *Proc. 23rd EVGA Working Meeting*, 191–195.

Kasdin N J (1995) Descrete Simulation of Colored Noise and Stochastic Processes and $1/f^{\alpha}$ Power Law Noise Generation. In: *Proc. IEEE*, 83, 802–826.

Kermarrec G, Schön S (2014) On the Mátern covariance family: a proposal for modeling temporal correlations based on turbulence theory. *J Geod*, 88(11), 1061–1079.

Klopotek G, Artz T, Bellanger A, Bourda G, Gerstl M, Gordon D, Haas R, Halsig S, Hjelle G, Hobiger T, Hugentobler U, Iddink A, Kirkvik A, Lambert S, Plank L, Schmid R, Shu F, Titov O, Tong F, Wang G (2016) Results from the VLBI Software Comparison Campaign 2015. In: D. Behrend, K. D. Baver, K. Armstrong (eds.), *IVS 2016 General Meeting Proceedings, "New Horizons with VGOS"*, 203–207.

Leek J, Artz T, Nothnagel A (2015) Optimized scheduling of VLBI UT1 intensive sessions for twin telescopes employing impact factor analysis. *J Geod*, 89(9), 911–924.

Nothnagel A, Artz T, Behrend D, Malkin Z (2016) International VLBI Service for Geodesy and Astrometry. Delivering high-quality products and embarking on observations of the next generation. *J Geod*, doi:10.1007/s00190-016-0950-5.

Petit G, Luzum B (2010) IERS Conventions 2010. *IERS Technical Note 35*, Verlag des Bundesamtes für Kartographie und Geodäsie, Frankfurt am Main, ISSN: 1019-4568, 2010.

Petrov L, Boy J-P (2004) Study of the atmospheric pressure loading signal in very long baseline interferometry observations. *J Geophys Res*, 109(B18):B03405.

Sekido M, Fukushima T (2006) A VLBI Delay Model for Radio Sources at a Finite Distance. *J Geod*, 80(3):137–149.

Schubert T, Halsig S, Iddink A, Jaron F, Nothnagel A (2017) Stochastic estimation of ZWD parameter in VLBI data analysis using a Square-Root Information Filter. In: R. Haas and G. Elgered (eds.), *Proc. 23rd EVGA Working Meeting* 257–260.

Tang G, Cao J, Han S, Hu S, Ren T, Chen L, Sun J, Wang M, Li Y, Li L (2014) Research on Lunar Radio Measurements by Chang'E-3. In: D. Behrend, K. D. Baver, K. L. Armstrong (eds.), *IVS 2014 General Meeting Proceedings, "VGOS: The New VLBI Network"* Science Press (Beijing), 473–477.

Impact of Station Clocks on UT1-TAI Estimates

E. Himwich, A. Bertarini, B. Corey, K. Baver, D. Gordon, L. La Porta

Abstract The importance of station clocks, and their corrections, on the determination of UT1-TAI is described. The results of tests verifying the effects they have are presented. The two constituents of the corrections, `fmout-gps` and the *Peculiar Offset*, are explained. The historical relative reference for the *Peculiar Offsets*, which causes a bias in UT1-TAI estimates, is described. A general outline of how to make a direct measurement of the *Peculiar Offsets*, to remove the associated bias, is discussed. We attempt to estimate the size of the current bias. Plans for future work are summarized.

Keywords UT1-TAI

1 Introduction

The time-tagging of VLBI data at the stations has a direct effect on estimates of UT1-TAI (hereafter referred to as "UT1"). Each station's time-tags are nominally in UTC, but with station dependent offsets. To correlate the data, it is necessary to utilize these offsets and correct for some instrumental delays. The offsets and instrumental delays are used during correlation to calculate the final time-tags. An overall error in the final time-tags will cause a bias, in the UT1 estimates from the data (Clark, 1997), *e.g.*, an overall error of $+1$ μs in the time-tags will shift UT1 by -1 μs.

The goal of this work is to eventually reduce the bias in UT1 estimates to less than ±0.1 μs. Until that is possible, we hope to keep the variations in the bias stable to better than the same ±0.1 μs level. The size of the bias and its variation is most critical for 24 hour VLBI experiments with long baselines. The UT1 formal errors for these experiments typical approach, and in some cases are less than, 1 μs. It is less important for short baseline experiments and intensives, which typically have larger formal errors, around 10 μs or larger.

Ed Himwich · Karen Baver · David Gordon
NVI, Inc., 7257D Hanover Parkway, Greenbelt, MD 20770, USA

Alessandra Bertarini · Laura La Porta
Reichert GmbH and BKG at MPIfR, Auf dem Hügel 69, DE-53121 Bonn, Germany

Brian Corey
MIT Haystack Observatory, 99 Millstone Hill Rd, Westford, MA 01886, USA

2 Background

In order for VLBI data to be correlated, the raw data streams need to be aligned at the correlator. This is accomplished by using a geometric model of the observations and the time-tags of the data. The raw time-tags of the data are nominally in UTC, but may be off by several μs. To correct the time-tags, the stations report the offsets of the raw time-tags relative to UTC as defined by GPS, so-called `fmout-gps`. The `fmout-gps` values are defined so that they represent how much earlier the time-tags are than UTC, so-called `clock_early`. These values are typically determined to a few nanoseconds.

Additionally, there are significant instrumental delays in the VLBI data path at the station that need to be taken into account. These can be as large as 100s of μs, but are more typically a few μs. To account for these instrumental effects, the correlators add corrections, known as the *Peculiar Offsets*, to the `fmout-gps` values. The *Peculiar Offsets* are also defined so that their sign is `clock_early`. Typically, unless a change is made to the instrumentation at the station, the *Peculiar Offset* for a given station is stable at a level of 50 nanoseconds or less.

The sum of the `fmout-gps` value and *Peculiar Offset* at a station yields the value *Used* as the correction for that station's time-tags, also with the sign of `clock_early`. The *Used* values change the effective time-tags of the raw data and consequently effectively change the time-tags of the resulting delays and rates.

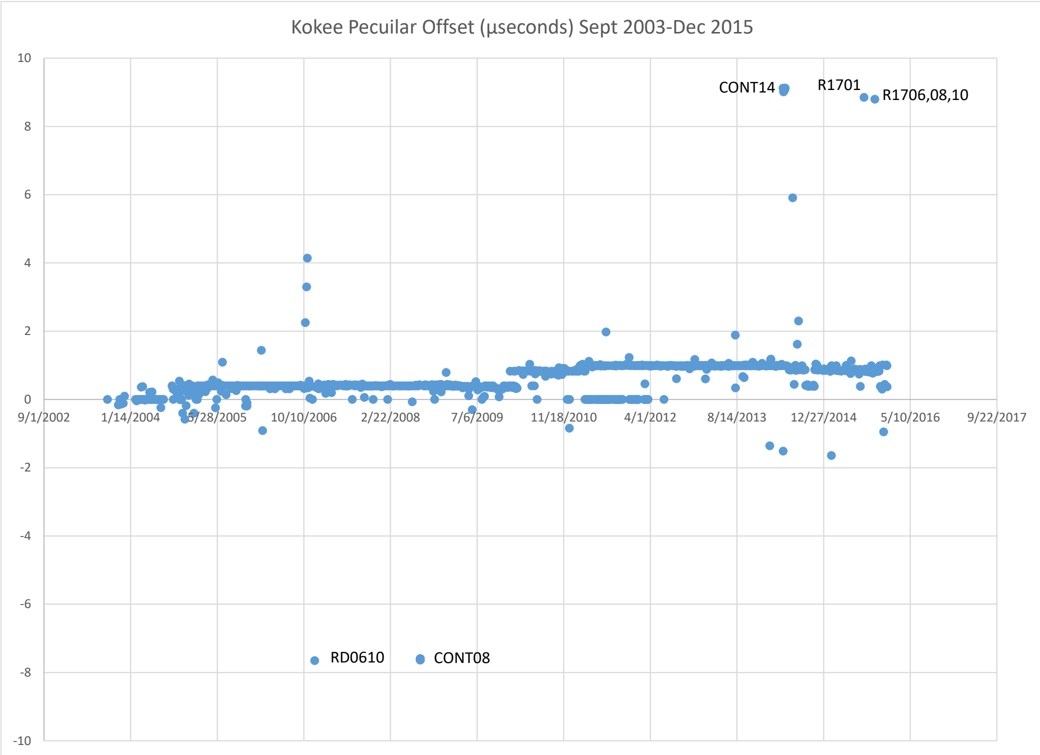

Fig. 1: History of Kokee Peculiar Offsets. See Section 6 *Relative Reference of Peculiar Offsets* for discussion.

The *Used* values have to be consistent between stations in an experiment to correlate the data successfully. However, only the relative values have to be consistent. The values for all the stations can be shifted by a constant amount, in particular by shifting all the *Peculiar Offsets*, and not affect the correlation. The resulting change in the effective time-tags of the output data due to a shift affects UT1. This shift UT1 is not due to the UT1 rate, which integrated over a period as short as a few μs is miniscule. One way to think about this effect is that if the time-tags of the data increase by some amount the `CALC` *a priori* theoretical model will rotate the earth farther by that amount and the resulting adjustment in UT1, to agree with the data, will decrease by the same amount.

3 Tests

Several tests were made to confirm the effect of the station clocks on UT1. The first test was made in 2004 by Axel Nothnagel, Kerry Kingham, and Dorothee Fischer (D. Fischer, personal communication, April 20, 2004). In this test, the data from Intensive experiment i04009 was re-correlated with all the station clocks offset by +1000.0 μs compared to the standard processing. The resulting UT1 value changed by −997.9 μs.

We made a similar test in 2017 using Intensive experiment q17072. In this test, the data was re-correlated with a −100.0 μs shift for all the station clocks compared to the standard processing. The resulting UT1 value changed by +100.8 μs.

Note that in both of these tests the resulting UT1 change was almost, but not exactly, the same magnitude as the change in the station clocks. This is probably due to intrinsic imperfections in the digital correlation process, such that small changes in the *a priori* model will cause changes in the delays at a small fraction of the delay formal error. The noise-level in the delay mapping appears to be small, but should be studied more fully since it is used in all routine processing.

We made a different test with q17072 by explictly changing the time-tags in the post correlation/fringe-fitting database by first +100.0 μs and then −100.0 μs compared to the standard database. The resulting UT1 values changed by −100.0 μs and +100.0 μs, respectively. Note that the UT1 changes were of the same magnitude as the overall *Peculiar Offset* shifts because no mapping of the observables was required.

4 fmout-gps

One of the two components of the *Used* clock correction is the `fmout-gps` value. This is normally measured at the station using a time-interval counter. It represents the delay between the time-tag assigned to the data (`fmout`) and UTC (`gps`). The `fmout` epoch is from a 1 PPS signal from the VLBI data formatter. The `gps` epoch is from a 1 PPS signal from a GPS receiver, tied to UTC. The sign of `fmout-gps` is such that if the time-tag is early, the value is positive, so-called `clock_early`.

The recorded values typically have single-shot measurement RMS scatters of about 0.03 μs or less. When the values from an entire experiment are fit to a line to determine the values used for correlation, the offset and rate values typically have uncertainties of a few nanoseconds and of about 1 part in 10^{-13}, respectively.

The `fmout-gps` value calibrates the sub-second portion of the difference in the formatter's time and UTC (integer second offsets are handled differently). This includes any offsets due to:

- The station's time reference (usually tied to a Hydrogen Maser) and its offset to UTC.
- The delays in the cables from the time reference to the formatter.
- Any formatter internal delays between the formatter's input time and its output time.

Changes in the above values are calibrated by `fmout-gps` and do not affect the *Peculiar Offsets*, which are covered next.

5 Peculiar Offsets

In addition to the `fmout-gps` value, the other component used to determine the *Used* clock offset is the *Peculiar Offset*. The *Peculiar Offset* value primarily represents the delay in the arrival of the VLBI signal to the point of insertion of the time-tag in the formatter compared to the arrival of the signal at the VLBI reference point of the antenna. It is the sum of the delays due to:

- Antenna optics
- Receiver
- IF Cables
- Back-end, up to time-tagging
- The cable from the formatter to the time-interval counter.
- Any effect of the counter set-up: trigger, etc. (may be negative)

minus the delays due to:

- Time-tag insertion after the `fmout` 1 PPS.
- The cable from the GPS receiver to the counter.

Any changes to the delays associated with these items will change the *Peculiar offset* for the station. Fortunately, these delays are usually stable, and small changes of a few 10s of nanoseconds, are negligible.

Historically the *Peculiar Offset* values have not been directly measured, only inferred to the relative difference between the stations. An arbitrary *de facto* overall reference was established in the past. This is discussed in the next section.

6 Relative Reference of Peculiar Offsets

The values of the *Peculiar Offsets* have a direct effect on UT1 estimates because they are a component of the *Used* clock corrections. However, they have not been directly measured. Instead, an arbitrary *de facto* reference was established in the past. The reference is 0 μs for the *Peculiar Offset* for the Kokee Park 20-m antenna using a VLBA formatter, in the 1990s. Since then this reference has typically been well maintained. A plot of the history of the *Peculiar Offsets* for the Kokee Park 20-m from September 2003 until December 2015 is shown in Figure 1. The remainder of this section discusses the features of this plot.

Ideally the *Peculiar Offset* would never change. However, some changes at a station are expected to cause changes in the *Peculiar Offset*.

Two changes in particular affected the *Peculiar Offset* at Kokee. The first was in 2004, when the station changed from using a VLBA formatter to a Mark IV formatter; this increased the *Peculiar Offset* by about +0.4 μs. The second change was in 2010, when they changed from a Mark IV formatter to a Mark 5 Sampler Module and Mark 5B Recorder; this increased the *Peculiar Offset* by about an additional +0.6 μs. Both of these shifts were approximately accounted for by the correlator by including them in the *Peculiar Offset* as can be seen in the plot.

Two other changes in the plot are expected. For the experiments marked "RD0610" and "CONT08" (the latter includes several individual points), the *Peculiar Offset* is shifted by −8 μs. This accounts for the fact that for these experiments the Mark IV formatter was used at a 16 Mbps track rate. There is a known −8 μs change compared to the other track rates, most notably the 8 Mbps that is normally used.

Conversely, the points marked “CONT14”, “R1701”, and “R1706,08,10” are off +8 μs, and that is incorrect. These experiments also used the 16 Mbps track rate, but at that time, Kokee Park 20-m was using a Mark 5 Sampler and Mark 5B Recorder and should not have had a *Peculiar Offset* shift. The observed shift is explained by the fact that a different station, Wettzell 20-m, was using a Mark IV formatter and its *Peculiar Offset* was not adjusted −8 μs. This had the effect of shifting the overall peculiar offsets by +8 μs, which in turn shifted UT1 by −8 μs. The IVS Coordinating Center is looking into fixing the databases with this shift.

As can be seen, there are several other points in the plot that differ from the expected values. It is not immediately clear if any of these represent a shift that would significantly affect UT1. The plot does include Intensive experiments, which have relatively large UT1 formal errors, which would make such variations relatively unimportant.

7 Correlator Use of Peculiar Offsets

Given that the handling of *Peculiar Offsets* has direct consequences for the values of UT1, a reasonable question to ask is why this is handled by the correlators instead of the geodetic analysis. There are three main reasons for this:

1. The correlators must manage the *Peculiar Offsets* in order to align the data for correlation anyway.
2. This approach agrees with historical usage.
3. For the IVS geodetic analysis to handle this issue, a new infrastructure would need to be developed and implemented by all analysis packages.

Keeping the *Peculiar Offset* handling at the correlators —only— avoids duplicate handling of information and allows the output delays to be used to estimate UT1 without applying corrections. How the overall bias in the historical data will be addressed after actual *Peculiar Offsets* have been measured is a different issue.

8 Measuring Peculiar Offsets

To determine the bias in UT1 due to the relative *Peculiar Offset* reference, and connect the TRF and CRF, the *Peculiar Offset* will need to be determined at one or more stations. This will include:

- Estimation of antenna optics delays
- Estimation of receiver delays
- Estimation/Measurement of IF cable delays
- Measurement of effective back-end delays
- Estimation/Measurement of differential cable delays to the `fmout-gps` time-interval counter
- Any effects of the counter set-up

The largest unknown is probably the back-end delays, particularly for the digital parts of the back-ends.

Although in principle, measuring the *Peculiar Offset* at one station would be sufficient, it is recommended to measure it at several to assess the consistency and average out random errors. It would be prudent to maintain a system for monitoring the *Peculiar Offsets* over the long term. The desired accuracy is a few 10s of nanoseconds.

We have attempted to estimate the size of the current bias in UT1 by estimating the actual *Peculiar Offset* for the Kokee Park 20-m when the value of overall 0 μs was being used. This value should also be the UT1 bias (same sign). Rough estimates of the contributions are:

- Antenna optics delay, about 0.015 μs
- Receiver delay, about 0.05 μs
- IF cable delay, about 0.5 μs.
- Back-end delay, which includes about 0.2 μs due to the filters
- Differential cable delays to the the `fmout-gps` time-interval counter, probably negligible, less than 0.010 μs
- Effects of the counter set-up, probably negligible

These items sum to about 0.75 μs. However, the delay in the digital electronics of the VLBA formatter, part of the “Back-end delay” is unknown. The effective delay includes the delay of the signal minus the delay in the time-tagging of the data. Without direct measurement, it is hard to know the effective delay, but examination of the circuit diagram could certainly help. The −8 μs shift in the Mark IV formatter *Peculiar Offset* moving from 8 to 16 Mbps track rate suggests that the effective delay, could be as large as several μs with the sign unknown. At this point, the best we can say is that the UT1 bias is probably somewhere in the range of a few μs, positive or negative.

9 Future Work

There are several items that need to be addressed in the future. An important one is to develop more formal procedures for keeping the *Peculiar Offsets* stable. This would probably include developing an “ensemble” approach based on averaging the offsets of a set of stations rather than the current approach, which relies on a single station. This will make UT1 less dependent on variations at a single station and should average out noise-like variations to make the overall *Peculiar Offsets* more stable. It should include outlier detection to avoid including stations in the ensemble that have significant changes from normal.

Another item to be addressed is correction of the CONT14 and R1 experiments affected by the +8 μs Peculiar Offsets. At the current time, there appear to be two promising methods for correcting the databases *a posteriori*:

1. Change the time-tags in the database. This approach will only be useful if all IVS analysis packages can handle non-integer second time-tags.
2. Map the multi-band delay observable using the delay observable.

We need to investigate which approach is best.

Another issue is that currently the *Peculiar Offsets* are set to split the difference between and S- and X-band data alignment during correlation. This should probably be changed to optimize X-band alignment and possibly use channel offsets to bring S-band into better alignment.

The current discussion of *Peculiar Offsets* is based on DiFX correlators used by the IVS. The analysis and procedures should be extended to other correlators to make sure all IVS results are consistent.

Until the actual *Peculiar Offsets* can be measured, the relative *Peculiar Offset* reference needs to be extended to VGOS observing. This will most likely be done using an observing network that has a mix of legacy and VGOS stations to allow the relative *Peculiar Offsets* to be determined.

Additionally, the noise level in the delay mapping should be studied and quantified.

10 Conclusion

Station timing measurements, `fmout-gps`, are required for accurate UT1-TAI. In addition, the *Peculiar Offsets* applied by the correlator need to be stable. We are investigating a more formal system to improve the relative *Peculiar Offset* stability. It will eventually be necessary to measure the actual *Peculiar Offsets* at one or more stations to remove the current bias in VLBI UT1-TAI results.

Acknowledgments

We would like to thank the many people who contributed to the advancement in the understanding of these issues over many years. These people include (in alphabetical order): Sergei Bolotin, Roger Cappallo, Tom Clark, Dorothee Fischer, John Gipson, David Hall, Kerry Kingham, Axel Nothnagel, Dan Smythe, and Mike Titus. We apologize for any omissions.

References

Clark T A (1997) High Accuracy, Low Cost Timing for Geodetic Applications: The "Totally Accurate Clock" And The Mark-4 VLBI Timing Initiative. Presented at the Wegener June '97 meeting.

The Influence of Phase Calibration at the Station Hobart12 on the ICRF

D. Mayer, J. Böhm, H. Krásná, L. McCallum

Abstract Sources in ICRF3 prototype solutions show a systematic shift in declination when compared to the ICRF2. One explanation for this effect is tropospheric mismodeling in the ICRF2. Another possible reason for this bias is a station dependent error from the Australian stations in the ICRF3. We found that the phase calibration system at the station Hobart12 introduces a spurious signal which propagates into source declination. The phase calibration system at Hobart12 was used during 440 sessions and was not used during 140 sessions of the ICRF3 data set (5830 session as of December 2016). When we remove the sessions where phase calibration was used we find that the declination bias vanishes. This indicates that the declination bias is due to a station dependent effect at Hobart12 and not due to tropospheric mismodeling in the ICRF2.

Keywords Phase calibration, ICRF3, Declination bias

1 Introduction

An important product of the geodetic and astrometric VLBI technique is the international celestial reference frame (ICRF). It is defined by the International Celestial Reference System (ICRS) with its current realisation being the ICRF2 (Ma et al., 2009; Fey et al., 2015). The ICRF2 incorporates geodetic VLBI data from 1979 until March 2009. It is defined by 295 defining sources.

The recently launched Gaia satellite mission will produce an optical celestial reference frame with comparable accuracy (Mignard et al., 2016; Petrov and Kovalev, 2016) in the near future (2018). This and the increased amount of data motivated the VLBI community to produce a new realisation of the ICRS which will be released in August 2018 at the 30th General Assembly of the International Astronomical Union in Vienna, Austria. It will be called ICRF3.

In geodetic VLBI the phase shifts induced by the instrumentation have to be corrected. This is done using a technique called phase calibration. A signal of known phase (set of tones) is injected into the front end of the instrumentation and later used for calibration (further information can be found in Sovers et al. (1998) and the references therein). This technique can also account for additional delays due to cable stretching and twisting. However, the uplink cable can cause additional uncompensated phase variation. Usually this is corrected with a cable calibration system which measures the length of this cable. Not all stations are equipped with such a system. The Australian stations do not have a cable calibration system.

There is another option which is used when the phase calibration fails or is not available. It is called manual phase calibration. During the fringe fitting stage, the individual phase offsets per band are manually set using a strong source as calibrator. In this case, the measured phase calibration signal is not used. Hence the phase calibration signal is not used.

2 Motivation

When comparing ICRF3 prototype solutions with the ICRF2, a clear bias in declination of the determined source positions (Figure 1) becomes evident. From here on we will simply refer to this bias as the declination bias. Different groups found that the addition of data from the Australian stations (Hobart12, Kath12M and Yarra12M) is causing this declination bias. However, the actual cause of the declination bias is yet unknown. One possible reason is that the new data from the southern stations correct a bias intrinsic to the ICRF2 (data

David Mayer · Johannes Böhm · Hana Krásná
Technische Universität Wien, TU Wien, Karlsplatz 13, AT-1040 Vienna, Austria

Lucia McCallum
University of Tasmania, Private Bag 37, 7001 Hobart, TAS, Australia

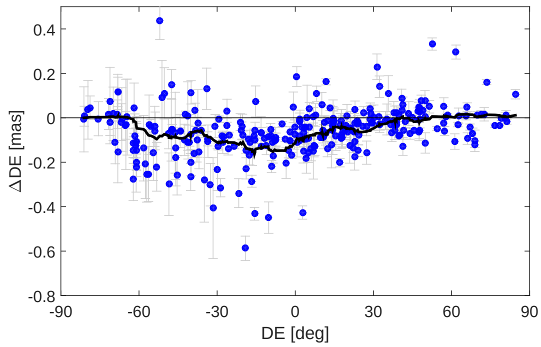

Fig. 1: Bias in declinations of the 295 defining sources as seen between the ICRF3 prototype solution by TU Wien and our own ICRF2 solution. Depicted are the defining sources and a moving average filter.

is mostly from northern stations). The southern sources were mainly observed under low elevation by northern stations. This magnifies tropospheric modeling errors and, because the troposphere has a known north-south gradient, could result in a bias in declination. If this is the case the southern stations helped to reveal this systematic effect and the new solution reflects the truth better. A second possible scenario is that the southern stations experience a systematic error and this distorts the ICRF. This is more critical because it means that the new solution has systematic errors.

In order to investigate this, we had a closer look at session AUG030, on Oct 07, 2016. We processed AUG030 once with the correction from the phase calibration and once with the manual phase calibration correction. Comparing the two solutions, we find a large difference in the group delays of up to 100–150 ps or 3–5 cm (Fig. 2). The differences seems to be mainly azimuth dependent with peaks at each end of the cable wrap. This is an indicator that a systematic error (possible cable twisting of the phase calibration uplink cable) might be introduced into the VLBI data.

The influence of such a systematic error on the CRF is discussed in the following sections.

3 Methodology

3.1 Data set

We used data from 1979 to 2016 (5830 sessions) to create ICRF solutions. In this data set we found ~ 140 sessions where the manual phase calibration correction was used (the phase calibration unit was either broken or not used) and ~ 440 sessions where the normal phase calibration correction was used at Hobart12.

3.2 Solutions

In total we created three test solutions (5250 sessions without Hobart12 plus different subsets of the sessions with Hobart12):

1. A first solution where the sessions with normal phase calibration at Hobart12 were used (5690 sessions in total).
2. A second solution where the sessions with manual phase calibration at Hobart12 were used (5390 sessions in total).
3. And a third solution where we reduced the number of sessions from the first solution to match the number of Hobart12 sessions of the second solution (5390 sessions in total).

We would expect the declination bias to become smaller when removing sessions (440 vs 140 sessions). The third solution was generated to mitigate this effect. In order to make this comparison as fair as possible we tried to keep the ratio of R1/R4 and Austral sessions similar in both data sets. Hence, the third solution incorporates ~ 60 R1/R4 sessions, ~ 60 Austral sessions and ~ 20 other sessions where the normal phase calibration correction was used.

4 Results and Discussion

The first solution, depicted in Figure 3, has a clear systematic bias in declination w.r.t. ICRF2 which is very similar to the declination bias seen when using the full set of 5830 sessions.

When looking at the difference plot between the first solution and the ICRF3 prototype solution with all data we do not see any systematic bias in declination, see Figure 4. This demonstrates that the removal of the 140 sessions where the manual phase calibration was used does not affect the declination bias.

However, looking at the difference in source declination of the second solution (using only sessions where the manual phase calibration correction was used at Hobart) w.r.t. the ICRF2 no bias is visible (Fig. 5). This suggests that removing the 440 sessions where normal phase calibration was used also removes the declination bias.

It is conceivable that 140 sessions are not enough to distinguish the declination bias from noise which is why test solution three was created, using a subset of 140 sessions from solution 1. As shown in Figure 6, the systematic is smaller when compared to Figure 3 (as expected, since we use less sessions) but still noticeable.

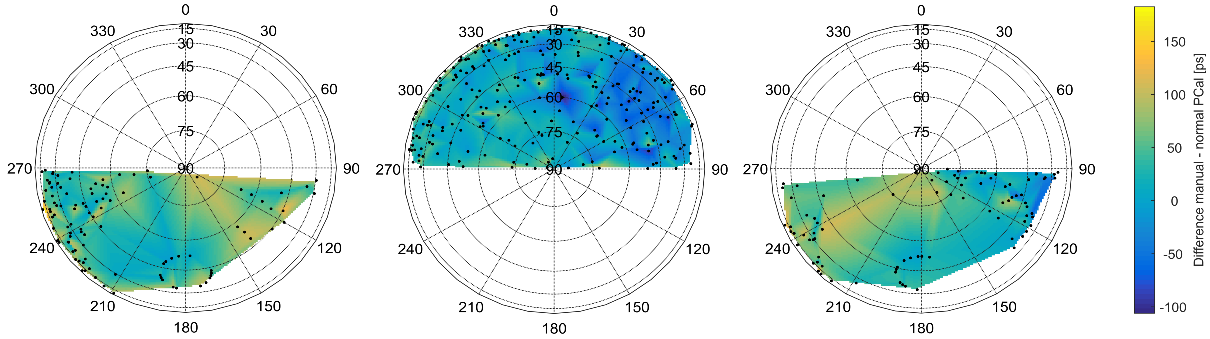

Fig. 2: Difference in group delays (only the baseline Hobart12-Hobart26 is depicted) of session AUS-GEO030 (October 2016) when analysed with the normal phase calibration and the manual phase calibration correction. The skyplot is split into three parts to resemble the different cable wraps counterclockwise, neutral and clockwise (from left to right).

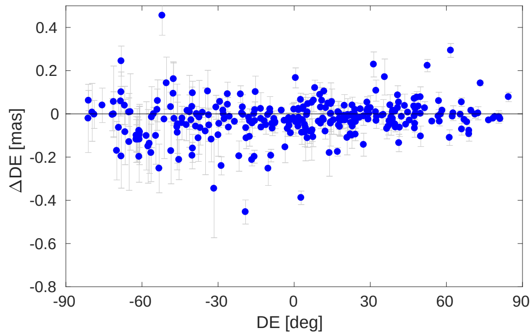

Fig. 5: Solution with 140 sessions where the manual phase calibration at Hobart12 was used. Depicted are the defining sources. The reference is our own ICRF2 solution.

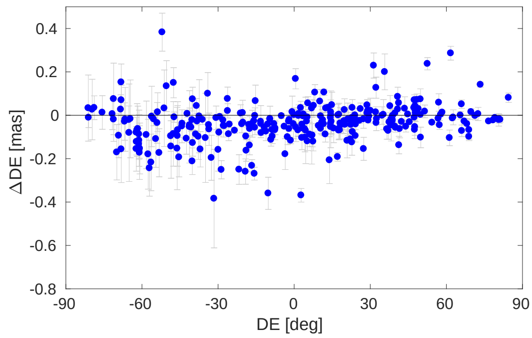

Fig. 6: Solution with a subset of 140 sessions where the normal phase calibration at Hobart12 was used. Depicted are the defining sources. The reference is our own ICRF2 solution.

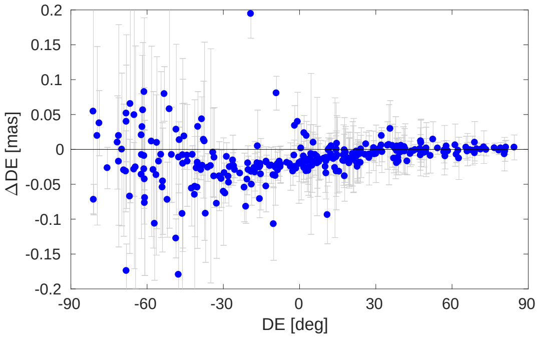

Fig. 7: Difference between solution two (140 manual phase calibration sessions) and solution three (140 normal phase calibration sessions). Depicted are the defining sources.

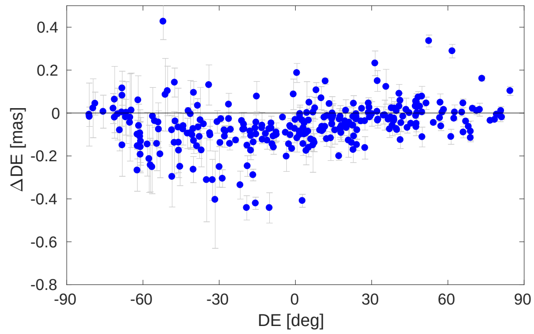

Fig. 3: Solution with 440 sessions where the normal phase calibration at Hobart12 was used. Depicted are the defining sources. The reference is our own ICRF2 solution.

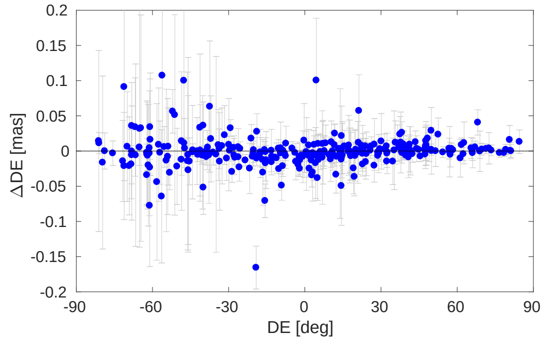

Fig. 4: Difference between our first test solution (440 normal phase calibration sessions) and the ICRF3 prototype solution (all 5830 sessions are used). Depicted are the defining sources.

This demonstrates that 140 sessions are enough to separate the declination bias from noise.

In order to see this effect even clearer we provide the difference plot of both (second and third) solutions, see Figure 7. A bias in declination which looks very similar to the declination bias is evident. This is further evidence that the declination bias is introduced by the normal phase calibration correction.

5 Conclusion

We found a clear (several centimeters) systematic difference in group delays at the station Hobart12 when we use the normal phase calibration versus manual phase calibration.

While a difference per se does not reveal any information about which solution is better, investigations of McCallum et al. (2017) (this edition) indicate that the measured phase calibration signal introduces additional systematic effects into the measurements, rather than correcting for them. This conclusion is supported with the findings of this contribution, looking at effects on the CRF.

When we remove all the sessions where normal phase calibration was used at Hobart12 (sessions where manual phase calibration is used are kept) from the ICRF3 data set, then the declination bias vanishes. We believe that this systematic error propagates into the source declination and causes a major part of the declination bias.

References

Fey A L, Gordon, D., Jacobs C S, Ma C., Gaume R A, Arias E F, Bianco G., Boboltz D A, Böckmann S, Bolotin S, Charlot P, Collioud A, Engelhardt G, Gipson J, Gontier A-M, Heinkelmann R, Kurdubov S, Lambert S, Lytvyn S, MacMillan D S, Malkin Z, Nothnagel A, Ojha R, Skurikhina E, Sokolova J, Souchay J, Sovers O J, Tesmer V, Titov O, Wang G, Zharov V (2015) The Second Realization of the International Celestial Reference Frame by Very Long Baseline Interferometry. *AJ*, 150, 58.

Ma C, Arias E F, Bianco G, Boboltz D A, Bolotin S L, Charlot P, Engelhardt G, Fey A L, Gaume R A, Gontier A-M, Heinkelmann R, Jacobs C S, Kurdubov S, Lambert S B, Malkin Z M, Nothnagel A, Petrov L, Skurikhina E, Sokolova J R, Souchay J, Sovers O J, Tesmer V, Titov O A, Wang G, Zharov V E, Barache C, Boeckmann S, Collioud A, Gipson J M, Gordon D, Lytvyn S O, MacMillan D S, Ojha R (2009) The Second Realization of the International Celestial Reference Frame by Very Long Baseline Interferometry. *IERS Technical Note 35*.

Ma C, Arias E F, Eubanks T M, Fey A L, Gontier A-M, Jacobs C S, Sovers O J, Archinal B A, Charlot P (1998) The International Celestial Reference Frame as Realized by Very Long Baseline Interferometry. *AJ*, 116, 516–546.

McCallum L, McCallum J, Lovell J (2017) The HOB experiments. In: R. Haas and G. Elgered (eds.), *Proc. 23rd EVGA Working Meeting*, 99–102.

Mignard F, Klioner S, Lindegren L, Bastian U, Bombrun A, Hernández J, Hobbs D, Lammers U, Michalik D, Ramos-Lerate M, Biermann M, Butkevich A, Comoretto G, Joliet E, Holl B, Hutton A, Parsons P, Steidelmüller H, Andrei A, Bourda G, Charlot P (2016) Gaia Data Release 1. Reference frame and optical properties of ICRF sources. *AAP*, 595, A5.

Petrov L, Kovalev Y Y (2016) On significance of VLBI/Gaia position offsets. *ArXiv e-prints*.

Sovers O J, Fanselow J L, Jacobs C S (1998) Astrometry and geodesy with radio interferometry: experiments, models, results. *Reviews of Modern Physics*, 70, 1393–1454.

K-band Celestial Reference Frame: Can it be Better Than S/X?

A. de Witt, C. S. Jacobs, A. Bertarini, D. Gordon, J. McCallum, J. Quick, J. Lovell, A. Nothnagel

Abstract K-band (24-GHz) VLBI observations are very rapidly realizing their potential to form the basis for the most accurate celestial reference frame (CRF) ever constructed. Relative to the standard S/X (2.3/8.4-GHz) observing bands, AGN at K-band have more compact source morphology and smaller core-shifts. This reduction in astrophysical systematics allows a more stable CRF at K-band. The only previous K-band CRF had 268 sources. With the 16-fold increase in data rate to 2 Gbps in our recently completed VLBA observations, we achieved a four-fold increase in sensitivity relative to previous observations. This allowed us to quickly double the number of sources to 551 while simultaneously improving the precision. In early 2017 we were awarded eight additional 24-hour VLBA sessions to continue the improvement of the K-band frame precision. With the inclusion of archival K-band Galactic Plane observations and recent dedicated observations in the Southern Hemisphere, we now have almost 800 sources in our K-band CRF. Our K-band CRF now has better precision than the international standard ICRF2. Our accuracy is currently limited by ~100 microarcsecond level zonal errors that we plan to address through increased southern observations using HartRAO-Hobart single-baselines. Our analysis of recently completed VLBA observations shows source position precision improving as the number of delay measurements to the −0.6 power. This improvement with number of observations shows that our additional observations will make rapid astrometric progress. We are optimistic that these observations will become the core of a K-band contribution to the ICRF3.

Aletha de Witt · Jonathan Quick
HartRAO, Krugersdorp, South Africa

Christopher Jacobs
JPL, California Institute of Technology/NASA, Pasadena, CA

Alessandra Bertarini
IGG, University of Bonn & MPIfR, Bonn, Germany

David Gordon
NVI, Inc./NASA GSFC, Greenbelt, MD, USA

Jamie McCallum · Jim Lovell
University of Tasmania, Hobart, Tasmania, Australia

Axel Nothnagel
IGG, University of Bonn, Bonn, Germany

Keywords Astrometry, 24 GHz, quasar, VLBI, reference frame, ICRF

1 Introduction

High precision VLBI measurements of positions of extragalactic radio sources define and maintain the current International Celestial Reference Frame (ICRF2; Ma et al, 2009), which forms the underlying basis for positional astronomy. Unfortunately, at the standard S/X frequencies, many ICRF sources exhibit spatially extended intrinsic structures that may vary with time, frequency and baseline projection. Such structure can introduce significant errors in the VLBI measurements thereby degrading the accuracy of the estimated sources positions (Charlot, 1990) and thus the stability of S/X-band celestial reference frames (CRFs).

However, on VLBI scales at higher radio frequencies, these extragalactic radio sources tend to exhibit more compact source structure and reduced core-shift. Thus, astrometric VLBI observations at higher radio frequencies permit the construction of a more accurate and well defined CRF which will also be advantageous in tying the VLBI reference frame to optical reference frames such as Gaia (Mignard et al., 2016).

In the last few years, considerable work has been done and significant progress made on defining CRFs at higher radio frequencies. Astrometric and imaging observations by Lanyi et al. (2010) and Charlot et al. (2010) provided a foundation for the development of a reference frame at K-band. However, the Lanyi et al. (2010) catalogue consists of only 268 sources with weak coverage in the mid-south and no coverage in the far south, several localised regions with no sources, especially near the galactic plane and uncertainties in source positions at the 100 µas level (see Figure 1). Additional observations to improve the precision and spatial coverage of the K-band CRF were thus needed.

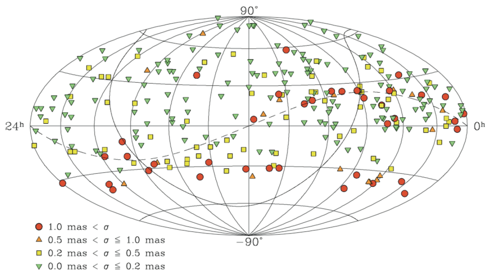

Fig. 1: Distribution of 268 sources at 24 GHz from ten, 24-hour observing sessions with the VLBA (Lanyi et al., 2010). Median formal uncertainties are 80 µas in $\alpha\cos(\delta)$ and 150 µas in δ.

Table 1: Summary of Observations.
*Sessions not yet included in the astrometric solution.

K-band Session Name	Date (yyyy-mm-dd)	K-band Session Name	Date (yyyy-mm-dd)
BR079A	2002.05.15	KS1601	2016.07.29
BR079B	2002.08.25	KS1602	2016.11.22
BR079C	2002.12.26	*KS1702**	*2017.04.12*
BL115A	2003.05.22	*KS1703**	*2017.04.23*
BL115B	2003.09.13	BJ083A1	2015.12.15
BL115C	2004.02.15	BJ083B	2016.01.28
BL122A	2004.12.14	BJ083C	2016.06.06
BL122B	2005.08.26	BJ083D	2016.06.20
BL122C	2006.07.09	UD001A	2017.01.08
BL122D	2007.03.30	UD001B	2017.01.26
BL151A	2008.07.10	UD001C	2017.02.23
BL151B	2008.12.18	UD001D	2017.03.04
BP125A	2006.06.04	*UD001E**	*2017.04.09*
BP125B	2006.06.11	*UD001F**	*2017.04.23*
BP125C	2006.10.20	*UD001G**	*2017.05.11*
KS1401	2014.05.04	*UD001H**	*2017.05.18*

Dedicated imaging and astrometric observations to improve the K-band CRF started in 2014. Our completed VLBA projects used a data rate of 2 Gbps achieving a four-fold increase in sensitivity to previous work allowing a tripling of the number of sources while simultaneously improving the precision. With the inclusion of archival K-band Galactic Plane observations and complementary observations in the Southern Hemisphere, there are now ~800 sources in the K-band CRF––comparable to the number of regularly observed S/X sources.

Our K-band CRF now has better precision than the international standard ICRF2 and better wRMS agreement with the Gaia data release 1 auxilliary catalog (Gaia DR1-aux; Mignard et al., 2016) than recent S/X CRFs. We are optimistic that these observations will become the core of a K-band contribution to the next generation international celestial reference frame, the ICRF3. In addition, multi-epoch maps will give us quantitative measures of the stability of the source structures. Preliminary imaging shows that these sources are compact on mas scales (de Witt et al., 2016).

2 Observations and Data Analysis

We completed observations for VLBA projects BJ083 (de Witt et al., 2016) and UD001. Each of the sessions was 24-hours in duration and we used a data rate of 2 Gbps. The scans were 120 seconds in duration and most sources were observed 3–4 times per session. We have also completed observations of five Southern Hemisphere sessions (KS1401 to KS1703), using the Hobart-26m and HartRAO-26m antennas. The sessions were all 24-hours in duration with a scan time of 2 minutes. Observations using a data rate of 2 Gbps started in August 2016. These Southern Hemisphere, single-baseline observations have already completed full sky coverage for the K-band CRF.

All of the sessions accumulated in all K-band work to date are listed in Table 1: 12 sessions from Lanyi et al. (2010), 3 VLBA Galactic Plane sessions from 2006 (Petrov et al., 2011), 5 Southern Hemisphere sessions from 2014, 2016 and 2017 and 12 VLBA sessions at 2 Gbps from 2015 to 2017. Only 26 of the 32 sessions listed were available to include in the astrometric solution presented in this paper at the time of publication. Sessions KS1702 and KS1703 as well as UD001E, F, G and H have not been included in the astrometric solution presented in § 3 and 3.

Correlation of the VLBI data since 2014 used the DiFX correlators (Deller et al., 2011) at Bonn University (KS sessions) or the VLBA (BJ083 and UD001 sessions). Fringe fitting was performed at the Bonn correlator using the Haystack Observatory Postprocessing System (HOPS) and the output converted into geodetic-style databases. Astrometric analysis of each session was made at the Goddard Space Flight Center (GSFC) using the Calc/Solve analysis package. A Solve global least squares solution was made using all the available sessions. The global solution solved for source positions, site positions, site velocities, and Earth Orientation Parameters (EOP). Our frame was aligned to ICRF2 with a no-net-rotation constraint using the 228 (of 295) ICRF2 defining sources in our data set.

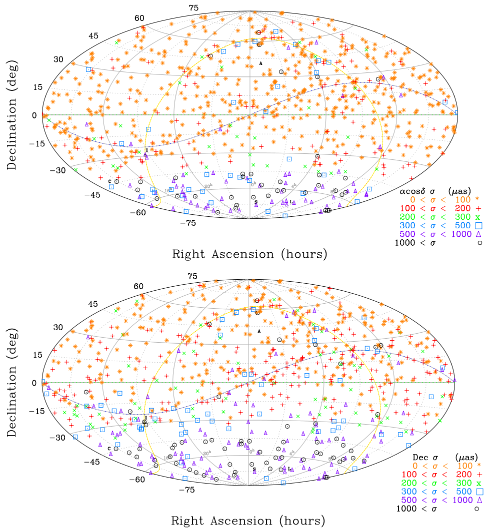

Fig. 2: The distribution of 788 sources at 24 GHz from twenty-six, 24-hour observing sessions (Lanyi et al., 2010; Petrov et al., 2011; de Witt et al., 2016). Parts a. and b. show the formal uncertainties in $\alpha\cos(\delta)$ and δ, respectively.

3 K-band Astrometric Catalog

There are now 788 sources in the K-band CRF, covering the full sky (Figures 2 and 3). The distribution of the formal position uncertainties from the K-band CRF are shown in Figure 2. The precision is much lower for $\delta < -45°$, where we only have a few sessions from single-baseline observations. Median formal uncertainties are 74 µas in $\alpha\cos(\delta)$ and 137 µas in δ. For comparison, the K and S/X median formal uncertainties for the 636 overlapping sources between K-band and ICRF2 and the 676 overlapping sources between K-band and the most recent S/X solution are listed in Table 2.

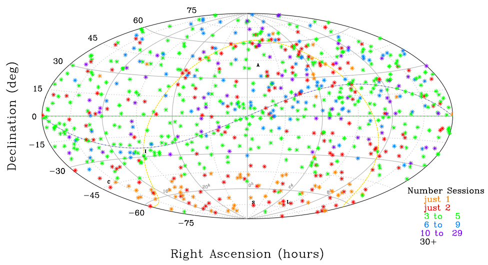

Fig. 3: The distribution of 788 sources at 24 GHz showing the number of sessions accumulated in all K-band work used in the astrometric solution presented in this paper.

Most of the VLBA's four-fold increase in sensitivity since earlier K-band reference frame work should translate into improved source position precision. The current K-band CRF shows source position precision improving as the number of delay measurements to the −0.6 power. We project improvement in precision with the addition of another 16 VLBA sessions (two sessions per month until around mid-2018), to ~38 and ~71 µas precision in $\alpha\cos(\delta)$ and δ, respectively. As summarized in Table 2, it can be seen that the current K-band CRF is already more precise than the ICRF2 and the projections indicate that the K-band CRF by mid-2018 may be comparable in precision to the current S/X frame.

The S/X CRF currently has only 794 sources with ten or more sessions per source. The distribution of sources in Figure 3 shows the number of K-band sessions accumulated per source. Considering that we need ~4-5 sessions to go through our list of 788 K-band CRF sources and assuming that we continue with two observing sessions per month, we project that we can meet the S/X standard for well observed sources (~10 sessions per source) by mid-2018.

Table 2: Median 1-σ formal uncertainties. Column 1 lists the band and date of catalog. Column 2 lists the number of sources or the number of overlapping sources between K and S/X catalogs, excluding sources with only one delay measurement and also outliers with > 5-σ differences in position between K and S/X catalogs.

Catalog	# Sources	$\alpha\cos(\delta)$ [µas]	δ [µas]
K-170324	768	74	137
K-projected	–	38	71
K-170324	636	66	122
S/X-ICRF2-090316	636	107	147
K-170324	676	70	129
S/X-170502	676	40	62

4 Catalog Comparisons

We compared our K-band astrometric catalog to the ICRF2 and the most recent S/X catalog (GSFC, S/X-gsfc-170502). We also compared the ICRF2 catalog to the most recent S/X catalog. For the various catalog comparisons we computed position differences in $\alpha\cos(\delta)$ and δ, respectively. Outlier sources, with more than 5-σ differences in position, were excluded. The results for all catalog comparisons are summarized in Table 3.

The current K-band CRF agrees about as well with the current S/X frame as the ICRF2 does, but with a much smaller $\Delta\delta$ vs. δ slope. The weighted RMS has also improved quite a bit with the recent S/X solution. In the K-band solution from Lanyi et al. (2010), the dominant systematic was the $\Delta\delta$ vs. δ slope at -4.7 ± 0.28 µas/deg, but we have reduce this slope to an insignificant -0.22 ± 0.13 µas/deg. However, there is a large

Table 3: Comparisons of astrometric catalogs at S/X and K bands. Column 1 lists the band and date of catalogs being compared. Column 2 lists the number of overlapping sources and column 3 lists the number of outliers with > 5-σ differences in position. Columns 4 & 5 list the $\Delta\alpha\cos(\delta)$ vs. δ slope and the $\Delta\delta$ vs. δ slope, respectively. Columns 6 & 7 list the associated weighted RMS differences about the weighted mean.

Catalogs Compared	# sources	# outliers (> 5-σ)	$\Delta\alpha\cos(\delta)$ vs. δ [µas/deg]	$\Delta\delta$ vs. δ [µas/deg]	wRMS $\alpha\cos(\delta)$ [µas]	wRMS δ [µas]
K-170324 – S/X-ICRF2-090316	636	13	-1.28 ± 0.14	1.18 ± 0.19	133	165
K-170324 – S/X-170502	676	24	-1.18 ± 0.08	-0.22 ± 0.13	105	133
S/X-170502 – S/X-ICRF2-090316	2977	24	0.04 ± 0.07	1.01 ± 0.08	116	138

Table 4: Comparisons of astrometric VLBI catalogs and the Gaia DR1-aux catalog (Jacobs et al., 2017). Column 1 lists the band and date of catalogs being compared, column 2 gives the number of overlapping sources. Columns 3 & 4 list the number and % of outliers with > 5-σ differences in position. Columns 5 & 6 list the associated weighted RMS differences about the weighted mean. Columns 7, 8 & 9 give the rotational alignment angles.

Catalogs Compared	# sources	# outliers (> 5-σ)	% outliers (> 5-σ)	wRMS $\alpha\cos(\delta)$ [µas]	wRMS δ [µas]	R_x [µas]	R_y [µas]	R_z [µas]
K-170324 – Gaia DR1-aux	481	13	2.6	439	455	100 ± 24	-7 ± 21	0 ± 23
S/X-170502 – Gaia DR1-aux	1984	106	5.0	536	544	32 ± 13	5 ± 11	28 ± 13

remaining systematic in $\Delta\alpha\cos(\delta)$ vs. δ at -1.18 ± 0.08 µas/deg.

Jacobs et al. (2017) also compared the K and S/X catalogs to the Gaia DR1-aux optical catalog. The summary presented in Table 4 hints that results improve by going to higher radio frequencies, with K-band showing a lower percentage of outliers and smaller scatter versus Gaia. Outliers with more than 5-σ differences in position were excluded from the comparison. It should be noted, however, that the results presented in Table 4 do not use the exact same objects for the S/X vs. Gaia and K vs. Gaia comparisons.

5 Ionosphere Calibration

Delays due to the ionosphere were computed as described in Lanyi et al. (2010), using GPS ionosphere maps produced by JPL. These maps are given at 2-hour intervals and have a resolution of 2.5° by 5° in latitude and longitude, respectively. Thus this method cannot account for short-term ionospheric variations, but should be able to remove a large fraction of the effects of the more slowly varying components of the ionosphere and greatly reduce the systematic effects of the ionosphere.

In Figure 4 we show the effect of including GPS obtained ionosphere calibration at K-band. On average the ionospheric calibrations do not affect right ascensions, but do make a 400 µas tilt in declinations. However, judging from the insignificant $\Delta\delta$ vs. δ slope of our GPS calibrated K vs. direct dual-band calibrated S/X (Table 3), we do not appear to be limited by the ionosphere. We also note that the current solar cycle is one of the weakest in the last century and this weak cycle is heading into its minimum. This means that the near future is expected to be an optimal time for single frequency observations.

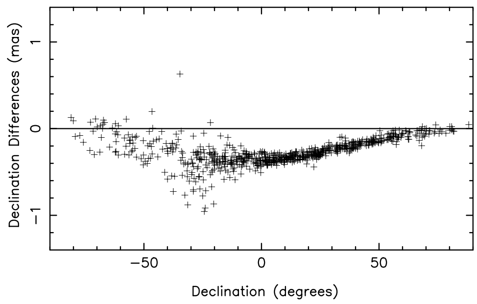

Fig. 4: The effect of including GPS obtained ionosphere calibration on $\Delta\delta$ (δ with GPS ionosphere calibration applied minus δ without GPS ionosphere calibration applied) as a function of δ, at K-band. The effect on RA (not shown) was negligible.

6 Conclusions

Our goal is to continue the improvement of the K-band CRF to match or exceed the precision of the future S/X and Gaia frames. Our current K-band frame is already more precise than the ICRF2, and the K-band precision is projected to be comparable to the current S/X frame at mid-2018. Our K-band results also have less scatter relative to Gaia than S/X catalogs and have a lower percentage of outliers. We believe that compared to the current SX-based IAU standard, the K-band work is a much more efficient use of resources to achieve a given level of astrometric precision while being far less susceptible to astrophysical systematics. Work now in progress to realize the full potential of the K-CRF includes increasing the temporal resolution of the GPS calibrations to 15 minutes and gathering more southern data including overlapping north-south baselines.

Noting that current S/X precision is very close to the systematic source structure floor of ~30 µas (Le Bail, 2017), S/X will soon not be able to improve any further while K-band's structure floor is expected to be a few times smaller allowing for improvement for years to come. K-band also compares well to S/X in the number of regularly observed sources. We are well on our way towards realizing K-band's potential to be the basis of a world class reference frame.

Acknowledgements

 U.S. Government sponsorship acknowledged for the work done at JPL-Caltech under a contract with NASA. The VLBA is operated by the LBO since Oct. 2016 and previously by the NRAO, both facilities of the National Science Foundation operated under cooperative agreement by Associated Universities. The authors gratefully acknowledge use of the VLBA under the USNO's time allocation. This work supports USNO's ongoing research into the celestial reference frame and geodesy. HartRAO is a facility of the National Research Foundation (NRF) of South Africa. The Hobart telescope is operated by the University of Tasmania and this research has been supported by AuScope Ltd., funded under the National Collaborative Research Infrastructure Strategy (NCRIS).

References

Charlot P (1990) Radio-source structure in astrometric and geodetic very long baseline interferometry. *AJ*, 99, 1309.

Charlot P, Boboltz D A, Fey A L, Fomalont E B, Geldzahler B J, Gordon D, Jacobs C S, Lanyi G E, Ma C, Naudet C Jâ Romney J D, Sovers O J, Zhang L D (2000) The Celestial Reference Frame at 24 and 43 GHz. II. Imaging. *AJ*, 139, 1713.

Deller A T, Brisken W F, Phillips C J, Morgan J, Alef W, Cappallo R, Middelberg E, Romney J, Rottmann H, Tingay S J, Wayth R (2011) DiFX-2: A More Flexible, Efficient, Robust, and Powerful Software Correlator. *PASP*, 123, 275.

de Witt A, Bertarini A, Jacobs C S, Quick J, Horiuchi S, Jung T, Lovell J, McCallum J, Bourda G, Charlot P (2016) Completing the K-band Celestial Reference Frame in the North. In: D. Behrend, K. D. Baver, K. L. Armstrong (eds.), *IVS 2016 General Meeting Proceedings "New Horizons with VGOS"*, NASA/CP-2016-219016, 302–306

Jacobs C S, Bertarini A, de Witt A, Garcia-Miro C, Gordon D, Horiuchi S, Lovell J, McCallum J, Mercolino M, Quick J, Snedeker L, Bourda G, Charlot P (2017) Tying Multiple Radio Wavelength Celestial Frames to the Gaia Optical Frame. Presented at: *Astrometry & Astrophysics in the Gaia Sky, IAU Symposium 330*, https://iaus330.sciencesconf.org/data/pages/Jacobs_Mac_Preview.pdf

Lanyi G E, Boboltz D A, Charlot P, Fey A L, Fomalont E B, Geldzahler B J, Gordon D, Jacobs C S, Ma C, Naudet C J, Romney J D, Sovers O J, Zhang L D (2010) The Celestial Reference Frame at 24 and 43 GHz. I. Astrometry. *AJ*, 139, 1695.

Le Bail K, Gordon D, Gipson J M, MacMillan D S (2017) Investigating the noise floor of VLBI source positions. In: R. Haas and G. Elgered (eds.), *Proc. 23rd EVGA Working Meeting*, 186–189.

Ma C, Arias E F, Bianco G, Boboltz D A, Bolotin S L, Charlot P, Engelhardt G, Fey A L, Gaume R A, Gontier A-M, Heinkelmann R, Jacobs C S, Kurdubov S, Lambert S B, Malkin Z M, Nothnagel A, Petrov L, Skurikhina E, Sokolova J R, Souchay J, Sovers O J, Tesmer V, Titov O A, Wang G, Zharov V E, Barache C, Boeckmann S, Collioud A, Gipson J M, Gordon D, Lytvyn S O, MacMillan D S, Ojha R (2009) The Second Realization of the International Celestial Reference Frame by Very Long Baseline Interferometry. *IERS Technical Note 35*.

Mignard F, Klioner S, Lindegren L, Bastian U, Bombrun A, Hernández J, Hobbs D, Lammers U, Michalik D, Ramos-Lerate M, Biermann M, Butkevich A, Comoretto G, Joliet E, Holl B, Hutton A, Parsons P, Steidelmüller H, Andrei A, Bourda G, Charlot P (2016) Gaia Data Release 1. Reference frame and optical properties of ICRF sources. *A&A*, 595, 16.

Petrov L, Kovalev Y Y, Fomalont E B, Gordon D (2011) The Very Long Baseline Array Galactic Plane Survey-VGaPS. *AJ*, 142, 35,

Investigating the Noise Floor of VLBI Source Positions

K. Le Bail, D. Gordon, J. M. Gipson, D. S. MacMillan

Abstract The noise floor of ICRF2 was at the level of 40μas. After eight years of various improvements (technique, measurements, models,...), we expect this level to have decreased significantly. The objective of this paper is to determine the noise floor of each source of the current VLBI solution using the Allan variance. The Allan variance quantifies the variance of time series at different sample periods, but it also gives access to time series statistical characteristics such as the type of noise in the series. When a time series exhibits flicker noise, it can be interpreted that any additional data will not add any more information and that the noise floor has been reached. For each source in the latest GSFC solution, we estimate the noise of the time series as a combination of white noise and flicker noise using least-squares on the Allan variance log-log curves. Each source is then quantified by its levels of white noise and flicker noise. From the latest GSFC solution (2017a) of time series for 4241 sources, 157 sources are selected after applying various criteria to obtain significant statistics, like the duration of the time series or the time span in between two observations. The Allan variance analysis determines two sets of sources: the dominant noise is flicker noise for 91 sources, and white noise for 66 sources. Some of the sources have noise floor values as low as 5 μas.

Keywords VLBI source positions, noise floor

1 Introduction

Many improvements were made since the ICRF2 was adopted by the IAU in 2009 replacing the ICRF1 on January 1, 2010 (see Table 1). In the eight years since ICRF2, the number of delay observations has more than doubled. There have been more than a thousand additional sources observed in S/X-band. And 675 sources have been now observed in X/Ka-band and 800 in K-band.

Karine Le Bail · David Gordon · John M. Gipson · Dan MacMillan
NVI, Inc. @ NASA/GSFC, 8800 Greenbelt Rd, Greenbelt, MD 20770, USA

Table 1: ICRFs evolution.

Parameter	**ICRF1** (1997)	**ICRF2** (2010)	**ICRF3** (2018)
Observation Dates	08/1979 - 07/1995 (16 years)	08/1979 - 03/2009 (29.5 years)	08/1979 - 12/2017 (38.5 years)
# Observations (group delays)	1.6M S/X	6.5M S/X	15 M S/X + X/Ka + K
# Defining Sources	212	295	200-300
# Sources S/X X/Ka K	608	3414	4400+ 675 800
Noise Floor	250 μas	40 μas	20-30 μas
Axis Stability	20 μas	10 μas	< 10 μas

The computation of the ICRF2 noise floor was done by a decimation test (IERS TN35, 2009) from the GSFC solution gsf08b. All experiments were ordered chronologically and divided into two sets selected by even or odd session to keep the same core network of observing stations. The declination and right ascension noise were then computed for each 15^{o} declination band in each solution derived from differences between positions in the two decimation solutions. Based on the number of observing sessions, the noise floor for declination and right ascension were 25 μas and 15 μas respectively. The ICRF2 noise floor was finally set at a conservative value of 40 μas, almost six times lower than the ICRF1 noise floor.

ICRF3 is expected to be released in 2018. We expect the noise floor to decrease significantly. The purpose of this paper is to determine the noise floor of the latest GSFC solution as an estimate of what the noise floor will be for ICRF3. The GSFC solution is presented in Section 2. Section 3 describes the method of time series analysis and gives a short overview of the Allan variance which is the statistical tool used to access the noise floor per source. Section 4 presents the results. Section 5 discusses the limitations of this method applied to our data. Section 6 discusses further work that needs to be done.

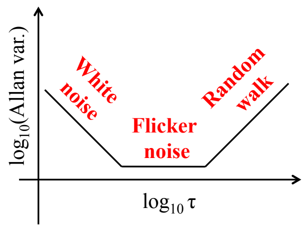

Fig. 1: Allan variance. Determination of noise scheme.

2 GSFC solution of source position time series - Description

In this paper we study the latest solution for source position time series processed at GSFC (gsf2017a), which was generated on April 14, 2017. It covers all databases from August 3, 1979 through March 27, 2017 for a total of 5696 sessions. In addition, it includes the VCS1-6, VCS-II, and UF1 A-D (VLBA) sessions. There are time series of positions for 4241 sources, but some of these are computed from only one epoch.

3 Computing noise floor with the Allan variance

The Allan variance is a statistical tool that gives the level and type of noise of a time series. For more details, the reader can refer to previous work in Le Bail and Gordon (2010) or from Allan (1966). The major drawback of this statistical tool when applied to VLBI position time series is that it has to be applied to regularly spaced time series. As with any other statistical tool, the significance of the results depends greatly on the number of points of the time series.

The observed VLBI data presents challenges for this statistical tool: there may be some large gaps between observations, the sessions may be scarce and/or the number of observations is limited. For these reasons, we chose to average the time series into three sets: yearly, 30-day, and 10-day averaged time series. In the case of a large gap, the portion of the time series after the large gap is the portion considered. We do not take into account data points before 1995 which are considered to be of lower quality.

Sources are then selected as follows.

1. GSFC solution gsf2017a: 4241 sources;
2. Sources with ten or more observations: 766 sources left.
3. Sources with good observation history (observed after 1995, more than five years of observation, more than two observations per session, more than one session per year, less than three years between two sessions, the number of additional points needed to regularize the series is less than 50% of the number of points in the series): 175 sources left.
4. Visual check of the homogeneity of the time series: 164 sources left.

The 164 remaining sources are then studied with the Allan variance and the type of noise is determined using the slope in the log-log plot of the Allan variance as a function of the sampling time (see Fig. 1).

4 Noise floor of GSFC solution 2017a

Out of the 164 sources studied, seven source series contained a random walk and were eliminated. These sources probably have too much structure for the Allan variance to be able to determine their noise. For the other 157 sources, we assumed that the noise is a combination of flicker noise and white noise. Using least-square estimation, we determined the level of noise for each noise type.

For 66 of the sources, the dominant noise is white noise, which implies that the quality of the data is still improving with time.

For the 91 remaining sources, the Allan variance curve shows flicker noise on the long-term, which means that the quality of the data is stabilized at a certain level of noise.

We determined the noise floor for each of these 157 sources by extracting the minimum of the Allan variance plot (curve $(log_{10}(AllanVariance), log_{10}(SamplingTime))$). Fig. 2 shows the values obtained for each source for each averaged time series (10-day averaging, 30-day averaging, and 1-year averaging). Plots for the 91 sources exhibiting flicker noise are on the left. Plots for the 66 sources exhibiting white noise are on the right.

For some sources, the noise floor is as low as $5\mu as$. It is obvious from Fig. 2 that the noise floor increases when the declination decreases. The sources in the south are scarce and may not be observed with as good geometry. This is also seen in the plots of the white noise sources: there are no sources south of $-50°$ that we stud-

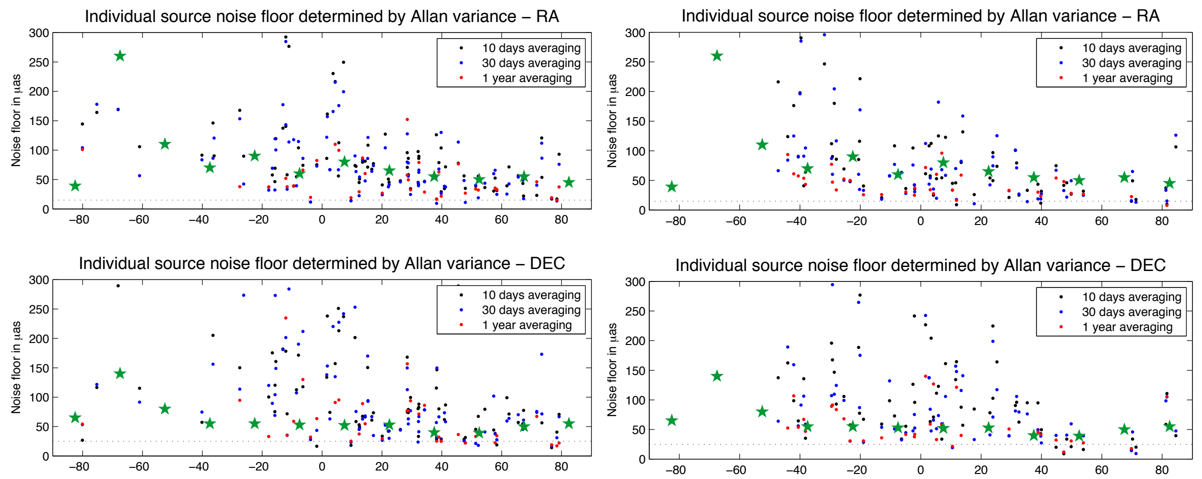

Fig. 2: Individual source noise floor determined by the Allan variance. Top: Right Ascension, bottom: Declination. Left: 91 sources exhibiting flicker noise. Right: 66 sources exhibiting white noise. Each plotted value is the minimum of the curve $(log_{10}(AllanVariance), log_{10}(SamplingTime))$. The green stars represent the values obtained by a decimation test to determine the noise floor of ICRF2 (IERS TN35, 2009). The dotted lines mark the overall noise floors determined in IERS TN35 (2009) (15 μas for Right Ascension and 25 μas for Declination).

ied, mostly due to the fact there are not enough observations for the sources in the south.

We added the information on the noise floor from IERS TN35 (2009) as green stars in Fig. 2. This may be difficult to compare as the IERS TN35 (2009) points represent an average value for all sources in a 15° declination bin, considering all sessions, whereas our study gives a point per source only for sources with good histories. However, the most recent GSFC solution seems to show an improvement in the noise floor compared to ICRF2.

5 Discussion

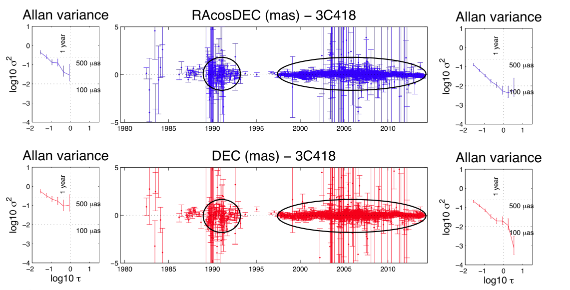

Fig. 3: Source 3C418. From poster presentation at the 2014 IVS GM Le Bail (2014). Time series (center) and two time spans Allan variance plots (right and left). The left plots show the Allan variances computed on 1989-1993 time series. The right plots show the Allan variances computed on 1997-2014 time series.

The homogeneity of the VLBI time series could also be debated. In Le Bail (2014), the source 3C418 is studied for two different time spans (from GSFC solution TS2014a). The Allan variance shows different determinations for the type and level of noise for these two different time spans (see Fig. 3). The noise of the time series studied on the time span 1989-1993 is determined to be white noise in both coordinates at the level of $200-400$ μas. The noise of the time series in the time span 1997-2014 is determined to be a combination of white noise and flicker noise for RAcos(DEC) and white noise for DEC with a noise level of 50 μas for RAcos(DEC) and 50 to 100 μas for DEC.

For some observed sources, it is apparent that the structure has a very strong effect. Fig. 4 illustrates this for the source 0607-157. The time series is presented along with the S-band images from the Bordeaux VLBI Image Database (BVID) at three different epochs (December 2008, July 2009, and October 2010). The change of structure of the source significantly impacts the time series.

6 Conclusion

The results of this study show that the noise floor of the current GSFC solution is lower than the estimated ICRF2 noise floor determined in IERS TN35 (2009). The two methods used are very different from each other, so to make a better comparison, we should apply our method to the 2009 ICRF2 time series.

With the imminent release of ICRF3, different analysis centers will submit their ICRF solutions. Among the Analysis Centers, there are different software packages, different models, and different processing strategies. It would be interesting to compare the noise floors

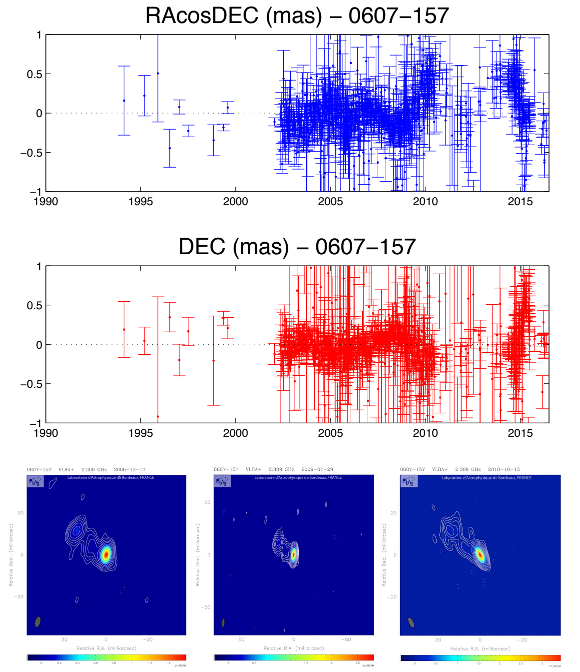

Fig. 4: Source 0607-157. Top: Time series from gsf2017a solution. Bottom: S-band images from BVID at three different epochs. From left to right: December 2008, July 2009, and October 2010.

of these different solutions as well as the final ICRF3 solution.

References

Allan D (1966) Statistics of Atomic Frequency Standards. In: *Proc. IEEE*, 54(2):221–230.

Fey A, Gordon D, Jacobs C S (eds.) (2009) The Second Realization of the International Celestial Reference Frame by Very Long Baseline Interferometry. Presented on behalf of the IERS / IVS Working Group, Alan Fey, David Gordon, and Christopher S. Jacobs (eds.). (IERS Technical Note; 35) Frankfurt am Main: Verlag des Bundesamts für Kartographie und Geodäsie, ISBN 3-89888-918-6.

Le Bail K, Gordon D (2010) Time-dependent Selection of an Optimal Set of Sources to Define a Stable Celestial Reference Frame. In: D. Behrend, K. Baver (eds.), *IVS 2010 General Meeting Proceedings "VLBI2010: From Vision to Reality"*, NASA/CP-2010-215864, 280–284.

Le Bail K, Gordon D, Gipson J M (2014) Evaluation of the Stability of ICRF2 in the Past Five Years using the Allan Variance. In: D. Behrend, K. D. Baver, K. L. Armstrong (eds.) *IVS 2014 General Meeting Proceedings "VGOS: The New VLBI Network"*, Science Press (Beijing), ISBN 978-7-03-042974-2, 395–398.

Two-component Structure of the Radio Source 0014+813 Using CONT14 Geodetic VLBI Observations

O. Titov, Y. Lopez, L. McCallum

Abstract We have developed a new approach to facilitate the structure delay for extended radio sources using the post-fit residuals calculated after adjustment of geodetic Very Long Baseline Interferometry (VLBI) observations by the standard method. No imaging of a radio source is required for that method. The simplest model of a radio source including two point-like components could be presented with four parameters (angular separation, orientation, flux ratio and difference of spectral indexes) at multi-baseline VLBI network for each baseline separately. We demonstrate the effectiveness of this approach on an example of radio source 0014+813 intensively observed during a two-week CONT14 campaign under the auspices of the International VLBI Service (IVS) in May 2014. Some large systematic differences in post-fit residuals for baselines of 5000 km and longer were detected. We estimated all four parameters for each baseline and determined the average characteristics of the 0014+813 radio structure at the frequency 8.4 GHz. The radio source is confirmed to consist of two components separated by 0.5 mas and aligned with a "north-south" direction. Implementation of the structure model to analysis of the CONT14 data set results in displacement of 0014+813 declination on 0.070 mas north with respect to its reference position.

Keywords VLBI, astrometry, active galactic nuclei, reference systems

Oleg Titov
Geoscience Australia, Australia

Yulia Lopez
Pulkovo Observatory, St. Petersburg, Russia

Lucia McCallum
University of Tasmania, Hobart, Australia

1 Introduction

At the milliarcsecond scale most frequently observed powerful extragalactic radio sources exhibit spatially extended intrinsic structures which are variable in both time and frequency. Such radio structures introduce sizeable effects in the VLBI measurements known as a structure delay (Charlot, 1990). That leads to astrometric coordinate instability 0.1-1 mas on timescale of months to years (Fey et al., 1997; Alberdi et al., 2000; Titov, 2007). First attempts modeling these effects starting circa 1980 (Charlot, 1990) have not shown success due to significant complication in radiostructure effect calculation both from astrophysical and astrometric VLBI observations (Charlot, 1990; Thomas, 1980; Sovers et al., 2002; Tornatore and Charlot, 2007). Recently, Xu et al. (2016) showed that the "closure delay" approach is capable to extract the structure effect from combination of the post-fit residuals of three baseline data. Nevertheless, this method meets other difficulties as it requires that observables from all three baselines should be available. Another suggestion by Charlot (1990) to fit the post-fit residuals for each individual baseline has not shown a progress so far. Thus, in this paper we first demonstrate the approach to facilitate the structure delay for extended radio sources using the post-fit residuals calculated after adjustment of geodetic Very Long Baseline Interferometry (VLBI) observations.

2 Processing CONT14-campaigns observations

For extended radio sources the structural delay can be so large (up to 500 ps) that the post-fit residuals have a noticeable systematic component considerably exceeding the stochastic errors. These systematics can be modeled by four parameters: angular separation between two components, mutual orientation angle, flux ratio and difference of spectral indexes (Charlot, 1990). We have applied this model to the radio source 0014+813, which was frequently observed during the two-week program CONT14 from May 6 to May 20, 2014 (Behrend et al., 2014). Located at high declination the radio source 0014+813 was observed during CONT14 round the clock (i.e. at any orientation of a baseline vector) by almost all baselines at the northern hemisphere. The quasar 0014+813 is known as one of the most powerful quasars in Universe (Hirabayashi et al., 1998; Ghisellini et al., 2009). It shows a powerful jet at 1.6 Ghz, oriented in the North-South direction at several mas from the core (Hirabayashi et al., 1998). At frequency of 8.4 GHz this jet lies at angular distance of 5 mas from the core (Fey and Charlot, 1997). Time series analysis of this object positions obtained with geodetic VLBI at 8.4 GHz reveal finding strong variations at declination in 1993-2010 with amplitude about 1 mas (Titov, 2007). During 1993–2002 the radio source 0014+813 was moving to the North, and after 2002 year to the South direction. At the same time interval its right ascension variation was negligible. Obviously, these variations are connected to the intrinsic structure variations. That is why we selected the radio source for search of the structure delay signal within the post-fit residuals after adjustment of the CONT14 VLBI observations.

3 Mathematical model of structure delay calculation

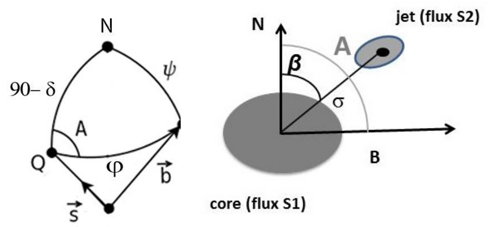

Fig. 1: Link of radio-structure and structure delay obtained from VLBI observations.

Let us consider the spherical triangle (Fig. 1) made of the baseline vector (**b**), radio source vector (Q) and the North Pole (N) in barycentric system. The spherical angles between the vectors create angles φ, ψ and $90° - \delta$. Variable angle A defines direction of the baseline projection vector **B** with respect to the N. Constant angle β, originated at the source core, defines the direction of the jet vector with respect to N. The vector **B** changes due to the Earth rotation and is aligned to the "source core" direction twice a day, with $A = \pm\beta$. Angle σ is the separation between core and jet.

In accordance to Charlot (1990) the structure delay could be presented by two terms, i.e.

$$\tau_1 = \frac{2\pi K}{\omega(1+K)} \frac{[1-\cos(2\pi R)]R}{K^2+2K\cos(2\pi R)+1}, \qquad (1)$$

$$\tau_2 = \frac{\Delta\alpha K}{\omega} \frac{\sin(2\pi R)}{K^2+2K\cos(2\pi R)+1}, \qquad (2)$$

where K is the ratio of two fluxes (Eq. 3). And R is the ratio between the separation of the components and the projection of the baseline along the "source-jet" direction (see Eq. 4),

$$K = \frac{S_2}{S_1}, \qquad (3)$$

$$R = \frac{B}{\lambda}\sigma_{12}\cos\beta\sin\varphi, \qquad (4)$$

where ω is the interference frequency, σ_{12} is the separation on Fig. 1, $\Delta\alpha = \alpha_1 - \alpha_2$ is the difference between the spectral indices of both components, λ is the wavelength and β is the jet azimuth (Fig. 1).

The phase centre of an extended radio source is referred to the radio source catalogue position. This lies between the core and jet in such way that $\sigma_{12} = \sigma_1 + \sigma_2$, where σ_1, σ_2 are the angles between the phase centre and the components ♯1 and ♯2, correspondingly. As the phase centre has not marked on the sky, the two angles are introduced mathematically, i.e. $\sigma_1 = \frac{S_2}{S_1+S_2}\sigma_{12}$. Then σ_1 could be calculated using Eq. 3 as follows:

$$\sigma_1 = \frac{K}{K+1}\sigma_{12} \qquad (5)$$

finally,

$$\sigma_2 = \sigma_{12} - \sigma_1. \qquad (6)$$

4 Results of applying model to 0014+813

The post-fit residuals of all baselines were approximated using Eq. 1 and Eq. 2 by searching of all possible combinations of all four parameters in a reasonable range (R from 0.3 to 3.0 with step size 0.15; K from 0.1 to 0.9 with step size 0.05; phase β from 60° to 240° with step size 12° and $\Delta\alpha$ from −1 to −5 with step size 0.133). The combination, providing the least weighted rms value, was chosen.

Fig. 2, 3 show the residuals and their fitting by the model (Eq. 1, Eq. 2) for four baselines. The coefficients are in Table 1 and Table 2. For shorter baselines the residuals do not reveal any special pattern, so only

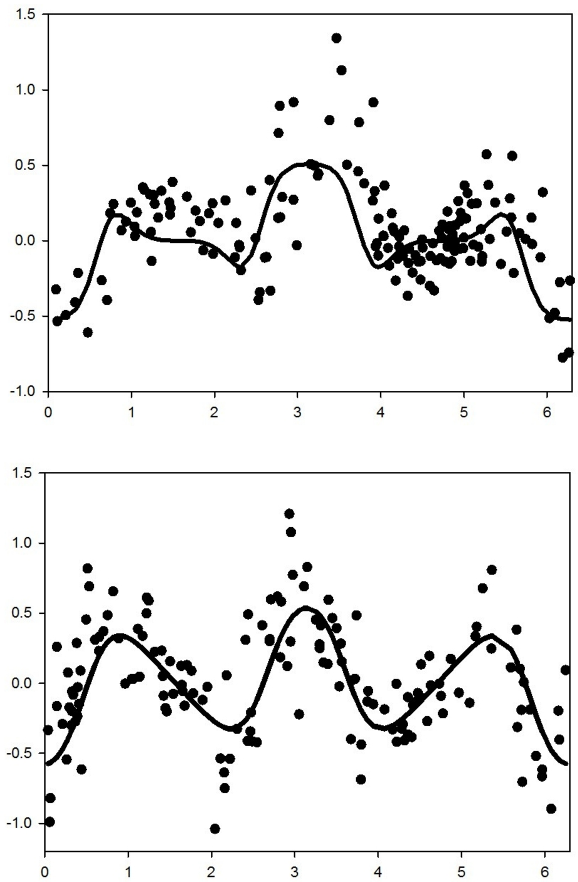

Fig. 2: Post-fit residuals (dots) and modeling (line) for Wettzell-Westford (upper) and Tsukub32 - Kokee (lower), unit: cm vs radians.

baselines longer than 5000 km needs to be modelled. It is essential that for the longest baselines the modeling requires both Eq. 1 and Eq. 2 as the fitting degrades without implementation of $\Delta\alpha$. Its estimate could reach $\Delta\alpha = -5$, and it is not clear whether this is caused by real nature of the active nuclei or some hidden instrument errors.

Table 1: Individual combinations of parameters for model fitting for some short baselines, as example.

Parameter	Wettzell – Onsala60	Wettzell – Matera	Wettzell – Yebes40M	Matera – Yebes40M
B (km)	920	990	1575	1667
R	2.70	1.65	1.65	1.35
K	0.10	0.10	0.20	0.20
β (deg)	84	168	192	156
$\Delta\alpha$	−1.0	−2.1	−1.0	−1.0
σ_{12} (ms)	0.25	0.15	0.28	0.23
rms (cm)	0.92	0.78	0.74	0.54
N	174	168	187	174

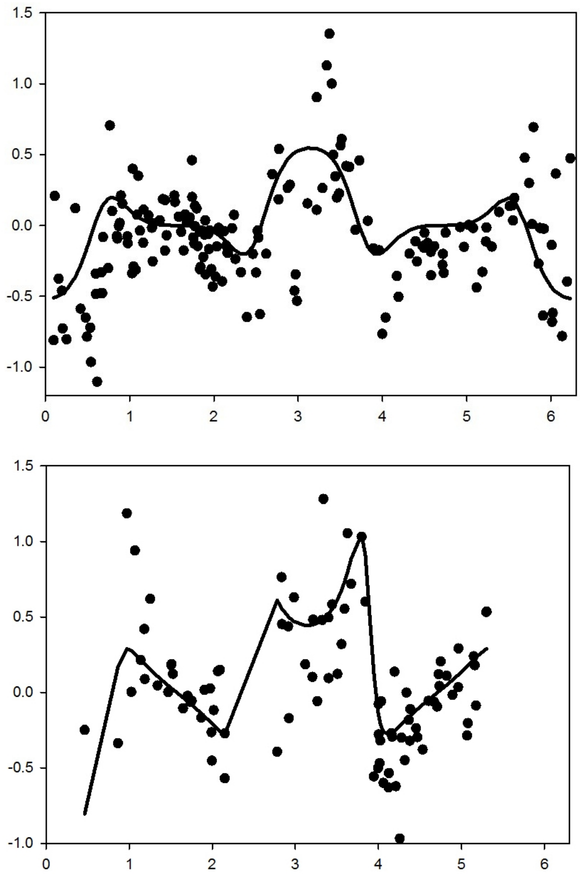

Fig. 3: Post-fit residuals (dots) and modeling (line) for Onsala60-Westford (upper) and Wettzell - Kokee (lower), unit: cm vs radians.

Table 2: Individual combinations of parameters for model fitting for some long baselines, as example.

Parameter	Wettzell – Westford	Tsukub32 – Kokee	Onsala60 – Westford	Wettzell – Kokee
B (km)	5998	5755	5601	10357
R	0.60	0.60	0.60	0.45
K	0.40	0.40	0.45	0.65
β (deg)	168	180	168	180
$\Delta\alpha$	−2.5	−5.0	−2.2	−3.9
σ_{12} (ms)	0.17	0.17	0.19	0.18
rms (cm)	0.24	0.30	0.33	0.32
N	163	150	173	91

In accordance with Charlot (1990), a standard two-component model of an extended synchrotron emitting radio source consists of an optically thick core with a positive spectral index ($\alpha_1 = +2.5$) and an optically thin jet with a negative spectral index ($\alpha_2 = -2.5$). More details are given by Dulk (1985). A chance of enlarging of the difference σ_{12} for extragalactic radio sources needs to be investigated.

5 Estimation of 0014+813 daily coordinate correction using structure delay model

Calculations of post-fit residuals were done in accordance with IERS Conventions 2010 (Petit and Luzum, 2010) by OCCAM (Titov et al., 2004) and VieVS (Böhm et al., 2009). The results obtained with both software are consistent. More detailed analysis is done with OCCAM only.

Fig. 4 shows daily estimates of the 0014+813 positions with respect to the ICRF2 coordinates. The correction to RA are small, whereas corrections to Dec vary from −0.4 to −0.7 mas with the mean value of −0.513 mas.

Fig. 5 and Table 3 show the effect of application of the structure delay model. The corrections to RA did not change essentially. The corrections to Dec shifted to the ICRF2 catalogue position (mean value −0.442 mas). The weighted rms reduced from 0.069 mas to 0.053 mas followed by improvement of the mean value uncertainty from 0.018 mas to 0.013 mas.

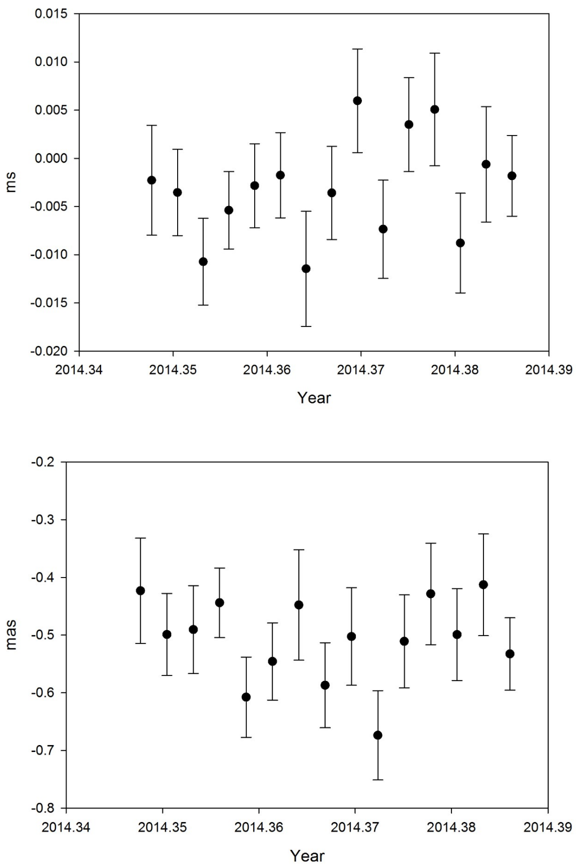

Fig. 4: Daily corrections to 0014+813 RA (upper) and Dec (lower) during CONT14 without application of the structure delay model.

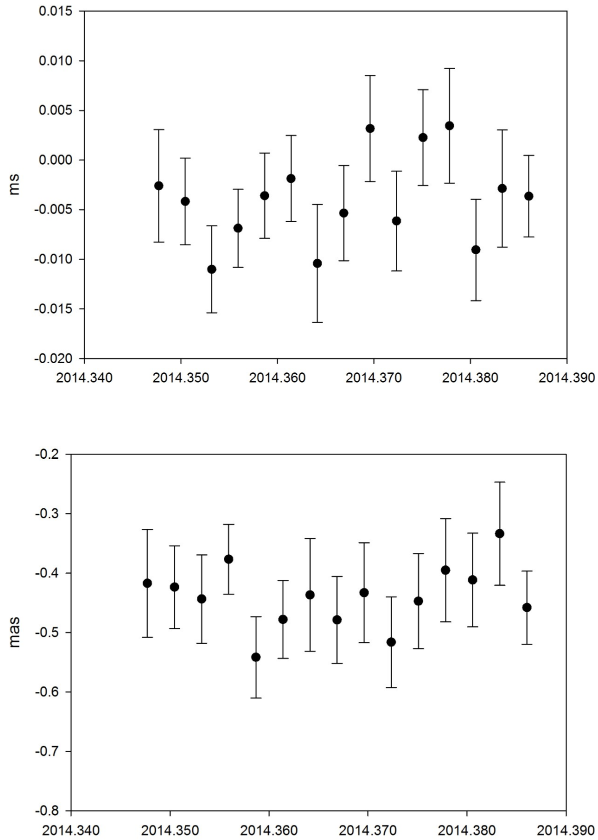

Fig. 5: Daily corrections to 0014+813 RA (upper) and Dec (lower) during CONT14 after application of the structure delay model.

We conclude that the jet located at scale of 5-10 mas does not affect the positions of 0014+813 at 8.4 GHz. Another jet at sub-mas scale is likely to exist and it should be responsible for the strong structure delay effect observed at post-fit residuals for baselines longer than 5000 km. The model needs both basic equations 1 and 2 to be used because the visual systematic pattern backs the large difference of the core and jet spectral indices. It is not clear whether the difference is caused by the real nature of the non-thermal emission or it is exaggerated by some instrumental factors.

Table 3: Comparison of the mean positions of radio source 0014+813 for CONT14 with and without application of the structure delay model.

Solution	Without structure delay	With structure delay
Mean RA correction (μsec)	-3.1 ± 1.2	-4.2 ± 1.1
Mean DE correction (μas)	-0.513 ± 0.018	-0.442 ± 0.013
Wrms on RA (μsec)	4.7	4.1
Wrms on DE (μas)	69	53

6 Acknowledgment

The paper is published with the permission of the CEO, Geoscience Australia

References

Alberdi A, Gómez J L, Marcaide J M, Marscher A P, Pérez-Torres M A (2000) 4C 39.25: Witnessing the interaction between a moving and a stationary component *Astron. Astrophys.*, 361, 529–534.

Behrend D, Thomas C, Himwich E, MacMillan D (2014) CONT14: Preparation and Prospects. In: D. Behrend, K. D. Baver, K. L. Armstrong (eds.), *IVS 2014 General Meeting Proceedings - "VGOS: The New VLBI Network"*, Science Press (Beijing), 196–200.

Böhm J, Böhm S, Nilsson T, Pany A, Plank L, Spicakova H, Teke K, Schuh H (2012) The new Vienna VLBI Software VieVS. In: S. Kenyon, M. C. Pacino, U. Marti (eds.) *Proc. IAG Scientific Assembly 2009*, IAG Symposia Series, 136, 1007–1011, doi:10.1007/978-3-642-20338-1_126.

Charlot P (1990) Radio-source structure in astrometric and geodetic very long baseline interferometry. *Astron. J.*, 99, 130–1326, doi:10.1086/115419.

Dulk G A (1985) Radio Emission from the Sun and Stars. *Annual Review of Astronomy and Astrophysics*, 23, 169–224, doi:10.1146/annurev.aa.23.090185.001125.

Fey A, Charlot P (1997) VLBA Observations of radio reference frame sources. II. Astrometric suitability based on observed structure. *Astroph. J. Suppl.*, 111, 95–142, doi:10.1086/313017.

Fey A, Eubanks M, Kingham K (1997) The Proper Motion of 4C 39.25. *Astron. J.*, 114, 2284, doi:10.1086/118648.

Ghisellini G et al. (2009) MNRAS, 399, 24 (2009).

Hirabayashi H, Hirosawa H, Kobayashi H et al. (1998) Overview and Initial Results of the Very Long Baseline Interferometry Space Observatory Programme. *Science*, 281(5384), 1825–1829, doi:10.1126/science.281.5384.1825.

Petit G, Luzum B (eds.) (2010) IERS Conventions (2010). *IERS Technical Note No. 36*, Frankfurt am Main: Verlag des Bundesamts für Kartographie und Geodäie, 179 pp., ISBN 3-89888-989-6.

Sovers O J, Charlot P, Fey A L, Gordon D (2002) Structure Corrections in Modeling VLBI Delays for RDV Data. In: N. R. Vandenberg, K. D. Baver (eds.) *IVS 2002 General Meeting Proceedings*, NASA Goddard Space Flight Centre, 243–247.

Thomas J (1980) NASA-JPL Publ., Pasadena, p. 80.

Titov O (2007) Apparent proper motions of radio sources from geodetic VLBI data *Astronomy Letters*, 33(7), 481–487, doi:10.1134/S1063773707070055.

Titov O, Tesmer V, Böhm J (2004) OCCAM v.6.0 Software for VLBI Data Analysis. In: N. R. Vandenberg, K. D. Baver (eds.) *IVS 2004 General Meeting Proceedings*, NASA/CP-2004-212255, 267–271.

Tornatore V, Charlot P (2007) The impact of radio source structure on European geodetic VLBI measurements. *J Geod*, 81, 469–478, doi:10.1007/s00190-007-0146-0.

Xu M H, Heinkelmann R, Anderson J A, Mora-Diaz J, Schuh H, Wang G L (2016) The Source Structure of 0642+449 Detected from the CONT14 Observations. *Astron. J.*, 152, 151, (2016). doi:10.3847/0004-6256/152/5/151.

Near-Field VLBI Delay Models – Implementation and Testing

F. Jaron*, S. Halsig, A. Iddink, L. McCallum, A. Nothnagel

Abstract VLBI observations of Earth satellites are of growing interest for geodetic applications, one reason being the possibility to improve the frame ties between ITRF and ICRF. The analysis chain for geodetic near-field VLBI observations, however, is still under construction, one important part being the modelling the VLBI delay. Near-field targets require special delay models, because the conventional models assume the observed target to be at infinite distance. Here we briefly present the theoretical background of near-field delay modelling and, in particular, the implementation of the Sekido and Fukushima (2006) and Duev et al. (2012) models into the VLBI analysis software ivg::ASCOT. We compare results to data acquired through VLBI observations of GPS satellites. We further investigate differences between the results obtained by our implementatiuciaons of the two models, and we discuss possibilities of simplification and optimization of the models for the special case of satellites orbiting the Earth observed by terrestial VLBI.

Keywords VLBI near-field models, geodetic VLBI, ivg::ASCOT

1 Introduction

The usual geodetic VLBI experiment consists in observing quasars (see, e.g., Sovers et al., 1998), i.e., natural radio sources emitting a noise-like signal with a flat spectrum (see, e.g., Romero et al., 2017, for a recent review), located in the far-field of the interferometer. Being in the far-field in this context means that the wavefronts of the observed signals appear as plane waves upon their arrival at the baseline (see, e.g., Ch. 2 in Thompson et al., 2017). In this case the IERS Conventions (2010) VLBI delay model can be applied.

There are, however, geodetic applications involving VLBI observations of sources which are located sufficiently close-by such that curvature of the wavefronts can no longer be neglected. Such applications include spacecraft tracking and observations of Earth satellites. The latter is of particular interest for geodesy, because it allows for better frame ties between celestial and terrestial reference frames (Plank, 2013). VLBI observations of near-field targets require appropriate delay models as developed by Sekido and Fukushima (2006, SF06 hereafter) and Duev et al. (2012, D+12 hereafter).

After briefly introducing the concepts behind near-field VLBI delay models in Sect. 2 we give some details about our implementation of the SF06 and the D+12 model in Sect. 3, where we discuss the issue of orbital information, comparison of the computed delays with observational data as well as comparison of the models against each other, and optimization of the models for the special case of terrestial VLBI observations of Earth satellites. Concluding in Sect. 4 we note that linearizing the satellite trajectory (Sect. 3.4) and formulation of the delay model in the GCRS (Sect. 3.5) leads to the existence of an analytical delay formula (Jaron et al., in prep.).

2 Near-Field Delay Modelling

The task of every VLBI delay model is to compute the difference in reception times of a signal at one station relative to the reception time of the same signal at another station. In near-field VLBI the situation is as follows: A moving target emits a radio signal at position x_0

* This research is supported by the Deutsche Forschungsgemeinschaft, DFG, project number No 318/14-1.

Frédéric Jaron · Sebastian Halsig · Andreas Iddink · Axel Nothnagel
Institute of Geodesy and Geoinformation – IGG Bonn, Nußallee 17, DE-53115 Bonn, Germany

Lucia McCallum
University of Tasmania, School of Physical Sciences, Private Bag 37, Hobart, 7001, Australia

at time t_0, the signal is received at station 1 at time t_1, and after a certain delay τ the signal is received at station 2 at time t_2, i.e., $\tau = t_2 - t_1$. The reference time for the delay is by convention the time t_1 of reception of the signal at station 1, $\tau = \tau(t_1)$. The time t_0 of emission of the signal, however, is not known a priori and has to be determined by solving the light-time equation,

$$t_0 = t_1 - \frac{|x_1(t_1) - x_0(t_0)|}{c} - \tau_{gr}, \qquad (1)$$

where τ_{gr} denotes the gravitational delay[2]. In general the light-time-equation has to be solved numerically and precise a priori knowledge about the trajectory $x_0(t)$ of the source is essential for this step.

Solving Eq. (1) is common to both the SF06 and the D+12 model. The next step is different:

- SF06 construct a “pseudo source vector” (see their Fig. 1 and their Eq. (12)) in order to derive a formula (their Eq. (20)) for the delay which bears a certain resemblence to the conventional far-field VLBI delay model (cf. Eq. (11.9) in IERS Conventions 2010).
- D+12 explicitely solve the second light-time-equation, i.e., the one for the signal propagation path from the source to station 2, fixing t_0 and solving for t_2.

For further details about these two delay models the reader is referred to the original papers. A short review of these can also be found in Jaron et al. (2017).

3 Implementation and Testing

We have implemented both the SF06 and the D+12 model in the VLBI analysis software ivg::ASCOT (Artz et al., 2016; Halsig et al., 2017)[3], written in C++. We solve the light-time-equation (1) with the Newton-Raphson method, which takes four iterations on average.

In order to test our implementation of the near-field VLBI delay models by SF06 and D+12 we make use of a session of VLBI observations of four GPS satellites carried out on August, 24, 2015 on the baseline Ceduna-Hobart26 (Plank et al., 2017).

[2] The gravitational is computed according to Eq. (17) in SF06. In our cases, however, the gravitational delay has always been in the order of 1 ps.

[3] The VLBI analysis software ivg::ASCOT is developped at the IGG in Bonn and is a toolbox for analysis, scheduling, and combination. Further information is available at `http://ascot.geod.uni-bonn.de/`.

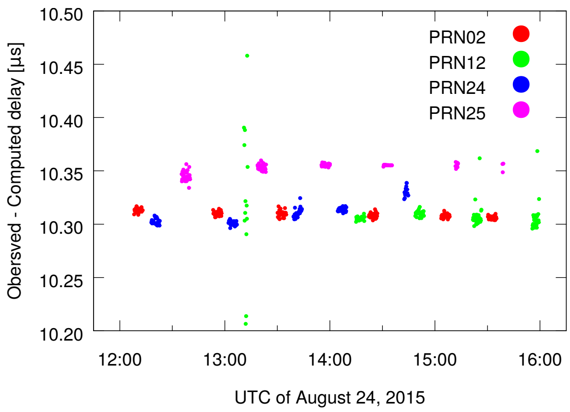

Fig. 1: Observed minus computed delays. The observed group delays are obtained by VLBI observations of GPS satellites on the baseline Ceduna-Hobart26 (Plank et al., 2017). The computed part is the result of our implementation of D+12, the results for SF06 look the same on this scale (see, however, Fig. 2).

3.1 Orbital Information

We use sp3 final ephemerides[4] as a priori information about GPS orbits. The orbital information is given in the form of text files[5] containing the three-dimensional position of every GPS satellite with a time resolution of 15 minutes. We interpolate all positional information within six hours around the considered epoch using Neville’s method. Since the variable storing the epoch has to contain the full information about the date we decided to store the date in the format of modified julian date (MJD). Using a regular double precision floating point number, however, would result in microseconds precision only, which is to coarse for our purpose. On the machine that we tested the implementation on, use of the data type “long double” results in twice the number of bytes reserved for the variable (“double” has 8 bytes, “long double” has 16 bytes). In this way we are able to evaluate the interpolation directly during the iteration.

Beside the position of the satellite, we use Neville’s method also to compute the instantaneous velocity of the satellites, a quantity which is necessary for solving the light-time-equation with the Newton-Raphson method and also for linearizing the trajectory of the satellite (as discussed in Sect. 3.4).

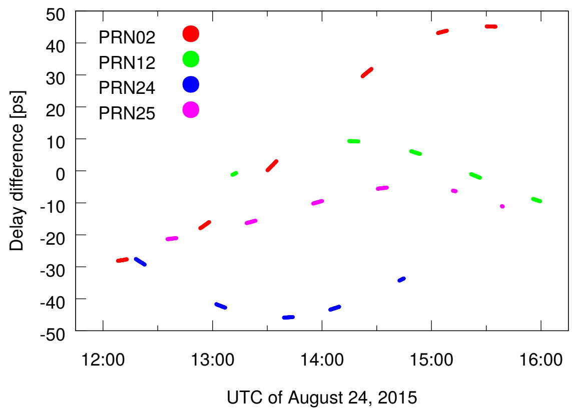

Fig. 2: Difference between the dalay computed with the SF06 model and the D+12 model, plotted against observational time.

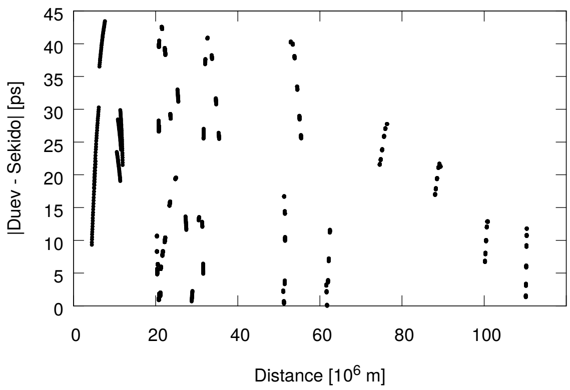

Fig. 3: Difference between the SF06 and the D+12 model plotted against the distance of the satellite from the middle of the baseline. Although there is not any obvious functional relationship visible here, there seems to be a tendency of smaller differences towards longer distances.

3.2 Comparison to Observational Data

Figure 1 shows the observed minus computed delays against observational time, shown here are the results for the D+12 model, the results for the SF06 model look indentical in the plotted scale (for a plot of the difference between the two models see Fig. 2). The overall offset of $\sim 10.3\,\mu$s can be explained as a clock offset between the stations. The origin of the systematic trends, which are even different for the individual satellites, is still under investigation, possible explanations include problems with the tracking, the unknown phase-center of the antenna array onboard the GPS satellites, and also the characteristics of the emitted signal itself.

3.3 Differences between the Models

Figure 2 shows the differences between the delays computed with the two models. For the example session considered here these differences are in the range of $\pm$50 ps, and there are again systematics trends for the individual satellites. Searches for a functional relationship of the model differences with geometrical or kinematical parameters as, e.g., elevation or the velocity of the satellite have so far remained elusive.

We investigated a possible relationship between the distance of the target from the observing telescopes. For that purpose we simulated a satellite on different orbital heights with a velocity a satellite would have at that height. We modified the sp3 final file accordingly and the remainder of the analysis chain was left unchanged. In Fig. 3 the resulting model differences are plotted against the distance of the satellite from the middle of the baseline Ceduna-Hobart26. A distinct functional relationship is not perceivable in this plot, but there seems to be a tendency of smaller differences as the distance increases. We have not found a difference grater than 50 ps in any comparison between the two models.

[4] Available, e.g., at `https://igscb.jpl.nasa.gov/components/prods_cb.html`.

[5] Detailed description at `ftp://igs.org/pub/data/format/sp3_docu.txt`.

3.4 Linearizing the Trajectory

Here we consider a possible simplification which also makes the computations more efficient. We evaluate the interpolation only once, i.e., at time t_1, to obtain the position $x_0(t_1)$ and velocity $v_0(t_1)$ of the target. During the iteration we then only evaluate the so obtained tangent around $x_0(t_1)$, i.e.,

$$x_0(t) = x_0(t_1) + t \cdot v_0(t_1). \tag{2}$$

The time argument t contains only the seconds relative to t_1 stored in a double precision floating point variable. The difference between the linearized method and the direct evaluation of the Neville interpolation is always in the order of 10^{-14} s as shown in Fig. 4, which is well below the detection limit of current VLBI.

3.5 BCRS vs. GCRS

The recommended reference system for the models by SF06 and D+12, aiming at computing the VLBI delay for any source in the near-field of VLBI, is the barycentric celestial reference system (BCRS) rather than the geocentric celestial reference system (GCRS). The rea-

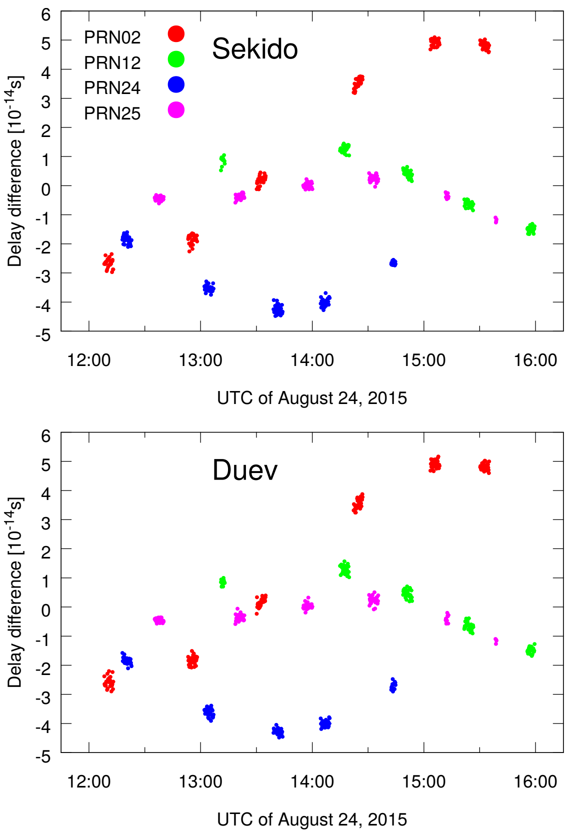

Fig. 4: Difference between the delay computed by linearizing the trajectory around the reception time at station 1 and by direct evaluation of the Neville interpolation of the sp3 final ephemerides with an increased floating point precision time argument, top panel SF06, bottom panel D+12.

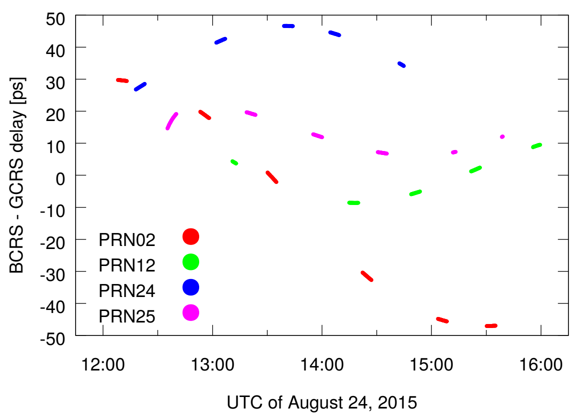

Fig. 5: Difference between the delay computed with D+12 performed in the BCRS and in the GCRS.

son is that the GCRS is not an inertial reference system since its origin, i.e., the barycenter of the Earth, is in orbit around the Sun and not in uniform motion. The BCRS, however, can be considered an intertial reference system for the purpose of computing VLBI delays.

In the here considered special case of satellites orbiting the Earth it would be beneficial to express the calculations in the GCRS, because it minimized the magnitude of all positions involved and hence their numerical precision. Since a GPS satellite is orbiting the Earth with an altitude of approximately 20000 km above the ground, the travel time of a signal from the satellite to an antenna on the Earth is around 67 ms. Over that short period of time the GCRS may possibly be approximated as an inertial reference system and here we investigate what difference it makes to apply that approximation.

Figure 5 shows the differences between the computed VLBI delay performed in the BCRS and in the GCRS. The difference for the here consideres case of GPS satellites are in the range of ±50 ps.

4 Conclusions

VLBI observations of near-field targets require especially suited delay models. We implemented the models by SF06 and D+12 into the VLBI analysis software ivg::ASCOT (Artz et al., 2016; Halsig et al., 2017). In order to test our implementation of these models we made use of one session of VLBI observations of GPS satellites (Plank et al., 2017). Here are our conclusions.

1. We tested both delay models by investigating the diffence between the observed group delay and the computed delay. The plot shown in Fig. 1 reveals that there are still systematic trends related to the individual satellites. Further investigation is needed to clarify whether these systematics are the result of, e.g., inaccurate tracking of the satellites, the unknown phase-center of the antenna array onboard the satellites, or the emitted signals themselves.
2. The results obtained with our implementation of both models have been found consistent up to 50 ps.
3. Linearizing the trajectory of the GPS satellites around one point determined by evaluating the interpolated position and velocity (Neville's method), and then only evaluating the so obtained tangent results in a computed delay which differs only by $\sim 10^{-14}$ s from the one obtained by evaluating the interpolation directly with a sufficiently precise time argument (see Fig. 4). This difference is well below the detection limit of current VLBI.
4. Performing the calculations in the GCRS affects the resulting computed delay by ±50 ps when compared to the results obtained in the BCRS.

The result that linearizing the trajectory (Sect. 3.4) and performing the calculations in the GCRS (Sect. 3.5) opens up new possibilities. Linearization leads to the existence of an analytical solution of the light-time-equation (Eq. (1)), and formulation in the GCRS simplifies the equations further. Benefits of an analytical near-field VLBI delay formula would include a gain in performance. The implication of the existence of partial derivatives of the delay model with respect to parameters of interest would be another important step towards the completion of an analysis chain for near-field geodetic VLBI (Jaron et al., in prep.).

References

Artz T, Halsig S, Iddink A, Nothnagel A (2016) ivg::ASCOT: Development of a New VLBI Software Package. In: D. Behrend, K. D. Baver, K. L. Armstrong (eds.), *IVS 2016 General Meeting Proceedings: "New Horizons with VGOS"*, NASA/CP-2016-219016, 217-221

Duev D A, Molera Calvés G, Pogrebenko S V, Gurvits L I, Cimó G,Bocanegra Bahamon T (2012) Spacecraft VLBI and Doppler tracking: algorithms and implementation. *A&A*, 541, A43.

Halsig S, Corbin A, Iddink A, Jaron F, Schubert T, Nothnagel A (2017) Current development progress in ivg::ASCOT. In: R. Haas and G. Elgered (eds.), *Proc. 23rd EVGA Working Meeting*, 167–171.

Hellerschmied A, Böhm J, Kwak Y, McCallum J, Plank L (2016) VLBI observations of GNSS satellites on the baseline Hobart-Ceduna. *EGU General Assembly Conference Abstracts, 18, 8895*.

IERS Conventions (2010) G. Petit, B. Luzum (eds.). *IERS Technical Note 36*, Frankfurt am Main: Verlag des Bundesamts für Kartographie und Geodäsie, 179 pp., ISBN 3-89888-989-6.

Jaron F, Halsig S, Iddink A, Nothnagel A, Plank L (2017) Near-field VLBI delay models (2017). In: A. Nothnagel and F. Jaron (eds.), *Proc. First International Workshop on VLBI Observations of Near-field Targets*, Schriftenreihe des Inst. f. Geodäsie u. Geoinformation, 54, ISSN 1864-1113, 23–27.

Jaron F, Halsig S, Iddink A, Nothnagel A (2017) An analytical GCRS near-field VLBI delay model. in prep.

Plank L (2013) VLBI satellite tracking for the realization of frame ties. PhD thesis, TU Wien.

Plank L, Hellerschmied A, McCallum J, Böhm J, Lovell J (2017) VLBI observations of GNSS-satellites: from scheduling to analysis. *J Geod*, 91:867, doi:10.1007/s00190-016-0992-8

Romero G E, Boettcher M, Markoff S, Tavecchio F (2017) Relativistic Jets in Active Galactic Nuclei and Microquasars. *Space Science Reviews*, 207(1–4), 5–61.

Sekido M, Fukushima T (2006) VLBI delay model for radio sources at finite distance. *J Geod*, 80:137, doi:10.1007/s00190-006-0035-y.

Sovers O J, Fanselow J L, Jacobs C S (1998) Astrometry and geodesy with radio interferometry: experiments, models, results. *Reviews of Modern Physics*, 70, 1393.

Thompson A R, Moran J M, Swenson G W, Jr. (2017) Interferometry and Synthesis in Radio Astronomy. 3rd ed., Springer.

Initial Estimations of the Lunar Lander Position by OCEL Observations

Z. Zhang, S. Han, A. Nothnagel, L. La Porta, S. Halsig, A. Iddink, F. Jaron, R. Haas, J. Lovell, A. Neidhardt, C. Plötz, G. Tang

Abstract The successful landing of the Chang'E-3 lunar lander, opened up the window for observing the moon with VLBI again after more than 40 years. *Observing Chang'E-3 with VLBI* (OCEL) is conducted as an IVS Research and Development project with 12 sessions observed and being processed. Presently, the position of the lunar lander on the Moon is in the focus to be determined. In this study, two OCEL observing sessions of the lunar lander have been processed preliminarily. Based on precise information of the moon's motion provided by ephemeris, the position of the lunar lander in a Moon-fixed system is determined. Since VLBI is much less sensitive to the radial direction, a constraint for the lunar distance is applied. The results show that with this constraint based on a priori information, a position of the lander on the Moon was determined which about ten meters off the position from Lunar Reconnaissance Orbiter results. Accuracy analyses are carried out with positioning results from other approaches. Analysis shows that the accuracy of the positioning with the preliminary observations is about 30 meters.

Axel Nothnagel · Laura La Porta · Sebastian Halsig · Andreas Iddink · Frédéric Jaroin · Z. Zhang
Institute of Geodesy and Geoinformation, University of Bonn, Nussallee 17, DE-53115 Bonn, Germany, e-mail: zhang@zism.ac.cn

Rüdiger Haas
Chalmers University of Technology, Onsala Space Observatory, SE-439 92 Onsala, Sweden

Jim Lovell
School of Mathematics and Physics, University of Tasmania, Private Bag 37, Hobart 7001, Australia,

Alexander Neidhardt
Technical University of Munich, Research Facility Satellite Geodesy, Geodetic Observatory Wettzell, Sackenrieder Str. 25, DE-93444 Bad Kötzting, Germany,

Christian Plötz
Federal Agency for Cartography and Geodesy, Geodetic Observatory Wettzell, Sackenrieder Str. 25, DE-93444 Bad Kötzting, Germany,

Geshi Tang · Songtao Han · Zhongkai Zhang
Beijing Aerospace Control Center, National Key Laboratory of Science and Technology on Aerospace Flight Dynamics, No. 120, Box 5130, Beijing, China, 100094,

Keywords VLBI, OCEL, Chang'E-3 lunar lander, Positioning

1 Introduction

As the only natural satellite of the Earth, holding the information of the Earth-Moon system dynamics and motions, the Moon has always been a prime object of interest for space sciences. For the first time in 1969, the Apollo program laid the groundwork to obtain direct geodetic measurements of the Moon. With the Apollo program, the Apollo Lunar Surface Experiments Package (ALSEP) (King, 1976) was carried to the Moon, which comprised a set of scientific instruments placed at the landing sites. With these instruments, VLBI observations were possible for a few years while Lunar Laser Ranging observations can be carried out today and beyond. These data have made significant contributions in many scientific fields.

The determination of coordinates of any lunar lander have always been of great importance for lunar investigations. Earlier studies have been carried out to estimate the coordinates of beacons on the lunar surface with VLBI observations. For instance, based on ALSEP Differential VLBI Observations, the uncertainties in the relative coordinates of ALSEP transmitter were reported by an MIT (Massachusetts Institute of Technology) research group to be 30 meters in the radial and 10 meters in the transverse components (King, 1976). Cao et al. (2016) used VLBI and unified X-band (UXB) observations of several hours arc from 4 stations to estimate the coordinates of the Chang'E-3 lunar lander and obtained coordinates in the Mean Earth (ME) frame which are different by 0.0025°, 0.0023° and 3 meters in latitude, longitude and altitude, respectively, from coordinates by Lunar Reconnaissance Orbiter (LRO) determinations (Mazarico et al., 2012).

In December 2013, the deployment of the Chang'E-3 lunar lander on the Moon and its capability to transmit X-band signals opened up the window for new lunar VLBI observations from the Earth again after more than 40 years (Zheng et al., 2004). The concept of *Observing Chang'E-3 Lander with VLBI* was firstly induced by Tang et al. (2014). Following observing proposals to the Observing Program Committee (OPC) of the International VLBI Service for Geodesy and Astrometry (IVS) (Nothnagel et al., 2017), four 24 hour sessions each were scheduled and conducted with subsets of the IVS observing network and 2 China Deep Space Network stations in 2014, 2015, and 2016 (Haas et al., 2017). Two of these sessions (OCEL-1 and OCEL-9) are available for geodetic analysis at the moment producing initial results for the lunar lander position.

2 Theory for the lunar lander positioning

Since the lunar lander is fixed to the surface of the Moon, the coordinates are approximately constant in the Moon-fixed coordinate frames without considering the tidal effects. Then its equations of motion only involves the transformation between the Moon-fixed coordinate frame(s) and the inertial frame. The locations of features on the lunar crust are usually described by coordinates expressed in the mean-Earth (ME) frame, in which the X axis is defined by the body-fixed axis that points toward the mean Earth direction and the Z axis points toward the mean rotation axis direction (Folkner et al., 2008, 2014). The ME frame is in contrast to the principal axis (PA) frame which considers the gravity field of the Moon. Coordinates in the ME frame (vector M) can be rotated into the PA frame (vector P) using

$$P = R_z(C) * R_y(B) * R_x(A) * M \quad . \qquad (1)$$

Conversely, coordinates in the PA frame can be rotated into the ME frame with

$$M = R_x(-A) * R_y(-B) * R_z(-C) * P \quad , \qquad (2)$$

where the R_x, R_y and R_z are the standard rotation matrices for right-handed rotations around the X, Y and Z axes, respectively, and A, B and C are the angles given in Table 1.

Because the procedure for calculating the constant rotation angles changed, there are different values of the constant angles for each JPL ephemeris listed in Table 1. By comparing the angles for DE403 (same as DE405) and DE421, the differences are up to about −0.15",

Table 1: The angles for transformation from the ME frame to the PA frame corresponding to the JPL ephemeris.

	DE403/DE405	DE421	DE430
Angle A (arcsecond)	0.1462	0.30	0.285
Angle B (arcsecond)	79.0768	78.56	78.580
Angle C (arcseond)	63.8986	67.92	67.573
Differences in PA (meters)	5.1/−1.0/2.6	0/0/0	0.6/−0.1/0.1

0.51" and −4.02",and the displacements in the PA frame from DE421 are 5.1, −1.0 and 2.6 meters, respectively. The constant rotation angles for DE421 and DE430 are below 1". Note that the angles for the transformation are computed only to first order. The second-order contribution is a rotation about 0.03"(0.25 meters on the lunar surface), and the error in the first-order expression is estimated to be half of that, i.e., 0.015"(0.11 meters). As we describe in Table 1, the differences of the three angles between DE430 and DE421 are 0.015", 0.020" and 0.347" (0.11, 0.16 and 2.9 meters), respectively.

The difference in the coordinates of a point on the surface of the Moon between the ME frame and the PA frame is approximately 860 meters. As recommended by the International Astronomical Union (IAU) for high precision working, e.g., spacecraft operations involving the orientation of the Moon, a lunar ephemeris should be used to obtain the libration angles for the Moon, which define the rotation from the PA frame to the inertial ICRF frame (Archinal et al., 2010). There are no equations of the motions for Euler angles referenced to the ME frame. The Euler angles provided by the JPL ephemeris are numerically integrated and inherently more accurate than the knowledge on the mean axes. The constant three-angle rotation from the PA frame to the ME frame is known less accurately than the integrated Euler angles, however this is enough for meter or lower level accuracy. Because of this, we use the coordinates in the PA frame for estimating the position of the lunar lander. It should be mentioned that the coordinates of the lunar lander obtained from LRO photographing data, which we use as a priori values, are in the ME frame. For comparison, our position estimates in the PA frame are thus converted to the ME frame a posteriori.

In this preliminary data analysis, we used only the lunar observations and those quasar observations designed for delay calibration purposes (Haas et al., 2017). With the calibration observations clock offsets were determined for segments of about two hours each in a very rudimentary least squares adjustment. These, together with corrections for the hydrostatic components of refraction, were used to roughly calibrate the observations. Of course, this is a very rough procedure but it is sufficient for a first quick glance at the observables (see Sec. refsec:results). Telescope coordinates from the ITRF2014 solution (Altamimi et al., 2016) were transformed with the usual correction models. Then a standard least squares adjustment is performed which estimates only the lunar lander position components.

3 Observation Data

Since currently no complete OCEL session is processed, a number of preliminarily processed observations from two sessions are used here for the initial estimation.

The raw data of OCEL sessions are correlated with the correlator software DiFX-2.4 (Deller et al., 2007). The fringe-fitting of the quasar observations is processed with HOPS-3.12(fourfit), and the lunar lander observations are fringe-fitted in a special DOR tone signal processing method (Kikuchi et al., 2004).

Table 2: The sessions and baselines of the observations used for the estimation.

Sessions	Baselines
OCEL-01 (RD1405)	BD-SH, HT-ZC, SH-ZC
	BD-KK, BD-WZ
OCEL-09 (RD1601)	BD-ZC, BD-HO, WZ-ZC
	BD-NY, NY-ZC, KK-NY

The OCEL-01 session was conducted in July, 2014, and the OCEL-09 in January, 2016. Five baselines from OCEL-01 and six baselines from OCEL-09 were used in the lunar lander positioning, and the number of the observations used were 119 and 89 respectively as shown in Table 2. The sessions provided observations of the lunar lander and of some nearby quasars (Haas et al., 2017). In addition, also a large number of standard VLBI observations had been gathered in these sessions but these are not used in this initial data analysis.

4 Results

According to the theory described above, the position of the lunar lander is estimated using about 200 successful VLBI observations. Taking the coordinates of the lunar lander from LRO as the a priori values, the corrections w.r.t. these coordinates from LRO in the PA frame are estimated (Table. 3). The adjustments to the Y and Z components are around 40 and 30 meters, but for the X component it is almost 500 meters. The reason is that the observations are hardly sensitive to this direction.

Table 3: The corrections w.r.t the coordinates of the lunar lander from LRO in the PA frame.

	X	Y	Z
Corrections in PA (m)	−491.5	−43.1	−30.4
STD (m)	34.9	3.8	2.9

The weighted RMS (WRMS) residual delay is only 30.8 ns which corresponds to about 9 m. This of course is still very rough but matches the position uncertainties.

For the lack of sensitivity of VLBI to the radial component, which corresponds to the X-axis of the Moon, a constraint needs to be introduced from a priori information. In this case, the lunar lander is fixed on the surface of the Moon with the distance between the center of the Moon and the lunar lander being introduced as a constant. This constraint can be formulated as

$$\sqrt{X^2+Y^2+Z^2} = \sqrt{X_0^2+Y_0^2+Z_0^2} = const., \qquad (3)$$

where X, Y and Z are the coordinates to be estimated, and X_0,Y_0 and Z_0 are the coordinates based on the a priori coordinates from LRO. With this constraint applied, the WRMS residual delay increases considerably to 44.9 ns but the X component reduces to a reasonable number (Table. 4). It should be taken into account that since the constraint is based on the a priori values, the accuracy of the a priori value heavily affects the positioning results. In some sense this is reflected in the increased formal error of this and the Z parameter.

Table 4: The corrections with constraint w.r.t. the coordinates of the lunar lander from LRO in PA frame.

	X	Y	Z
Corrections in PA (m)	10.0	−4.3	−10.9
STD (m)	25.4	2.5	11.3

The photographic positioning results of the lunar lander from LRO are given in the ME frame, based on the JPL ephemeris DE421 and a radius of the Moon 1737.4 km. Table 5 shows the polar coordinates of the lander from the initial VLBI estimation, from the VLBI estimation with constraint and from LRO, all in the ME frame. The differences are 0.0096° in latitude, −0.0021° in longitude and −343 m in altitude between the coordinates from VLBI estimation and LRO. With the constraint, the differences are improved to −0.0005°, −0.0002° and 0 meters in latitude, longitude and altitude respectively.

At this point, we should also discuss the accuracy of the reference position of the lander stemming from LRO

Table 5: The geodetic coordinates of the lunar lander from the initial VLBI estimation, from the VLBI estimation with constraint and from LRO, all in the ME frame.

	VLBI (Tab. 3)	VLBI (Tab. 4) with constraint	LRO
Latitude (°)	44.1310	44.1209	44.1214
Longitude (°)	−19.5137	−19.5118	−19.5116
Altitude (m)	−2983	−2640	−2640

photography. The camera on LRO is reported to have a resolution of up to 0.5 meters (Mazarico et al., 2012; Liu et al., 2015). After some modifications to the control of the lunar orbiter laser altimeter (LOLA) during the mission, the accuracy of the photographic positioning with a single photograph of LRO is estimated to be about 20 meters. This accuracy can be increased by stacking a number of photographs (Mazarico et al., 2012; Liu et al., 2015). Comparing our results with those from LRO based on different numbers of photographs shows differences in the range of 0.0003° to 0.0005° corresponding to about 9 to 15 m on the lunar surface which are just within the accuracy of LRO positioning 20 meters (Table. 6).

From the initial spacecraft navigation observations (Cao et al., 2016; Li et al., 2014) more results are available for comparison. Compared to positioning results from VLBI and Unified X Band (UXB) measurements for range and range rate observations in the initial mission period (2014), our results differ by about 50 meters and 80 meters, respectively (Table. 6). However, these reference results are based on a much smaller number of observations. So, presuming that the accuracy of the LRO photographic positioning is just 20 meters, our results agree quite well with these references even though we have just applied a very rough analysis scheme.

Table 6: Current positioning results with different approaches and data. VLBI+UXB from Cao et al. (2016) and Li et al. (2014).

Approaches	Latitude (°)	Longitude (°)
VLBI, this paper	44.1209	−19.5118
LRO (1 photograph)	44.1214	−19.5116
LRO (5 photographs)	44.1213	−19.5115
LRO (14 photographs)	44.1219	−19.5113
Mission VLBI+UXB (initial)	44.1189	−19.5093
Mission VLBI+UXB	44.1206	−19.5124

5 Conclusions

This paper describes a very preliminary determination of the position of the Chang'E-3 lunar lander. With about 200 VLBI group delay observations the position is estimated in a very rough least squares solution. Considering that VLBI has hardly any sensitivity in the radial direction, a constraint based on the a priori information from LRO is applied. With this constraint, the position difference in radial direction relative to LRO photographic positioning reduces from 500 m to about 10 meters. Also the differences in the transverse directions are estimated to have the same magnitude of about 10 meters. These results are very motivating for refined analyses both in fringe fitting and VLBI modelling with more data of more observing sessions.

References

Altamimi Z, Rebischung P, Métivier L, Xavier C (2016) ITRF2014: A new release of the International Terrestrial Reference Frame modeling nonlinear station motions. *J. Geophys. Res. Solid Earth*, 121, doi:10.1002/2016JB013098.

Archinal B A, A'Hearn M F, Bowell E, Conrad A, Consolmagno G J, Courtin R, Fukushima T, Hestroffer D, Hilton J L, Krasinsky G A, Neumann G, Oberst J, Seidelmann P K, Stooke P, Tholen D J, Thomas P C, Williams I P (2010) Report of the IAU working group on cartographic coordinates and rotational elements: 2009. *Celestial Mechanics and Dynamical Astronomy*, 109(2), 101–135, doi:10.1007/s10569-010-9320-4.

Cao J, Zhang Y, Hu S, Huang Y, Chen M (2016) An Analysis of Precise Positioning and Accuracy of the CE–3 Lunar Lander Soft Landing. *Geomatics and Information Science of Wuhan University*.

Deller A T, Tingay S J, Bailes M, West C (2007) DiFX: A Software Correlator for Very Long Baseline Interferometry Using Multiprocessor Computing Environments. *Publ. Astronomical Society of the Pacific*, 119:318–336, 2014.

Folkner W M, Williams J G, Doggs D H (2008) The planetary and lunar ephemerides DE421. *JPL IOM 343R-08-003*.

Folkner W M, Williams J G, Doggs D H, Park R S, Kuchynka P (2014) The planetary and lunar ephemerides DE430 and DE431. *Interplanet. Netw. Prog. Rep*.

Haas R, Halsig S, Han S, Iddink A, Jaron F, La Porta L, Lovell J, Neidhardt A, Nothnagel A, Plötz C, Tang G, Zhang Z (2017) Observing the Chang'E-3 Lander with VLBI (OCEL) - Technical Setups and First Results. In: A. Nothnagel, F. Jaron (eds.), *Proc. First International Workshop on VLBI Observations of Near-field Targets*, Schriftenreihe des Inst. f. Geodäsie u. Geoinformation, 54, ISSN 1864-1113, 41–64.

Kikuchi F, Kono Y, Yoshikawa M, Sekido M, Ohnishi M, Murata Y, Ping J, Liu Q, Matsumoto K, Asari K, Tsuruta S, Hanada H, Kawano N (2004) VLBI observation of narrow bandwidth signals from the spacecraft. *Earth Planets Space*, 56(11), 1041–1047, doi:10.1186/BF03352546.

King R W (1976) Precision Selenodesy via Differential Very-Long Baseline Interferometry. Ph.D. Thesis, Massachusetts Institute of Technology, Cambrige, Mass.

Li P, Huang Y, Chang S (2014) Positioning for the Chang'E-3 lander and rover using Earth-based observations. *Chinese Science Bulletin*, 59, 3162, doi:10.1360/N972014-00207.

Liu B, Di K C, Wang B F, Tang G, Xu B, Zhang L, Liu Z (2015) Positioning and precision validation of Chang'E–3 Lander based on multiple LRO NAC images. *Chinese Science Bulletin*, 60, 2750, doi:10.1360/N972015-00336.

Mazarico E, Rowlands D D, Neumann G A, Smith D E, Torrence M H, Lemoine F G, Zuber M T (2012) Orbit determination of the Lunar Reconnaissance Orbiter. *J Geod*, 86(3),193–207, doi:10.1007/s00190-011-0509-4.

Nothnagel A, Artz T, Behrend D, Malkin Z (2017) International VLBI Service for Geodesy and Astrometry – Delivering high-quality products and embarking on observations of the next generation. *J Geod*, 91(7), 711–721, doi:10.1007/s00190-016-0950-5.

Tang G, Cao J, Han S, Hu S, Ren T, L. Chen L, Sun J, Wang M, Li Y, Li L (2014) Research on Lunar Radio Measurements by Chang'E-3. In: D. Behrend, K. D. Baver, K. L. Armstrong (eds.), *IVS 2014 General Meeting Proceedings VGOS: "The New VLBI Network"*, Science Press, Beijing, 473–477.

Zheng W, Huang Y, Chen Z, Wang G, Liu Q, Tong F, Li P, Tong L, Shu F (2004) Real-time and High-Accuracy VLBI in the CE-3 Mission. In: D. Behrend, K. D. Baver, K. L. Armstrong (eds.), *IVS 2014 General Meeting Proceedings VGOS: "The New VLBI Network"*, Science Press, Beijing, 466–472.

Update on VLBI Data Analysis at ESA/ESOC

C. Flohrer, E. Schönemann, T. Springer, R. Zandbergen, W. Enderle

Abstract ESA's Navigation Support Office is providing the geodetic reference for ESA missions mainly based on the processing of the satellite-geodetic techniques GNSS, SLR and DORIS. Since 2016 the Navigation Support Office is extending its expertise to include VLBI processing and analysis. This effort will establish ESA's capability to determine the absolute orientation of the Earth and therewith enable the Navigation Support Office to provide a fully independent set of Earth orientation parameters for ESA missions. ESOC's software package NAPEOS will become capable of combining all four geodetic techniques on the observation level and thus supporting GGOS, the Global Geodetic Observing System.
The VLBI delay model is now fully implemented following the IERS 2010 standards. With the current implementation in NAPEOS observation residuals of the level of 2-3 cm are reached. This result is expected and can be further improved by applying a better clock model and allowing for VLBI parameter estimation. The paper discusses briefly the current status and future plans of the VLBI implementation in NAPEOS and shows example residuals. The question as to which space-time coordinate systems to use for the various parameters of the VLBI delay model is addressed as well.

Keywords VLBI data analysis, NAPEOS, space-time coordinate systems

1 Introduction

In 2015 ESA's Navigation Support Office started to extend its processing capabilities for VLBI tracking data to complete ESA's capabilities in generating independent Earth Orientation Parameters (EOP). In addition this capability would allow ESA to contribute to the IVS service as an analysis centre and to enhance its contribution to the IERS service with UTI-UTC and nutation products. Finally it would enable ESOC's software package NAPEOS (ESA/ESOC, 2009) to combine all space-geodetic techniques at the observation level, bringing together the strengths of the individual techniques.

NAPEOS (NAvigation Package for Earth Orbiting Satellites) is capable of processing data from various satellite-geodetic techniques, such as GNSS, SLR, DORIS, and altimetry, individually but also combined at the observation level. This leads to the challenge to incorporate a new observation type into an existing software package. On the one hand it has the advantage that the developer can access already existing modules and algorithms and the combined processing of the various techniques comes almost for free. On the other hand, however, it implies a lot of integration and testing effort and proper book-keeping.

In Section 2 we briefly review the results achieved in 2016, followed by the current status of the VLBI implementation in NAPEOS in Section 3. The next steps planned for the VLBI data processing in NAPEOS are highlighted in Section 4. Finally, in Section 5, we discuss the problem of different coordinate time scales involved in the VLBI delay model and their proper usage.

2 Results achieved in 2016

Various implementation steps are needed to enable basic VLBI data processing in NAPEOS. The main ones can be summarised as:

- radio source and VLBI station database set up
- VLBI observation reading
- VLBI observation modelling
- VLBI observation corrections
- VLBI parameter estimation

Claudia Flohrer · Erik Schönemann · Tim Springer · René Zandbergen · Werner Enderle
Navigation Support Office, ESA/ESOC, Robert-Bosch-Str. 11, DE-64293 Darmstadt, Germany

In 2016 we were able to present initial results at the 9th IVS General Meeting (Flohrer et. al, 2016). Our data processing starts with VLBI observations read from NGS card files. In the future, this format can be replaced by the vgosDB format based on NETcdf files. A basic VLBI observation model was implemented in NAPEOS, only considering the main terms. Observation corrections such as the gravitational delay, axis offsets, and cable delays had not been included. Also, no parameters had been estimated, with the exception of constant clock offsets w.r.t. a reference clock. With this basic implementation we could present O-C residuals at the 0.5 m level. By correcting the observations for the instrumental delay caused by the axis offset we could reduce the O-C residuals to the 10 cm level.

3 Current status

Meanwhile we fully implemented the Consensus model from Eubanks et.al (1991) into NAPEOS, adding also the gravitational delay according to the recipe provided in the IERS 2010 conventions (Petit and Luzum, 2010). The entire observation modelling was successfully validated against the VieVS software (Böhm et. al, 2012).

Table 1 summarises the processing standards and models used in our current implementation of VLBI in NAPEOS. We use the observed VLBI delay as provided by the correlator, which is considered to be equal to a Terrestrial Time (TT) coordinate time interval d_{TT}. No transformation is done to Geocentric Coordinate Time (TCG). With this choice we follow the generally accepted approach of the VLBI analysis centres. The space coordinates resulting from the VLBI analysis x_{TT} are thus called TT-compatible. They can be transformed into a TCG system (as recommened by the IAU), i.e. the Geocentric Celestial Reference System (GCRS), by a simple rescaling

$$x_{TCG} = \frac{x_{TT}}{1 - L_G} \tag{1}$$

(see Petit and Luzum, 2010).

NAPEOS uses the latest IERS models and standards (Petit and Luzum, 2010) for Earth Orientation Parameters (EOPs) and displacement of reference points. See Table 1 for further details.

We use the Saastamoinen model for the a priori tropospheric delay model together with the GMF mapping functions. The antenna axis offset is applied using the antenna information file provided by Nothnagel (2009). Other technique-specific effects are not yet taken into account, such as cable delay and thermal deformation of the antenna.

We have not yet enabled the parameter estimation of the main VLBI parameters, such as EOPs, station coordinates, and source coordinates. These parameters are kept fixed w.r.t. their a priori values.

A simple clock model is applied using a piece-wise linear function. For each station clock, one offset and a drift every 6 hours is estimated w.r.t. a chosen reference clock. No automatic clock jump detection has been implemented yet, neither a polynomial function for the clock model. Both are foreseen in a next implementation step.

We enabled the estimation of tropospheric parameters, namely tropospheric wet zenith delays and tropospheric gradients with North and East component mapped with the wet GMF mapping function. Troposphere parameters are set up as piece-wise linear functions every 1 hour. Tropospheric gradients are estimated every 24 hours.

With this approach we processed 24 h sessions obtaining O-C residuals on the order of 2-3 cm. As an example, Figure 1 shows O-C residuals in centimetres for session 15MAR23XA_N004, for 2850 observations of 21 baselines to 50 sources. There are three different solutions marked in different colours. Orange labels the solution without any troposphere estimates. Only piece-wise linear station clocks have been estimated every 6 hours. The light blue solution is similar to orange but adding piece-wise linear zenith wet delays every 1 hour. Dark blue adds tropospheric gradients every 24 hours on top.

Table 2 summarises the RMS values of the residuals in cm (and in ps for convenience). Without allowing for the estimation of any troposphere parameter, the RMS value is at the 10 cm level. Estimating wet zenith delays decreases the RMS significantly to 2.77 cm. It can be slightly further decreased to 2.61 cm by estimating tropospheric gradients.

The achieved residual level is still a factor of two higher then the standard residual level achieved by the IVS analysis centres in a routine VLBI data processing. However, with the current state of the VLBI implementation in NAPEOS this result is very satisfying. Further improvements are expected by applying a better clock model and allowing the parameter estimation for station coordinates and EOPs (see next section).

4 Next steps

With the current implementation status we are ready to participate in the next VLBI Analysis Software Comparison Campaign (VASCC), see Klopotek et. al (2016), to validate our VLBI delay model.

Table 1: VLBI processing standards and models used for the current VLBI implementation in NAPEOS.

Reference frames	
Time argument	coordinate time TT is used for the VLBI observations leading to TT-compatible TRS spatial coordinates, the VLBI delays provided by the correlators are equivalent to a TT coordinate interval (assuming that the proper time of the station clocks, used to record the signal, has the same rate as TT)
Inertial frame	• Barycentric (BCRF): ICRF2 reference frame realised by a set of source positions consistent with J2000.0, given in the IVS source name translation table (https://gemini.gsfc.nasa.gov/ solve_save/-IVS_SrcNamesTable.txt) mainly based on IERS TN35 (Fey et al., 2009) • Geocentric (GCRF): mean equator and equinox of 2000 Jan 1.5 (J2000.0)
Terrestrial frame	ITRF2008 reference frame realised through a set of station coordinates and velocities given in the IVS internal realisation ITRF2008-TRF-IVS.SNX
Precession	IAU 2006/2000A precession-nutation model
Nutation	IAU 2006/2000A precession-nutation model, daily dx and dy corrections (celestial pole offset) from IERS Bulletin-A are applied
Polar motion, UT1	interpolated from IERS Bulletin-A, updated daily, with the restoration of subdaily variations due to ocean tidal and libration effects using IERS 2010 (Petit and Luzum, 2010) models: • ocean tidal effects: diurnal and semi-diurnal variations in pole coordinates and UT1 applied (using IERS routine ORTHO_EOP.F) • libration effects: prograde diurnal and semi-diurnal nutations in polar motion applied (using IERS routine PMSDNUT2.F), semi-diurnal libration in UT1 applied (using IERS routine UTLIBR.F)
Displacement of reference points	
Solid Earth tides	IERS 2010
Solid Earth pole tides	IERS 2010, mean pole removed by quadratic trend until 2010 / linear trend from 2010
Oceanic pole tides	not applied
Ocean tidal loading	consistent with IERS 2010, site-dependent amps/phases from free ocean tide loading provider (Bos and Scherneck, 2017) for FES-2004 (Lyard et al., 2006) tide model including centre of mass correction, NEU site displacement computed using HARDISP.F from D. Agnew
Atmospheric pressure loading	not applied
Non-tidal loading	not applied
Ionospheric delay	Ionospheric group delay correction applied from observation file (NGS)
A priori tropospheric delay model	
A priori hydrostatic zenith delay	Saastamoinen model (Saastamoinen, 1972), with meteorological data from observation file
A priori wet zenith delay	none
Mapping function	GMF dry (Böhm et. al, 2006)
A priori gradients	none
Technique-specific effects	
Antenna axis offset	applied using the antenna information file (http://vlbi.geod.uni-bonn.de/Analysis/Thermal/ antenna-info.txt) provided by Nothnagel (2009)
Cable delay	not applied
Thermal antenna deformation	not applied
Station eccentricities	not applied
Source structure	not applied
Geometric/relativistic delay model	
Consensus model	applied following the IERS 2010 conventions
Planetary ephemerides	DE405 (Standish, 1998) for all planets, Sun, Moon using coordinate time TDB as input
GM values	from IERS 2010 and DE405 (see Section 5 for details)
Parameter treatment	
Polar motion	fixed
Nutation (Celestial pole offset)	fixed
UT1-UTC	fixed
Source coordinates	fixed
Station coordinates	fixed
Station clocks	estimated piece-wise linear every 6 hours (w.r.t. a fixed reference clocks)
Troposphere	• Wet zenith delay: estimated piece-wise linear every 1 hours • Mapping function: partial is GMF wet (Böhm et. al, 2006) • Gradients: North and East gradients estimated piece-wise linear per 24 hours

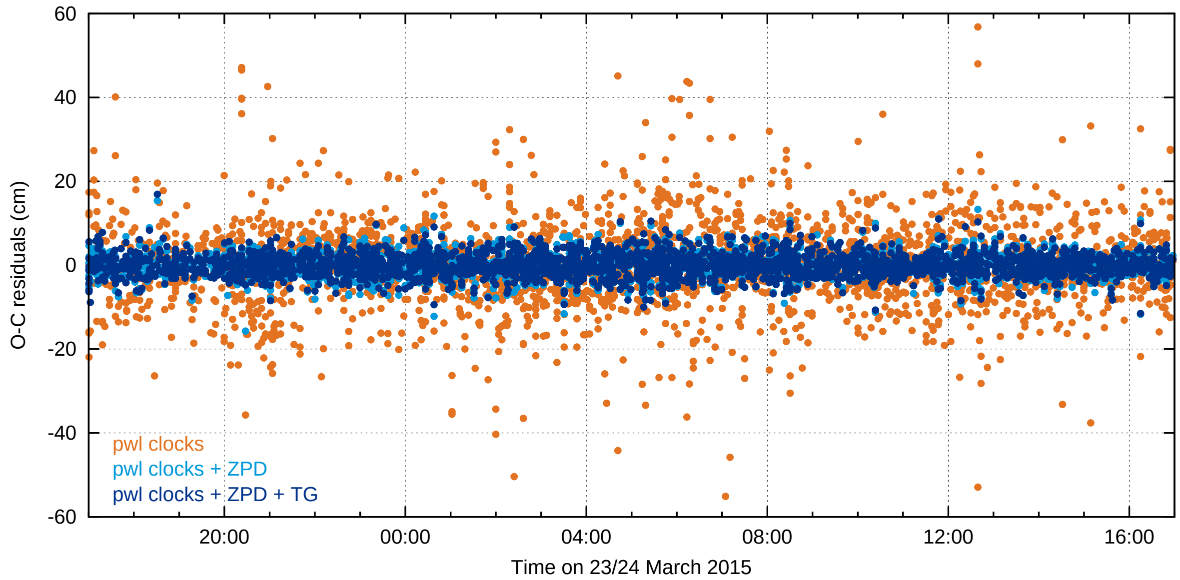

Fig. 1: O-C residuals (in cm) from the example session 15MAR23XA_N004 for three different solutions: (pwl clocks) with piece-wise linear clocks estimated every 6 hours, (pwl clocks + ZPD) additionally with piece-wise linear tropospheric zenith wet delays every 1 hour, (pwl clocks + ZPD +TG) additionally with tropospheric gradients every 24 hours.

In the upcoming future we plan to extend the current VLBI implementation in NAPEOS by the following steps:

- implement observation weighting and outlier detection
- add observation correction due to cable delay
- add observation correction due to instrumental delay caused by thermal deformation
- implement automatic clock jump detection algorithm
- implement polynomial function for clock model
- add partial derivatives for remaining parameters (EOPs, station coordinates)

Once these steps have been achieved a full VLBI based parameter estimation can be done. As NAPEOS has already the capabilities to process and combine various observation types, we also aim for a combined parameter estimation (combining at the observation level), starting with GNSS and VLBI.

Table 2: RMS values of O-C residuals from the example session (in cm and ps) for three different solutions: (a) with piece-wise linear clocks estimated every 6 hours, (b) additionally with piece-wise linear tropospheric zenith wet delays every 1 hour, (c) additionally with tropospheric gradients every 24 hours.

Solution ID	RMS (cm)	RMS (ps)
(a) pwl clocks	10.46	348.9
(b) pwl clocks + ZPD	2.77	92.4
(c) pwl clocks + ZPD + TG	2.61	87.1

5 On the sound usage of space-time coordinate systems in the Consenus model

The Consensus model (Eubanks et.al, 1991) given in the IERS conventions (Petit and Luzum, 2010) has become an agreed standard to model the VLBI delay. It was derived from a combination of five different relativistic models and combines quantities defined in both reference systems, the Barycentric Celestial Reference System (BCRS) and the Geocentric Celestial Reference System (GCRS). Both reference systems have corresponding coordinate time scales, namely Barycentric Coordinate Time (TCB) and Geocentric Coordinate Time (TCG). In addition there are scaled versions, Terrestrial Time TT (renamed from Terrestrial Dynamic Time TDT, being a scaled version of TCG)

Table 3: Parameters of space-time coordinate systems and their relationships. Scaling factors are defined as $F = 1 - L_B$ and $L = 1 - L_G$, with the defining constants L_B and L_G (Petit and Luzum, 2010), from Klioner (2008).

BCRS	**TCB**	**TDB**
Coordinate time	$t = TCB$	$t^* = TDB = Ft + t_0$
Spatial coordinates	x	$x^* = Fx$
Mass parameter	μ	$\mu^* = F\mu$
GCRS	**TCG**	**TCB**
Coordinate time	$T = TCG$	$T^{**} = TT = LT$
Spatial coordinates	X	$X^{**} = LX$
Mass parameter	μ	$\mu^{**} = L\mu$

and Barycentric Dynamic Time (TDB, being a scaled version of TCB). Both scalings have no physical meaning, but were chosen for convenience in order to make the difference between the proper time of an observer on the rotating geoid and these two coordinate time scales evaluated along his trajectory as small as possible.

The post-newtonian equations hold irrespective of the use of TCB and TDB time, if additional scalings are also used for derived quantities as the spatial coordinates and mass parameters of Sun, Earth, Moon and planets. The equations given in Table 3 allow, according to Klioner (2008), to scale coordinate time, spatial coordinates and mass parameters from one space-time coordinate system to another, using the defining constants $L_B = 1.550519768 \times 10^{-8}$ and $L_G = 6.969290134 \times 10^{-10}$. These scalings make it possible to retain exactly the same form of the principle dynamical equations in the BCRS and the GCRS.

When implementing the VLBI delay model into a software package one gets inevitably confronted with the following questions: Which space-time coordinate systems have to be used for spatial coordinates and mass parameters in the Consensus model? And consequently, are there any quantities which have to be rescaled? The authors did not find clear answers to these questions. This may be due to the fact that the coordinate time scales TCB and TCG were introduced at the same time or even after the definition of the Consensus model, i.e. by IAU resolutions A4 (in 1991) and B1.9 (in 2000).

We found another aspect worth addressing, as it may be a potential source of confusion. Earth and solar parameter mass values can be found in the IERS conventions as well as in the JPL ephemerides files. The IERS conventions give the TCB-compatible value for the solar mass parameter and the TCG-compatible value for the Earth mass parameter. The JPL ephemerides give TDB-compatible values for both Earth and solar mass parameters. Table 4 summarises the mass parameter values from the latest three IERS conventions (1996, 2003, 2010) and from the JPL ephemerides files DE403, DE405, and DE241. The values in blue are the original values taken from the reference. All other values are derived from the blue ones by using the scaling factors L_B and L_G. We found that values from the IERS conventions and the JPL ephemerides differ and also change over time. Note that TCB- and TCG-compatible values of the mass parameters are the same in both GCRS and BCRS.

In the following, we summarise the parameters of the Consensus model under question. Our assumptions of the parameter values to be used within the model are stated in italic type.

Spatial coordinates from JPL ephemerides: The barycentric position of Sun, Earth, Moon, and planets are derived from the JPL planetary ephemerides. To request the spatial coordinates the input time argument needs to be TDB. The numerical value of the spatial coordinates provided by the JPL ephemerides are TDB-compatible x^*. Are the barycentric spatial coordinates used in the Consensus model supposed to be TCB-compatible? If yes, we have to rescale the numerical values of spatial coordinates derived from the JPL ephemerides from TDB-compatible to TCB-compatible values by

$$x = F^{-1} x^*. \tag{2}$$

Note, as the TCB-compatible velocities coincide with the TDB-compatible velocities, no rescaling is required for velocities.

The authors assumption: to use TCB-compatible values x for the position of Sun, Earth, Moon, and planets, i.e. rescale the spatial coordinates derived from the JPL ephemerides.

Solar mass parameter: The solar mass parameter, also named heliocentric gravitational constant, is given in the IERS conventions as TCB-compatible value $\mu_\odot$. It is also provided in the JPL ephemerides but as TDB-compatible value $\mu^*_\odot$. The TCB-compatible value can be derived by

$$\mu_\odot = F^{-1} \mu^*_\odot. \tag{3}$$

It should be noted that the value has changed over time for the different IERS conventions. The latest value from IERS 2010 conventions is derived from the DE421 JPL ephemerides, whereas the value from IERS 2003 conventions is compatible with DE405 JPL ephemerides.

The authors assumption: to use the TCB-compatible value $\mu_\odot$ from the latest IERS conventions.

Planetary mass parameters: The mass parameters of the planets are also available in the JPL ephemerides. They are provided as a ratio of TDB-compatible values $\mu^*_\odot/\mu^*_J$. Are the planetary mass parameters for the gravitational delay computation supposed to be TCB-compatible values? If yes, we have to multiply the inverse of the given ratio by the TCB-compatible solar mass parameter to obtain the planetary mass parameter

$$\mu_J = \frac{\mu^*_J}{\mu^*_\odot} \mu_\odot. \tag{4}$$

This implicitly rescales the planetary mass parameters from TDB- to TCB-compatible values. But special care has to be taken to use a $\mu_\odot$ value consistent with $\mu^*_\odot$ provided in the very same JPL ephemerides file.

The authors assumption: to use the TCB-compatible value μ_J derived from the JPL ephemerides using Equation 4, with $\mu_\odot$ being the TCB-compatible value of the

Table 4: Mass parameters for Sun and Earth (also referred to as Heliocentric and Geocentric gravitational constants) derived from IERS conventions and JPL ephemerides files for different coordinate time scales (TCB, TCG, TDB, TT)). Blue values are given in the reference. Black values have been derived from blue by rescaling using the scaling factors L_G and L_B (Petit and Luzum, 2010).

	IERS Conventions			JPL ephemerides		
	TN21 (1996) (McCarthy, 1996)	**TN32 (2003)** (McCarthy and Petit, 2004)	**TN36 (2010)** (Petit and Luzum, 2010)	**DE403** (Standish et. al, 1995)	**DE405** (Standish, 1998)	**DE421** (Folkner et. al, 2009)
	Heliocentric gravitational constant ($\times 10^{20} m^3 s^{-2}$)					
TCB, TCG	1.32712**400000**	1.32712**442076**	1.32712**442099**	1.32712**442081**	1.32712**442076**	1.32712**442099**
TDB	1.32712**397942**	1.32712**440018**	1.32712**440041**	1.32712**440023**	1.32712**440018**	1.32712**440041**
TT	1.32712**399908**	1.32712**441984**	1.32712**442007**	1.32712**441989**	1.32712**441984**	1.32712**442007**
	Geocentric gravitational constant ($\times 10^{14} m^3 s^{-2}$)					
TCB, TCG	3.986004**418**	3.986004**418**	3.986004**418**	3.986004**418**	3.986004**391**	3.986004**424**
TDB	3.986004**356**	3.986004**356**	3.986004**356**	3.986004**356**	3.986004**329**	3.986004**362**
TT	3.986004**415**	3.986004**415**	3.986004**415**	3.986004**415**	3.986004**388**	3.986004**421**

solar mass parameter derived from the very same JPL ephemerides.

Earth mass parameter: The TCB-compatible value of the Earth mass parameter $\mu_\oplus$ is the very same in latest three IERS conventions (1996, 2003, 2010) and corresponds to the TDB-compatible value as given in the DE403 ephemerides. But it has different values in the DE405 and DE421 ephemerides. Why do the latest JPL ephemerides use a different value then the latest IERS conventions (or vice verca)? And which value should be taken? Special attention has to be paid for software packages that also process data of Earth-orbiting satellites and need to use the TT-compatible value for the geopotential.

The authors assumption: to use the TCB-compatible value $\mu_\oplus$ from the latest IERS conventions.

Although the order of magnitude of the scaling effects is below the 1 ps level accuracy of the Consensus model, it might be worth discussing the presented questions and agreeing on the usage of space-time coordinates systems in the Consensus model. This would remove one potential error source with almost no costs assuming that the required changes are simple scaling factors.

6 Conclusions

ESA's Navigation Support Office continues its efforts toward VLBI data analysis. The VLBI delay model is now fully implemented into our software package NAPEOS. The current O-C residual level is at the 2-3 cm level. This result corresponds with our expectations, in particular considering the current level of implementation. We are confident to lower the residual level by a factor of two with the next implementation steps. Full parameter estimation capabilities still have to be enabled. As a next step we will replace our simple piece-wise linear station clock model by a polynomial function and we will enable parameter estimation for station coordinates and EOPs.

We also presented some open questions related to the topic of space-time coordinate systems and their usage in the Consensus model. We look forward to receiving feedback from the scientific community.

References

Böhm J, Böhm S, Nilsson T, Pany A, Plank L, Spicakova H, Teke K, Schuh H (2012) The new Vienna VLBI Software VieVS. In: S. Kenyon, M. C. Pacino, U. Marti (eds.), *Proc. IAG Scientific Assembly 2009*, International Association of Geodesy Symposia Series, 136, 1007–1011.

Böhm J, Niell A, Tregoning P, Schuh H (2006) Global Mapping Function (GMF): A new empirical mapping function based on numerical weather model data. *Geophys. Res. Lett.*, 33, L07304, doi:10.1029/2005GL025546.

Bos M. S., Scherneck H-G (2017) Ocean tide loading provider. `http://holt.oso.chalmers.se/loading/`

ESA/ESOC (2009): NAPEOS Mathematical Models and Algorithms, DOPS-SYS-TN-0100-OPS-GN.

Eubanks T. M. (ed.) (1991) *Proc. U. S. Naval Observatory Workshop on Relativistic Models for Use in Space Geodesy*, U. S. Naval Observatory, Washington, D. C.

Fey A, Gordon D, Jacobs C S (eds.) (2009) The Second Realization of the International Celestial Reference Frame by Very Long Baseline Interferometry, presented on behalf of the IERS / IVS Working Group. *IERS Technical Note 35*, Frankfurt am Main: Verlag des Bundesamts für Kartographie und Geodäsie, ISBN 3-89888-918-6.

Flohrer, C., E. Schönemann, T. Springer, R. Zandbergen, and W. Enderle (2016) VLBI processing at ESOC. In: D. Behrend, K. D. Baver, K. L. Armstrong (eds.), *Proc. IVS 2016 General Meeting 2016: "New Horizons with VGOS"*, NASA/CP-2016-219016, 261–264.

Folkner W M, Williams J G, Boggs D H (2009) The Planetary and Lunar Ephemeris DE 421. *IPN Progress Report 42-178*.

Klioner S A (2008) Relativistic scaling of astronomical quantities and the system of astronomical units. *A&A*, 478, 951–958.

Klopotek G, Artz T, Bellanger A, Bourda G, Gerstl M, Gordon D, Haas R, Halsig S, Hjelle G A, Hobiger T, Hugentobler U, Iddink A, Kirkvik A S, Lambert S, Plank L, Schmid R, Shu F, Titov O, Tong F, Wang G, Xu M, Zheng W (2016) Results from the VLBI Analysis Software Comparison Campaign 2015. In: D. Behrend, K. D. Baver, K. L. Armstrong (eds.), *IVS 2016 General Meeting Proceedings: "New Horizons with VGOS"*, NASA/CP-2016-219016, 203–207.

Lyard F, Lefevre F, Letellier T, Francis O (2006) Modeling the global ocean tides. Modern insights from FES2004. *Ocean Dyn.*, 56(5-6), 394–415, doi:10.1007/s10236-006-0086-x.

McCarthy D D, Petit G (eds.) (2004) IERS Conventions (2003). *IERS Technical Note 32*, Frankfurt am Main: Verlag des Bundesamts für Kartographie und Geodäsie, ISBN 3-89888-884-3.

McCarthy D D (ed.) (1996) IERS Conventions (1996). *IERS Technical Note 21*, Paris, Central Bureau of IERS - Observatoire de Paris.

Nothnagel A (2009) Conventions on thermal expansion modelling of radio telescopes for geodetic and astrometric VLBI. *J Geod*, 83(3), 787–792, doi:10.1007/s00190-008-0284-z.

Petit G, Luzum B (eds.) (2010) IERS Conventions (2010). *IERS Technical Note 36*, Frankfurt am Main: Verlag des Bundesamts für Kartographie und Geodäsie, ISBN 3-89888-989-6.

Saastamoinen J (1972) Contributions to the theory of atmospheric refraction. *J Geod*, 46(3), 279–298.

Standish E M, Newhall X X, Williams J G, Folkner W M (1995) JPL Planetary and Lunar Ephemerides, DE403/LE403. *JPL IOM 314.10-127*.

Standish E M (1998) JPL Planetary and Lunar Ephemerides, DE405/LE405. *JPL IOM 312.F-98-048*.

DOGS-RI: New VLBI Analysis Software at DGFI-TUM

Y. Kwak, M. Gerstl, M. Bloßfeld, D. Angermann, R. Schmid, M. Seitz

Abstract OCCAM has served as the main VLBI software at DGFI-TUM for more than 20 years. For more flexibility and compatibility, DGFI-TUM started to develop its own VLBI software called DOGS-RI. DOGS-RI is a software library of the DGFI Orbit and Geodetic Parameter Estimation Software (DOGS) package which also includes the software libraries for SLR analysis and intra-/inter-technique combinations. That will give a possibility to keep consistency between software libraries sharing common modules. To validate DOGS-RI, we conducted internal comparisons with the OCCAM solutions and external comparisons with the IVS combined solution. In this paper, we introduce the structure and features of DOGS-RI and some validation results. We also discuss future plans for the software and for the VLBI analysis at DGFI-TUM.

Keywords VLBI, IVS, DOGS-RI, VLBI analysis software

1 Introduction

The German Geodetic Research Institute of Technical University of Munich (DGFI-TUM) is an IVS operational Analysis Center (AC) and made use of OCCAM (Titov et al., 2004) as the main software for Very Long Baseline Interferometry (VLBI) analysis since the 1990s. Despite its long history of commitment, DGFI-TUM decided a transition to a new VLBI analysis software in order to reach more flexibility and compatibility.

The new DGFI VLBI software is named "DOGS-RI" (Ralf et al., 2015) since it is one of the software libraries of the DGFI Orbit and Geodetic Parameter Estimation Software (DOGS) package that supports the software libraries for Satellite Laser Ranging (SLR) analysis and intra- and inter-technique combinations (Fig. 1). Within the DOGS package, common modules are shared by the different libraries in order to reach consistency between the techniques.

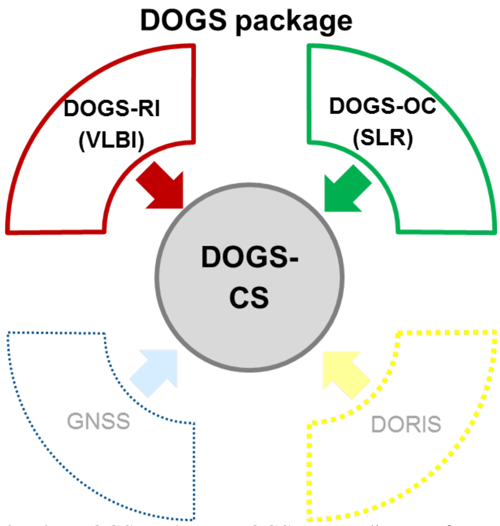

Fig. 1: The DOGS package. DOGS-RI (Radio Interferometry): VLBI analysis, DOGS-OC (Satellite observations as SLR): SLR analysis, DOGS-CS (Combination and Solution): intra- and inter-technique combination. The DOGS package does not support analyses of GNSS and DORIS. Nevertheless, it is able to read the normal equation systems out of SINEX files from those techniques and conduct the combination with DOGS-CS.

2 DOGS-RI

Figure 2 shows the simplified flow chart of DOGS-RI. The whole procedure is similar to other VLBI softwares. It is developed by FORTRAN language and therefore it gives a consistency with other libraries in DGFI softwares, especially DOGS package. Moreover, most geodetic and astronomical subroutines, e.g.

Younghee Kwak · Michael Gerstl · Mathis Bloßfeld · Detlef Angermann · Ralf Schmid · Manuela Seitz
Deutsches Geodätisches Forschungsinstitut, Technische Universität München (DGFI-TUM), Arcisstr. 21, DE-80333 München, Germany

International Earth Rotation and Reference Systems Service (IERS) Conventions and Standards of Fundamental Astronomy (SOFA), are written and provided by FORTRAN language. Therefore, DOGS-RI easily adopts them and thereby we can expect the exactly intended outputs.

The following items are the important new features of DOGS-RI:

- DOGS-RI adheres to the IERS 2010 Conventions strictly and thereby guarantees the international standards.
- Producing nutation parameters with celestial offsets, i.e. dX and dY, instead of $d\psi$ and $d\epsilon$ is now available.
- A common adjustment of multiple sessions, i.e. a global solution, is possible.
- Because of more flexible parameterization, it is easier to set up the consistent parameterization and combine with other space geodetic techniques.
- The option for automatic de-selection of sources with fewer observations is available.
- More exclusion options for problematic baselines, outliers, and incorrect cable calibrations are implemented.
- The handling of station coordinates and jumps are improved.

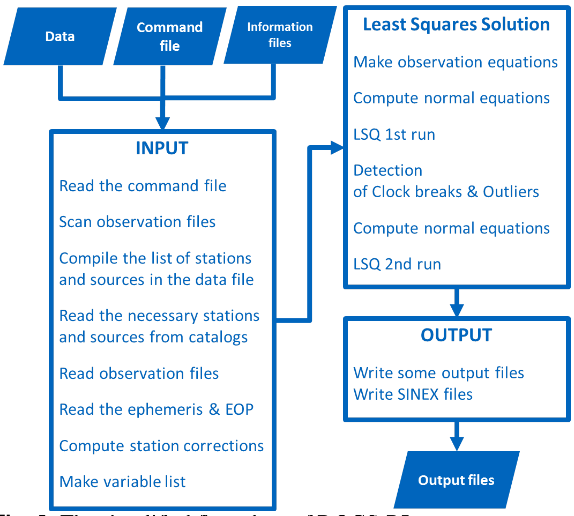

Fig. 2: The simplified flow chart of DOGS-RI

In 2015, DGFI-TUM participated in the VLBI Analysis Software Comparison Campaign with DOGS-RI. The aim of the campaign was to compare the theoretical delays that were computed by different VLBI analysis software packages (Klopotek et. al, 2016). Thereby, we could validate the theoretical modeling of DOGS-RI. The root mean square (RMS) of the residuals between the theoretical delays is a sub-mm level when the theoretical delays by DOGS-RI were compared to the other VLBI analysis softwares.

3 Internal Validation

It is most crucial to confirm that DOGS-RI produces reliable and consistent solutions. To validate the quality of the products, which are computed by DOGS-RI, they are compared with the OCCAM solutions in terms of Terrestrial Reference Frame (TRF) and Earth Orientation Parameters (EOP). We processed all types of the IVS sessions (1,682 sessions) over a time period of 12 years (2005.0-2017.0).

Table 1 shows the Helmert transformation parameters between OCCAM and DOGS-RI solutions with respect to DTRF2014 (Seitz et al., 2016). All the components are comparable within a sub-mm level. Especially the scale parameters agree most. Figure 3 depicts the time series of the scale parameters between OCCAM and DOGS-RI solutions.

Table 1: Helmert transformation parameters of OCCAM and DOGS-RI solutions with respect to DTRF2014. The weighted root mean squared values (WRMS) and weighted mean values (WMEAN) are the statistics from the time series. The unit is cm.

	OCCAM		DOGS-RI	
	WRMS	WMEAN	WRMS	WMEAN
Tx	0.47	0.59	0.51	0.58
Ty	0.58	0.10	0.63	0.02
Tz	0.46	-0.14	0.43	-0.11
Rx	0.49	-0.40	0.50	-0.47
Ry	0.38	-0.40	0.47	-0.37
Rz	0.42	0.16	0.44	0.15
Scale	0.65	0.06	0.65	0.06

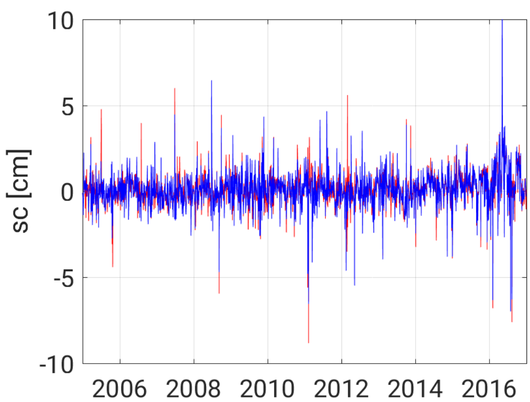

Fig. 3: The time series of the scale parameters of DOGS-RI (blue) and OCCAM (red) solutions.

We also compared the DOGS-RI and OCCAM solutions with IERS 08 C04 EOP series (http://hpiers.obspm.fr/eop-pc/). Table 1 shows the WRMS and WMEAN of the differences with respect to IERS 08 C04 EOP series. The x-pole, y-pole, and UT1-UTC of DOGS-RI agree with those of OCCAM within sub-mm in length on the surface of the Earth. At present, DOGS-RI is able to provide the celestial offsets (dX and dY) for the nutations. Figure 4 shows the comparison of DOGS-RI and OCCAM for dX and dY with respect to IERS 08 C04 EOP series. The dX and dY of the OCCAM solutions are converted from dψ and dϵ values.

The dX components are comparable within 3 μas. In contrast, the dY component of OCCAM solutions has a drift since around 2009 and the reason is unclear. We presume that it could be caused by the outdated convention models in OCCAM. The DOGS-RI solutions show more stable results and can even detect the flaws of OCCAM.

Table 2: The WRMS and WMEAN of the EOP, which are estimated by OCCAM and DOGS-RI, with respect to IERS 08 C04 series. The units are mas for x-pole, y-pole, dX, and dY and ms for UT1-UTC.

	OCCAM		DOGS-RI	
	WRMS	WMEAN	WRMS	WMEAN
x-pole	0.231	0.126	0.237	0.104
y-pole	0.239	0.126	0.242	0.142
UT1-UTC	0.020	-0.005	0.021	-0.006
dX	0.058	0.007	0.060	0.010
dY	0.071	-0.129	0.061	-0.006

4 External Validation

The DOGS-RI solutions are also assessed externally by comparing to the IVS combination solutions. Here, only the DOGS-RI solutions from 2011.0 to 2017.0 are validated. Figure 5 shows the station coordinate repeatability of NYALES20 station. The DOGS-RI solution (DGFI) shows the reliable quality compared to the combination and other AC solutions. Table 3 shows the statistics of the dX components of the IVS AC solutions including the DOGS-RI solution (DGFI). The offset, formal errors (σ), RMS, WRMS of the residuals of the DOGS-RI solution with respect to the IVS combination solution are pretty reasonable compared to those of other IVS ACs. The other components are of the same quality (not shown in this paper).

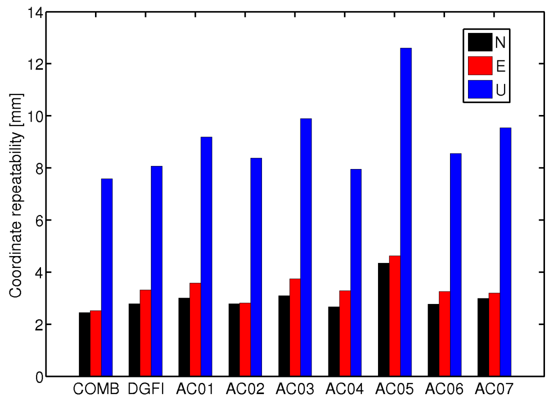

Fig. 5: Station coordinate repeatability of NYALES20 station (courtesy of S. Bachmann at BKG). Each bar group depicts the IVS combination solution or IVS AC solutions. The bars of one triple represent north (black), east (red), and up (blue) components.

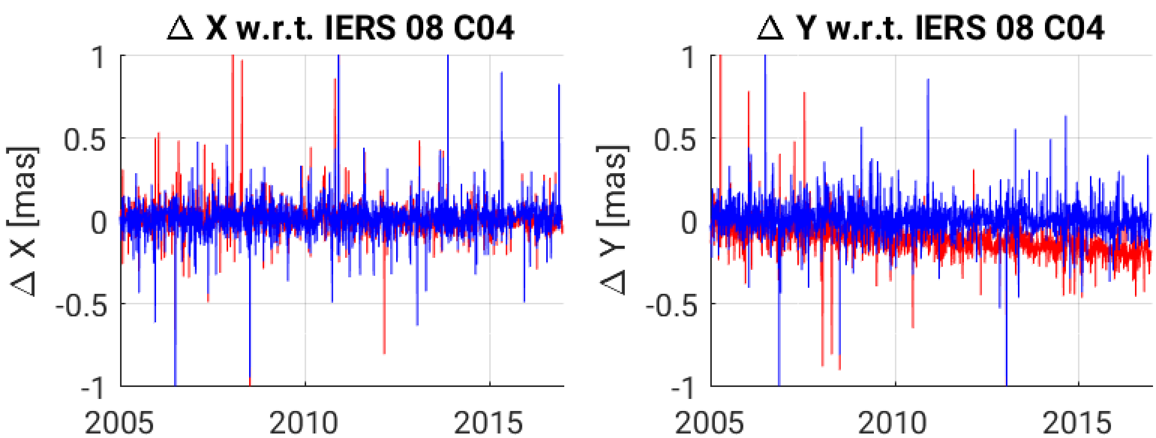

Fig. 4: Celestial offsets from DOGS-RI (blue) and OCCAM (red) solutions with respect to IERS 08 C04 EOP series.

Table 3: Comparison of the dX components of all the ACs with respect to the IVS combination solution. The unit is μas.

	DGFI	AC01	AC02	AC03	AC04	AC05	AC06
Offset	-5.6	-6.6	-3.0	-3.9	-4.2	6.7	11.6
σ	1.5	1.6	0.9	2.4	0.8	0.9	1.3
RMS	55.2	63.4	36.8	90.1	38.2	36.2	49.5
WRMS	39.9	43.1	23.2	53.1	22.3	23.3	33.5

5 Outlook

In order to make DOGS-RI operational completely, the IVS Combination Center recommends rather longer-term (more than 13 years) validation to rule out long-term systematic effects and to guarantee the quality of the product. This work will be done under cooperation with the IVS Combination Center.

DOGS-RI will be developed further and extended for more features. Currently, we are switching from ITRF2008 to ITRF2014 as a priori station coordinates. Supporting vgosDB should be the next urgent task because the IVS Directing Board made the decision that “from September 30, 2017, the sole data format for any type of exchange and long term storage will be vgosDB."

Acknowledgements

This study was funded by the German Research Foundation (DFG) within the Research Unit “Space-Time Reference Systems for Monitoring Global Change and for Precise Navigation in Space" (FOR 1503). The authors would like to thank IVS for providing the data (Schuh and Behrend, 2012). The authors also appreciate Sabine Bachmann’s (BKG) validation through VLBI intra combination.

References

Klopotek G, Artz T, Bellanger A, Bourda G, Gerstl M, Gordon D, Haas R, Halsig S, Hjelle G A, Hobiger T, Hugentobler U, Iddink A, Kirkvik A S, Lambert S, Plank L, Schmid R, Shu F, Titov O, Tong F, Wang G, Xu M, Zheng W (2016) Results from the VLBI Analysis Software Comparison Campaign 2015. In: D. Behrend, K. D. Baver, K. L. Armstrong (eds.), *IVS 2016 General Meeting Proceedings: "New Horizons with VGOS"*, NASA/CP-2016-219016, 203–207.

Schmid R, Gerstl M, Seitz M, D. Angermann D (2015) DGFI Analysis Center Annual Report 2014. In: K. D. Baver, D. Behrend, K. L. Armstrong (eds.), *IVS 2014 Annual Report*, NASA/TP-2015-217532, 210–212.

Schuh H, Behrend D (2012) VLBI: a fascinating technique for geodesy and astrometry. *J Geodyn* 61:68-80.

Seitz M, Bloßfeld M, Angermann D, Schmid R, Gerstl M, Seitz F (2016) The new DGFI-TUM realization of the ITRS: DTRF2014 (data). Deutsches Geodätisches Forschungsinstitut, Munich, doi:10.1594/PANGAEA.864046.

Titov O, Tesmer V, Böhm J. OCCAM v.6.0 software for VLBI data analysis. In: N. Vandenberg, K. Baver (eds.), *IVS 2004 General Meeting Proceedings*, NASA/CP-2004-212255, 267–271.

Ocean Tide Loading - Where we are Standing

H.-G. Scherneck, M. S. Bos, R. M. S. Fernandes

Abstract The actual state of affairs in ocean tide loading is reviewed, including the Free Ocean Tide Loading Service. As of current, the service computes loading parameters from a range of ocean tide models, eleven harmonic species in time and gridded in space at resolutions as given in the 27 data sources, adding local improvement with a high-resolution coastline model. In the context of this conference, we concentrate on vertical and horizontal displacement. The advent of tide models with 1/8×1/8 degree resolution strained the computation on the machine at Onsala Space Observatory beyond practicability. One of our measures was to relay the computation to a dedicated computer at SEGAL UBI/IDL. Another was to retain the 1/8 degree resolution only near coasts, making use of the quad-tree algorithm already engaged in the coastline process. The presentation shows the attainable gain in precision by comparing parameters based on (a) lower-resolution models, (b) on 1/8 degree resolution throughout, (c) on the mixed resolution representation, and (d) on a mapping approach that, by inherent limitation, skips the coastline resolution altogether. The latter method will be detailed; we will present the options it offers to prospective users. The options include fast retrieval of displacements at random locations from a disseminated set of grid files, which could be attractive primarily in the context of fast evolving space geodetic networks.

Keywords Site displacements, Ocean tide loading

Hans-Georg Scherneck
Onsala Space Observatory, Department of Earth, Space and Environment, Chalmers University of Technology, SE-439 92 Onsala, Sweden

Machiel S. Bos · Rui M. S. Fernandes
SEGAL Space & Earth Geodetic Analysis Laboratory, University of Beira Interior and Instituto Dom Luiz, Rua Marquês d'Àvila e Bolama, 6201-001 Covilhã, Portugal

1 Introduction

Ocean tides cause up to centimetre level displacements of the Earth surface that are observed by space geodetic techniques. Therefore, ocean tide loading corrections have been in use in VLBI software for over thirty years. The GNSS technique is more recent but the number of stations has grown rapidly to a few thousands and the IGS is striving for comparable accuracy demands as the IVS. Anticipating the foreseeable work load of computing ocean tide loading coefficients, Scherneck and Bos (2002) launched an automated, internet-based user service in 2001, called the Free Ocean Tide Loading Provider (henceforth called OLP). An OLP client may choose among 27 ocean tide models and specify up to 100 station positions per request. The computation of coefficients is based on a convolution integral of a global tide model with a Green's function. The latter represents the deformation of the Earth's surface due to a point load on an elastic, spherically symmetric Earth (Farrell, 1972; Bos and Scherneck, 2013). In the next sections we present the details of the computation of the OTL coefficients and discuss the improvements of the OLP we envision for the near future.

2 Ocean tide Models and Coastlines

Since the launch of the TOPEX/Poseidon satellite in 1992, the oceanographic community has produced global ocean tide models with ever increasing spatial resolution, from a wider range of observation sources, and has extended the park of methods in charting and hydrodynamic modelling. Table 1 gives a short overview of the ocean tide models that have been published over the years. For historic reasons we also include the model of Schwiderski (1980), which predates the satellite altimetry era; it has a spatial resolution of 1°. The most recent ocean tide models provided by the Toulouse group, FES2012 and

Table 1: Time line of ocean tide models, time they became available, number of nodes per degree (reciprocal grid constant) and the number of frequencies (waves). The last column contains the thickness of the compensating tide layer for harmonic M_2 for conserving its mass.

Model	year	1/resol	nr. of waves	compensation (mm)
Schwiderski	1980	1	11	7.30
TPXO.5	1994	2	11	0.90
CSR3	1994	2	8	0.41
CSR4	1994	2	8	0.56
FES94.1	1994	2	11	3.80
FES95.2	1995	2	12	1.19
FES98	1998	4	11	1.74
FES99	1999	4	15	1.33
GOT99.2b	1999	2	11	0.22
NAO.99b	2000	2	23	1.32
GOT00.2	2000	2	11	0.15
FES2004	2004	8	17	0.57
TPXO.6.2	2004	4	11	0.54
AG06	2006	4	11	0.26
TPXO.7.0	2002	4	11	0.23
TPXO.7.1	2007	4	11	0.22
EOT08a	2008	8	13	0.46
TPXO.7.2	2009	4	11	0.06
DTU10	2010	8	13	0.47
EOT11a	2011	8	14	0.61
GOT4.7/GOT4.8	2011	2	12	0.10
OSU12	2012	4	13	0.30
FES2012	2012	16	11	0.49
Hamtide	2014	8	11	0.11
TPXO8-Atlas	2014	30	9	0.21
FES2014b	2014	16	34	0.16

FES2014b, have a grid spacing of 1/16°. More details about the early ocean tide models are given by Shum et al. (1997) while Stammer et al. (2014) review the more recent ones.

Figure 1 shows for harmonic M_2 the vector difference between ocean loading displacements computed from Schwiderski-FES94.1, FES2004-GOT00.2 and between FES2014-TPXO.7.2. The first shows difference of the order of 10 cm, indicating the tremendous effect of including satellite altimetry data into the model. The second panel shows that around 2000-2004 there were still remaining errors near the coast and in the polar region. The third panel shows that with the most recent models these errors are further reduced.

The models with 1/8° spatial resolution already required a wall clock computing time of up to two hours per OLP request with hundred stations. On an average day, the OLP machine at Onsala is occupied with jobs for more than 12 hours. The recent models would raise this four-fold, creating an ever-increasing backlog of OTL requests.

As a provisory solution, requests involving FES2012 or FES2014b are currently relayed to SEGAL. There, the computation uses reduced ocean grids at 1/4° in the open ocean and the 1/16° resolution near the coast in order to represent the complex shelf and bay tides. The latter also ensures a better fit with the coastline. Penna et al. (2008) showed that the coastline resolution is a critical step; especially with the early models that have grid constants of one or one-half degree, tide loads on complicated coasts are insufficiently represented when geodetic sites are located there at short distances. The OLP employs a quad-tree algorithm that inter- and extrapolates at ever finer resolution between the global grid and the coastline, which is taken from the high-resolution database of the GMT package (Wessel and Smith, 1998; Bos and Baker, 2005).

The higher resolution of the recent models implies a slightly lower accuracy demand on the quad-tree filling between regular grid and coastline. Yet, this step does not appear to become obsolete if we require sub-millimetre precision for the leading tide M_2 (as a rule of thumb, the error level is about two times the M_2 error when all eleven tide waves are included; this estimate takes also the missing signal from unrepresented waves into account). As an example of an outright error in ocean representation of the global FES2014b grid is shown in Figure 2. It represents the area of the southern Malacca peninsula and one can note the white area in the left map. Fortunately, the tide is low there and the nearest GNSS station of the IGS station, NTUS, is at a respectable distance (marked with a black cross). Also note that much fewer wet nodes are located on land than dry ones in the sea, judging from the GMT full-resolution coastline. Recently a version of FES2014b has been made available that has tidal grid cells extrapolated over land, resolving this problem. However, such an extrapolation is also performed inside our OTL software. The OTL map to the right is computed using the fast gridding method, see section 3.

3 Fast OTL computations and Green's functions

In response to the afore mentioned long computation times, a fast Fourier algorithm was devised to compute the loading effects from the global, regular tide grids. It computes the global deformation field with the same grid constants. Thus, the results can be stored once-for-all. The CPU-time is proportional to $N^3 \log N$ (instead of $\propto N^4$ in the straight approach), where N is the number of grid nodes in one dimension. The whole set of global OTL maps can be computed in 25 hours (next generation ocean tide models would eventually need a more powerful computer) instead of months using a program such as CARGA (Bos and Baker 2005). The new imple-

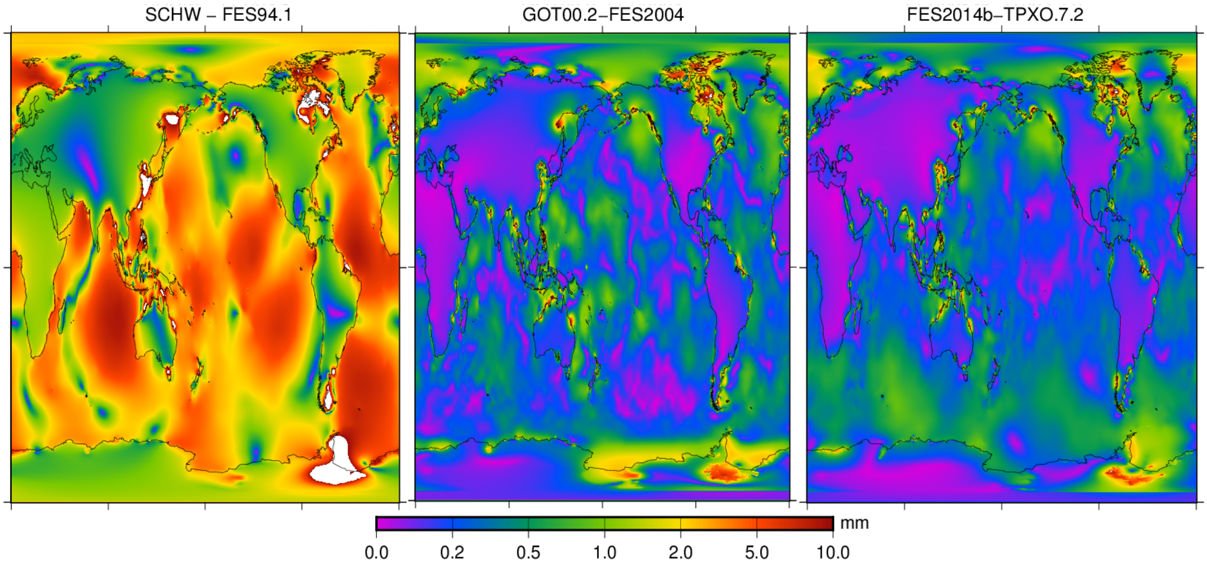

Fig. 1: Modulus of difference between OTL fields, Schwiderski & FES94.1 (left), FES2004 & GOT00.2 (middle) and FES2014b & TPXO.7.2 (right), evidencing the impact of the global coverage in satellite altimetry in the GOT- and TPXO-model suites. Shown is the vertical component of M_2

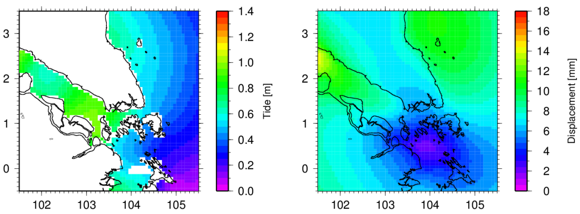

Fig. 2: A land-sea representation error in FES2014b at the southern Malacca peninsula, note the white area in the left diagram. Fortunately, the tide is low there and the nearest GNSS station of the IGS station, NTUS, is at a respectable distance (marked with a black cross). Also note that much fewer wet nodes are located on land than dry ones in the sea, judging from the GMT full-resolution coastline. The map to the right is from the fast gridding method.

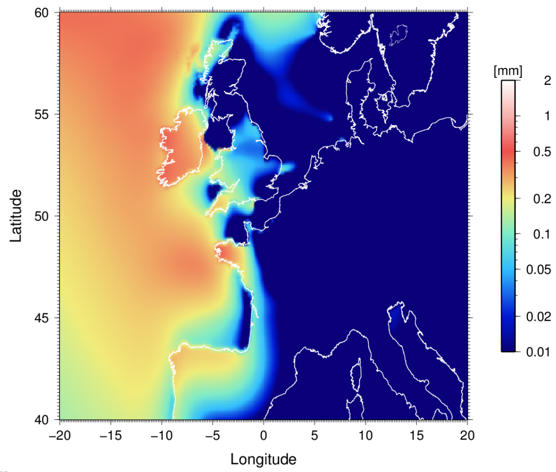

Fig. 3: Effect of integration of Green's function versus point-load approximation. Shown is the modulus of the difference in the case of radial displacement for M_2 computed from the HAMTIDE ocean model using fast convolution.

mentation of the Fast OTL algorithm strikes a balance between speed and precision; for instance, the Green's functions' hemispheric symmetry is utilized, and the function is integrated over grid boxes if they are within a critical distance. This implies that the load is distributed like a uniform quadrangular tile. Without integration, a load would resemble an infinitely dense mass point at the centre of a grid cell. The impact of integration versus the central point-load approximation is shown in Figure 3 as the modulus of the difference for the case of radial displacement computed from the HAMTIDE M_2 map (implying that load distribution abides by the grid's 1/8° jagged land-sea pattern). Note that integration was still performed in the case where a load cell acts on the corresponding field cell; that specific contribution to the response is uninteresting at field points on land, which is the usual condition conserning space geodetic sites.

For some stations that are within a 10-50 km range of the coast, we noted that it is still necessary to subdivide the ocean tide grid cells around the station to keep the numerical error below the 0.1-0.3 mm level per harmonic. However, this quad-tree subdivision is only necessary in a limited region near these sites. Efforts to come to specific thresholds and terms with this task are currently in progress. The ambition is that differences between different ocean models would stand out above measures of increased precision, where the latter should arrive at less than a millimetre when time series are produced, i.e. all waves are added together. Figure 4 shows an example for the spread of loading phasors from a sample of ocean tide models, Green's functions

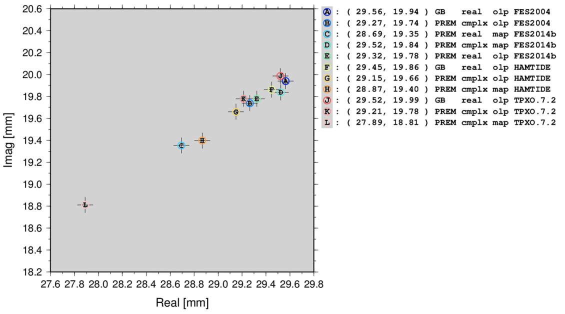

Fig. 4: Loading phasors for vertical displacement of tide M_2 at the VLBI site BRFT, Fortaleza, Brazil. Shorthands for Green's functions: Earth structure from `GB` - Gutenberg-Bullen, `PREM` - Anderson and Dziewonski; `real` - elastic earth, `cmplx` - anelastic earth. Shorthands for methods: `olp` - Ocean loading provider (Internet service with high-resolution coastlines), `map` - fast mapping algorithm, no coastline refinement.

and processing methods for VLBI station BRFT, Fortaleza, Brazil, harmonic M_2, up component. It shows OTL values computed using the internet ocean tide loading provider with high-resolution coastlines (olp) and the fast mapping algorithm (map), with no coastline refinement. It also shows OTL values computed using various Green's functions such as the one of Gutenberg-Bullen (GB), Anderson and Dziewonski (PREM). The latter has been computed assuming a pure elastic Earth (real) or a constant absorption band from 1s to the period of M_2 (cmplx). The latter includes anelasticity effects that are mostly produced in the asthenosphere, see Bos et al. (2015) for more details.

The reader might wonder why we keep the tide waves of the OLP to the set published by Schwiderski (1980)? First, although recent catalogues include species in addition to S_{sa}, M_m, M_f, Q_1, O_1, P_1, K_1, N_2, M_2, S_2 and K_2, the sets are inconsistent and thus cumbersome to employ in routine geodetic analyses. Second, the BLQ format adopted in a range of softwares still seems to enjoy wide use. If an option to include all available waves pertaining to a model catalogue is introduced, the tables of loading coefficients would be issued in the HARPOS format thanks to its extendibility. Readers may notify us of their opinion.

4 OTL time series

In the previous section, we noted that the OTL coefficients are given as a set of amplitudes and phase-lags for 11 major harmonics. The displacement time series are computed by simply summing the various periodic functions:

$$u(t) = \sum_{i=1}^{11} A_i \cos(\omega_i t + \chi_i + \phi_i) \tag{1}$$

where A_i is the amplitude, χ_i the astronomical argument at $t = 0$, and ϕ_i the phase-lag value provided by the OLP.

However, the full tidal potential has many more constituents, see Wenzel (1997) or Agnew (2007). These must be considered if one is to produce an accurate time series. Here, there are basically two methods, one to interpolate an admittance spectrum from the harmonics given at distinct frequencies, and another to invoke the response method of Munk and Cartwright (1966) (see also Lambert, 1974). Each has its own drawback. The response method requires a totally revised method to generate time series of predictions, the admittance method needs to separate between gravitational and radiational (including atmospheric) generation of tidal components. In each case we must distinguish response or admittance functions by spherical harmonic degree. Sun's seasonally varying radiation affects S_1 and S_2 and their neighbour waves at one, two and three cycles per year beat frequency. Conflation of effects is more complicated still in the case of the solar annual tide S_a where altimetry also senses steric, thermal expansion of water, which does not cause direct loading effects in the open ocean; however, the annual cycle does not keep ocean mass conserved. Thus, ocean models for S_1 must be derived from time-stepped products like ECCO (Forget et al., 2015). As ECCO represents the non-tidal ocean, adding the equilibrium response to the solar gravitational tide might be a reasonable approximation.

Talking about equilibrium response, there are additional ocean loading effects at periods or quasi-periods longer than one year, where dynamics play a subordinate role. This concerns forcing by polar motion and the lunar nodal tide at 18.6 yr period (Tapley et al., 1993). The longer the forcing period, the more retarded strain will be released due to mantle anelasticity.

5 Outlook

A comprehensive revision of means and methods to predict ocean tide loading effects is on the way, planned for publication during the coming year. For instance, clients of the OTL service will be able to choose among a range of Green's functions that depend on the viscoelastic structure of the earth with a parameterized frequency dependence. The full resolution of all ocean tide models will be utilized, augmented with yet higher resolution coastlines to represent the loads accurately also in complicated settings. The ambition to arrive at precisions of less than 1 mm RMS error in time series also in complicated cases will require testing with observations, preferably using both VLBI and GNSS techniques.

References

Agnew D (2007) Earth tides. In: T. Herring (ed.), *Treatise on Geophysics: Geodesy*, Elsevier, 163–195.

Bos M S, Baker T F (2005) An estimation of the errors in the gravity ocean tide loading computations. *J Geodesy*, 79:50–63.

Bos M S, Scherneck H-G (2013) Computation of Green's functions for ccean tide loading. In: G. Xu (ed.), *Sciences of Geodesy - ii*. Springer Berlin Heidelberg, 1–52.

Farrell W E (1972) Deformation of the earth by surface loads. *Rev. Geophys. Space Phys.*, 10:761–797.

Forget G, Campin J-M, Heimbach P, Hill C N, Ponte R M, Wunsch C (2015) ECCO version 4: an integrated framework for non-linear inverse modeling and global ocean state estimation. *Geosci. Model Dev.*, 8(10):3071–3104.

Lambert A (1974) Earth tide analysis and prediction by the response method. *J. Geophys. Res.* 79(32):4952–4960.

Munk W H, Cartwright D E (1966) Tidal spectroscopy and prediction. *Phil. Trans. R. Soc. A*, 259(1105):533–581.

Penna N T, Bos M S, Baker T F, Scherneck H-G (2008) Assessing the accuracy of predicted ocean tide loading displacement values. *J Geod*, 82:893–907.

Scherneck H-G, Bos M S (2002) Displacements due to ocean tide and atmospheric loading using modern sea level records. In: N. R. Vandenberg, K. D. Baver (eds.), *IVS General Meeting 2002 Proceedings*.

Schwiderski E W (1980) On charting global ocean Tides. *Rev. Geophys. Space Phys.*, 18(1):243–268.

Shum C K, Woodworth P L, Andersen O B, Egbert G D, Francis O, King C, Klosko S M, Le Provost C, Li X, Molines J M, Parke M E, Ray R D, Schlax M L, Stammer D, Tierney C C, Vincent P, Wunsch C (1997) Accuracy assesment of recent ocean tide models. *J. Geophys. Res.*, 102(C11), 25173–25194, doi:10.1029/97JC00445.

Stammer D, Ray R D, Andersen O B, Arbic B K, Bosch W, Carrère L, Cheng Y, Chinn D S, Dushaw B D , Egbert G D, Erofeeva S Y, Fok H S, Green J A M, Griffiths S, King M A, Lapin V, Lemoine F G, Luthcke S B, Lyard F, Morison J, Müller M, Padman L, Richman J G, Shriver J F, Shum C K, Taguchi E, Yi Y (2014) Accuracy assessment of global barotropic ocean tide models. *Reviews of Geophysics*, 52: 243–282.

Tapley B D, Schutz B E, Eanes R J, Ries J C, Watkins M (1993) Lageos Laser Ranging Contributions to Geodynamics, Geodesy, and Orbital Dynamics. In: D. E. Smith, D. L. Turcotte (eds.), *Contributions of Space Geodesy to Geodynamics: Earth Dynamics*. Geodynamics Series, American Geophysical Union, Washington, D. C., 147–173, doi:10.1029/GD024p0147.

Wenzel H-G (1997) Tide-generating potential for the earth. In: H. Wilhelm, W. Zürn, H.-G. Wenzel (eds.), *Tidal phenomena*. Springer, 9–26.

Wessel P, Smith W H F (1998) New, improved version of the Generic Mapping Tools released. *EOS Trans. AGU*, 79:579.

An Empirical Atmospheric Tidal Loading Solution for Particular VLBI Stations

A. Girdiuk, M. Schindelegger, J. Böhm

Abstract Tidal atmospheric loading causes small but periodic reference point displacements that are conventionally treated in the space geodetic analysis reductions. On the one hand, numerical model estimates of these displacement signals are provided, e.g., by TU Wien, Goddard Space Flight Center (GSFC) or the Global Geophysical Fluid Center (GGFC). On the other hand, with the large data base of modern Very Long Baseline Interferometry (VLBI) observations and the high precision of other reduction models, the small effects of the tidal atmospheric loading variations can be determined directly in the analysis. Here, by utilizing the Vienna VLBI and Satellite Software (VieVS), hourly station coordinates are obtained and particular measures are taken to mitigate the obvious correlations with tropospheric parameters. Specifically, the hourly intervals of zenith wet delay estimates are replaced by six-hourly intervals, similar to the estimation interval of tropospheric gradients. Retrieved time series (06/2011–02/2016) of positions for station Katherine, Australia, reveal amplitudes of the diurnal atmospheric signal in the range (0.5 – 1.5) mm with a confidence interval of 1.5 mm (threefold formal error) as provided by single session solutions for different analysis setups. Generally, these amplitudes exhibit fair agreement with estimates from the applied loading models, that is cosine and sine amplitudes: (−0.6 mm; 0.7 mm) for the TU Wien solution, (−0.4 mm; 0.5 mm) for GSFC and (−0.8 mm; 1.0 mm) for GGFC.

Keywords Atmospheric tides, harmonic variations of station positions, single session solution

Anastasiia Girdiuk · Michael Schindelegger · Johannes Böhm
TU Wien, Geodesy and Geoinformation, Advanced Geodesy, Gußhausstraße 27-29/E120, AT-1040, Vienna, Austria

1 Introduction

Atmospheric tides are regular variations induced by solar insolation and appear with Sun-locked periods of 24 and 12 hours. These geophysical phenomena are visible in geodetic parameters, i.a., Earth Rotation and variations of station positions. This paper focuses on the less studied harmonic variations in Very Long Baseline Interferometry (VLBI) station positions. Currently, various numerical models — TU Wien (Wijaya et al., 2013), Goddard Space Flight Center (GSFC) (Petrov and Boy, 2004) or the Global Geophysical Fluid Center (GGFC) (van Dam, 2010) — provide station position corrections associated with atmospheric loading. Routine VLBI analysis takes into account atmospheric loading reductions, along with other distortions due to solid Earth tides and ocean tides as recommended by the IERS Conventions (Petit and Luzum, 2010). Atmospheric tidal loading induces one of the smallest displacements of the reference points on the crust with amplitudes mostly at or below the 1 millimetre level. These obvious systematic influences are required to be considered in the analysis. The proper determination of these small variations is one of the challenges imposed on the modern geodetic VLBI observations. To achieve this goal in the present paper, loading results from numerical weather models are reviewed to pinpoint VLBI stations with large-magnitude atmospheric tidal variations. Because the modern geodetic VLBI technique approaches the millimetre accuracy level, the tidal loading maxima are probed, and station Katherine in Australia is found to be a suitable example. In detail, hourly station positions at Katherine estimated in single sessions solutions are favored over the standard parametrization, in which station coordinates have only one estimate per session. This modification requires to adjust the tropospheric parameter evaluation interval because of correlations with station positions. A compromise is found in changing the zenith wet delay interval from 1 hour to 6 hour. Additionally, the impact of other reductions and parametrization is studied to test the hourly station

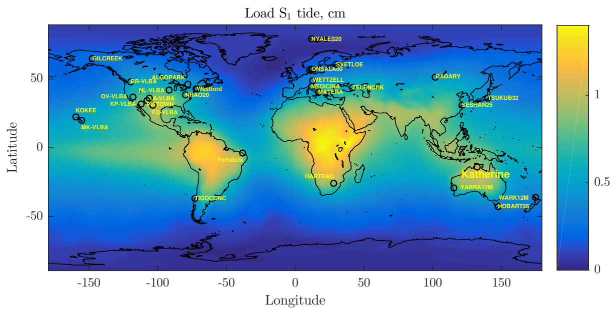

Fig. 1: Amplitudes of S_1 atmospheric tidal loading as provided by the TU Wien model.

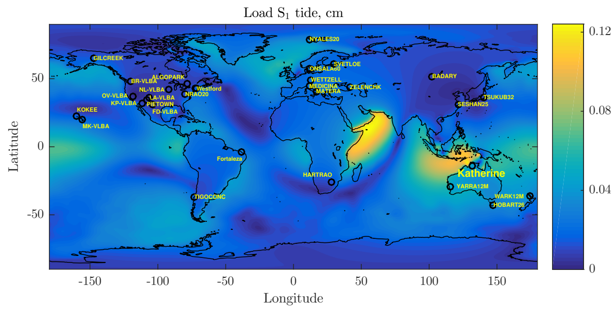

Fig. 2: Amplitudes of S_1 ocean tidal loading as provided by the FES2014b model.

position time series reliability. To meet this challenge, the method of the least squares adjustment (LSA) at the frequencies of atmospheric tides is applied to obtain an empirical tidal solution for station Katherine.

2 Numerical loading solutions

Using pressure data from numerical circulation models, station position corrections induced by the atmospheric tides S_1 and S_2 can be deduced for a set of components in Radial, East and North directions (REN system) for each station. For S_1 (the diurnal atmospheric oscillation), the maximal displacement is concentrated in the radial direction illustrated in Fig. 1, because it receives the most of the tidal loading power. The model calculated at TU Wien exemplifies the distribution of the atmospheric impact on the Earth's crust including maximum and minimal values. Other available models (GSFC and GGFC) possess rather similar scattering and amplitude patterns.

In Fig. 1 the VLBI station Hartrao can be found close to the equatorial area where the atmospheric tidal loading attains largest values over the South African continent. Yet, the load tide amplitude at this station is smaller than the corrections at the station Katherine in Australia provided by numerical models. The numerical corrections (cosine and sine amplitudes) to the Katherine position are (−0.6 mm; 0.7 mm) for the TU Wien solution, (−0.4 mm; 0.5 mm) for the GSFC model and (−0.8 mm; 1.0 mm) for GGFC. These small magnitudes cause certain difficulties in terms of the detection in VLBI analysis; yet, being systematic influences on daily and sub-daily time scales, their estimation should be feasible.

Larger loading effects in the diurnal and semi-diurnal bands belong to the effect of the ocean tides. As a rule, ocean tide loading is introduced in VLBI reductions for 8 major tides (Q_1, O_1, P_1, K_1, N_2, M_2, S_2, K_2) and 3 long term tides (Mf, Mm, Ssa), where S_2 denotes the frequency corresponding to a period of 12 hour, thus matching the frequency band of the atmospheric S_2 tide. The oceanic S_2 tide induces maximal loading values at VLBI station Fortaleza (South America, 1.1 cm) and at the same time the atmospheric tide S_2 is less then 1 mm. This coincidence of atmospheric and oceanic contributions is unavoidable and required to be considered properly for both studied frequencies, i.e. S_1 and S_2. In the VLBI reductions, following the IERS Conventions example, ocean tides are taken into account commonly by means of the FES2004 ocean model. Girdiuk et al. (2016a,b) compared tidal loadings from different providers, and rather similar solutions in terms of VLBI baseline length repeatabilities are found when the underlying ocean model is changed. Here, the last available version of the FES numerical ocean model series (Letellier et al., 2004) FES2014b (Aviso, 2014) is chosen for reductions because this model includes the ocean response to the atmospheric forcing at the S_1 frequency (Fig. 2). Older models, for instance FES2004, do not consider S_1. At the station of interest in this paper, Katherine, the corrections due to the S_1 load tide based on FES2014b (shown in Fig. 2) are found to be approximately 0.4 mm.

3 Single session solution modifications

Almost 390 24 h VLBI sessions were assembled for the period of June, 2011 – Feb, 2016, in which the station Katherine participates. This relatively short but dense time series of 5 years were processed by solving each session with the LSA using the Vienna VLBI and Satellite Software (VieVS) (Böhm et al., 2012). An additional criterion for the selection of a session is that it contains observations at more than 5 stations. This requirement for the network is necessary because station Katherine has to be excluded from the datum, so that the rest of the stations (4 antennas) is enough for its realization. The datum can be realized by a part of the antennas per session. The main reason for excluding Katherine from the datum is that in our analysis the station positions for Katherine are evaluated at hourly intervals to resolve daily and sub-daily variations. This scheme is in contrast to the standard approach where the station coordinates are estimated once per session or fixed to a priori values.

In the standard approach (Schuh and Böhm, 2013) of solving VLBI observations in single session solutions, the design matrix is set up for:

1. Clocks:piecewise linear offsets at hourly intervals plus a linear and quadratic terms per session;
2. Tropospheric parameters: Zenith Wet Delay (ZWD) at hourly intervals and tropospheric gradients in North and East directions (NGR and EGR) at 6-hour intervals.
3. Earth Orientation Parameters daily constant value;
4. Station coordinates once per session;
5. Source coordinates once per session.

Given the elevation angle dependence for both the station heights and the ZWD (Sovers et al., 1998), and the associated correlations in the inversion, the estimation interval of one of them has to be modified. The hourly station coordinates are the subject of this paper, thus the ZWD is evaluated at 6-hour intervals for all solutions presented below in this paper. Yet, some undesired dependencies are retained in the solutions. In order to reduce some of them, ray-traced delays were applied to the NGR and EGR as well as to the ZWD because this approach might be more accurate in application to the VLBI observations (Hofmeister, 2016), so a statistical formal error level improvement was expected. Hence, solutions with gradients fixed to their a priori values were used in addition to the standard strategy. Therefore, for the one atmospheric loading variant (Sect. 2) four solutions were obtained.

Concerning the rest of reductions and constraints applied in the processing, we follow the common approach widely used at TU Wien and given by Krásná et al. (2014). The only difference in the reductions is that the atmospheric tidal loading is excluded from the station position corrections, but the corrections due to ocean loading are introduced using FES2014b, so that the oceanic contribution at the S_1 frequency is included. In this way, oceanic and atmospheric contributions are considered separately, and explicit emphasis can be given to the atmospheric part.

4 An empirical assessment

Hourly station position variations for the station Katherine are obtained in the geocentric rectangular coordinate frame as provided in VieVS single session solutions. In order to facilitate numerical model comparisons, these time series can be transformed to the REN system in a straight-forward manner by a rotation matrix at the angle of latitude and longitude of the location. These hourly estimates are supplied with formal errors of the stochastic model in VieVS. However, the time series is contaminated for various reasons, among them insufficient network geometry as the most prominent factor (Girdiuk et al., 2016c). Influences from these sporadic outliers can not be mitigated through the formal error analysis. To remove these outliers, a better approach is to limit the hourly station position time series by 10 cm condition in X and Y directions, and 7 cm in Z.

Finally, the LSA is undertaken to retrieve atmospheric tidal contributions from the hourly time series of station positions. A similar approach was implemented by Girdiuk et al. (2016c) for the high-frequency Earth Rotation Parameter analysis, but in this paper we introduce the pre-defined frequencies S_1 and S_2 only. The results of this assessment for four VLBI solutions described above are demonstrated in Fig. 3 for the primary S_1 radial component. The circles indicate formal errors, i.e. $3\,\sigma$ (1.5 mm), $2\,\sigma$ (1.0 mm) and $1\,\sigma$ (0.5 mm). These levels are almost the same for all shown solutions, so the width of the circles on the plot should underline this fact. Fig. 3 illustrates the substantial empirical estimates of the S_1 load tide in radial direction. Unfortunately, modeled values are found under the $3\,\sigma$ reliability level, but the atmospheric tides estimates obtained for Katherine have a good agreement with these models except for some separation in phase (see Fig. 3). Also, due to noise in the time series, improved results using ray-tracing instead of VMF1 (Böhm et al., 2006) to better account for the troposphere is not evident. And, the significant difference of about 1 mm between the strategy of fixing gradients and estimating them does not allow to validate the ray-tracing or VMF1 approach. In future, a larger number of observations for station Katherine will increase the reliability of such assessments based on lower formal error statistics.

Some distortions of the final results (Fig. 3) can arise from the applied method of the LSA at two pre-defined frequencies because of possible leakage from side lobes. In fact, the large-amplitude ocean tides P_1 and K_1 (see Table 8.2a of the IERS Conventions) are the closest to the frequency S_1 and, by this reason, might corrupt loading estimates at this frequency. Note that the gravitationally induced S_1 constituent is a product of the P_1 and K_1 side lobes as derived from the tide generating potential. This oceanic variation is of a small amplitude and its impact is neglected in the station position variations. But, the atmospheric impact at the frequency S_1 has a completely different source, that is, diurnal atmospheric pressure variations induce regular motions of

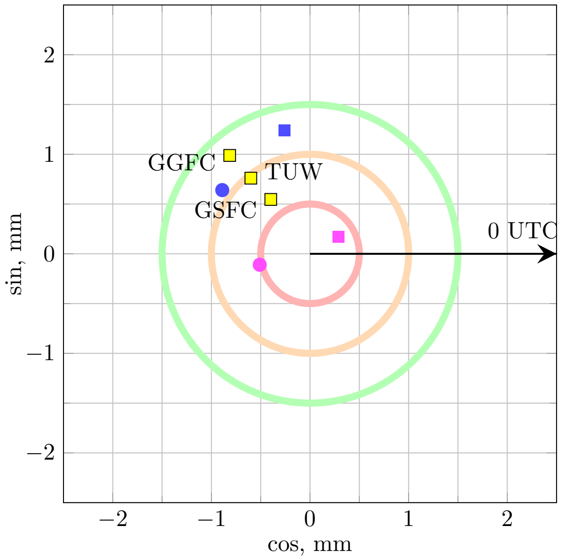

Fig. 3: Atmospheric tides retrieved in harmonic variations of station positions of radial component for Katherine. The 1 σ level of standard deviations is depicted on both planes as circle of pink color, 2 σ as orange color, and 3 σ as green color; squares mark ray-tracing, circles denote VMF1, pink color represents solutions where gradients are fixed, blue where gradients are estimated. The phase reference is Greenwich midnight (0 UTC).

the crust at the order of 1 mm as provided by the numerical models (TU Wien, GSFC, GGFC). Also, the atmosphere forces the ocean to vary at the same frequency as atmospheric tides. As we have seen, FES2014b provides this hydrodynamic response at the S_1 line (Fig. 2); see also Ray and Egbert (2004). At the frequency of S_2, the atmospheric forcing is difficult to distinguish from the oceanic S_2 influence because the semi-diurnal ocean tide S_2 is one of the main lobes in the tide generating potential and possesses amplitudes which are approximately 10 times bigger than the response to the meteorological S_2 signal (Arbic, 2005). Evidently, an improper account of ocean tidal loading can lead to uncertainties in the evaluation of the amplitude and phase of the atmospheric tidal loading contribution.

5 Conclusions

On the one hand, atmospheric tidal loading estimates are available from various numerical models, where three of them were investigated and this study revealed the maximum contribution at the VLBI station Katherine. On the other hand, using modern VLBI observations we retrieved atmospheric tidal signals in hourly station position variations for station Katherine. This empirical result was cleansed from the ocean response to the atmospheric forcing at the S_1 frequency using a load tide solution from the most recent ocean model FES2014b. We presented here results for the atmospheric-induced S_1 load tide in the radial component mainly to exemplify the involved magnitude of signals. It became clear that the time series need to be extended to achieve lower formal errors and a more robust empirical assessment. Although the reliability level of the obtained atmospheric tidal loading estimates at the S_1 frequency may be critical we find that the agreement between numerical loading models and VLBI-based results is encouraging.

References

Arbic B K (2005) Atmospheric forcing of the oceanic semidiurnal tide. *Geophys. Res. Lett.*, 32(2), ISSN 1944-8007, doi:10.1029/2004GL021668.

Aviso (2014) FES2014 is distributed by Aviso (`http://www.aviso.altimetry.fr/`. Copyright: 2014- ongoing Legos/Noveltis/Cnes/CLS.

Girdiuk A, Schindelegger M, Böhm J (2016a) Tidal Atmospheric Loading and VLBI. In: *IVS General Meeting 2016 Proceedings: " "*,

Girdiuk A, Schindelegger M, Böhm J (2016b) Tidal atmospheric and ocean loading in VLBI analysis. *EGU General Assembly Conference Abstracts*, 18, 4498.

Girdiuk A, Schindelegger M, Madzak M, Böhm J (2016) Detection of the Atmospheric S_1 Tide in VLBI Polar Motion Time Series. *International Association of Geodesy Symposia*, 1–7, doi:10.1007/1345_2016_234.

Hofmeister A (2016) Determination of path delays in the atmosphere for geodetic VLBI by means of ray-tracing. Department f. Geodäsie u. Geoinformation / Höhere Geodäsie, `http://resolver.obvsg.at/urn:nbn:at:at-ubtuw:1-3444`.

Böhm J, Böhm S, Nilsson T, Pany A, Plank L, Spicakova H, Teke K, Schuh H (2012) The new Vienna VLBI Software VieVS. In: S. Kenyon, M. C. Pacino, and U. Marti (eds.), *Proc. of IAG Scientific Assembly 2009*, International Association of Geodesy Symposia Series, 136, 1007–1011, doi:10.1007/978-3-642-20338-1_126.

Böhm J, Werl B, Schuh H (2006) Troposphere mapping functions for GPS and very long baseline interferometry from European Centre for Medium-Range Weather Forecasts operational analysis data. *J. Geophys. Res.*, 111, doi:10.1029/2005JB003629.

Krásná H, Böhm J, Plank L, Nilsson T, Schuh H (2014) Atmospheric Effects on VLBI-derived Terrestrial and Celestial Reference Frames. In: C. Rizos, P. Willis (eds.), *Earth on the edge: science for a sustainable planet*, International Association of Geodesy Symposia, 139, 203–208, doi:10.1007/978-3-642-37222-3_26

Letellier T, Lyard F, Lefevre F (2004) The new global tidal solution: FES2004. *Proc. Ocean Surface Topography Science Team Meeting, St. Petersburg, Florida*

Petit G, Luzum B (eds.) (2010). IERS Conventions (2010). *IERS Technical Note*, 36, Frankfurt am Main: Verlag des Bundesamts für Kartographie und Geodäsie.

Petrov L, Boy J P (2004) Study of the atmospheric pressure loading signal in very long baseline interferometry observations. *J. Geophys. Res.*, 109:B03405, doi:10.1029/2003JB002500.

Ray R D, Egbert G D (2004) The Global S1 Tide. *J. Physical Oceanography*, 34(8), 1922–1935.

Schuh H, Böhm J (2013) Very long baselines interferometry for geodesy and astronomy. In: G. Xu (ed.), *Sciences of geodesy–II: innovations and future developments*, 339–376, doi:10.1007/978-3-642-28000-9_7.

Sovers O J, Fanselow J L, Jacobs C S (1998) Astrometry and geodesy with radio interferometry: Experiments, models, results. *Reviews of Modern Physics*, 70, 1393–1454, doi:10.1103/RevModPhys.70.1393.

van Dam T (2010) Updated October 2010. NCEP Derived 6-hourly, global surface displacements at 2.5° x 2.5° spacing. Data set accessed YYYY-MM-DD at `http://geophy.uni.lu/ncep-loading.html`.

Wijaya D, Böhm J, Karbon M, Krasna H, Schuh H (2013) Atmospheric pressure loading. In: J. Böhm, H. Schuh (eds.), *Atmospheric effects in space geodesy*, 137–158.

Twin Telescope Tests: Assessing Station Oriented Systematic Errors

C. S. Jacobs, C. García-Míro, S. Horiuchi, L. G. Snedeker

Abstract Each of NASA's three Deep Space Network sites has multiple large antennas capable of acquiring VLBI data. The long range plan is to have four 34-meter beam waveguide antennas at each site. At present Goldstone has three, Canberra has three, and Madrid has two with two more under construction. These antennas offer the opportunity to do connected element interferometry (CEI) over the few hundred meter baselines within each complex. Given that all antennas within a site are of nominally the same structural design, are run off the same clock, observe through almost the same atmosphere, and are subject to almost the same geophysics, doing CEI experiments is an excellent way to probe the limits of VLBI accuracy and expose station-specific systematic errors. This paper will report the results of just such tests which achieved about 0.2 mm baseline precision per pass. Some stations exhibit more than 1 mm systematics. Based on this data we will discuss the implications for whether the IAG's goal of 1 mm station stability in VLBI geodesy is possible for large antennas.

Keywords VLBI, reference frame, ITRF, quasar, AGN, station stability

Christopher Jacobs
JPL, California Institute of Technology/NASA, Pasadena, CA

Cristina García Míro
Madrid Deep Space Communications Complex/NASA, ISDEFE, Madrid, Spain

Shinji Horiuchi
Canberra Deep Space Communications Complex/NASA, CSIRO, Canberra, Australia

Larry Snedeker
Goldstone Deep Space Communications Complex/NASA, SaiTech, Ft. Irwin, CA

1 Introduction

Modern geodetic techniques have an important role to play in many aspects of society. Driven by concerns about global sea level rise, the International Association of Geodesy (IAG) has set requirements for the next generation International Terrestrial Reference Frame (ITRF) to have an accuracy of ±1 mm in global positioning (e.g. Beutler et al. (2009)). Current Very Long Baseline Interferometry (VLBI) measurements have errors much larger than this ±1 mm goal. Tropospheric fluctuations in refractivity, largely from water vapor (e.g. Treuhaft and Lanyi (1987)), stochastic variations in station clocks, and extended source morphology (e.g. Charlot (1990)) are commonly cited as the major sources of error in VLBI. Are these the only error sources larger than 1 mm?

This paper leverages a short baseline (200–300 m) configuration so that most of the tropospheric, clock, (global) geophysical, and source structure errors common mode away thereby revealing underlying instrumental errors. Furthermore, because the experiments discussed here used antennas of nominally the same design, structural deformation due to gravity loading should largely common mode. Thermal expansion should common mode to the extent that both antennas are in the same thermal environment. Note that our previous work (Jacobs and Rius (1989)) using antennas of radically different sizes and designs i.e. the 70-m (DSS 63) and the old non-beam waveguide 34-m (DSS 65) could not leverage common mode-ing of structural errors to anywhere near the ±1 mm accuracy goal of the current work.

Geophysical motion should common mode away to the extent that both antennas are attached to the same piece of stable bedrock. In summary, these experiments have the potential to be a null test to verify the preceding assumptions that most error sources common mode away down to the accuracy goal level of ±1 mm. Our experience at NASA's Goldstone site circa 2005 accomplished just such verification. However, the data from our Madrid site indicated that not all antennas performed at the ±1 mm accuracy level.

2 Observations and Data Analysis

As shown in Table 1, a series of short baseline Connected Element Interferometry (CEI) passes were done between 2014 and 2017 at the Canberra and Madrid Deep Space Network (DSN) sites. The CEI technique we used is virtually the same as VLBI except that, unlike VLBI, both stations were synchronized to the same H_2 maser clock thereby virtually eliminating clock variations as an error source—other than minor differences in clock distribution to the two antennas.

The observation schedules were designed to sample the full range of azimuth, cable wrap, and elevation using the strong ICRF2 defining sources (Ma et al, 2009) which have sufficiently accurate astrometric positions to be fixed a priori for the short ~200 m baselines under consideration. Sky coverage was optimized within the constraint of keeping slew times manageable by nodding up and down in elevation while rotating in azimuth in steps on the order of 20°. The schedule moved through the full range of cable wrap including the full 360° of azimuth plus reaching a full quadrant from both clockwise and counterclockwise directions. This schedule strategy separates geometric baseline effects due to azimuth changes from cable wrap effects. Sessions were typically 4–8 hours and done at night when possible to minimize thermal gradients.

We used the DSN 34-meter beam waveguide (Imbriale, 2002) antennas to observe X-band (8200–8600 MHz) with Right Circular Polarization. The data were downconverted by subtracting 8100 MHz, sent over cables to the control room where the analog signal was digitized by the Wideband VLBI Science Recorder (Rogstad et al., 2009) with 2-bit resolution, and channelized into 12 channels each 8 MHz wide for a total data rate of 384 Mbps per station. The data were e-transferred to JPL, correlated with the SOFTC software correlator (Lowe, 2006), and fringe fit with the CFit software to produce group delays and phase delay rates. These observables were then modelled using the MODEST software (Sovers et al., 1998). We estimated parameters for a differential baseline vector, differential zenith troposphere, and differential time-linear residual clock.

Table 1: Summary of Observations. All sessions used X-band RCP recorded at 384 Mbps.

Date	stations	Scans	wRMS (psec)
	Canberra		
2014 05 28	DSS 34–35	317	4.6
2014 07 12	DSS 34–35	132	6.3
2014 07 19	DSS 34–35	153	2.7
2014 07 25	DSS 34–35	261	11.2
2016 06 18	DSS 34–35	178	4.4
2016 07 14	DSS 34–36	111	3.7
2016 07 17	DSS 34–36	125	11.4
2016 09 23	DSS 34–36	188	3.3
	Madrid		
2015 12 05	DSS 54–55	119	5.2
2016 01 31	DSS 54–55	132	5.4
2016 05 07	DSS 54–55	167	4.1
2016 07 09	DSS 54–55	93	5.2
2017 01 03	DSS 54–55	188	3.3

3 Delay Scatter Results

Table 1 shows the dates, the pair of Deep Space Stations (DSS), the number of scans and the wRMS group delay scatter. Most passes show a scatter of 3–6 psec or 1–2 mm. There are two passes close to 4 mm scatter. As an example, Fig. 1 shows the group delay vs. time on 2014 May 28 on the DSS 34 to DSS 35 baseline. The 4.5 psec scatter is equivalent to about 1.4 mm. The points with orange color coding are close to the sun suggesting that thermal effects may be increasing the delay scatter at the start of the pass.

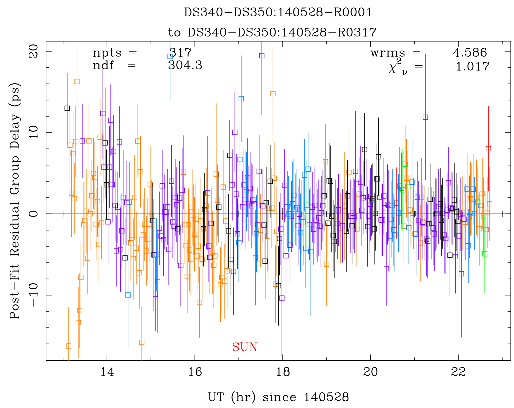

Fig. 1: Group delay scatter on Australia's DSS 34 to DSS 35 baseline on 2014 May 28. Orange indicates scans near the Sun.

4 Case Study: Madrid Systematic Error Level

The Madrid complex is shown in Fig. 2. Within this complex, the DSS 54 to DSS 55 baseline was measured five times between 2015 Dec. and 2017 Jan. Fig. 3 shows the baseline length scatter is extremely stable with a WRMS scatter of 0.11 mm. Fig. 4 shows the vertical scatter is 0.26 mm excepting the outlier session on 2016 Jul 09 which had a sunrise in the middle. Thus the length and vertical results confirm our expectation that errors should common mode away down to the 1 mm level.

By the time the 4^{th} session's results were analyzed, we were becoming increasingly concerned that there was a differential velocity between DSS 54 and DSS 55 which might eventually damage an antenna. Thus we began to focus on the foundations.

5 Antenna Foundation

Foundations are critical to the stability of the antenna's position and thus the intra-complex baseline vectors that we are measuring. Our starting assumption is that all antennas within a given complex are firmly attached to the same piece of bedrock thereby eliminating any geophysically induced differential motion from slippage or seasonal variation in underlying groundwater. Fig. 7 shows the foundation work for the under-construction DSS 56 antenna as of 2016 Nov 10.

This photograph reveals the sub-surface geology within a few 100 m of the antennas we measured (DSS 54 and 55). The surface soil extends 0–10 m after which one observes a mixture of soil and rock. To the left, the terrain is almost bedrock, but has an underlying thin seam of soil which might allow seismic movement or ground water induced changes. The construction seeks to get below these seams to solid bedrock before laying the concrete foundation shown in Fig. 7.

This quick lesson in foundations failed to reveal why the east and north were not stable. And, in fact, when the results of the 5th and final session were analyzed, both the east and north values came down thereby breaking the linear trend. We note that a 6th session done after these results were presented also went against the linear trend and began to suggest that we are seeing a seasonal effect of unknown origin. We have begun to consider a range of effects such as differential thermal environment due to the downward topography going from DSS 54 to DSS 55 (Fig. 2) or phase and delay effects from antenna pointing errors (Gorham & Rochblatt, 1998) or—returning to foundations—local hydrological effects such as groundwater getting under one of the foundations.

6 Conclusions

The goal of the twin telescope baseline measurements discussed in this paper has been to measure the baseline in an environment in which most error sources difference away so that variations in individual antennas can be isolated and studied. We have presented a series of short baseline Connected Element Interferometry (CEI) sessions from NASA's Deep Space Network complexes with eight passes from Canberra, Australia and five passes from Madrid, Spain. These passes had 1 to 4 mm of group delay scatter per session. The Canberra, Australia baselines were generally stable to near the ± 1 mm level.

The early Madrid measurements showed a trend of a few mm/yr in the horizontal components. Only later did it appear that the 2016 Jul 09 session was an outlier—not only the obvious vertical but also the horizontal components. Removing that outlier session, wRMS scatters become 0.29 mm in east, 0.18 mm in north, 0.22 mm in vertical, and 0.08 mm in length.

Our previous experience, especially at the Goldstone complex, has been that the vertical component has a factor of several higher scatter than the horizontal components. This is expected because (1) vertical is determined from $< 90°$ of elevation range vs. the horizontal's 360° range of observations and (2) troposphere degrades the vertical more than horizontal.

Efforts to understand these results are ongoing. At this time, the small sample size makes it difficult to establish an outlier with certainty. Our plan is to make measurements of the DSS 54 to DSS 55 baseline at roughly quarterly intervals with the hope that outliers and seasonal effects can be well separated as a step towards understanding the error budget in this class of measurements. Once we understand the instrumental and possible local geophysical and hydrological effects on these short intra-complex baselines to the 1 mm level, we will have achieved a small but important step towards the goal of global geodesy at the 1 mm level.

However, the horizontal baseline history raised questions. Both the East (Fig. 5) and North (Fig. 6) components showed a monotonic, roughly linear increase for the first four sessions at the level of ≈ 3 mm/yr.

Fig. 2: Aerial view of NASA's Madrid Deep Space Communications Complex. There are three active 34-m antennas (DSS 54, 55, and 65), a 70-m (DSS 63), an inactive 34-m antenna (DSS 61), and two 34-m antennas under construction (DSS 53 & 56). The four antennas DSS 53, 54, 55, and 56 are all nominally of the same beam waveguide design (Imbriale, 2002).

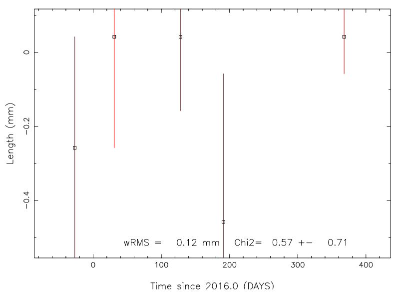

Fig. 3: Length vs. time, DSS 54−55. WRMS = 0.12 mm

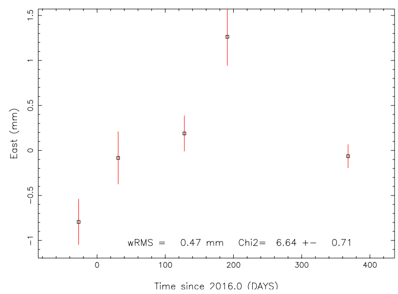

Fig. 5: East vs. time for DSS 54−55. WRMS = 0.47 mm

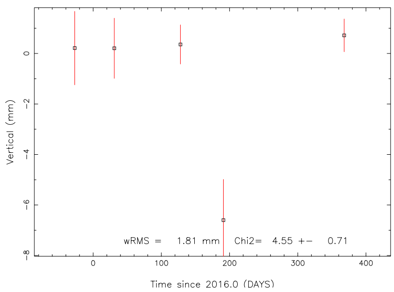

Fig. 4: Vertical vs. time, DSS 54−55. WRMS = 1.81 mm

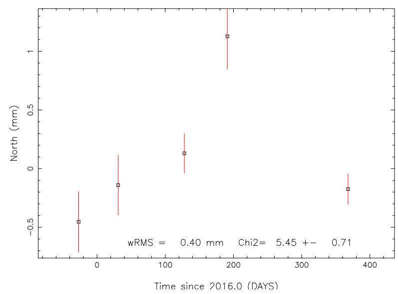

Fig. 6: North vs. time for DSS 54−55. WRMS = 0.40 mm

Acknowledgements

 U.S. Government sponsorship acknowledged for the work done at JPL-Caltech under a contract with NASA. Thanks to Hana Krásná and Marisa Nickola for comments which improved this paper and to María Benítez-Balseiro for the tour of the DSS 53 and DSS 56 foundations.

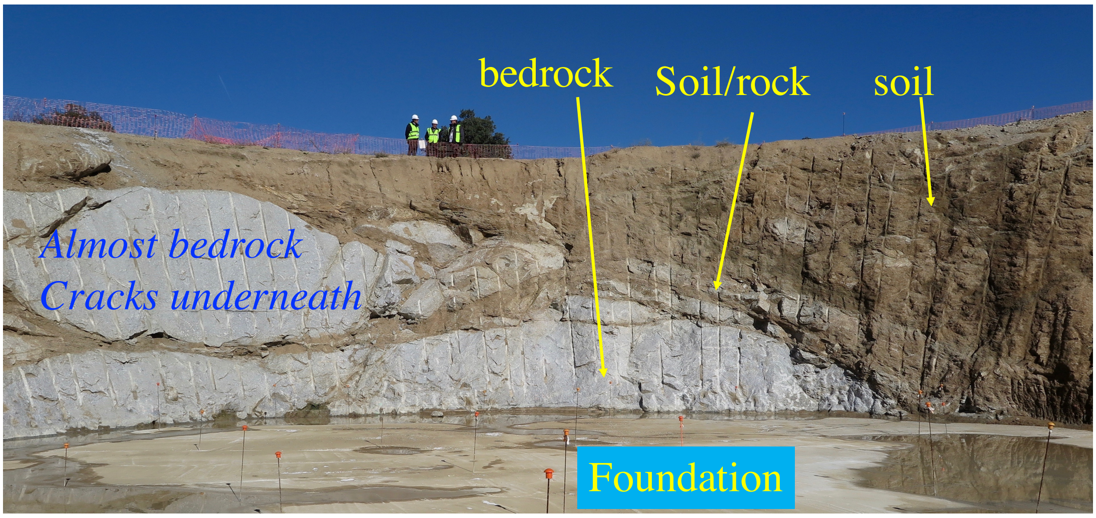

Fig. 7: Progress as of 2016 Nov. 10th on the construction of the foundation for a new 34-meter beam waveguide antenna, Deep Space Station (DSS) 56. Foundations are intended to be attached to solid bedrock to provide stable baselines throughout the complex.

References

Charlot P (1990) Radio-source Structure in Astrometric and Geodetic VLBI. *AJ*, 99, 1309–1326, http://adsabs.harvard.edu/abs/1990AJ.....99.1309C

Beutler G, Pearlman M, Plag H-P, Neilan R, Rothacher M, Rummel R (2009) Global Geodetic Observing System - Meeting the Requirements of a Global Society on a Changing Planet in 2020. In: H.-P. Plag, M. Pearlman (eds.) Towards GGOS in 2020, 273–281, https://link.springer.com/chapter/10.1007/978-3-642-02687-4_10

Gorham P W, Rochblatt D J (1998) Effect of Antenna-Pointing Errors on Phase and Interferometric Delay. *JPL TDA Prog. Report*, 42–132, https://ipnpr.jpl.nasa.gov/progress_report/42-132/132H.pdf

Imbriale W A (2002) Large Antennas of the Deep Space Network, Chapter 8: The 34-Meter Beam-Waveguide Operational Antennas. In: J. Yuen (ed.) *Deep Space Communications and Navigation Series*, DESCANSO Monograph 4, 225–255, https://descanso.jpl.nasa.gov/monograph/series4/Mono4_Ch8.pdf

Jacobs C S, Rius A (1989) VLBI Surveying between DSS63 and DSS65. *Proc. 7th EVGA*, 64–67, http://adsabs.harvard.edu/abs/1989ebga.conf...64J

Lowe S T (2006) SOFTC: A Software Correlator for VLBI. *NASA Technical Report Server*, NASA Tech Briefs, 43, http://adsabs.harvard.edu/abs/2006ntb..rept...43L

Ma C, Arias E F, Bianco G, Boboltz D A, Bolotin S L, Charlot P, Engelhardt G, Fey S L, Gaume R A, Gontier A M, Heinkelmann R, Jacobs C S, Kurdubov S, Lambert S B, Malkin Z M, Nothnagel A, Petrov L, Skurikhina E, Sokolova J R, Souchay J, Sovers O J, Tesmer V, Titov O A, Wang G, Zharov V E, Barache C, Böckmann S, Collioud A, Gipson J M, Gordon D G, Lytvyn S O, MacMillan D S, Ojha R (2009) The Second Realization of the International Celestial Reference Frame by VLBI. In: A. Fey, D. Gordon, C.S. Jacobs (eds.) *IERS Tech Note No. 35*, http://adsabs.harvard.edu/abs/2009ITN....35....1M

Rogstad S, Navarro R, Finley S, Goodhart C, Proctor R, Asmar S (2009) The Portable Radio Science Receiver (RSR). *JPL IPN Progress Report*, 42–178, https://ipnpr.jpl.nasa.gov/progress_report/42-178/178B.pdf

Sovers O J, Fanselow J L, Jacobs C S (1998) Astrometry and Geodesy with Radio Interferometry: Experiments, Models, Results. *Rev. Mod. Phys.*, 70(4), http://adsabs.harvard.edu/abs/1998RvMP...70.1393S

Truehaft R N, Lanyi G E (1987) The Effect of the Dynamic Wet Troposphere on Radio Interferometric Measurements. *Radio Sci.*, 22, 251–265, http://adsabs.harvard.edu/abs/1987RaSc...22..251T

Estimating Common Tropospheric Parameters for Co-located VLBI Antennas

T. Nilsson, K. Balidakis, S. Glaser, M. Karbon, R. Heinkelmann, H. Schuh

Abstract We test the effect of estimating common zenith wet delays (ZWD) and gradients for co-located VLBI telescopes. We find that the station coordinate repeatabilities are improved slightly when doing so, especially if the sky coverage obtained when considering the observations of both telescopes is better than that of a single one. Furthermore, we find that the repeatability of the baseline vector between the two telescopes is improved, especially in the vertical component by more than 50 %.

Keywords VLBI, Kalman filter, Troposphere, co-location

1 Introduction

Co-located VLBI telescopes, located less than 1 km apart, are subject to approximately the same tropospheric effects. Thus it should be possible to estimate common tropospheric parameters for these telescopes. This will reduce the number of parameters needed to be estimated in the VLBI data analysis, what should lead to an increase in the precision of the estimated parameters (e.g., the station coordinates). Thus, the estimation of common tropospheric parameters will be of great interest especially in the future, since the upcoming VGOS (VLBI Global Observing System) network will contain several twin telescopes.

Nilsson et al. (2015a) performed simulations for a potential future VGOS network, with one twin telescope. They showed that the station coordinates for the twin telescope improve if common tropospheric parameters for the twin telescope are estimated. In particular, a significant improvement in the baseline between the two telescopes was found; when estimating common ZWD (zenith wet delay) the repeatability of the vertical component of the baseline was improved by more than 50 %.

In recent years many new VGOS-type telescopes have been constructed, in many cases at stations already equipped with a legacy VLBI antenna. For several of these new telescopes, initial operation in standard IVS sessions have already commenced, using S/X receivers. Relatively often the new and the legacy antennas observe in the same session, thus providing excellent data to test the estimation of common tropospheric parameters. In this work we perform such a test, considering four sites with co-located VLBI telescopes.

2 Data analysis

We analyzed all VLBI sessions from 2010 until early 2017 containing any of the following co-locations (in total 210 sessions): Wettzell, Germany (WETTZELL and WETTZ13N, 92 sessions), Yebes, Spain (YEBES40M and RAEGEYEB, 14 sessions), Hobart, Australia (HOBART26 and HOBART12, 86 sessions), and HartRAO, South Africa (HARTRAO and HART15M, 21 sessions). The data were analyzed with the Kalman filter module in the VieVS@GFZ Software (Nilsson et al., 2015). The analysis options were more or less standard, estimating station coordinates, radio source coordinates, Earth Orientation Parameters, ZWD, gradients, and clocks. Four different solutions were calculated, each with different handling of the tropospheric parameters (ZWD and gradients) at co-located telescopes:

None The tropospheric parameters were estimated independently for each telescope

Grad. Common gradient parameters were estimated for the co-located telescopes

Tobias Nilsson · Robert Heinkelmann · Harald Schuh
Helmholtz-Centre Potsdam, GFZ German Research Centre for Geosciences, Telegrafenberg, DE-14473 Potsdam, Germany

Kyriakos Balidakis

Susanne Glaser · Maria Karbon · Harald Schuh
Technische Universität Berlin, Institute for Geodesy and Geoinformation Science, Berlin, Germany

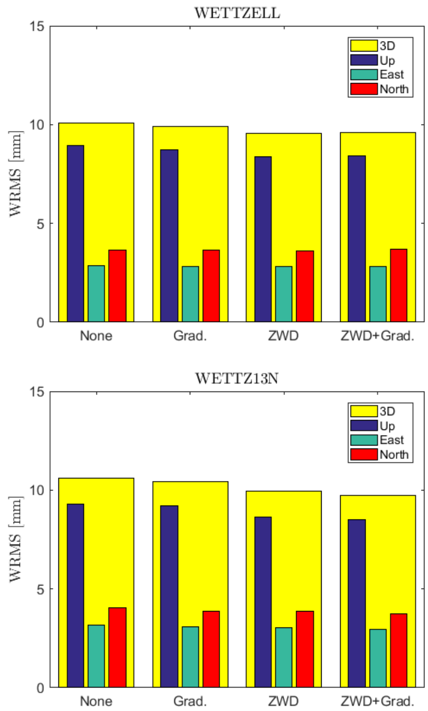

Fig. 1: Station position repeatabilities for WETTZELL (top) and WETTZ13N (bottom) from the four different solutions.

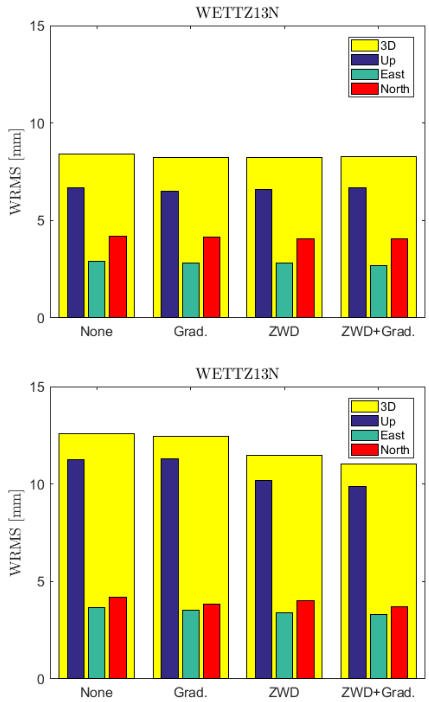

Fig. 2: Station position repeatabilities for WETTZ13N from the four different solutions, considering only sessions with a low (top) and high (bottom) improvement in sky coverage when considering both telescopes compared to WETTZ13N only.

ZWD Common ZWD parameters were estimated for the co-located telescopes

ZWD+Grad. Common ZWD and gradient parameters estimated

When estimating common ZWDs it is important to correct a priori for the ZWD and ZHD differences which exist due to the telescopes being at different heights. This was done using the formulas for the tropospheric ties presented in Teke et al. (2011).

2.1 Station positions

As an example, Fig. 1 shows the station position repeatabilities of the two telescopes in Wettzell, Germany (WETTZELL and WETTZ13N), from the four solutions. We can note a slight (6 %) improvement when estimating common ZWD. The results from the other co-locations are similar.

In general, we would expect an improvement in the station position repeatabilities if the sky coverage obtained when considering the observations from both telescopes is better then what is obtained from only one. This was found in the simulations performed by Nilsson et al. (2015a). If the two telescopes are always scheduled to the same source (i.e., the sky coverage from both telescopes is the same as from one), there are practically no improvements in the station position repeatabilities, while if the telescopes are always scheduled to different sources (i.e., the sky coverage from both telescopes is clearly better than from one) the repeatabilities improve by about 15 %. Hence, it is interesting to look at how the co-located telescopes in our study are scheduled, i.e., how the sky coverage obtained using both telescopes compare to that of only one.

In general, the co-located telescopes have often been scheduled to the same source, although not always. To study the effect of this in more detail, we looked at the results obtained from two sub-sets of sessions: one containing the 28 sessions where the improvement in sky coverage comparing both telescopes relative to one are the lowest, and one sub-set containing the 26 session with the highest improvement. The sky-coverage was calculated using the method described in Sun et al. (2013). The results for the station position repeatabilities can be seen in Fig. 2. We can see that when there is no improvement in sky coverage, there is no significant improvement in the repeatabilities when estimating common tropospheric parameters, while for the sessions with the highest sky coverage improvement the repeabilities improve by about 9 % when estimating common ZWD and gradients.

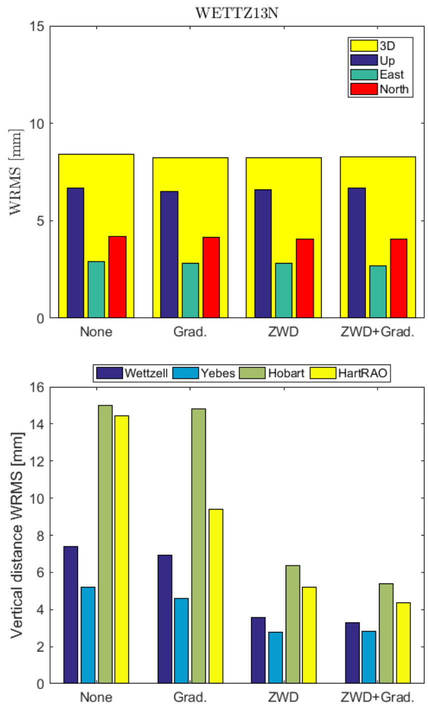

Fig. 3: Repeatabilites of the baseline length (top) and vertical component of the baseline (bottom) for the four co-location stations and for the four different solutions.

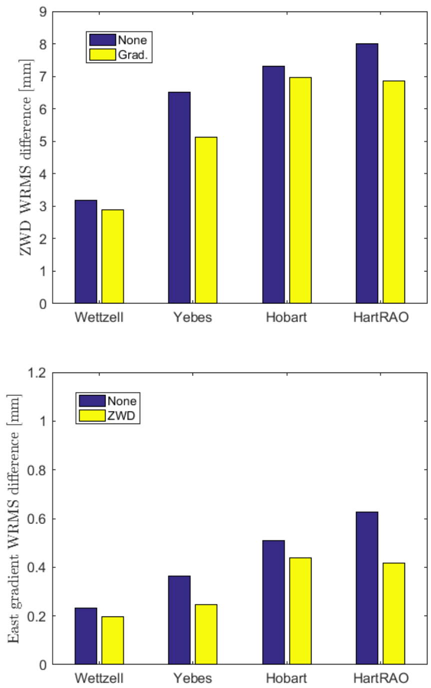

Fig. 4: Repeatabilities of the estimated ZWD (top) and East gradients (bottom) of the co-located telescopes.

2.2 Local baseline

Figure 3 shows the repeatabilities of the lengths and vertical components of the baselines between the co-located antennas. For all stations except HartRAO we can see that the repeatability of the baseline length improves when common gradients are estimated. The largest impact is, however, in the vertical components. When estimating a common ZWD, the repeatabilities of the vertical distances are all reduced by more than 50 %. This agrees well with the simulation results from Nilsson et al. (2015a).

We also looked at the mean baseline lengths obtained from the different solutions. No significant differences could be seen, and the values also agree within the formal errors with the results from local tie measurements. Thus, there are no significant systematic effects introduced in the baselines when estimating common tropospheric parameters.

3 Tropospheric parameters

We also studied the effect on the tropospheric parameters. Figure 4 shows the RMS difference between the ZWD estimates of the co-located antennas for the “None” and “Grad.” solutions, as well as the RMS differences in the East gradient estimates from the “None” and “ZWD” solutions. For all stations, the RMS differences between the ZWD/gradients decrease when common gradients/ZWD are estimated. This further confirms that the VLBI solution is improved when common tropospheric parameters of co-located telescopes are estimated.

4 Conclusions

The results of this work confirm the simulation results of Nilsson et al. (2015a) using real observations. Estimating common tropospheric parameters can improve the station coordinate estimates, provided that the observations are schedules in such a way that the sky coverage obtained by two telescopes is significantly better than that of just one. Thus this should be considered when making the schedules. The main improvement found was in the baseline vector, especially in the vertical component when estimating common ZWD. Thus, this is a technique for obtaining a precise baseline vector, e.g., for validation of the local tie measurements.

The estimation of common tropospheric parameters is also of great interest in inter-technique combinations, e.g, between VLBI, GNSS, and/or DORIS (Heinkelmann et al., 2016). The fact that it is working well when considering VLBI only, gives great hope that it will also be beneficial when combining VLBI with other microwave space geodetic techniques.

Acknowledgements

The authors thank the IVS for providing the VLBI used in this work (Nothnagel et al., 2015, 2017).

References

Heinkelmann R, P. Willis P, Deng Z, Dick G, Nilsson T, Soja B, Zus F, Wickert J, Schuh H (2016) Multi-technique comparison of atmospheric parameters at the DORIS co-location sites during CONT14. *Adv. Space Res.*, 58(12):2758–2773, doi:10.1016/j.asr.2016.09.023.

Nilsson T, Karbon M, Soja B, Heinkelmann R, Lu C, Schuh H (2015a) Atmospheric modeling for co-located VLBI antennas and twin telescopes. *J Geod*, 89:655–665, doi:10.1007/s00190-015-0804-6.

Nilsson T, Soja B, Karbon M, Heinkelmann R, Schuh H (2015b) Application of Kalman filtering in VLBI data analysis. *Earth Planets Space*, 67(136):1–9, doi:10.1186/s40623-015-0307-y.

Nothnagel A, Artz T, Behrend D, Malkin Z (2017) International VLBI Service for Geodesy and Astrometry. *J Geod*, 91(7): 711–721, doi:10.1007/s00190-016-0950-5.

Nothnagel A et al. (2015) The IVS data input to ITRF2014. *International VLBI Service for Geodesy and Astrometry*, GFZ Data Services, doi:10.5880/GFZ.1.1.2015.002.

Sun J, Böhm J, Nilsson T, Krásná H, Böhm S, Schuh H (2013) New VLBI2010 scheduling strategies and implications on the terrestrial reference frames. *J Geod*, submitted.

Teke K, Böhm J, Nilsson T, Schuh H, Steigenberger P, Dach R, Heinkelmann R, Willis P, Haas R, Garcia-Espada S, Hobiger T, Ichikawa R, Shimizu S (2011) Multi-technique comparison of troposphere zenith delays and gradients during CONT08. *J Geod*, 85(7):395–413, doi:10.1007/s00190-010-0434-y.

Implementation of the vgosDb Format at the GSFC VLBI Analysis Center

S. Bolotin, K. Baver, J. Gipson, D. Gordon, D. MacMillan

Abstract The IVS Working Group 4 developed a new format to store and exchange data obtained from geodetic VLBI observations. The new data format, vgosDb, will replace existing Mk3 databases this year. At GSFC we developed software that implements the vgosDb format and that will be used routinely to convert correlator output to the new data storage format. In this paper we outline the current status of the transition of VLBI data flow to use the vgosDb format.

Keywords VLBI data analysis software, vgosDb

1 Introduction

Data produced at a correlator are subject to various changes before they become available to an end user. Historically, the results of correlation and fringe fitting of VLBI observations are stored in a binary self-descriptive file called a *database*. The format of the database file and the implementation of input/output operations were developed in the early 1970s. Since then, the databases have been used as a standard for data exchange in the geodetic VLBI community.

The database format has disadvantages, mostly caused by hardware and software limitations that existed in the period when the format was developed. In addition, the format was not well documented. Several attempts to replace the database format with an alternative were made in the last few decades, but none of these were successful. The anticipated vast increase in the number of VLBI observations and the emergence of VLBI Geodetic Observing System (VGOS) technology prompted the IVS Directing Board to establish the IVS Working Group on Data Structures. Efforts undertaken by the group were eventually realized in the creation of the new VLBI data format, *vgosDb*, see Gipson (2012); Gipson et al. (2014).

In accordance with the vgosDb format, the VLBI data of one session are stored in various files in the form of {*key* ⇒ *value*}. Each file represents an atomic piece of data, e.g., observed values with their standard deviations, or station coordinates. An additional feature is that it is possible to keep alternative models or approaches to the editing of observations in the same session data tree. A set of data files that is available to the user is specified in a special file called a *wrapper file*. It is possible to have more than one wrapper file for one VLBI session.

2 vgosDb-compatible VLBI Data Analysis Software

First results of the implementation of the vgosDb format by the GSFC VLBI group were shown in 2013. The legacy VLBI data analysis software, global solve, is ready to use data in the vgosDb format, see Gipson (2015). A part of the solve distribution package is the utility db2vgosDB, which converts data of a VLBI session from the database format into the vgosDb format. The next generation VLBI data analysis software, *ν*Solve, is capable of working with the new format (Bolotin et al., 2014).

In addition, vgosDb-compatible utilities were developed to support the transition to the vgosDb format. These utilities replace the legacy utilities dbedit, calc and pwxcb/dbcal.

The first utility, dbedit, creates database files from correlator output and fringe files. Routinely, it is executed at a correlator, and the database file for each band is then sent to one of the VLBI data centers.

The software calc generates the theoretical values of a delay and a delay rate, the partials with respect to estimated parameters and a set of intermediate values that

Sergei Bolotin · Karen Baver · John M. Gipson · David Gordon · Daniel S. MacMillan
NVI, Inc., NASA GSFC Code 61A, 8800 Greenbelt Road, Greenbelt, Maryland 20771 USA

allows one to turn on or off in data analysis some particular effect.

The purpose of the pair of utilities, pwxcb and dbcal, is to extract, validate, edit (if necessary), and put into a database the information that is contained in the Field System log files produced by each station that participated in a VLBI session. Usually, two types of data are extracted: cable calibration measurements and meteorological parameters.

The new vgosDb-compatible utilities, vgosDbMake (which replaces dbedit), vgosDbCalc (a vgosDb-compatible modification of calc software) and vgosDbProcLogs (which replaces pwxcb/dbcal), are part of the new VLBI data analysis software developed at NASA GSFC (Bolotin et al., 2010) and currently distributed in one package under the common name "nusolve".

The utilities vgosDbMake and vgosDbProcLogs have the same design as other parts of νSolve software as well as the same software development environment.

The utilities are designed to operate on any POSIX compatible operating system. We use C++ as the programming language due to its power, flexibility, and portability. The GNU Build System is used to make the software distribution portable. The software consists of two parts:

- Space geodesy library: a library where data structures and algorithms are implemented (about 90 % of the total source code).
- Executables vgosDbMake and vgosDbProcLogs: drivers that call library functions and organize work with an end user (about 10 % of the total source code).

Such organization of the software allows us to share the source code between applications and reuse it in other projects.

The software has a modular structure that makes it flexible and scalable. A module is a logical block of code that is loosely tied with other parts of the software. Obviously, not all the modules will be used by vgosDbMake and vgosDbProcLogs. On the other hand, the modular design of the software allow us to easily add the functionality of the utilities to the interactive VLBI data editor, νSolve.

Modification of the program calc to be compatible with vgosDb is done in a different way. A set of functions that mimics the Mk3 database handler programming interface has been created. These functions replace database functions with vgosDb input/output operations. In this case we do not need to modify the calc source code at all, but just need to link the software with the emulator of the Mk3 database handler library.

The distribution of the software package "nusolve" is available on the following FTP site:

ftp://gemini.gsfc.nasa.gov/pub/misc/slb/nusolve-latest.tar.gz

The file *nusolve-latest.tar.gz* is a symbolic link to the latest nusolve distribution. In addition, there is a file *NEWS* that outlines major modifications in the current version of the software.

The software distribution contains instructions on how to compile the source codes and to run the utilities as well as user guides for each of the utlities. A collection of necessary files containing *a priori* data is also in the distribution. It should be noted that one of these files, the table of the Earth rotation parameters, needs to be updated on a regular basis.

3 Use of the VLBI Data in the vgosDb Format

The vgosDb format is used in routine data analysis utilizing the set of the two vgosDb compatible software packages: solve and νSolve.

Before switching to the new vgosDb format we made the VLBI observations in this format available for public access in two groups of files. The first is the data that are distributed by the official IVS ftp sites. The vgosDb files for this set can be downloaded from

ftp://gemini.gsfc.nasa.gov/pub/vgosDB_IVS/

The second collection of the vgosDb files corresponds to the GSFC-analyzed VLBI observations. It can be obtained from

ftp://gemini.gsfc.nasa.gov/pub/vgosDB_GSFC/

The main difference between the two data sets is in the data editing options. These publicly accessible data will help users to transition to the new format.

The first practical use of the VLBI observations in the vgosDb format was reported by MIT Haystack Observatory (Niell et al., 2016). All VGOS-related observations since January 2016 were analyzed with the vgosDb data flow. These observations include broadband VGOS sessions with up to three stations and S/X sessions using mixed Mark4 and broadband stations.

4 Conclusions

Our group will switch to the new VLBI data format in 2017. At the time of writing we are performing extensive testing of the software, the legacy solve package, and new utilities from the nusolve distribution. We strongly encourage all VLBI data analysis centers to switch to the new VLBI data format.

Acknowledgements

We are grateful to Tim Morin, Mike Titus and Arthur Niell, of the MIT Haystack Observatory for installing, testing, and helping debug the vgosDb format compatible utilities.

References

Bolotin S, Gipson J M, MacMillan D S (2010) Development of a New VLBI Data Analysis Software. In: D. Behrend, K. D. Baver (eds.), *IVS 2010 General Meeting Proceedings*, NASA/CP-2010-215864, NASA GSFC, Maryland, 197–201.

Gipson J M (2012) IVS Working Group 4: VLBI Data Structures. In: D. Behrend, K. D. Baver (eds.), *IVS 2012 General Meeting Proceedings*, NASA/CP-2012-217504, NASA GSFC, Maryland, 212–221.

Bolotin S, Baver K D, Gipson J M, Gordon D, MacMillan D S (2014) The VLBI data analysis software *ν*Solve: development progress and plans for the future. In: D. Behrend, K. D. Baver, K. L. Armstrong (eds.), *IVS 2014 General Meeting Proceedings*, ISBN 978-7-03-042974-2, Science Press, Beijing, China, 253–257.

Gipson J, Böhm J, Bolotin S, Gordon D, Hobiger T, Jacobs C S, Kurdubov S, Nothnagel A, Sovers O, Titov O, Takiguchi H (2014) Final Report of IVS Working Group 4 (WG4) on Data Structures. In: K. D. Baver, D. Behrend, K. L. Armstrong (eds.), *IVS 2013 Annual Report*, NASA/TP-2014-217522, NASA GSFC, Maryland, 11–25.

Gipson J M (2015) *Practical Uses of VGOSDB Format*. In: R. Haas, F. Colomer (eds.) *Proc. 22nd EVGA Working Meeting*. ISBN 978-989-20-6191-7, 97–101.

Niell A, Cappallo R, Corey B, Eckert C, Elosegui P, McWhirter R, Rajagopalan G, Ruszczyk C, Titus M (2016) VGOS Observations with Westford, GGAO, and the New Station at Kokee, Hawaii. In: D. Behrend, K. D. Baver, K. L. Armstrong (eds.) *IVS 2016 General Meeting Proceedings*, NASA/CP-2016-219016, NASA GSFC, Maryland, 44–48.

Automated Ambiguity Resolution With Clustering and Analysis of Intensive Sessions Within ivg::ASCOT

A. Corbin, S. Halsig, A. Iddink, F. Jaron, A. Nothnagel

Abstract The first steps for analysing VLBI sessions include ambiguity resolution and ionospheric correction as well as extracting cable calibration and applying meteorological data. An automated procedure for these steps has been developed within the software package ivg::ASCOT.
The multi-band delays may be ambiguous. Resolving those ambiguities is a crucial step because unsolved ones will propagate into the subsequent solution. In a first step, an adjustment is performed using ambiguity free single band delays with down-weighted multi-band delays and estimating only clock parameters. The multi-band delay residuals are computed with these parameters and the ambiguities are then resolved with agglomerative hierarchical clustering. This distance-based clustering technique computes a dendrogram and creates clusters with the known ambiguity spacing. So far, the procedure works reliably for Intensive Sessions involving two stations. The validity of the approach is tested by carrying out the full session adjustment incorporating zenith wet delays and UT1-UTC. The resulting UT1-UTC time series is compared with results from other analysis centers to evaluate the performance of the automated procedure. Based on experiences with these sessions, the functionality is currently being expanded to networks of stations.

Keywords Intensive Sessions, ambiguity resolution, clustering, automating, UT1

Armin Corbin · Sebastian Halsig · Andreas Iddink · Frédéric Jaron · Axel Nothnagel
Rheinische Friedrich-Wilhelms Universität Bonn, Institute of Geodesy and Geoinformation, Nußallee 17, DE-53115 Bonn, Germany

1 Introduction

The solar time UT1 is the most variable of all Earth Orientation Parameters. In order to achieve precise and continuous measurements of UT1, Intensive Sessions have been established. They are performed daily and last for one hour. This relatively short observation time assures a fast shipping and correlation of the experiments (Schnell, 2006).
Since April 2016 a procedure for automated analysis of Intensive Sessions is implemented within the software package ivg::ASCOT (Analysis Scheduling Combination Toolbox, Artz et al. (2016)). ivg::ASCOT is written in C++ and developed by the VLBI group of the Institute of Geodesy and Geoinformation (IGG) of the University of Bonn (Germany).
The new software component is able to download sessions using the vgosDB format (Bolotin et al., 2016), extract meteorological and cable calibration information from the logfiles, resolve the ambiguities, and finally calculate the ionospheric correction without any interaction. Afterwards an independent solution can be performed to obtain the target parameters.

2 Uncovering ambiguities

Ambiguities occur due to the way the signals are processed in the fringe fitting software. The standard deviation of the delay decreases inversely proportional to the recorded bandwidth. However, due to limited memory capacity not the entire bandwidths of the X and S band are recorded. Instead, small channels that are deliberately scattered across the band are used.
By applying the correlation to a single channel the single band delays are obtained. They are free of ambiguities but have a comparably high standard deviation caused by the small bandwidth of each channel in MHz range.
With the bandwidth synthesis technique it is possible to

achieve better delay accuracies with limited recording bandwidth (Rogers, 1970). The resulting delays are called multi-band delays that may posses ambiguities.

In order to uncover those ambiguities a simple least squares adjustment (Meissl, 1982) is performed. The observation vector

$$\boldsymbol{\ell} = \begin{bmatrix} \tau_{SB} \\ \tau_{MB} \end{bmatrix} \tag{1}$$

contains both, ambiguity free single band delays τ_{SB} as well as ambiguous multi-band delays τ_{MB}. In the stochastic model the multi-band delays get very large variances so that only the single band delays contribute to the solution

$$\Sigma\{\mathcal{L}\} = \begin{bmatrix} \Sigma\{\tau_{SB}\} & \mathbf{0} \\ \mathbf{0} & \Sigma\{\tau_{MB}\} \end{bmatrix}, \ \Sigma\{\tau_{MB}\} = \begin{bmatrix} 10^{18} & & \\ & \ddots & \\ & & 10^{18} \end{bmatrix}. \tag{2}$$

The only estimated parameters are polynomials of degree one (offset and rate) to estimate the clock behavior. The previously extracted air pressure is used to correct the delay caused by the hydrostatic part of the troposphere. An ionosphere correction is not possible at this point. The deformation of the Earth and relativistic delays are considered, too. Other effects do not need to be considered at this point (Shaffer, 1995).
In the next step, the residuals of the multi-band delays are examined for each baseline. If ambiguities exist the residuals show strong banding about the delay ambiguities (Shaffer, 1995). Fig. 1 shows the multi-band residuals for session 14APR06XK which is a good example for typical multi-band delay residuals.

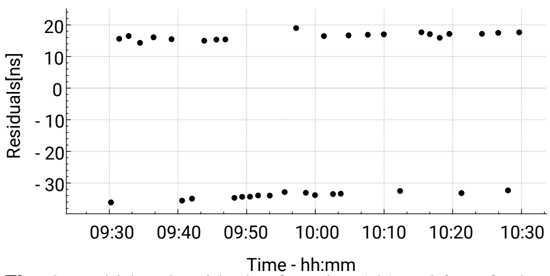

Fig. 1: Multi-band residuals of session 14APR06XK for baseline WzTs (the only baseline). Two groups of residuals are clearly separated by the ambiguity spacing of 50 ns.

The clearly visible step size corresponds to the known ambiguity spacing (here 50 ns). In Fig. 2, the corresponding residuals of the single-band delays are plotted. As expected they are free of ambiguities.
In order to resolve the ambiguities each residual r_i has to be shifted by a multiple $k_i \in Z$ of the ambiguity spacing a so that all residuals are on the same level

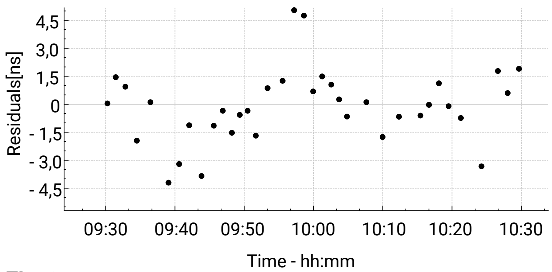

Fig. 2: Single-band residuals of session 14APR06XK for baseline WzTs (the only baseline). Single-band delays are free of ambiguities but have a larger variance.

$$\hat{r}_i = r_i + k_i \cdot a \,. \tag{3}$$

Ambiguity free multi-band delays are obtained by shifting them with the same correction $k_i \cdot a$. An algorithm to determine each k_i is presented in Section 3.

3 Resolving ambiguities

The problem of finding residuals sharing the same multiplier k can be solved with clustering algorithms. The agglomerative hierarchical clustering (AHC) technique (Manning et al., 2009) is used here. Agglomerative means that at the beginning every data point is its own cluster. These clusters will be merged successively until there is only one cluster left.
The clustering results can be visualised with a dendrogram (Fig. 3). A merge between two clusters is represented with a horizontal line in the dendrogram. The y coordinate of those lines coorespondes to the distance between two merged clusters (Manning et al., 2009).
Before running AHC the metric, the linkage type, and the separation method, have to be determined.
The time of the observations is neglected here, so the data is one dimensional. In 1D space, the choice of metric (euclidean, city-block, ...) has no impact.
The linkage type (Fig. 4) determines how the distance (similarity) between two clusters is computed. Single linkage selects in each cluster one point, so that the distance is minimized. Complete linkage selects the points that maximize the distance. Average linkage calculates the average of pairwise distances without pairs within the same cluster. In 1D space this is equal to the distance of the cluster centroids. The average linkage is used here, because the clusters are normally distributed and therefore the distance between the means is computed.
In the dendrogram all data points are merged to one cluster. This cluster can be subdivided either through

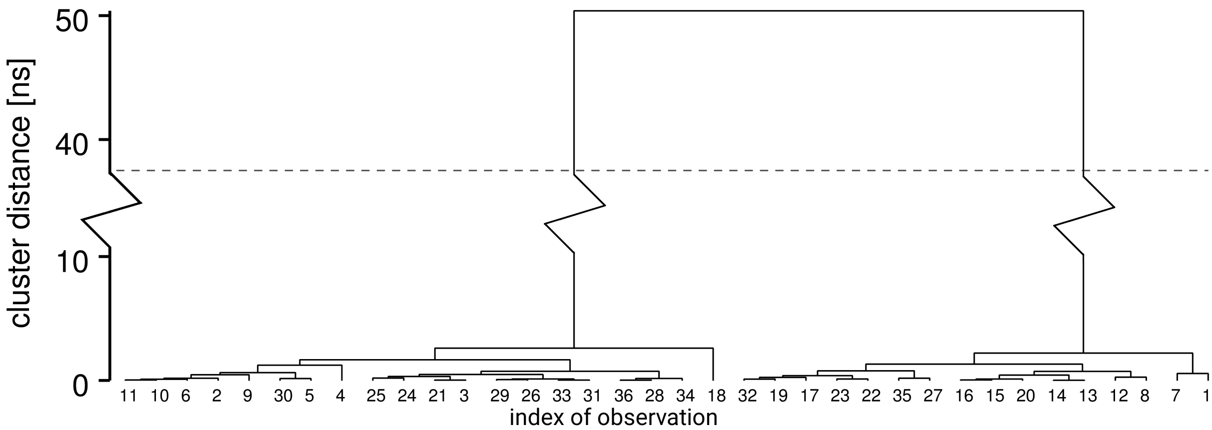

Fig. 3: Dendrogram for the multi-band residuals of session 14APR06XK for baseline WzTs. It visualises the clustering results. Each horizontal bar represents a merge. The distance between two merged clusters is plotted on the y-axis. The dashed line shows the cut at 75 % of the ambiguity spacing, that generates two clusters. The index of observation corresponds to the chronologically sorted residuals in Fig. 1 beginning on the left.

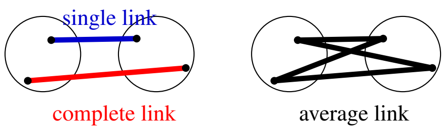

Fig. 4: Linkage types according to Manning et al. (2009). They determine how the distance between two clusters is measured: **single linkage:** minimum distance, **complete linkage:** maximum distance, **average linkage:** average of pairwise distances without pairs within the same cluster

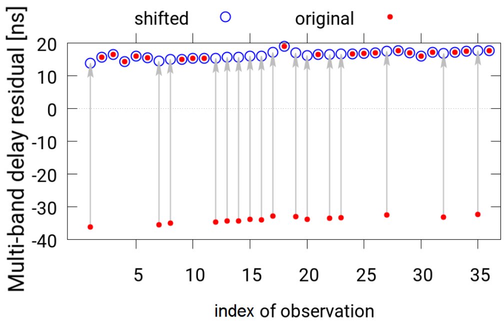

Fig. 5: The multi-band residuals of session 14APR06XK are on one line (the blue circles ◯) after shifting the initial residuals (the red dots •). The ambiguities have been resolved successfully for this baseline.

defining the number of clusters or by defining a threshold. This threshold represents the minimum similarity needed to build a cluster. Here, the number of clusters is not known beforehand. Therefore, the residuals are separated with a threshold. Since the clusters are separated by one or more multiples of the ambiguity spacing this threshold can be easily determined. The gray dashed line in Fig. 3 shows a threshold that corresponds to 75 % of the ambiguity spacing. Here, it cuts the dendrogram into two clusters.

The cluster with the most points is chosen as the reference cluster. If there are clusters with a similar number of points, the one having a mean residual delay closest to zero is chosen. All other clusters are shifted to it if necessary. Thereto, the differences between the cluster centroids and the centroid of the reference cluster are computed. This difference is divided by the ambiguity spacing and rounded. The result is the multiplier k. The shifted residuals for session 14APR06XK are shown in Fig. 5.

So far only the ambiguities for individual baselines have been resolved. If only one baseline is involved in a session no more action is necessary but if the session consists of more baselines, the triangle closure condition has to be satisfied: In each triangle, formed by the baselines, the sum of the averaged residuals of each baseline $\bar{r}^{(i)}$ has to be approximately zero. Deviations from zero of a few nanoseconds are to be expected at this point since only a few clock parameters are estimated and not all corrections are used.
For one triangle the condition is

$$\sum_{i=1}^{3} \underbrace{\frac{1}{n_i}\sum_{j=1}^{n_i} r_j^{(i)}}_{\bar{r}^{(i)}} \overset{!}{\approx} 0, \tag{4}$$

with i denoting the baseline index, n_i the number of observation for the i-th baseline and $r_j^{(i)}$ the j-th residual in the i-th baseline. The situation is illustrated in Fig. 6. Considering the orientation of the baseline vectors, the loop closing condition for that specific triangle is

$$\bar{r}^{(\overrightarrow{AB})} + \bar{r}^{(\overrightarrow{BC})} - \bar{r}^{(\overrightarrow{AC})} \overset{!}{\approx} 0\,. \tag{5}$$

Another interpretation of the condition is that the sum of two mean residuals has to yield the third one

$$\bar{r}^{(\overrightarrow{AB})} + \bar{r}^{(\overrightarrow{BC})} \overset{!}{\approx} \bar{r}^{(\overrightarrow{AC})}. \tag{6}$$

So far, this condition is not implemented in ivg::ASCOT.

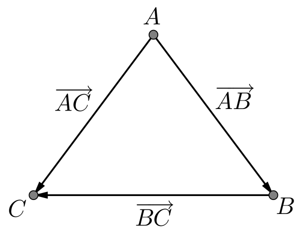

Fig. 6: Triangle closure: The sum of the averaged baseline-wise residuals in this triangle has to be appropriately zero.

4 Results

In order to validate the automated analysis procedure developed in this study, intensive sessions are analysed, resulting in time series of UT1 – TAI. To check the results they are compared with a reference solution. As reference solution the 'bkgint14.eopi' intensive solution[1] from the Bundesamt für Kartographie und Geodäsie (BKG) Leipzig is used. It includes all Intensive sessions since 1999. The only estimated parameters are clock and tropospheric zenith parameters as well as UT1. The terrestrial frame is fixed to the VTRF2008a (VLBI terrestrial reference frame) and the celestial frame to the ICRF2 (Fey et al., 2009). The solution has been executed with CALC/SOLVE (Ma et al., 1990).
In order to compare a time series with the reference solution, the series is subtracted from the reference time series

$$\begin{aligned} \Delta &= (\mathrm{UT1_{BKG}} - \mathrm{TAI}) - (\mathrm{UT1} - \mathrm{TAI}) \quad &(7)\\ &= \mathrm{UT1}_{BKG} - \mathrm{UT1}. \quad &(8) \end{aligned}$$

Since TAI is included in both time series it is eliminated through the subtraction. The quality of the solution that is compared with the reference is rated by this difference.

All available intensive sessions from 2007 until 2017 have been processed with the automated procedure. Afterwards, an independent solution was carried out with the same parameters as the BKG solution. However, instead of the VTRF2008 the VTRF2014 was used. The differences for UT1 between these solutions is shown in Fig. 7. Some statistics to the differences can be found in Table 1.
The median of the difference is 4 μs and the WRMS is 20 μs. Considering that deviations in the magnitude of a 'few tens of microseconds' can be explained with different 'analysis strategies, geophysical models, software and reference frames' (Schnell, 2006) the INT1 results agree very well with the BKG solution.

Table 1: Statistic properties of the differences between the BKG solution and the automated procedure.

[μsec]	INT 1	INT 2	ALL
median	−3	−15	−4
WRMS.	14	28	20

The behavior of the INT2 sessions is rather unexpected. In the first part a yearly signal is visible. Furthermore, there is a bias from the middle of 2011 to the end of 2012 and a drift at the end. Both effects are probably caused by earthquake induced changes in the terrestrial reference frames.
Fig. 7 shows only differences between -160 μs and 160 μs. However, there are 51 sessions with higher differences that are not visible. 20 of these sessions involve more than one baseline, in 16 sessions too many observations have been eliminated, 10 have not corrected clock jumps or strange clock behavior, and 5 sessions had other errors.
The sessions with differences between 50 μs and 160 μs have also been examined. Most differences can be explained with the causes mentioned above.

5 Conclusions

The automated processing of VLBI-Intensive sessions works well for most sessions with only one baseline. The ambiguity resolution with AHC works without any problems as long as the multi-band residuals are not affected by severe clock behavior deviations.
To overcome the problems with sessions involving more than one baseline, the triangle closure condition is currently implemented.

[1] ftp://ivs.bkg.bund.de/pub/vlbi/ivsproducts/eopi/bkgint14.eopi.txt

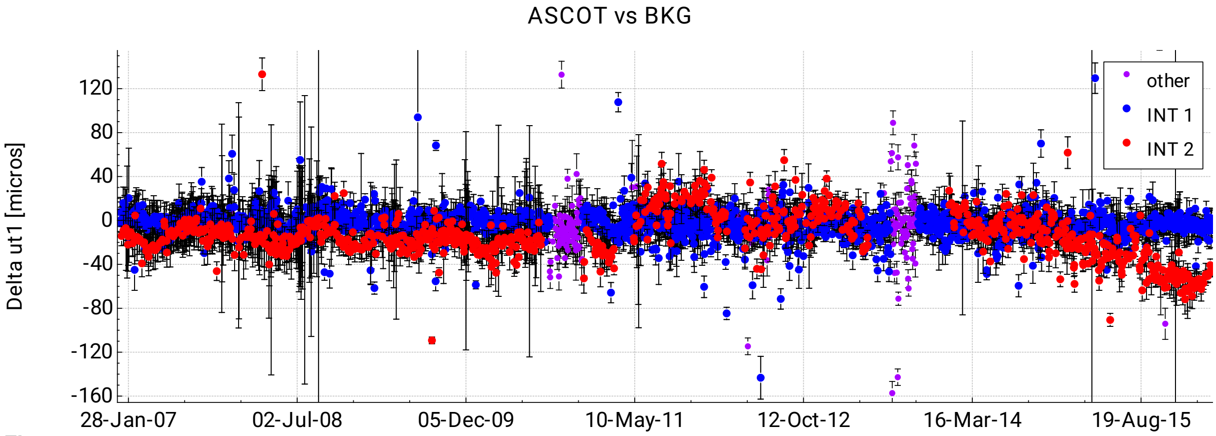

Fig. 7: Difference in UT1 between the BKG solution and the automated procedure. In total 3330 sessions between 2007 and 2017 are plotted. Statistics to this time series can be found in Table 1. The bias of the INT2 sessions from the middle of 2011 to the end of 2012 as well as a drift at the end are probably caused by earthquake induced changes in the terrestrial reference frames.

References

Artz T, Halsig S, Iddink A, Nothnagel A (2016) ivg::ASCOT: The development of a new vlbi software package. In: D. Behrend, K. D. Baver, K. L. Armstrong (eds.), *IVS 2016 General Meeting Proceedings, "New Horizons with VGOS"*, 217–221.

Bolotin S, Bave K, Gipson J, Gordon D, MacMillan D S (2016) Transition to the vgosdb format. In: D. Behrend, K. D. Baver, K. L. Armstrong (eds.), *IVS 2016 General Meeting Proceedings, "New Horizons with VGOS"*, 222–224.

Fey A, Gordon D, Jacobs C S (eds.) (2009) The Second Realization of the International Celestial Reference Frame by Very Long Baseline Interferometry. *IERS Technical Note*, 35, Verlag des BKG, Frankfurt am Main.

Ma C, Sauber J, Bell L, Clark T, Gordon D, Himwich W, Ryan J (1990) Measurement of horizontal motions in Alaska using very long baseline interferometry. *J. Geophys. Res.: Solid Earth*, 95(B13), 21991–22011.

Manning C D, Raghavan P, Schütze H (2009) An Introduction to information Retrival. Cambridge University Press, Cambridge, England.

Meissl P (1982) Least squares adjustment a modern approach. *Mitteilungen der geodätischen Institute der Technischen Universität Graz*, 43.

Rogers A E (1970) Very long baseline interferometry with large effective bandwidth for phase-delay measurements. *Radio Science*, 5(10), 1239–1247.

Schnell D (2006) Quality aspects of short duration VLBI observations for UT1 determinations. PhD thesis, Institut für Geodäsie und Geoinformation, Universität Bonn. http://hss.ulb.uni-bonn.de/2006/0918/0918.pdf.

Shaffer D B (1995) Geodetic Measurements with VLBI. In: J. A. Zensus, P. J. Diamond, P. J. Napler (eds.), *Very long baseline interferometry and the VLBA*, ASP Conference Series, 82, 345–361

Characterization of the Astrometric Stability of the Radio Sources With the Allan Variance

C. Gattano, S. Lambert, C. Bizouard

Abstract We provide a classification of the VLBI radio sources based on their astrometric stability and, hence, their suitability to carry the axes of a reference frame. This classification is based on the Allan variance which we apply to radio source position time series adjusted on geodetic VLBI observations since 1979. We introduce a threshold providing a flexibility in the definition of a "stable source". Finally, we expose two statistical tools to estimate the stability of celestial frames that will be realized on the basis of this classification.

Keywords astrometry, stability, allan variance, sources classification

1 Introduction

The International Celestial Reference System [ICRS] is nowadays realized through a set of extragalactic radio sources observed by the VLBI and selected on the basis of their astrometric stability. But the set of the "core" radio sources - defining the system axes - varies between the difference releases of the ICRF. In 2018, a new subset will be chosen for realizing the ICRF3 axes. This subset will have to answer all the upcoming challenges, e.g., linking each frequency-dependent reference frame such as the radio ones : S/X (conventional), K-band (see de Witt et al. in these proceedings) ; and the optical one realized by Gaia (Mignard et al., 2016; Lindegren et al., 2016).

Our work aims at giving an objective characterization of the radio sources that can be selected to participate in the definition of the CRF - the so called "defining sources". We rigorously establish the astrometric stability of all the sources observed by VLBI and for which the observations are available on the International VLBI Service (IVS, Nothnagel et al., 2015) database, see the details in section 2. For that, coordinates time series of each sources are precisely determined as explained in section 3 and the stability of the series are computed using the Allan Variance by a method explained in section 4. It leads to a new classification of the sources with respect to this stability given by the colours and the levels of the noise at different time scales within the time series. An overview of this classification is presented in section 5. Finally we present two statistical tools in section 6 in order to estimate the stability of future CRFs that we will realize on the basis of our Allan variance-based classification.

It is to be noted that our work is progressing to automation for frequent updates.

2 Data sets

We used all the diurnal geodetic VLBI sessions available on the IVS database, that is 6 327 in which 5 928 sources were observed. Only sources that have a large observational history can be characterized by means of studying their position time series. Moreover some sources cannot be easily available, depending on the strategy behind the data treatment. For example, a strategy for which we only adjust sources positions for each session and consider all the other parameters to their a priori modelled values enables to determine positions of 4 121 sources only. This data analysis produces Fig. 1 which gives an overview of the sources accessibility, that is the number of sources with respect to the number of sessions. For example, if we selected sources observed in more than 100 sessions, we would restrict ourselves to only 300 sources, that is roughly 7 % of the 4 121 sources easily available. Up to 1 000 sessions, less than 2.5 % is reachable. In our stability study, we reduce our set of data to 710 sources observed in 10 sessions or more.

César Gattano · Sébastien Lambert · Christian Bizouard
SYRTE, Observatoire de Paris, PSL Research University, CNRS, Sorbonne Universités, UPMC Univ. Paris 06, LNE, Paris, France

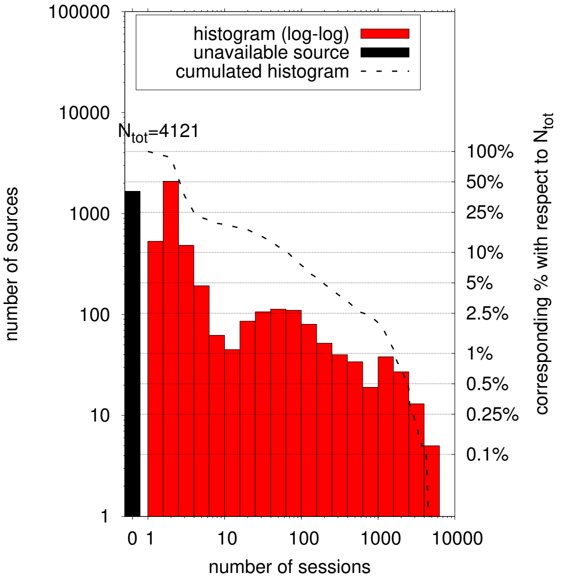

Fig. 1: Histogram of VLBI sources with respect to the number of good sessions. The black bar represents the number of sources that may be unavailable depending on the complexity of the VLBI analysis strategy used. The black dashed curve is the cumulative plot from right to left of the red histogram.

3 Determine sources astrometric instabilities

Our first task was to determine astrometric time series for all VLBI sources. To this aim, we built a composite solution of 11 different adjustments (see Fig. 2) inspired from (Ma et al., 1990). All the details of the analysis strategy not mentioned below can be found in the OPA technical file[1] From a first adjustment called `REFER`, we retrieved the astrometric instabilities for the 39 special handling sources (Ma et al., 1990). Then, in the additional ten adjustments, `SOL01` to `10`, 10 % of all the other sources adjusted globally in `REFER`, are adjusted locally. In each of the `SOL` adjustments, a no-net rotation constraint is applied to 90 % of the ICRF2 defining sources. By doing so we reduce the noise level of our sources astrometric instabilities by a factor of two with respect to time series obtained to a straightforward solution in independent mode in which all sources are estimated locally.

4 Estimate sources astrometric stability

We used the Allan variance (Allan, 1966; Rutman, 1978) to quantify the stability of each sources, allowing us to discriminate noises colour and estimate their levels at perceptible time scales through Allan diagrams (see Fig. 3). The Allan variance estimator is

$$\sigma^2(t,\tau) = \frac{\sum^{k} 1/2\,(\bar{y}_k - \bar{y}_{k+1})^2}{N}$$

where t is the epoch of the first observation, τ is the measurements period and N their number. We computed both Allan diagrams on $\Delta\alpha\cos\delta$ and $\Delta\delta$ for all selected sources and we analyse the noise at each time scale.

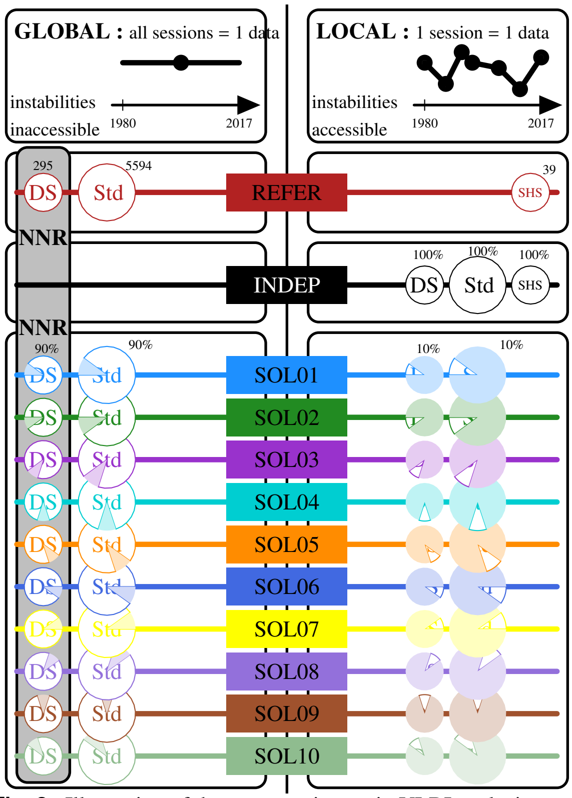

Fig. 2: Illustration of the astrometric part in VLBI analysis strategy for each adjustment that determines astrometric instabilities of sources. REFER + SOL01 to 10 = composite solution ; INDEP = independent solution. NNR = subset of sources on which a no-net rotation constraint is applied.

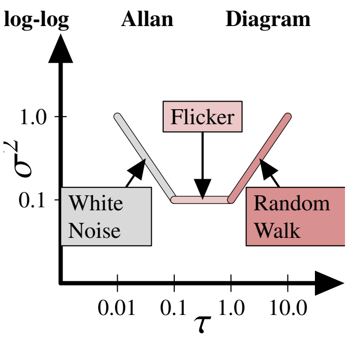

	Drift in Allan diagram
Red noise also called Random walk	1
Pink noise also called Flicker noise	0
White noise	-1

Fig. 3: Illustration of an Allan diagram for a perfect artificial noisy signal with three different types of noise, each one dominating at different time scales.

[1] → `ftp://ivsopar.obspm.fr/vlbi/ivsproducts/eops/opa2017a.eops.txt`

Our classification is built on three categories. The first one, referred to as `AV0` are sources dominated by a white noise at most of the time scales or by flicker noise otherwise. The second one, referred to as `AV1`, are sources that can present a red noise behaviour at intermediate time scale, but not at long time scale where it is dominated by white noise. Finally, the last class, referred to as `AV2`, are all others sources showing an unstable behaviour, i.e., red noise at long time scale.

Our estimation of sources stability includes the determination of the lowest white noise level that returns a pessimist limit on the source potential as defining sources (its corresponding Allan diagram maximizes the computed Allan diagrams built on the observations). It means that the determination of the source position will be better than this hypothetical purely white noise source. This information can be used to roughly resume the noise level of the source without taking into account the details at each time scales.

Finally, and because our method appears to be too severe in determining stable sources (`AV0`), we implement a statistical validation test based on Monte Carlo analysis. The result of the test may rehabilitate `AV1` and `AV2` sources into the `AV0` class. For a given source, the test consists of resampling with white noise and computing the Allan variance, and averaging over 1 000 times. Because of the irregular, finite sampling, a white noise can show false drifts from the expected -1-slope in its Allan diagram, especially at the longest time scale. Consequently, we computed a scatter plot of all the 1 000 Allan diagrams and superimposed it to the real Allan diagrams of the sources. Then we retrieve a percentage of white noise that drifts more than the Allan diagrams of the source. The bigger the percentage, the better the chance than the observed drifts on the source Allan diagrams are not statistically significant.

5 Classification overview and prospects in defining sources selection

Without the MC validation test, our method returns a very pessimistic overview of only 60 stable sources over the 710 well observed and 361 unstable. Nevertheless when we apply the validation test with the loosest threshold, the number of stable sources increase to 561. So, our classification established an adjustable hierarchy that can be used in the context of selecting defining sources. For example, after fixing the threshold for the validation test, one can select only the `AV0` sources. A preferable strategy would be to combine the `AV` classes and the noise level information in order to determine defining sources. External information could be used as well in the selection process, such as the source structure index (Charlot, 1990). Such selection strategies will be our future field of investigation in order to realize several celestial reference frames and compare their stability.

6 Statistical tool to estimate CRF stability

Even if we have not get through the selection process yet, we have already implement two statistical tools to estimate the stability of a celestial reference frame.

A first one is inspired from Lambert (2013). It estimates the time stability by comparing orientation of annual versions of a celestial reference frame to a common reference. In Fig. 6, we show an example for the ICRF2. We defined annual ICRF2 by computing the yearly mean position on the previous astrometric instabilities of each defining sources observed during the corresponding year. Then we adjust three rotation parameters, A_1 around (Ox), A_2 around (Oy) and A_3 around (Oz), to align each annual CRF on the frame taken as reference, i.e. the official positions of ICRF2 sources in the example of this example. The variations of those parameters return the stability of the CRF. For the ICRF2, the stability is estimated to 60 μas.

The second tool consists in randomly drawn M defining sources over N_{DS} in total (N_{DS}=295 for the ICRF2) 1 000 times and estimate the mean rotation angles A_1, A_2, A_3 and theirs standard deviation, given M. The example of the ICRF2 concerning the parameter A_1 around (Ox) axis is shown in Fig. 7 with the ratio M/N in abscissa. The standard deviation gives informations about the stability of the frame. It cannot quantify it with a unique number but it is a great tool to compare stabilities between axis or frames. In the case of ICRF2, we can conclude that A_3 angle of rotation is more stable than A_2 which is more stable than A_1 because A_3 has the lowest σ-curve and A_1, the highest.

7 Conclusion

We establish a new classification of VLBI radio-sources. Three classes are composing the solution: sources `AV0` with a stable behaviour, sources `AV2` with an unstable long-term behaviour and intermediate sources `AV1`. The distribution of the sources in this classification is user-depedent throught a threshold that can be modified in order to restrict or loose a statis-

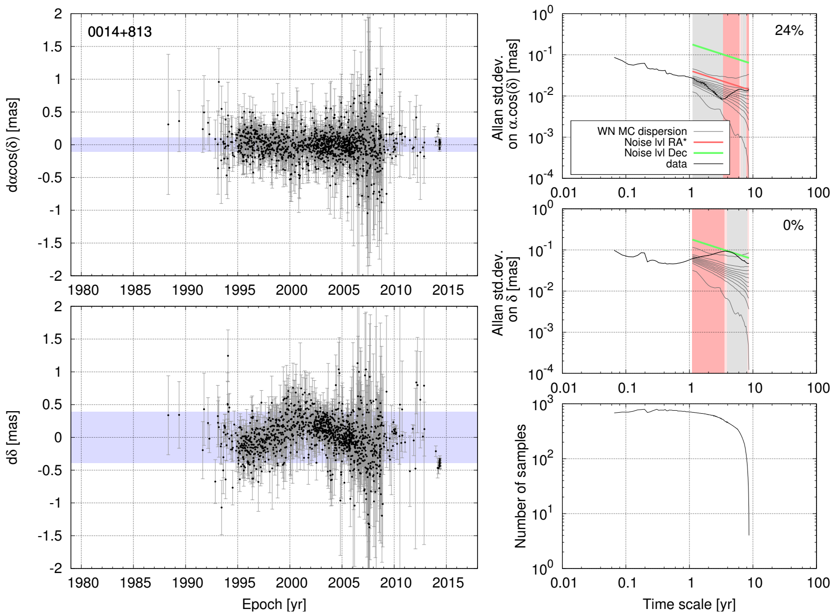

Fig. 4: Example of 0014+813 astrometric instabilities and its corresponding Allan diagrams on $\Delta\alpha\cos\delta$ and $\Delta\delta$. Coloured backgrounds indicated the type of noise respecting the Fig. 3 colour scheme. Green and red straight lines show the minimum white noise level necessary too hide all other coloured noise effects. The grey dispersion curves are a Monte-Carlo-based statistical validation test (see the text for more details).

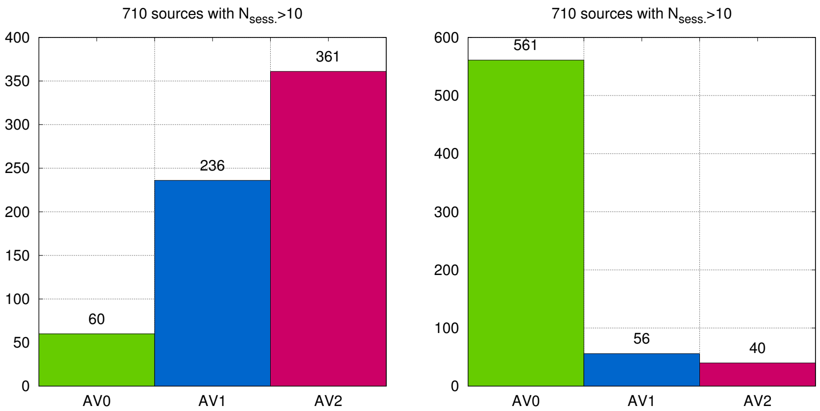

Fig. 5: Classification overview in the most pessimistic scenario (left), where the statistical threshold was fixed at 100 %, and the most optimistic scenario (right), where the statistical threshold was fixed at 0 %.

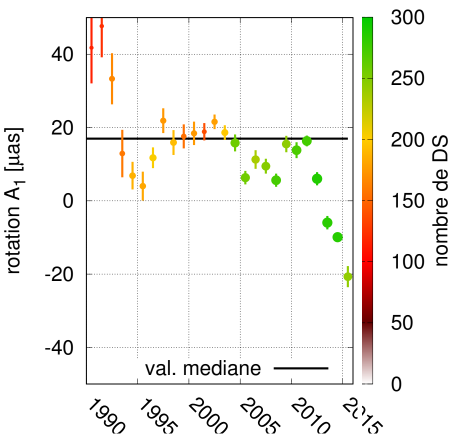

Fig. 6: Example of ICRF2 time stability according to the angle of rotation around (Ox) axis.

Fig. 7: Example of coherence in stability for 1 000 ICRF2 randomly drawn sub-frames according to the angle of rotation around (Ox) axis.

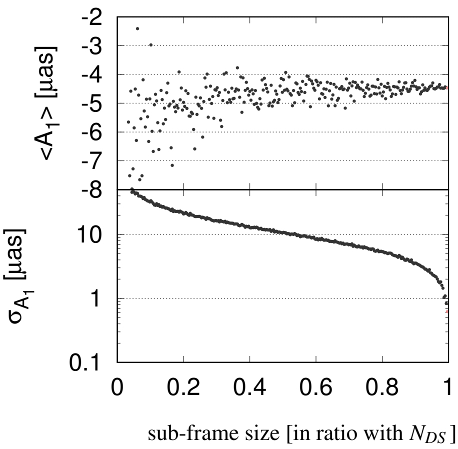

tical constraint defining the border of stable/unstable behaviours.

This classification brings accurate additional information for the selection of defining sources in the realization of a celestial reference frame. Moreover the astrometric variability defined by the instabilities that we adjust accurately on the observation is also rich on astrophysical information about active galactic nuclei [AGN] plasma jet. Their study may answer some questions such as the origin of the instabilities or help to understand physical particularities of sources that are well-suited for geodetic observations and that should be preferred in the VLBI scheduling.

References

Allan D W (1966) Statistics of atomic frequency standards. *IEEE Proceedings*, 54, 221–230, doi:10.1109/PROC.1966.4634

Arias E F, Charlot P, Feissel M, Lestrade J-F (1995) The extragalactic reference system of the International Earth Rotation Service, ICRS. *Astron. Astrophys.*, 303, 604–608,

Charlot P (1990) Radio-source structure in astrometric and geodetic VLBI. *Astron. J.*, 99, 1309–1326. doi:10.1086/115419

Fey A L, Gordon, D., Jacobs C S, Ma C., Gaume R A, Arias E F, Bianco G., Boboltz D A, Böckmann S, Bolotin S, Charlot P, Collioud A, Engelhardt G, Gipson J, Gontier A-M, Heinkelmann R, Kurdubov S, Lambert S, Lytvyn S, MacMillan D S, Malkin Z, Nothnagel A, Ojha R, Skurikhina E, Sokolova J, Souchay J, Sovers O J, Tesmer V, Titov O, Wang G, Zharov V (2015) The Second Realization of the International Celestial Reference Frame by Very Long Baseline Interferometry. *Astron. J.*, 150(58), doi:10.1088/0004-6256/150/2/58

Lambert S (2013) Time stability of the ICRF2 axes. *Astron. Astrophys.*, 553, A122, doi:10.1051/0004-6361/201321320

Lindegren L, Lammers U, Bastian U, Hernández J, Klioner S, Hobbs D, Bombrun A, Michalik D, Ramos-Lerate M, Butkevich A, Comoretto G, Joliet E, Holl B, Hutton A, Parsons P, Steidelmüller H, Abbas U, Altmann M, Andrei A, Anton S, Bach N, Barache C, Becciani U, Berthier J, Bianchi L, Biermann M, Bouquillon S, Bourda G, Brüsemeister T, Bucciarelli B, Busonero D, Carlucci T, Castañeda J, Charlot P, Clotet M, Crosta M, Davidson M, de Felice F, Drimmel R, Fabricius C, Fienga A, Figueras F, Fraile E, Gai M, Garralda N, Geyer R, González-Vidal J J, Guerra R, Hambly N C, Hauser M, Jordan S, Lattanzi M G, Lenhardt H, Liao S, Löffler W, McMillan P J, Mignard F, Mora A, Morbidelli R, Portell J, Riva A, Sarasso M, Serraller I, Siddiqui H, Smart R, Spagna A, Stampa U, Steele I, Taris F, Torra J, van Reeven W, Vecchiato A, Zschocke S, de Bruijne J, Gracia G, Raison F, Lister T, Marchant J, Messineo R, Soffel M, Osorio J, de Torres A, O'Mullane W (2016) Gaia Data Release 1. Astrometry: one billion positions, two million proper motions and parallaxes. *Astron. Astrophys.*, 595, A4, doi:10.1051/0004-6361/201628714

Ma C, Arias E F, Eubanks T M, Fey A L, Gontier A M, Jacobs C S, Sovers O J, Archinal B A, Charlot P (1990) The International Celestial Reference Frame as Realized by VLBI. *Astron. J.*, 116, 516–546, doi:10.1086/300408

Mignard F, Klioner S, Lindegren L, Bastian U, Bombrun A, Hernández J, Hobbs D, Lammers U, Michalik D, Ramos-Lerate M, Biermann M, Butkevich A, Comoretto G, Joliet E, Holl B, Hutton A, Parsons P, Steidelmüller H, Andrei A, Bourda G, Charlot P (2016) Gaia Data Release 1. Reference frame and optical properties of ICRF sources. *Astron. Astrophys.*, 595, A5, doi:10.1051/0004-6361/201629534

Nothnagel et al. (2015) The IVS data input to ITRF2014. doi:10.5880/GFZ.1.1.2015.002

Rutman J (1978) Characterization of phase and frequency instabilities in precision frequency sources - 15yrs of progress. *IEEE Proceedings*, 66, 1048–1075.

Schuh H, Behrend D (2012) VLBI: A fascinating technique for geodesy and astrometry. *J Geodynamics*, 61, 68–80, doi:10.1016/j.jog.2012.07.007

Where – A New Software for Geodetic Analysis

A.-S. Kirkvik, G. A. Hjelle, M. Dähnn, I. Fausk, E. Mysen

Abstract At the Norwegian Mapping Authority we are currently developing Where, a new software for geodetic analysis. Where is built on our experiences with the GEOSAT software, and will be able to analyse data from geodetic techniques such as VLBI, SLR and GNSS. The software is mainly written in Python. The code is quick to write and the architecture is easily extendable and maintainable, while at the same time taking advantage of well-tested libraries like the SOFA and IERS packages. At the moment the VLBI analysis is close to ready. Comparison to other softwares show that theoretical delay computations in Where are consistent with those. Development of SLR and GNSS analysis is well under way, while DORIS is postponed.

Keywords VLBI, Python, Where, Software, VASCC, Comparison

1 Introduction

Where is a new software for geodetic analysis, currently being developed at the Norwegian Mapping Authority. Where is based on experiences from working with the GEOSAT software (Kierulf et al., 2010), and is intended to be able to analyse data from multiple space geodetic techniques used in the creation of reference frames.

The last decade the Norwegian Mapping Authority has increased its contributions to global reference frames. Currently, a new fundamental station is being built at Ny-Ålesund with VLBI, SLR, GNSS and DORIS. The Norwegian Mapping Authority has also contributed to passing a UN resolution on global geodesy and the importance of Global Geodetic Reference Frames[1]. The Where project is the third leg in this effort, developing a new tool for the analysis of space geodetic data.

Full VLBI analysis of daily sessions will soon be possible with Where and this paper will briefly explain the implementation strategy in Where. Some results from tests to verify the implementation of the theoretical model will be shown. Finally, an outline of the remaining activities to complete the VLBI pipeline is presented. Analysis of SLR and GNSS is in development, while DORIS analysis is postponed.

2 Architecture

Where is mainly implemented in Python. The Python ecosystem for data science is very rich and powerful. Python is Open Source and freely available on all major platforms[2]. In addition, Python smoothly interfaces with other languages like C and Fortran, which allows Where to use the `SOFA`[3] and `IERS` (IERS contributors) Fortran libraries directly. Python also provides a comprehensive set of libraries. Where utilizes several well known packages such as `numpy`[4], `scipy`[5], and `matplotlib`[6] as well as more specialized packages like `astropy` (Astropy Collaboration et al., 2013), `pint`[7] and `jplephem`[8].

Where stores the analysis output in HDF5[9] and JSON[10] files. To explore the output a simple graphical interface called There based on `matplotlib` is also

Ann-Silje Kirkvik · Geir Arne Hjelle · Michael Dähnn · Ingrid Fausk · Eirik Mysen
Norwegian Mapping Authority, Geodetic Institute, Kartverksveien 21, NO-3511 Hønefoss, Norway

[1] URL `ggim.un.org/UN_GGIM_wg1.html`
[2] URL `python.org`
[3] URL `iausofa.org`
[4] URL `numpy.org`
[5] URL `scipy.org`
[6] URL `matplotlib.org`
[7] URL `pint.readthedocs.io`
[8] URL `pypi.python.org/pypi/jplephem`
[9] URL `hdfgroup.org`
[10] URL `json.org`

Fig. 1: A screen-shot of There. There is a graphical tool developed to look into the results and analysis done by Where.

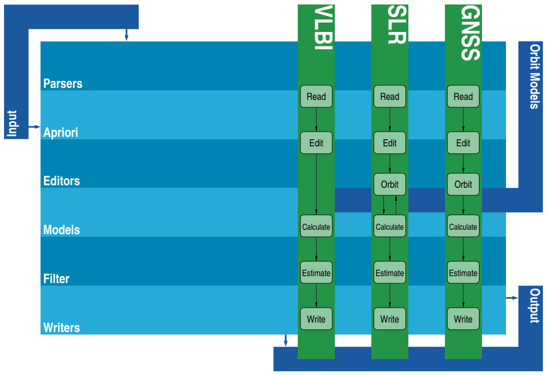

Fig. 2: An overview of the architecture of Where. Pipelines for the analysis of the different techniques is shown as vertical bars. Horisontal lines represent packages that to some extent can be reused across techniques.

being developed. A screen-shot from There is shown in Figure 1.

Where works on the basis of a pipeline that is split into several stages, see Figure 2. First, observation files are processed in the *read* stage and converted to an internal Where data structure. Next, in the *edit* stage bad observations are discarded and other filters such as an elevation cut off angle can be applied. Next, theoretical delays are calculated and a quadratic clock polynomial is estimated in the *calculate* stage. At this stage the analyst can inspect the residuals to identify for instance clock breaks and bad cable calibration data and update the configuration file for the edit stage accordingly. The *edit* and *calculate* stage needs to be run again if any changes are made. Next, station positions and other target parameters such as Earth orientation parameters can then be estimated in the *estimate* stage. Finally, results are written to disk in proper formats in the *write* stage.

3 Implementation

A VLBI model consistent with current conventions is fully implemented. In Where, the theoretical delay τ is calculated according to

$$\begin{aligned} \tau = & \tau_{\text{geom}} + \tau_{\text{grav}} + \Delta\tau_{\text{tropo}} + \Delta\tau_{\text{axis}} - \\ & \Delta\tau_{\text{therm}} + \tau_{\text{clock}} - \Delta\tau_{\text{cable}} + \tau_{\text{iono}}, \end{aligned} \tag{1}$$

with the notation

$$\Delta\tau_x = \tau_x(\text{station}_2) - \tau_x(\text{station}_1). \tag{2}$$

The geometric and gravitational delays τ_{geom} and τ_{grav} follow the consensus model in chapter 11 of the 2010 IERS Conventions (Petit and Luzum, 2010). The geocentric velocity of a receiver, w_i, in the consensus model is implemented as

$$w_i(t) = Q(t)\dot{R}(t)W(t)x_i \tag{3}$$

where t is the epoch of the observation. Furthermore, $Q(t)$, $R(t)$ and $W(t)$ are the transformation matrices discussed in chapter 5 of the 2010 IERS Conventions (Petit and Luzum, 2010) and $\dot{R}(t)$ is the time derivative of $R(t)$. Finally, x_i is the coordinate of the receiver in a terrestrial reference frame.

Gravitational delays are included for the Sun, the Earth, the Moon, Mercury, Venus, Mars, Jupiter, Saturn, Uranus, Neptune and Pluto. The planet ephemerides are calculated using the Python package `jplephem`[8] which reads the Satellite Planet Kernel files provided by JPL and computes three-dimensional positions and velocities for the planets.

The tropospheric delay τ_{tropo} is implemented according to chapter 9 in the 2010 IERS Conventions (Petit and Luzum, 2010) with VMF1 (Böhm et al., 2006) as default mapping functions. When available, routines from `IERS` (IERS contributors) are used to calculate the delay due to the troposphere.

The delays due to axis offset τ_{axis} and thermal deformation τ_{therm} are implemented based on (Nothnagel, 2009). To account for the time delay in the thermal deformation model a sine function is fitted to the temperature data to estimate the temperature at 2 and 6 hours before the observation epochs. The elevation angle is not corrected for refractivity, and antennas with a radome are not treated differently than those without.

The ionospheric delay τ_{iono} and cable delay τ_{cable} are used directly as provided on the observation file. The delay due to clock synchronization issues τ_{clock} is an estimated second degree polynomial for all stations except one station that is kept fixed as a reference station.

The apriori station coordinates are projected to the observation epochs using the linear model provided

Table 1: VLBI Models and apriori data supported by Where. A configuration file is used to choose between the different options.

EOP	Lagrange interpolated C04 time series with corrections for high frequency ocean tides and liberations
Reference frames	ITRF2008/2014 (no post-seismic deformations) and ICRF2
Ephemerides	DE405, DE421, DE430
Displacement models	Atmospheric pressure loading, Eccentricity vector, Ocean tidal loading, Ocean pole tides, Solid Earth tides, Solid Earth pole tides
Troposphere	GMF, GPT, GPT2, GPT2w, VMF1
VLBI models	Axis offset, Cable calibration, Geometric and gravitational delay, Ionosphere, Thermal deformation
Estimation	Kalman Filter with continuous piece-wise linear functions
Partial derivatives	Clock, Polar motion and rate, ΔUT1 and rate, Celestial pole offset, Source coordinates, Station position, Zenith wet delay, Horizontal gradients

with the reference frame. The station displacement models from chapter 7 in the IERS Conventions 2010 are then applied to model the variations in the station coordinates during the observation period. Table 1 gives an overview of the models currently available for Where. The station displacement models are based on the `IERS` (IERS contributors) routines that are available.

The transformation between a terrestrial reference frame and a geocentric celestial frame is implemented using `SOFA`[3] routines. The applied method is IAU 2006/2000A, CIO based using the X, Y series as described in section 5.6 in SOFA Tools for Earth Attitude (IAU SOFA Tools). The Earth orientation parameters are interpolated to the observation epochs and corrected for ocean tides and liberations using `IERS` (IERS contributors) routines as described in chapter 5 of the 2010 IERS Conventions (Petit and Luzum, 2010).

To handle the various time scales needed in a typical VLBI analysis, Where utilizes the `Time` class of the `astropy` library (Astropy Collaboration et al., 2013). However, to ensure consistency, the transition between UT1 and UTC is overridden by a custom implementation based on the apriori UT1-UTC time series. Likewise, the transition between TT and TDB is overridden by the method and software described in chapter 10 of the 2010 IERS Conventions (Petit and Luzum, 2010). For now, all the delay models and station displacement models are calculated using the arrival time at the first station of a baseline.

The estimation is done using a Kalman filter with a Modified Bryson-Frazier smoother (Bierman, 2006). Currently, the clock errors and troposphere (wet delay and gradients) are modeled using continuous piece-wise linear functions. The Kalman filter solution is converted to reduced normal equations using results from (Mysen, 2017). Table 1 summarizes the parameters that can be estimated.

4 Test results

In 2015/2016 Grzegorz Klopotek at Chalmers University of Technology in Sweden carried out a VLBI Analysis Software Comparison Campaign (VASCC). The goal of the campaign was to compare computed theoretical delays from different software packages. In total 11 different software packages contributed to the campaign and the results where presented at the IVS General Meeting in South Africa in 2016 (Klopotek et al., 2016).

The Norwegian Mapping Authority provided solutions to VASCC using the legacy software GEOSAT (Kierulf et al., 2010). However, as development of the new software progressed a new VASCC solution using Where was computed. This solution was compared with VASCC solutions from the software packages c5++ (Hobiger et al., 2010) and VieVS (Böhm et al., 2012).

The VASCC data-set includes two networks of stations: one with four stations on the southern hemisphere (SH) and one with five stations on the northern hemisphere (NH). Virtual observations of one radio source for each network are scheduled every minute for 15 days, from June 22nd to July 7th 2015. This yielded a total number of 129600 observations for the southern network and 216000 observations for the northern network. A leap second is introduced at midnight June 30th.

Not all terms of the theoretical delay (1) are included in the campaign. The VASCC delay model includes geometric and gravitational delay from the IERS 2010 Conventions (Petit and Luzum, 2010). Also the delay through the troposphere (Petit and Luzum, 2010) (hydrostatic delay with GMF mapping function) and delay due to thermal deformations (with constant temperatures) and axis offset as described by (Nothnagel, 2009) are included. Delays due to cable calibration, the ionosphere and clocks are ignored. Site displacement models includes solid Earth tides, solid Earth pole tides, ocean tidal loading (FES2004) and ocean loading pole tides according to (Petit and Luzum, 2010). The ver-

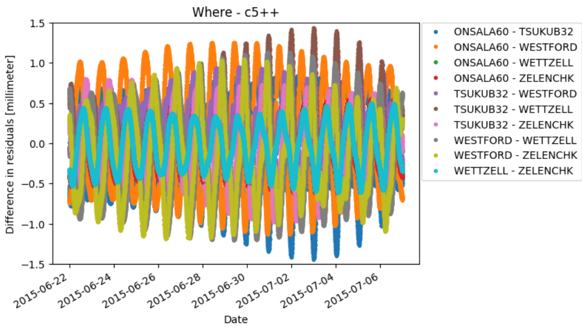

Fig. 3: Difference in theoretical delay between Where and c5++ for each baseline in the northern network used in the VASCC. The RMS of all differences is 0.49 mm.

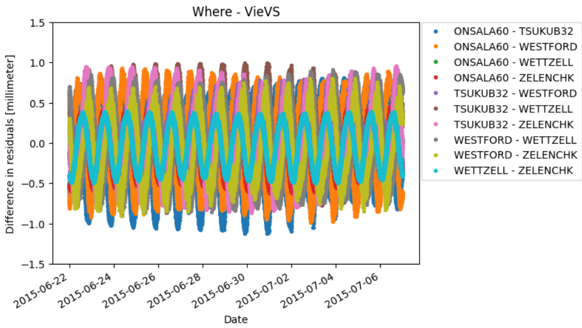

Fig. 4: Difference in theoretical delay between Where and VieVS for each baseline in the northern network used in the VASCC. The RMS of all differences is 0.44 mm.

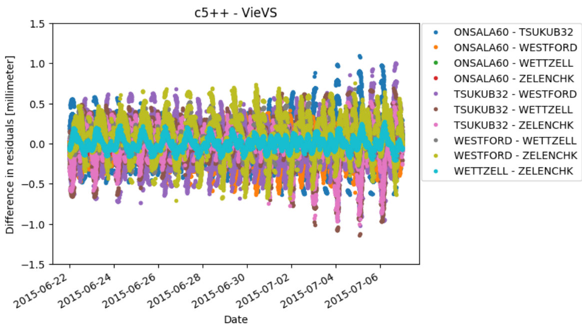

Fig. 5: Difference in theoretical delay between c5++ and VieVS for each baseline in the northern network used in the VASCC. The RMS of all differences is 0.21 mm.

sion of the IERS Conventional mean pole model used in VASCC is 2010. Atmospheric pressure loading and eccentricity vectors are ignored. The apriori EOP time series is corrected for ocean tides and liberation effects with periods less than two days according to (Petit and Luzum, 2010).

In the original campaign six software packages got sub-millimeter agreement when comparing the RMS of the difference in theoretical delays for both networks together over the whole period. The largest RMS difference between two of these software packages was 0.71 mm and the smallest difference was 0.17 mm. The absolute value of the largest difference in residual among these packages was 2.68 mm and the smallest difference was 0.83 mm. The solutions from two of the these six software packages, c5++ (Hobiger et al., 2010) and VieVS (Böhm et al., 2012), were compared with Where and the results are summarized in Tables 2 and 3. Figures 3, 4 and 5 show the difference between Where, c5++ and VieVS for the northern network. For the southern network the differences in residuals are slightly smaller.

Table 2: RMS of difference [mm] between Where, c5++ and VieVS for the northern (NH, above diagonal) and southern (SH, below diagonal) network.

		NH		
		Where	**c5++**	**VieVS**
SH	**Where**	⋄	0.49	0.44
	c5++	0.18	⋄	0.21
	VieVS	0.43	0.39	⋄

Table 3: Maximum absolute difference [mm] between Where, c5++ and VieVS for the northern (NH, above diagonal) and southern (SH, below diagonal) network.

		NH		
		Where	**c5++**	**VieVS**
SH	**Where**	⋄	1.44	1.12
	c5++	0.63	⋄	1.14
	VieVS	1.28	1.09	⋄

5 Conclusions and future work

The comparison with the VASCC results indicate that the VLBI delay model in Where is consistent with existing software packages and current conventions. The VASCC data-set has been valuable in the development and testing of Where. An extension of the campaign to include for instance the VMF1 mapping function and partial derivatives is encouraged.

The *estimation* and *write* stages in Where are implemented, but some testing remains. Where can read both `NGS` and `vgosDb` files, but requires that the ionosphere and ambiguities are provided in the observation files.

The Norwegian Mapping Authority is an associated analysis center within the IVS and the short term plan is to finish a stable version of Where capable of producing normal equations that can be used for IVS products (Behrend, 2013). Additionally, the short term plan is to implement support for the post-seismic deformation models in ITRF2014 (Altamimi et al., 2016).

The next step is to combine solutions from individual sessions to investigate the behavior of for instance station coordinates over time. This work is intended to monitor and ensure good data quality from the new antennas at Ny-Ålesund. Later, we will investigate the possibilities for solving the ionosphere and ambiguities in the next step towards creating an independent analysis software.

References

Altamimi Z, Rebischung P, Métivier L, Collilieux X (2016) ITRF2014: A new release of the International Terrestrial Reference Frame modeling nonlinear station motions. *J. Geophys. Res.: Solid Earth*, 121, 6109–6131. doi:10.1002/2016JB013098.

Astropy Collaboration, et al. Astropy: A community python package for astronomy. *Astronomy & Astrophysics*, 558: A33, Oct. 2013. doi:10.1051/0004-6361/201322068. URL www.astropy.org.

Behrend D (2013) Data Handling within the International VLBI Service *Data Science Journal*, 12, WDS81–WDS84, ISSN 1683-1470, doi:10.2481/dsj.WDS-011

Böhm J, Werl B, Schuh H (2006) Troposphere mapping functions for GPS and VLBI from ECMWF operational analysis data. *J. Geophys. Res.: Solid Earth*, 111(B2), 2156–2202, doi:10.1029/2005JB003629

Böhm J, Böhm S, Nilsson T, Pany A, Plank L, Spicakova H, Teke K, Schuh K (2012) The new Vienna VLBI software VieVS. In: S. Kenyon, M. C. Pacino, U. Marti (eds.) *Geodesy for Planet Earth: Proc. 2009 IAG Symposium* IAG Symposia Series, 136, 1007–1011, doi:10.1007/978-3-642-20338-1_126.

Bierman G J (2006) Factorization Methods for Discrete Sequential Estimation. Dover publications. ISBN 9780486449814

Hobiger T, Otsubo T, Sekido M, Gotoh T, Kubooka T, Takiguchi H (2010) Fully automated VLBI analysis with c5++ for ultra-rapid determination of UT1. *Earth, Planets and Space*, 62(12):933–937, doi:10.5047/eps.2010.11.008.

IAU SOFA Board. SOFA Tools for Earth Attitude. http://www.iausofa.org/publications/sofa_pn.pdf

IERS contributors. IERS software collection. ftp://maia.usno.navy.mil/conventions/2010.

Kierulf H P, Andersen P-H, Boeckmann S, Kristiansen O (2010) VLBI analysis with the multi-technique software GEOSAT. In D. Behrend, K. D. Baver (eds.), *IVS 2010 General Meeting Proceedings - "VLBI2010: From Vision to Reality"*, NASA/CP-2010-215864, 207–211, ivscc.gsfc.nasa.gov/publications/gm2010/kierulf.pdf.

Klopotek G, Artz T, Bellanger A, Bourda G, Gerstl M, Gordon D, Haas R, Halsig S, Hjelle G A, Hobiger T, Hugentobler U, Iddink A, Kirkvik A S, Lambert S, Plank L, Schmid R, Shu F, Titov O, Tong F, Wang G, Xu M, Zheng W (2016) Results from the VLBI Analysis Software Comparison Campaign 2015. In: D. Behrend, K. D. Baver, K. L. Armstrong (eds.), *IVS 2016 General Meeting Proceedings: "New Horizons with VGOS"*, NASA/CP-2016-219016, 203–207, URL ftp://ivscc.gsfc.nasa.gov/pub/general-meeting/2016/pdf/042_klopotek_etal.pdf.

Mysen E (2017) On the equivalence of Kalman filtering and least-squares estimation. *Journal of Geodesy*, 91(1):41–52, doi:10.1007/s00190-016-0936-3.

Nothnagel A (2009) Conventions on thermal expansion modelling of radio telescopes for geodetic and astrometric VLBI. *J Geod*, 83(8):787–792, doi:10.1007/s00190-008-0284-z.

Petit G, Luzum B (eds.) IERS Conventions 2010, *IERS Technical Note* 36, Frankfurt am Main: Verlag des Bundesamts für Kartographie und Geodäsie, URL www.iers.org/IERS/EN/Publications/Technical\protect\discretionary{\char\hyphenchar\font}{}{}Notes/tn36.html.

Improvements of the Stochastic Model of the VLBI Data Analysis in VieVS@GFZ

N. Mammadaliyev, R. Heinkelmann, T. Nilsson, H. Schuh

Abstract In geodetic VLBI, usually the least-squares adjustment method is applied for the estimation of the unknown parameters. The complete model of the least-squares adjustment contains the full variance-covariance matrix of the observables. However, the current stochastic model of the VLBI analysis software VieVS@GFZ includes only diagonal elements in the weight matrix of the observations that depend e.g. on the uncertainties provided by the VLBI correlation process. The observations are assumed to be independent. A number of studies had shown that modeling the stochastic model as a diagonal matrix affects the accuracy of the estimated parameters and the parameters themselves. The aim of this study is the improvement of the variances by incorporating all error sources affecting the "observed minus computed" delays, and the modeling of additional covariances in order to obtain a more realistic stochastic model in terms of a fully populated variance-covariance matrix. In order to evaluate possible improvements, the extended stochastic model will be applied to the analysis of the continuous VLBI campaign 2014 (CONT14) data using the VieVS@GFZ VLBI analysis software. The results demonstrate that an extended, fully populated variance-covariance matrix provides different adjusted parameters with more realistic formal errors.

Keywords Stochastic Model, CONT14, Station Dependent Correlation

Nijat Mammadaliyev · Harald Schuh
Technische Universität Berlin, IGG, Straße des 17. Juni 135, DE-10623 Berlin, Germany

Robert Heinkelmann · Tobias Nilsson · Harald Schuh
Deutsches GeoForschungsZentrum, GFZ, Telegrafenberg, DE-14473 Potsdam, Germany

1 Introduction

The standard stochastic information of the VLBI observations is derived during the correlation process. Furthermore, the observations are assumed to be independent, i.e. the noise of different observations is uncorrelated. This is equivalent to modeling the covariance matrix as diagonal. Neglecting other error sources and the correlation between observations can cause too optimistic errors of the parameters and wrong parameter estimates (Gipson, 2007).

In this study, possible error sources are added into the stochastic model in order to improve the variances. Many of them cause correlation between observations. In order to obtain covariances, the station dependent error sources were investigated. These errors are constant for all observations involving a station within a certain time interval.

Following section describes several implemented stochastic models in VieVS@GFZ analysis software.

Section 3 presents results of these stochastic models. The baseline length repeatability is used as a quality assessment method and χ^2 values are presented to validate different solutions. Moreover estimated Earth Orientation Parameters (EOP) and baseline scatter obtained from different stochastic models were compared.

2 Stochastic Models

In order to analyze geodetic VLBI data, usually the Gauss-Markoff model is applied to determine the unknown parameters. In this study, eleven different stochastic models have been investigated for the analysis of 15 CONT14 session (Fig. 1).

	Co-variance matrix			1-sigma standard error								
	Main Diagonal	Block Diagonal	Full Populated	σobs	σion	σtrop	σtherm	σAO	σcal	σsour	σcom	σconst
setup1	X			X								
setup2	X			X	X							
setup3	X			X	X	X						
setup4	X			X	X	X	X					
setup5	X			X	X	X	X	X				
setup6	X			X	X	X	X	X	X			
setup7	X			X	X	X	X	X	X	X		
setup8	X			X	X	X	X	X	X	X	X	
setup9	X			X	X							X
setup10		X		X	X	X	X	X	X	X	X	
setup11			X	X	X	X	X	X	X	X	X	

Fig. 1: Different stochastic properties.

2.1 Improvement of the Variances

The traditional stochastic model is derived as a product of the common variance level σ_0^2 and the cofactor matrix **Q**. Usually, in VLBI analysis, cofactor matrix **Q** is a main diagonal matrix and consists of the formal error of observations.

The standard assumption in VLBI data analysis (setup1) is that, the formal error of the observations σ_i are defined equal to the measurement noise σ_{meas}, which is derived during the correlation process. However, under this assumption, the χ^2 value of the solution is much larger than 1, an indication for unmodeled error sources.

$$\sigma_i^2 = \sigma_{meas}^2 \quad ,i = 1,2,...,n$$

Another error source is due to ionospheric effect on the VLBI signals. In the setup2, we add the delay ionospheric correction formal error, which is provided in the NGS file, into the stochastic model to analyze the data. Variances of the observations are estimated as:

$$\sigma_i^2 = \sigma_{meas}^2 + \sigma_{ion}^2$$

One of the other significant error sources in the VLBI data analysis is the mismodelled troposphere. In the setup3 we investigate a delay tropospheric correction formal error σ_{trop} and add it to the stochastic model. The formal error of the delay tropospheric correction was calculated based on the accuracy of the zenith hydrostatic delay, mapping function and a priori gradients.

Other error sources are, due to antenna thermal deformation σ_{therm}, axis offsets σ_{AO}, instrumental calibration σ_{cal}, source structure σ_{sour}, investigated and added into stochastic model at setups 4, 5, 6, 7 respectively. For the source structure formal error median absolute closure quantities are used (Xu et al., 2017).

Formal errors of the computed delays σ_{com} were derived based on station and source position errors, EOP errors, and errors in geophysical models. Setup8 contains all mentioned error source. The variances of observations are derived as follows:

$$\sigma_i^2 = \sigma_{meas}^2 + \sigma_{ion}^2 + \sigma_{trop}^2 + \sigma_{therm}^2 + \\ + \sigma_{AO}^2 + \sigma_{cal}^2 + \sigma_{sour}^2 + \sigma_{com}^2$$

The standard stochastic model of the VieVS@GFZ analysis software is defined at setup9. It is main diagonal matrix and consists of the variance of the observation, ionospheric delay and a 1 cm constant σ_{const}^2. The constant part is added to cover deficiencies in the functional model.

$$Q = \begin{bmatrix} \sigma_{obs1}^2 + \sigma_{ion1}^2 + \sigma_{const}^2 & \cdots & 0 \\ \vdots & \ddots & \vdots \\ 0 & \cdots & \sigma_{obsn}^2 + \sigma_{ionn}^2 + \sigma_{const}^2 \end{bmatrix}$$

2.2 Addition of the Covariances

The complete stochastic model of the Gauss-Markoff model consists of the fully populated variance-covariance matrix. However, off diagonal elements are set to zero and only main diagonal elements are used to analyze the geodetic VLBI data. Generally the main diagonal elements consist of the σ_{meas} and additional σ_{const} to cover the deficits of the modeling. Or instead of the rigorous constant part, additional noise is iteratively added to the formal error of the observations in order to improve the variances of the observations.

In this study, the station dependent error sources are investigated. Because the station dependent error sources are time-invariant, they affect all observations involving certain station in the same way. Therefore, station dependent error sources introduce correlations between observations in case of common stations.

Under the following assumptions, correlation is considered between the observations:

1. **Block diagonal matrix -** Correlations of observations within the same scan are considered (setup10)
2. **Fully populated matrix -** Correlations of all observations within a session are considered (setup11).

The correlation between the observations is calculated as:

$$q = \sigma_{trop}^2 + \sigma_{therm}^2 + \sigma_{AO}^2 + \sigma_{cal}^2$$

where σ_{trop} are the 1-σ errors of the troposphere delay, σ_{therm} are 1-σ errors of the thermal deformation,

σ_{AO} are 1-σ errors of the axis offset and σ_{cal} are 1-σ errors of the instrumental calibration.

3 Test results of different stochastic models

For this test, 15 CONT14 sessions were processed with the VieVS@GFZ analysis software (Nilsson et al., 2011) with eleven different stochastic models. CONT14 sessions deliver high quality continuous data over a short period of time from VLBI observation. Therefore, they should be more sensitive to improvements in the analysis (Gipson, 2007).

For all the solutions a priori station coordinates and their accuracies are taken from ITRF2008, a priori source coordinates and their accuracies are taken from ICRF2 and a priori EOP and their accuracies from IERS 08 C04.

The χ^2 values for each day of the CONT14 sessions are given in Fig. 2 to validate the different solutions. If the weights of the observations are given correctly, the χ^2 value of the session should be close to unity.

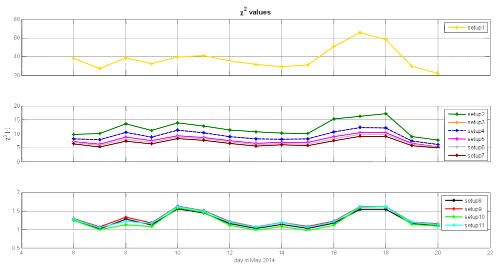

Fig. 2: χ^2 values for each day of the CONT14 session for validation of the different stochastic models.

It is clearly seen in Figure 2 that, σ_{meas} is much smaller, therefore χ^2 value is much larger than it should be (setup1). Including other error sources into the stochastic model increases the formal error of the individual observations and therefore decrease the χ^2 value of the session. Additionally, introducing co-variances improves the stochastic model, so χ^2 values get closer to 1. Figure 2 demonstrates that the improved stochastic model gives more realistic errors and consequently better estimates.

Figure 3 shows baseline length repeatability to asses the quality of the different solutions. Baseline length repeatability is calculated for all baselines observed in the CONT14 session, in total 136 baselines. Improvement of the stochastic model significantly decreases the wRMS. As one can see, the repeatability of the correlated approach (setup10) is better than the uncorrelated approach. The average improvement is ≈3 mm (20 %) with respect to setup1 or ≈0.4 mm (4 %) with respect to setup9 for the Westford - Yarragadee baseline.

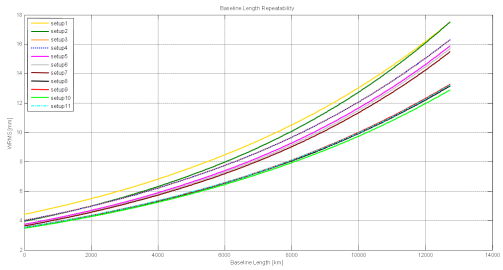

Fig. 3: Baseline length repeatability for all stochastic model.

Figure 4 shows the differences in baseline scatter between the standard solution of the VieVS@GFZ analysis software (setup9) and a solution using the stochastic model with improved variances (setup8). The repeatabilities of the stochastic model with improved variances (setup 8) are better for 100 baselines compared to the standard VieVS@GFZ model (setup 9) and the average improvement is 0.06 mm.

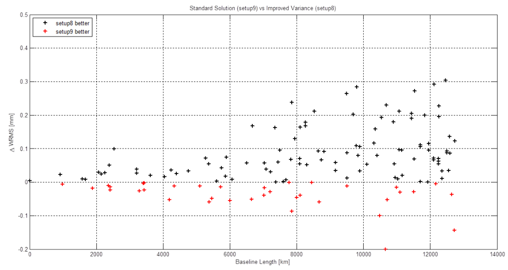

Fig. 4: Standard solution (setup9) vs. Improved variances (setup8).

Figure 5 shows the difference in baseline scatter between the standard solution of the VieVS@GFZ analysis software (setup9) and a solution using the stochastic model with the block diagonal variance-covariance matrix, where observations within the same scan are correlated (setup10). The repeatabilities of the correlated approach (setup 10) are better for 107 baselines compared to the setup 9 and the average improvement is 0.21 mm.

Figure 6 shows the differences in baseline lengths scatter between the setup8 and setup10. The repeatabilities of the setup 10 are better for 95 baselines compared to the setup 8 and the average improvement is 0.15 mm.

In addition, we compare EOP parameters (x_{pol} and y_{pol}) obtained from the different stochastic models. Table 1 represents the results of the analysis with different stochastic properties. Considering additional error sources in the stochastic model slightly improves the results. The wRMS of the polar motion residuals are lower

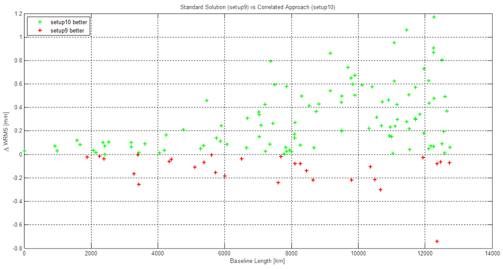

Fig. 5: Standard solution (setup9) vs. Correlated approach (setup10).

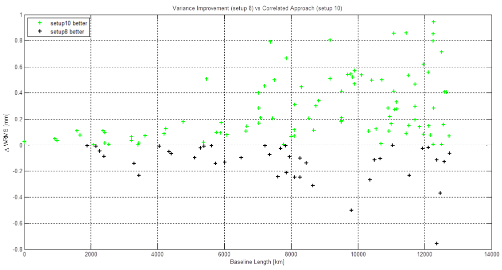

Fig. 6: Variance improvement (setup8) vs. Correlated approach (setup10).

when the improved stochastic model is used. Polar motion parameter differences between setup9 and setup10 reach up to 10 μas for x_{pol} and up to 3 μas for y_{pol}

Table 1: Comparison of the EOP.

EOP Parameters	x_{pol} (μas)		y_{pol} (μas)	
	wRMS	**Chg. %**	**wRMS**	**Chg. %**
setup1	132.6	-	139.4	-
setup2	108.5	18.2	134.2	3.7
setup3	103.4	22.0	129.1	7.4
setup4	103.4	22.0	129.1	7.4
setup5	95.8	27.8	123.1	11.7
setup6	94.3	28.9	122.2	12.3
setup7	92.2	30.5	122.5	12.1
setup8	**84.6**	**36.2**	104.7	24.9
setup9	86.2	35.0	105.1	24.6
setup10	87.6	33.9	**104.3**	**25.1**
setup11	85.5	35.5	105.6	24.2

4 Conclusions

In this study, we presented several alternative stochastic models to the standard. We demonstrate that including error sources into the stochastic model reduces the baseline lengths scatter and decreases χ^2 values. It also leads to more realistic formal errors and slightly improves the results. Generally the larger improvement is achieved on the longer baseline.

The effect on baseline lengths and global parameters, here EOP, clearly documented that the stochastic model not only affects the formal errors but also the parameters themselves. We recommend applying an enhanced stochastic model for VLBI analysis. Currently we do not recommend a specific stochastic model, because our results are still preliminary and we have to extend our evaluation using more VLBI data.

References

Altamimi Z, Collilieux X, Métivier L (2011) ITRF2008: An improved solution of the international terrestrial reference frame. *J Geod*, 85, 457–473.

Bizouard C, Gambis D (2009) The Combined Solution C04 for Earth Orientation Parameters Consistent with International Terrestrial Reference Frame 2005. In: H. Drewes (ed.), *Geodetic Reference Frames*, IAG Symposia 134, 265–270.

Böhm J, Werl B, Schuh H (2006). Troposphere mapping functions for GPS and Very Long Baseline Interferometry from European Centre for Medium-Range Weather Forecasts operational analysis data. *J. Geophys. Res.*, 111.

Böhm J, Urquhart L, Steigenberger P, Heinkelmann R, Nafisi V, Schuh H (2012) A Priori Gradients in the Analysis of Space Geodetic Observations. In: Z. Altamimi, X. Collilieux (eds.), IAG Symposia 138, 105–109.

Fey A L , Gordon D, C. S. Jacobs, C. Ma, R. A. Gaume, E. F. Arias, G. Bianco, Boboltz D A, Böckmann S, Bolotin S, Charlot P, Collioud A, Engelhardt G, Gipson J, Gontier A-M, Heinkelmann R, Kurdubov S, Lambert S, Lytvyn S, MacMillan D S, Malkin Z, Nothnagel A, Ojha R, Skurikhina E, J. Sokolova J, Souchay J, Sovers O J, Tesmer V, Titov O, Wang G, Zharov V (2015) The second realization of the international celestial reference frame by very long baseline interferometry. *Astronomical J.*, 150(58):1–16, doi:10.1088/0004-6256/150/2/58.

Gipson J M (2007) Incorporating Correlated Station Dependent Noise Improves VLBI Estimates. In: J. Böhm, A. Pany, H. Schuh (eds.), *Proc. 18th EVGA Working Meeting*, 129–134.

Gipson J M, MacMillan D S, Petrov L (2008) Improved Estimation in VLBI through Better Modeling and Analysis. In: A. Finkelstein, D. Behrend (eds.), *IVS 2008 General Meeting Proceedings*, 157–162.

Petit G, Luzum B (eds.) (2010) IERS Conventions 2010. *IERS Technical Note No. 36*, Frankfurt am Main: Verlag des Bundesamts fur Kartographie und Geodäsie.

Tesmer V, Kutterer H (2004) An Advanced Stochastic Model for VLBI Observations and its Application to VLBI Data Analysis. In: N. R. Vandenberg, K. D. Baver (eds.), *IVS 2004 General Meeting Proceedings*, 296–300.

Schuh H, Wilkin A (1989) Determination of Correlation Coefficients between VLBI-Observations. In: A. Rius (ed.), *Proc. 7th EVGA Working Meeting*, 79–91.

Xu M H, R. Heinkelmann R, Anderson J M, Mora-Diaz J, Karbon M, Schuh H, Wang G L (2017) The impacts of source structure on geodetic parameters demonstrated by the radio source 3C371. *J Geod*, 91, 767–781.

Nilsson T, Böhm J, Böhm S, Madzak M, Nafisi V, Plank L, Spicakova H, Sun J, Tierno Ros C, Schuh H (2011) Status and future plans for the Vienna VLBI Software VieVS. In: W. Alef, S. Bernhart, A. Nothnagel (eds.), *Proc. 20th EVGA Working Meeting*, 93–96.

The GFZ-VLBI-TRF Solution

T. Nilsson, S. Glaser, M. Karbon, B. Soja, R. Heinkelmann, H. Schuh

Abstract We present a VLBI Terrestrial Reference Frame (TRF) solution based on the results of the Kalman filter module in the VieVS@GFZ software; the GFZ-VLBI-TRF. In this work, we demonstrate the properties of this solution and compare it to a similar VLBI TRF based on the results from the classical least squares module in VieVS@GFZ. We also make comparisons to several recent official TRF solutions, namely the ITRF2014, the DTRF2014, the JTRF2014, and the latest IVS TRF solution. In general, an agreement with these TRF was on the the level of 1–2 mm or better was found, except for a 4.7 mm scale difference w.r.t. ITRF2014. Furthermore, we study the impact of different handling of the Celestial Reference Frame (CRF), as well as the session types included in the solution.

Keywords VLBI, Terrestrial Reference Frame, Kalman filter

1 Introduction

Recently, a Kalman filter module has been implemented in the GFZ version of the Vienna VLBI Software (VieVS, Böhm et al., 2012), VieVS@GFZ (Nilsson et al., 2015; Soja et al., 2015). A Kalman filter has the advantage over the classical least-squares method (LSM) that it allows for better modeling of randomly varying parameters, such as the station clocks and the tropospheric parameters. It has been shown (e.g., Nilsson et al., 2015) that this improved modeling lead to slightly better results for the baseline lengths and Earth Orientation Parameters (EOP) estimated in a single-session analysis, compared when using the classical LSM module in VieVS@GFZ.

In this work, we investigate how the usage of the Kalman filter module impact s the results of a global solution, in particular the estimation of a VLBI-only Terrestrial Reference Frame (TRF). This is done by first analyzing almost all (4967) 24-h geodetic VLBI sessions from 1990 until 2017 with the Kalman filter module. Then the results of these single-session analyses are combined in a global solution to estimate a VLBI TRF, which we call the GFZ-VLBI-TRF. This TRF is then compared to a similar TRF based on the results of the LSM module in VieVS@GFZ, using the same set of sessions, as well as to several recent official TRF solution: the ITRF2014 (Altamimi et al., 2016), the DTRF2014 (Seitz et al., 2016), the JTRF2014 (Wu et al., 2015), and the latest IVS TRF (IVS_TRF2015b)[1].

2 Data analysis

We analyzed 4967 24-h geodetic VLBI sessions from the time period 1990 until the beginning of 2017 with the Kalman filter module. In total, these sessions contained 133 stations (see Fig. 1 for their activity). The a priori station coordinates and the radio source coordinates were taken from DTRF2014 and IRCF2 (Fey et al., 2015), respectively. In the data analysis, we estimated station coordinates, radio source coordinates (as session-wise offsets), EOP (parametrized by offsets and rates), zenith wet delays, tropospheric gradients, and station clocks (all modeled as random walk processes). For each session, we then calculated a datum-free normal equation matrix N and the corresponding right hand

Tobias Nilsson · Robert Heinkelmann · Harald Schuh
Helmholtz-Centre Potsdam, GFZ German Research Centre for Geosciences, Telegrafenberg, DE-14473 Potsdam, Germany

Susanne Glaser · Kyriakos Balidakis · Maria Karbon · Harald Schuh
Technische Universität Berlin, Institute for Geodesy and Geoinformation Science, Berlin, Germany

Benedikt Soja
Jet Propulsion Laboratory, California Institute of Technology, Pasadena, USA

[1] http://www.ccivs.bkg.bund.de

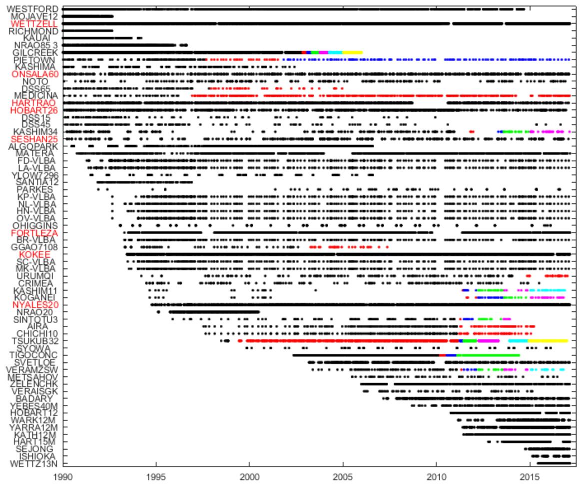

Fig. 1: Activities of the antennas included in the GFZ-VLBI-TRF solution (only antennas participating in more than 50 sessions are shown). A change of color indicates that a break has been introduced. Stations with names in red are included in the TRF datum.

side vector **b**, following the algorithm presented by Mysen (2017):

$$\mathbf{N} = \mathbf{C}^{-1} - \mathbf{C}_0^{-1} \tag{1}$$

$$\mathbf{b} = \mathbf{C}^{-1}\mathbf{x} \tag{2}$$

where $\mathbf{x}$ is the vector of the estimated parameters, $\mathbf{C}$ its variance-covariance matrix, and $\mathbf{C}_0$ the variance-covariance matrix of the a priori values for the station coordinates, radio source coordinates, and EOP.

The session-wise normal equations were then stacked to form a global normal equation system for the station positions and the velocities. All other parameters were reduced session-wise. Breaks in the positions and/or the velocities were introduced whenever needed due to antenna repairs or earthquakes, see Fig. 1. The breaks applied were in principle the same as those in DTRF2014, plus one additional at URUMQI in 2014 (antenna repair) and some additional breaks needed to describe the post-seismic motion at stations that have been affected by earthquakes. Only at breaks due to antenna repairs, the velocities were kept constant, and at breaks introduced to describe the post-seismic motion, conditions were applied to keep the coordinates continuous. Finally, the global normal equation system was inverted to obtain the positions and velocities. To do this, we applied No-Net-Translation (NNT) and No-Net-Rotation (NNR) conditions relative to DTRF2014 for eight stations (see Fig. 1). Velocities of co-located stations were constrained to be identical. Furthermore, velocities of 25 stations having an observation period spanning less than one week were fixed to the a priori DTRF2014 values.

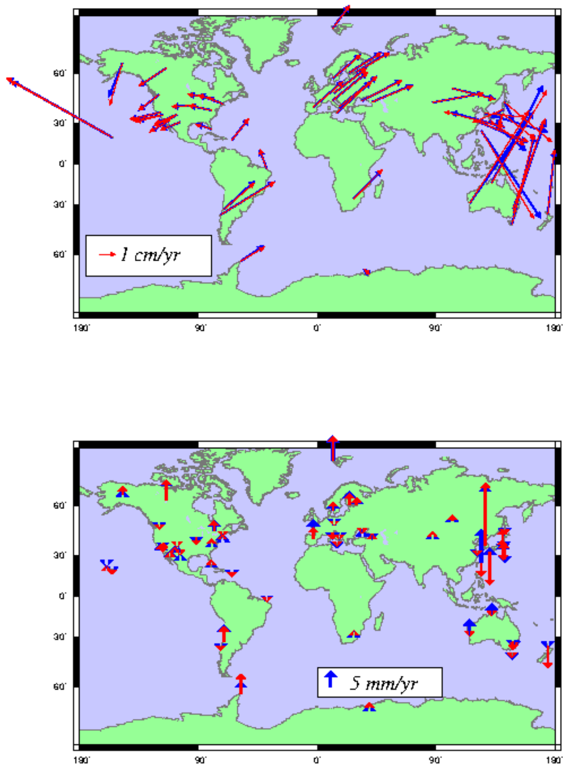

Fig. 2: Horizontal (top) and vertical (bottom) velocities at epoch 2005.0 from the GFZ-VLBI-TRF (red) and ITRF2014 (blue).

For comparison, we also analyzed all the sessions with the LSM module in VieVS@GFZ. The normal equations obtained from this analysis were also stacked and inverted as described above, to create a reference TRF based on the results of the LSM module. This TRF we denote as the LSM-TRF.

3 Results

Figure 2 shows the horizontal and vertical velocities from the GFZ-VLBI-TRF as well as from ITRF2014. We can note that the velocities from the two catalogs are generally in good agreement. Some significant differences can be observed for some stations in Japan. One reason for these differences could be the handling of the post-seismic motions (ITRF2014 uses special post-seismic functions, while the GFZ-VLBI-TRF applies piece-wise linear functions), since the Japanese stations are all affected by earthquakes. Another reason is that these stations are mostly observing in domestic Japanese sessions (e.g. the JADE sessions) and are thus poorly connected to the global sessions.

Table 1: Helmert transformation parameters (translation T_x, T_y, and T_z, rotation R_x, R_y, and R_z, and scale S) at epoch 2005.0 between the GFZ-VLBI-TRF and several other TRFs (see Sec. 3). All values are in mm.

	T_x	T_y	T_z	R_x	R_y	R_z	S
LSM-TRF	0.1	0.0	-0.3	-0.1	-0.2	-0.1	0.2
ITRF2014	-0.6	2.8	0.5	1.5	-0.7	1.2	4.7
DTRF2014	0.3	0.1	-0.4	0.2	-0.0	-0.0	-0.4
IVS_TRF2015b	-2.1	-1.4	-0.3	-0.4	-0.2	2.6	0.0
JTRF2014	1.3	3.3	2.2	0.9	-0.7	0.2	1.6
Fix def.	0.0	0.0	0.0	0.1	0.1	-0.0	-0.7
Glob sou.	0.3	-0.1	-0.2	-0.1	-0.4	-0.3	0.3
Large netw.	-0.2	0.0	0.1	0.0	0.2	0.1	-0.1
1990-1999	-2.6	-0.7	8.8	2.5	6.6	1.5	0.5
2000-2009	-0.5	-0.7	0.2	-0.6	0.4	-0.2	0.6
2010-2017	-1.8	3.5	-1.5	0.5	0.6	-3.0	0.0
R1 & R4	-0.1	-0.5	-0.5	-1.0	-0.2	-0.0	-0.6

Table 2: Time derivatives of the Helmert transformation parameters (translation $\dot{T}_x$, $\dot{T}_y$, and $\dot{T}_z$, rotation $\dot{R}_x$, $\dot{R}_y$, and $\dot{R}_z$, and scale $\dot{S}$) at epoch 2005.0 between the GFZ-VLBI-TRF and several other TRFs (Sec. 3). All values are in mm/year. JTRF2014 does not provide velocities, thus it is not included in this table.

	$\dot{T}_x$	$\dot{T}_y$	$\dot{T}_z$	$\dot{R}_x$	$\dot{R}_y$	$\dot{R}_z$	$\dot{S}$
LSM-TRF	0.09	-0.04	-0.08	-0.08	-0.11	-0.03	-0.02
ITRF2014	-0.11	0.33	-0.02	0.21	0.26	0.04	0.10
DTRF2014	-0.11	0.04	0.07	0.05	0.10	0.02	-0.01
IVS_TRF2015b	-0.12	0.26	-0.13	0.02	0.13	0.01	0.03
Fix def.	-0.02	0.02	-0.02	-0.01	0.04	-0.01	-0.00
Glob. sou.	-0.07	0.05	0.04	0.04	0.09	0.01	0.01
Large netw.	0.02	-0.00	-0.02	-0.01	-0.01	-0.01	0.02
1990-1999	-0.60	-0.16	1.07	0.29	0.81	0.19	0.11
2000-2009	0.26	-0.20	-0.21	-0.19	-0.01	0.28	-0.06
2010-2017	0.27	-0.34	0.08	-0.01	-0.14	0.27	-0.00
R1 & R4	0.04	0.03	0.02	0.10	-0.02	0.00	0.07

3.1 Helmert transformation parameters

The 14 Helmert transformation parameters at epoch 2005.0 between the GFZ-VLBI-TRF and the LSM-TRF, ITRF2014, DTRF2014, IVS_TRF2015b, and JTRF2014 are presented in Table 1 (positions) and Table 2 (velocities). We can note that the best agreement is found with the LSM-TRF. This is not surprising since it is based on the same data set. Thus, we can conclude that using a Kalman filter instead of LSM in the single-session analysis has only a small impact on the resulting TRF. We can further note a relatively good agreement (sub-mm) with the DTRF2014. This could be expected since the DTRF2014 coordinates were used as a priori coordinates for the GFZ-VLBI-TRF. We can also note a significant scale difference (4.7 mm) relative to ITRF2014. There is also a notable scale difference of 1.6 mm relative to JTRF2014, whereas the agreement with the scales of the other TRFs is very good (<0.5 mm). This confirms that there is a scale offset between the VLBI scale and the ITRF2014 scale.

3.2 Handling of radio source positions

We also investigated how the handling of the radio source coordinates affects the estimated TRF. In the GFZ-VLBI-TRF the radio sources were estimated session-wise (applying NNR to the ICRF2 defining sources). However, other possibilities could be to estimate the sources globally, or to fix certain sources. Thus, we calculated two other TRF solutions, differing from the GFZ-VLBI-TRF only for the handling of the radio source coordinates. In one solution (Fix def.) we fixed the coordinates of the ICRF2 defining sources to their ICRF2 values, while the others were estimated session-wise (i.e., like what was done for ITRF2014). In the other solution (Glob. sou.) we estimated the radio source coordinates as global parameters (except for the ICRF2 special handling sources which were estimated session-wise), applying NNR to the ICRF2 defining sources.

The Helmert transformation parameters between these two solutions and the GFZ-VLBI-TRF are also shown in Tables 1 and 2. We can see that the differences are small, at most some tenths of a millimeter. Hence, the handling of the radio source position does not have a significant effect on the TRF.

3.3 Selection of observing sessions

To study the impact on the selection of observing sessions, we calculated several solutions based on only a sub-set of sessions. One solution (Large netw.) included only sessions with large observing networks (the volume of the polyhedron spanned by the station network being larger than 10^{18} m^2, 3869 session), one only sessions between the beginning of 1990 until the end of 1999 (1982 sessions), one with sessions from 2000 until 2009 (1684 sessions), one with sessions between 2010 and 2017 (1301 sessions), and one including only the IVS-R1 and R4 sessions (1550 sessions). The Helmert transformation parameters between the GFZ-VLBI-TRF and these solutions are also presented in Tables 1 and 2. We can note that using only sessions with large network volumes, as well as only the R1 and R4 sessions, does not change the Helmert parameters significantly. This fact shows that sessions with large networks, and in particular the R1 and R4 sessions (the networks of the R1 and R4 sessions are usually large, only four sessions have a network smaller than 10^{18} m^2), are the most important sessions for the VLBI-TRF. The largest differences can be seen for the case using only sessions from 1990-1999, probably due to the smaller networks and lower data quality in these years.

4 Conclusions

We have demonstrated that it is possible to create normal equations from a Kalman filter solution and to combine these to estimate VLBI-TRFs. The resulting TRF, the GFZ-VLBI-TRF, has a similar quality as one created based on the normal equations from the LSM module in VieVS@GFZ. The GFZ-VLBI-TRF agrees well with other recent TRFs, with the differences being similar to the general differences between these TRFs.

In the future we will investigate the possibility of also using a Kalman filter for the combination, thus creating a TRF solution completely based on Kalman filtering. First investigations in this direction have been performed by Soja et al. (2016).

Acknowledgements

The authors thank the IVS for providing the VLBI used in this work (Nothnagel et al., 2015, 2017).

References

Altamimi Z, Rebischung P, Métivier L, Collilieux X (2016) ITRF2014: A new release of the international terrestrial reference frame modeling nonlinear station motions. *J. Geophys. Res. Solid Earth*, 121:6109–6131, 2016. doi:10.1002/2016JB013098.

Böhm J, Böhm S, Nilsson T, Pany A, Plank L, Spicakova H, Teke K, Schuh H (2012) The new Vienna VLBI software. In: S. Kenyon, M. C. Pacino, U. Marti (eds.), *IAG Scientific Assembly 2009*, IAG Symposia, 136, 1007–1011, Springer, doi:10.1007/978-3-642-20338-1_126.

Fey A L , Gordon D, C. S. Jacobs, C. Ma, R. A. Gaume, E. F. Arias, G. Bianco, Boboltz D A, Böckmann S, Bolotin S, Charlot P, Collioud A, Engelhardt G, Gipson J, Gontier A-M, Heinkelmann R, Kurdubov S, Lambert S, Lytvyn S, MacMillan D S, Malkin Z, Nothnagel A, Ojha R, Skurikhina E, J. Sokolova J, Souchay J, Sovers O J, Tesmer V, Titov O, Wang G, Zharov V (2015) The second realization of the international celestial reference frame by very long baseline interferometry. *Astronomical J.*, 150(58):1–16, doi:10.1088/0004-6256/150/2/58.

Mysen E (2017) On the equivalence of Kalman filtering and least-squares estimation. *J. Geodesy*, 91(1):41–52. doi:10.1007/s00190-016-0936-3.

Nilsson T, Soja B, Karbon M, Heinkelmann R, Schuh H (2015) Application of Kalman filtering in VLBI data analysis. *Earth Planets Space*, 67(136):1–9, doi:10.1186/s40623-015-0307-y.

Nothnagel A, Artz T, Behrend D, Malkin Z (2017) International vlbi service for geodesy and astrometry. *J Geod*, 91(7):711–721, doi:10.1007/s00190-016-0950-5.

Nothnagel A et al. (2015) The IVS data input to ITRF2014. *International VLBI Service for Geodesy and Astrometry*, GFZ Data Services, doi:10.5880/GFZ.1.1.2015.002

Seitz M, Bloßfeld M, Angermann D, Schmid R, Gerstl M, Seitz F (2016) The new DGFI-TUM realization of the ITRS: DTRF2014 (data). doi:10.1594/PANGAEA.864046.

Soja B, Nilsson T, Karbon M, Zus F, Dick G, Deng Z, Wickert J, Heinkelmann R, Schuh H (2015) Tropospheric delay determination by Kalman filtering VLBI data. *Earth Planets Space*, 67(144):1–16, doi:10.1186/s40623-015-0293-0.

Soja B, Nilsson T, Balidakis K, Glaser S, Heinkelmann R, Schuh H (2016) Determination of a terrestrial reference frame via Kalman filtering of very long baseline interferometry data. *J. Geodesy*, 90(12):1311–1327, doi:10.1007/s00190-016-0924-7.

Wu X, Abbondanza C, Altamimi Z, Chin T M, Collilieux X, Gross R S, Heflin M B, Jiang Y, Parker J W (2015) KALREF-a Kalman filter and time series approach to the international terrestrial reference frame realization. *J. Geophys. Res.: Solid Earth*, 120(5):3775–3802, doi:10.1002/2014JB011622.

Stochastic Estimation of ZWD Parameter in VLBI Data Analysis Using a Square-Root Information Filter

T. Schubert, S. Halsig, A. Iddink, F. Jaron, A. Nothnagel

Abstract Many parameters of VLBI data analysis, such as the zenith wet delay (ZWD), underlie stochastic processes and require a stochastic rather than a deterministic modeling. In contrast to a classical least-squares approach, filtering offers a way of sequential processing of parameter estimation. We perform filtering with a Kalman Filter and extend this to a Square-Root Information Filter which provides a higher numerical stability. For validating the results, numerical weather models (MERRA and ECMWF) and a classical least-squares approach are applied. We find that the results highly depend on the stochastic modeling (filter tuning), i.e., the correct assessment of process noise variances, which is to be derived from post-fit residuals, and external meteorological data.

Keywords ZWD estimation, Stochastic parameter estimation, Kalman Filter, Square-Root Information Filter

1 Introduction

In this study, we perform different methods of stochastic parameter estimation in comparison to classical least squares methods. Stochastic estimation is valuable if quantities like clocks and troposphere show a clear and persistent stochastic behavior, e.g., driven by physics. In principle, a stochastic behaviour or process is predicted into a parameter. A stochastic approach works on the basis of observations and yields parameters at each observation period.

The reference solution for all comparisons is a least-squares approach (LSA) using continuous piecewise linear functions (CPWLFs). It is a pseudo-stochastic approach as we can control the variability of the parameter by the interval length. For the ZWD parameter it is common to have hourly piecewise linear functions.

A filtering method has the advantage of sequentially processing the observations. The benefits are considered to be improved runtime and possible real-time applications. The Square-Root Information Filter (Bierman, 1977) is advantageous for weakly defined and badly conditioned systems which generally applies to VLBI analysis (Artz et al., 2016a). The main aspect of this work is the comparison of the Kalman Filter and the Square-Root Information Filter.

The first application of a Kalman Filter in VLBI analysis has been reported by Herring et al. (1990). Recent works of Nilsson et al. (2015) and Soja et al. (2015) deal with TRF-determinations and ZWD-estimations using the Kalman Filter. The filter model follows that of Soja (2016).

2 Analysis Options and Data

We concentrate on independent session solutions using a similar parametrization for all methods. The focus is on zenith wet delay (ZWD) estimation with modeling of stochastic behavior. Next to the necessary accounting for clock polynomial and offsets, a stochastic approach could optionally be added for them. EOPs, station and source coordinates stay fixed to the ITRF2014 and ICRF2 catalogs (Fey et al., 2015).

For validation, two sessions of the IVS (Nothnagel et al., 2016) are used, i.e., `04JAN05XA` (IVS-R1) and `15APR26XA` (IVS-AUS). The AUS-sessions are especially suited for stochastic methods due to the high number of observations per station.

It is common to estimate only stochastic offsets in the filter solution (Soja, 2016). Thus, the clock polynomial and one ZWD offset for the whole session (per station) are estimated in a LSA pre-solution, such that only zero mean stochastic offsets are left in the residuals.

We implemented the Kalman Filter (KF) and Square-

Till Schubert · Sebastian Halsig · Andreas Iddink · Frédéric Jaron · Axel Nothnagel
Institute of Geodesy and Geoinformation, University of Bonn, Nußallee 17, DE-53115 Bonn, Germany

Root Information Filter (SRIF) in the analysis software ivg::ASCOT (Halsig et al., 2017; Artz et al., 2016b) and compared the results and runtime.

Fig. 1: Logo of the VLBI analysis software package ivg::ASCOT (IGG VLBI Group - Analysis, Scheduling and Combination Toolbox).

3 Kalman Filter Model

In the Kalman Filter model, the system equation is constructed by transition matrices F and B of mostly identity structure:

$$x_{k+1} = F \cdot x_k + B \cdot w_k. \tag{1}$$

States x_k, process noise w_k and observations z_k have corresponding covariance matrices $x_k \sim \Sigma_k$, $w_k \sim Q_k$ and $z_k \sim R_k$. The Kalman Filter is treated as a linear time variant system as we can only correct for selective observations at each iteration. Thus, we obtain subsets of the (linearized) Jacobian matrix as the measurement matrix H_k in the measurement equation

$$z_k = H_k \cdot x_k + v_k. \tag{2}$$

Filter tuning includes the choice of correct noise variances and adjustment of initial state covariances to ensure convergence of states. We follow the Random Walk approach of Soja (2016) where the state transition is of identity structure $F_{i,i} = 1$. The diagonal entries of the process noise covariance matrix are PSD-values $Q_{i,i} = \Phi_{RW} \Delta t$ which are derived from the noise level of Allan-Variance plot (Soja, 2016). The smoothness of the filter output is controlled by the filter tuning. Reducing the variances on behalf of the process noise leads to less noisy and smoother results.
For the filter solution we implemented a scan-wise iteration. A forward running filter and backward running filter are combined via smoothing to obtain all states being estimated from all observation. The convergence of the filter to a steady-state depends on the initial states and the respective initial covariances Σ_{x_0}. Due to the uncertain aprioris, Σ_{x_0} might be set as high as possible, however, limited by numerical problems. The number of runs can be set to an arbitrary number. The last two runs contribute to the smoothing.

4 The Square-Root Information Filter (SRIF)

The second solution type, the Square-Root Information Filter, combines two concepts with different advantages for the data processing. Both concepts exist individually but are mostly realized together. Firstly, the information filter is an inverse covariance filter. Instead of propagating states and state covariance matrices the filter works with an information vector y_k and an information matrix Y_k which are defined as:

$$y_k = \Sigma_k^{-1} x_k, \tag{3}$$

$$Y_k = \Sigma_k^{-1}. \tag{4}$$

The concept enables initialization with no information, i.e., $y_{k=0} = \mathbf{0}$ and $Y_{k=0} = \mathbf{0}$, which is beneficial when apriori parameters are unknown.
Secondly, in the Square-Root representation a positive-definite matrix $R_k = R_{Chol}^T R_{Chol} = R_k^{T/2} R_k^{1/2}$ is split up into Cholesky-factors, the so called square roots. The same applies to the other covariance matrices. More precisely, the square roots of the inverse

$$R_k^{-1} = R_k^{-1/2} R_k^{-T/2} \tag{5}$$

are needed.
Continuous storage and propagation of the covariance matrices as decomposed matrices has shown advantageous for the numerical stability and robustness towards rounding errors. Besides, the concept is expected to outperform for weakly defined and badly conditioned systems.
For the filter solution the construction of a pre-array allows that the Kalman time and measurement update can be done at once (Bierman, 1977; Anderson and Moore, 1979). The process of triangularizing the pre-array using orthogonal transformations yields a post-array with sub-matrices

$$T \begin{pmatrix} Q_k^{-1/2} & 0 & Q_k^{-1/2} \cdot w_k \\ S_k^{-1} \cdot F_k^{-1} \cdot B_k & S_k^{-1} \cdot F_k^{-1} & S_k^{-1} \cdot x_k \\ 0 & R_k^{-1/2} \cdot H_k & R_k^{-1/2} \cdot z_k \end{pmatrix} = \begin{pmatrix} (Q_k^{-1} + B_k^T \cdot \Sigma_k \cdot B_k)^{-1/2} & * & * \\ 0 & S_{k+1}^{-1} & y_{k+1} \\ 0 & 0 & E_{k+1} \end{pmatrix} \tag{6}$$

from which the processed states and covariances can be recovered. Efficient algorithms are based on LAPACK[1] and BLAS[2] routines (Vanbegin and Verhaegen, 1989). Note that equivalent square-root smoothers also exist.

[1] http://www.netlib.org/lapack/
[2] http://www.openblas.net/

5 Validation using ECMWF and MERRA

The zenith wet delay derived from numerical weather models serves as validation of the estimated parameters. The ECMWF offers the ERA-Interim reanalysis[3].
MERRA-2 (Bosilovich et al., 2016) provides zenith wet delays in the form of integrated or total column water vapor (IWV) in units of atmospheric science, i.e. kg/m^2. It converts to metric units by

$$ZWD = k \cdot IWV \tag{7}$$

using a factor k stemming from the ideal gas law and depending on the mean atmospheric temperature T_M (Bevis et al., 1994; Nothnagel, 2000)

$$k = \frac{10^6}{\rho_W \cdot R_v \cdot (\frac{k_3}{T_M} + k_2')} \tag{8}$$

$$\text{with} \quad \begin{aligned} R_v &= 8314.34\ J\ kmol^{-1}\ K^{-1} \\ M_w &= 18.0152\ kg/kmol \\ k_2' &= 17\ K/hPa \\ k_3 &= 373900 K^2/hPa \\ \rho_W &\approx 1\ kg/l. \end{aligned}$$

The mean atmospheric temperature can be derived from surface temperature T_0 using an approximate formula (Nothnagel, 2000):

$$T_M = 70.2 + 0.72 \cdot T_0. \tag{9}$$

The following table has an overview of the common global numerical weather models and their resolutions. Interpolation is done bilinearly in space and linearly in time. ERA-Interim data is included in the Vienna Mapping Functions (VMF1, Böhm et al. (2006)) which are used in the modelling of the hydrostatic component.

Table 1: Specifications of numerical weather models.

	MERRA-2	ERA-Interim
Zenith wet delay	TQV=IWV	ZWD
Temperature	Surface T_0	Surface T_0
Temporal resolution	$1h$	$6h$
Spatial resolution	0.625°x0.5° $\approx 56km$	$79km$

[3] http://apps.ecmwf.int/datasets/data/interim-full-daily

6 Results

As Figure 2 shows, the filter solutions follow the LSA solution as well as the numerical weather models. The filter solutions successfully show sub-daily variations in the ZWD parameter. Its variability seems reasonable. SRIF and KF don't show any significant differences. Although few parts of the KF show slightly more variation they still proceed in parallel.
Table 2 includes a runtime comparison for two sessions. The Square-Root Information Filter takes substantially less time than the conventional Kalman Filter. The AUS-session with less stations and more observations is more expensive to process. In general, the SRIF can be run with higher (less accurate) covariance matrix of initial states, which leads to less influence of wrong initial parameters.

Table 2: Runtime comparison for 3 runs.

Session	#obs	#stat	SRIF	KF
R1 04JAN05XA	904	6	85.5 sec	184.2 sec
AUS 15APR26XA	2560	3	136.7 sec	731.2 sec

7 Conclusion

Kalman-Filtering has shown to be useful for a stochastic parameter estimation in VLBI data analysis. The SRIF has an advantages concerning runtime. Though, the results show that there are no significant impacts of the numerical instabilities in VLBI analysis which would make the SRIF absolutely necessary. An analogous conclusion is found in Artz et al. (2016a) where the numerical problems have shown to be noncritical. Nonetheless, the SRIF remains favorable due to the optimal numerical computation. The assessment of the numerical advantages of the filter can be extended to the condition number.
The optimization of the filter tuning is still ongoing. It is crucial for the results, but it is not trivial and needs to be linked to a method like Allan-Variance. Here, the method by Soja (2016) is appropriate to estimate the noise characteristics. However, a more complete description of signal and noise can be achieved using e.g. the power spectral density information, which the Random Walk modeling cannot incorporate. So, research will be carried out towards the prediction of arbitrary stochastic processes into the parameters.

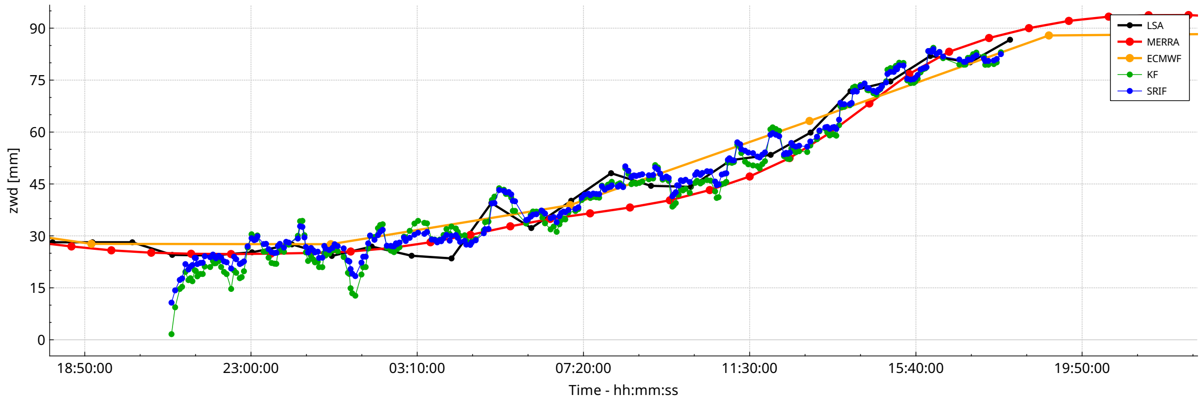

Fig. 2: ZWD-estimates of session `04JAN05XA` for WETTZELL: The KF (green) and SRIF (blue) are plotted next to the pseudo-stochastic LSA approach in black. The numerical weather models are shown in red (MERRA) and orange (ERA-Interim).

References

Anderson B, Moore J (1979) *Optimal Filtering*. Prentice-Hall, Englewood Cliffs, NJ.

Artz, T., S. Halsig, A. Iddink, A. Nothnagel, und C. Tegtmeier (2016a). *Constraining Least-Squares VLBI Solutions*. In: D. Behrend, K. D. Baver, K. L. Armstrong (eds.), *IVS 2016 General Meeting Proceedings, "New Horizons with VGOS"*, NASA/CP-2016-219016, 193–197.

Artz T, Halsig S, Iddink A, Nothnagel A (2016b) ivg::ASCOT: The Development of a new VLBI Software Package. In: D. Behrend, K. D. Baver, K. L. Armstrong (eds.), *IVS 2016 General Meeting Proceedings, "New Horizons with VGOS"*, NASA/CP-2016-219016, 217–221.

Bevis M., Businger S, Chiswell S, Herring T A, Anthes R A, Rocken C, Warw R H (1994) GPS Meteorology: Mapping Zenith Wet Delays onto Precipitable Water. *J. Appl. Meteor.*, 33(3), 379–386.

Bierman G (1977) *Factorization Methods for Discrete Sequential Estimation*. Academic Press, New York.

Böhm J, B. Werl B, Schuh H (2006) Troposphere mapping functions for GPS and VLBI from European Centre For Medium-Range Weather Forecasts (ECMWF) operational analysis data. *J. Geophys. Res.: Solid Earth*, 111(B2).

Bosilovich M G, Lucchesi R, Suarez M (2016) MERRA-2: File Specification. *GMAO Office Note*, No. 9 (Version 1.1), 73 pp, available from `http://gmao.gsfc.nasa.gov/pubs/office_notes`.

Fey A L , Gordon D, C. S. Jacobs, C. Ma, R. A. Gaume, E. F. Arias, G. Bianco, Boboltz D A, Böckmann S, Bolotin S, Charlot P, Collioud A, Engelhardt G, Gipson J, Gontier A-M, Heinkelmann R, Kurdubov S, Lambert S, Lytvyn S, MacMillan D S, Malkin Z, Nothnagel A, Ojha R, Skurikhina E, J. Sokolova J, Souchay J, Sovers O J, Tesmer V, Titov O, Wang G, Zharov V (2015) The second realization of the international celestial reference frame by very long baseline interferometry. *Astron J*, 150(58):1–16, doi:10.1088/0004-6256/150/2/58.

Halsig S, Corbin A, Iddink A, Jaron F, Schubert T, Nothnagel A (2017) Current development progress in ivg::ASCOT. In: R. Haas and G. Elgered (eds.), *Proc. 23rd EVGA Working Meeting*, 167–171.

Herring T A, Davis J L, Shapiro I I (1990) Geodesy by radio interferometry: The application of Kalman Filtering to the analysis of very long baseline interferometry data. *J. Geophys. Res.: Solid Earth*, 95(B8), 12561–12581.

Nilsson T, Soja B, Karbon M, Heinkelmann R, Schuh H (2015) Application of Kalman filtering in VLBI data analysis. *Earth Planets Space*, 67(1), 136.

Nothnagel A (2000) Der Einfluss des Wasserdampfes auf die modernen raumgestützten Messverfahren. In: *Mitteilungen des Bundesamtes für Kartographie und Geodäsie*, Volume 16, Frankfurt am Main. Verlag des Bundesamtes für Kartographie und Geodäsie.

Nothnagel A, Artz T, Behrend D, Malkin Z (2016) International VLBI Service for Geodesy and Astrometry. *J Geod*, 91(7), 711–721, doi:10.1007/s00190-016-0950-5

Soja B, Nilsson T, Karbon M, Zus F, Dick G, Deng Z, Wickert J, Heinkelmann R, Schuh H (2015) Tropospheric delay determination by Kalman filtering VLBI data. *Earth Planets Space*, 67(1), 144.

Soja B (2016) Anwendung eines Kalman Filters in der Auswertung von VLBI-Daten. PhD thesis. *Scientific Technical Report STR 16/06*, Deutsches GeoForschungsZentrum, Potsdam.

Vanbegin M, Verhaegen M (1989) Algorithm 675: Fortran Subroutines for Computing the Square Root Covariance Filter and Square Root Information Filter in Dense or Hessenberg Forms. *ACM Trans. Math. Softw.*, 15, 243–256.

Comparison of Least-Squares and Kalman Filter Solutions From Different VLBI Analysis Centers

E. Tanır Kayıkçı , Ö. Karaaslan

Abstract IVS Analysis Centers apply various statistical methods, namely Least-Squares (LSQ) method, the Kalman Filter (KF) method, the Square-Root Information Filter (SRIF) and the Least-Squares Collocation (LSQC) method and consider the behavior of stochastic parameters in different approaches. The majority of geodetic VLBI analysis software uses LSQ, e.g., CALC/SOLVE software, Vienna VLBI Software (VieVS) and OCCAM. QUASAR and OCCAM use LSQC. Kalman filters or square-root information filters are applied in OCCAM and SteelBreeze. Even thought Kalman Filter is not one of the commonly used techniques in VLBI analysis software, it has some advantages to determine short-term random variations in the estimation of tropospheric delays and clocks which might affect accuracy of estimated parameters accuracies. In Least-Squares (LSQ), parameters are described as constant through different measurement epochs. LSQ estimation supposes that the parameters that we want to estimate are constant for all observation equations in the problem. Nevertheless we can have the case that certain parameters in the same problem might have variations based on the time, atmosphere or any other causes. However, in Kalman Filter estimation procedure, parameters can have variations at each epoch and their behaviors can be described statistically so this procedure allows the estimation of instantaneous changes. Additionally, with the Least-Squares estimation method; each observation requires the computation of a multidimensional matrix inverse. Computations with the Kalman Filter method are simpler and faster, so the method is very convenient when a number of parameter changes must be quickly analyzed. In this study, we first consider comparison of KF and LSQ solutions from different IVS analysis centers to some ideas about the procedures which can be implemented in Kalman Filter output to make it combinable with LSQ results are given for VLBI intra-technique combination.

Emine Tanır Kayıkçı · Özge Karaaslan
Karadeniz Technical University, Engineering Faculty, Department of Geomatics Engineering, TR-61080, Trabzon, Turkey, etanir@ktu.edu.tr, ozgekaraaslan@ktu.edu.tr

Keywords Kalman Filter, Least-Squares, IVS analysis, VLBI

1 Introduction

IVS Analysis Centers using different VLBI analysis softwares CALC/SOLVE, VieVS, OCCAM and QUASAR) consider the behaviour of stochastic parameters in different approaches and apply various statistical methods, namely

- Least-Squares (LSQ) method,
- Kalman Filter (KF) method,
- Square-Root Information Filter (SRIF)
- Least-Squares Collocation (LSQC)

Kalman Filter (KF) has some advantages to determine short-term random variations in the estimation of tropospheric delays and clocks which might affect accuracy of estimated parameters accuracies. Likely the most common optimal filtering technique is that developed by Kalman for estimating the state of a linear system. For example, given a linear system model and any measurements of its behaviour, plus statistical models which characterize system and measurement errors, plus initial condition information, the Kalman filter describes how to process the measurement data. On the other hand, the Kalman filter per se does not solve the problem of establishing an optimal measurement timetable, or of design in the being of parameter uncertainties, or of how to get over computational errors. Other design criteria, in addition to those used to derive the filtering algorithm must be imposed to resolve these questions. **Least-Squares (LSQ)** supposes that the parameters that we want to estimate are constant for all observation equations in the problem. We can have the case that certain parameters in the same problem might

Table 1: Current VLBI ACs and used statistical methods and software packages were listed.

Station	Weekends [UT]	Weekdays [UT]
CALC/SOLVE	LSQ	CGS
		BKG/IGGB
		GSFC
		Italy INAF
		Paris OPAR
		SHAO
		Tsukuba
		U.S. VLBI
OCCAM	KF	SPU
		IAA
	LSQC	GSFC
VIEVS	LSQ	KTU-GEOD IVS
		Milan PMD
		Tsukuba VLBI
		Vienna Special
	KF	GFZ
QUASAR	LSQC	IAA VLBI
GEOSAT	KF	NMA
C++		ICT
		Tsukuba VLBI
ARIADNA	LSQ	SAI

have variations based on the time, atmosphere or any other causes. Vector and matrix methods are especially fit in the application of least-squares estimation techniques. A specific example of least-squares estimation occurs in curve-fitting problems, where it is wished to obtain a functional form of some chosen order that best fits a given set of measurements. The criterion for goodness of fit is to minimize the sum of squares of differences between measurements and the "estimated" functional form or curve. In **Kalman Filter** estimation procedure, parameters can have variations at each epoch and their behaviours can be described statistically so this procedure allows the estimation of instantaneous changes. In **Least-Squares** estimation method; each observation requires the computation of a multidimensional matrix inverse. Computations with the **Kalman Filter** method are simpler and faster, so the method is very convenient when a number of parameter changes must be quickly analyzed.

(CGS:Matera CGS VLBI Analysis Center; BKG/IGGB: BKG/IGGB VLBI Analysis Center; GSFC: GSFC VLBI Analysis Center; Italy INAF:Italy INAF Analysis Center; Paris OPAR:Paris Observatory Analysis Center; SHAO: SHAO Analysis Center; Tsukuba VLBI: Tsukuba VLBI Analysis Center; U.S. VLBI: U.S. Naval Observatory VLBI Analysis Center; SPU:Analysis Center of Saint Petersburg University; IAA:IAA VLBI Analysis Center; GSFC: GSFC VLBI Analysis Center; Milan PMD: Milan University of Technology Analysis Center; Vienna Special:Vienna Special Analysis Center; KTU-GEOD IVS:KTU-GEOD IVS Analysis Center; GFZ:GFZ Analysis Center (developing); ICT:Analysis Center at the National Institute of ICT; IAA:IAA VLBI Analysis Center; NMA:The Norwegian Mapping Authority Analysis Center; SAI:SAI of Lomonosov VLBI Analysis Center)

2 METHODS

Kalman Filter Kalman (1960) as a type of Least-Squares can be obtained by using the iterative parameter estimation from LSQ point of view. By using Kalman Filter estimation in VLBI analysis to compute geodetic parameters, previously used polynomials models in least-square method are taken place by stochastic models. In this study it is shown that how Kalman Filter equations are related the theory of Least Squares (, Zarraoa 1992,S; Marmion, 2006).

2.1 Least-Squares adjustment

Observations are expressed as a function of unknown parameters as

$$l = Ax \tag{1}$$

which is means of matrix notation of the linear model. The inverse of covariance matrix is

$$P = Q_{ll}^{-1} \tag{2}$$

The solution is

$$x = (A^T PA)^{-1} A^T Pl \tag{3}$$

or general form is

$$x = N^{-1} b \tag{4}$$

Where

A $n \times u$ matrix of given coefficients with full rank,
x $u \times 1$ vector of unknowns,
l $n \times 1$ vector of observations,
P $n \times n$ positive definite weight matrix,
Q $n \times n$ variance-covariance matrix,
n, u number of observations and number of unknowns respectively.

2.2 Sequential adjustment

Improves the solution by using new measurement, observation model is divided into two sets (Eq.1, 2)

$$l_k = Ax_k + V_k \tag{5}$$

$$l_{k+1} = Ax_{k+1} + V_{k+1} \tag{6}$$

Then the solution x_k is calculated as follow

$$x_k = (A^T PA)^{-1} A^T P l_k = N^{-1} b_k \tag{7}$$

($N = A^T PA$ and $b = A^T P$, Eq.7). The next measurements is a little various from the previous one

$$l_{k+1} = l_k + \Delta l \tag{8}$$

Then the solution x_{k+1} is

$$x_{k+1} = ((A^T PA)^{-1} A^T P l_{k+1}) = N^{-1} b_{k+1} \tag{9}$$

$$x_{k+1} = x_k + N^{-1} A^T P (l_{k+1} - l_k) \tag{10}$$

$$K = (A^T PA)^{-1} A^T P \tag{11}$$

The updated equation takes the following form

$$x_{k+1} = x_k + K(l_{k+1} - (Ax)_k) \tag{12}$$

Ax_k may be considered as a prediction l_{k+1} of before any measurements are conducted. The Kalman Filter is based on sequential adjustment in the static case.

2.3 Kalman Filter

Kalman Filter is based on sequential adjustment in the static case. All observations up to epoch t are used to obtain optimal estimations of the unknowns. In a dynamic system, the state vector is time dependent, and it may be predicted for any instant k by means of system equations. The predicted values are then updated by the use of observations, which contain information of the state vector. *Forward Kalman Filter*; non-stochastic parameters, e.g., position of ground VLBI site, radio source coordinates and the EOP parameters are estimated. Backward Kalman Filter; stochastic parameters, e.g., clock components and atmosphere disturbance parameters are estimated. Smoothing is applied to get estimates of stochastic parameters at each epoch as a weighted mean of forward and backward estimate (Nilsson et al., 2015; Gelb, 2001; , Mysen 2016).

For summary, Kalman Filter uses state at the epoch of t to estimate the observations at time of $1 + t$ by using series of observations with the following steps: prior estimation measurements, updates and prediction. For prior estimation; input a priori estimate $\widehat{x_0^-}$ and its error covariance matrix $Q_0{}^-$, establish R_k and W_k (System noise). For measurement, doing observations l_k. For update; Compute Kalman gain

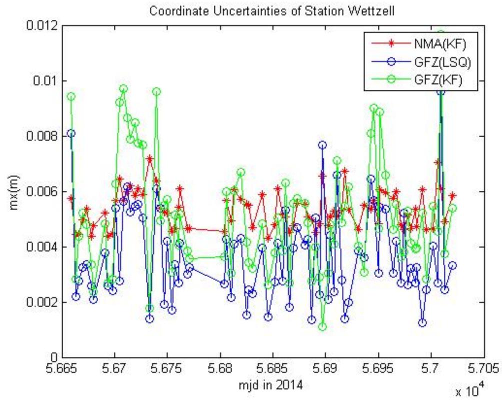

Fig. 1: X coordinate uncertanities of station Wettzell in year 2014.

$K_k = Q_k{}^- A_k{}^T (A_k Q_k{}^- A_k{}^T + R_k)^{-1}$, update estimate with measurement
$\widehat{x_0} = \widehat{x_0^-} K_k (l_k - A_k \widehat{x_0}^-)$ and compute error covariance for updated estimate $Q_k = (I - K_k A_k) Q_k{}^-$. And for prediction $\widehat{x_0^-} = T_k \widehat{x_0}$ and $Q_{k+1}^- = T_k Q_k T_k{}^T + W_k$.

This series is known forward Kalman Filter in Kalman 1960. $x_F(i)$, $C_F(i,i)$ is estimate of parameters and its covariance matrix for each epoch as for forward Kalman Filter and $x_B(i)$, $C_B(i,i)$ is for backward Kalman Filter. $x_S(i)$, $C_S(i,i)$ is estimation results for parameters and its covariance matrix from smoothing and calculating as shown below (Eq. 13, 14, 15),

$$x_S = x_F + C^T (x_B - x_F) \tag{13}$$

$$C^T = I - C = C_F (C_F - C_B)^{-1} \tag{14}$$

$$C_S = (C_F{}^{-1} + C_B{}^{-1})^{-1} \tag{15}$$

3 APPLICATION

Daily SINEX file of GFZ, estimated parameters: source positions, station positions (to estimate station positions a datum has to be added (e.g. NNR+NNT datum), earth orientation: Pole coordinates, UT1-UTC, dX, and dY piece-wise-linear continuous function with temporal resolution of 2 days, Zenith troposphere (per station, Troposphere gradient, Clock model. Daily SINEX file of NMA, estimated parameters: In the un-reduced NEQS: ZWD, 2 horizontal *gradients*, linear clocks, xpol, $xpole_rate$, $ypole_rate$, UT, LOD, xnut, ynut, sta and right ascension and declination of the radio. Datum constraints (NNR/NNT conditions on stations, or NNR on sources). Statistics from daily SINEX outputs of GFZ (LSQ), GFZ(KF) and NMA (KF) are compared. Fig. 1, Fig. 2 and Fig. 3 are given below.

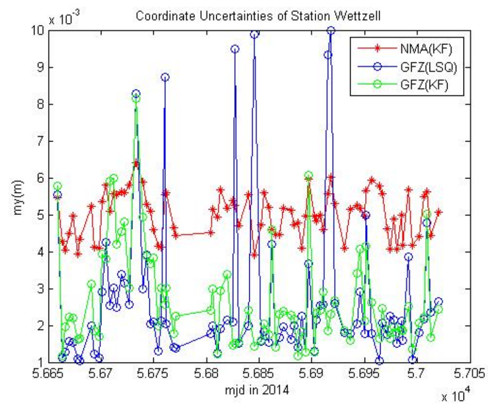

Fig. 2: Y coordinate uncertanities of station Wettzell in year 2014.

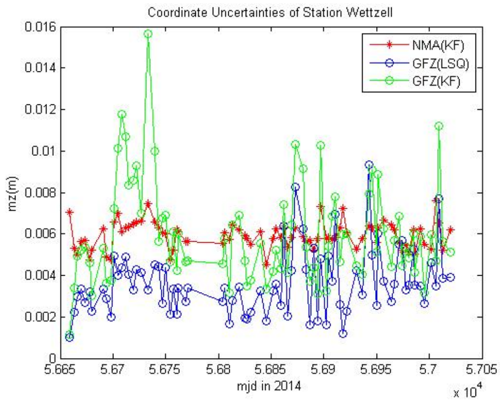

Fig. 3: Z coordinate uncertanities of station Wettzell in year 2014.

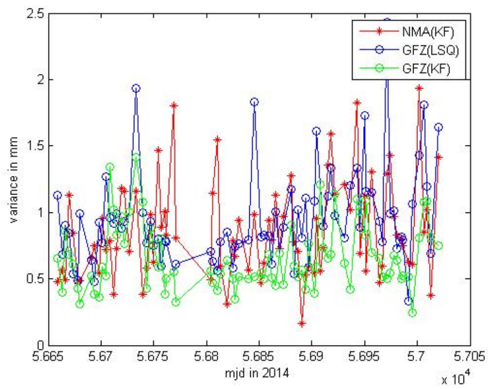

Fig. 4: Variance factor of station Wettzell in year 2014

When we look at Fig. 1 for X coordinate uncertanties, the best results is GFZ(LSQ). NMA(KF) solutions are the highest. When we look at Fig. 2 for Y coordinate uncertanities, the best results is GFZ(LSQ) and there are leaps at some points. NMA(KF) solutions are the highest. When we look at Fig. 3 for Z coordinate uncertanities, the best results is GFZ(LSQ). There are leaps at some points GFZ(KF) solutions. Uncertainties results for station coordinate Wettzell from NMA (KF), GFZ(KF) and GFZ(LSQ) in year 2014 is shown below (Fig. 1, Fig. 2 and Fig. 3). m_x, m_y, m_z values are approx-

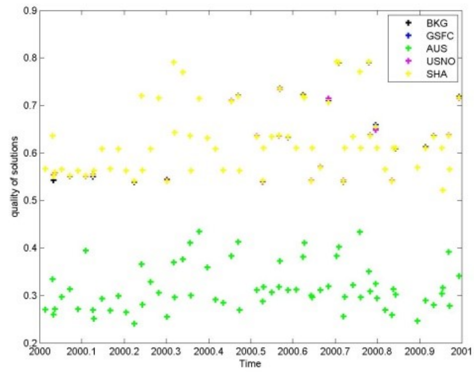

Fig. 5: Quality of AC solutions (Tanır, 2008).

imately small from 0,01. When we look at Fig. 4 for variance factor,the best result is GFZ(KF).

4 FUTURE WORK

Future work dedicated to improve daily SINEX output data from Kalman Filter solutions of VLBI observations which can be used for combination aim efficiently. And we will work like Tanır (2008) 2008 shown below. In Tanır (2008), only AUS AC is used Kalman Filter. But now, GFZ, IAA, NMA AC are used Kalman Filter, too. Our new work is combination LSQ and KF for with three KF solutions and three LSQ solutions. The same ACs KF and LSQ solutions will be used in new work, GFZ.

4.1 Quality of AC Solutions

Quality of AUS solution is not as good as the other ACs BKG, GSFC; SHA and USNO (Fig. 5). The software or user dependent errors might cause such a difference. Some additional calculations to daily SINEX AUS solutions to make them combinable and comparable to LSQ solutions as explained in detailed with above equations. Such calculations require some matrix manipulations e.g., matrix reduction, changing on column and row order in covariance matrix and changing of row order in solution vector which might lead some cumulating errors in resulting normal equation matrix and normal equation vector (Tanır, 2008).

The average mean error $\mu = \sqrt{\frac{tr(M^{-1}}{u}}]$ and M $u \times u$ precision matrix $M = 1/\sigma^2 N$

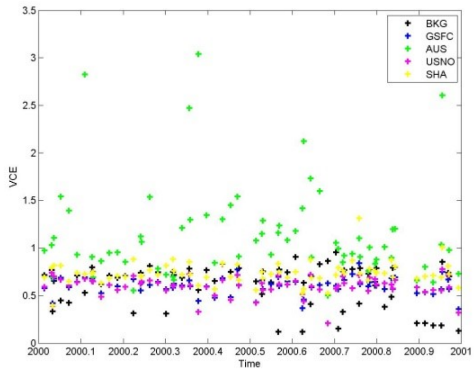

Fig. 6: VCE scaling factors of AC solutions (Tanır, 2008).

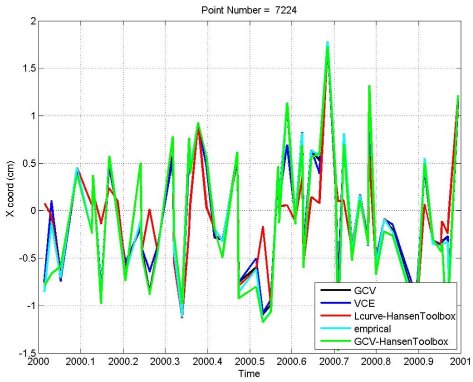

Fig. 7: Results for station X coordinates WETTZELL (Tanır, 2008).

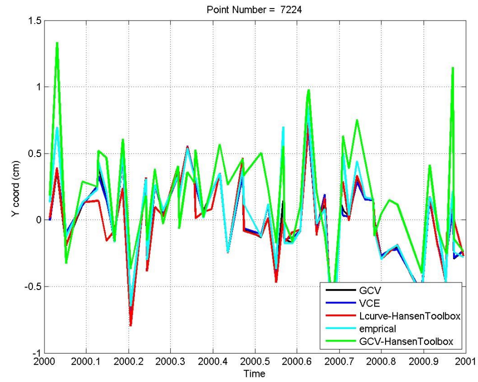

Fig. 8: Results for station Y coordinates WETTZELL (Tanır, 2008).

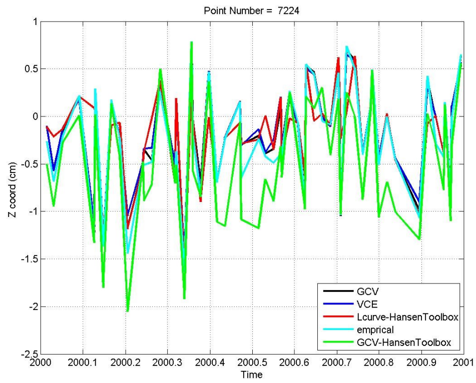

Fig. 9: Results for station Z coordinates WETTZELL (Tanır, 2008).

4.2 VCE scaling factors of AC Solutions

4 AC solutions in year 2000 (LSQ) were combined with VLBI AUS solution (KF) by using two-step combination algorithm with different regularization parameters and VCE results were used as scaling factors for combination (Fig. 6) (Tanır, 2008).

Differences between combination and ITRF2000 results for station coordinates WETTZELL from KF and LSQ combination in year 2000 (Fig. 7, Fig. 8 and Fig. 9)

5 Acknowledgements

We acknowledge IVS for providing the data analysed in this study.

References

Gelb A (2001) Applied Optimal Estimation. *Massachusetts Institute of Technology Press*, London England, 18th edition.

Kalman R E (1960) A New Approach to Linear Filtering and Prediction Problems. *the ASME–Journal of Basic Engineering*, 82:Series D,35–45.

Marmion M (2006) Airborne attitude estimation using a Kalman filter. Master Thesis, UNIS – The University Centre of Svalbard (Longyearbyen, Norway) NTNU – Norwegian University of Science and Technology (Trondheim, Norway) ENSIEG – Superior National School of Electrical Engineering Part of the Polytechnic National Institute of Grenoble (INPG) (Grenoble, France)

Mysen E (2017) On The Equivalence of Kalman Filtering and Least-Squares Estimation. *J Geod*, 91(1), 41–52, doi:10.1007/s00190-016-0936-3.

Nilsson T (2015) Application of Kalman Filtering in VLBI Data Analysis. *Earth Planets Space*, 67:136.

Salzmann M (1993) Least-Squares Filtering and Testing For Geodetic Navigation Applications. *Publication on Geodesy*, 37.

Tanır E (2008) A Study About Optimal Intra-technique Combination of VLBI Analysis Center Solutions. Ph.D. Thesis, Vienna University of Technology, Austria.

Zarraoa N (1992) Estudio de Movimientos Relativos en Europa Mediante Una Red De Radiointerferometrìa Geodèesica. Ph.D. Thesis, Universidad Complutense de Madrid.

Index of authors

EVGA 2017 scientific programme

15 May 2017

08:45-09:00	Welcome	R. Haas
Session-T1	**Chair: Evgeny Nosov**	
09:00-09:15	Technological Development for VGOS at Yebes Observatory	J. A. López Fernández
09:15-09:30	Broadband VLBI System GALA-V and Its Application for Geodesy and Frequency Transfer	M. Sekido
09:30-09:45	Sensitivity and antenna noise temperature analysis of Onsala Twin Telescopes 3 – 18 GHz	J. Flygare
09:45-10:00	Design, implementation and tests of the signal Chain for the Twin Telescopes at Onsala Space Observatory	M. Pantaleev
10:00-10:30	**Coffee break**	
Session-T2	**Chair: José Antonio López Fernández**	
10:30-10:45	Improvement of PCAL signal distribution on RT-32 radio telescopes of "Quasar" VLBI network	E. Nosov
10:45-11:00	VLBI - DORIS Interference Investigation at Wettzell	T. Schüler
11:00-11:15	Paraboloid deformation investigations of the Onsala 20 m radio telescope with terrestrial laser scanning	A. Nothnagel
11:15-11:30	Unified Model for Surface Fitting of Radio Telescope Reflectors	C. Eschelbach
11:30-11:45	**Stretch your legs break**	
Session-T3	**Chair: Axel Nothnagel**	
11:45-12:00	On the way to regular, transatlantic VGOS sessions using an Elevenfeed and DBBC2s	A. Neidhardt
12:00-12:15	The Jumping Jive Monitoring Work Package: centralized System Monitoring and Automation as key feature also for VGOS	A. Neidhardt
12:15-12:30	VGOS 1.1: A DBE Opportunity and Data Transmission Challenge	B. Petrachenko
12:30-12:45	A Year of Dynamic Observing	J. Lovell
12:45-13:45	**Lunch break**	
Session-T4	**Chair: Bill Petrachenko**	
13:45-14:00	An IVS pilot study for distributed correlation in the VGOS era	A. Bertarini
14:00-14:15	Real-time eVLBI at JIVE using the SFXC software correlator	A. Keimpema
14:15-14:30	Correlation at UTAS	J. McCallum
14:30-14:45	Towards Cloud Correlation of VLBI Data	S. Weston
14:45-15:15	**Coffee break**	

Session-T5	**Chair: Alessandra Bertarini**	
15:15-15:30	The progress of VLBI terminal and correlator in SHAO	W. Zheng
15:30-15:45	Ultra-wide band receiver for SHAO VGOS station	B. Li
15:45-16:00	Recent Progress in Cryogenic MMIC Design of SHAO	Y. Chen
Session-A1		
16:00-16:15	A celestial reference frame based on Kalman filtering	B. Soja
16:15-16:30	**Stretch your legs break**	
Session-O1	**Chair: John Gipson**	
16:30-16:45	VGOS development for Ishioka 13-m antenna	T. Wakasugi
16:45-17:00	VGOS Interoperability Observing Sessions - Results, Lessons Learned, and Guidelines	C. Ruszczyk
17:00-17:15	Bonn Correlator: Preparing for VGOS and EHT	W. Alef
17:15-17:30	Linear polarizers in VLBI: offline conversion into a circular basis	I. Marti-Vidal
17:30-17:45	**Stretch your legs break**	
Session-O2	**Chair: Johannes Böhm**	
17:45-18:00	The HOB experiments	L. McCallum
18:00-18:15	Proposed establishment of a Fundamental Geodetic Station in Antarctica	L. Combrinck
18:15-18:30	Simulation Results for KOKEE12M-WETTZ13S 'Intensives'	J. Gipson
18:30-18:45	Optimal tag-along station locations for VLBI Intensive sessions	N. Kareinen
18:45-20:45	**Poster session**	

16 May 2017

Session-O3	**Chair: Sabine Bachmann**	
09:00-09:15	Recent developments in scheduling with VieVS	M. Schartner
09:15-09:30	VLBI with GNSS-signals on an intercontinental baseline	R. Haas
09:30-09:45	Simulations of VLBI-only spacecraft orbit determination	T. Hobiger
09:45-10:00	Lunar observations and geodetic VLBI - A simulation study	G. Klopotek
10:00-10:30	**Coffee break**	
Session-A2	**Chair: Rüdiger Haas**	
10:30-10:45	ITRS realizations in the framework of ITRF2014: impact of different TRF parameterizations on VLBI combined products	S. Bachmann
10:45-11:00	Determining the Galactocentric acceleration vector from VLBI and its impact on the terrestrial reference frame	H. Krásná
11:00-11:15	INT2b - determination of UT1 with parallel Intensive sessions	S. Halsig
11:15-11:30	Impact of station clocks on UT1-TAI estimates	E. Himwich
11:30-11:45	**Stretch your legs break**	

Session-A3	**Chair: Aletha de Witt**		
11:45-12:00	CONT14 Imaging and Closure Analysis of Source Structure Effects: Part 1 Imaging Results	J. Anderson
12:00-12:15	CONT14 Imaging and Closure Analysis of Source Structure Effects: Part 2 Closure Analysis	M. Xu
12:15-12:30	The application of ray-traced delays for the ICRF3	D. Mayer
12:30-12:45	Towards the third realization of the International Celestial Reference Frame	P. Charlot
12:45-13:45	**Lunch break**	
Session-A4	**Chair: James Anderson**	
13:45-14:00	K-band Celestial Frame: can it be better than S/X ?	A. de Witt
14:00-14:15	Investigating the noise floor of VLBI source positions	K. Le Bail
14:15-14:30	Structure of the radio source 0014+813 using CONT14 geodetic VLBI observations	O. Titov
14:30-14:45	Absolute astrometry of weak sources with the AOV	F. Shu
14:45-15:15	**Coffee break**	
Session-A5	**Chair: Patrick Charlot**	
15:15-15:30	Near-field VLBI delay models - Implementation and testing	F. Jaron
15:30-15:45	Initial Study of Lunar Librations by VLBI Observations of the ChangE-3 Lunar Lander	Z. Zhang
15:45-16:00	Update on VLBI data analysis at ESOC C. Flohrer	
16:00-16:15	DOGS-RI: new VLBI analysis software at DGFI-TUM	Y. Kwak
16:15-16:30	**Stretch your legs break**	
Session-A6	**Chair: Lucia McCullum**	
16:30-16:45	Ocean tide loading - where we are standing	H.-G. Scherneck
16:45-17:00	An empirical atmospheric tidal loading solution for particular VLBI stations	A. Girdiuk
17:00-17:15	Twin Telescope Tests: Assessing Station Oriented Systematic Errors	C. Jacobs
17:15-17:30	Estimating common tropospheric parameters for co-located VLBI antennas	T. Nilsson
17:30-17:45	Closing session	R. Haas
19:00-23:00	**Conference dinner**	

EVGA 2017 poster contributions

Technology Sessions		
P1.01	Geometric variations of a geodetic telescope	S. Bergstrand
P1.02	Accuracy assessment of the two WVRs, Astrid and Konrad, at the Onsala Space Observatory	P. Forkman
P1.03	Time and frequency distribution for the Onsala Twin-Telescopes	L. Helldner
P1.04	Communication, Coordination, and Automation for future Geodetic Infrastructures of the VLBI-capabilities for future challenges	A. Neidhardt
P1.05	The MIT/NASA Broadband Signal Chain - Present State, VGOS compliance, and Beyond	C. Ruszczyk
P1.06	DBBC3: The new flexible, wide-band VLBI backend status	G. Tuccari
P1.07	BRAND: A very wide-band receiver for the EVN	G. Tuccari
Observations Sessions		
P2.01	GFZ Simulations of VLBI Observations of E-GRASP/Eratosthenes	J. Anderson
P2.02	Reduction of the IVS-INT01 UT1 Formal Error through New Sked Algorithms	K. D. Baver
P2.03	Planning of the Continuous VLBI Campaign 2017 (CONT17)	D. Behrend
P2.04	The Onsala Twin Telescopes project	G. Elgered
P2.05	Geodetic VLBI Correlation at the Vienna Scientific Cluster	J. Gruber
P2.06	Argentinean-German Geodetic Observatory (AGGO)	H. Hase
P2.07	Status of RANGD project	P. Jaroenjittichai
P2.08	Status of RAEGE Network	J. A. López Fernández
P2.09	Metsähovi Geodetic Fundamental Station - current status of the new VGOS site	G. Molera Calvés
P2.10	HartRAO antenna axis offset and its effect on troposphere modelling and antenna coordinates	M. Nickola
P2.11	VLBI at GARS O'Higgins - 25 years of operation and recent developments	V. Thorandt
P2.12	The Sheshan VGOS station progress on construction	G. Wang
Analysis Sessions		
P3.01	Calculating integrated water vapor trends from VLBI, GNSS and NWM	K. Balidakis
P3.02	Implementation of the vgosDb format at the GSFC VLBI Analysis Center	S. Bolotin
P3.03	Automated ambiguity resolution with clustering and analysis of Intensive Sessions	A. Corbin
P3.04	Classification of VLBI radio-sources by astrometric stability using Allan Variance	C. Gattano
P3.05	Current development progress in ivg::ASCOT	S. Halsig
P3.06	Where - A New Software for Geodetic Analysis	G. Hjelle
P3.07	The impact of the TRF on the CRF	M. Karbon
P3.08	Improvements of the stochastic model of the VLBI data analysis in VieVS@GFZ	N. Mammadaliyev
P3.09	Copula-based analysis of correlation structures in VLBI data analysis	S. Modiri
P3.10	The GFZ VLBI TRF solutions	T. Nilsson
P3.11	Stochastic estimation of ZWD parameter in VLBI data analysis	T. Schubert

	using a Square-Root Information Filter	
P3.12	CONT14 Data Analysis	E. Skurikhina
P3.13	VLBI Analysis at the IAA	E. Skurikhina
P3.14	Comparison of least squares and KalmanFilter solutions from different IVS analysis centers	E. Tanır Kayıkçı
P3.15	IVS Primary Data Center and Analysis Center at BKG	V. Thorandt

EVGA 2017 list of participants

Name	**Affiliation and Email address**
Alef, Walter	MPIfR, Germany walef@mpifr-bonn.mpg.de
Anderson, James M	GFZ, Germany anderson@gfz-potsdam.de
Bachmann, Sabine	BKG, Germany sabine.bachmann@bkg.bund.de
Behrend, Dirk	NVI, Inc./NASA GSFC, USA dirk.behrend@nasa.gov
Bergstrand, Sten	RISE, Sweden sten.bergstrand@ri.se
Bertarini, Alessandra	University of Bonn, Germany abertari@mpifr-bonn.mpg.de
Böhm, Johannes	TU Wien, Austria johannes.boehm@tuwien.ac.at
Campbell, Bob	JIVE, The Netherlands campbell@jive.eu
Charlot, Patrick	Laboratoire d'Astrophysique de Bordeaux, France charlot@obs.u-bordeaux1.fr
Cho, Jungho	Korea Astronomy & Space Science Institute, South Korea jojh@kasi.re.kr
Colomer, Francisco	JIVE, The Netherlands colomer@jive.eu
Combrinck, Ludwig	HartRAO, South Africa ludwig@hartrao.ac.za
Conway, John	Chalmers University of Technology, Sweden john.conway@chalmers.se
de Witt, Aletha	HartRAO, South Africa alet@hartrao.ac.za
Elgered, Gunnar	Chalmers University of Technology, Sweden gunnar.elgered@chalmers.se
Eschelbach, Cornelia	Frankfurt University of Applied Sciences, Germany cornelia.eschelbach@fb1.fra-uas.de
Fan, Jin	National Astronomy Observatory of China
Fath, Henrik	Frankfurt University of Applied Sciences, Germany hfath@stud.fra-uas.de
Flohrer, Claudia	ESOC - Navigation Support Office, Germany claudia.flohrer@esa.int
Flygare, Jonas	Chalmers University of Technology, Sweden jonas.flygare@chalmers.se
Forkman, Peter	Chalmers University of Technology, Sweden peter.forkman@chalmers.se

Gattano, César	Observatoire de Paris, SYRTE, France cesar.gattano@obspm.fr
Gipson, John	NASA GSFC/NVI Inc, USA john.m.gipson@nasa.gov
Girdiuk, Anastasiia	TU Wien, Austria anastasiia.girdiuk@geo.tuwien.ac.at
Gomez–Gonzalez, Jesus	IGN, Spain jggonzalez@fomento.es
Gruber, Jakob	TU Wien, Austria jakob.franz.gruber@geo.tuwien.ac.at
Haas, Rüdiger	Chalmers University of Technology, Sweden rudiger.haas@chalmers.se
Halsig, Sebastian	University of Bonn, Germany halsig@igg.uni-bonn.de
Hao, Longfei	Yunnan Observatories, China haolongfei@ynao.ac.cn
Hase, Hayo	BKG, Germany hayo.hase@bkg.bund.de
Hawarey, Mosab	Geodesic Dome Company, Jordan mhawarey@yahoo.com
Helldner, Leif	Chalmers University of Technology, Sweden leif.helldner@chalmers.se
Himwich, Ed	NVI, Inc. / GSFC, USA ed.himwich@nasa.gov
Hjelle, Geir Arne	Norwegian Mapping Authority, Norway geir.arne.hjelle@kartverket.no
Hobiger, Thomas	Chalmers University of Technology, Sweden thomas.hobiger@chalmers.se
Jacobs, Christopher	JPL, USA christopher.s.jacobs@jpl.nasa.gov
Jaroenjittichai, Phrudth	NARIT, Thailand phrudth@narit.or.th
Jaron, Frédéric	University of Bonn, Germany jaron@igg.uni-bonn.de
Karaaslan, Özge	Karadeniz Technical University, Turkey ozgekaraaslan@ktu.edu.tr
Kareinen, Niko	Chalmers University of Technology, Sweden niko.kareinen@chalmers.se
Keimpema, Aard	JIVE, The Netherlands keimpema@jive.eu
Kirkvik, Ann-Silje	Norwegian Mapping Authority, Norway ann-silje.kirkvik@kartverket.no
Klopotek, Grzegorz	Chalmers University of Technology, Sweden grzegorz.klopotek@chalmers.se
Krásna, Hana	TU Wien, Austria

	hana.krasna@geo.tuwien.ac.at
Kwak, Younghee	DGFI - TUM, Germany younghee.kwak@tum.de
Kylenfall, Ulf	Chalmers University of Technology, Sweden ulf.kylenfall@chalmers.se
Lanotte, Roberto	E-GEOS Centro di Geodesia Spaziale CGS/ASI Matera, Italy, roberto.lanotte@e-geos.it
Le Bail, Karine	NVI, Inc. at GSFC/NASA, USA karine.lebail@nasa.gov
Li, Bin	SHAO, China bing@shao.ac.cn
Li, Zhixuan	Yunnan Observatories, China lzx@ynao.ac.cn
Lopez Fernandez, José Antonio	CDT IGN Yebes, Spain jalfernandez@fomento.es
Lopez Ruiz, Samuel	CDT IGN Yebes, Spain samuel.lopez@oan.es
Lösler, Michael	Frankfurt University of Applied Sciences, Germany michael.loesler@fb1.fra-uas.de
Lovell, Jim	UTAS, Australia jim.lovell@utas.edu.au
Ma, Chopo	NASA GSFC, USA chopo.ma@nasa.gov
Mammadaliyev, Nicat	GFZ, Germany nicat.mammadaliyev@campus.tu-berlin.de
Marti-Vidal, Ivan	Chalmers University of Technology, Sweden ivan.marti-vidal@chalmers.se
Mayer, David	TU Wien, Austria david.mayer@tuwien.ac.at
McCallum, Lucia	UTAS, Australia jamie.mccallum@utas.edu.au
McCallum, Jamie	UTAS, Australia jamie.mccallum@utas.edu.au
Modiri, Sadegh	GFZ, Germany sadegh@gfz-potsdam.de
Molera Calves, Guifré	FGI, Finland guifre.moleracalves@maanmittauslaitos.fi
Müskens, Arno	University of Bonn, Germany mueskens@mpifr.de
Negusini, Monia	IRA - INAF, Italy negusini@ira.inaf.it
Neidhardt, Alexander	FESG - TUM, Germany neidhardt@fs.wettzell.de
Niell, Arthur	MIT Haystack Observatory, USA aniell@haystack.mit.edu

Nilsson, Tobias	GFZ, Germany nilsson@gfz-potsdam.de
Nosov, Evgeny	IAA RAS, Russia nosov@iaaras.ru
Nothnagel, Axel	University of Bonn, Germany nothnagel@uni-bonn.de
Pantaleev, Miroslav	Chalmers University of Technology, Sweden miroslav.pantaleev@chalmers.se
Petrachenko, Bill	NRCan, Canada bill.petrachenko@nrc.gc.ca
Porcas, Richard	MPIfR, Germany porcas@mpifr-bonn.mpg.de
Ruszczyk, Chester	MIT Haystack Observatory, USA chester@mit.edu
Schartner, Matthias	TU Wien, Austria matthias.schartner@tuwien.ac.at
Scherneck, Hans-Georg	Chalmers University of Technology, Sweden hans-georg.scherneck@chalmers.se
Schubert, Till	University of Bonn, Germany s7tischu@uni-bonn.de
Schüler, Torben	Geodetic Observatory Wettzell, BKG, Germany schueler@fs.wettzell.de
Sekido, Mamoru	NICT, Japan sekido@nict.go.jp
Shu, Fengchun	SHAO, China sfc@shao.ac.cn
Skurikhina, Elena	IAA, Russia sea@iaaras.ru
Soja, Benedikt	JPL, USA bsoja@jpl.nasa.gov
Tanır Kayıkçı, Emine	Karadeniz Technical University, Turkey eminetanir@gmail.com
Thorandt, Volkmar	BKG, Germany volkmar.thorandt@bkg.bund.de
Titov, Oleg	Geoscience Australia oleg.titov@ga.gov.au
Tuccari, Gino	INAF, Italy, & MPIfR, Germany tuccari@mpifr-bonn.mpg.de
Vermeulen, René	ASTRON, The Netherlands rvermeulen@astron.nl
Wakasugi, Takahiro	GSI, Japan wakasugi-t96kg@mlit.go.jp
Wang, Guangli	SHAO, China wgl@shao.ac.cn
Weston, Stuart	AUT, New Zealand stuart.weston@aut.ac.nz

Xu, Minghui	SHAO, China mhxu@shao.ac.cn
Xu, Yonghua	Yunnan Observatories, China yhx@ynao.ac.cn
Yang, Jian	Chalmers University of Technology, Sweden jian.yang@chalmers.se
Yang, Jun	Chalmers University of Technology, Sweden jun.yang@chalmers.se
Zhang, Zhongkai	University of Bonn, Germany zzk.caesar@gmail.com
Zheng, Weimin	SHAO, China zhwm@shao.ac.cn

VGOS system compatibility meeting

Gino Tuccari

INAF Istituto di Radioastronomia (Italy) and Max Planck Institut für Radiastronomie (Germany)

In the framework of the 23rd Working Meeting of the European VLBI Group for Geodesy and Astrometry on 17/05/2017 a splinter meeting was held about the topic of 'VGOS technology compatibility'.

The meeting was attended by a group of people which are actively involved in the development of VGOS systems and the establishment of VGOS stations. The current status of deployment of antennas, receivers, backends, and recorders was reported. The overall goal of the meeting was to compare systems, identify potential differences, and to promote maximum compatibility between the systems in order to reach the common performance goals of VGOS.

Detailed information on the stations and their VGOS systems was collected in a table (see below). Even if this table definitely requires upgrades and corrections, it reflects the current and future status of the various stations. Station representatives as well as receiver and system developers were invited to keep the table properly updated. The table was added to the V2C wiki pages and will be mirrored on the IVS Technology Coordinator web pages.

During the splinter meeting the information collected in the table was discussed in detail. It became clear that a common line was basically followed, however with some differences and different options. Several groups were experimenting with different observing modes and opportunities.

It was generally agreed that there is a necessity to align the frequency range as much as possible and to adopt a basic observing mode. The latter is to use several 32 MHz bandwidth channels that can be flexibly tuned in the entire input frequency range, as described in the proof-of-concept documents, however leaving open to experiment with different bandwidth and modes, too. In particular to be mentioned here is the Japanese broadband system that operates with a tunable 1 GHz bandwidth. Experimental observations with compatible systems for evaluation and comparison were encouraged.

The IVS Technology Coordinator proposed to contact a number of actively involved people in order to maintain the compatibility table and to discuss the evolution of the current and newly proposed observing modes.

Reports on the status will be presented during IVS meetings and at the Directing Board.

1 WESTFORD, GGAO12M, and KOKEE12M

Site name	Westford	GGAO	Kokee
SEFD (Jy)	broadband	broadband	broadband
2	2500	2500	2500
5	2500	2500	2500
9	2500	2500	2500
14	2500	2500	2500
Antenna			
Date ready	now	now	2015/09
Optics	prime	cass	cass
Az slew rate (°/s)	3	5	12
El slew rate (°/s)	1	1,25	6
Diameter (m)	18	12,1	12,1
efficiency (%)			
2	40	50	50
5	40	50	50
9	40	50	50
14	40	50	50
Front End			
Date ready	now	now	2016/01
Tsys (K)			
2	50	50	50
5	50	50	50
9	50	50	50
14	50	50	50
Band1			
Name	broadband	broadband	broadband
Start freq (GHz)	**2,2**	**2,2**	**2,2**
Stop freq (GHz)	**14**	**14**	**14**
npol	**2**	**2**	**2**
pol type	**linear**	**linear**	**linear**

PCAL			
Date ready	now	now	2016/01
injection	pre LNA	pre LNA	pre LNA
generator	Mk3	digital	digital
freq spacing (MHz)	**5**	**5**	**5**
Noise Diode			
Date ready	now	now	2015/09
installed	yes	yes	yes
synchronous (Hz)	**10-100**	**10-100**	**10-100**
Cable Cal			

Date ready	2015/03	2015/03	2016/01
Type	new	new	new
Down-converter			
Date ready	now	now	2016/01
Band 1			
Type	**up-down**	**up-down**	**up-down**
nband	4x2	4x2	4x2
1st stage			
filter start (GHz)	na	na	na
filter stop (GHz)	na	na	na
lo start (GHz)	23	23	23
lo stop (GHz)	33	33	33
lo res (KHz)	400	400	400
2nd stage			
filter start (GHz)	20	20	19
filter stop (GHz)	22	22	21
lo start (GHz)	22,5	22,5	22
lo stop (GHz)	na	na	23
lo res (KHz)	fixed	fixed	200
3rd stage			
filter start (GHz)	na	na	2
filter stop (GHz)	na	na	3
lo start (GHz)	na	na	1,9
lo stop (GHz)	na	na	2,1
lo res (KHz)	na	na	0,001
Nyquist			
Start (MHz)	512	512	512
Stop (MHz)	1024	1024	1024
Net range			
Start (GHz)	1	1	2
Stop (GHz)	11,5	11,5	13,5

Sampler			
Date ready	now	now	2016/01
Input bandwidth (MHz)	**512**	**512**	**512**
Nyquist zone	**2**	**2**	**2**
Sample clock (MHz)	1024	1024	1024
bits/sample	8	8	8
Total No. of IF's	**4x2**	**4x2**	**4x2**

Digital Back End (DBE)			
Type	**RDBE**	**RDBE**	**RDBE**
No. DBE per site	**4**	**4**	**4**
No. IF's per DBE	**2**	**2**	**2**
DDC	**na**	**na**	**na**
PFB			
No. per DBE	**2**	**2**	**2**
Chan BW (MHz)	**32**	**32**	**32**
Chan per DBE	**16**	**16**	**16**

Recorder			
Type	**Mk6**	**Mk6**	**Mk6**
No. per site	1	1	2
Network			
Data rate (Gbps)	20	1	0,1

2 WETTZ13S and WETTZ13N

Site name	TTW1		TTW2
Receiver type	Tri-band		Wideband
SEFD (Jy)			
2,3	1500	4,0	1100
8,5	800	6,0	1000
30,0	3500	8,0	900
		10,0	1200
Antenna			
Date ready	now		now
Optics	ring focus		ring focus
Az slew rate (°/s)	12		12
El slew rate (°/s)	6		6
Diameter (m)	13,2		13,2
efficiency (%)			
2,3	65	4,0	55
8,5	80	6,0	65
32,0	64	8,0	65
		10,0	60
Front End			
Date ready	now		now
Tsys (K)			
2,3	40	4,0	34
8,5	35	6,0	31
32,0	100	8,0	27
		10,0	30
Band1			
Name	S-band		band
Start freq (GHz)	**2**		**1**
Stop freq (GHz)	**2,8**		**14**
npol	**2**		**2**
pol type	**circular**		**linear**
Band2			
Name	X-band		
Start freq (GHz)	**7**		
Stop freq (GHz)	**9,5**		
npol	**2**		
pol type	**circular**		
Band3			
Name	Ka-band		
Start freq (GHz)	**28**		
Stop freq (GHz)	**33**		
npol	**2**		
pol type	**circular**		
PCAL			
Date ready	March 15		June 16
injection	pre LNA		post LNA
generator	Wettzell		Wettzell
freq spacing (MHz)	**1;5;10**		**5**
Noise Diode			
Date ready	March 15		August 17
installed	now		no
synchronous (Hz)	**on/off/80 Hz**		na
Cable Cal			

Date ready	autumn 15		Oct. 2017	
Type	own design		new design	
Down-converter				
Date ready	now		now	
Band 1				
Type	**down**		**down**	
nband	2		2	
1st stage		1st stage		
filter start (GHz)	2,1	filter start (GHz)	2,8	
filter stop (GHz)	2,7	filter stop (GHz)	4	
lo start (GHz)	1,5	lo start (GHz)	1	
lo stop (GHz)	3	lo stop (GHz)	6	
lo res (KHz)	0,001	lo res (KHz)	0,001	
Nyquist		Nyquist		
Start (MHz)	0	Start (MHz)	0	
Stop (MHz)	512	Stop (MHz)	1536	
Net range		Net range		
Start (GHz)	2	Start (GHz)	3	
Stop (GHz)	3	Stop (GHz)	4	
Band 2	1. Converter			
Type	**up-down**		**down**	
nband	**2**			
1st stage		1st stage		
filter start (GHz)	7	filter start (GHz)	4,6	
filter stop (GHz)	9,5	filter stop (GHz)	6,6	
LO start (GHz)	11	LO start (GHz)	1	
LO stop (GHz)	13,4	LO stop (GHz)	6	
lo res (KHz)	0,001	lo res (KHz)		
2nd stage		2nd stage	0,001	
filter start (GHz)	20	filter start (GHz)		
filter stop (GHz)	22	filter stop (GHz)		
LO start (GHz)	19,5	LO start (GHz)		
LO stop (GHz)	na	LO stop (GHz)		
LO res	fixed	LO res		
Nyquist		Nyquist		
Start (MHz)	512	Start (MHz)	0	
Stop (MHz)	2560	Stop (MHz)	1536	
Net range		Net range		
Start (GHz)	7	Start (GHz)	4,7	
Stop (GHz)	9,5	Stop (GHz)	6,5	
Band3		Band3		Band 4
Type	**down-down**		**down**	**down**
nband	**2**			
1st stage		1st stage		
filter start (GHz)	27	filter start (GHz)	5,75	10
filter stop (GHz)	33	filter stop (GHz)	8,25	12,5
LO start (GHz)	16,5	LO start (GHz)	1	9
LO stop (GHz)	22,5	LO stop (GHz)	6	12
lo res (KHz)	0,001	lo res (KHz)	0,001	0,001
2nd stage		2nd stage		
filter start (GHz)	10,25	filter start (GHz)		
filter stop (GHz)	12,25	filter stop (GHz)		
LO start (GHz)	9,75	LO start (GHz)		

LO stop (GHz)	na	LO stop (GHz)		
LO res	fixed	LO res		
Nyquist		Nyquist		
Start (MHz)	512	Start (MHz)	0	0
Stop (MHz)	2560	Stop (MHz)	1536	1536
Net range		Net range		
Start (GHz)	27	Start (GHz)	6	10
Stop (GHz)	33	Stop (GHz)	7,5	12,5

Sampler				
Date ready	now		now	
Type	**DBBC**		**DBBC**	
Input bandwidth (MHz)	**512**	Input bandwidth (MHz)	**512**	
Nyquist zone	**4**	Nyquist zone	**4**	
Sample clock (MHz)	1024	Sample clock (MHz)	1024	
bits/sample	8	bits/sample	8	
Total No. of IF's	**4**		**4**	
Digital Back End (DBE)				
Type	**DBBC**		**DBBC**	**ADS3000+**
No. DBE per site	**2**		**2**	**2**
No. IF's per DBE	**4**		**4**	**4**
DDC				
No. per DBE	**16**		**16**	**4**
Chan BW (MHz)	**1 to 16**		**1 to 16**	**1 to 16**
Sideband	**UL**		**UL**	**UL**
LO Res (KHz)	**10**		**10**	**10**
PFB				
No. per DBE	**4**		**4**	**4**
Chan BW (MHz)	**32**		**32**	**32**
Chan per DBE	**30**		**30**	**16**

Recorder			
Type	**Mk5B+**	**Mark5**	**Mark6**
No. per site	2	2	1
Network			
Data rate (Gbps)	1	1	

3 RAEGYEB

Site name	Yebes	Yebes	
Receiver type	tri-band	Broad-band	
SEFD (Jy)			
2	1700	3GHz?	?
9	1600	8GHz?	2600
32	5400	12GHz?	5000
Antenna			
Date ready	now	now	
Optics	ring focus	ring focus	
Az slew rate (°/s)	12	12	
El slew rate (°/s)	6	6	
Diameter (m)	13,2	13,2	
efficiency (%)			
2	70	3GHz?	
9	70	8GHz?	
32	38	12GHz?	

Front End		
Date ready	not available	now
Tsys (K)		
2	50	3GHz?
9	50	8GHz?
32	100	12GHz?
Band1		
Name	S-band	Broad-band
Start freq (GHz)	**2,2**	**2**
Stop freq (GHz)	**2,7**	**14**
npol	**2**	**2**
pol type	**circular**	**linear**
Band2		
Name	X-band	
Start freq (GHz)	**7**	
Stop freq (GHz)	**9,5**	
npol	**2**	
pol type	**circular**	
Band3		
Name	Ka-band	
Start freq (GHz)	**28**	
Stop freq (GHz)	**32**	
npol	**2**	
pol type	**circular**	

PCAL		
Date ready	now	now
injection	pre LNA	pre LNA
generator	Yebes	Yebes
freq spacing (MHz)	**1**	**5**

Noise Diode		
Date ready	now	now
installed	yes	yes
synchronous (Hz)	80 Hz	80 Hz

Cable Cal		
Date ready	now	now
Type	Mk3	
Down-converter		
Date ready	now	now
Band 1		
Type	**fixed down**	
nband	2	
1st stage		
filter start (GHz)	2,2	
filter stop (GHz)	2,7	
lo start (GHz)	1,7	
lo stop (GHz)	na	
lo res (KHz)	fixed	
Nyquist		
Start (MHz)	500	
Stop (MHz)	1000	
Net range		
Start (GHz)	2,2	
Stop (GHz)	2,7	
Type	**up-down**	**up-down**
nband	2	4
1st stage		
filter start (GHz)	7	2
filter stop (GHz)	9,5	14
LO start (GHz)	10	24,25
LO stop (GHz)	13	34,75
LO res	mHz	400KHz
2nd stage		
filter start (GHz)	19,35	19,75
filter stop (GHz)	20,25	22,25
LO start (GHz)	19,25	22,25
LO stop (GHz)	na	22,25
LO res	fixed	fixed
Nyquist		
Start (MHz)	100	DC
Stop (MHz)	1000	1000
Net range		
Start (GHz)	7	
Stop (GHz)	9,5	
Band3		
Type	down-down	
nband	2	
1st stage		
filter start (GHz)	28	
filter stop (GHz)	33	
LO start (GHz)	15	
LO stop (GHz)	20	
LO res	mHz	
2nd stage		
filter start (GHz)	12,75	
filter stop (GHz)	13,25	
LO start (GHz)	12,25	

LO stop (GHz)	na
LO res	fixed
Nyquist	
Start (MHz)	500
Stop (MHz)	1000
Net range	
Start (GHz)	28
Stop (GHz)	33

Sampler	
Date ready	now
Type	**ADB**
Input bandwidth (MHz)	**500/1000**
Nyquist zone	**2**
Sample clock (MHz)	1024
bits/sample	8
Total No. of IF's	**2**
Digital Back End (DBE)	
Type	**RDBE-G**
No. DBE per site	**4**
No. IF's per DBE	**2**
DDC	
No. per DBE	**4**
Chan BW (MHz)	**1,2,4,8,16,32,64,128**
Sideband	**UL**
LO Res (KHz)	**15625**
PFB	
No. per DBE	
Chan BW (MHz)	**32**
Chan per DBE	**32**

Recorder	
Type	**Mark6**
No. per site	2
Network	
Data rate (Gbps)	10

4 HOBART12

Site name	Hobart12
SEFD (Jy)	broadband
2	~3500?
5	~3000?
9	~3000?
14	~3500?
Antenna	
Date ready	Now.
Optics	Cassegrain.
Az slew rate (°/s)	300 d/min
El slew rate (°/s)	75 d/min
Diameter (m)	12
efficiency (%)	
2	50%?
5	60%?
9	60%?
14	50%?

Front End	
Date ready	Mid-2017
Tsys (K)	
2	90K?
5	80K?
9	80K?
14	90K?
Band1	
Name	broadband
Start freq (GHz)	**2,2**
Stop freq (GHz)	**14**
npol	**2**
pol type	**Linear**

PCAL	
Date ready	now
injection	Injected from probe in feed
generator	Callisto design.
freq spacing (MHz)	5

Noise Diode	
date ready	Now
installed	
synchronous (Hz)	

Cable Cal	
Date ready	N/A
Type	N/A
Down-converter	
Date ready	Now
Sub-band 1	
Type	**Fixed**
nband	2
1st stage	
filter start (GHz)	~3
filter stop (GHz)	7
lo start (GHz)	4,1
lo stop (GHz)	13,4
lo res (KHz)	100
Nyquist	
Start (MHz)	0
Stop (MHz)	4096
Net range	
Start (GHz)	3
Stop (GHz)	7
Sub-band 2	
Type	**Fixed**
nband	2
1st stage	
filter start (GHz)	6
filter stop (GHz)	10
lo start (GHz)	4,1
lo stop (GHz)	13,4
lo res (KHz)	100
Nyquist	
Start (MHz)	0
Stop (MHz)	4096
Net range	
Start (GHz)	6
Stop (GHz)	10
Sub-band 3	
Type	Fixed
nband	2
1st stage	
filter start (GHz)	9,5
filter stop (GHz)	13,5
lo start (GHz)	4,1
lo stop (GHz)	13,4
lo res (KHz)	100
Nyquist	
Start (MHz)	0
Stop (MHz)	4096
Net range	
Start (GHz)	9,5
Stop (GHz)	13,5

Sampler	
Date ready	now
Input bandwidth (MHz)	4096
Nyquist zone	1
Sample clock (MHz)	8192
bits/sample	10
Total No. of IF's	3x2
Digital Back End (DBE)	
Type	**DBBC3-6L6H**
No. DBE per site	**1**
No. IF's per DBE	**6**
DSC (phase 1)	
No. per DBE	**6**
Chan BW (MHz)	**4096**
Sideband	**U|L**
LO Res (KHz)	**na**
DDC-OCT (phase 2)	
No. per DBE	**>=6**
Chan BW	**2048, 1024**
Sideband	**U|L**
LO Res (KHz)	**1000**
DDC (phase 2)	
No. per DBE	**6*8**
Chan BW	**2-128**
Sideband	**U&L**
LO Res (KHz)	**10**
PFB (phase 3)	
No. per DBE	**6**
Chan BW (MHz)	**256**
Chan per DBE	**8*16 (15+1)**
DDC/PFB | FPB/DDC (phase 3)	
No. per DBE	**> 6*2**
Chan BW	**2-128**
Sideband	**U&L**
LO Res (KHz)	**variable**
Recorder	
Type	**Flexbuff**
No. per site	1
Network	
Data rate (Gbps)	10

5 ISHIOKA and KASHIM34

Site name	Ishioka	Ishioka	Kashima
Receiver type	tri-band	QRFH	QRFH
SEFD (Jy)			
2	1400	(no value)	(no value)
9	1500	2000	2000
32	(not yet)	(no value)	(no value)
Antenna			
Date ready	now	now	now
Optics	ring focus	ring focus	ring focus
Az slew rate (°/s)	12	12	12
El slew rate (°/s)	6	6	6
Diameter (m)	13,2	13,2	13,2
efficiency (%)			
2	70	(not yet)	(not yet)
9	70	(not yet)	(not yet)
32	(not yet)	(not yet)	(not yet)
Front End			
Date ready	now	now	now
Tsys (K)			
2	49	(not yet)	(not yet)
9	52	(not yet)	(not yet)
32	(not yet)	(not yet)	(not yet)
Band1			
Name	S-band	Broadband	Broadband
Start freq (GHz)	**2,2**	**3**	**3**
Stop freq (GHz)	**2,4**	**14**	**14**
npol	**1**	**2**	**2**
pol type	**circular**	**linear**	**linear**
Band2			
Name	X-band		
Start freq (GHz)	**8,18**		
Stop freq (GHz)	**8,98**		
npol	**1**		
pol type	**circular**		
Band3			
Name	Ka-band		
Start freq (GHz)			
Stop freq (GHz)			
npol			
pol type	**circular**		
PCAL			
Date ready	now	now	
injection	pre LNA	pre LNA	
generator	AES	AES	
freq spacing (MHz)	5	5	
Noise Diode			
Date ready	now	(not yet)	
installed	yes	(not yet)	
synchronous (Hz)	(No Func)		

Cable Cal			
Date ready	now	now	
Type	NICT	NICT	
Down-converter			
Date ready	now	now	now
Band 1			
Type	**fixed down**	**flexible up-down**	**direct sampling**
nband	1	4	
1st stage			
filter start (GHz)	2,2	27,928	
filter stop (GHz)	2,4	29,928	
lo start (GHz)	2,02	15,44	
lo stop (GHz)	na	26,416	
lo res (KHz)	fixed	100	
Nyquist			
Start (MHz)	0	0	
Stop (MHz)	500	1024	
Net range			
Start (GHz)	2,2	3	
Stop (GHz)	2,4	14	
Band 2			
Type	**fixed down**		
nband	1		
1st stage			
filter start (GHz)	8,18		
filter stop (GHz)	8,592		
LO start (GHz)	8,08		
LO stop (GHz)	na		
LO res	fixed		
Nyquist			
Start (MHz)	100		
Stop (MHz)	512		
Net range			
Start (GHz)	8,18		
Stop (GHz)	8,592		
Band3			
Type	**fixed down**		
nband	1		
1st stage			
filter start (GHz)	8,592		
filter stop (GHz)	8,98		
LO start (GHz)	8,08		
LO stop (GHz)	na		
LO res	fixed		
Nyquist			
Start (MHz)	512		
Stop (MHz)	1000		
Net range			
Start (GHz)	8,592		
Stop (GHz)	8,98		

Sampler			
Date ready	now	now	now
Type	ADS3000+	ADS3000+	K6
Input bandwidth (MH	512	512	16384
Nyquist zone	1or2	3or4	2
Sample clock (MHz)	2048	2048	16384
bits/sample	8	8	3
Total No. of IF's	4	4	2(nominal), 4(extended)
Digital Back End (DBE)			
Type	**ADS3000+**	**ADS3000+**	**GALAS(OCTAD-G)**
No. DBE per site	**1**	**4**	
No. IF's per DBE	**4**	**4**	
DDC			
No. per DBE	**16**	**16**	**4(nominal),8(extended)**
Chan BW (MHz)	**4 to 32**	**4 to 32**	**1024**
Sideband	**UorL**	**UorL**	
LO Res (KHz)	**0,001**	**0,001**	**1**
PFB			
No. per DBE	**(No func)**	**(No func)**	
Chan BW (MHz)	**(No func)**	**(No func)**	
Chan per DBE	**(No func)**	**(No func)**	

Recorder		
Type	**K5VSI**	**K5VSI**
No. per site	2	4
Network		
Data rate (Gbps)	10	10

6 ONSA13NE and ONSA13SW

Site name	ONSA13NE	ONSA13SW	notes
SEFD (Jy)	broadband	broadband	
2	?	?	not know yet
5	?	?	not know yet
9	?	?	not know yet
14	?	?	not know yet
Antenna			
Date ready	now	now	
Optics	ring-focus	ring-focus	
Az slew rate (°/s)	720 deg/min	720 deg/min	
El slew rate (°/s)	360 deg/min	360 deg/min	
Diameter (m)	13,20	13,20	
efficiency (%)			
2	?	?	not know yet
5	?	?	not know yet
9	?	?	not know yet
14	?	?	not know yet
Front End			
Date ready	summer 2017	summer 2017	
Tsys (K)			
2	?	?	not know yet
5	?	?	not know yet
9	?	?	not know yet
14	?	?	not know yet
Band1			
Name	broadband	broadband	
Start freq (GHz)	**3**	**2,2**	
Stop freq (GHz)	**15**	**14**	
npol	**2**	**2**	
pol type	**linear**	**linear**	

PCAL		
Date ready	now	now
injection	launch into feed	launch into feed
generator	CDMS Haystack	CDMS Haystack
freq spacing (MHz)	1	1
Noise Diode		
date ready	now	now
synchronous (Hz)	80	80

Cable Cal		
Date ready	now	now
Type	radio-optical	radio-optical
Down-converter		
Date ready	now	now
Sub-band 1		
Type	**quasi-fixed down**	**quasi-fixed down**
nband	2	2
1st stage		
filter start (GHz)		
filter stop (GHz)		
lo start (GHz)	4 100	4 100
lo stop (GHz)	13 400	13 400
lo res (KHz)	100	100
Nyquist		
Start (MHz)	0	0
Stop (MHz)	4096	4096
Net range		
Start (GHz)	0	0
Stop (GHz)	15.0	15.0
Sub-band 2		
Type	**quasi-fixed down U|L**	**quasi-fixed down U|L**
nband	2	2
1st stage		
filter start (GHz)		
filter stop (GHz)		
lo start (GHz)	4 100	4 100
lo stop (GHz)	13 400	13 400
lo res (KHz)	100	100
Nyquist		
Start (MHz)	0	0
Stop (MHz)	4096	4096
Net range		
Start (GHz)	0	0
Stop (GHz)	15.0	15.0
Sub-band 3		
Type	**quasi-fixed down U|L**	**quasi-fixed down U|L**
nband	2	2
1st stage		
filter start (GHz)		
filter stop (GHz)		
lo start (GHz)	4 100	4 100
lo stop (GHz)	13 400	13 400
lo res (KHz)	100	100
Nyquist		
Start (MHz)	0	0
Stop (MHz)	4096	4096
Net range		
Start (GHz)	0	0
Stop (GHz)	15.0	15.0
Sub-band 4		
Type	quasi-fixed down U|L	quasi-fixed down U|L
nband	2	2

1st stage		
filter start (GHz)		
filter stop (GHz)		
lo start (GHz)	4 100	4 100
lo stop (GHz)	13 400	13 400
lo res (KHz)	100	100
Nyquist		
Start (MHz)	0	0
Stop (MHz)	4096	4096
Net range		
Start (GHz)	0	0
Stop (GHz)	15.0	15.0
Sampler		
Date ready	now	now
Type	ADB3L	ADB3L
Input bandwidth (MHz)	4096	4096
Nyquist zone	1	1
Sample clock (MHz)	8192	8192
bits/sample	10	10
Total No. of IF's	4x2	4x2
Digital Back End (DBE)		
Type	**DBBC3-L**	**DBBC3-L**
No. DBE per site	**1**	**1**
No. IF's per DBE	**8**	**8**
DSC (phase 1)		
No. per DBE	**8**	**8**
Chan BW (MHz)	**4096**	**4096**
Sideband	**U|L**	**U|L**
LO Res (KHz)	**na**	**na**
DDC-OCT (phase 2)		
No. per DBE	**>=8**	**>=8**
Chan BW	**2048, 1024**	**2048, 1024**
Sideband	**U|L**	**U|L**
LO Res (KHz)	**1000**	**1000**
DDC (phase 2)		
No. per DBE	**8*8**	**8*8**
Chan BW	**2-128**	**2-128**
Sideband	**U&L**	**U&L**
LO Res (KHz)	**10**	**10**
PFB (phase 3)		
No. per DBE	**8**	**8**
Chan BW (MHz)	**256**	**256**
Chan per DBE	**8*16 (15+1)**	**8*16 (15+1)**
DDC/PFB | FPB/DDC (phase 3)		
No. per DBE	**> 8*2**	**> 8*2**
Chan BW	**2-128**	**2-128**
Sideband	**U&L**	**U&L**
LO Res (KHz)	**variable**	**variable**
Recorder		
Type	**FILA40G/Flexbuff**	**FILA40G/Flexbuff**
No. per site	1	1
Network		
Data rate (Gbps)	10	10

7 BADAR13M and ZELEN13M

Site name	Badary	Zelenchukskaya
Receiver type	Tri-band	Tri-band
SEFD (Jy)		
2,4	1000*	1100*
7,5	650*	750*
28,5	2000*	1900*
Antenna		
Date ready	now	now
Optics	ring focus	ring focus
Az slew rate (°/s)	12	12
El slew rate (°/s)	6	6
Diameter (m)	13,2	13,2
efficiency (%)		
2,4	70*	70*
7,5	80*	80*
28,5	75*	75*
Front End		
Date ready	now	now
Tsys (K)		
2,4	35*	40*
7,5	25*	30*
28,5	75*	70*
Band1		
Name	S-band	S-band
Start freq (GHz)	**2,2**	**2,2**
Stop freq (GHz)	**2,6**	**2,6**
npol	**2**	**2**
pol type	**circular**	**circular**
Band2		
Name	X-band	X-band
Start freq (GHz)	**7**	**7**
Stop freq (GHz)	**9,5**	**9,5**
npol	**2**	**2**
pol type	**circular**	**circular**
Band3		
Name	Ka-band	Ka-band
Start freq (GHz)	**28**	**28**
Stop freq (GHz)	**34**	**34**
npol	**2**	**2**
pol type	**circular**	**circular**
PCAL		
Date ready	now	now
injection	pre LNA	pre LNA
generator	IAA design	IAA design
freq spacing (MHz)	1; 2	1; 2
Noise Diode		
Date ready	now	now
installed	yes	yes
synchronous (Hz)	on/off	on/off
Cable Cal		
Date ready	now	now
Type	IAA design	IAA design

Down-converter				
Date ready	now	now		
Band 1				
Type	down	down		
nband	2	2		
1st stage				
filter start (GHz)	2,2	2,2		
filter stop (GHz)	2,6	2,6		
lo start (GHz)	3,6	3,6		
lo stop (GHz)	3,7	3,7		
lo res (KHz)	100	100		
Nyquist				
Start (MHz)	1024	1024		
Stop (MHz)	1536	1536		
Net range				
Start (GHz)	2,2	2,2		
Stop (GHz)	2,6	2,6		
Band 2	1. Converter	1. Converter	2. Converter	3.Converter
Type	up-down	up-down	up-down	up-down
nband	2	2	2	2
1st stage				
filter start (GHz)	7	7	7	7
filter stop (GHz)	9,5	9,5	9,5	9,5
LO start (GHz)	24	23,5	23,5	23,5
LO stop (GHz)	25,5	25,5	25,5	25,5
lo res (KHz)	400	400	400	400
2nd stage				
filter start (GHz)	16	16	16	16
filter stop (GHz)	17	17	17	17
LO start (GHz)	15	15	15	15
LO stop (GHz)	na	na	na	na
LO res	fixed	fixed	fixed	fixed
Nyquist				
Start (MHz)	1024	1024	1024	1024
Stop (MHz)	2048	2048	2048	2048
Net range				
Start (GHz)	7	7	7	7
Stop (GHz)	9,5	9,5	9,5	9,5
Band 3	1. Converter	1. Converter	2. Converter	3.Converter
Type	down-down	down-down	down-down	down-down
nband	2	2	2	2
1st stage				
filter start (GHz)	28	28	28	28
filter stop (GHz)	34	34	34	34
LO start (GHz)	17,5	21,5	21,5	21,5
LO stop (GHz)	22,5	27	27	27
lo res (KHz)	400	400	400	400
2nd stage				
filter start (GHz)	10,5	6,5	6,5	6,5
filter stop (GHz)	11,5	7,5	7,5	7,5
LO start (GHz)	12,5	5,5	5,5	5,5
LO stop (GHz)	na	na	na	na
LO res	fixed	fixed	fixed	fixed
Nyquist				
Start (MHz)	1024	1024	1024	1024
Stop (MHz)	2048	2048	2048	2048

Net range				
Start (GHz)	28	28	28	28
Stop (GHz)	34	34	34	34

Sampler		
Date ready	now	now
Input bandwidth (MHz)	512	512
Nyquist zone	3	3
Sample clock (MHz)	1024	1024
bits/sample	8	8
Total No. of IF's	8	8
Digital Back End (DBE)		
Type	**BRAS**	**BRAS**
No. DBE per site	**1**	**1**
No. IF's per DBE	**8**	**8**
DDC	**na**	**na**
PFB	**na**	**na**
No. per DBE		
Chan BW (MHz)		
Chan per DBE		

Recorder		
Type	**DRS / Mk5C**(under repair)	**DRS / Mk5C**
No. per site	1 / 1	1 / 1
Network		
Data rate (Gbps)	2	2

Inauguration of the Onsala twin telescopes on 18 May 2017

The Onsala twin telescopes. (Photo: Roger Hammargren)

The inauguration is described as follows. First we give a brief summary of the event. Thereafter follow transcriptions of the speeches. Most of them were delivered in Swedish but assuming that the typical reader of these proceedings prefer the English language, we have made a best effort translating these speeches. Photos from the day of the inauguration follow and finally we include a number of photos documenting the construction work, from the clearing of the ground until the telescopes are completed.

The inauguration of the Onsala twin telescopes

On Thursday, 18 May 2017, the Onsala twin telescopes were inaugurated with a ceremonial event. More than 200 international and national guests, including the EVGA participants, veterans of the first transatlantic VLBI observations in 1968, as well as regional governors and representatives of Chalmers, participated in the festivity.

The inauguration day at Onsala was sunny and warm, with temperatures up to 21 °C but rather windy, as can be expected for a site located right at the coast line. The festivity guests gathered in a tent that had been erected next to the southern twin telescope. Here they followed an interesting program.

The Onsala twin telescopes on 18 May 2017.
(Photo: Onsala Space Observatory)

First, Prof. John Conway, the director of the Onsala Space Observatory, gave a welcome address. Then Prof. Stefan Bengtsson, President of Chalmers University of Technology, gave a speech, followed by a speech by Dr. Axel Nothnagel, chairman of the International VLBI Service for Geodesy and Astrometry (IVS).

After that, the twin sisters Malin and Josefin Flyckt, members of the Swedish Astronomical Youth Association, gave a speech. They addressed in particular the importance of inspiring cutting-edge technology and research for young people and the coming generations, and also highlighted the value of being twins.

This was followed by showing NASA's cartoon film on the principles of geodetic VLBI, which was accompanied by simultaneous life narration in Swedish, performed by Assoc. Prof. Maria Sundin from Gothenburg University.

Finally, the actual inauguration started. Prof. Lena Sommestad, county governor of Hallands län, and Lisbeth Schultze, acting county governor of Västra Götalands län gave speeches and expressed how important the Onsala Space Observatory and Chalmers University of Technology are for the two counties. Then the whole festivity party left the tent and gathered around the table with the two start buttons. The governors pressed the two starter buttons, and the telescopes started to move. Accompanied by saxophone music performed by Mikael Högdahl the telescopes started a coordinated dance. This gave the spectators a glimpse of how future VGOS operations at Onsala may look like. The Onsala twin telescopes were inaugurated!

After the telescope dance, the festivity continued with a lunch inside and outside of the tent. After lunch, several guided tours allowed the guests to visit the many scientific instrument installations at the observatory. These include the twin telescopes, the 25 m and 20 m telescopes, and the Onsala tide gauge station using conventional pneumatic, radar, and laser sensors, as well as the GNSS-R tide gauge and GNSS reference installations.

Welcome address by Prof. John Conway, Director of the Onsala Space Observatory

Prof. John Conway
(Photo: Onsala Space Observatory)

It is my great pleasure to welcome you all to this inauguration of the Onsala twin telescopes!

I want to especially welcome Hallands and Västra Götalands governors Lena Sommestad and Lisbeth Schultze and I would also like to welcome our other distinguished guests, colleagues and friends who are here to share with us this happy occasion.

Since we have both many international and Swedish guests here today the programme of this inauguration will be bi-lingual. One language will of course be Swedish, for the other language, although I have heard rumours that in the near future English may no longer be a major language in Europe... I will anyway mostly speak English – with a few words in Swedish at the end.

The new Onsala twin telescopes which we inaugurate today forms part of a world-wide network of radio telescopes that is designed to use observations of the most distant objects in the universe to measure relative positions on the Earth down to millimetre accuracy.

The technique of combining together worldwide networks of dishes to create one giant synthetic telescope is known as Very Long Baseline Interferometry or VLBI. This year marks the 50th anniversary of the first successful VLBI observations made using two telescopes in Canada in 1967; one year later in 1968 the older brother of the Onsala twin telescopes the Onsalas 25 m telescope formed the European end of the very first transatlantic VLBI experiment. Onsala has therefore been involved from the very earliest days of VLBI and remains highly active today in VLBI as applied to both geoscience and to astronomy. With the construction of the twin telescopes Onsala takes its next step into the future of geo-VLBI with two specially designed rapidly moving telescopes which will observe thousands of distant quasars per day which will improve the accuracy for measuring by a factor of ten.

It is an amazing fact, that shows the connectedness and beauty of science, that in order to fully understand our Earth we must use observations of the most distant objects in the universe. It would I expect come as a surprise to many people, and against common sense, that looking outward into space is necessary to understand the Earth below our feet, but so it is. The twin telescopes will be involved in nothing less than in connecting the Earth with the stars.

As well as connecting astronomy with the Earth the twin telescopes also connect basic and applied science. The information obtained as part of the global network, measures changes in the orientation and rotation rate of the Earth which in turn tells us about processes occurring deep within our planet and also the effects of human induced global change. In addition, the twin telescopes, will give vital contributions to accurate navigation on Earth, which you exploit whenever you use GPS in your car or use google maps on your smartphone. Future applications of self-driving cars, drones and applications for other industries we have yet to invent, will make use of the data from the Onsala twin telescopes.

I would like to thank the Knut and Alice Wallenberg foundation and Chalmers for the generous funding provided for the construction of the Onsala twin telescopes and would also like to thank the prime contractor for the telescope structure MT Mechatronics. I would also like to thank the Swedish Research council, Vetenskapsrådet, for their long-term support of geo-VLBI operations at Onsala.

I would like to end by thanking everyone at Onsala Space Observatory, which have contributed to the construction of the twin telescopes and their equipment. This is the largest construction project made here since 1976 when the 20-meter telescope was built. The twin telescopes is a project that started before my time as a director. The construction was begun and led by Gunnar Elgered, Rüdiger Haas, and my predecessor Hans Olofsson. Onsala's infrastructure staff have had a great deal of commitment in the building process, without you this project would never have been possible. I never stop being surprised by what we can do at the Onsala Space Observatory. I would like to thank you all for your hard work.

We did it together!

Speech by Prof. Stefan Bengtsson, President of Chalmers University of Technology

Prof. Stefan Bengtsson
(Photo: Onsala Space Observatory)

It's incredibly fun to be here today when we take the next step in developing Onsala. This is one of Chalmers' three locations where work is carried out. We have been here since the 40's with activities connected to space and Earth and there has been many and incredibly important results from this research facility over the years, and it has gradually evolved.

It has meant incredibly much scientifically and is for Chalmers an amazing research infrastructure, but it has also had a role in regional development that you may never think about. The development of the receivers required here gave in turn the research base that attracts high technology industry in high-frequency and high-speed electronics to Gothenburg, which in turn reinforced educational efforts and research, which in turn increased the opportunities for Onsala to act scientifically. Here you can see a good example of how regional growth can take place between different types of actors, despite the fact that the issues that are scientifically studied and the purpose of the facility, is indeed very basic science.

Today we take the next step with the twin telescopes. Here it is our own planet, as we heard John describe, which is the goal of the studies, and what I understand when I've read a bit about this, it now opens up completely new possibilities to make accurate measurements of the dynamics of our planet.

We usually say that Chalmers is a university of technology and natural science, and for us, the basic science that is done in Onsala, and in other parts of our activities, is incredibly important. It is hard to imagine a successful university of technology, which does not ensure to have curiosity driven research, found in basic science and mathematics.

With regard to Onsala and the development here, Chalmers has together with the Swedish Research Council, and many others, taken long-term responsibility, with contributions, with long-term funding, and we are prepared to continue to do so because we see the great value and the amazing opportunities that are connected to the facility here. Not the least, such a facility is important for increasing interest and understanding for natural science and technology in the country of young people. We know that we need to interest young people to study natural sciences, and to choose the path within the research, perhaps. What we are doing here today in a lot of ways is a commitment to the future partly from the aspect I just mentioned, and of course for many years to continue to pursue, and we will have new opportunities for conducting world-class research.

So I want to end by saying that I'm incredibly pleased that we now have these telescopes in place. It will be amazingly exciting and see what results they will be able to contribute with.

I wish to congratulate Onsala, the department, and the international science community to the access to new amazing instruments and wish you all the best to take full advantage of these instruments. Chalmers as a whole is prepared to support this also in the future. My final word to you here at Onsala is:

You are amazing and we are so happy to have you in our university!

Thank you!

Speech by Dr. Axel Nothnagel, Chair of the International VLBI Service for Geodesy and Astrometry (IVS)


Dr. Axel Nothnagel
(Photo: Onsala Space Observatory)

Dear Stefan Bengtson
(President of Chalmers University of Technology),

Dear John Conway
(Director of Onsala Space Observatory),

Dear staff members of this magnificent observatory,

Dear guests of the inauguration ceremony!

It is a great pleasure for me to extend the greetings and best wishes of the IVS; the International VLBI Service for Geodesy and Astrometry, for the inauguration of the new twin telescopes of the Onsala Space Observatory.

In fact, only a few of you will be aware that we are virtually standing at the cradle of European transatlantic geodetic VLBI. Olof Rydbeck and Bernt Rönnäng carried out the first geodetic VLBI observations between Onsala and Haystack Observatory near Boston with a Mark I system in 1977 and 1978 reaching a precision of several centimeters. Another milestone was set by the first Mark III observations between Onsala and North America with the Mark III system on January 21, 1981, where the precision of the baseline length result was improved to the order of 1–2 cm. Within a few years a series of observing sessions across the Atlantic, a major scientific breakthrough was documented: The proof of the existence of plate motion, or as is more common language, of continental drift. In a scientific paper in early 1986, Tom Herring and co-authors showed that North America and Europe were separating by 17 mm per year. Other authors were Chopo Ma, who is here today as well, and in particular the Onsala colleagues Bernt Rönnäng. Göran Lundqvist and Gunnar Elgered. Since then the Onsala Space Observatory with its 20 m radio telescope has carried out successfully hundreds of geodetic VLBI observing sessions producing a wealth of data and results. Onsala Space Observatory is an indispensable corner stone of IVS operations today.

The pleasure about this is the greater in that today we mark further progress in technology and scientific possibilities with the inauguration of the Onsala twin telescopes. These telescopes will be within the first in the world which will help to achieve the 1 mm accuracy goal in global reference frames which we need to reach for a reliable monitoring of global change. Being close to the sea here, sea level rise is certainly one of the most prominent effects. Without long-term stable reference frames of ground stations, like this one, and the link to the orbits of the altimeter satellites, sea level variations cannot be monitored reliably and I do not need to address the consequences. The twin telescopes will allow experimental setups and observing configurations which will be really unique. Over and beyond geodetic challenges, the telescopes will also help to push atmospheric sciences forward because the behavior of the signals observed with the telescopes provides direct information of the atmosphere above. In the name of the IVS and its members, I like to express our gratitude to the Wallenberg Foundation and Chalmers University of Technology for their efforts and investments into these telescopes. Finally, I would like to congratulate all of you on having such nice new instruments and I wish all of us that the telescopes will carry out very many successful observations.

Thank you for your attention.

Speech by Malin and Josefin Flyckt, members of the Swedish Astronomical Youth Association

The twin sisters Malin and Josefin Flyckt, members of the Swedish Astronomical Youth Association. (Photo: Hans-Georg Scherneck)

Hi!

My name is Malin — and my name is Josefin, we are 17 years old and are currently in the first year at the high school Bäckängskolan in Borås.

Malin: I am studying natural sciences

Josefin: and I study social sciences

As we said, we both study at Bäckängskolan, which when we searched for high school were the obvious choice for us, as it has a wide range of programmes, with good teachers and a good study environment, where everyone may be just who they want to be and have the opportunity to become just who and what they want. We are both very curious and would like to explore the world around us.

Malin: For me, space is a place for endless possibilities (literally endless) a brand new world (literally) opened to us humans. I have been fascinated by space since i was little, but the real interest only came when I went in the eighth grade. It was then I figured out what I wanted to do with my life. I wanted to be an astronaut. To get out into space and to see everything is a tempting thought to me.

Josefin: I have always thought space is something very fascinating. Imagine you have one soccer field and you put out a pea somewhere on the field. The pea represents the Earth and the soccer field represents our expanding universe, all unexplored. All opportunities and places we have not yet discovered, places and opportunities that we do not even know we can discover yet. Stars, nebulosor, atomic to atomic, everything is so simple yet so complicated. And we're just a tiny piece of this gigantic phenomenon. Who will not be marveled by that thought? Being involved in this was a must for me.

Malin: But, if the telescope was never invented, if we never had the desire and curiosity to explore space, what is outside, I could never have had this dream. My dream of being an astronaut would never have been possible unless it was for the telescope. Looking out into the interstellar formations had not been possible.

Josefin: I totally agree with Malin, if it were not for that idea and to look into space, we would not have been here today, right? It was because of this, our common interest in space, to which we joined the Astronomical Youth, an organisation where young people's interest in space is taken advantage of and can be developed together with other young people with the same interest. They also organise events to go on where you can learn more about space and to join astronomy camps where you have the opportunity to meet like-minded people. For us, Astronomical Youth means that we can develop our interest and satisfy our present curiosity.

Malin: Even though I and Josefin are basically the same, we have chosen to take different ways. However, we still work as one, just like the telescope.

Josefin: Today, the twin telescopes will be inaugurated, so what are the benefits of being a twin? When we were small we used to send pieces between a narrow hole in the wall that went between our rooms. For example, if we had been sent to our rooms because we were too messy or interrupted each other, we could send small pieces through this hole in the wall messages we have written to still be able to communicate with each other.

Malin: Like twins, we share DNA and very many of our properties, which means we can work effectively with each other and take advantage of our similarities, but we look at things with different eyes. This is a similarity to the twin telescopes. So, we as twins understand really the advantage of building telescopes in pairs, though still with a certain distance between them. Even though we are in different places, we can still work together – as one. So we believe and know that these telescopes will work well and make a big difference to Sweden's and the world's research and science.

Josefin: We as young people think it is very important to focus on research, especially in an area like this that inspires so much.

Malin and Josefin: Concluding, we together wish all researchers and engineers that will work with the telescopes a lot of success!

Assoc. Prof. Maria Sundin's simultaneous life narration accompanying NASA's short cartoon film on VLBI

Assoc. Prof. Maria Sundin gives a simultaneous life narration in Swedish accompanying NASA's short cartoon film on VLBI. (Photo: Hans-Georg Scherneck)

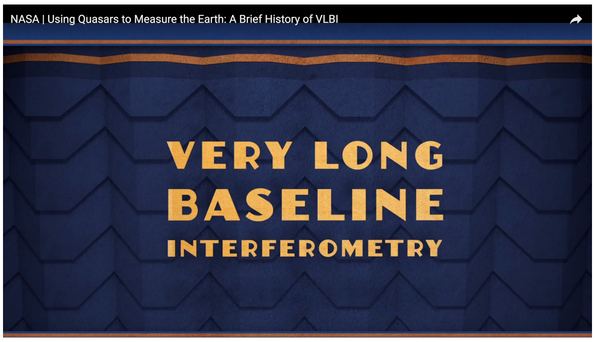

See e.g.
`https://www.youtube.com/watch?v=IVB8kArRZ6I`
for an English version
and `https://youtu.be/G04cDzU8sXE`
for a narration in Swedish.

An example collection of screen shots from NASA's cartoon film on VLBI.

Speech by Prof. Lena Sommestad, county governor of Hallands län

Prof. Lena Sommestad.
(Photo: Hans-Georg Scherneck)

Professor Bengtsson, President of Chalmers,
Professor Conway, Professor Nothnagel,
ladies and gentlemen.

It is a great honor for me, as Governor of the province of Halland, to conduct this opening ceremony, together with my colleague in Västra Götaland, Lisbeth Schultze. We will both talk in Swedish; my apologies; but before turning to the Swedish language, I would like to wish all foreign guests welcome to Halland.
We are pleased to have you here, in these beautiful surroundings.

My friends. The time has come to inaugurate Onsala's new twin telescopes. We have already had a first insight into the staggering possibilities that the new telescopes mean – opportunities for scientific adventures and progress, opportunities for international cooperation, and opportunities for building knowledge of significance to our planet and our common future. I would like to congratulate Chalmers and Onsala Space Observatory to these twin telescopes and the opportunities that are now being opened.

I appreciate that you here at the opening ceremony are spinning on the line of twinning opportunities! As a governor in Halland, I feel a joy for today's opening, for several reasons. When we gather here today, with the new telescopes in front of us, we are reminded – first and foremost – of the fact that few "insatser" are so crucial for scientific development and excellence, as a top-class research infrastructure. And historically, the telescope stands as the symbol of the development, where ever-increasingly refined tools and instruments have helped us to measure, understand and shape the world around us with increasing accuracy.

Throughout centuries, the telescope has been the mind of knowledge, enlightenment, progress. One of the major challenges facing the Swedish science community right now, as you know, is precisely the research infrastructure; how we can afford to invest in the new, increasingly advanced facilities that modern science requires. Not least in this perspective, it is gratifying that today at the Onsala Space Observatory we can inaugurate two new telescopes that further strengthen Swedish researchers' ability to contribute to increased knowledge about the Earth and its movements.

And never before has such knowledge been as anxious as now. We need better knowledge of the Earth and the Earth system to handle the challenges ahead of us – from population growth to climate threats. Sustainable development requires knowledge. When we stand here today, I also feel joyful for the exciting international collaboration that the twin telescopes makes possible, and which carries on your research area, geodesy. You need each other and each other's telescopes. The two telescopes that we see in front of us are part of a global network. Only if you work together can you achieve your goals. And this essentially scientifically-based collaboration, at the same time holds a message that goes beyond science and measurement technology. Like other researchers who explore the earth system, you help to understand our shared responsibility for the planet, and to realise our dependence on each other. The world's population is growing. Poverty countries develop toward industrialisation and increased prosperity. Progress is great, but the threats to ecosystems and climate are also growing, day by day. Research has a key role to build networks, and to create consensus on the conditions human beings have to deal with.

Finally, as a governor in Halland County, on the border with the city of Gothenburg, I feel delighted that within the county limits, in the beautiful Kungsbacka municipality, we have a scientific environment of such a high international class. You contribute to a dynamic knowledge and growth region here in western Sweden, but you also have an important role to play as a scientific actor in the county and the municipality.

Something that I particularly appreciate is that you actively contribute to spreading scientific knowledge in easily accessible form, especially among the young people. Here to the observatory, school classes come to learn about astronomy and geoscience. Here you arrange the "day and Night of Astronomy". You recently contributed to the Gothenburg Science Festival. And best of all – on Mother's Day you always invite the public, a day for families to enjoy this breathtaking beautiful place, while learning more about both the Earth and the universe. I – as a twin myself – note that this year you have special prize for twins – a pair of twins can come here for the price of one, the twin telescopes to honor. What a nice initiative! I'll see if I can attract my very best twin sister here. I would like to thank you for the efforts you make. You share your special knowledge, but you are also – in a broader sense – ambassadors of science, in the important tradition of enlightenment and democracy that has shaped our societies. It is important in a time when research progress and respect for scientific knowledge are needed more than ever before.

The twin telescopes stand as a symbol of science's progress, but they also stand as a symbol of a common future, based on knowledge and global cooperation.

And with these words I would like to hand over to my colleague, Lisbeth Schulze, Västra Götaland County.

Speech by Lisbeth Schultze, acting county governor of Västra Götalands län


Lisbeth Schultze.
(Photo: Onsala Space Observatory)

In the autumn of 1970, 47 years ago, two persons were here on Onsalahalvön and picked mushrooms.

One was Victor Hasselblad. The other was Edwin "Buzz" Aldrin, who had previously photographed the moon with Victor Hasselblad's camera, which was developed and manufactured in Gothenburg.

Here we stand today at the inauguration of the twin telescopes. The similarities are quite striking.

We observe and document other celestial bodies and remote galaxies to increase our knowledge of our own planet. Why did they choose Hasselblad's camera at the moon landing? Because they wanted the camera with the best optics! The twin telescopes are part of a world-leading research network with other telescopes, because research at Chalmers is at the forefront!

The telescopes are a striking manifestation of the prominent scientific research going on in Western Sweden. It makes me happy and proud also because I know how important scientific research is to further develop strong and prosperous societies.

How can Western-Swedish industry, such as automotive and textile industries, be so strong when labor costs are much lower in many other parts of the world? Well, it is because scientific research and technological achievements, with Chalmers as a key player, develop and modernise our industrial operations so that they are strong in meeting the future. And because there is well established cooperation between academia, industry and society.

Warm congratulations on the twin telescope activities. I will follow it with great interest!

Selected photos from the inauguration

The inauguration guests listen concentrated to the speeches.
(Top photo: Sofie Haldén. Bottom photo: Onsala Space Observatory)

The two county governors Lena Sommestad (centre, left) and Lisbeth Schultze (center, right) press the start buttons and the Onsala twin telescopes start to dance, accompanied by saxophone music performed by Mikael Högdahl. John Conway (right), Robert Cumming (left) and Claas-Tido Dörnath, the site manager from MT Mechatronics during the installation phase (far right background), are massively impressed by the show! (Photo: Onsala Space Observatory)

The Onsala twin telescopes perform their inauguration dance.
(Photo: Onsala Space Observatory)

The celebration guests watch the OTT inauguration dance.
(Photo: Hans-Georg Scherneck)

Flowers for the county governors, presented by the twin sisters Klara and Ellen Helldner Larsson. (Photo: Onsala Space Observatory)

Finally, a happy director! (Photo: Onsala Space Observatory)

Double twins: The twin sisters Malin and Josefin Flyckt with the twin telescopes. (Photo: Onsala Space Observatory)

Dirk Behrend (left) and Oleg Titov (right), possible candidates to become the honoured twin patron saints of the twin telescopes? (Photo: Hans-Georg Scherneck)

Bernt Rönnäng (left) and his wife Eva, with Francisco Colomer (right). Bernt was one of the pioneers starting up the VLBI activities at the observatory already in the 1960ies. (Photo: Hans-Georg Scherneck)

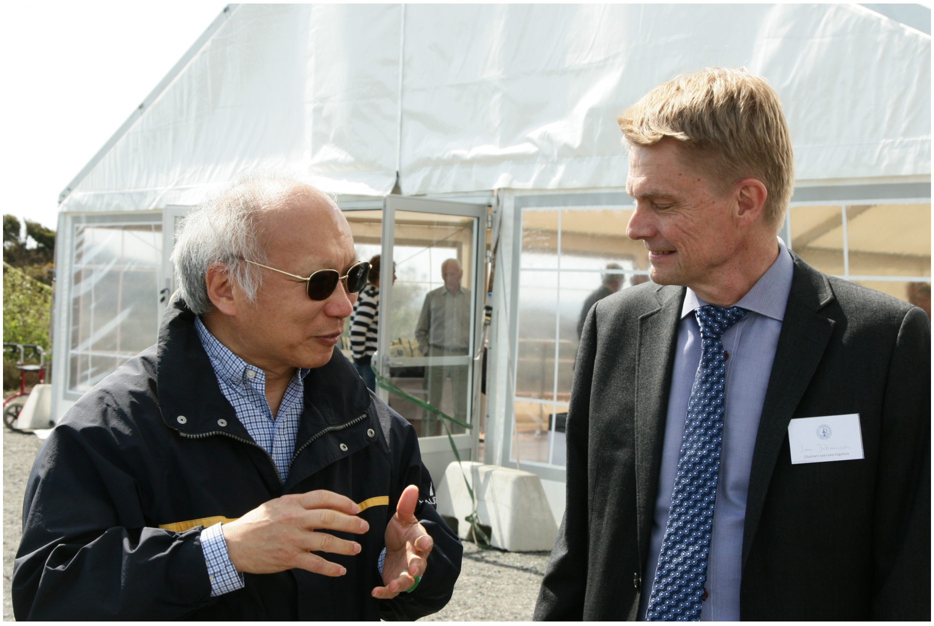

Chopo Ma (left) and Jan Johansson (right). (Photo: Hans-Georg Scherneck)

Selected photos from the construction phase

The infrastructure work has started. (Photo: Lars Wennerbäck)

The foundations are being constructed. (Photo: Lars Wennerbäck)

Work on the concrete tower for the southern telescope. (Photo: Rüdiger Haas)

The concrete towers are ready. (Photo: Rüdiger Haas)

Most of the telescope parts have arrived. (Photo: Roger Hammargren)

The reflectors have been assembled. (Photo: Roger Hammargren)

Lift of the azimuth cabin of the southern telescope. (Photo: Gunnar Elgered)

The reflector is lifted on the northern telescope. (Photo: Leif Helldner)


(Photo: Rüdiger Haas)


(Photo: Rüdiger Haas)

ISBN 978-91-88041-09-8